

UNIVERSITÀ
DEGLI STUDI
DI PADOVA

Sede Amministrativa: Università degli Studi di Padova

Dipartimento di Ingegneria Industriale

CORSO DI DOTTORATO DI RICERCA IN: INGEGNERIA INDUSTRIALE

CURRICOLO: INGEGNERIA ENERGETICA

CICLO XXIX

Synchronous Reluctance Machines: Eccentricity Analysis and Design Criteria

Direttore della Scuola:

CH.MO PROF. PAOLO COLOMBO

Coordinatore d'Indirizzo:

CH.MO PROF. LUISA ROSSETTO

Supervisore:

CH.MO PROF. NICOLA BIANCHI

Dottorando: ING. HANAFY MAHMOUD

31 January 2017

Acknowledgments

Firstly, I would like to express my sincere gratitude to Prof. Nicola Bianchi, for always being an enthusiastic supervisor throughout my doctoral period. I am truly grateful to him for trusting in my ability to complete this work and for his valuable suggestions and ideas during this work. I am also indebted to Prof. Silverio Bolognani for his invaluable encouragement.

A special thank to Giacomo, Prof. Luigi Alberti and "our" technician Mosè for their irreplaceable help and support during my Ph.D. activity.

I express my gratitude to ERASMUS MUNDUS FATIMA AL-FIHRI for giving me this opportunity to spend my doctoral period at the Electric Drive Laboratory of Padova. These years have been a wonderful and memorable period. I am very grateful to all members of EDLab.

Lastly, but definitely not the least, I like to express all of my sincere and appreciated thanks to my parents and my sisters for encouraging me during my doctoral period. Besides, I like to express my greatest love to my wife Samia, my son Mahmoud, and my daughter Rahaf for their invaluable encouragement and support during my study.

Padova, 15 November 2016

Hanafy Mahmoud

This Thesis is written in \LaTeX .
An electronic version is available at: <http://paduaresearch.cab.unipd.it>

Contents

Sommario	1
Preface	5
1 Synchronous reluctance motor	11
1.1 Operating principle	11
1.2 Development history	12
1.3 Model and basic characteristics	16
1.3.1 Relation between the load angle and the current angle	19
1.3.2 The electromagnetic torque derivation	19
1.3.3 Power factor computation	22
1.4 Real behavior of the motor	24
1.4.1 Saturation effect	25
1.4.2 Cross saturation effect	26
1.4.3 Slotting effect	27
1.5 Operating regions	28
I Linear Analytical Computation	31
2 Analytical model of concentric REL motor	33
2.1 Stator electric loading	33
2.2 Stator magnetic potential	36
2.3 The air-gap flux density	37
2.4 Rotor magnetic potential	37
2.4.1 One flux barrier per pole	37
2.4.2 Two flux barriers per pole	39

2.4.3	Three flux barriers per pole	41
2.5	Electromagnetic torque computation	44
2.5.1	One flux barrier per pole	44
2.5.2	Two flux barriers per pole	45
2.5.3	Three flux barriers per pole	46
2.6	Rotor iron losses due to eddy currents	47
3	Analytical model of eccentric REL motor	51
3.1	Introduction	51
3.2	Stator electric loading and magnetic potential	53
3.3	Air-gap flux density distribution	54
3.4	Rotor magnetic potential	56
3.4.1	One flux barrier per pole	56
3.4.2	Two flux barriers per pole	59
3.4.3	Three flux barriers per pole	64
3.5	Electromagnetic torque	69
3.5.1	One flux barrier per pole	69
3.5.2	Two flux barriers per pole	71
3.5.3	Three flux barriers per pole	73
3.6	Radial magnetic pressure and force	75
3.7	Rotor iron losses	75
4	Performance analysis of concentric and eccentric REL machine	77
4.1	Geometrical data of the stator and rotor	77
4.2	FE model	78
4.3	FE validation of the concentric REL motor analytical model	80
4.3.1	Air-gap flux density	80
4.3.2	Electromagnetic torque	82
4.3.3	Magnetic radial force	83
4.3.4	Rotor iron losses	84
4.4	FE validation of the eccentric REL motor analytical model	86
4.4.1	Static eccentricity case	87
4.4.2	Dynamic eccentricity case	99
4.4.3	The effect of eccentricity distance and electrical loading on the radial force	110

5	Different rotor geometries and stator windings	111
5.1	Introduction	111
5.2	Rotor structure with symmetric and asymmetric flux-barriers	112
5.2.1	Comparison in case of static rotor eccentricity	114
5.2.2	Comparison in case of dynamic rotor eccentricity	115
5.3	Fractional-Slot Stator windings	118
5.3.1	Winding comparison in case of no eccentricity	118
5.3.2	Winding comparison in case of static rotor eccentricity	121
5.3.3	Windings comparison in case of dynamic rotor eccentricity	124
5.3.4	Iron saturation impact including the complete stator FE model	126
5.4	Conclusions	127
6	Comparison between eccentric REL and PMAREL motors	131
6.1	Introduction	131
6.2	Comparison in healthy case (no eccentricity)	133
6.3	Comparison in static eccentricity case	136
6.4	Comparison in dynamic eccentricity case	138
6.5	Comparison in combined eccentricity case	140
6.6	Conclusions	144
7	Analytical comparison of REL and SPM machines with eccentricity	147
7.1	Introduction	147
7.2	Analytical model of concentric SPM motor	149
7.2.1	Relation between the field intensity and flux density for different regions	150
7.2.2	Analytical solution of magnetic field in region <i>I</i> and <i>II</i>	150
7.3	Analytical model of eccentric SPM motor	155
7.4	Results of the analytical model of concentric SPM motor	159
7.5	Analytical comparison between SPM and REL motors	160
7.5.1	Case of uniform displacement of the rotor axis	161
7.5.2	Case of displacement of rotor axis at one end	163
7.5.3	Case of similar and opposite displacement of rotor axis	164
7.6	Accuracy comparison of the two models	165
7.7	A rapid prediction of the air-gap flux density	166
7.8	FE comparison of complete stator SPM, REL, and PMAREL motors	167
7.8.1	Comparison in healthy case (no eccentricity)	167
7.8.2	Comparison in static eccentricity case	167

7.8.3	Comparison in dynamic eccentricity case	169
7.8.4	Comparison in combined eccentricity case	170
7.9	Conclusions	171
II Non-Linear Analytical Computation		173
8	Analytical model of REL motor considering iron saturation and slotting effect	175
8.1	The effect of stator slotting	175
8.2	Saturation effect modeling	178
8.2.1	Basic idea of the saturation factor computation	178
8.2.2	The second example	182
8.2.3	Saturation factors of concentric REL motor	184
8.2.4	Stator saturation factors	184
8.2.5	Rotor saturation factors	185
8.2.6	Saturation factors of eccentric REL motor	192
8.2.7	Stator saturation factors	195
8.2.8	Rotor saturation factors	197
8.3	Experimental validation	201
8.3.1	The machine	201
8.3.2	Bench layout	201
8.3.3	Implementation procedure	202
8.3.4	Results Comparison and discussion	203
8.4	Conclusions	205
III Analytical Design of the REL and PMAREL Motors		207
9	Practical approach to design the PM in PMAREL motors robust toward the demagnetization	209
9.1	Introduction	209
9.2	The no load flux density of the PM	211
9.2.1	Complete model to predict the no-load flux density	211
9.2.2	Correction for lower size PM	213
9.2.3	Simplified model to compute the no-load flux density	215
9.2.4	PM width selection	217
9.2.5	Example and FE validation	217
9.3	Computation of the current reaction	218

9.3.1	Complete model to predict the PM stress	219
9.3.2	Simplified model to predict the PM stress	220
9.3.3	PM thickness selection	221
9.3.4	Flux barriers end angles	222
9.3.5	Example and FE validation	224
9.4	Rotor iron ribs effect	225
9.4.1	Complete model	226
9.4.2	Simplified model	226
9.4.3	Example and FE Validation	227
9.4.4	Electric loading effect on the operating points of the PMs	228
9.5	Conclusions	229
10	Fast Synthesis of REL and PMAREL Motors	231
10.1	Introduction	231
10.2	Determination of the main REL motor dimensions	232
10.3	Selection of the ends of the flux barriers	233
10.4	Selection of the geometry of the flux barriers	238
10.5	Computation of the iron rib thickness	243
10.6	Selection of the PM width	244
10.6.1	complete model analysis	246
10.6.2	Simplified model analysis	247
10.7	Computation of the PM thickness	248
10.7.1	complete model analysis	249
10.7.2	Simplified model analysis	249
10.8	Example	249
10.9	Conclusion	252
IV	Graphical User Interface Application	255
11	User interface application for concentric and eccentric REL motor	257
11.1	The main body of the application	257
11.2	User application interface form	258
11.3	Input and output data interface	261
11.4	Model of REL motor with one barrier	263
11.5	Model of REL motor with two barrier	267
11.6	Model of REL motor with three barrier	268
11.7	The results of the application	270

Conclusions and future work	271
Appendix A	273
Appendix B	277
Bibliography	279
List of Symbols	289

Sommario

Negli ultimi vent'anni l'interesse per le macchine sincrone a riluttanza è notevolmente cresciuto. Lo sviluppo e la ricerca dedicata a questi motori, supportata dai diversi vantaggi che presentano rispetto ad altri tipi di macchine, ha permesso a questa tipologia di macchina di guadagnarsi una quota di mercato in diverse applicazioni industriali. I motori a riluttanza offrono una più alta densità di coppia rispetto ai motori asincroni. Tuttavia, se confrontati con i motori sincroni a magneti permanenti, essi presentano una densità di coppia ed una efficienza minori. Tale decremento delle prestazioni rispetto alle macchine a magneti permanenti è tuttavia compensato dalla complessiva riduzione del costo di costruzione del rotore.

In aggiunta, essi presentano una struttura rotorica più robusta delle macchine sincrone a magneti superficiali e consentono di ottenere un più ampio range di funzionamento a potenza costante. I principali svantaggi delle macchine sincrone a riluttanza sono il basso fattore di potenza e le elevate oscillazioni di coppia. Il primo svantaggio, correlato alla assenza di alcun sistema di eccitazione sul rotore, viene normalmente mitigato attraverso l'introduzione di magneti permanenti all'interno delle barriere di flusso. Questo tipo di configurazione prende il nome di motore a riluttanza assistita da magneti permanenti. Il secondo svantaggio, ossia l'eccessivo torque ripple, è dovuto all'elevato contenuto armonico della forza magnetomotrice che interagisce con l'anisotropia rotorica. Diversi approcci sono stati proposti in letteratura allo scopo di ridurre tali oscillazioni, tra i quali: (a) lo skewing del rotore, (b) barriere rotoriche geo-metricamente asimmetriche rispetto all'asse interpolare, (c) barriere rotoriche asimmetriche rispetto all'asse polare, (d) equa distribuzione delle barriere lungo la periferia del rotore, e (e) l'ottimizzazione della intera geometria delle barriere.

Il grande interesse suscitato negli ultimi anni è dovuto principalmente a due motivi: (i) l'aumento di costo delle terre rare, utilizzate in magneti ad elevato contenuto energetico (Nd-FeB e SmCo); (ii) la crescente richiesta di macchine ad alta efficienza. Pertanto, il motore a riluttanza e il motore a riluttanza assistito da magneti permanenti stanno diventando concorrenti di entrambe le macchine a magneti permanenti e macchine a asincrone in molte applicazioni. Un altro vantaggio intrinseco delle macchine sincrone a riluttanza è che non inducono tensione a vuoto, quando il rotore è fermo, conseguentemente le correnti di corto circuito e coppie frenanti che si possono creare a causa dei guasti elettrici, sono trascurabili. Per quanto concerne l'aspetto controllistico è doveroso sottolineare il crescente interesse verso le macchine sincrone a riluttanza. Tale interesse è sostanzialmente giustificato dalla naturale propensione della stessa macchina ad essere controllata senza alcun sensore di velocità.

Sebbene vi sia un grande interesse per questo tipo di macchine, ci sono pochi lavori sulla progettazione analitica del loro rotore, ad esempio su come selezionare gli angoli di fine barriera, il dimensionamento dei ponticelli di ferro ed dettagli sulla progettazione robusta nei confronti della smagnetizzazione dei magneti permanenti. Nella maggior parte dei casi la macchina riluttanza viene analizzata mediante analisi agli elementi finiti. I risultati sono precisi e utili per realizzare una geometria specifica, ma si riferiscono ad una particolare soluzione perdendo generalità. In altre parole, è difficile trovare regole generali per progettare macchine a riluttanza. Per colmare questa lacuna, questa tesi si propone di fornire un approccio analitico utile alla determinazione di una geometria preliminare del motore, come punto di partenza per un'ottimizzazione successiva. La progettazione accurata dei ponticelli di ferro del rotore e gli effetti sulla forza elettromagnetica che agisce sul rotore con diversi gradi di eccentricità sono considerati. Questo lavoro di tesi è suddiviso in quattro parti principali.

Un modello analitico basato sul circuito magnetico equivalente a parametri concentrati del motore a riluttanza viene presentato e discusso nella prima parte. Questo modello studia il rendimento magnetico del motore sincrono a riluttanza concentrica. Lo stesso modello analitico è utilizzato per lo studio di differenti casi di eccentricità ed il loro impatto sulle prestazioni del motore a riluttanza. Motori a riluttanza con diversi tipi di avvolgimenti statici e diverse geometrie di rotore, simmetriche ed asimmetriche, vengono considerate. Lo stesso metodo viene applicato a motori a riluttanza con magneti permanenti e confrontata con il motore a riluttanza eccentrico. I risultati prodotti dai modelli utilizzati vengono confrontati tramite simulazioni agli elementi finiti. Inoltre, un confronto analitico tra il motore a riluttanza e motore a magneti permanenti superficiali viene condotta in diversi casi di eccentricità.

La seconda parte si propone di stimare in modo più accurato le forze elettromagnetiche agenti sul rotore, considerando l'effetto delle cave di statore e la caduta di tensione magnetica dovuta alla effettiva curva B-H del lamierino ferromagnetico. Il modello analitico è indicato per macchine con e senza presenza di eccentricità. Infine, misure sperimentali vengono condotte per validare la bontà dei modelli analitici ed agli elementi finiti.

Nella terza parte, si propone un approccio analitico per la progettazione del motore a riluttanza assistito da magneti permanenti. La larghezza e lo spessore dei magneti sono scelti in modo da realizzare la densità di flusso a vuoto al traferro desiderata e resistere alla smagnetizzazione che si possono presentare in condizioni di sovraccarico. Infine, un rapido approccio analitico e multi-obiettivo è proposto per la progettazione preliminare di motori a riluttanza e motori a riluttanza assistiti.

Nella quarta parte è stata sviluppata un'interfaccia utente grafica per l'analisi del motore a riluttanza. Questa applicazione stima i potenziali scalari magnetici di statore e rotore, la densità di flusso al traferro, la coppia elettromagnetica, la forza magnetica che agisce sul rotore. I parametri di ingresso di questa applicazione sono:

- dati geometrici dello statore e del rotore,
- carico elettrico (kA / m), e la sua fase (grado elettrico)
- il tipo di geometria del rotore, ad esempio, simmetrico o asimmetrico (Macaone),
- Numero di barriere di flusso per polo del rotore,
- il tipo di eccentricità o nessuna eccentricità, per esempio, il caso con rotore concentrico,

- il valore di eccentricità.

Perciò, l'utente può usare l'applicazione per stimare le prestazioni della macchina.

Struttura della tesi

Di seguito, il contenuto di ciascun capitolo della tesi viene brevemente descritto:

Parte I – Calcolo lineare

Il capitolo 1 descrive brevemente la teoria di base, la storia dello sviluppo, il modello, il diagramma vettoriale, e le principali caratteristiche del motore sincrono a riluttanza. Inoltre, viene discusso il comportamento non lineare ed il funzionamento del motore sincrono a riluttanza. Nel capitolo 2 viene riportato il modello analitico lineare del motore sincrono a riluttanza concentrica con uno, due e tre barriere di flusso per polo di rotore. Questo modello è basato sul circuito magnetico equivalente a parametri concentrati. L'obiettivo principale di questo modello è il calcolo del potenziale scalare magnetico di statore e rotore, la densità di flusso al traferro, la coppia elettromagnetica, le perdite nel ferro del rotore, e le forze radiali che agiscono sul rotore. Il capitolo 3 presenta la derivazione del modello analitico lineare del motore sincrono a riluttanza eccentrica con uno, due e tre flusso barriere per polo di rotore. Anche in questo caso le grandezze sopra citate vengono calcolate considerando entrambi i casi di eccentricità. Capitolo 4 illustra l'impatto di entrambi i casi di eccentricità sul motore a riluttanza. Per un insieme prestabilito di dati geometrici del motore a riluttanza, i risultati di entrambi i modelli analitici "sani" e in condizioni di guasto vengono confrontati. L'impatto dell'eccentricità sul potenziale magnetico del rotore, la densità di flusso al traferro, la forza magnetica e la coppia vengono determinate. La validazione dei modelli analitici citati viene effettuata attraverso l'analisi agli elementi finiti. Nel capitolo 5 viene evidenziato l'impatto di diversi tipi di avvolgimenti di statore e diverse geometrie di rotore sulla forza magnetica radiale in entrambi i casi di eccentricità. Entrambi i modelli analitici vengono implementati nel corso di questo studio. Ancora una volta, i risultati sono confermati da analisi agli elementi finiti. Il capitolo 6 mostra il confronto agli elementi finiti tra il motore a riluttanza e assistito da magnete in entrambi i casi di eccentricità. L'impatto di diverse geometrie del rotore e dimensioni barriera sono presi in considerazione in questo confronto. Il capitolo 7 presenta un modello analitico per motore sincrono a magneti permanenti superficiali in entrambi i casi sani ed eccentricità. Successivamente, il confronto analitico tra il motore sincrono a riluttanza e magnete permanente superficiale viene effettuato. Lo spostamento assiale uniforme e non uniforme del rotore viene introdotto in questo confronto.

Parte II – calcolo non lineare

Il capitolo 8 introduce il modello analitico non lineare del motore sincrono a riluttanza concentrico. Questo modello considera l'effetto dell'apertura di cava e le cadute di tensione magnetica che avvengono nel ferro del motore. Poi viene proposto il modello analitico non lineare del motore sincrono a riluttanza soggetto a eccentricità. I risultati sono confermati dai modelli agli elementi finiti. Infine viene condotta una prova sperimentale per valutare le forze magnetiche calcolate.

Parte III – Procedura di progettazione

Nel capitolo 9 presenta un approccio analitico alla scelta delle dimensioni dei magneti nei motori sincroni a riluttanza assistita. L'approccio analitico è presentato sia considerando che trascurando la presenza dei ponticelli magnetici. Inoltre si è applicata una semplificazione realistica all'approccio analitico per ricavare le dimensioni del magnete rapidamente. La larghezza e lo spessore del magnete sono selezionati in modo da avere la densità di flusso magnetico desiderata al traferro a vuoto, e in modo tale da resistere alla smagnetizzazione causata dalla corrente a carico. Il Capitolo 10 riassume la procedura analitica per la progettazione dei motori sincroni a riluttanza e riluttanza assistita.

Parte IV – Graphical User Interface Application

Introduce la prima versione dell'applicazione grafica sviluppata per l'analisi del motore sincrono a riluttanza. I modelli lineari presentati nei capitoli 2 e 3 della prima parte della tesi sono implementati in linguaggio di programmazione C++ e ambiente Qt. Grazie allo strumento sviluppato, le prestazioni dei motori sincroni a riluttanza concentrici ed eccentrici possono essere semplicemente stimate utilizzando questa applicazione.

Preface

This Preface describes the motivation and the main contributions of the thesis. The contents of each Chapter of the thesis are briefly summarized. Finally, a list of publications of the author is reported.

Background

Nowadays, the interest in the synchronous reluctance machines is growing up due to their several merits in comparison to other machine types. These machines offer high torque density with respect to the induction machines. Their torque density is slightly lower than permanent magnet synchronous machines even though the lower performance is compensated by a much cheaper rotor. Since synchronous reluctance machines do not induce voltage when the stator is not supplied, there are not short circuit currents and braking torques due to the electrical faults, e.g. they have high fault tolerant capability. In addition, synchronous reluctance machine has a robust structure, and a wide constant power speed range.

For these aforementioned reasons, these machines are employed in several applications. However, there is a prominent defect of this kind of machines which is the low power factor. This defect is addressed by assisting the motor by permanent magnets within the flux barriers of the rotor leading to the permanent magnet assisted synchronous reluctance motor.

In addition, these kinds of machines has high torque ripple. This is due to the high harmonic content in the magneto motive force which interacts with the rotor anisotropy. Several approaches are proposed to reduce the torque ripple, such as: (a) using skewed rotor, (b) adopting two different flux-barrier geometries in the same lamination, i.e., asymmetric rotor, (c) using equally spaced the flux-barrier ends along the rotor periphery, and (d) optimization approaches were applied to smooth the torque.

The synchronous reluctance machine is becoming of great interest in the last years, due to two key reasons: (i) the increase of rare earth permanent magnet cost and (ii) the increasing request of high-efficiency machines. Therefore, the reluctance motor and the ferrite permanent assisted reluctance motor are becoming competitors of both surface-mounted permanent magnet machines and induction machines in many applications. Such motors are also becoming particularly interesting when the control is based on the sensor-less rotor position detection.

Even if there is a great interest in this kind of machines, there is a few work about the analytical design of their rotor, e.g. about how to select the end barrier angles, designing

the iron ribs, and designing the permanent magnet robust towards the demagnetization. In the majority of the cases the reluctance machine is analyzed by using finite element analysis. The results are precise and useful for achieving a specific geometry to be prototyped, but they refer to that particular solution and they lose generality. In other words, it is difficult to find general rules to design reluctance machines, since the analysis approach is focused on a single objective.

During the manufacturing process, there are some manufacturing imprecision, such as mass unbalance, bearing tolerance, shaft bow, and etc., cause eccentricity fault. Eccentricity may cause magnetic and dynamic problems with additional vibrations, noises, and torque pulsations. Although the eccentricity faults in induction and permanent magnet motors are extensively investigated, there are a few publications on synchronous reluctance machines with eccentricity. It is important to study the effect of rotor eccentricity on these machines because of their high anisotropy and critical iron parts in the rotor (iron ribs). For the aim of designing the iron ribs thicknesses, the unbalanced magnetic force acting on these ribs should be accurately estimated.

Main contribution of the thesis

This thesis aims to give an useful analytical approach for reaching a preliminary geometry of both synchronous reluctance and permanent magnet assisted synchronous reluctance motors, as starting point for a successive optimization. For more accurate design of the rotor iron ribs, the electro-magnetic force acting on the rotor, in different rotor eccentricity cases, are analytically computed. In addition, a comparative studies (analytically and FE) between the synchronous reluctance, permanent magnet assisted, and surface mounted permanent magnet machines, in different eccentricity cases, is carried out. Therefore, this thesis is divided into four main parts.

At the first part, an analytical model based on the magnetic equivalent lumped network of the reluctance motor is discussed. This model studies the magnetic performance of the concentric synchronous reluctance motor. Then, this analytical model is adopted in order to study the impact of different eccentricity scenarios (static and dynamic eccentricity) on the reluctance motor. Different stator windings configurations (distributed and concentrated windings) and different rotor geometries (symmetric and asymmetric rotor) are considered. After that, the eccentric synchronous reluctance machine is compared with the eccentric permanent magnet assisted synchronous reluctance machine. The impact of the barrier dimensions, the rotor geometry, and the permanent magnet type is highlighted in this comparison. Furthermore, an analytical comparison between the reluctance motor and the surface mounted permanent magnet motor is carried out in different cases of eccentricity. The axial non uniform displacement of the rotor axis from the stator axis, at one end and both ends of the axis, are involved in this analytical comparison.

The second part aims to achieve more realistic estimation of the electromagnetic forces acting on the rotor by considering the effect of stator slots and the magnetic voltage drop due to the actual B-H curve of the motor iron. The analytical model is developed for both eccentric and concentric synchronous reluctance motor. Then, an experimental validation of the analytical and FE analysis is carried out.

At the third part, an analytical approach for designing the permanent magnet of the permanent magnet assisted reluctance motor is proposed. The width and the thickness are selected

so as to achieve the desired no-load air-gap flux density and resist the demagnetization under the desired loading conditions, respectively. Both complete and simplified analytical analyses are discussed. In addition, the analytical approach is presented in both cases of neglecting and considering the rotor iron ribs. Then, from the previously mentioned three parts of this thesis, a rapid multi-objectives analytical approach is proposed to achieve the initial design of the synchronous reluctance and permanent magnet assisted synchronous reluctance motors.

Finally, at the fourth part, a graphical user interface application for concentric and eccentric synchronous reluctance motor is developed. This application estimates stator and rotor scalar magnetic potential, air-gap flux density, electromagnetic torque, magnetic force acting on the rotor. The input parameters of this application are

- the geometrical data of the stator and rotor,
- the electric loading (kA/m), the electric load angle in (electric degree),
- the rotor geometry type, e.g., symmetric or asymmetric rotor geometry,
- number of flux-barriers per rotor pole,
- eccentricity type or no eccentricity, e.g., healthy case,
- the eccentricity value.

Then, the user can run the application to estimate the magnetic performance of both concentric and eccentric synchronous reluctance motor.

Outline of the thesis

Hereafter, the contents of the each chapter of the thesis are briefly described:

Part I–Linear Computation

Chapter 1 describes briefly the basic theory, the development history, the model, the vector diagram, and the main characteristics of the synchronous reluctance motor. In addition, the non-linear behavior is discussed. Then, the operating regions of the synchronous reluctance motor are highlighted.

Chapter 2 reports the linear analytical model of the concentric synchronous reluctance motor with one, two, and three flux-barriers per rotor pole. This model is based on the equivalent lumped-parameter magnetic network. The main target of this model is to compute stator and rotor scalar magnetic potential, air-gap flux density, electromagnetic torque, rotor iron losses, and the electromagnetic radial force acting on the rotor.

Chapter 3 presents the derivation of the linear analytical model of the eccentric synchronous reluctance motor with one, two, and three flux-barriers per rotor poles. Once again, both stator and rotor scalar magnetic potential, air-gap flux density, electromagnetic torque, electromagnetic force acting on the rotor, and the rotor iron losses are computed. Both eccentricity cases are considered.

Chapter 4 illustrates the impact of both eccentricity cases on the magnetic performance of the synchronous reluctance motor. For a given geometrical data of reluctance motor in this chapter, the results of both healthy and faulty analytic models are compared. The impact of eccentricity on the rotor scalar magnetic potential, the air-gap flux density, the magnetic force and the torque is highlighted. The validation of aforementioned analytical models by means of finite element analysis is carried out.

Chapter 5 highlights the impact of different stator windings and different rotor geometries on the radial magnetic force in both cases of eccentricity. Both analytical models are implemented during this study. Once again, the results are confirmed by finite element analysis.

Chapter 6 shows the comparison between the synchronous reluctance motor and permanent magnet assisted reluctance motor in both cases of eccentricity. Different rotor geometries and barrier dimensions impact are taken into account in this comparison, besides different permanent magnets are considered.

Chapter 7 presents an analytical model for surface mounted permanent magnet synchronous motor in both healthy and eccentricity cases. Then, the analytical comparison between the synchronous reluctance motor and surface mounted permanent magnet motor is carried out. Uniform and non-uniform axial displacement of the rotor axis from the stator axis are introduced in this comparison.

Part II–NON Linear Computation

Chapter 8 introduces the non-linear analytical model of the concentric synchronous reluctance motor. This model considers the slotting effect and the magnetic voltage drop in the motor actual iron. Then, the non-linear analytical model of the eccentric synchronous reluctance motor is proposed. The results are confirmed by the FE results. Then, an experimental validation of computed magnetic force is carried out.

Part III–Implementation of The Design Procedure

Chapter 9 presents an analytical approach for designing the permanent magnets dimensions for the permanent magnet assisted reluctance motor. The analytical approach is presented in both cases of neglecting and considering the rotor iron ribs. In addition, a realistic simplification is applied to this analytical approach to achieve the dimensions of the PM rapidly. The width and the thickness are selected so as to achieve the desired no-load air-gap flux density and resist the demagnetization under the desired loading conditions, respectively.

Chapter 10 presents a fast analytical synthesis of the synchronous reluctance and permanent magnet assisted reluctance motors. This design approach is multi objective, as well as, consumes short computation times. FE analysis and experimental results validates the results of the analytical approach.

Part IV–Graphical User Interface Application

shows the first version of the developed graphical user interface application of the synchronous reluctance motor. The linear analytical models presented in chapters 2 and 3 of the first part of the thesis are implemented using C++ programming and Qt environment. Then, the magnetic performance of the concentric and eccentric synchronous reluctance motor can be simply estimated by using this friendly user application.

List of publications

Several parts of this Ph.D. thesis have been presented by the author during his Ph.D. course in international conferences and journals. Hereafter the publications are listed in a chronological order:

- **Mahmoud H.** and Bianchi N., "*Eccentricity in Synchronous Reluctance Motors–Part I : Analytical and Finite–Element Models*". In IEEE Transactions on Energy Conversion, vol. 30, no. 2, pp. 745-753, 2015, DOI: 10.1109/TEC.2014.2384535.
- **Mahmoud H.** and Bianchi N., "*Eccentricity in Synchronous Reluctance Motors–Part II: Different Rotor Geometry and Stator Windings*". In IEEE Transactions on Energy Conversion, vol. 30, no. 2, pp. 754-760, 2015, DOI: 10.1109/TEC.2014.2384534.
- **Mahmoud H.** and Bianchi N., "*Comparison between synchronous reluctance and interior permanent magnet motors with eccentricity*". In IEEE Workshop on Electrical Machines Design, Control and Diagnosis (WEMDCD 2015), Torino, Italy, 26-27 March 2015, p. 22-27, DOI: 10.1109/WEMDCD.2015.7194484.
- **Mahmoud H.** and Bianchi N., "*Analytical comparison of synchronous reluctance and surface permanent magnet machines with rotor eccentricity*". In IEEE Energy Conversion Congress and Exposition (ECCE 2015), Montreal, QC, USA, 20-24 Sept. 2015, p. 1765 - 1772, DOI: 10.1109/ECCE.2015.7309909.
- Bianchi N. and **Mahmoud H.**, "*An Analytical Approach to Design the PM in PMAREL Motors Robust Toward the Demagnetization*". In IEEE Transactions on Energy Conversion, vol. 31, no. 2, pp. 800-809, 2016, DOI:10.1109/TEC.2016.2523556.
- Bianchi N., **Mahmoud H.**, and Bolognani S., "*Fast synthesis of permanent magnet assisted synchronous reluctance motors*". In IET Electric Power Applications Journal, Volume 10, Issue 5, pp. 312-318, 2016, DOI: 10.1049/iet-epa.2015.0240.
- **Mahmoud H.** and Bianchi N., "*Comparison between Synchronous Machines with Eccentricity: Reluctance and Permanent Magnets*". In 23rd International Symposium on Power Electronics, Electrical Drives, Automation, and Motion (SPEEDAM 2016), Capri Island, Italy, 22-24 June 2016, p. 394-400, DOI: 10.1109/SPEEDAM.2016.7525863.
- **Mahmoud H.** and Bianchi N., "*Magnetic Field Analytical Computation in Synchronous Reluctance Machines Considering the Iron Saturation*". In IEEE Energy Conversion Congress and Exposition (ECCE 2016), Milwaukee, WI, USA, 18-22 Sept. 2016.
- **Mahmoud H.** and Bianchi N., "*An Improved Analytical Model of Eccentric Synchronous Reluctance Machines Considering the Iron Saturation and Slotting Effect*". In XXII th International Conference on Electrical Machines (ICEM'2016), Lausanne, Switzerland, 4-7 Sept. 2016.
- Degano M., **Mahmoud H.**, and Bianchi N., "*Synchronous Reluctance Machine Analytical Model Optimization and Validation Through Finite Element Analysis*". In XXII th International Conference on Electrical Machines (ICEM'2016), Lausanne, Switzerland, 4-7 Sept. 2016.

Synchronous reluctance motor

In this chapter, the basic working principle of synchronous reluctance (REL) motor is explained. Then, the development history of this kind of motors is summarized. In addition, the model, the vector diagram, and the main characteristics of the motor are reported. The non-linear behavior of the REL motor is discussed. Hereafter, the operating regions of the REL motor are highlighted.

1.1. Operating principle

SYNCHRONOUS reluctance (REL) motor operating principle is based on the reluctance concept. This concept can be clarified by Fig.1.1. Since an anisotropic rotor is placed in a magnetic field with a defined direction, as shown in Fig.1.1 (a), the reluctance torque is produced. This torque is due to the interaction of the non-uniform magnetic reluctance in both d and q axes of the anisotropic rotor and the magnetic field. The magnetic reluctance in the d -axis direction is much lower than that in the q -axis direction. From Fig.1.1 (a), there are an angle δ between the magnetic field and the d -axis of the rotor. For the sake of reducing the whole system potential energy to reduce the field distortion, the reluctance torque is produced to align the d -axis of the rotor with the magnetic field. Therefore, the rotor rotates to be in position (b), as shown in Fig.1.1 (b).

On the contrary, the magnetic reluctance is uniform for the isotropic rotor, as shown in 1.2. Therefore, if the magnetic field is applied on this rotor, the reluctance torque is zero.

For the REL motor, the rotating magnetic field is produced by the multi-phase winding of the stator. A traditional stator with distributed winding, as used in the induction motor, is used to avoid the sub harmonics produced by the fractional slot concentrated winding (FSCW). If the load angle δ is kept constant between the magnetic field and the rotor d -axis, the electromagnetic energy will be continuously converted to mechanical energy. This can be done by controlling the current angle of the machine [1]. In addition, the main parameter affects the torque is the stator current.

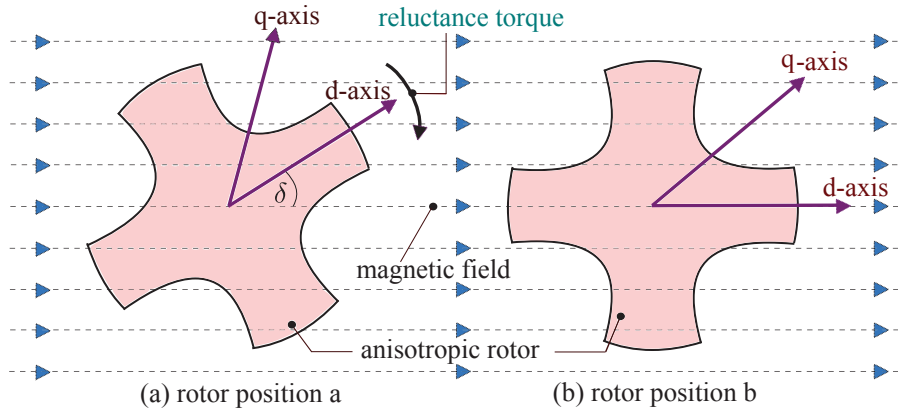


Figure 1.1: Cross section of an anisotropic rotor placed in a magnetic field.

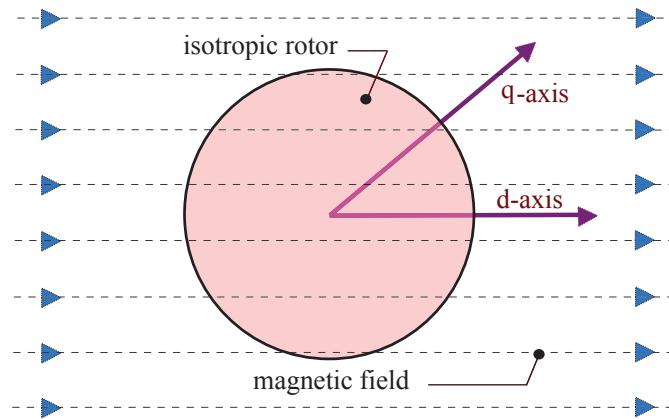


Figure 1.2: Cross section of an isotropic rotor placed in a magnetic field.

1.2. Development history

The pure synchronous motor shown in Fig.1.1 is one of oldest types of electric motors, antedating the induction motor by many years [2]. At this time, the technology of switching devised of the inverters was poor. This means that there were not motor inverters to start the motor, as well as, this motor does not start directly on line. Therefore, the rotor is replaced by a cage rotor, as in Fig.1.3. However, the cage causes a reduction in the saliency ratio which yields to impair the power factor and the efficiency of motor comparing to the cage-less one. Therefore, this motor had poor performance comparing with the other alternating current (ac) machines.

Although, nowadays, the REL motor can start by the modern inverter technology, suitable field oriented control and PWM technique without inserting the cage to the rotor, there are high noise and torque pulsation [3]. From [4], these noise and torque pulsations were eliminated by increasing the air-gap length which yields to effectively eliminate the power density and efficiency of this motor. Therefore, other rotor geometries are developed as in Fig. 1.4 and Fig. 1.5.

In Fig. 1.4 (a), by removing teeth from the rotor of a conventional induction motor, the rotor saliency can be achieved. However, in the resulting rotor geometry, the saliency ratio

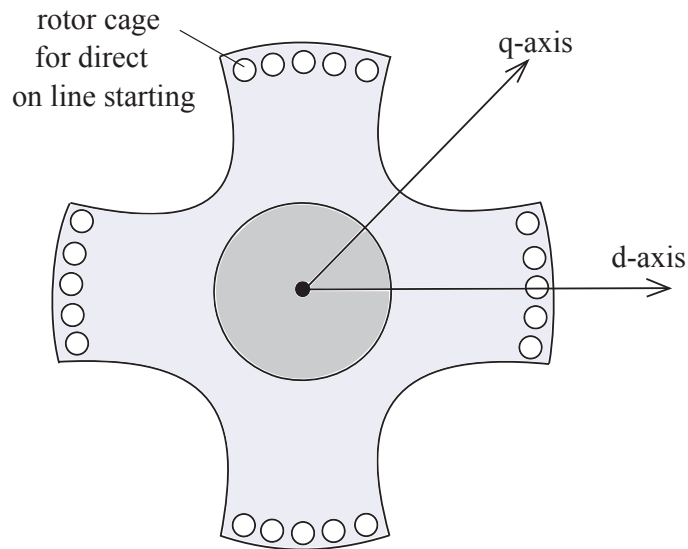


Figure 1.3: Cross section of synchronous motor with cage windings in the rotor for the starting direct online purpose.

($\xi = L_d/L_q$) is less than 3. Fig. 1.4 (b) shows the rotor of an ordinary salient-pole synchronous motor without the excitation windings. Nevertheless, the saliency ratio is still low. As in [5, 6], the saliency ratio for this rotor geometry was reported equal to 3, decreasing to about 2.5 under load. However, in [7], several variants of this geometry were considered. The saliency ratio was reported not higher than 3.8.

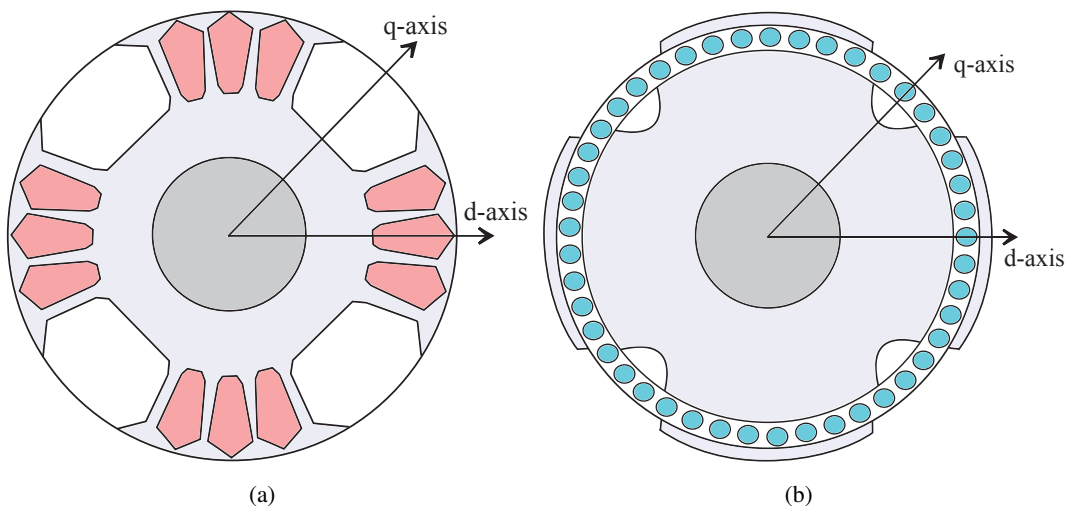


Figure 1.4: Cross section of two classes of synchronous reluctance rotor design resulted by: (a) modifying the rotor of traditional induction motor and (b) removing the excitation winding from the salient-pole synchronous motor.

The so-called single-layer flux-barrier rotors are illustrated in Fig. 1.5. By adding flux-barrier of a non magnetic material in the q-axis below the cage windings, as in Fig. 1.5 (a), the rotor saliency was achieved. This rotor geometry allows the motor to start direct online.

Other geometry is shown in Fig. 1.5 (b). By removing the permanent magnet from the interior permanent magnet motor, the flux barrier insulation is achieved. The saliency ratio of these kind of rotor geometries were reported about 6-8, as in [6, 8].

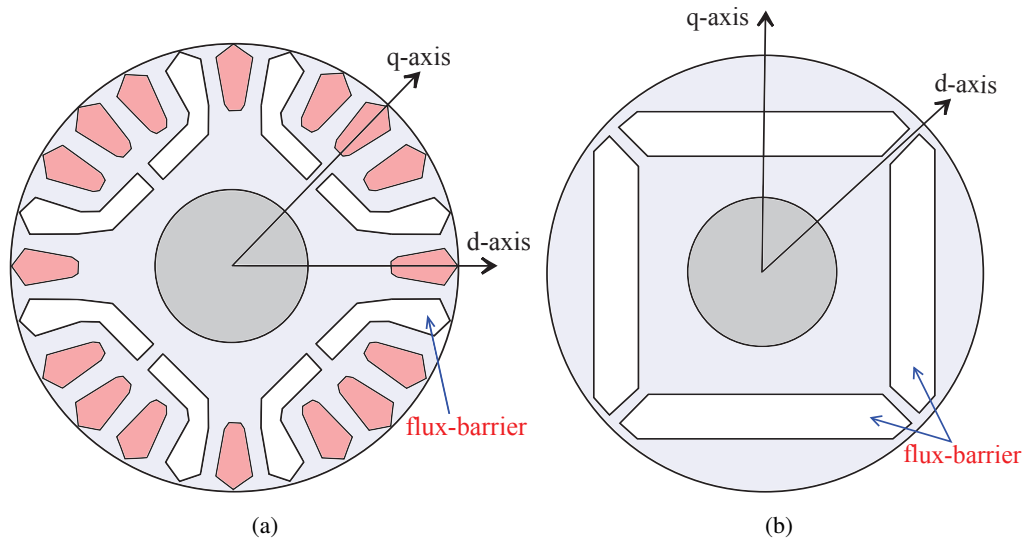


Figure 1.5: Cross section of the so-called single-layer flux-barrier rotor geometries resulted by (a) adding flux-barrier below the cage windings and (b) removing the permanent magnet from the interior permanent magnet motor.

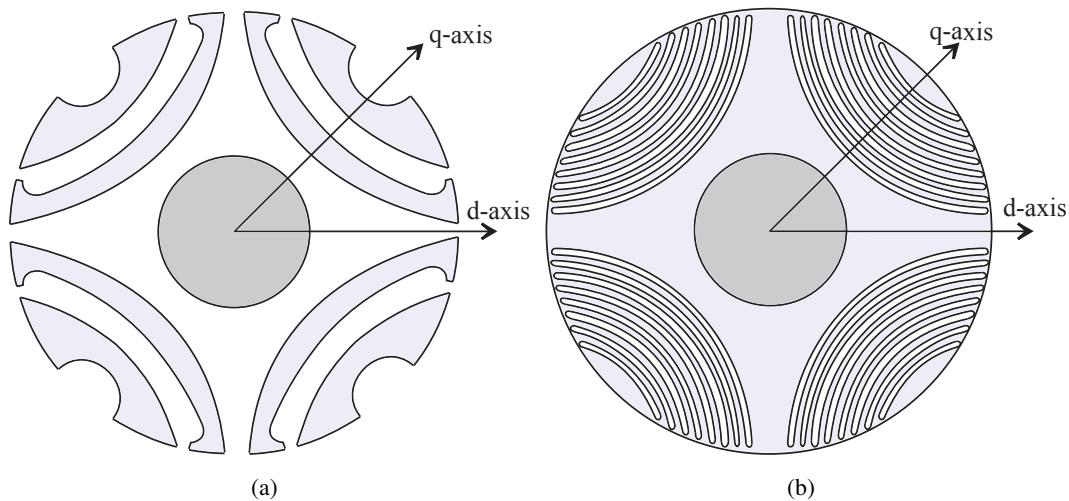


Figure 1.6: Cross section of (a) the transversally laminated anisotropy (TLA) rotor proposed by Kostko and (b) its developed multiple flux barrier geometry.

As early as 1923, Kostko [2] investigated the aforementioned rotor geometries. His opinion in the inferiority of these geometries is mainly due to the faulty form of the rotor. To increase the torque, it is necessary to prevent, as much as possible, the formation of the transverse field. The usual practise is to cut out that part of the rotor where the q-axis field would be maximum, as shown in all aforementioned strategies. However, in these design strategies, some of the

useful d -axis fields are lost. Then, he proposed the rotor design based on multiple flux barriers, 'segmental' geometry, and a q -axis channel, as shown in Fig. 1.6. However, the mechanical aspects were disregarded as shown in Fig. 1.6 (a). According to Kostko's work, there are two possible solutions for the rotor design development, as reported in [9]. They are described as follows:

- (a) axially-laminated anisotropic (ALA) solution [10, 11], as shown in Fig. 1.7. The laminations are probably shaped, insulated to each other by magnetically and electrically passive material. Then, the resulting stacks are connecting through the pole holder to the center part of where the shaft is connected to,
- (b) transversally laminated anisotropic (TLA) solution, as shown in Fig. 1.8. The laminations are punched in the traditional way. Thin ribs are left to hold the rotor segments together. To achieve the anisotropy, these ribs should be magnetically saturated results an additional leakage component of the q - axis flux. This leakage causes loss of the torque. This torque loss can be limited to $\sim 5\%$ of the rated torque in the $10 \div 100$ N.m range and up to ~ 5000 rpm [9].

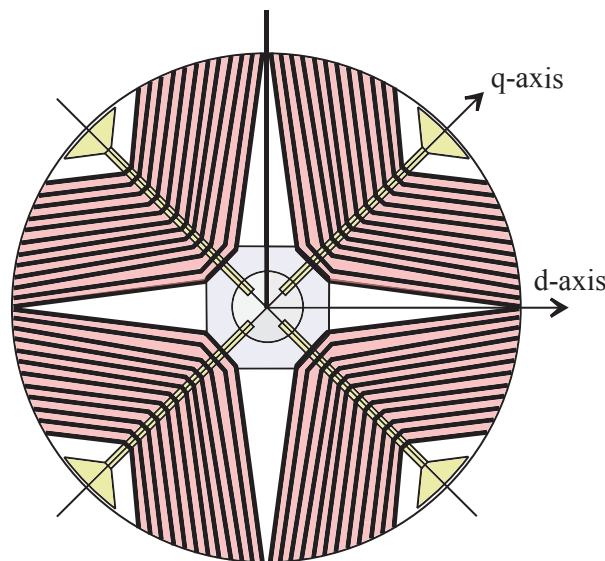


Figure 1.7: Cross section of the axial laminated anisotropic rotor (ALA).

Both TLA and ALA design solutions have been investigated and compared together considering the mechanical strength, saliency ratio, iron losses, starting on line capability, and the manufacturing process.

Firstly, for mechanical strength point of view, the TLA rotor gives mechanical strength to the rotor stack, in an easy and cheap way, as shown in Fig. 1.8. Secondly, for the saliency ratio, TLA has lower saliency ratio than ALA. This reduction is due to the iron ribs, which leads to reduce the magnetic reluctance in the q -axis direction (R_q). By other words, the iron ribs increases L_q , which yields to limit the saliency ratio. This L_q can be minimized by reducing the thicknesses of the rotor iron ribs. However, the thicknesses of these ribs are restricted by the mechanical stress. The mechanical stresses on these ribs raises from the centrifugal force and

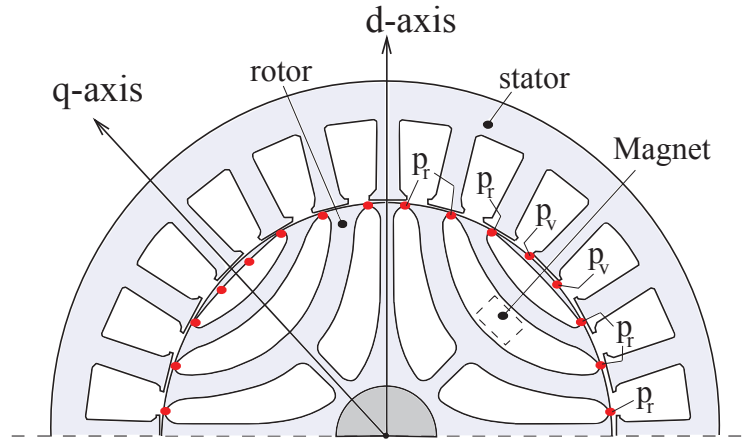


Figure 1.8: Cross section of the TLA rotor with equal space between the equivalent rotor slots.

the magnetic force acting on the rotor. For the TLA rotor shown in Fig. 1.8, we must content ourselves with the value ten for the saliency ratio ξ . On the contrary, due to the absent of the iron ribs in case of axial laminated rotor geometry, as shown in Fig. 1.7, the saliency ratio is high. Saliency ratio values for the c-type rotors, shown in Fig. 1.7, are normally above ten, and at their best even above 15 [6, 8].

Thirdly, for line start motors, the segmental rotor reached a high state of development in the work of [6, 12–14]. Fourthly, as the stator slots are considered, the rotor iron losses are resulted. These iron losses can be reduced in the TLA rotor. Nevertheless, the iron losses is high in ALA rotor, as reported in [3, 15–18]. Finally, the TLA is more suitable for the industrial manufacturing. Hence, the TLA rotor is preferred and attracts most of the researchers and industry to study it and developing its performance.

1.3. Model and basic characteristics

This section briefly describes the model of the REL motor. Then, the main characteristics of this motor are discussed. Fig. 1.9 shows the complete equivalent circuit of the REL motor [1, 3, 19]. Nowadays, the technology of the electric drives allows the REL motor to start-up without inserting the damper windings in the rotor, and hence, the rotor losses resulted from these windings are eliminated. As a consequent, the motor efficiency and power factor are improved. Therefore, the damper winding can be removed from the equivalent circuit shown in Fig. 1.9. In addition, the iron losses are disregarded, as in [19]. Referring to the previous assumptions, the equivalent circuit can be simplified as in Fig. 1.10.

By the notations of Fig. 1.10, the stator terminal voltage vector in stationary reference frame is given by

$$v_s = R_s i_s + \frac{d\lambda_s}{dt} \quad (1.1)$$

where i_s are the amplitude of the stator current vector, R_s is winding resistance, and λ_s is the amplitude of the stator flux linkage vector. λ_s is computed as

$$\lambda_s = (L_{s\sigma} + L_m) i_s \overset{\text{or}}{\equiv} \lambda_{s\sigma} + \lambda_m \quad (1.2)$$

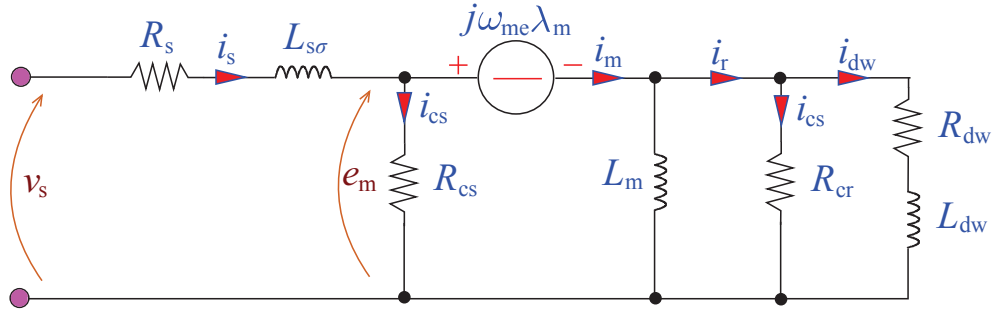


Figure 1.9: Equivalent circuit according to the stator stationary reference frame for a REL motor.

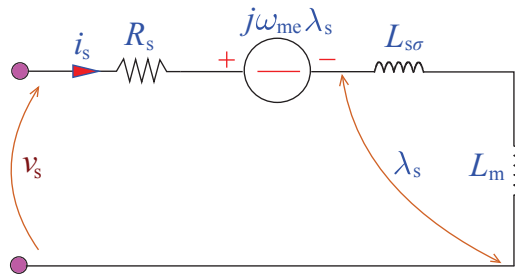


Figure 1.10: Simplified equivalent circuit according to the stator stationary reference frame for a REL motor.

where $L_{s\sigma}$, L_m is the stator leakage inductance and magnetizing inductance per phase, respectively. As in eq. (1.2), λ_s consists of the leakage flux linkage of the stator $\lambda_{s\sigma}$ and the flux linkage of the air-gap λ_m .

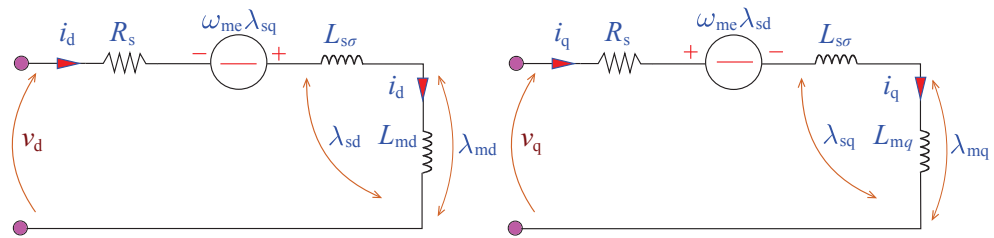


Figure 1.11: Equivalent circuit according to the synchronous reference frame for a REL motor.

Since the rotor of the REL motor has different inductances in d and q axes, as the salient pole machine without excitation, the model can be presented in the synchronous reference frame. The equivalent circuit is split into two circuits according to d and q axes, as in Fig. 1.11. From Fig. 1.12, v_s , i_s , and λ_s are referred to both d and q axes, respectively, as

$$v_s = v_d + jv_q \tag{1.3}$$

$$i_s = i_d + ji_q \tag{1.4}$$

$$\lambda_s = \lambda_{sd} + j\lambda_{sq} \tag{1.5}$$

Then, the voltage equations are rewritten as

$$v_d = R_s i_d + \frac{d\lambda_{sd}}{dt} - \omega_{me} \lambda_{sq} \quad (1.6)$$

$$v_q = R_s i_q + \frac{d\lambda_{sq}}{dt} + \omega_{me} \lambda_{sd} \quad (1.7)$$

where ω_{me} is the electrical angular speed of the motor. λ_{sd} and λ_{sq} are the flux linkage components in d and q axes directions, respectively. They are given by

$$\lambda_{sd} = \lambda_{md} + \lambda_{s\sigma d} = (L_{md} + L_{s\sigma}) i_d \stackrel{\text{or}}{=} L_d i_d \quad (1.8)$$

$$\lambda_{sq} = \lambda_{mq} + \lambda_{s\sigma q} = (L_{mq} + L_{s\sigma}) i_q \stackrel{\text{or}}{=} L_q i_q \quad (1.9)$$

The vector diagram of the REL motor model is shown in Fig. 1.12, where a -axis presents the reference of the stator stationary reference frame, θ is the angle of the d -axis measured from a -axis, i.e. it refers to the rotor position, α_i^e is the angle of the current vector referring to the d -axis, ϕ is the phase angle between the stator voltage and current vectors, which determines the power factor ($\cos(\phi)$). δ_m and δ are the angles of the air-gap flux linkage and stator flux linkage referring to the d -axis, respectively. δ is also called the load angle.

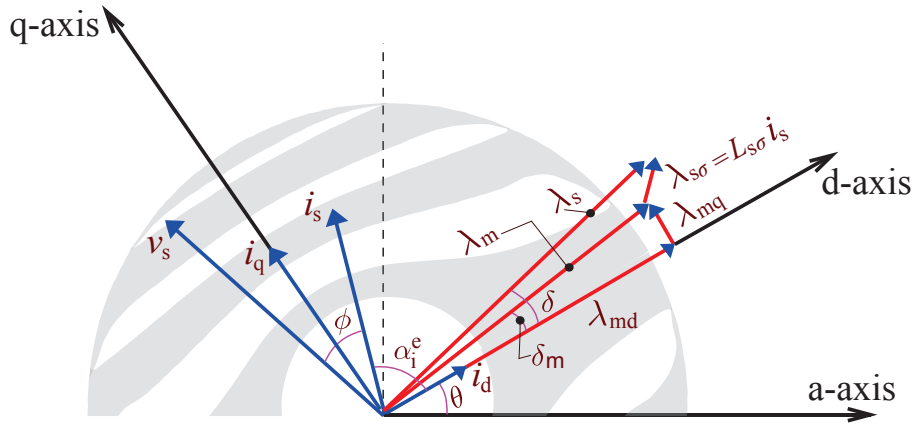


Figure 1.12: Vector diagram of a REL motor at the nominal operating point.

1.3.1. Relation between the load angle and the current angle

From the vector diagram shown in Fig. 1.12, the load angle δ is computed as

$$\delta = \tan^{-1}\left(\frac{\lambda_{sq}}{\lambda_{sd}}\right) = \tan^{-1}\left(\frac{L_q i_q}{L_d i_d}\right) = \tan^{-1}\left(\frac{1}{\xi} \frac{i_q}{i_d}\right) \quad (1.10)$$

Of course, the current angle can be computed from i_d and i_q as

$$\alpha_i^e = \tan^{-1}\left(\frac{i_q}{i_d}\right) \quad (1.11)$$

Thus, the load angle is given by

$$\delta = \tan^{-1}\left(\frac{1}{\xi} \tan(\alpha_i^e)\right), \quad \text{or} \quad \tan(\delta) = \frac{1}{\xi} \tan(\alpha_i^e) \quad (1.12)$$

Both δ and α have effect on the machine performance, as well as, the saliency ratio ξ .

1.3.2. The electromagnetic torque derivation

From the interaction between the stator current vector and the flux linkage vector, the electromagnetic torque can be computed [19], as

$$T = \frac{3}{2}p(\vec{\lambda}_s \times \vec{i}_s) \quad (1.13)$$

where p is the number of pole pairs. Substituting eqs. (1.4) and (1.5) in eq. (1.13), it results

$$T = \frac{3}{2}p(\lambda_{sd}i_q - \lambda_{sq}i_d) = \frac{3}{2}p\left(\frac{\lambda_{sd}\lambda_{sd}}{L_q} - \frac{\lambda_{sd}\lambda_{sd}}{L_d}\right) = \frac{3}{2}p\lambda_{sd}\lambda_{sd}\left(\frac{1}{L_q} - \frac{1}{L_d}\right) \quad (1.14)$$

By substituting $\lambda_s = v_s/\omega_{me}$ in eq. (1.14), the electromagnetic torque can be expressed as a function of the motor saliency, the amplitude of the stator voltage space vector v_s , and the load angle, as

$$\begin{aligned} T &= \frac{3}{2}p\lambda_s^2\left(\frac{L_d - L_q}{L_d L_q}\right) \cos(\delta) \sin(\delta) = \frac{3}{2}p\lambda_s^2\left(\frac{L_d - L_q}{2L_d L_q}\right) \sin(2\delta) \\ &= \frac{3}{2}pv_s^2\left(\frac{L_d - L_q}{2\omega_{me}^2 L_d L_q}\right) \sin(2\delta) \end{aligned} \quad (1.15)$$

Similarly, from eq. (1.14), the electromagnetic torque can be expressed as a function of the motor saliency, the amplitude of the stator current space vector i_s , and the current angle α_i^e , as

$$T = \frac{3}{2}p(L_d - L_q)i_d i_q = \frac{3}{2}p(L_d - L_q)i_s^2 \sin(2\alpha_i^e) \quad (1.16)$$

In fact, the electromagnetic torque shown in eq. (1.15) does not consider the variation of the co-energy with the variation of the rotor position $\frac{\partial W'_m}{\partial \theta_m}$. This point is discussed deeply in [20]. From eq. (1.15), at constant voltage, the effect of the load angle and the ξ of the rotor on the electromagnetic torque are studied, as shown in Fig. 1.13. It is noted that the maximum torque is achieved at $\delta = \frac{\pi}{4}$. In addition, the impact of ξ on the electromagnetic torque is highlighted.

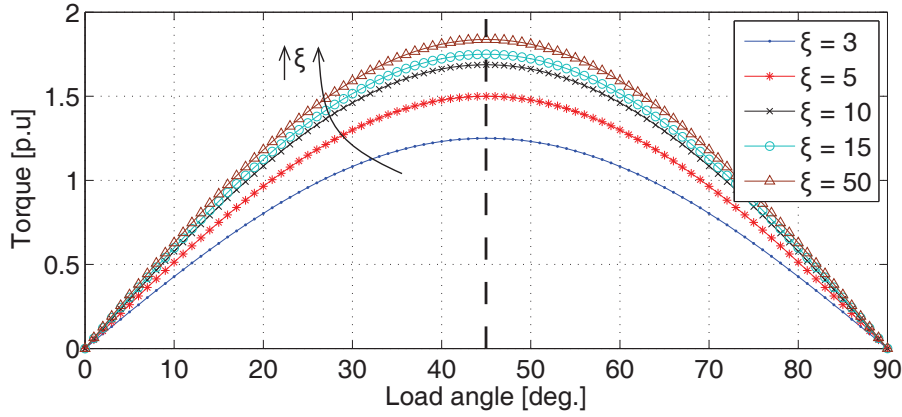


Figure 1.13: The electromagnetic torque versus the load angle at different saliency ratios of the REL motor.

Due to the relation between the load angle and the current angle reported in eq. (1.12), the electromagnetic torque can be presented as

$$T = \frac{3}{2} p v_s^2 \left(\frac{L_d - L_q}{2\omega_{me}^2 L_d L_q} \right) \sin\left(2 \tan^{-1}\left(\frac{1}{\xi} \tan(\alpha_i^e)\right)\right) \quad (1.17)$$

Then, for a given voltage, the impact of the current angle and ξ on the electromagnetic torque is studied as shown in Fig. 1.14.

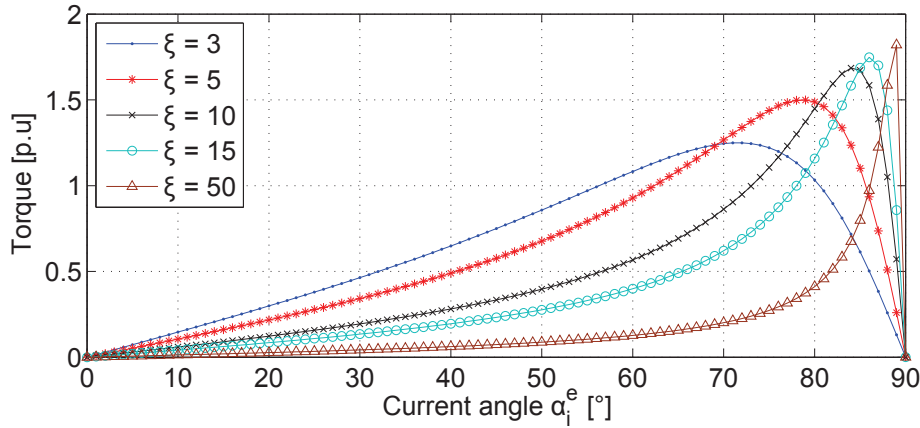


Figure 1.14: The electromagnetic torque versus the current angle at different saliency ratios of the REL motor.

From eq. (1.17), at $\xi \simeq 10$, the impact of the current angle on the electromagnetic torque is studied at different voltage levels, as shown in Fig. 1.15. It is noted that the maximum torque is achieved at $\alpha_{ie} = \tan^{-1}(\xi)$ for different voltage values. Therefore, this operating condition is called maximum torque per voltage (MTPV). The value of current angle of the MTPV is reduced due to the iron saturation. This point will be discussed deeply later.

Analogously, the impact of the current angle on the electromagnetic torque is studied at different current levels and $\xi \simeq 10$, as shown in Fig. 1.16. It is noted that the maximum torque is obtained at $\alpha_i^e = 45^\circ$ for all current values, which is called maximum torque per ampere

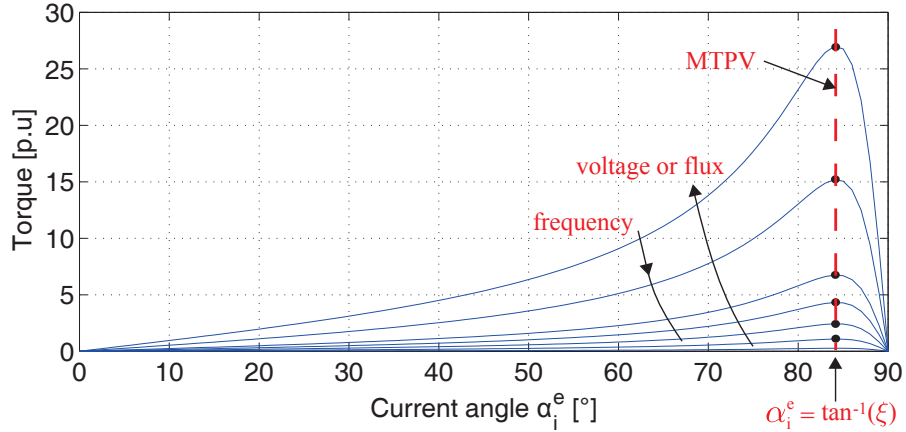


Figure 1.15: The electromagnetic torque versus the current angle at constant stator flux, which shows the MTPA of a REL motor.

(MTPA). The value of current angle of the MTPA is increased due to the iron saturation. This point will be discussed deeply later.

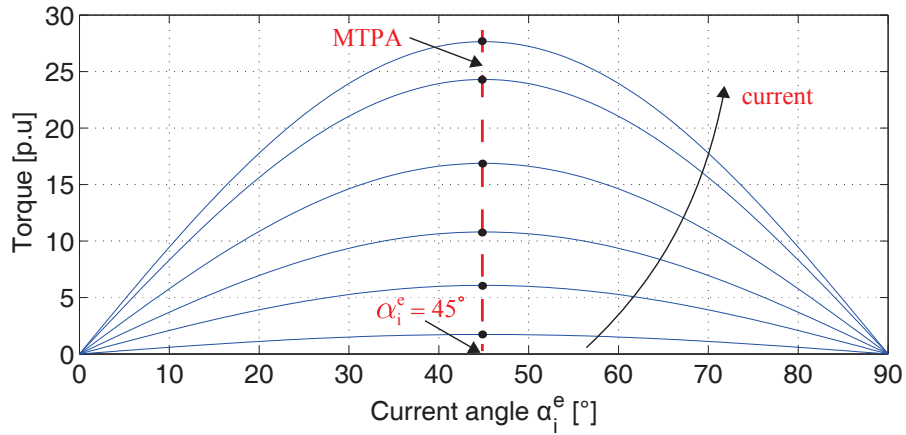


Figure 1.16: The electromagnetic torque versus the current angle, which shows the MTPA of a REL motor.

Fig. 1.17 shows block diagram, which concludes the model of the REL motor. The electrical equations are the voltage equations and the electromagnetic torque equation, as in eqs. (1.6), (1.7) and (1.16), respectively. The relation of the mechanical load torque and the electromagnetic torque (the load equation) is given by

$$T = T_L + B\omega_m + J \frac{d\omega_m}{dt} \tag{1.18}$$

where T_L is the load torque, B is the viscous friction coefficient, J is the moment of inertia of the rotor, and ω_m is the mechanical angular speed of the rotor, which given by $p\omega_{me}$.

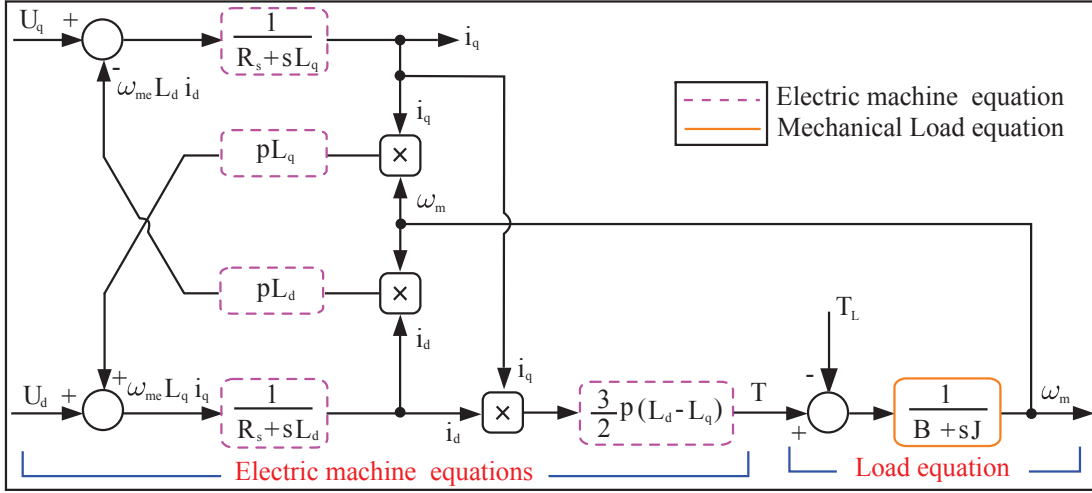


Figure 1.17: Reluctance motor block diagram in synchronous reference frame.

1.3.3. Power factor computation

From Fig. 1.12, the power factor $\cos(\phi)$ can be computed.

$$\cos(\phi) = \cos\left(\frac{\pi}{2} - \alpha_i^e + \delta\right) \quad (1.19)$$

By neglecting the stator resistive losses and the iron losses, it is possible to express the balance of the electromechanical energy conversion as:

$$\frac{3}{2} p v_s i_s \cos(\phi) = T \omega_{me} \quad (1.20)$$

where v_s is given by $\omega_{me} \lambda_s$ and T is computed in eq. (1.16). Besides, the amplitudes of the flux linkage λ_s and current vector i_s are given by

$$\lambda_s = \sqrt{\lambda_d^2 + \lambda_q^2}, \quad \text{and} \quad i_s = \sqrt{i_d^2 + i_q^2} \quad (1.21)$$

By substituting eq. (1.16) and eq. (1.21) in eq. (1.20), the power factor is computed as

$$\cos(\phi) = \frac{(L_d - L_q) i_d i_q}{\sqrt{(L_d i_d)^2 + (L_q i_q)^2} \sqrt{i_d^2 + i_q^2}} \quad (1.22)$$

The power factor is expressed as function of the d and q axes currents and the saliency ratio. In order to study the effect of the current angle on the power factor, the previous expression

shown in eq. (1.22) can be simplified as follows

$$\begin{aligned}
 \cos(\phi) &= \frac{L_q (\xi - 1) i_d i_q}{L_q i_q \sqrt{\left(\frac{L_d i_d}{L_q i_q}\right)^2 + 1} \sqrt{i_d^2 + i_q^2}} \\
 &= \frac{(\xi - 1) \frac{i_d}{\sqrt{i_d^2 + i_q^2}}}{\sqrt{\left(\frac{\xi}{\tan(\alpha_i^e)}\right)^2 + 1}} = \frac{(\xi - 1) \cos(\alpha_i^e)}{\sqrt{\xi^2 \left(\frac{\cos^2(\alpha_i^e)}{\sin^2(\alpha_i^e)}\right) + 1}} \\
 &= \frac{(\xi - 1)}{\sqrt{\xi^2 \left(\frac{1}{\sin^2(\alpha_i^e)}\right) + \left(\frac{1}{\cos^2(\alpha_i^e)}\right)}} = (\xi - 1) \sqrt{\frac{\sin(2\alpha_i^e)}{2(\tan(\alpha_i^e) + \xi^2 \cot(\alpha_i^e))}}
 \end{aligned} \tag{1.23}$$

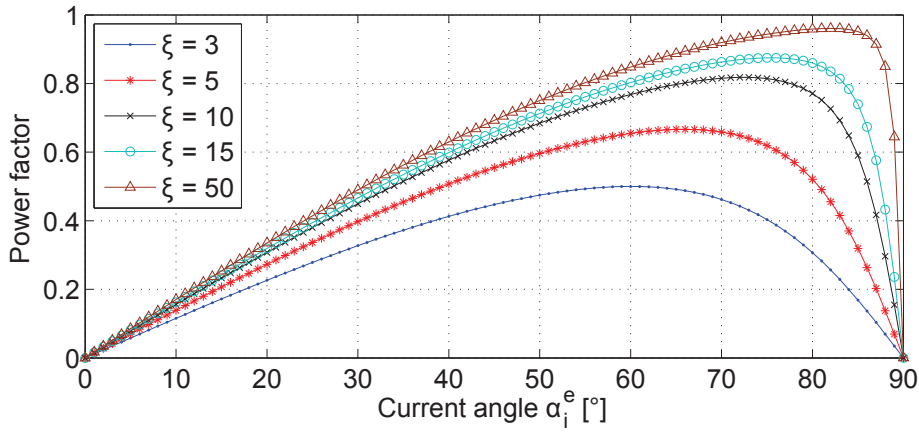


Figure 1.18: The power factor of a REL motor as a function of current angle at different saliency ratios.

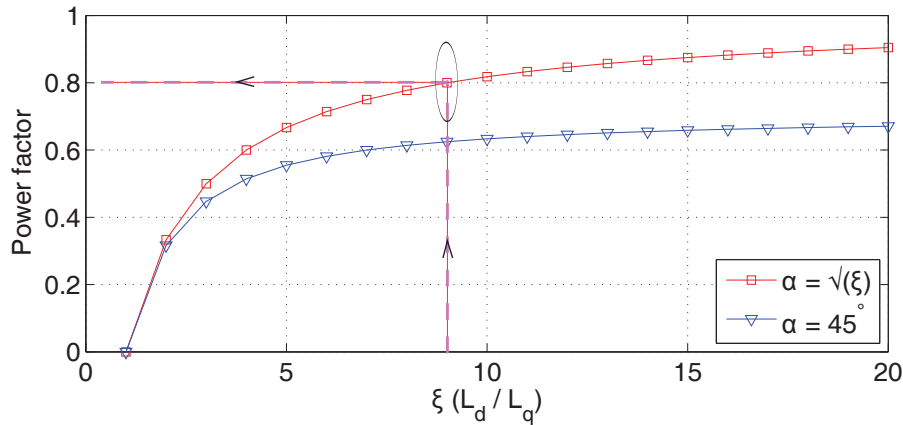


Figure 1.19: The Power factor versus the saliency ratio variation.

Fig. 1.18 and eq. (1.23), highlight the dependency of the power factor on the saliency ratio and the current angle. Practically, $\xi = 50$ cannot be achieved. In addition, Fig. 1.19 shows that the impact of ξ on the power factor is strongly reduced for $\xi > 10$. For each, ξ , the maximum

value of the power factor depends on the current angle, as shown in Fig. 1.18. The current angle, which gives the maximum power factor, is computed as

$$\frac{d \cos(\phi)}{d\alpha_i^e} = 0 \quad (1.24)$$

Hence, the power factor obtain its maximum at current angle equal to

$$\alpha_i^e = \tan^{-1}(\sqrt{\xi}) \quad i.e., \quad \frac{i_q}{i_d} = \sqrt{\frac{L_d}{L_q}} = \sqrt{\xi} \quad (1.25)$$

By substituting eq. (1.25) in eq. (1.23), the maximum power factor is given by

$$\cos(\phi) = \frac{\xi - 1}{\xi + 1} \quad (1.26)$$

Fig. 1.19 shows the power factor variation with ξ variation at two different current angles. One of them results the maximum power factor and the other one is equal to 45° . It is noted that, to achieve power factor equal to 0.8, $\xi = 9$ is sufficient for the maximum power factor curve and it is impossible to reach this value at the other power factor curve [6]. The effect of load angle variation on the power factor at different ξ is shown in Fig. 1.20.

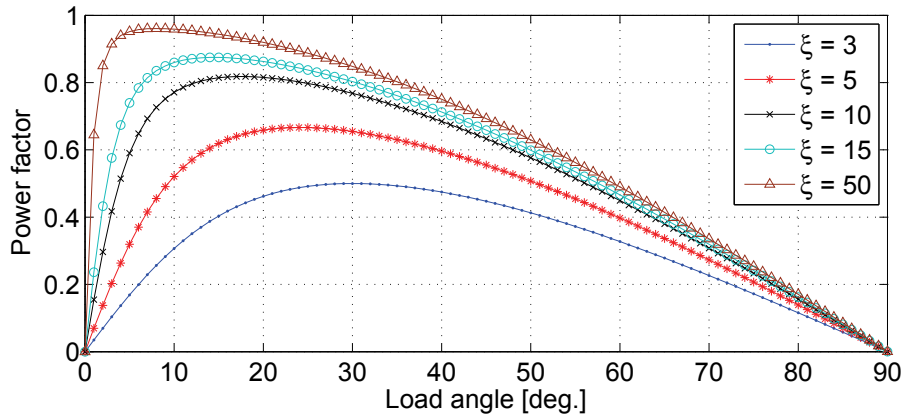


Figure 1.20: The power factor of a REL motor as a function of load angle at different saliency ratios.

1.4. Real behavior of the motor

All theoretical analyses shown in the previous section are based on the linear characteristic of λ_d and λ_q , as reported in eqs. (1.8) and (1.9). However, there are some nonlinearity results from the saturation, the cross saturation, and the stator slotting effect. Thus, λ_d and λ_q are expressed as a function of both i_d and i_q to include the saturation and cross saturation effect. In addition, the dependency on the rotor position θ is included in order to include the slotting effect. Therefore, the general expressions of λ_d and λ_q are

$$\begin{aligned} \lambda_d &= \lambda_d(i_d, i_q, \theta) \\ \lambda_q &= \lambda_q(i_d, i_q, \theta) \end{aligned} \quad (1.27)$$

1.4.1. Saturation effect

For a REL motor with actual B-H curve of the iron, the finite element analysis (FEA) is used to compute λ_d as a function of i_d ($\lambda_d(i_d)$) and λ_q as a function of i_q ($\lambda_q(i_q)$). Then, the saturation effect on both λ_d and λ_q can be studied, as shown in Fig. 1.21. It is noted that λ_d of the real model is always lower than that results from the linear model due to the saturation effect. In addition, λ_q is little bit reduced with i_q increasing. This means that the linear relation $\lambda_q = L_q i_q$ is valid with a little error. However, the cross saturation and slotting effect change this linear relation.

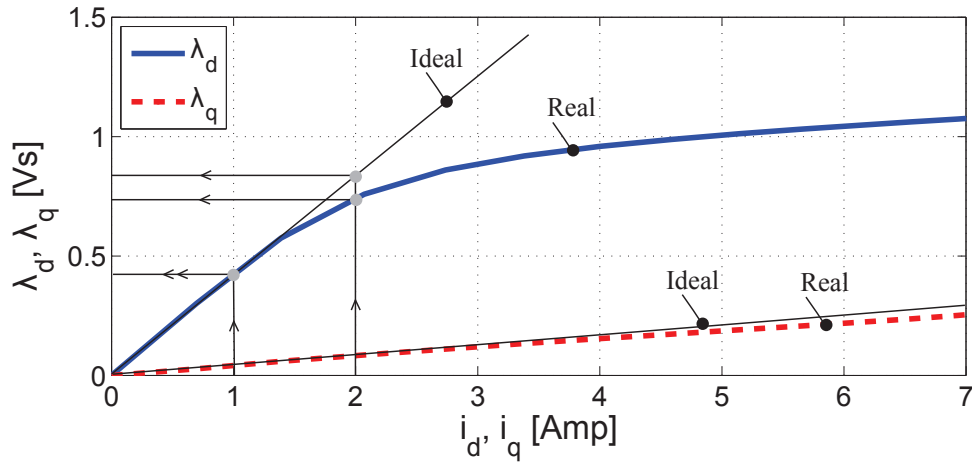


Figure 1.21: The magnetizing characteristic of d and q axes resulted from the FEA for a REL motor.

The magnetic saturation effect on the REL motor operating regions, i.e., MTPA and MTPV, is studied [1]. By comparing the linear model with the real model, as in Fig. 1.22, it is concluded that the saturation effect shifts the current angle of the maximum torque to a higher value. Once again, from Fig. 1.21, it is noted that λ_d is reduced due to the saturation. As a consequent, L_d is reduced, which yields to reduce the rotor saliency ratio ξ . From Fig. 1.22, it is noted that the current angle is increased to reduce i_d in order to compensate the reduction occurred in L_d .

From eq. (1.17), it is noted that, the maximum torque is achieved when the term $(1/L_q - 1/L_q) \sin(2 \tan^{-1}(\frac{1}{\xi} \tan(\alpha)))$ is maximized. There are three variables should be considered in this term, which are L_q , L_d , and α_i^e . By increasing the stator flux, the behavior of these variables under the saturation condition is: L_q is not so sensitive to this saturation, L_d is reduced, and, as a consequent, ξ is reduced. The current angle is reduced in order to compensate the decrease occurred in L_d or to minimize the term $1/L_d$, as shown in Fig. 1.23. This affects the MTPV of the machine.

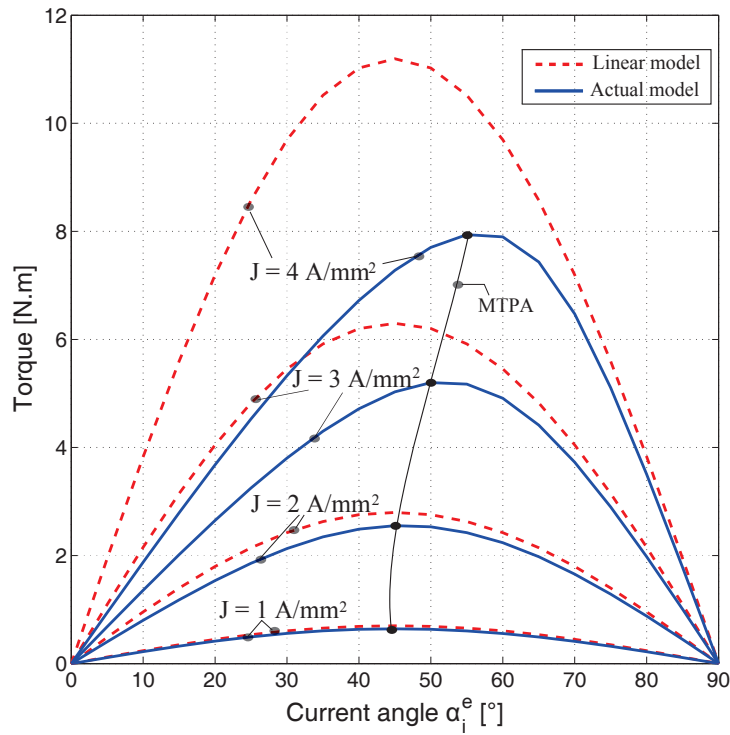


Figure 1.22: The impact of the saturation on the MTPA of a REL motor.

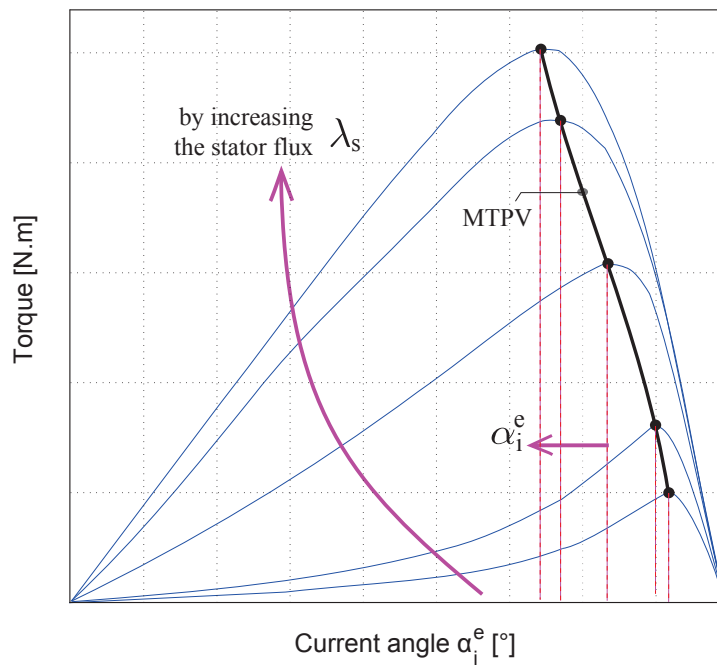


Figure 1.23: The impact of the saturation on the MTPV of a REL motor.

1.4.2. Cross saturation effect

The impact of the current in one axis of the d,q frame on the flux linkage of the another axis is called cross saturation effect. Indeed, the iron saturation of one axis depends on the respective

current and secondarily to the current of the other axis. So the flux linkage equation became:

$$\begin{aligned}\lambda_d &= \lambda_d(i_d, i_q) \\ \lambda_q &= \lambda_q(i_d, i_q)\end{aligned}\quad (1.28)$$

The cross saturation is mainly due to the shared iron parts between the d - and q - axes. In addition, the iron ribs increase this effect [1]. Fig. 1.24 shows the experimental measurements of λ_d and λ_q of real REL motor. It is noted that λ_d is reduced due to increasing i_q . In addition, λ_q is reduced by increasing i_d . The reduction of the L_d has a negative effect on the motor performance. It causes a reduction in the motor torque. The cross effect has to be considered specially, when the motor is controlled by a sensorless control technique [1, 21, 22].

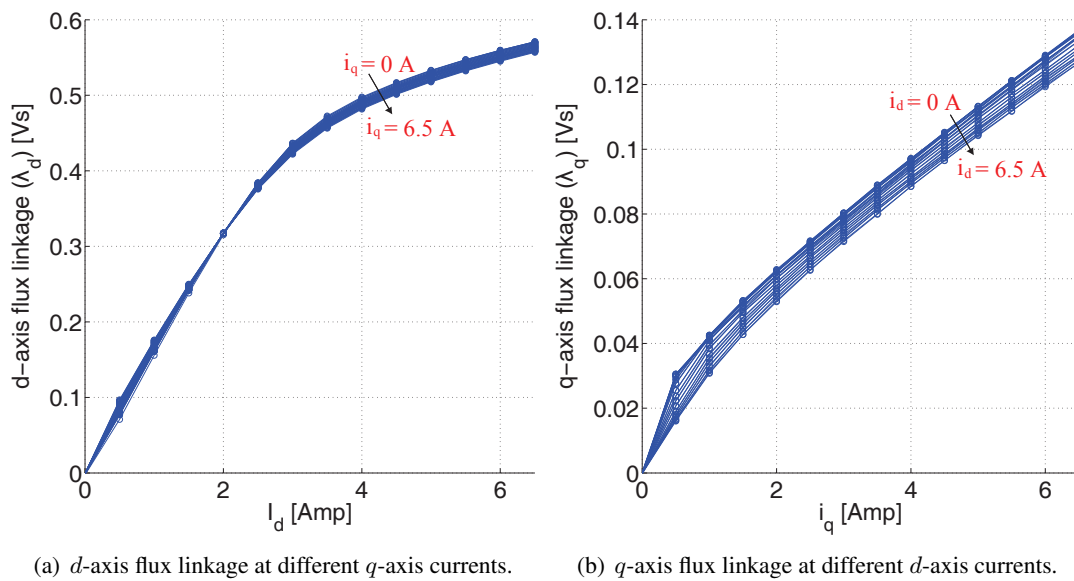


Figure 1.24: Real magnetic flux trajectory of a REL machine prototype.

1.4.3. Slotting effect

Due to the interaction between the stator teeth and the rotor segments during the rotor rotation, there are a variation of the inductances L_d and L_q . In addition, an interconnection effect between the two inductances L_{dq} is resulted [23]. For one stator slot pitch, there are three situations of the rotor segments with respect to the stator teeth, as follows

- when they are aligned, as shown in Fig. 1.25 (a),
- when they are in opposition, as shown in Fig. 1.25 (b),
- when the rotor segment is in intermediate position between the stator tooth and slot, as shown in Fig. 1.25 (c) and Fig. 1.25 (d).

For position (a), the magnetic reluctance is at its minimum value and therefore L_d is at maximum value. On the contrary, for position (b), the magnetic reluctance is at its maximum

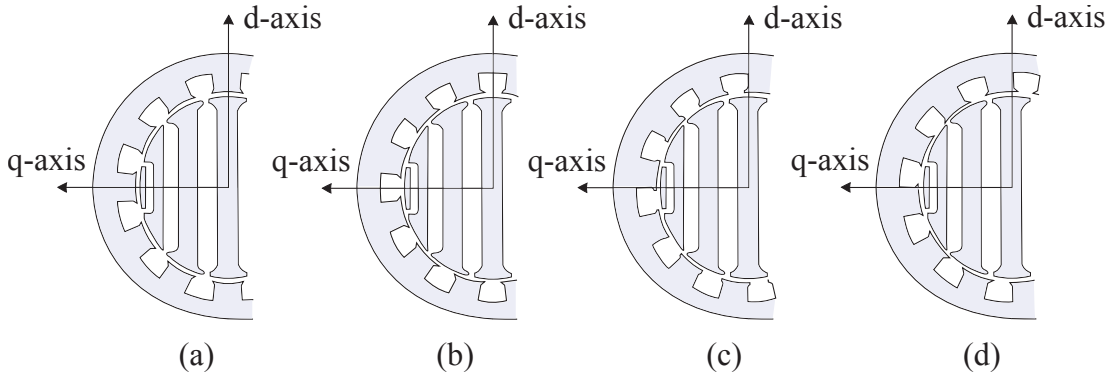


Figure 1.25: The different situations of the rotor segments with respect to the stator teeth during the rotor rotation.

value and L_d is at minimum value. As in [3, 23], there are similar behavior of L_q . On the other hand, for position (c), circulation flux paths are present, as produced by the difference in the stator and rotor magnetic potentials. These paths produces an additional contribution to another axis inductance, e.g, if the main flux is applied in d - axis, there are an additional contribution to L_q and vice versa [23]. This contribution depends on the rotor position.

Due to the dependency of L_d and L_q on the rotor position, the torque ripple is produced. There are some techniques proposed in the literature to reduce the torque ripple in synchronous REL machines [23–29]. In addition, high flux fluctuations in the rotor segments are generated, which leads to high iron losses in the rotor. Therefore, the slotting effect should be considered during the rotor design [30].

1.5. Operating regions

In general, the electric motor operating regions should be within the voltage and current limits of this motor. The voltage limit depends on the winding insulation limit. The maximum current is based on the thermal limit, which depends on the used cooling system. In addition, it depends on the demagnetization current limit, in case of permanent magnet motors. Moreover, the capacity of the electric drive has an impact on these limits.

To study the operating regions of the REL motor, the steady state condition is assumed. Therefore, all symbols can be expressed as capital letters. The voltage and current limits in the synchronous reference frame are expressed [31], as

$$U_d^2 + U_q^2 \leq U_N^2 \quad (1.29)$$

$$I_d^2 + I_q^2 \leq I_N^2 \quad (1.30)$$

where $U_N = \sqrt{\frac{2}{3}}U_{nominal}$ is the amplitude of the stator voltage space vector which is the peak value of the nominal phase voltage ($U_{nominal}/\sqrt{3}$). Besides, $I_N = \sqrt{2}I_{nominal}$ is the amplitude of the stator current space vector which is the peak value of the nominal phase current $I_{nominal}$. The star connection is considered for the stator windings in this study.

By neglecting the stator resistance in eqs. (1.6) and (1.7), the expression of U_d and U_q at steady state condition is

$$\begin{aligned} U_d &= -\omega_{me}L_qI_q \\ U_q &= \omega_{me}L_dI_d \end{aligned} \quad (1.31)$$

By substituting eq. (1.31) in eq. (1.29), the voltage limit can be expressed as function of the stator current, as

$$(\omega_{me}L_qI_q)^2 + (\omega_{me}L_dI_d)^2 \leq U_N^2 \quad (1.32)$$

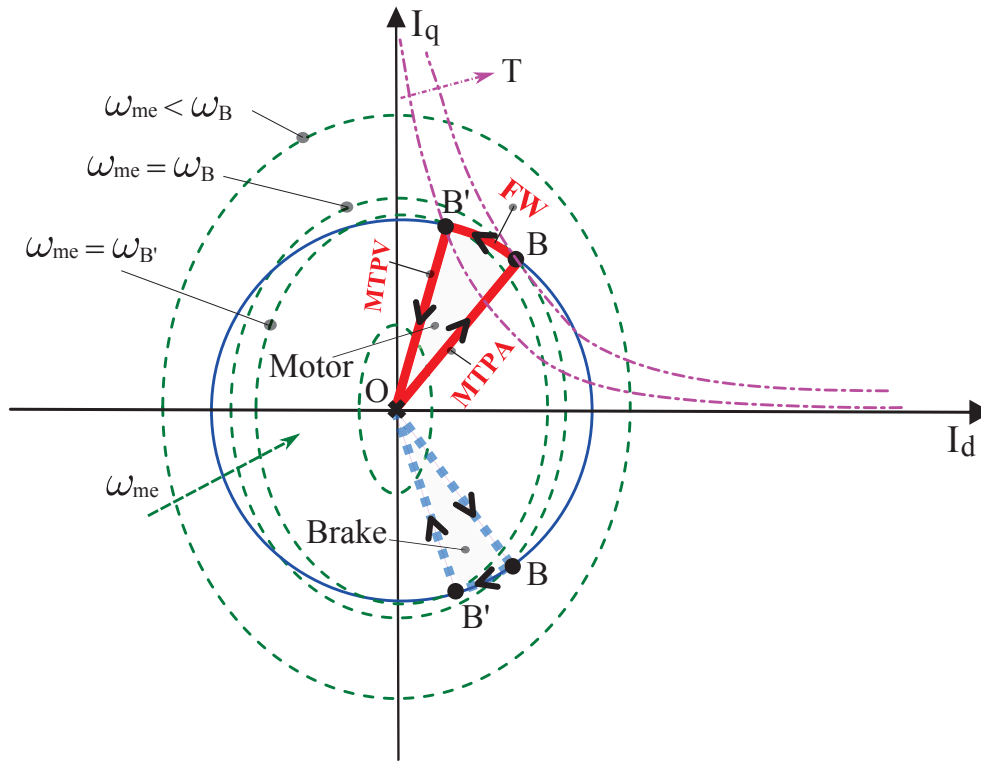


Figure 1.26: Operating limits and working points of a REL motor.

From eq. (1.30), the current limit is presented as a circle with a radius equal to I_N , as shown in Fig. 1.26. From eq. (1.32), the voltage limit is reached at the base speed ω_B . It is presented as an ellipse, as shown in Fig. 1.26. From eq. (1.16), the torque loci in the synchronous rotating frame, is presented by a family of hyperboles with asymptotes locate in the $d-$ axis and $q-$ axis, as shown in Fig. 1.26. The REL motor runs in three different control regions as follows:

Region I (Constant torque region): Below the base speed (ω_B), it is possible to produce the maximum torque satisfying the voltage and current constrains by applying MTPA control. The maximum available torque obtained by the MTPA control T_N is achieved at the base speed, when the torque hyperbole tangent to the current circle limit (at Point B , in Fig. 1.26). From

eqs. (1.30) and (1.32), the base speed can be computed as

$$\omega_B = \frac{\sqrt{2}U_N}{I_N\sqrt{L_d^2 + L_q^2}} \quad (1.33)$$

Region II (Constant volt-ampere region, flux weakening): Above the base speed, the current vector controlled by flux weakening (FW) control. Since, the voltage is kept constant and the speed increases, according to $v = \omega_{me}\lambda$, the flux is reduced. By increasing the current angle, off course, the d -axis current (I_d) is reduced and the q -axis current (I_q) is increased. According to Fig. 1.21, the flux linkages in both d and q axes are changed due to the change of I_d and I_q . However, the reduction of the flux linkage λ_d is more than the increase of the λ_q , and hence, the total flux is reduced and the flux weakening is achieved. By changing the current angle, the current vector trajectory moves along the current limit circle up to speed $\omega_{B'}$, as shown in Fig. 1.26.

Region III (Decreasing volt-ampere region, flux weakening): From Fig. 1.26, the motor speed $\omega_{B'}$ is achieved, when the current limit circle intersect with the MTPV trajectory. Then, for speeds above $\omega_{B'}$, the optimum current vector is achieved by applying the MTPV control, as shown in Fig. 1.26.

Fig. 1.27 shows the electromagnetic torque versus the motor speed. In addition, the three operating regions mentioned above are highlighted.

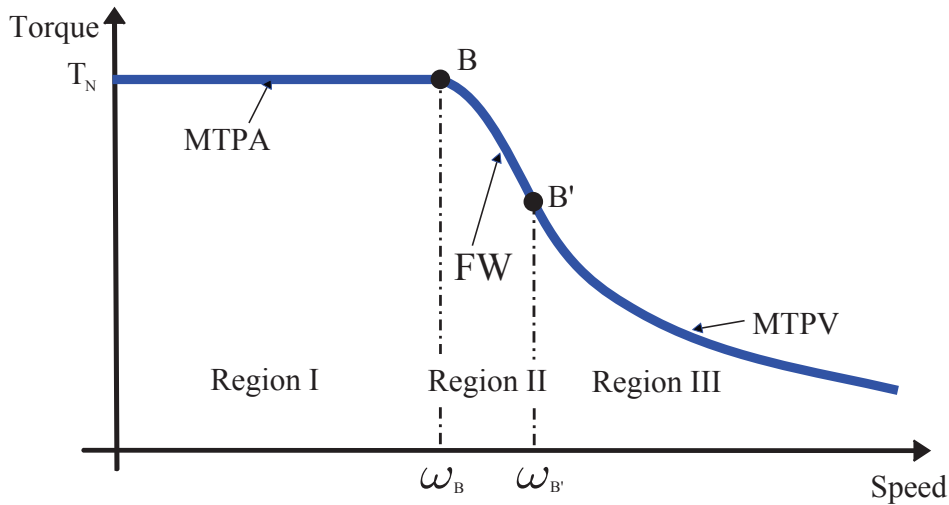


Figure 1.27: Torque versus speed for a REL motor.

Part I

Linear Analytical Computation

Analytical model of concentric REL motor

This chapter describes the analytical model of the concentric REL machine. This model is based on a lumped-parameter magnetic network. The aim of the model is to compute the air-gap flux density distribution for different rotor positions, determine the electromagnetic torque and the torque ripple of the machine, and finally estimate the rotor iron losses. The model is presented for REL machine with one, two, and three flux barriers per rotor pole.

2.1. Stator electric loading

The conventional stator, with distributed windings, is replaced by an equivalent conductive sheet with infinitesimal thickness. This sheet is placed in the inner surface of the stator. The actual distribution of the slots coils are presented by a conductor density distribution function ($n_d(\theta_s)$) along this sheet. Starting from one coil with single-turn, as shown in Fig.2.1, the conductor density distribution function can be derived.

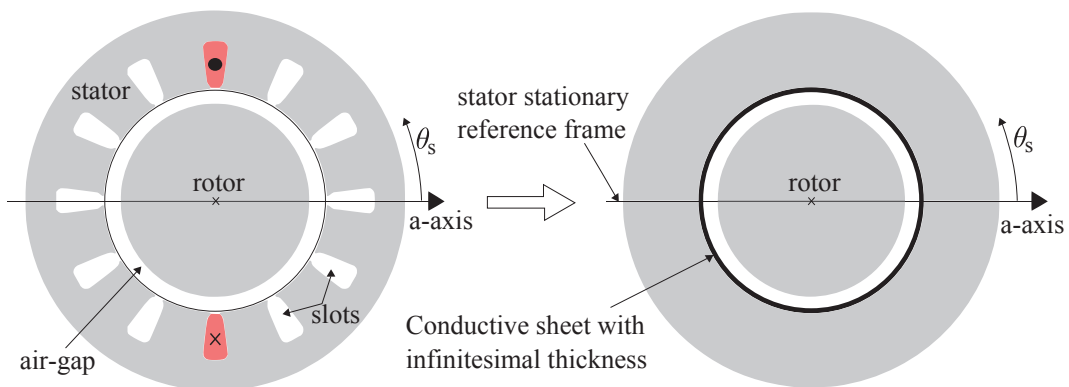


Figure 2.1: Cross section of the stator windings and its conductor density distribution.

From Fig.2.1, the relative conductor distribution function plot is drawn, as shown in Fig.2.2.

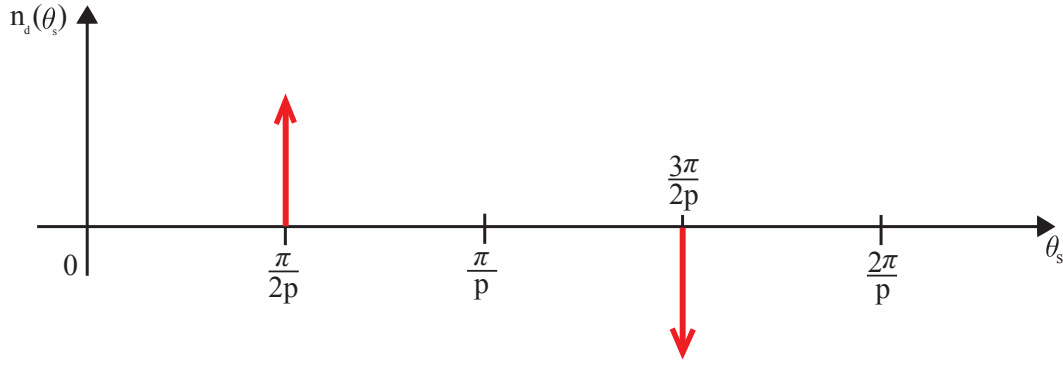


Figure 2.2: The conductor distribution function corresponding to the stator windings shown in Fig.2.1.

It can be expressed as

$$n_d(\theta_s) = \hat{n} \left\{ \delta\left(\theta_s - \frac{\pi}{2p}\right) - \delta\left(\theta_s - \frac{\pi}{2p} - \frac{\pi}{p}\right) \right\} \quad (2.1)$$

where θ_s is the coordinate angle (mechanical degrees), in the stator stationary reference frame, as shown in Fig.2.3. $\delta(\cdot)$ is the Dirac delta impulse. \hat{n} is the amplitude of the impulse function. It can be computed by integrating $n_d(\theta_s)$ for semi period. From Fig.2.2, this integration has to result one conductor. Then \hat{n} is computed as

$$\int_0^{\frac{\pi}{p}} n_d(\theta_s) \frac{D}{2} d\theta_s = \int_0^{\frac{\pi}{p}} \hat{n} \delta\left(\theta_s - \frac{\pi}{2p}\right) \frac{D}{2} d\theta_s = 1 \Rightarrow \hat{n} = \frac{2}{D} \quad (2.2)$$

where D is the inner diameter of the stator. As a consequent, $n_d(\theta_s)$ is given by

$$n_d(\theta_s) = \frac{2}{D} \left\{ \delta\left(\theta_s - \frac{\pi}{2p}\right) - \delta\left(\theta_s - \frac{3\pi}{2p}\right) \right\}, \quad \theta_s \in \left[0, \frac{2\pi}{p}\right] \quad (2.3)$$

where 2 presents the number of conductor per pole pair. In addition, the previous expression presents $n_d(\theta_s)$ for the first pole only. Therefore, it has to be repeated through the following operator.

$$Per_T\{f(t)\} = \sum_{\nu=-\infty}^{\nu=+\infty} f(t - \nu T) \quad (2.4)$$

Then

$$n_d(\theta_s) = \frac{2}{D} Per_{\frac{2\pi}{p}} \left\{ \delta\left(\theta_s - \frac{\pi}{2p}\right) - \delta\left(\theta_s - \frac{3\pi}{2p}\right) \right\} \quad (2.5)$$

From eq. (2.5) and Fig.2.2, it is noted that $n_d(\theta_s)$ is a periodic function, odd, and has half-wave symmetry. Thus, its Fourier series coefficients are given by

$$b_\nu = \frac{2p}{2\pi} \int_0^{\frac{2\pi}{p}} n_d(\theta_s) \sin(\nu\theta_s) d\theta_s = \frac{2p}{\pi} \int_0^{\frac{\pi}{p}} \frac{2}{D} \delta\left(\theta_s - \frac{\pi}{2p}\right) \sin(\nu\theta_s) d\theta_s = \frac{4p}{\pi D} \sin\left(\nu \frac{\pi}{2p}\right) \quad (2.6)$$

where ν is the mechanical space harmonic order. By replacing $2p$ by the number of series conductors per phase (N_s) and introducing the winding factor ($k_w^{\nu^e}$), the series of conductor distribution function per phase is

$$n_d(\theta_s) = \frac{2}{\pi D} N_s \sum_{\nu^e=1}^{+\infty} k_w^{\nu^e} \sin\left(\frac{\nu^e \pi}{2}\right) \sin(\nu^e p \theta_s) \quad (2.7)$$

where ν^e is the electrical space harmonic order. For three phase winding, with an integer number of slots per pole per phase (q), ν^e can be expressed as $6k+1$, where $k = 0; \pm 1; \pm 2; \pm 3; \dots$, [20]. The previous conductor density distribution function can be written for the three phases of the stator windings as follows

$$n_{da}(\theta_s) = \frac{2}{\pi D} N_s \sum_{\nu^e=1}^{+\infty} k_w^{\nu^e} \sin\left(\frac{\nu^e \pi}{2}\right) \sin(\nu^e p \theta_s) \quad (2.8)$$

$$n_{db}(\theta_s) = \frac{2}{\pi D} N_s \sum_{\nu^e=1}^{+\infty} k_w^{\nu^e} \sin\left(\frac{\nu^e \pi}{2}\right) \sin\left(\nu^e \left(p \theta_s - \frac{2\pi}{3}\right)\right) \quad (2.9)$$

$$n_{dc}(\theta_s) = \frac{2}{\pi D} N_s \sum_{\nu^e=1}^{+\infty} k_w^{\nu^e} \sin\left(\frac{\nu^e \pi}{2}\right) \sin\left(\nu^e \left(p \theta_s - \frac{4\pi}{3}\right)\right) \quad (2.10)$$

Since the current-control drive feeds the REL motor, the currents are synchronized with the rotor position θ_m [32]. They can be expressed as

$$i_a(\theta_m) = \hat{I} \cos(p\theta_m + \alpha_i^e) \quad (2.11)$$

$$i_b(\theta_m) = \hat{I} \cos\left(p\theta_m + \alpha_i^e - \frac{2\pi}{3}\right) \quad (2.12)$$

$$i_c(\theta_m) = \hat{I} \cos\left(p\theta_m + \alpha_i^e - \frac{4\pi}{3}\right) \quad (2.13)$$

Hence, the linear current density distribution is computed as

$$\begin{aligned} K_s(\theta_s) &= n_{da}(\theta_s)i_a(\theta_m) + n_{db}(\theta_s)i_b(\theta_m) + n_{dc}(\theta_s)i_c(\theta_m) \\ &= \frac{2}{\pi D} N_s \hat{I} \sum_{\nu^e=1}^{+\infty} \sin\left(\frac{\nu^e \pi}{2}\right) k_w^{\nu^e} \left[\sin(\nu^e p \theta_s) \cos(p\theta_m + \alpha_i^e) + \right. \\ &\quad \left. \sin\left(\nu^e \left(p \theta_s - \frac{2\pi}{3}\right)\right) \cos\left(p\theta_m + \alpha_i^e - \frac{2\pi}{3}\right) + \right. \\ &\quad \left. \sin\left(\nu^e \left(p \theta_s - \frac{4\pi}{3}\right)\right) \cos\left(p\theta_m + \alpha_i^e - \frac{4\pi}{3}\right) \right] \end{aligned} \quad (2.14)$$

so that

$$K_s(\theta_s) = \sum_{\nu^e=1}^{+\infty} \hat{K}_{s\nu^e} \sin(\nu^e p \theta_s - p \theta_m - \alpha_i^e) \quad (2.15)$$

where $\hat{K}_{s\nu^e}$ is given by

$$\hat{K}_{s\nu^e} = \frac{3N_s \hat{I} k_w^{\nu^e}}{\pi D} \sin\left(\frac{\nu^e \pi}{2}\right) \quad (2.16)$$

From eq. (2.15), it is noted that $K_s(\theta_s)$ is a series of rotating waveforms. When $\nu^e = p$, the distribution moves synchronously with the rotor, whereas for different values of ν^e , the waveforms move asynchronously with the rotor. The linear current density reported in eq. (2.15) is called the electric loading of the machine.

2.2. Stator magnetic potential

By integrating the electric loading, the stator scalar magnetic potential referring to the stator reference frame, is given by

$$U_s(\theta_s) = \int K_s(\theta_s) \frac{D}{2} d\theta_s \quad (2.17)$$

By substituting eq. (2.15) in eq. (2.17), it results

$$U_s(\theta_s) = -\frac{D}{2} \sum_{\nu^e=1}^{+\infty} \frac{\hat{K}_{s\nu^e}}{p\nu^e} \cos(\nu^e p\theta_s - p\theta_m - \alpha_i^e) \quad (2.18)$$

The synchronous or d,q reference frame and the stationary reference frame are highlighted in Fig.2.3. The two reference frames are linked together by the following equation

$$\theta_s = \theta_m + \theta_r \quad (2.19)$$

where θ_m refers to the rotor position or the angle between the rotating d-q reference frame and the stationary frame (mechanical degrees) and θ_r is the coordinate angle (mechanical degrees), in the rotating d-q reference frame. Thus, the electric loading and the scalar magnetic potential of the stator can be expressed in the d,q frame as

$$K_s(\theta_r) = \sum_{\nu^e=1}^{+\infty} \hat{K}_{s\nu^e} \sin(\nu^e p\theta_r - (\nu^e - 1)\omega_{me}t - \alpha_i^e) \quad (2.20)$$

$$U_s(\theta_r) = -\frac{D}{2} \sum_{\nu^e=1}^{+\infty} \frac{\hat{K}_{s\nu^e}}{p\nu^e} \cos(\nu^e p\theta_r - (\nu^e - 1)\omega_{me}t - \alpha_i^e) \quad (2.21)$$

At steady state the rotor position is linked to the its speed by $\omega_{me} = p\theta_m$. Both $K_s(\theta_r)$ and $U_s(\theta_r)$ of the fundamental harmonic are highlighted in Fig.2.3.

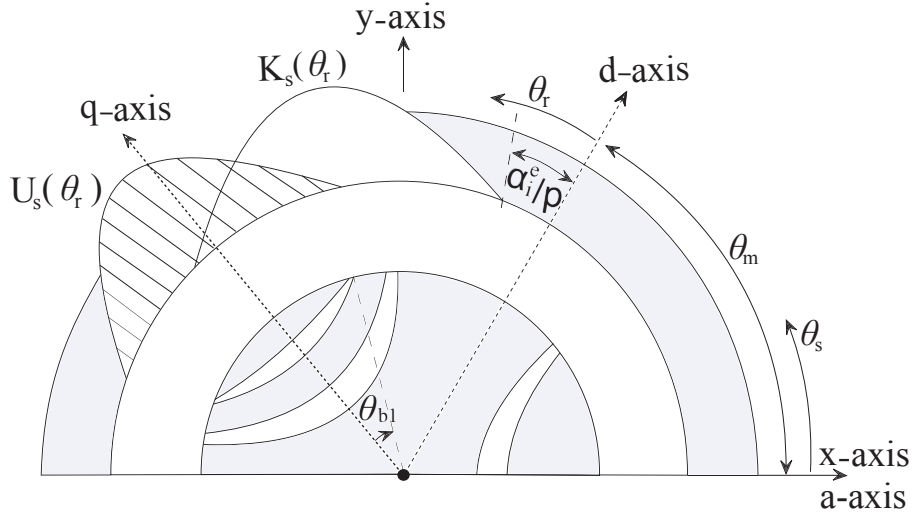


Figure 2.3: Distribution of $K_s(\theta_s)$ and $U_s(\theta_s)$ in different reference frames. Only the fundamental harmonics are represented. All angles are in mechanical degrees.

2.3. The air-gap flux density

Due to the stator magnetic potential, the magnetic flux flows through the rotor. As a consequent, the rotor islands assume magnetic potential proportional to the magnetic reluctance of each flux-barrier and the flux following through it. The distributions of the magnetic potential of both stator and rotor are reported in Fig.2.4. By neglecting the magnetic saturation occurs in the stator and rotor iron (i.e., $\mu_{iron} = \infty$), the air gap magnetic flux density is computed as

$$B_g(\theta_r) = \mu_o \frac{-U_s(\theta_r) + U_r(\theta_r)}{g} \quad (2.22)$$

where μ_o is the free space permeability, g is the air-gap length, and $U_r(\theta_r)$ is the rotor scalar magnetic potential.

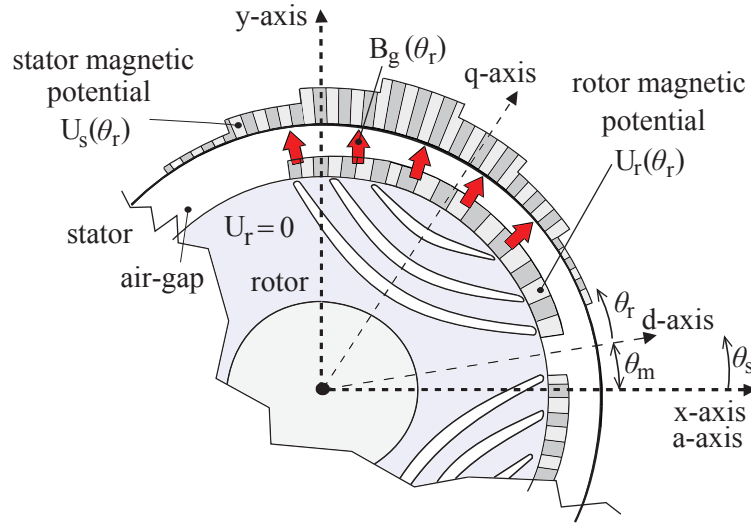


Figure 2.4: Rotor magnetic reaction and air-gap flux density.

2.4. Rotor magnetic potential

2.4.1. One flux barrier per pole

Fig.2.5 shows the linearized geometry of one rotor pole of a REL machine and its corresponding lumped magnetic network. The scalar magnetic potential of the rotor island bordered by the flux-barrier, as shown in Fig. 2.5 (a), can be considered as a constant and null elsewhere (i.e., is null at the rotor channels shown in Fig. 2.5 (a)).

In Fig. 2.5 (a), θ_{b1} is the half of the flux barrier ends angle. From Fig. 2.5 (b), R_{g1} refers to the magnetic reluctance of the air gap over the rotor island and R_{g2} and R_{g3} refer to the reluctance of the remainder air-gap over the pole ends or channels. In addition, R_{b1} refers to the magnetic reluctance of the flux-barrier. It is given by $R_{b1} = t_{b1}/(\mu_o l_{b1} L_{stk})$. From the magnetic network, the scalar magnetic potential of the rotor island (U_{r1}) can be computed as

$$U_{ri} = \phi_{bi} R_{bi} \quad (2.23)$$

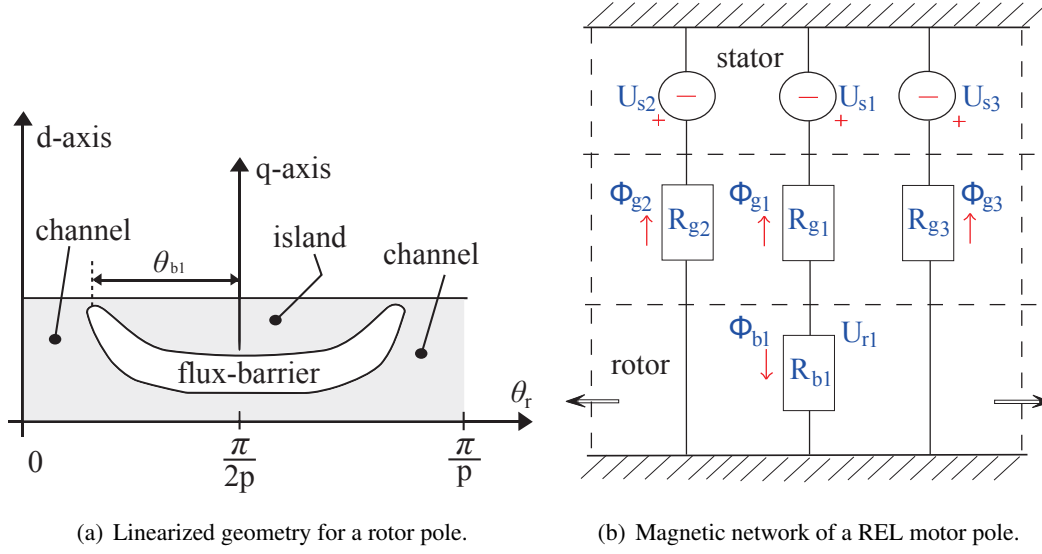


Figure 2.5: REL machine with one flux-barrier per pole.

where the subscript "i" refers to the rank of the flux barrier in case of multiple barriers per pole (for one barrier per pole, $i = 1$). ϕ_{b1} is the magnetic flux flowing through the flux-barrier. It is given by

$$\phi_{b1} = \int_{\frac{\pi}{2p} - \theta_{b1}}^{\frac{\pi}{2p} + \theta_{b1}} -B_g(\theta_r) L_{stk} \frac{D}{2} d\theta_r = \int_{\frac{\pi}{2p} - \theta_{b1}}^{\frac{\pi}{2p} + \theta_{b1}} \mu_o \frac{U_s(\theta_r) - U_{r1}}{g} L_{stk} \frac{D}{2} d\theta_r \quad (2.24)$$

where L_{stk} is the stack length of the motor. By substituting eq. (2.24) in eq. (2.23), U_{r1} is computed as

$$U_{r1} = \frac{t_{b1}}{\mu_o L_{stk} l_{b1}} \int_{\frac{\pi}{2p} - \theta_{b1}}^{\frac{\pi}{2p} + \theta_{b1}} \mu_o \frac{U_s(\theta_r) - U_{r1}}{g} L_{stk} \frac{D}{2} d\theta_r = \frac{Dt_{b1}}{2gl_{b1}} \int_{\frac{\pi}{2p} - \theta_{b1}}^{\frac{\pi}{2p} + \theta_{b1}} (U_s(\theta_r) - U_{r1}) d\theta_r \quad (2.25)$$

then,

$$U_{r1} \left[1 + \frac{Dt_{b1}}{2gl_{b1}} (2\theta_{b1}) \right] = \frac{Dt_{b1}}{2gl_{b1}} \int_{\frac{\pi}{2p} - \theta_{b1}}^{\frac{\pi}{2p} + \theta_{b1}} U_s(\theta_r) d\theta_r = a \int_{\frac{\pi}{2p} - \theta_{b1}}^{\frac{\pi}{2p} + \theta_{b1}} U_s(\theta_r) d\theta_r \quad (2.26)$$

where the dimensionless coefficient a depends on the geometrical data of the rotor and the air-gap length and is given by

$$a = \frac{\frac{Dt_{b1}}{2gl_{b1}}}{1 + \frac{Dt_{b1}}{gl_{b1}} (\theta_{b1})} \quad (2.27)$$

Finally, U_{r1} is given by

$$\begin{aligned} U_{r1} &= -aD \sum_{\nu^e} \frac{\hat{K}_{\nu^e}}{(\nu^e \pi)^2} \cos \left(\frac{\nu^e p}{2} + (\nu^e - 1) \omega_{me} t - \alpha_i^e \right) \sin(\nu^e p \theta_{b1}) \\ &= -aD \sum_{\nu^e} \frac{\hat{K}_{\nu^e}}{(\nu^e p)^2} \cos(\lambda_{\nu^e}) \cdot \sin(\nu^e p \theta_{b1}) \end{aligned} \quad (2.28)$$

where λ_{ν^e} is expressed as

$$\lambda_{\nu^e} = \frac{\nu^e \pi}{2} + (\nu^e - 1)\omega_{me}t - \alpha_i^e \quad (2.29)$$

2.4.2. Two flux barriers per pole

Analogously, for REL motor with two flux-barriers per pole, the magnetic potential of the rotor islands can be derived. The linear geometry of a rotor pole is shown in Fig. 2.6 (a). The magnetic network presents one pole of the machine is shown in Fig. 2.6 (b). The subscript "1" is used for the outer island, and the subscript "2" is used for the inner island.

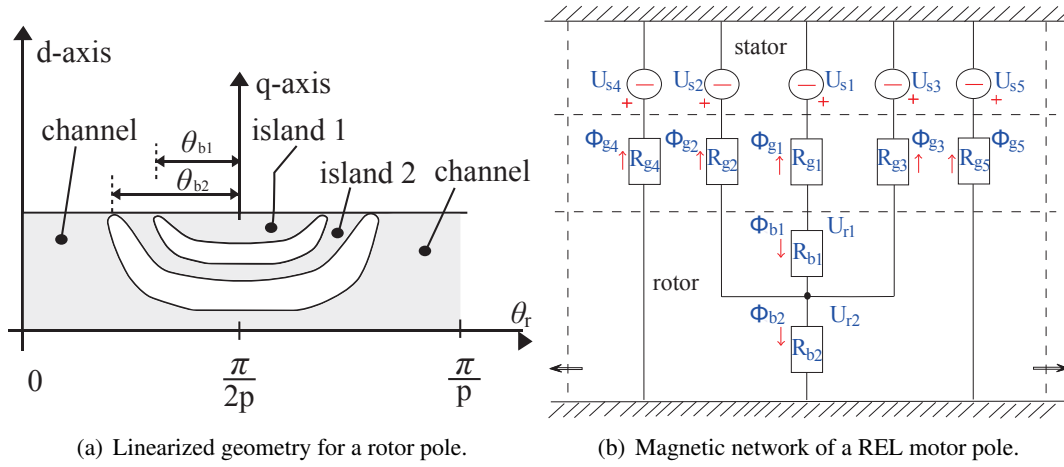


Figure 2.6: REL machine with two flux-barriers per pole.

From the magnetic network, the scalar magnetic potential of the first island (U_{r1}) is computed as

$$\begin{aligned} U_{r1} &= \phi_{b1} R_{b1} + U_{r2} \\ &= \left[\int_{\frac{\pi}{2p} - \theta_{b1}}^{\frac{\pi}{2p} + \theta_{b1}} \mu_o \frac{U_s(\theta_r) - U_{r1}}{g} L_{stk} \frac{D}{2} d\theta_r \right] \frac{t_{b1}}{\mu_o L_{stk} l_{b1}} + U_{r2} \\ &= \frac{Dt_{b1}}{2gl_{b1}} \left[\int_{\frac{\pi}{2p} - \theta_{b1}}^{\frac{\pi}{2p} + \theta_{b1}} (U_s(\theta_r) - U_{r1}) d\theta_r \right] + U_{r2} \end{aligned} \quad (2.30)$$

then from

$$U_{r1} \left[1 + \frac{Dt_{b1}}{2gl_{b1}} 2\theta_{b1} \right] = \frac{Dt_{b1}}{2gl_{b1}} \int_{\frac{\pi}{2p} - \theta_{b1}}^{\frac{\pi}{2p} + \theta_{b1}} U_s(\theta_r) d\theta_r + U_{r2} \quad (2.31)$$

It is possible to express the magnetic potential of the outer island as

$$U_{r1} = a \int_{\frac{\pi}{2p} - \theta_{b1}}^{\frac{\pi}{2p} + \theta_{b1}} U_s(\theta_r) d\theta_r + bU_{r2} \quad (2.32)$$

where the dimensionless coefficient b is given by

$$b = \frac{1}{1 + \frac{Dt_{b1}}{gl_{b1}} \theta_{b1}} \quad (2.33)$$

and U_{r2} is the scalar magnetic potential of the inner island. From the magnetic network, it is given by

$$U_{r2} = \phi_{b2} R_{b2} \quad (2.34)$$

By substituting $\phi_{b2} = \phi_{b1} - \phi_{g2} - \phi_{g3}$ in eq. (2.34), U_{r2} is computed as

$$U_{r2} = \left[\phi_{b1} + \int_{\frac{\pi}{2p}-\theta_{b2}}^{\frac{\pi}{2p}-\theta_{b1}} \mu_o \frac{U_s(\theta_r) - U_{r2}}{g} L_{stk} \frac{D}{2} d\theta_r + \int_{\frac{\pi}{2p}+\theta_{b1}}^{\frac{\pi}{2p}+\theta_{b2}} \mu_o \frac{U_s(\theta_r) - U_{r2}}{g} L_{stk} \frac{D}{2} d\theta_r \right] \frac{t_{b2}}{\mu_o L_{stk} l_{b2}} \quad (2.35)$$

Substituting $\phi_{b1} = (U_{r1} - U_{r2})/R_{b1}$ in eq. (2.35), it results

$$\begin{aligned} U_{r2} &= \left[\frac{U_{r1} - U_{r2}}{\frac{t_{b1}}{l_{b1}}} + \int_{\frac{\pi}{2p}-\theta_{b2}}^{\frac{\pi}{2p}-\theta_{b1}} \frac{U_s(\theta_r) - U_{r2}}{g} \frac{D}{2} d\theta_r + \int_{\frac{\pi}{2p}+\theta_{b1}}^{\frac{\pi}{2p}+\theta_{b2}} \frac{U_s(\theta_r) - U_{r2}}{g} \frac{D}{2} d\theta_r \right] \frac{t_{b2}}{l_{b2}} \\ &= \frac{l_{b1} t_{b2}}{t_{b1} l_{b2}} \left[a \int_{\frac{\pi}{2p}-\theta_{b1}}^{\frac{\pi}{2p}+\theta_{b1}} U_s(\theta_r) d\theta_r + b U_{r2} \right] - \frac{l_{b1} t_{b2}}{t_{b1} l_{b2}} U_{r2} - \frac{D t_{b2}}{g l_{b2}} U_{r2} (\theta_{b2} - \theta_{b1}) \\ &+ \frac{D t_{b2}}{2 g l_{b2}} \left[\int_{\frac{\pi}{2p}-\theta_{b2}}^{\frac{\pi}{2p}-\theta_{b1}} U_s(\theta_r) d\theta_r + \int_{\frac{\pi}{2p}+\theta_{b1}}^{\frac{\pi}{2p}+\theta_{b2}} U_s(\theta_r) d\theta_r \right] \end{aligned} \quad (2.36)$$

and hence,

$$\begin{aligned} U_{r2} \left[1 - (b-1) \frac{l_{b1} t_{b2}}{t_{b1} l_{b2}} + \frac{D t_{b2}}{g l_{b2}} (\theta_{b2} - \theta_{b1}) \right] &= \\ a \frac{t_{b2} l_{b1}}{l_{b2} t_{b1}} \int_{\frac{\pi}{2p}-\theta_{b1}}^{\frac{\pi}{2p}+\theta_{b1}} U_s(\theta_r) d\theta_r + \frac{D t_{b2}}{2 g l_{b2}} \left[\int_{\frac{\pi}{2p}-\theta_{b2}}^{\frac{\pi}{2p}-\theta_{b1}} U_s(\theta_r) d\theta_r + \int_{\frac{\pi}{2p}+\theta_{b1}}^{\frac{\pi}{2p}+\theta_{b2}} U_s(\theta_r) d\theta_r \right] \end{aligned} \quad (2.37)$$

Consequently, U_{r2} can be expressed as

$$\begin{aligned} U_{r2} &= c \underbrace{\int_{\frac{\pi}{2p}-\theta_{b1}}^{\frac{\pi}{2p}+\theta_{b1}} U_s(\theta_r) d\theta_r}_{S_1} + d \left\{ \underbrace{\int_{\frac{\pi}{2p}-\theta_{b2}}^{\frac{\pi}{2p}-\theta_{b1}} U_s(\theta_r) d\theta_r + \int_{\frac{\pi}{2p}+\theta_{b1}}^{\frac{\pi}{2p}+\theta_{b2}} U_s(\theta_r) d\theta_r}_{S_2} \right\} \\ &= c S_1 + d S_2 \end{aligned} \quad (2.38)$$

where the coefficients c and d are given by

$$c = \frac{a \frac{t_{b2} l_{b1}}{l_{b2} t_{b1}}}{1 - \frac{t_{b2} l_{b1}}{l_{b2} t_{b1}} (b-1) + \frac{D t_{b2}}{g l_{b2}} (\theta_{b2} - \theta_{b1})} \quad (2.39)$$

$$d = \frac{\frac{D t_{b2}}{2 g l_{b2}}}{1 - \frac{t_{b2} l_{b1}}{l_{b2} t_{b1}} (b-1) + \frac{D t_{b2}}{g l_{b2}} (\theta_{b2} - \theta_{b1})} \quad (2.40)$$

The integration S_1 and S_2 reported in eq. (2.38) are solved. Then, their solutions are reported as

$$S_1 = \sum_{\nu^e} -\frac{\hat{K}_{\nu^e}}{(\nu^e p)^2} D \cos(\lambda_{\nu^e}) \cdot \sin(\nu^e p \theta_{b1}) \quad (2.41)$$

$$S_2 = \sum_{\nu^e} -\frac{\hat{K}_{\nu^e}}{(\nu^e p)^2} D \cos(\lambda_{\nu^e}) [\sin(\nu^e p \theta_{b2}) - \sin(\nu^e p \theta_{b1})] \quad (2.42)$$

By substituting eqs. (2.41) and (2.42) in eq. (2.38), U_{r2} is resulted as

$$U_{r2} = \sum_{\nu^e} -\frac{\hat{K}_{\nu^e}}{(\nu^e p)^2} D \rho_2 \cos(\lambda_{\nu^e}) \quad (2.43)$$

Again, by substituting eq. (2.43) in eq. (2.32), U_{r1} is achieved as

$$U_{r1} = \sum_{\nu^e} -\frac{\hat{K}_{\nu^e}}{(\nu^e p)^2} D \rho_1 \cos(\lambda_{\nu^e}) \quad (2.44)$$

where the coefficients ρ_1 and ρ_2 are given by

$$\rho_1 = (a + b(c - d)) \sin(\nu^e p \theta_{b1}) + bd \sin(\nu^e p \theta_{b2}) \quad (2.45)$$

$$\rho_2 = (c - d) \sin(\nu^e p \theta_{b1}) + d \sin(\nu^e p \theta_{b2}) \quad (2.46)$$

2.4.3. Three flux barriers per pole

Once again, the linearized geometry of one pole of a REL motor with three flux-barriers and its corresponding equivalent magnetic network are shown in Fig. 2.7. From the magnetic network, it is noted that U_{r1} can be expressed as in eq. (2.32). In addition, U_{r2} is computed as

$$U_{r2} = \phi_{b2} R_{b2} + U_{r3} \quad (2.47)$$

The simplification of the previous expression is similar to that carried out in case of two flux-barriers per pole, as in eqs. (2.35) to (2.38). However, an additional term (U_{r3}) is added to the derivation. Hence, U_{r2} can be expressed as

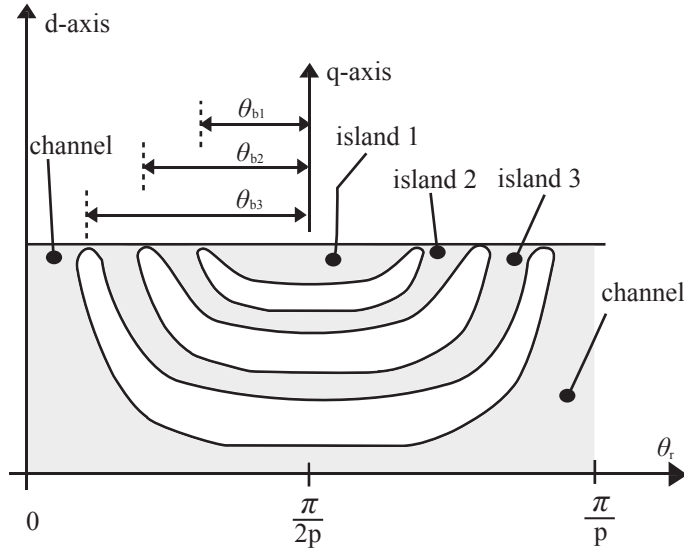
$$U_{r2} = c \underbrace{\int_{\frac{\pi}{2p} - \theta_{b1}}^{\frac{\pi}{2p} + \theta_{b1}} U_s(\theta_r) d\theta_r}_{S_1} + d \left\{ \underbrace{\int_{\frac{\pi}{2p} - \theta_{b2}}^{\frac{\pi}{2p} - \theta_{b1}} U_s(\theta_r) d\theta_r + \int_{\frac{\pi}{2p} + \theta_{b1}}^{\frac{\pi}{2p} + \theta_{b2}} U_s(\theta_r) d\theta_r}_{S_2} \right\} + z U_{r3} \quad (2.48)$$

where the coefficient z is given by

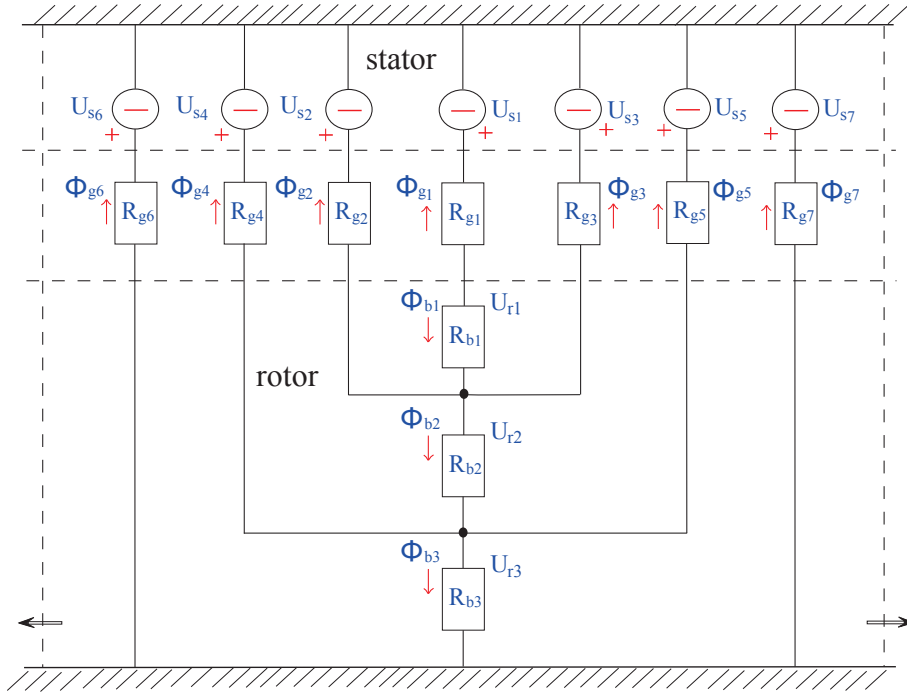
$$z = \frac{1}{1 - \frac{t_{b2} l_{b1}}{l_{b2} t_{b1}} (b - 1) + \frac{D t_{b2}}{g l_{b2}} (\theta_{b2} - \theta_{b1})} \quad (2.49)$$

From the magnetic network shown in Fig. 2.7 (b), the magnetic potential of the third island U_{r3} is computed as

$$U_{r3} = \phi_{b3} \cdot R_{b3} \quad (2.50)$$



(a) Linearized geometry for a rotor pole.



(b) Magnetic network of a REL motor pole.

Figure 2.7: REL machine with three flux-barriers per pole.

By substituting $\phi_{b3} = \phi_{b2} - \phi_{g4} - \phi_{g5}$ in eq. (2.50), it results in

$$\begin{aligned}
 U_{r3} = & \left[\phi_{b2} + \int_{\frac{\pi}{2p} - \theta_{b2}}^{\frac{\pi}{2p} - \theta_{b3}} \mu_0 \frac{U_s(\theta_r) - U_{r3}}{g} L_{stk} \frac{D}{2} d\theta_r \right. \\
 & \left. + \int_{\frac{\pi}{2p} + \theta_{b2}}^{\frac{\pi}{2p} + \theta_{b3}} \mu_0 \frac{U_s(\theta_r) - U_{r3}}{g} L_{stk} \frac{D}{2} d\theta_r \right] \frac{t_{b3}}{\mu_0 L_{stk} l_{b3}}
 \end{aligned} \tag{2.51}$$

Substituting $\phi_{b2} = (U_{r2} - U_{r3})/R_{b2}$ in eq. (2.51), it results

$$\begin{aligned}
 U_{r3} &= \left[\frac{U_{r2} - U_{r3}}{\frac{t_{b2}}{l_{b2}}} + \int_{\frac{\pi}{2p} - \theta_{b3}}^{\frac{\pi}{2p} - \theta_{b2}} \frac{U_s(\theta_r) - U_{r3}}{g} \frac{D}{2} d\theta_r + \int_{\frac{\pi}{2p} + \theta_{b2}}^{\frac{\pi}{2p} + \theta_{b3}} \frac{U_s(\theta_r) - U_{r3}}{g} \frac{D}{2} d\theta_r \right] \frac{t_{b3}}{l_{b3}} \\
 &= \frac{l_{b2}t_{b3}}{t_{b2}l_{b3}} [cS_1 + dS_2] - \frac{l_{b2}t_{b3}}{t_{b2}l_{b3}} U_{r3} - \frac{Dt_{b3}}{gl_{b3}} U_{r3} (\theta_{b3} - \theta_{b2}) \\
 &\quad + \frac{Dt_{b3}}{2gl_{b3}} \left[\underbrace{\int_{\frac{\pi}{2p} - \theta_{b3}}^{\frac{\pi}{2p} - \theta_{b2}} U_s(\theta_r) d\theta_r + \int_{\frac{\pi}{2p} + \theta_{b2}}^{\frac{\pi}{2p} + \theta_{b3}} U_s(\theta_r) d\theta_r}_{S_3} \right]
 \end{aligned} \tag{2.52}$$

then from

$$U_{r3} \left[\underbrace{1 - (z-1) \frac{l_{b2}t_{b3}}{t_{b2}l_{b3}} + \frac{Dt_{b3}}{gl_{b3}} (\theta_{b3} - \theta_{b2})}_{den} \right] = c \frac{l_{b2}t_{b3}}{t_{b2}l_{b3}} S_1 + d \frac{l_{b2}t_{b3}}{t_{b2}l_{b3}} S_2 + \frac{Dt_{b3}}{2gl_{b3}} S_3 \tag{2.53}$$

U_{r3} is expressed as

$$U_{r3} = mS_1 + nS_2 + qS_3 \tag{2.54}$$

where the coefficients m , n , and q are functions of the coefficient den . All of these coefficients are given by

$$m = \frac{c \frac{l_{b2}t_{b3}}{t_{b2}l_{b3}}}{den} \tag{2.55}$$

$$n = \frac{d \frac{l_{b2}t_{b3}}{t_{b2}l_{b3}}}{den} \tag{2.56}$$

$$q = \frac{\frac{Dt_{b3}}{2gl_{b3}}}{den} \tag{2.57}$$

$$den = \left[1 - (z-1) \frac{l_{b2}t_{b3}}{t_{b2}l_{b3}} + \frac{Dt_{b3}}{gl_{b3}} (\theta_{b3} - \theta_{b2}) \right] \tag{2.58}$$

The integrations S_1 and S_2 are reported in eqs. (2.41) and (2.42) whereas, the integration S_3 is solved following the same procedure used for solving the integration S_2 . The solution of S_3 is reported as

$$S_3 = \sum_{\nu^e} -\frac{\hat{K}_{\nu^e}}{(\nu^e p)^2} D \cos(\lambda_{\nu^e}) [\sin(\nu^e p \theta_{b3}) - \sin(\nu^e p \theta_{b2})] \tag{2.59}$$

By substituting eqs. (2.41), (2.42) and (2.59) in eq. (2.54), U_{r3} is expressed as

$$U_{r3} = \sum_{\nu^e} -\frac{\hat{K}_{\nu^e}}{(\nu^e p)^2} D \rho_3 \cos(\lambda_{\nu^e}) \tag{2.60}$$

Once again, by substituting eqs. (2.41), (2.42) and (2.60) in eq. (2.48), U_{r2} is achieved as

$$U_{r2} = \sum_{\nu^e} -\frac{\hat{K}_{\nu^e}}{(\nu^e p)^2} D \rho_2 \cos(\lambda_{\nu^e}) \tag{2.61}$$

From eqs. (2.41) and (2.61), the expression of U_{r1} is

$$U_{r1} = \sum_{\nu^e} -\frac{\hat{K}_{\nu^e}}{(\nu^e p)^2} D \rho_1 \cos(\lambda_{\nu^e}) \quad (2.62)$$

where the coefficients ρ_1 , ρ_2 , and ρ_3 are given by

$$\rho_1 = (a + b(c - d + z(m - n))) \sin(\nu^e p \theta_{b1}) + (b(d + z(n - q))) \sin(\nu^e p \theta_{b2}) + bzq \sin(\nu^e p \theta_{b3}) \quad (2.63)$$

$$\rho_2 = (c - d + z(m - n)) \sin(\nu^e p \theta_{b1}) + (d + z(n - q)) \sin(\nu^e p \theta_{b2}) + qz \sin(\nu^e p \theta_{b3}) \quad (2.64)$$

$$\rho_3 = (m - n) \sin(\nu^e p \theta_{b1}) + (n - q) \sin(\nu^e p \theta_{b2}) + q \sin(\nu^e p \theta_{b3}) \quad (2.65)$$

2.5. Electromagnetic torque computation

Once stator and rotor scalar magnetic potential distributions are achieved, the air-gap flux density is computed as in eq. (2.22). Hence, the Lorentz's force density along the air-gap surface is given by $B_g(\theta_r)K_s(\theta_r)$. The torque is obtained by integrating the Lorentz's force density along the air-gap surface and then multiplying the integration by the radius $D/2$. It results

$$\begin{aligned} \tau_m &= -\frac{D}{2} \int_0^{2\pi} B_g(\theta_r) K_s(\theta_r) \frac{DL_{stk}}{2} d\theta_r = -\frac{D}{2} \int_0^{2\pi} \mu_o \frac{-U_s(\theta_r) + U_r(\theta_r)}{g} K_s(\theta_r) \frac{DL_{stk}}{2} d\theta_r \\ &= \frac{\mu_o D^2 L_{stk}}{4} \left[\underbrace{\int_0^{2\pi} \frac{U_s(\theta_r) K_s(\theta_r)}{g} d\theta_r}_{\text{null}} + \int_0^{2\pi} \frac{-U_r(\theta_r) K_s(\theta_r)}{g} d\theta_r \right] \end{aligned} \quad (2.66)$$

The first part of the previous integration is null, because the Fourier series expansions of $U_s(\theta_r)$, and $K_s(\theta_r)$ are orthogonal functions. Thus the integration of the product of them is null. So the torque equation is reduced to

$$\tau_m = \frac{-\mu_o D^2 L_{stk}}{4} \int_0^{2\pi} \frac{U_r(\theta_r) K_s(\theta_r)}{g} d\theta_r \quad (2.67)$$

2.5.1. One flux barrier per pole

Due to the symmetry of the rotor poles, the torque components of the poles are equal. Therefore, the total torque of the motor is achieved by multiplying the number of poles by the torque component of one pole, as reported in the following

$$\tau_m = \frac{-\mu_o D^2 L_{stk}}{4} (2p) \int_0^{\frac{\pi}{p}} \frac{U_r(\theta_r) K_s(\theta_r)}{g} d\theta_r \quad (2.68)$$

Once again, the rotor magnetic potential is null at the rotor channels. Thus, the electromagnetic torque is given by

$$\tau_m = \frac{-\mu_o D^2 L_{stk}}{4} (2p) \int_{\frac{\pi}{2p} - \theta_{b1}}^{\frac{\pi}{2p} + \theta_{b1}} \frac{U_{r1} K_s(\theta_r)}{g} d\theta_r \quad (2.69)$$

Substituting eqs. (2.20) and (2.28) in eq. (2.69), the electromagnetic torque is expressed as

$$\tau_m = \frac{\mu_o D^2 L_{stk} (2p) a D \sum_{\nu^e} \frac{\hat{k}_{\nu^e}}{(\nu^e p)^2} \cos(\lambda_{\nu^e}) \sin(\nu^e p \theta_{b1})}{4g} \cdot \int_{\frac{\pi}{2p} - \theta_{b1}}^{\frac{\pi}{2p} + \theta_{b1}} \sum_{\xi_a} \hat{k}_{\xi_a} \sin(\xi_a p \theta_r + (\xi_a - 1) \omega_{me} t - \alpha_i^e) d\theta_r \quad (2.70)$$

then

$$\tau_m = \frac{\mu_o D^3 L_{stk} a}{g} \sum_{\nu^e} \frac{\hat{K}_{\nu^e}}{(\nu^e p)^2} \cos(\lambda_{\nu^e}) \sin(\nu^e p \theta_{b1}) \cdot \sum_{\xi_a} \frac{\hat{K}_{\xi_a}}{\xi_a} \sin(\lambda_{\xi_a}) \cdot \sin(\xi_a p \theta_{b1}) \quad (2.71)$$

Letting

$$\lambda_{\xi_a} = \frac{\xi_a \pi}{2} + (\xi_a - 1) \omega_{me} t - \alpha_i^e \quad (2.72)$$

$$k_\tau = \frac{\mu_o D^3 L_{stk}}{g} \quad (2.73)$$

Consequently, the electromagnetic torque is expressed as

$$\tau_m = a k_\tau \sum_{\nu^e} \frac{\hat{k}_{\nu^e}}{(\nu^e p)^2} \cos(\lambda_{\nu^e}) \cdot \sin(\nu^e p \theta_{b1}) \sum_{\xi_a} \frac{\hat{k}_{\xi_a}}{(\xi_a p)} \sin(\lambda_{\xi_a}) \cdot \sin(\xi_a p \theta_{b1}) \quad (2.74)$$

2.5.2. Two flux barriers per pole

Similarly, the electromagnetic torque can be computed for REL motor with two flux-barriers per pole as

$$\tau_m = \frac{-\mu_o D^2 L_{stk}}{4} (2p) \left[\int_{\frac{\pi}{2p} - \theta_{b1}}^{\frac{\pi}{2p} + \theta_{b1}} \frac{U_{r1} K_s(\theta_r)}{g} d\theta_r + \int_{\frac{\pi}{2p} - \theta_{b2}}^{\frac{\pi}{2p} - \theta_{b1}} \frac{U_{r2} K_s(\theta_r)}{g} d\theta_r + \int_{\frac{\pi}{2p} + \theta_{b1}}^{\frac{\pi}{2p} + \theta_{b2}} \frac{U_{r2} K_s(\theta_r)}{g} d\theta_r \right] \quad (2.75)$$

Substituting eqs. (2.20), (2.43) and (2.44) in eq. (2.75), it results

$$\tau_m = \frac{\mu_o D^3 L_{stk}}{2g} p \sum_{\nu^e} \frac{\hat{k}_{\nu^e}}{(\nu^e p)^2} \cos(\lambda_{\nu^e}) \left[\underbrace{\rho_1 \int_{\frac{\pi}{2p} - \theta_{b1}}^{\frac{\pi}{2p} + \theta_{b1}} K_s(\theta_r) d\theta_r}_{G1} + \rho_2 \left(\underbrace{\int_{\frac{\pi}{2p} - \theta_{b2}}^{\frac{\pi}{2p} - \theta_{b1}} K_s(\theta_r) d\theta_r + \int_{\frac{\pi}{2p} + \theta_{b1}}^{\frac{\pi}{2p} + \theta_{b2}} K_s(\theta_r) d\theta_r}_{G2} \right) \right] \quad (2.76)$$

The integrations G_1 and G_2 are solved as

$$G_1 = \int_{\frac{\pi}{2p}-\theta_{b1}}^{\frac{\pi}{2p}+\theta_{b1}} K_s(\theta_r) d\theta_r = \sum_{\xi_a} \frac{2\hat{K}_{\xi_a}}{\xi_a p} \sin(\lambda_{\xi_a}) \sin(\xi_a p \theta_{b1}) \quad (2.77)$$

$$G_2 = \int_{\frac{\pi}{2p}-\theta_{b2}}^{\frac{\pi}{2p}-\theta_{b1}} K_s(\theta_r) d\theta_r + \int_{\frac{\pi}{2p}+\theta_{b1}}^{\frac{\pi}{2p}+\theta_{b2}} K_s(\theta_r) d\theta_r = \sum_{\xi_a} \frac{2\hat{K}_{\xi_a}}{\xi_a p} \sin(\lambda_{\xi_a}) [\sin(\xi_a p \theta_{b2}) - \sin(\xi_a p \theta_{b1})] \quad (2.78)$$

Thus, the electromagnetic torque expression can be simplified as

$$\begin{aligned} \tau_m = k_\tau \sum_{\nu^e} \frac{\hat{k}_{\nu^e}}{(\nu^e p)^2} \cos(\lambda_{\nu^e}) & \left[(\rho_1 - \rho_2) \sum_{\xi_a} \frac{\hat{K}_{\xi_a}}{\xi_a} \sin(\lambda_{\xi_a}) \sin(\xi_a p \theta_{b1}) \right. \\ & \left. + \rho_2 \sum_{\xi_a} \frac{\hat{K}_{\xi_a}}{\xi_a} \sin(\lambda_{\xi_a}) \sin(\xi_a p \theta_{b2}) \right] \end{aligned} \quad (2.79)$$

2.5.3. Three flux barriers per pole

Applying the same computation procedure used with one flux-barrier and two flux-barriers per pole, the electromagnetic torque in case of three flux-barriers per pole is computed as

$$\begin{aligned} \tau_m = \frac{-\mu_o D^2 L_{stk}}{4} (2p) & \left[\int_{\frac{\pi}{2p}-\theta_{b1}}^{\frac{\pi}{2p}+\theta_{b1}} \frac{U_{r1} K_s(\theta_r)}{g} d\theta_r + \int_{\frac{\pi}{2p}-\theta_{b2}}^{\frac{\pi}{2p}-\theta_{b1}} \frac{U_{r2} K_s(\theta_r)}{g} d\theta_r \right. \\ & \left. + \int_{\frac{\pi}{2p}+\theta_{b1}}^{\frac{\pi}{2p}+\theta_{b2}} \frac{U_{r2} K_s(\theta_r)}{g} d\theta_r + \int_{\frac{\pi}{2p}-\theta_{b3}}^{\frac{\pi}{2p}-\theta_{b2}} \frac{U_{r3} K_s(\theta_r)}{g} d\theta_r + \int_{\frac{\pi}{2p}+\theta_{b2}}^{\frac{\pi}{2p}+\theta_{b3}} \frac{U_{r3} K_s(\theta_r)}{g} d\theta_r \right] \end{aligned} \quad (2.80)$$

Substituting eqs. (2.20) and (2.60) to (2.62) in eq. (2.80), it results

$$\begin{aligned} \tau_m = \frac{\mu_o D^3 L_{stk}}{2g} p \sum_{\nu^e} \frac{\hat{k}_{\nu^e}}{(\nu^e p)^2} \cos(\lambda_{\nu^e}) & \left[\underbrace{\rho_1 \int_{\frac{\pi}{2p}-\theta_{b1}}^{\frac{\pi}{2p}+\theta_{b1}} K_s(\theta_r) d\theta_r}_{G_1} \right. \\ & + \rho_2 \left(\underbrace{\int_{\frac{\pi}{2p}-\theta_{b2}}^{\frac{\pi}{2p}-\theta_{b1}} K_s(\theta_r) d\theta_r + \int_{\frac{\pi}{2p}+\theta_{b1}}^{\frac{\pi}{2p}+\theta_{b2}} K_s(\theta_r) d\theta_r}_{G_2} \right) \\ & \left. + \rho_3 \left(\underbrace{\int_{\frac{\pi}{2p}-\theta_{b3}}^{\frac{\pi}{2p}-\theta_{b2}} K_s(\theta_r) d\theta_r + \int_{\frac{\pi}{2p}+\theta_{b2}}^{\frac{\pi}{2p}+\theta_{b3}} K_s(\theta_r) d\theta_r}_{G_3} \right) \right] \end{aligned} \quad (2.81)$$

The solutions of both integration terms G_1 and G_2 are reported in eqs. (2.77) and (2.78). In addition the integration G_3 is solved as

$$G_3 = \int_{\frac{\pi}{2p}-\theta_{b3}}^{\frac{\pi}{2p}-\theta_{b2}} K_s(\theta_r) d\theta_r + \int_{\frac{\pi}{2p}+\theta_{b2}}^{\frac{\pi}{2p}+\theta_{b3}} K_s(\theta_r) d\theta_r = \sum_{\xi_a} \frac{2\hat{K}_{\xi_a}}{\xi_a p} \sin(\lambda_{\xi_a}) [\sin(\xi_a p \theta_{b3}) - \sin(\xi_a p \theta_{b2})] \quad (2.82)$$

By substituting eqs. (2.77), (2.78) and (2.82) in eq. (2.81), the electromagnetic torque is simplified as

$$\begin{aligned} \tau_m = k_\tau \sum_{\nu^e} \frac{\hat{k}_{\nu^e}}{(\nu^e p)^2} \cos(\lambda_{\nu^e}) & \left[(\rho_1 - \rho_2) \sum_{\xi_a} \frac{\hat{K}_{\xi_a}}{\xi_a} \sin(\lambda_{\xi_a}) \sin(\xi_a p \theta_{b1}) \right. \\ & \left. + (\rho_2 - \rho_3) \sum_{\xi_a} \frac{\hat{K}_{\xi_a}}{\xi_a} \sin(\lambda_{\xi_a}) \sin(\xi_a p \theta_{b2}) + \rho_3 \sum_{\xi_a} \frac{\hat{K}_{\xi_a}}{\xi_a} \sin(\lambda_{\xi_a}) \sin(\xi_a p \theta_{b3}) \right] \end{aligned} \quad (2.83)$$

2.6. Rotor iron losses due to eddy currents

The iron losses of a generic motor lamination consist of the sum of hysteresis and eddy currents losses. Both of them can be estimated through Steinmetz formula as follows

$$p_{fe} = p_{hy} + p_{ec} = k_{hy} B^\beta f + k_{ec} B^2 f^2 \quad (2.84)$$

where k_{hy} and k_{ec} are the hysteresis and eddy current constants. Their values are computed from the data sheet of the lamination by implementing the curve fitting. β is the Steinmetz constant, often approximated as $\beta \simeq 2$ [33, 34].

This section focuses on the analytical estimation of the rotor eddy currents losses, which are higher than the hysteresis losses specially at high speed, i.e., at high frequency, as reported in eq. (2.84). The hysteresis losses are disregarded in this study.

For the i -th rotor island, all the harmonics cause losses ($p_{ec_{island_i}}$) which are proportional, with K'_{ec} , to the energy of the time-variation of the flux density in the i -th rotor island (B_{island_i}). Hence, $p_{ec_{island_i}}$ is given by

$$p_{ec_{island_i}} = \frac{K'_{ec}}{T} \int_0^T \left(\frac{\partial B_{island_i}}{\partial t} \right)^2 dt = \frac{K'_{ec}}{T} \int_0^T \left(\frac{\partial B_{island_i}}{\partial \theta_m} \frac{\partial \theta_m}{\partial t} \right)^2 d\theta_m \quad (2.85)$$

where K'_{ec} is the generic eddy current constant and $T = 2\pi/w_{me}$ is the period. Since the flux density in the i -th rotor island B_{island_i} is decomposed in its Fourier series

$$B_{island_i}(\theta_m) = \sum_h B_{h_{island_i}} \sin(h\theta_m + \gamma_h) \quad (2.86)$$

Its time-variation can be computed as

$$\frac{\partial B_{island_i}}{\partial \theta_m} = \sum_h B_{h_{island_i}} h \cos(h\theta_m + \gamma_h) \quad (2.87)$$

where h is the order of the spatial harmonic of the i -th rotor island flux density. Then, $p_{ec_{island_i}}$ expression is simplified as

$$\begin{aligned} p_{ec_{island_i}} &= \frac{K'_{ec} \omega_{me}^2}{2\pi} \int_0^{2\pi} \sum_h B_{h_{island_i}}^2 h^2 \cos^2(h\theta_m + \gamma_h) d\theta_m \\ &= \frac{K'_{ec} 4\pi^2 f^2}{2\pi} \sum_h B_{h_{island_i}}^2 h^2 \pi \\ &= K_{ec} f^2 \sum_h B_{h_{island_i}}^2 h^2 \end{aligned} \quad (2.88)$$

where $K'_{ec} = K_{ec}/2\pi^2$ and f is the frequency related to the rotor speed (n), by $f = pn/60$. From eq. (2.85), it can be noted the big impact of both the speed of the motor and the harmonic order on the eddy currents losses. The computation of the flux density variation in the i -th rotor island during the rotor rotation is carried out in the following.

Fig. 2.8 (a) shows cross section of one pole of REL motor. The flux enters, goes out, and flowing through the i -th rotor island (ϕ_{in_i} , ϕ_{out_i} , and ϕ_{island_i}) are highlighted. It is assumed that ϕ_{island_i} is constant and equal to the flux flowing in the middle of the island itself. Fig. 2.8 (b) presents the equivalent magnetic network of the island considering the aforementioned assumption. This approach is valid for REL motor with any number of flux-barriers per pole.

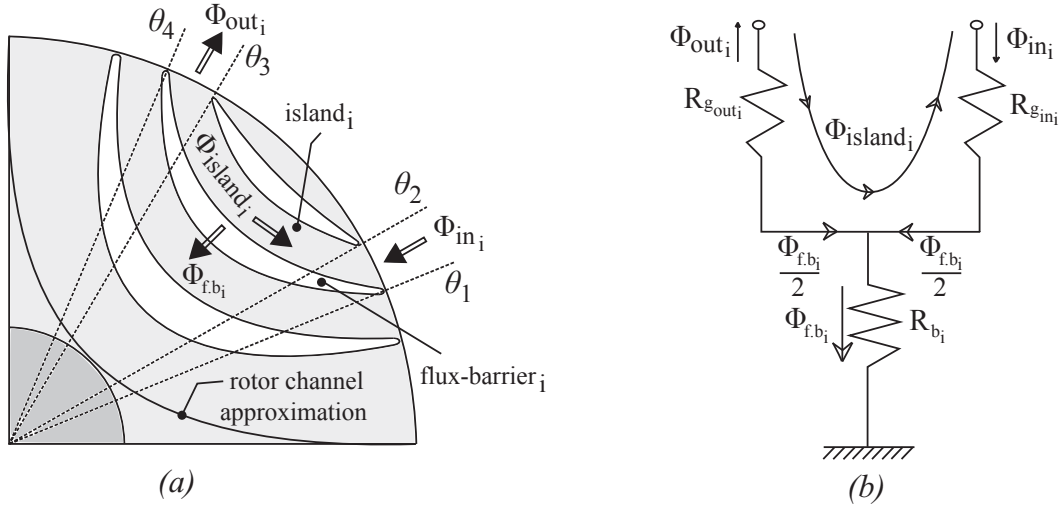


Figure 2.8: The computation of the magnetic flux flowing through the i -th rotor island is explained by (a) cross section of the rotor pole and (b) a simple magnetic network.

From the air-gap flux density distribution, ϕ_{in_i} and ϕ_{out_i} are computed as

$$\phi_{in_i} = \int_{\theta_1}^{\theta_2} B_g(\theta_r) \frac{D}{2} L_{stk} d\theta_r \quad (2.89)$$

$$\phi_{out_i} = \int_{\theta_3}^{\theta_4} B_g(\theta_r) \frac{D}{2} L_{stk} d\theta_r \quad (2.90)$$

The magnetic flux flowing through the i -th flux barrier ($\phi_{f.b_i}$) is given by

$$\phi_{f.b_i} = |\phi_{in_i}| - |\phi_{out_i}| \quad (2.91)$$

then, ϕ_{island_i} can be expressed as

$$\phi_{island_i} = |\phi_{in_i}| - \frac{\phi_{f.b_i}}{2} = |\phi_{out_i}| + \frac{\phi_{f.b_i}}{2} = \frac{|\phi_{in_i}| + |\phi_{out_i}|}{2} \quad (2.92)$$

Finally, the flux density of the i -th island is computed as

$$B_{island_i} = \frac{\phi_{island_i}}{w_{r_i} L_{stk}} \quad (2.93)$$

The computation of B_{island_i} is carried out at different rotor positions. Then, the previous procedure of computing $p_{ec_{island_i}}$ can be applied. The computation should be implemented on all rotor islands and channels. For simplicity, the rotor channel is simplified as shown in Fig. 2.8 (a). Then, the same computation technique is applied on it. Finally, eddy currents losses of all rotor islands and channels are summed together to get the total eddy currents losses in the rotor.

Analytical model of eccentric REL motor

This chapter deals with the derivation of the analytical model of the eccentric REL machine. Both static and dynamic eccentricity cases are considered. This model estimates the main electromagnetic quantities of the REL machine: stator and rotor scalar magnetic potentials, the air-gap flux density distribution, the electromagnetic torque, the radial magnetic pressure distribution on the rotor surface, and finally the radial magnetic force on the rotor. Besides, this model estimates the flux density variation in the rotor islands and channels, and hence the rotor iron losses are estimated.

3.1. Introduction

Synchronous reluctance machines are profitably adopted in applications where high torque density, overload capability, wide constant-power speed range are required [24, 35–37]. Nevertheless, the design of this kind of machines is rather complex, due to the interaction between the rotor anisotropy and the high harmonic content in the stator magneto-motive force (MMF). Thus, the use of the fundamental harmonic only is not enough. In addition, the high MMF harmonics can cause local saturation, with a further increase of the torque ripple. Several works are available in literature investigating the proper design of the rotor geometry, so as to increase the average torque and reduce the torque ripple [24, 28, 38–41].

Nevertheless, it is important to study the effect of rotor eccentricity on this machine because of its high anisotropy. Since the thicknesses of iron ribs should be carefully designed to sustain the mechanical stress resulted from the centrifugal force and the magnetic force on the rotor, the unbalanced magnetic force on the rotor, which resulted in eccentricity case, should be taken into account. However, the rotor eccentricity in synchronous reluctance machine has been marginally investigated. In addition, eccentricity has a strong effect in comparison with other machine types, for instance induction machines [42] or surface mounted permanent magnet machines [43, 44]. Thus, this report deals with an accurate study of the eccentricity effect in a synchronous reluctance machine.

There are many different reasons for rotor eccentricity, however, the most common reasons are stated [45], as incorrect bearing positioning during assembly, worn bearings, bent rotor shaft, and operation at critical speed creating rotor "whirl", etc.,. This analytical model deals with two types of rotor eccentricity, which are the static and dynamic eccentricity cases.

The static rotor eccentricity occurs when the rotor is shifted from the center of the stator, and rotates around its center, as shown in Fig. 3.1 (b). The dynamic rotor eccentricity occurs when the rotor is shifted from the center of the stator, and rotates around the stator center, as shown in Fig. 3.1 (c). In both cases of eccentricity, the smaller air-gap is on the right hand side (positive x-axis direction), as shown in Fig. 3.1 (b) and Fig. 3.1 (c). The healthy motor, i.e. with no rotor eccentricity, is also shown in Fig. 3.1 (a). It will be considered for the sake of comparison.

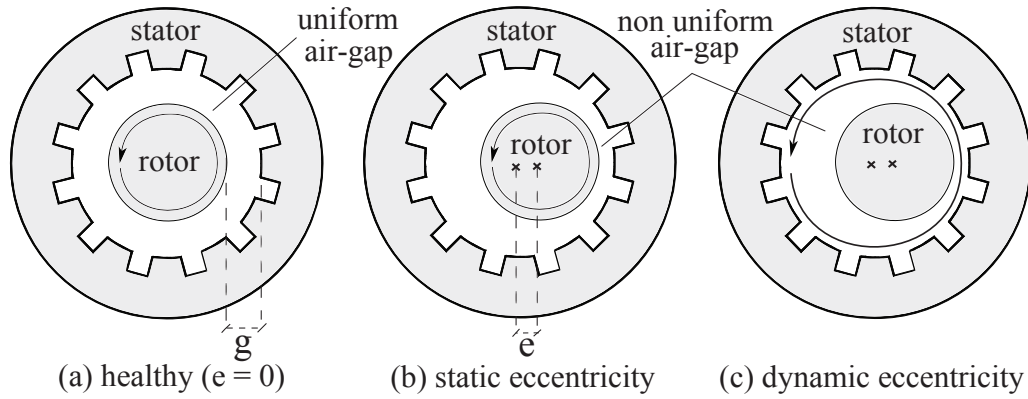


Figure 3.1: cross section of a motor describes the different types of rotor eccentricity.

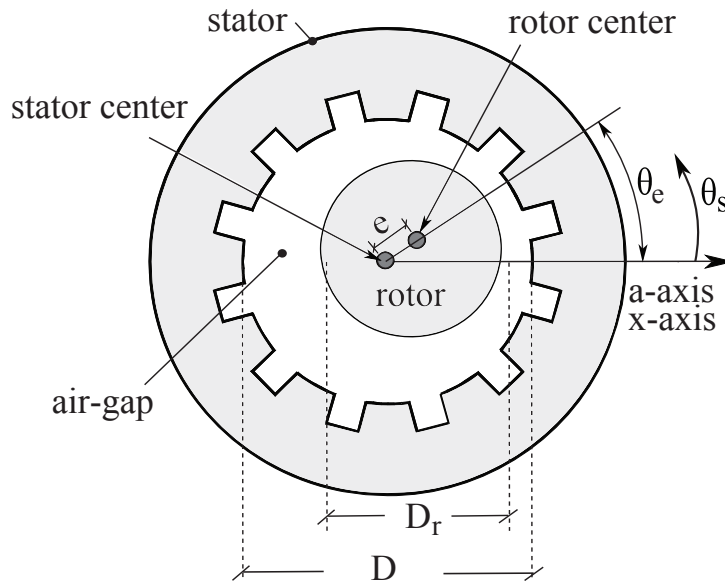


Figure 3.2: Air-gap length variation with the rotor rotation, in case of static eccentricity.

The mathematical formula describes the non-uniform air-gap length in case of static eccentricity is firstly proposed in [45–47]. As shown in Fig. 3.2, the air-gap length variation is fixed with rotor rotation (i.e., independent of the rotor position). It is given by

$$g(\theta_s) = g - e \cos(\theta_s) = g[1 - \Delta \cos(\theta_s - \theta_e)] \quad (3.1)$$

where

- e is the eccentricity distance between the stator axial center and the rotor axial center,
- $\Delta = e/g$ is the relative eccentricity, given by the ratio of the rotor displacement and the air-gap length.
- θ_e is the angle of the minimum air-gap length or the initial angle of the eccentricity referring to the stator stationary reference frame (mechanical degrees).

Then, this variation is discussed in case of dynamic eccentricity as in [48]. Fig. 3.3 shows that the air-gap length variation depends on the rotor position, in case of dynamic eccentricity. Hence, the analytical presentation for this air-gap length variation, as a function of θ_s in the stator reference frame, is given by

$$g(\theta_s) = g - e \cos(\theta_s - \theta_m) = g[1 - \Delta \cos(\theta_s - \theta_m - \theta_e)] \quad (3.2)$$

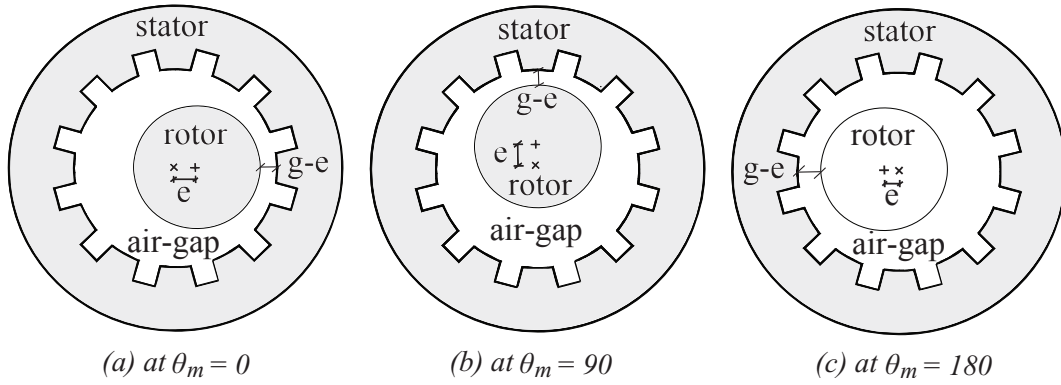


Figure 3.3: Air-gap length variation with the rotor rotation, in case of dynamic eccentricity, with $\theta_e = 0^\circ$.

The expressions of the air-gap length variation for both static and dynamic eccentricity can be rewritten in the synchronous reference frame, as in eqs. (3.3) and (3.4), respectively.

$$g(\theta_r) = g[1 - \Delta \cos(\theta_r + \theta_m - \theta_e)] \quad (3.3)$$

$$g(\theta_s) = g[1 - \Delta \cos(\theta_r - \theta_e)] \quad (3.4)$$

3.2. Stator electric loading and magnetic potential

Since, the stator windings are fed by its currents, the stator magneto-motive force (MMF) is generated. This MMF does not depend on the rotor type or the rotor position. By another word, the eccentricity has no impact on the stator MMF. Thus, the expressions of the stator electric loading and scalar magnetic potential are the same for both concentric and eccentric rotor motor. They are reported in eqs. (2.20) and (2.21). The main parameter affected by the eccentricity is the air-gap length, which yields to affect the air-gap flux density distributions, and hence, the rotor scalar magnetic potential.

3.3. Air-gap flux density distribution

Similar to the concentric rotor case, the air-gap flux density distributions in both cases of rotor eccentricity (i.e., static and dynamic rotor eccentricity) is computed by neglecting the magnetic voltage drop in the iron. It can be expressed, in d,q reference frame, as

$$B_g(\theta_r) = \mu_o \frac{-U_s(\theta_r) + U_r(\theta_r)}{g(\theta_r)} \quad (3.5)$$

From the derivation reported in the previous chapter, it is noted that the integration of the air-gap flux density distribution is needed in order to compute the rotor magnetic potential and the electromagnetic torque, as highlighted in eqs. (2.24) and (2.66), respectively. However, in eccentricity case, the symbolic integration of $B_g(\theta_r)$ is complicated due to the cosine function in the denominator. Therefore, for the aim of simplifying this integration, the air-gap is split into different regions. Then, the integration is implemented on each region considering the average of air-gap length variation in each region (\bar{g}_{region}), i.e., as a constant value. The number of these regions (n_g) depends on the number of pole pairs (p) and number of flux-barriers per pole (N_b). It can be expressed as

$$n_g = 4N_b p \quad (3.6)$$

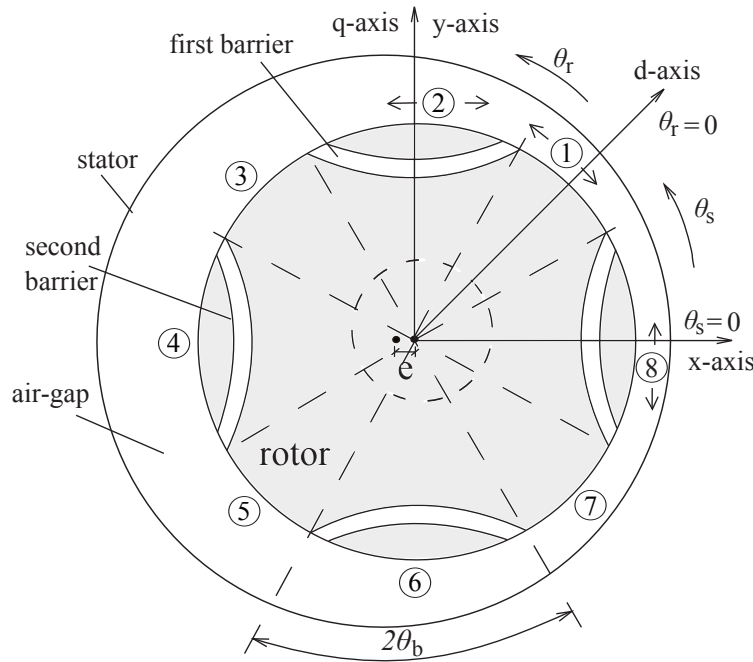


Figure 3.4: Cross section of eccentric internal rotor REL machine.

To better clarify, REL motor with single flux-barrier per pole is used, as an example. Fig. 3.4 shows the different air-gap regions or integration regions, which is given by ($n_g = 8$). Then, the average of the air-gap length variation is computed and considered as a constant during the integration for these regions, as shown in Fig. 3.5. The generic expression of the average air-gap length over a region boarded by the angles (γ_1 and γ_2) is called ($\bar{g}_{\gamma_1 \rightarrow \gamma_2}$). This

general expression is computed in case of static eccentricity, in the stator stationary reference frame, as

$$\begin{aligned} \bar{g}_{\gamma_1 \rightarrow \gamma_2} &= \frac{1}{\gamma_2 - \gamma_1} \int_{\gamma_1}^{\gamma_2} g [1 - \Delta \cos(\theta_s - \theta_e)] d\theta_s \\ &= g \left[1 - \frac{2\Delta}{\gamma_2 - \gamma_1} \cos\left(\frac{\gamma_1 + \gamma_2}{2} - \theta_e\right) \sin\left(\frac{\gamma_2 - \gamma_1}{2}\right) \right] \end{aligned} \quad (3.7)$$

Similarly, $\bar{g}_{\gamma_1 \rightarrow \gamma_2}$, in case of dynamic eccentricity, in the stator stationary reference frame, is expressed as

$$\begin{aligned} \bar{g}_{\gamma_1 \rightarrow \gamma_2} &= \frac{1}{\gamma_2 - \gamma_1} \int_{\gamma_1}^{\gamma_2} g [1 - \Delta \cos(\theta_s - \theta_m - \theta_e)] d\theta_s \\ &= g \left[1 - \frac{2\Delta}{\gamma_2 - \gamma_1} \cos\left(\frac{\gamma_1 + \gamma_2}{2} - \theta_m - \theta_e\right) \sin\left(\frac{\gamma_2 - \gamma_1}{2}\right) \right] \end{aligned} \quad (3.8)$$

The two previous expressions can be rewritten in the synchronous reference frame, as following

$$\bar{g}_{\gamma_1 \rightarrow \gamma_2} = g \left[1 - \frac{2\Delta}{\gamma_2 - \gamma_1} \cos\left(\frac{\gamma_1 + \gamma_2}{2} + \theta_m - \theta_e\right) \sin\left(\frac{\gamma_2 - \gamma_1}{2}\right) \right] \quad (3.9)$$

$$\bar{g}_{\gamma_1 \rightarrow \gamma_2} = g \left[1 - \frac{2\Delta}{\gamma_2 - \gamma_1} \cos\left(\frac{\gamma_1 + \gamma_2}{2} - \theta_e\right) \sin\left(\frac{\gamma_2 - \gamma_1}{2}\right) \right] \quad (3.10)$$

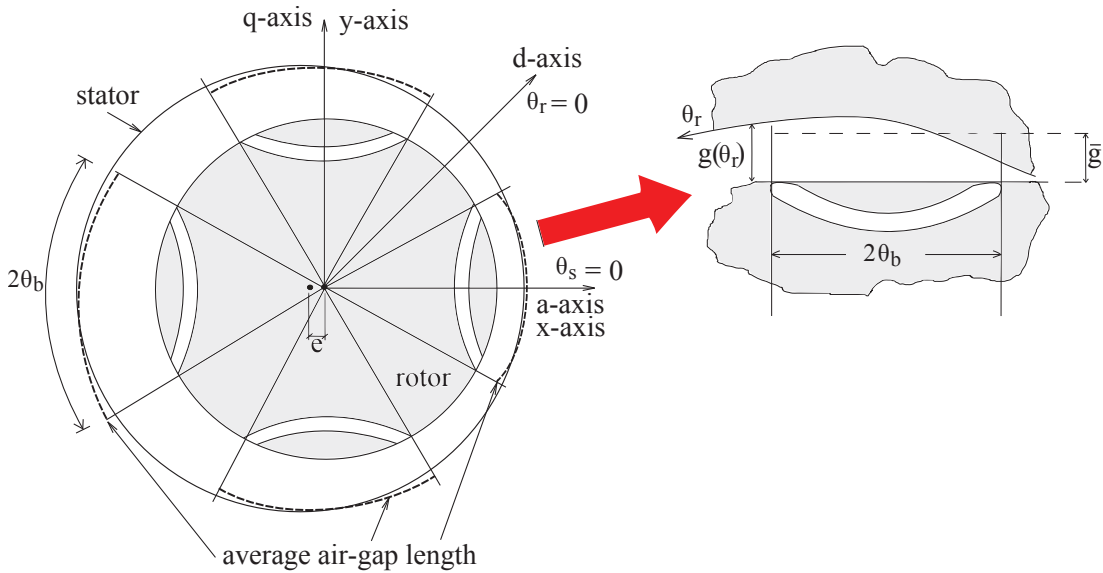


Figure 3.5: The air-gap length approximation of REL machine with eccentric rotor.

3.4. Rotor magnetic potential

3.4.1. One flux barrier per pole

As stated in the previous chapter, the rotor magnetic potential is exist only on the islands boarded by the flux-barriers and null on the rotor channels. As reported in eq. (2.22), due to the uniform air-gap distribution, there is symmetry of the air-gap flux density distributions over the poles, however, their signs are changed depending on each pole polarity. Consequently, the amplitude of rotor scalar magnetic potential, which based on magnetic flux as reported in Fig. 2.5 (b), is similar for all poles, and its sign is changed depending on each pole polarity. That's why the rotor magnetic potential is computed only for one pole in the previous chapter.

On the contrary, for the eccentric REL machine, due to the non-uniform air-gap length variation, there are unbalance in the flux density distribution over the poles. Hence, the amplitude of the rotor magnetic potential is not the same for all poles. Thus, it is necessary to compute the rotor magnetic potential for each pole separately. The non-uniform air-gap length distribution is highlighted in the generic linearized geometry of the REL machine with one barrier, which shown in Fig. 3.6.

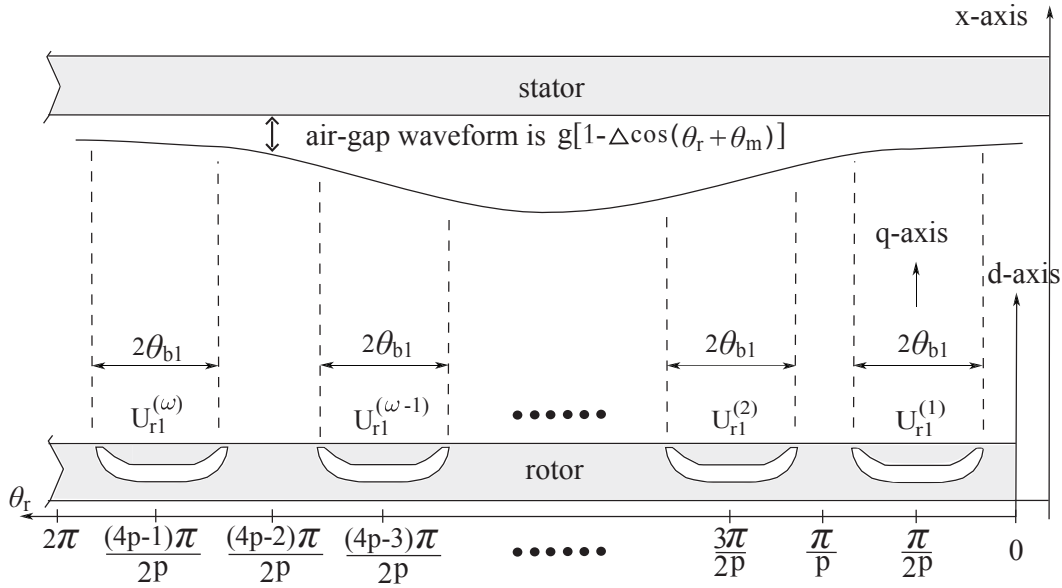


Figure 3.6: Linearized geometry for four-pole rotor with one flux-barrier. $\theta_e = 0^\circ$.

At the first, the scalar magnetic potential of the rotor island of the first pole ($U_{r1}^{(1)}$) is computed, where the superscript "1" refers to the rank of the poles, as shown in Fig. 3.6. Referring to the magnetic network shown in Fig. 2.5 (b) and eq. (2.23), $U_{r1}^{(1)}$ is given by $U_{r1}^{(1)} = \phi_{b1}^{(1)} R_{b1}$. Once, the magnetic flux flowing through the flux barrier is achieved as following

$$\begin{aligned} \phi_{b1}^{(1)} &= \int_{\frac{\pi}{2p} - \theta_{b1}}^{\frac{\pi}{2p} + \theta_{b1}} -B_g(\theta_r) L_{stk} \frac{D}{2} d\theta_r = \int_{\frac{\pi}{2p} - \theta_{b1}}^{\frac{\pi}{2p} + \theta_{b1}} \mu_o \frac{U_s(\theta_r) - U_{r1}^{(1)}}{g(\theta_r)} L_{stk} \frac{D}{2} d\theta_r \\ &= \frac{\mu_o D L_{stk}}{2\bar{g}_{(\frac{\pi}{2p} - \theta_{b1}) \rightarrow (\frac{\pi}{2p} + \theta_{b1})}} \left[\int_{\frac{\pi}{2p} - \theta_{b1}}^{\frac{\pi}{2p} + \theta_{b1}} U_s(\theta_r) d\theta_r - 2\theta_{b1} U_{r1}^{(1)} \right] \end{aligned} \quad (3.11)$$

The island magnetic potential can be expressed as

$$\begin{aligned} U_{r1}^{(1)} &= \frac{Dt_{b1}}{2l_{b1}\bar{g}_{(\frac{\pi}{2p}-\theta_{b1})\rightarrow(\frac{\pi}{2p}+\theta_{b1})}} \left[\int_{\frac{\pi}{2p}-\theta_{b1}}^{\frac{\pi}{2p}+\theta_{b1}} U_s(\theta_r) d\theta_r - 2\theta_{b1} U_{r1}^{(1)} \right] \\ &= a_1 \int_{\frac{\pi}{2p}-\theta_{b1}}^{\frac{\pi}{2p}+\theta_{b1}} U_s(\theta_r) d\theta_r \end{aligned} \quad (3.12)$$

where $\bar{g}_{(\frac{\pi}{2p}-\theta_{b1})\rightarrow(\frac{\pi}{2p}+\theta_{b1})}$ is the average of the air-gap length between the two angles $\frac{\pi}{2p} - \theta_{b1}$ and $\frac{\pi}{2p} + \theta_{b1}$. By substituting these two angles in eqs. (3.9) and (3.10), this average air-gap length can be obtained in both static and dynamic eccentricity cases, respectively. Then, they are given by

$$\bar{g}_{(\frac{\pi}{2p}-\theta_{b1})\rightarrow(\frac{\pi}{2p}+\theta_{b1})} = g \left[1 - \frac{\Delta}{\theta_{b1}} \cos\left(\frac{\pi}{2p} + \theta_m - \theta_e\right) \sin(\theta_{b1}) \right] \quad (3.13)$$

$$\bar{g}_{(\frac{\pi}{2p}-\theta_{b1})\rightarrow(\frac{\pi}{2p}+\theta_{b1})} = g \left[1 - \frac{\Delta}{\theta_{b1}} \cos\left(\frac{\pi}{2p} - \theta_e\right) \sin(\theta_{b1}) \right] \quad (3.14)$$

Hence, the dimensionless coefficient a_1 is expressed, in static eccentricity case, as

$$a_{1_{static}} = \frac{\frac{Dt_{b1}}{2gl_{b1} \left[1 - \frac{\Delta}{\theta_{b1}} \cos\left(\frac{\pi}{2p} + \theta_m - \theta_e\right) \sin(\theta_{b1}) \right]}}{1 + \frac{Dt_{b1}}{2gl_{b1} \left[1 - \frac{\Delta}{\theta_{b1}} \cos\left(\frac{\pi}{2p} + \theta_m - \theta_e\right) \sin(\theta_{b1}) \right]} 2\theta_{b1}} \quad (3.15)$$

and, in dynamic eccentricity case, as

$$a_{1_{dynamic}} = \frac{\frac{Dt_{b1}}{2gl_{b1} \left[1 - \frac{\Delta}{\theta_{b1}} \cos\left(\frac{\pi}{2p} - \theta_e\right) \sin(\theta_{b1}) \right]}}{1 + \frac{Dt_{b1}}{2gl_{b1} \left[1 - \frac{\Delta}{\theta_{b1}} \cos\left(\frac{\pi}{2p} - \theta_e\right) \sin(\theta_{b1}) \right]} 2\theta_{b1}} \quad (3.16)$$

Substituting eq. (2.21) in eq. (3.12), it results

$$\begin{aligned} U_{r1}^{(1)} &= a_1 \sum_{\nu^e} \int_{\frac{\pi}{2p}-\theta_{b1}}^{\frac{\pi}{2p}+\theta_{b1}} \frac{-\hat{K}_{\nu^e} D}{\nu^e p} \cos(\nu^e p \theta_r + (\nu^e - 1)\omega_{met} - \alpha_i^e) d\theta_r \\ &= -a_1 D \sum_{\nu^e} \frac{\hat{K}_{\nu^e}}{(\nu^e p)^2} \cos(\lambda_{\nu_1^e}) \sin(\nu^e p \theta_{b1}) \end{aligned} \quad (3.17)$$

Letting

$$\lambda_{\nu_1^e} = \frac{\nu^e \pi}{2} + (\nu^e - 1)\omega_{met} - \alpha_i^e \quad (3.18)$$

Similarly, the derivation of the magnetic potential of the rotor island of the second pole is carried out. It results

$$\begin{aligned} U_{r1}^{(2)} &= \phi_{b1}^{(2)} R_{b1} \\ &= \frac{Dt_{b1}}{2l_{b1}\bar{g}_{(\frac{3\pi}{2p}-\theta_{b1})\rightarrow(\frac{3\pi}{2p}+\theta_{b1})}} \left[\int_{\frac{3\pi}{2p}-\theta_{b1}}^{\frac{3\pi}{2p}+\theta_{b1}} U_s(\theta_r) d\theta_r - 2\theta_{b1} U_{r1}^{(2)} \right] \\ &= a_2 \int_{\frac{3\pi}{2p}-\theta_{b1}}^{\frac{3\pi}{2p}+\theta_{b1}} U_s(\theta_r) d\theta_r \end{aligned} \quad (3.19)$$

where $\bar{g}_{(\frac{3\pi}{2p} - \theta_{b1}) \rightarrow (\frac{3\pi}{2p} + \theta_{b1})}$ is the average of the air-gap length between the two angles $\frac{3\pi}{2p} - \theta_{b1}$ and $\frac{3\pi}{2p} + \theta_{b1}$. To achieve this average value in static and dynamic eccentricity cases, these two angles are substituted in eqs. (3.9) and (3.10), and hence,

$$\bar{g}_{(\frac{3\pi}{2p} - \theta_{b1}) \rightarrow (\frac{3\pi}{2p} + \theta_{b1})} = g \left[1 - \frac{\Delta}{\theta_{b1}} \cos\left(\frac{3\pi}{2p} + \theta_m - \theta_e\right) \sin(\theta_{b1}) \right] \quad (3.20)$$

$$\bar{g}_{(\frac{3\pi}{2p} - \theta_{b1}) \rightarrow (\frac{3\pi}{2p} + \theta_{b1})} = g \left[1 - \frac{\Delta}{\theta_{b1}} \cos\left(\frac{3\pi}{2p} - \theta_e\right) \sin(\theta_{b1}) \right] \quad (3.21)$$

Consequently, the coefficient a_2 is computed in both static and dynamic eccentricity cases, respectively, as

$$a_{2_{static}} = \frac{\frac{Dt_{b1}}{2gl_{b1} \left[1 - \frac{\Delta}{\theta_{b1}} \cos\left(\frac{3\pi}{2p} + \theta_m - \theta_e\right) \sin(\theta_{b1}) \right]}}{1 + \frac{\frac{Dt_{b1}}{2gl_{b1} \left[1 - \frac{\Delta}{\theta_{b1}} \cos\left(\frac{3\pi}{2p} + \theta_m - \theta_e\right) \sin(\theta_{b1}) \right]}}{2\theta_{b1}}} \quad (3.22)$$

$$a_{2_{dynamic}} = \frac{\frac{Dt_{b1}}{2gl_{b1} \left[1 - \frac{\Delta}{\theta_{b1}} \cos\left(\frac{3\pi}{2p} - \theta_e\right) \sin(\theta_{b1}) \right]}}{1 + \frac{\frac{Dt_{b1}}{2gl_{b1} \left[1 - \frac{\Delta}{\theta_{b1}} \cos\left(\frac{3\pi}{2p} - \theta_e\right) \sin(\theta_{b1}) \right]}}{2\theta_{b1}}} \quad (3.23)$$

Once again, substituting eq. (2.21) in eq. (3.19), it results

$$\begin{aligned} U_{r1}^{(2)} &= a_2 \sum_{\nu^e} \int_{\frac{3\pi}{2p} - \theta_{b1}}^{\frac{3\pi}{2p} + \theta_{b1}} \frac{-\hat{K}_{\nu^e}}{\nu^e} \frac{D}{2p} \cos(\nu^e p \theta_r + (\nu^e - 1)\omega_m t - \alpha_i^e) d\theta_r \\ &= -a_2 D \sum_{\nu^e} \frac{\hat{K}_{\nu^e}}{(\nu^e p)^2} \cos(\lambda_{\nu_2^e}) \sin(\nu^e p \theta_{b1}) \end{aligned} \quad (3.24)$$

Letting

$$\lambda_{\nu_2^e} = \frac{3\nu^e \pi}{2} + (\nu^e - 1)\omega_m t - \alpha_i^e \quad (3.25)$$

Furthermore, the magnetic potential of the rotor island of the third pole is computed following the same derivation applied for the first and the second pole. It is resulted as

$$\begin{aligned} U_{r1}^{(3)} &= a_3 \sum_{\nu^e} \int_{\frac{5\pi}{2p} - \theta_{b1}}^{\frac{5\pi}{2p} + \theta_{b1}} \frac{-\hat{K}_{\nu^e}}{\nu^e} \frac{D}{2p} \cos(\nu^e p \theta_r + (\nu^e - 1)\omega_m t - \alpha_i^e) d\theta_r \\ &= -a_3 D \sum_{\nu^e} \frac{\hat{K}_{\nu^e}}{(\nu^e p)^2} \cos(\lambda_{\nu_3^e}) \sin(\nu^e p \theta_{b1}) \end{aligned} \quad (3.26)$$

Letting

$$\lambda_{\nu_3^e} = \frac{5\nu^e \pi}{2} + (\nu^e - 1)\omega_m t - \alpha_i^e \quad (3.27)$$

and the coefficient a_3 in both eccentricity cases is given by

$$a_{3_{static}} = \frac{\frac{Dt_{b1}}{2gl_{b1} \left[1 - \frac{\Delta}{\theta_{b1}} \cos\left(\frac{5\pi}{2p} + \theta_m - \theta_e\right) \sin(\theta_{b1}) \right]}}{1 + \frac{\frac{Dt_{b1}}{2gl_{b1} \left[1 - \frac{\Delta}{\theta_{b1}} \cos\left(\frac{5\pi}{2p} + \theta_m - \theta_e\right) \sin(\theta_{b1}) \right]}}{2\theta_{b1}}} \quad (3.28)$$

$$a_{3dynamic} = \frac{\frac{Dt_{b1}}{2gl_{b1} \left[1 - \frac{\Delta}{\theta_{b1}} \cos\left(\frac{5\pi}{2p} - \theta_e\right) \sin(\theta_{b1}) \right]}}{1 + \frac{Dt_{b1}}{2gl_{b1} \left[1 - \frac{\Delta}{\theta_{b1}} \cos\left(\frac{5\pi}{2p} - \theta_e\right) \sin(\theta_{b1}) \right]}} 2\theta_{b1} \quad (3.29)$$

Finally, from the results of the first three poles, the general expression of the magnetic potential of the rotor island of the w -th pole is

$$\begin{aligned} U_{r1}^{(w)} &= a_w \sum_{\nu^e} \int_{\frac{x(w)\pi}{2p} - \theta_{b1}}^{\frac{x(w)\pi}{2p} + \theta_{b1}} \frac{-\hat{K}_{\nu^e} D}{\nu^e} \frac{D}{2p} \cos(\nu^e p \theta_r + (\nu^e - 1)\omega_{me} t - \alpha_i^e) d\theta_r \\ &= -a_w D \sum_{\nu^e} \frac{\hat{K}_{\nu^e}}{(\nu^e p)^2} \cos(\lambda_{\nu_w^e}) \sin(\nu^e p \theta_{b1}) \end{aligned} \quad (3.30)$$

where w is a number related to the rank of pole where the average air-gap length or the magnetic potential is calculated. It is given by $w = 1, 2, 3, \dots, 2p$ and $X(w) = (2w - 1)$. The angle $\lambda_{\nu_w^e}$ is expressed as

$$\lambda_{\nu_w^e} = \frac{X(w)\nu^e\pi}{2} + (\nu^e - 1)\omega_{me} t - \alpha_i^e \quad (3.31)$$

In static eccentricity case, the coefficient a_w is given by

$$a_{wstatic} = \frac{\frac{Dt_{b1}}{2gl_{b1} \left[1 - \frac{\Delta}{\theta_{b1}} \cos\left(\frac{X(w)\pi}{2p} + \theta_m - \theta_e\right) \sin(\theta_{b1}) \right]}}{1 + \frac{Dt_{b1}}{2gl_{b1} \left[1 - \frac{\Delta}{\theta_{b1}} \cos\left(\frac{X(w)\pi}{2p} + \theta_m - \theta_e\right) \sin(\theta_{b1}) \right]}} 2\theta_{b1} \quad (3.32)$$

and in dynamic eccentricity case, is given by

$$a_{wdynamic} = \frac{\frac{Dt_{b1}}{2gl_{b1} \left[1 - \frac{\Delta}{\theta_{b1}} \cos\left(\frac{X(w)\pi}{2p} - \theta_e\right) \sin(\theta_{b1}) \right]}}{1 + \frac{Dt_{b1}}{2gl_{b1} \left[1 - \frac{\Delta}{\theta_{b1}} \cos\left(\frac{X(w)\pi}{2p} - \theta_e\right) \sin(\theta_{b1}) \right]}} 2\theta_{b1} \quad (3.33)$$

3.4.2. Two flux barriers per pole

Analogously, for REL motor with two flux-barriers per pole, the general expressions of the magnetic potentials of the rotor islands per pole can be derived. The non-uniform air-gap length distribution is highlighted in the generic linearized geometry of the REL machine with two barriers, which shown in Fig. 3.7.

From the magnetic network, shown in Fig. 2.6 (b), the scalar magnetic potential of the first island of the first pole ($U_{r1}^{(1)}$) is computed as

$$\begin{aligned} U_{r1}^{(1)} &= \phi_{b1}^{(1)} \cdot R_{b1} + U_{r2}^{(1)} \\ &= \left[\int_{\frac{\pi}{2p} - \theta_{b1}}^{\frac{\pi}{2p} + \theta_{b1}} \mu_o \frac{U_s(\theta_r) - U_{r1}}{\bar{g}_{(\frac{\pi}{2p} - \theta_{b1}) \rightarrow (\frac{\pi}{2p} + \theta_{b1})}} L_{stk} \frac{D}{2} d\theta_r \right] \frac{t_{b1}}{\mu_o L_{stk} l_{b1}} + U_{r2} \\ &= \frac{Dt_{b1}}{2\bar{g}_{(\frac{\pi}{2p} - \theta_{b1}) \rightarrow (\frac{\pi}{2p} + \theta_{b1})} l_{b1}} \left[\int_{\frac{\pi}{2p} - \theta_{b1}}^{\frac{\pi}{2p} + \theta_{b1}} U_s(\theta_r) d\theta_r - 2\theta_{b1} U_{r1} + U_{r2} \right] \end{aligned} \quad (3.34)$$

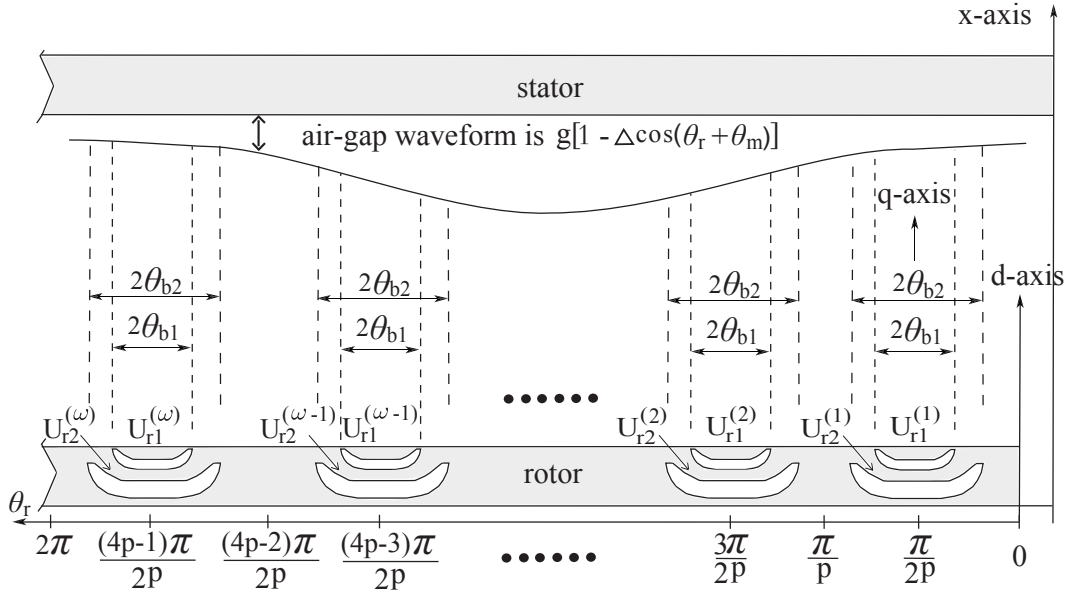


Figure 3.7: Linearized geometry for four-pole rotor with two flux-barriers. $\theta_e = 0^\circ$.

and hence,

$$U_{r1}^{(1)} = a_1 \int_{\frac{\pi}{2p} - \theta_{b1}}^{\frac{\pi}{2p} + \theta_{b1}} U_s(\theta_r) d\theta_r + b_1 U_{r2}^{(1)} \quad (3.35)$$

where the dimensionless coefficient b_1 , in case of static eccentricity, is given by

$$b_{1_{static}} = \frac{1}{1 + \frac{Dt_{b1}}{2gl_{b1} \left[1 - \frac{\Delta}{\theta_{b1}} \cos\left(\frac{\pi}{2p} + \theta_m - \theta_e\right) \sin(\theta_{b1}) \right]}} 2\theta_{b1} \quad (3.36)$$

and in case of dynamic eccentricity, is given by

$$b_{1_{dynamic}} = \frac{1}{1 + \frac{Dt_{b1}}{2gl_{b1} \left[1 - \frac{\Delta}{\theta_{b1}} \cos\left(\frac{\pi}{2p} - \theta_e\right) \sin(\theta_{b1}) \right]}} 2\theta_{b1} \quad (3.37)$$

Besides, $U_{r2}^{(1)}$ is the scalar magnetic potential of the inner island of the first pole and is given by

$$\begin{aligned} U_{r2}^{(1)} &= \phi_{b2}^{(1)} R_{b2} = (\phi_{b1}^{(1)} - \phi_{g2}^{(1)} - \phi_{g3}^{(1)}) R_{b2} \\ &= \left[\phi_{b1}^{(1)} + \int_{\frac{\pi}{2p} - \theta_{b2}}^{\frac{\pi}{2p} - \theta_{b1}} \mu_\circ \frac{U_s(\theta_r) - U_{r2}^{(1)}}{\bar{g}(\frac{\pi}{2p} - \theta_{b2}) \rightarrow (\frac{\pi}{2p} - \theta_{b1})} L_{stk} \frac{D}{2} d\theta_r + \right. \\ &\quad \left. + \int_{\frac{\pi}{2p} + \theta_{b1}}^{\frac{\pi}{2p} + \theta_{b2}} \mu_\circ \frac{U_s(\theta_r) - U_{r2}^{(1)}}{\bar{g}(\frac{\pi}{2p} + \theta_{b1}) \rightarrow (\frac{\pi}{2p} + \theta_{b2})} L_{stk} \frac{D}{2} d\theta_r \right] \frac{t_{b2}}{\mu_\circ L_{stk} l_{b2}} \end{aligned} \quad (3.38)$$

Then, it can be simplified as

$$\begin{aligned} U_{r2} &= \left[\frac{U_{r1} - U_{r2}}{\frac{t_{b1}}{l_{b1}}} + \int_{\frac{\pi}{2p} - \theta_{b2}}^{\frac{\pi}{2p} - \theta_{b1}} \frac{U_s(\theta_r) - U_{r2}}{\bar{g}(\frac{\pi}{2p} - \theta_{b2}) \rightarrow (\frac{\pi}{2p} - \theta_{b1})} \frac{D}{2} d\theta_r + \right. \\ &\quad \left. + \int_{\frac{\pi}{2p} + \theta_{b1}}^{\frac{\pi}{2p} + \theta_{b2}} \frac{U_s(\theta_r) - U_{r2}}{\bar{g}(\frac{\pi}{2p} + \theta_{b1}) \rightarrow (\frac{\pi}{2p} + \theta_{b2})} \frac{D}{2} d\theta_r \right] \frac{t_{b2}}{l_{b2}} \end{aligned} \quad (3.39)$$

Substituting eq. (3.35) in eq. (3.39), it results

$$\begin{aligned}
U_{r2} = & \frac{l_{b1}t_{b2}}{t_{b1}l_{b2}} \left[a \int_{\frac{\pi}{2p}-\theta_{b1}}^{\frac{\pi}{2p}+\theta_{b1}} U_s(\theta_r) d\theta_r + bU_{r2} \right] - \frac{l_{b1}t_{b2}}{t_{b1}l_{b2}} U_{r2} + \\
& + \frac{Dt_{b2}}{2\bar{g}_{(\frac{\pi}{2p}-\theta_{b2}) \rightarrow (\frac{\pi}{2p}-\theta_{b1})} l_{b2}} \int_{\frac{\pi}{2p}-\theta_{b2}}^{\frac{\pi}{2p}-\theta_{b1}} U_s(\theta_r) d\theta_r + \frac{Dt_{b2}}{2\bar{g}_{(\frac{\pi}{2p}+\theta_{b1}) \rightarrow (\frac{\pi}{2p}+\theta_{b2})} l_{b2}} \int_{\frac{\pi}{2p}+\theta_{b1}}^{\frac{\pi}{2p}+\theta_{b2}} U_s(\theta_r) d\theta_r \\
& - \frac{Dt_{b2}}{2\bar{g}_{(\frac{\pi}{2p}-\theta_{b2}) \rightarrow (\frac{\pi}{2p}-\theta_{b1})} l_{b2}} U_{r2}(\theta_{b2} - \theta_{b1}) - \frac{Dt_{b2}}{2\bar{g}_{(\frac{\pi}{2p}+\theta_{b1}) \rightarrow (\frac{\pi}{2p}+\theta_{b2})} l_{b2}} U_{r2}(\theta_{b2} - \theta_{b1})
\end{aligned} \tag{3.40}$$

Referring to the static eccentricity case, the coefficients $A_{1_{static}}$ and $B_{1_{static}}$ are defined as

$$A_{1_{static}} = \bar{g}_{(\frac{\pi}{2p}-\theta_{b2}) \rightarrow (\frac{\pi}{2p}-\theta_{b1})} = g - \frac{2g\Delta}{\theta_{b2} - \theta_{b1}} \cos \left(\frac{\frac{\pi}{p} - \theta_{b1} - \theta_{b2}}{2} + \theta_m - \theta_e \right) \sin \left(\frac{\theta_{b2} - \theta_{b1}}{2} \right) \tag{3.41}$$

$$B_{1_{static}} = \bar{g}_{(\frac{\pi}{2p}+\theta_{b1}) \rightarrow (\frac{\pi}{2p}+\theta_{b2})} = g - \frac{2g\Delta}{\theta_{b2} - \theta_{b1}} \cos \left(\frac{\frac{\pi}{p} + \theta_{b1} + \theta_{b2}}{2} + \theta_m - \theta_e \right) \sin \left(\frac{\theta_{b2} - \theta_{b1}}{2} \right) \tag{3.42}$$

Once again, in the dynamic eccentricity case, the coefficients $A_{1_{dynamic}}$ and $B_{1_{dynamic}}$ are defined as

$$A_{1_{dynamic}} = \bar{g}_{(\frac{\pi}{2p}-\theta_{b2}) \rightarrow (\frac{\pi}{2p}-\theta_{b1})} = g - \frac{2g\Delta}{\theta_{b2} - \theta_{b1}} \cos \left(\frac{\frac{\pi}{p} - \theta_{b1} - \theta_{b2}}{2} - \theta_e \right) \sin \left(\frac{\theta_{b2} - \theta_{b1}}{2} \right) \tag{3.43}$$

$$B_{1_{dynamic}} = \bar{g}_{(\frac{\pi}{2p}+\theta_{b1}) \rightarrow (\frac{\pi}{2p}+\theta_{b2})} = g - \frac{2g\Delta}{\theta_{b2} - \theta_{b1}} \cos \left(\frac{\frac{\pi}{p} + \theta_{b1} + \theta_{b2}}{2} - \theta_e \right) \sin \left(\frac{\theta_{b2} - \theta_{b1}}{2} \right) \tag{3.44}$$

and hence,

$$\begin{aligned}
U_{r2}^{(1)} \left[1 - (b-1) \frac{l_{b1}t_{b2}}{t_{b1}l_{b2}} + \left(\frac{D}{2A_1} + \frac{D}{2B_1} \right) (\theta_{b2} - \theta_{b1}) \frac{t_{b2}}{l_{b2}} \right] = \\
= \frac{t_{b2}l_{b1}}{l_{b2}t_{b1}} a_1 \int_{\frac{\pi}{2p}-\theta_{b1}}^{\frac{\pi}{2p}+\theta_{b1}} U_s(\theta_r) d\theta_r + \frac{Dt_{b2}}{2A_1 l_{b2}} \int_{\frac{\pi}{2p}-\theta_{b2}}^{\frac{\pi}{2p}-\theta_{b1}} U_s(\theta_r) d\theta_r + \frac{Dt_{b2}}{2B_1 l_{b2}} \int_{\frac{\pi}{2p}+\theta_{b1}}^{\frac{\pi}{2p}+\theta_{b2}} U_s(\theta_r) d\theta_r
\end{aligned} \tag{3.45}$$

As a consequent, $U_{r2}^{(1)}$ can be expressed as

$$U_{r2}^{(1)} = c_1 \underbrace{\int_{\frac{\pi}{2p}-\theta_{b1}}^{\frac{\pi}{2p}+\theta_{b1}} U_s(\theta_r) d\theta_r}_{S_1} + d_1 \underbrace{\int_{\frac{\pi}{2p}-\theta_{b2}}^{\frac{\pi}{2p}-\theta_{b1}} U_s(\theta_r) d\theta_r}_{S_2} + f_1 \underbrace{\int_{\frac{\pi}{2p}+\theta_{b1}}^{\frac{\pi}{2p}+\theta_{b2}} U_s(\theta_r) d\theta_r}_{S_3} \tag{3.46}$$

where the coefficients c_1 , d_1 , and f_1 depend on the type of the eccentricity due to their dependency of the coefficients a_1 , b_1 , A_1 , and B_1 . They are given by

$$c_1 = \frac{a_1 \frac{t_{b2} t_{b1}}{l_{b2} t_{b1}}}{1 - \frac{t_{b2} t_{b1}}{l_{b2} t_{b1}} (b_1 - 1) + \left(\frac{D}{2A_1} + \frac{D}{2B_1}\right) (\theta_{b2} - \theta_{b1}) \frac{t_{b2}}{l_{b2}}} \quad (3.47)$$

$$d_1 = \frac{\frac{D}{2A_1} \frac{t_{b2}}{l_{b2}}}{1 - \frac{t_{b2} t_{b1}}{l_{b2} t_{b1}} (b_1 - 1) + \left(\frac{D}{2A_1} + \frac{D}{2B_1}\right) (\theta_{b2} - \theta_{b1}) \frac{t_{b2}}{l_{b2}}} \quad (3.48)$$

$$f_1 = \frac{\frac{D}{2B_1} \frac{t_{b2}}{l_{b2}}}{1 - \frac{t_{b2} t_{b1}}{l_{b2} t_{b1}} (b_1 - 1) + \left(\frac{D}{2A_1} + \frac{D}{2B_1}\right) (\theta_{b2} - \theta_{b1}) \frac{t_{b2}}{l_{b2}}} \quad (3.49)$$

The solution of the integration S_1 is reported in eq. (2.41), whereas the two integrations S_2 and S_3 are solved as

$$S_2 = \int_{\frac{\pi}{2p} - \theta_{b2}}^{\frac{\pi}{2p} - \theta_{b1}} U_s(\theta_r) d\theta_r = \sum_{\nu^e} -\frac{\hat{k}_{\nu^e}}{(\nu^e p)^2} \frac{D}{2} [\sin(\lambda_{\nu^e 1} - \nu^e p \theta_{b1}) - \sin(\lambda_{\nu^e 1} - \nu^e p \theta_{b2})] \quad (3.50)$$

$$S_3 = \int_{\frac{\pi}{2p} + \theta_{b1}}^{\frac{\pi}{2p} + \theta_{b2}} U_s(\theta_r) d\theta_r = \sum_{\nu^e} -\frac{\hat{k}_{\nu^e}}{(\nu^e p)^2} \frac{D}{2} [\sin(\lambda_{\nu^e 1} + \nu^e p \theta_{b2}) - \sin(\lambda_{\nu^e 1} + \nu^e p \theta_{b1})] \quad (3.51)$$

From eqs. (2.21), (3.46), (3.50) and (3.51), $U_{r2}^{(1)}$ can be rewritten as

$$\begin{aligned} U_{r2}^{(1)} &= c_1 S_1 + d_1 S_2 + f_1 S_3 \\ &= \sum_{\nu^e} -\frac{\hat{K}_{\nu^e}}{(\nu^e p)^2} D c_1 \cos(\lambda_{\nu^e 1}) \sin(\nu^e p \theta_{b1}) \\ &\quad + \sum_{\nu^e} -\frac{\hat{K}_{\nu^e}}{(\nu^e p)^2} \frac{D}{2} d_1 \left[\sin(\lambda_{\nu^e 1} - \nu^e p \theta_{b1}) - \sin(\lambda_{\nu^e 1} - \nu^e p \theta_{b2}) \right] \\ &\quad + \sum_{\nu^e} -\frac{\hat{K}_{\nu^e}}{(\nu^e p)^2} \frac{D}{2} f_1 \left[\sin(\lambda_{\nu^e 1} + \nu^e p \theta_{b2}) - \sin(\lambda_{\nu^e 1} + \nu^e p \theta_{b1}) \right] \end{aligned} \quad (3.52)$$

Consequently, by substituting eq. (3.52) in eq. (3.35), $U_{r1}^{(1)}$ can be rewritten as

$$\begin{aligned} U_{r1}^{(1)} &= -\sum_{\nu^e} \frac{\hat{K}_{\nu^e}}{(\nu^e p)^2} \cos(\lambda_{\nu^e 1}) \sin(\nu^e p \theta_{b1}) [a_1 + b_1 c_1] \\ &\quad - \sum_{\nu^e} \frac{\hat{K}_{\nu^e}}{(\nu^e p)^2} \frac{D}{2} b_1 d_1 \left[\sin(\lambda_{\nu^e 1} - \nu^e p \theta_{b1}) - \sin(\lambda_{\nu^e 1} - \nu^e p \theta_{b2}) \right] \\ &\quad - \sum_{\nu^e} \frac{\hat{K}_{\nu^e}}{(\nu^e p)^2} \frac{D}{2} b_1 f_1 \left[\sin(\lambda_{\nu^e 1} + \nu^e p \theta_{b2}) - \sin(\lambda_{\nu^e 1} + \nu^e p \theta_{b1}) \right] \end{aligned} \quad (3.53)$$

Similarly, the magnetic potentials of the rotor islands of the second and third poles are computed. Then, from the resulted expressions of the rotor islands magnetic potential, the general

formulas of the magnetic potential of the inner and outer islands for the w -th pole are reported in eqs. (3.54) and (3.55).

$$\begin{aligned}
U_{r2}^{(w)} &= \sum_{\nu^e} -\frac{\hat{K}_{\nu^e}}{(\nu^e p)^2} D c_w \cos(\lambda_{\nu^e w}) \sin(\nu^e p \theta_{b1}) \\
&+ \sum_{\nu^e} -\frac{\hat{K}_{\nu^e}}{(\nu^e p)^2} \frac{D}{2} d_w \left[\sin(\lambda_{\nu^e w} - \nu^e p \theta_{b1}) - \sin(\lambda_{\nu^e w} - \nu^e p \theta_{b2}) \right] \\
&+ \sum_{\nu^e} -\frac{\hat{K}_{\nu^e}}{(\nu^e p)^2} \frac{D}{2} f_w \left[\sin(\lambda_{\nu^e w} + \nu^e p \theta_{b2}) - \sin(\lambda_{\nu^e w} + \nu^e p \theta_{b1}) \right]
\end{aligned} \tag{3.54}$$

$$\begin{aligned}
U_{r1}^{(w)} &= -\sum_{\nu^e} \frac{\hat{K}_{\nu^e}}{(\nu^e p)^2} \cos(\lambda_{\nu^e w}) \sin(\nu^e p \theta_{b1}) [a_w + b_w c_w] \\
&- \sum_{\nu^e} \frac{\hat{K}_{\nu^e}}{(\nu^e p)^2} \frac{D}{2} b_w d_w \left[\sin(\lambda_{\nu^e w} - \nu^e p \theta_{b1}) - \sin(\lambda_{\nu^e w} - \nu^e p \theta_{b2}) \right] \\
&- \sum_{\nu^e} \frac{\hat{K}_{\nu^e}}{(\nu^e p)^2} \frac{D}{2} b_w f_w \left[\sin(\lambda_{\nu^e w} + \nu^e p \theta_{b2}) - \sin(\lambda_{\nu^e w} + \nu^e p \theta_{b1}) \right]
\end{aligned} \tag{3.55}$$

where the general expressions of the coefficients $b_{w_{static}}$, $A_{w_{static}}$, and $B_{w_{static}}$, in static eccentricity case, are given by

$$b_{w_{static}} = \frac{1}{1 + \frac{D t_{b1}}{2 g l_{b1} \left[1 - \frac{\Delta}{\theta_{b1}} \cos\left(\frac{X(w)\pi}{2p} + \theta_m - \theta_e\right) \sin(\theta_{b1}) \right]} 2 \theta_{b1}} \tag{3.56}$$

$$A_{w_{static}} = g \left[1 - \frac{2\Delta}{\theta_{b2} - \theta_{b1}} \cos\left(\frac{X(w)\pi}{2p} - \frac{\theta_{b1} + \theta_{b2}}{2} + \theta_m - \theta_e\right) \sin\left(\frac{\theta_{b2} - \theta_{b1}}{2}\right) \right] \tag{3.57}$$

$$B_{w_{static}} = g \left[1 - \frac{2\Delta}{\theta_{b2} - \theta_{b1}} \cos\left(\frac{X(w)\pi}{2p} + \frac{\theta_{b1} + \theta_{b2}}{2} + \theta_m - \theta_e\right) \sin\left(\frac{\theta_{b2} - \theta_{b1}}{2}\right) \right] \tag{3.58}$$

and in dynamic eccentricity cases, are given by

$$b_{w_{dynamic}} = \frac{1}{1 + \frac{D t_{b1}}{2 g l_{b1} \left[1 - \frac{\Delta}{\theta_{b1}} \cos\left(\frac{X(w)\pi}{2p} - \theta_e\right) \sin(\theta_{b1}) \right]} 2 \theta_{b1}} \tag{3.59}$$

$$A_{w_{dynamic}} = g \left[1 - \frac{2\Delta}{\theta_{b2} - \theta_{b1}} \cos\left(\frac{X(w)\pi}{2p} - \frac{\theta_{b1} + \theta_{b2}}{2} - \theta_e\right) \sin\left(\frac{\theta_{b2} - \theta_{b1}}{2}\right) \right] \tag{3.60}$$

$$B_{w_{dynamic}} = g \left[1 - \frac{2\Delta}{\theta_{b2} - \theta_{b1}} \cos\left(\frac{X(w)\pi}{2p} + \frac{\theta_{b1} + \theta_{b2}}{2} - \theta_e\right) \sin\left(\frac{\theta_{b2} - \theta_{b1}}{2}\right) \right] \tag{3.61}$$

Hence, the expressions of the coefficients c_w , d_w , and f_w , which depends on the coefficients a_w , b_w , A_w , and B_w , are generalized as

$$c_w = \frac{a_w \frac{t_{b2} l_{b1}}{l_{b2} t_{b1}}}{1 - \frac{t_{b2} l_{b1}}{l_{b2} t_{b1}} (b_w - 1) + \left(\frac{D}{2A_w} + \frac{D}{2B_w} \right) (\theta_{b2} - \theta_{b1}) \frac{t_{b2}}{l_{b2}}} \quad (3.62)$$

$$d_w = \frac{\frac{D}{2A_w} \frac{t_{b2}}{l_{b2}}}{1 - \frac{t_{b2} l_{b1}}{l_{b2} t_{b1}} (b_w - 1) + \left(\frac{D}{2A_w} + \frac{D}{2B_w} \right) (\theta_{b2} - \theta_{b1}) \frac{t_{b2}}{l_{b2}}} \quad (3.63)$$

$$f_w = \frac{\frac{D}{2B_w} \frac{t_{b2}}{l_{b2}}}{1 - \frac{t_{b2} l_{b1}}{l_{b2} t_{b1}} (b_w - 1) + \left(\frac{D}{2A_w} + \frac{D}{2B_w} \right) (\theta_{b2} - \theta_{b1}) \frac{t_{b2}}{l_{b2}}} \quad (3.64)$$

3.4.3. Three flux barriers per pole

The linearized geometry of a REL motor, with $2p$ poles and three flux-barriers per each pole is shown in Fig. 3.8. From the magnetic network shown in Fig. 2.7 (b), it is noted that $U_{r1}^{(1)}$ can be expressed as in eq. (3.35). In addition, $U_{r2}^{(1)}$ is computed as

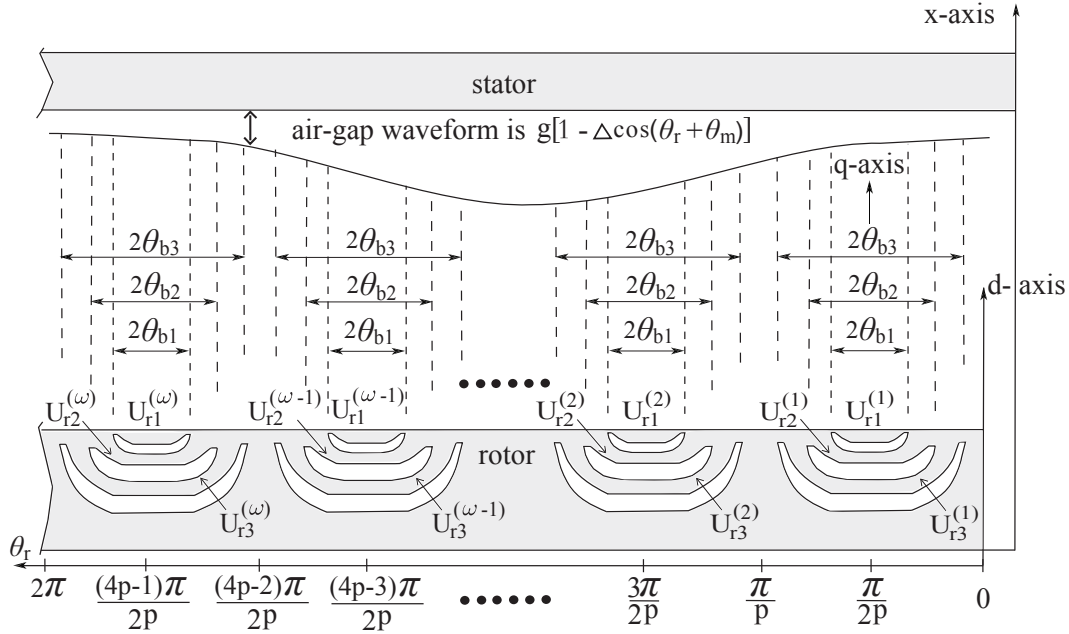


Figure 3.8: Linearized geometry for four-pole rotor with three flux-barriers. $\theta_e = 0^\circ$.

$$U_{r2} = \phi_{b2}^{(1)} R_{b2} + U_{r3}^{(1)} \quad (3.65)$$

The simplification of the previous expression is similar to that carried out in case of two flux-barriers per pole, as in eqs. (3.38) to (3.40), (3.45) and (3.46). However, an additional term (U_{r3}), which is the magnetic potential of the inner island bordered by the broader barrier, is

added to the derivation. Hence, U_{r2} can be expressed as

$$U_{r2}^{(1)} = c_1 \underbrace{\int_{\frac{\pi}{2p}-\theta_{b1}}^{\frac{\pi}{2p}+\theta_{b1}} U_s(\theta_r) d\theta_r}_{S_1} + d_1 \underbrace{\int_{\frac{\pi}{2p}-\theta_{b2}}^{\frac{\pi}{2p}-\theta_{b1}} U_s(\theta_r) d\theta_r}_{S_2} + f_1 \underbrace{\int_{\frac{\pi}{2p}+\theta_{b1}}^{\frac{\pi}{2p}+\theta_{b2}} U_s(\theta_r) d\theta_r}_{S_3} + z_1 U_{r3}^{(1)} \quad (3.66)$$

where the coefficient z_1 is given by

$$f_1 = \frac{1}{1 - \frac{t_{b2}t_{b1}}{l_{b2}l_{b1}}(b_1 - 1) + \left(\frac{D}{2A_1} + \frac{D}{2B_1}\right)(\theta_{b2} - \theta_{b1})\frac{t_{b2}}{l_{b2}}} \quad (3.67)$$

Once again, from the magnetic network shown in Fig. 2.7 (b), the magnetic potential of the third island $U_{r3}^{(1)}$ is computed as

$$\begin{aligned} U_{r3}^{(1)} &= \phi_{b3}^{(1)} R_{b3} \\ &= \left[\phi_{b2}^{(1)} + \int_{\frac{\pi}{2p}-\theta_{b3}}^{\frac{\pi}{2p}-\theta_{b2}} \mu_o \frac{U_s(\theta_r) - U_{r3}^{(1)}}{\bar{g}_{(\frac{\pi}{2p}-\theta_{b3}) \rightarrow (\frac{\pi}{2p}-\theta_{b2})}} L_{stk} \frac{D}{2} d\theta_r + \right. \\ &\quad \left. + \int_{\frac{\pi}{2p}+\theta_{b2}}^{\frac{\pi}{2p}+\theta_{b3}} \mu_o \frac{U_s(\theta_r) - U_{r3}^{(1)}}{\bar{g}_{(\frac{\pi}{2p}+\theta_{b2}) \rightarrow (\frac{\pi}{2p}+\theta_{b3})}} L_{stk} \frac{D}{2} d\theta_r \right] \frac{t_{b3}}{\mu_o L_{stk} l_{b3}} \end{aligned} \quad (3.68)$$

Substituting $\phi_{b2}^{(1)} = (U_{r2}^{(1)} - U_{r3}^{(1)})/R_{b2}$ in eq. (3.68), it results

$$\begin{aligned} U_{r3}^{(1)} &= \left[\frac{U_{r2}^{(1)} - U_{r3}^{(1)}}{\frac{t_{b2}}{l_{b2}}} + \frac{D}{2} \int_{\frac{\pi}{2p}-\theta_{b3}}^{\frac{\pi}{2p}-\theta_{b2}} \frac{U_s(\theta_r) - U_{r3}^{(1)}}{\bar{g}_{(\frac{\pi}{2p}-\theta_{b3}) \rightarrow (\frac{\pi}{2p}-\theta_{b2})}} d\theta_r + \right. \\ &\quad \left. + \frac{D}{2} \int_{\frac{\pi}{2p}+\theta_{b2}}^{\frac{\pi}{2p}+\theta_{b3}} \frac{U_s(\theta_r) - U_{r3}^{(1)}}{\bar{g}_{(\frac{\pi}{2p}+\theta_{b2}) \rightarrow (\frac{\pi}{2p}+\theta_{b3})}} d\theta_r \right] \frac{t_{b3}}{l_{b3}} \end{aligned} \quad (3.69)$$

Substituting $U_{r2}^{(1)}$, which reported in eq. (3.66), in eq. (3.69), it results

$$\begin{aligned} U_{r3}^{(1)} &= \frac{l_{b2}t_{b3}}{t_{b2}l_{b3}} \left[c_1 S_1 + d_1 S_2 + f_1 S_3 + z_1 U_{r3}^{(1)} \right] - \frac{l_{b2}t_{b3}}{t_{b2}l_{b3}} U_{r3}^{(1)} - \\ &\quad - \left[\frac{Dt_{b3}}{2\bar{g}_{(\frac{\pi}{2p}-\theta_{b3}) \rightarrow (\frac{\pi}{2p}-\theta_{b2})} l_{b3}} + \frac{Dt_{b3}}{2\bar{g}_{(\frac{\pi}{2p}+\theta_{b2}) \rightarrow (\frac{\pi}{2p}+\theta_{b3})} l_{b3}} \right] U_{r3}^{(1)} (\theta_{b3} - \theta_{b2}) \\ &\quad + \frac{Dt_{b3}}{2\bar{g}_{(\frac{\pi}{2p}-\theta_{b3}) \rightarrow (\frac{\pi}{2p}-\theta_{b2})} l_{b3}} \underbrace{\int_{\frac{\pi}{2p}-\theta_{b3}}^{\frac{\pi}{2p}-\theta_{b2}} U_s(\theta_r) d\theta_r}_{S_4} + \\ &\quad + \frac{Dt_{b3}}{2\bar{g}_{(\frac{\pi}{2p}+\theta_{b2}) \rightarrow (\frac{\pi}{2p}+\theta_{b3})} l_{b3}} \underbrace{\int_{\frac{\pi}{2p}+\theta_{b2}}^{\frac{\pi}{2p}+\theta_{b3}} U_s(\theta_r) d\theta_r}_{S_5} \end{aligned} \quad (3.70)$$

The coefficient x_1 refers to the average air-gap length between the two angles $\frac{\pi}{2p} - \theta_{b3}$ and $\frac{\pi}{2p} - \theta_{b2}$, besides, the coefficient y_1 refers to the average air-gap length between the two angles

$\frac{\pi}{2p} + \theta_{b2}$ and $\frac{\pi}{2p} + \theta_{b3}$. For static eccentricity cases, the two coefficients are given by

$$x_{1_{static}} = \bar{g}_{(\frac{\pi}{2p}-\theta_{b3}) \rightarrow (\frac{\pi}{2p}-\theta_{b2})} = g - \frac{2g\Delta}{\theta_{b3} - \theta_{b2}} \cos \left(\frac{\frac{\pi}{p} - \theta_{b2} - \theta_{b3}}{2} + \theta_m - \theta_e \right) \sin \left(\frac{\theta_{b3} - \theta_{b2}}{2} \right) \quad (3.71)$$

$$y_{1_{static}} = \bar{g}_{(\frac{\pi}{2p}+\theta_{b2}) \rightarrow (\frac{\pi}{2p}+\theta_{b3})} = g - \frac{2g\Delta}{\theta_{b3} - \theta_{b2}} \cos \left(\frac{\frac{\pi}{p} + \theta_{b2} + \theta_{b3}}{2} + \theta_m - \theta_e \right) \sin \left(\frac{\theta_{b3} - \theta_{b2}}{2} \right) \quad (3.72)$$

and, for the dynamic eccentricity case, are expressed as

$$x_{1_{static}} = \bar{g}_{(\frac{\pi}{2p}-\theta_{b3}) \rightarrow (\frac{\pi}{2p}-\theta_{b2})} = g - \frac{2g\Delta}{\theta_{b3} - \theta_{b2}} \cos \left(\frac{\frac{\pi}{p} - \theta_{b2} - \theta_{b3}}{2} - \theta_e \right) \sin \left(\frac{\theta_{b3} - \theta_{b2}}{2} \right) \quad (3.73)$$

$$y_{1_{static}} = \bar{g}_{(\frac{\pi}{2p}+\theta_{b2}) \rightarrow (\frac{\pi}{2p}+\theta_{b3})} = g - \frac{2g\Delta}{\theta_{b3} - \theta_{b2}} \cos \left(\frac{\frac{\pi}{p} + \theta_{b2} + \theta_{b3}}{2} - \theta_e \right) \sin \left(\frac{\theta_{b3} - \theta_{b2}}{2} \right) \quad (3.74)$$

$$U_{r3}^{(1)} = c_1 \frac{l_{b2}t_{b3}}{t_{b2}l_{b3}} S_1 + d_1 \frac{l_{b2}t_{b3}}{t_{b2}l_{b3}} S_2 + f_1 \frac{l_{b2}t_{b3}}{t_{b2}l_{b3}} S_3 + \frac{l_{b2}t_{b3}}{t_{b2}l_{b3}} (z_1 - 1) U_{r3}^{(1)} - \left[\frac{Dt_{b3}}{2x_1 l_{b3}} + \frac{Dt_{b3}}{2y_1 l_{b3}} \right] (\theta_{b3} - \theta_{b2}) U_{r3}^{(1)} + \frac{Dt_{b3}}{2x_1 l_{b3}} S_4 + \frac{Dt_{b3}}{2y_1 l_{b3}} S_5 \quad (3.75)$$

$$U_{r3}^{(1)} \underbrace{\left[1 - (z_1 - 1) \frac{l_{b2}t_{b3}}{t_{b2}l_{b3}} + \left(\frac{D}{2x_1} + \frac{D}{2y_1} \right) (\theta_{b3} - \theta_{b2}) \frac{t_{b3}}{l_{b3}} \right]}_{den_1} = c_1 \frac{l_{b2}t_{b3}}{t_{b2}l_{b3}} S_1 + d_1 \frac{l_{b2}t_{b3}}{t_{b2}l_{b3}} S_2 + f_1 \frac{l_{b2}t_{b3}}{t_{b2}l_{b3}} S_3 + \frac{Dt_{b3}}{2x_1 l_{b3}} S_4 + \frac{Dt_{b3}}{2y_1 l_{b3}} S_5 \quad (3.76)$$

thus,

$$U_{r3}^{(1)} = m_1 \underbrace{\int_{\frac{\pi}{2p}-\theta_{b1}}^{\frac{\pi}{2p}+\theta_{b1}} U_s(\theta_r) d\theta_r}_{S_1} + n_1 \underbrace{\int_{\frac{\pi}{2p}-\theta_{b2}}^{\frac{\pi}{2p}-\theta_{b1}} U_s(\theta_r) d\theta_r}_{S_2} + q_1 \underbrace{\int_{\frac{\pi}{2p}+\theta_{b1}}^{\frac{\pi}{2p}+\theta_{b2}} U_s(\theta_r) d\theta_r}_{S_3} + j_1 \underbrace{\int_{\frac{\pi}{2p}-\theta_{b3}}^{\frac{\pi}{2p}-\theta_{b2}} U_s(\theta_r) d\theta_r}_{S_4} + h_1 \underbrace{\int_{\frac{\pi}{2p}+\theta_{b2}}^{\frac{\pi}{2p}+\theta_{b3}} U_s(\theta_r) d\theta_r}_{S_5} \quad (3.77)$$

where

$$den_1 = \left[1 - (z_1 - 1) \frac{l_{b2}t_{b3}}{t_{b2}l_{b3}} - \left(\frac{D}{2x_1} + \frac{D}{2y_1} \right) (\theta_{b3} - \theta_{b2}) \frac{t_{b3}}{l_{b3}} \right] \quad (3.78)$$

$$m_1 = \frac{c_1 \frac{l_{b2}t_{b3}}{t_{b2}l_{b3}}}{den_1} \quad (3.79)$$

$$n_1 = \frac{d_1 \frac{l_{b2} t_{b3}}{t_{b2} l_{b3}}}{den_1} \quad (3.80)$$

$$q_1 = \frac{f_1 \frac{l_{b2} t_{b3}}{t_{b2} l_{b3}}}{den_1} \quad (3.81)$$

$$j_1 = \frac{\frac{Dt_{b3}}{2x_1 l_{b3}}}{den_1} \quad (3.82)$$

$$h_1 = \frac{\frac{Dt_{b3}}{2y_1 l_{b3}}}{den_1} \quad (3.83)$$

The symbolic solution of the integrations S_1 , S_2 , and S_3 have been reported in eqs. (2.41), (3.50) and (3.51). Nevertheless S_4 , and S_5 are solved as following:

$$S_4 = \int_{\frac{\pi}{2p} - \theta_{b3}}^{\frac{\pi}{2p} - \theta_{b2}} U_s(\theta_r) d\theta_r = \sum_{\nu^e} -\frac{\hat{K}_{\nu^e}}{(\nu^e p)^2} \frac{D}{2} [\sin(\lambda_{\nu^e 1} - \nu^e p \theta_{b2}) - \sin(\lambda_{\nu^e 1} - \nu^e p \theta_{b3})] \quad (3.84)$$

$$S_5 = \int_{\frac{\pi}{2p} + \theta_{b2}}^{\frac{\pi}{2p} + \theta_{b3}} U_s(\theta_r) d\theta_r = \sum_{\nu^e} -\frac{\hat{K}_{\nu^e}}{(\nu^e p)^2} \frac{D}{2} [\sin(\lambda_{\nu^e 1} + \nu^e p \theta_{b3}) - \sin(\lambda_{\nu^e 1} + \nu^e p \theta_{b2})] \quad (3.85)$$

Finally $U_{r3}^{(1)}$, can be expressed as

$$\begin{aligned} U_{r3}^{(1)} &= \sum_{\nu^e} -\frac{\hat{K}_{\nu^e}}{(\nu^e p)^2} D m_1 \cos(\lambda_{\nu^e 1}) \sin(\nu^e p \theta_{b1}) \\ &+ \sum_{\nu^e} -\frac{\hat{K}_{\nu^e}}{(\nu^e p)^2} \frac{D}{2} n_1 [\sin(\lambda_{\nu^e 1} - \nu^e p \theta_{b1}) - \sin(\lambda_{\nu^e 1} - \nu^e p \theta_{b2})] \\ &+ \sum_{\nu^e} -\frac{\hat{K}_{\nu^e}}{(\nu^e p)^2} \frac{D}{2} q_1 [\sin(\lambda_{\nu^e 1} + \nu^e p \theta_{b2}) - \sin(\lambda_{\nu^e 1} + \nu^e p \theta_{b1})] \\ &+ \sum_{\nu^e} -\frac{\hat{K}_{\nu^e}}{(\nu^e p)^2} \frac{D}{2} j_1 [\sin(\lambda_{\nu^e 1} - \nu^e p \theta_{b2}) - \sin(\lambda_{\nu^e 1} - \nu^e p \theta_{b3})] \\ &+ \sum_{\nu^e} -\frac{\hat{K}_{\nu^e}}{(\nu^e p)^2} \frac{D}{2} h_1 [\sin(\lambda_{\nu^e 1} + \nu^e p \theta_{b3}) - \sin(\lambda_{\nu^e 1} + \nu^e p \theta_{b2})] \end{aligned} \quad (3.86)$$

By substituting eqs. (3.41), (3.50) and (3.51) in eq. (3.66), $U_{r2}^{(1)}$ is finally expressed as

$$\begin{aligned} U_{r2}^{(1)} &= \sum_{\nu^e} -\frac{\hat{K}_{\nu^e}}{(\nu^e p)^2} D c_1 \cos(\lambda_{\nu^e 1}) \sin(\nu^e p \theta_{b1}) \\ &+ \sum_{\nu^e} -\frac{\hat{K}_{\nu^e}}{(\nu^e p)^2} \frac{D}{2} d_1 [\sin(\lambda_{\nu^e 1} - \nu^e p \theta_{b1}) - \sin(\lambda_{\nu^e 1} - \nu^e p \theta_{b2})] \\ &+ \sum_{\nu^e} -\frac{\hat{K}_{\nu^e}}{(\nu^e p)^2} \frac{D}{2} f_1 [\sin(\lambda_{\nu^e 1} + \nu^e p \theta_{b2}) - \sin(\lambda_{\nu^e 1} + \nu^e p \theta_{b1})] + z_1 U_{r3}^{(1)} \end{aligned} \quad (3.87)$$

Once again, by substituting eq. (3.41) in eq. (3.35), the final expression of $U_{r2}^{(1)}$ can be achieved as

$$U_{r1}^{(1)} = -a_1 D \sum_{\nu^e} \frac{\hat{K}_{\nu^e}}{(\nu^e p)^2} \cos(\lambda_{\nu^e 1}) \sin(\nu^e p \theta_{b1}) + b_1 U_{r2}^{(1)} \quad (3.88)$$

Analogously, the magnetic potentials of the three rotor islands of the second and third poles are computed. Then, the general formulas of the magnetic potential of the three islands for the w -th pole are reported as

$$U_{r1}^{(w)} = -a_w D \sum_{\nu^e} \frac{\hat{K}_{\nu^e}}{(\nu^e p)^2} \cos(\lambda_{\nu^e w}) \sin(\nu^e p \theta_{b1}) + b_w U_{r2}^{(w)} \quad (3.89)$$

$$\begin{aligned} U_{r2}^{(w)} &= \sum_{\nu^e} -\frac{\hat{K}_{\nu^e}}{(\nu^e p)^2} D c_w \cos(\lambda_{\nu^e w}) \sin(\nu^e p \theta_{b1}) \\ &+ \sum_{\nu^e} -\frac{\hat{K}_{\nu^e}}{(\nu^e p)^2} \frac{D}{2} d_w [\sin(\lambda_{\nu^e w} - \nu^e p \theta_{b1}) - \sin(\lambda_{\nu^e w} - \nu^e p \theta_{b2})] \\ &+ \sum_{\nu^e} -\frac{\hat{K}_{\nu^e}}{(\nu^e p)^2} \frac{D}{2} f_w [\sin(\lambda_{\nu^e w} + \nu^e p \theta_{b2}) - \sin(\lambda_{\nu^e w} + \nu^e p \theta_{b1})] + z_w U_{r3}^{(w)} \end{aligned} \quad (3.90)$$

and

$$\begin{aligned} U_{r3}^{(w)} &= \sum_{\nu^e} -\frac{\hat{K}_{\nu^e}}{(\nu^e p)^2} D m_w \cos(\lambda_{\nu^e w}) \sin(\nu^e p \theta_{b1}) + \\ &\sum_{\nu^e} -\frac{\hat{K}_{\nu^e}}{(\nu^e p)^2} \frac{D}{2} n_w [\sin(\lambda_{\nu^e w} - \nu^e p \theta_{b1}) - \sin(\lambda_{\nu^e w} - \nu^e p \theta_{b2})] \\ &+ \sum_{\nu^e} -\frac{\hat{K}_{\nu^e}}{(\nu^e p)^2} \frac{D}{2} q_w [\sin(\lambda_{\nu^e w} + \nu^e p \theta_{b2}) - \sin(\lambda_{\nu^e w} + \nu^e p \theta_{b1})] \\ &+ \sum_{\nu^e} -\frac{\hat{K}_{\nu^e}}{(\nu^e p)^2} \frac{D}{2} j_w [\sin(\lambda_{\nu^e w} - \nu^e p \theta_{b2}) - \sin(\lambda_{\nu^e w} - \nu^e p \theta_{b3})] \\ &+ \sum_{\nu^e} -\frac{\hat{K}_{\nu^e}}{(\nu^e p)^2} \frac{D}{2} h_w [\sin(\lambda_{\nu^e w} + \nu^e p \theta_{b3}) - \sin(\lambda_{\nu^e w} + \nu^e p \theta_{b2})] \end{aligned} \quad (3.91)$$

where

$$z_w = \frac{1}{1 - \frac{t_{b2} l_{b1}}{l_{b2} t_{b1}} (b_w - 1) + \left(\frac{D}{2A_w} + \frac{D}{2B_w}\right) (\theta_{b2} - \theta_{b1}) \frac{t_{b2}}{l_{b2}}} \quad (3.92)$$

$$x_w = g \left[1 + \frac{\Delta}{\theta_{b3} - \theta_{b2}} \left(\sin\left(\theta_m + \frac{X(w)\pi}{2p} - \theta_{b3}\right) - \sin\left(\theta_m + \frac{X(w)\pi}{2p} - \theta_{b2}\right) \right) \right] \quad (3.93)$$

$$y_w = g \left[1 + \frac{\Delta}{\theta_{b3} - \theta_{b2}} \left(\sin\left(\theta_m + \frac{X(w)\pi}{2p} + \theta_{b2}\right) - \sin\left(\theta_m + \frac{X(w)\pi}{2p} + \theta_{b3}\right) \right) \right] \quad (3.94)$$

$$den_w = \left[1 - (z_w - 1) \frac{l_{b2} t_{b3}}{t_{b2} l_{b3}} - \left(\frac{D}{2x_w} + \frac{D}{2y_w}\right) (\theta_{b3} - \theta_{b2}) \frac{t_{b3}}{l_{b3}} \right] \quad (3.95)$$

$$m_w = \frac{c_w \frac{l_{b2} t_{b3}}{t_{b2} l_{b3}}}{den_w} \quad (3.96)$$

$$n_w = \frac{d_w \frac{l_{b2} t_{b3}}{t_{b2} l_{b3}}}{den_w} \quad (3.97)$$

$$q_w = \frac{f_w \frac{l_{b2} t_{b3}}{t_{b2} l_{b3}}}{den_w} \quad (3.98)$$

$$j_w = \frac{\frac{Dt_{b3}}{2x_w l_{b3}}}{den_w} \quad (3.99)$$

$$h_w = \frac{\frac{Dt_{b3}}{2y_w l_{b3}}}{den_w} \quad (3.100)$$

3.5. Electromagnetic torque

This section deals with the derivation of the general formula of the electromagnetic torque of REL motor with one, two, and three flux barriers per pole. Both static and dynamic eccentricity cases are considered. Again, due to the non-uniform air-gap length variation, there is no symmetry of the air-gap flux density distribution over the motor poles. Consequently, the computation of the electromagnetic torque should be carried out separately for each pole. Then, the total torque is obtained by summing all torque components results by all poles.

3.5.1. One flux barrier per pole

The general expression of the electromagnetic torque is reported in eq. (2.67). Considering the different poles, it can be expressed as

$$\begin{aligned} \tau_m = & \frac{-\mu_o D^2 L_{stk}}{4} \left[\underbrace{\int_{\frac{\pi}{2p}-\theta_{b1}}^{\frac{\pi}{2p}+\theta_{b1}} \frac{U_{r1}^{(1)}(\theta_r) K_s(\theta_r)}{\bar{g}(\frac{\pi}{2p}-\theta_{b1}) \rightarrow (\frac{\pi}{2p}+\theta_{b1})} d\theta_r}_1 + \underbrace{\int_{\frac{3\pi}{2p}-\theta_{b1}}^{\frac{3\pi}{2p}+\theta_{b1}} \frac{U_{r1}^{(2)}(\theta_r) K_s(\theta_r)}{\bar{g}(\frac{\pi}{2p}-\theta_{b1}) \rightarrow (\frac{\pi}{2p}+\theta_{b1})} d\theta_r}_2 \right. \\ & \left. + \underbrace{\int_{\frac{5\pi}{2p}-\theta_{b1}}^{\frac{5\pi}{2p}+\theta_{b1}} \frac{U_{r1}^{(3)}(\theta_r) K_s(\theta_r)}{\bar{g}(\frac{\pi}{2p}-\theta_{b1}) \rightarrow (\frac{\pi}{2p}+\theta_{b1})} d\theta_r}_3 + \dots + \underbrace{\int_{\frac{X(w)\pi}{2p}-\theta_{b1}}^{\frac{X(w)\pi}{2p}+\theta_{b1}} \frac{U_{r1}^{(w)}(\theta_r) K_s(\theta_r)}{\bar{g}(\frac{X(w)\pi}{2p}-\theta_{b1}) \rightarrow (\frac{X(w)\pi}{2p}+\theta_{b1})} d\theta_r}_{2p} \right] \quad (3.101) \end{aligned}$$

For simplicity, the torque components of the first and second poles are derived, and then the general formula of the torque component results by the w -th pole is derived. As stated before the magnetic potential is exist only on the rotor islands and null on the rotor channels.

Therefore, the electromagnetic torque results for the first pole τ_m^1 is computed as

$$\begin{aligned}\tau_m^{(1)} &= \frac{-\mu_o D^2 L_{stk}}{4} \int_{\frac{\pi}{2p} - \theta_{b1}}^{\frac{\pi}{2p} + \theta_{b1}} \frac{U_{r1}^{(1)} K_s(\theta_r)}{\bar{g}_{(\frac{\pi}{2p} - \theta_{b1}) \rightarrow (\frac{\pi}{2p} + \theta_{b1})}} d\theta_r \\ &= \frac{-\mu_o D^2 L_{stk} U_{r1}^{(1)}}{4\bar{g}_{(\frac{\pi}{2p} - \theta_{b1}) \rightarrow (\frac{\pi}{2p} + \theta_{b1})}} \int_{\frac{\pi}{2p} - \theta_{b1}}^{\frac{\pi}{2p} + \theta_{b1}} K_s(\theta_r) d\theta_r\end{aligned}\quad (3.102)$$

The average air-gap lengths, for both eccentricity cases, are reported in eqs. (3.13) and (3.14). Then, substituting $U_{r1}^{(1)}$ and $K_s(\theta_r)$, which reported in eqs. (2.20) and (3.17), respectively, and $\bar{g}_{(\frac{\pi}{2p} - \theta_{b1}) \rightarrow (\frac{\pi}{2p} + \theta_{b1})}$, in eq. (3.102), it results

$$\tau_m^{(1)} = \frac{\mu_o D^2 L_{stk} a_1 D}{2\bar{g}_{(\frac{\pi}{2p} - \theta_{b1}) \rightarrow (\frac{\pi}{2p} + \theta_{b1})}} \sum_{\nu^e} \frac{\hat{K}_{\nu^e}}{(\nu^e p)^2} \cos(\lambda_{\nu^e 1}) \sin(\nu^e p \theta_{b1}) \sum_{\xi_a} \frac{\hat{K}_{\xi_a}}{(\xi_a p)} \sin(\lambda_{\xi_1}) \sin(\xi_a p \theta_{b1}) \quad (3.103)$$

Letting

$$\lambda_{\xi_1} = \frac{\xi_a \pi}{2} + (\xi_a - 1) \omega_{me} t - \alpha_i^e \quad (3.104)$$

$$k_{\tau 1} = \frac{\mu_o D^3 L_{stk}}{2\bar{g}_{(\frac{\pi}{2p} - \theta_{b1}) \rightarrow (\frac{\pi}{2p} + \theta_{b1})}} \quad (3.105)$$

So the first component of the torque (τ_{m1}) is given by:

$$\tau_m^{(1)} = a_1 k_{\tau 1} \sum_{\nu^e} \frac{\hat{K}_{\nu^e}}{(\nu^e p)^2} \cos(\lambda_{\nu^e 1}) \sin(\nu^e p \theta_{b1}) \sum_{\xi_a} \frac{\hat{K}_{\xi_a}}{(\xi_a p)} \sin(\lambda_{\xi_1}) \sin(\xi_a p \theta_{b1}) \quad (3.106)$$

The computation of electromagnetic torque is repeated for the second pole. The integration limits are changed to $\frac{3\pi}{2p} - \theta_{b1}$ and $\frac{3\pi}{2p} + \theta_{b1}$. Then, the electromagnetic torque is given by

$$\begin{aligned}\tau_m^{(2)} &= \frac{-\mu_o D^2 L_{stk}}{4} \int_{\frac{3\pi}{2p} - \theta_{b1}}^{\frac{3\pi}{2p} + \theta_{b1}} \frac{U_{r1}^{(2)} K_s(\theta_r)}{\bar{g}_{(\frac{3\pi}{2p} - \theta_{b1}) \rightarrow (\frac{3\pi}{2p} + \theta_{b1})}} d\theta_r \\ &= \frac{-\mu_o D^2 L_{stk} U_{r1}^{(2)}}{4\bar{g}_{(\frac{3\pi}{2p} - \theta_{b1}) \rightarrow (\frac{3\pi}{2p} + \theta_{b1})}} \int_{\frac{3\pi}{2p} - \theta_{b1}}^{\frac{3\pi}{2p} + \theta_{b1}} K_s(\theta_r) d\theta_r\end{aligned}\quad (3.107)$$

Once again, by substituting the expressions of $U_{r1}^{(2)}$, $K_s(\theta_r)$, which are reported in eqs. (2.20) and (3.24), in eq. (3.107), it results

$$\tau_m^{(2)} = a_2 k_{\tau 2} \sum_{\nu^e} \frac{\hat{K}_{\nu^e}}{(\nu^e p)^2} \cos(\lambda_{\nu^e 2}) \sin(\nu^e p \theta_{b1}) \sum_{\xi_a} \frac{\hat{K}_{\xi_a}}{(\xi_a p)} \sin(\lambda_{\xi_2}) \sin(\xi_a p \theta_{b1}) \quad (3.108)$$

Letting

$$\lambda_{\xi_2} = \frac{3\xi_a \pi}{2} + (\xi_a - 1) \omega_{me} t - \alpha_i^e \quad (3.109)$$

$$k_{\tau 2} = \frac{\mu_o D^3 L_{stk}}{2\bar{g}_{(\frac{3\pi}{2p} - \theta_{b1}) \rightarrow (\frac{3\pi}{2p} + \theta_{b1})}} \quad (3.110)$$

Similarly, the same computations are carried out for the third pole. Then, the results are

$$\tau_m^{(3)} = a_3 k_{\tau 3} \sum_{\nu^e} \frac{\hat{K}_{\nu^e}}{(\nu^e p)^2} \cos(\lambda_{\nu^e 3}) \sin(\nu^e p \theta_{b1}) \sum_{\xi_a} \frac{\hat{K}_{\xi_a}}{(\xi_a p)} \sin(\lambda_{\xi 3}) \sin(\xi_a p \theta_{b1}) \quad (3.111)$$

Letting

$$\lambda_{\xi 3} = \frac{5\xi_a \pi}{2} + (\xi_a - 1)\omega_{me} t - \alpha_i^e \quad (3.112)$$

$$k_{\tau 3} = \frac{\mu_o D^3 L_{stk}}{2\bar{g}_{(\frac{5\pi}{2p} - \theta_{b1}) \rightarrow (\frac{5\pi}{2p} + \theta_{b1})}} \quad (3.113)$$

From eqs. (3.106), (3.108) and (3.111), the general expression of the electromagnetic torque of the w -th pole is achieved as

$$\tau_m^{(w)} = a_w k_{\tau w} \sum_{\nu^e} \frac{\hat{K}_{\nu^e}}{(\nu^e p)^2} \cos(\lambda_{\nu^e w}) \sin(\nu^e p \theta_{b1}) \sum_{\xi_a} \frac{\hat{K}_{\xi_a}}{(\xi_a p)} \sin(\lambda_{\xi w}) \sin(\xi_a p \theta_{b1}) \quad (3.114)$$

where

$$\lambda_{\xi w} = \frac{X(w)\xi_a \pi}{2} + (\xi_a - 1)\omega_{me} t - \alpha_i^e \quad (3.115)$$

$$k_{\tau w} = \frac{\mu_o D^3 L_{stk}}{2\bar{g}_{(\frac{X(w)\pi}{2p} - \theta_{b1}) \rightarrow (\frac{X(w)\pi}{2p} + \theta_{b1})}} \quad (3.116)$$

Finally, the total electromagnetic torque of the motor can be expressed as

$$\tau_m = \sum_{w=1}^{w=2p} a_w k_{\tau w} \sum_{\nu^e} \frac{\hat{K}_{\nu^e}}{(\nu^e p)^2} \cos(\lambda_{\nu^e w}) \sin(\nu^e p \theta_{b1}) \sum_{\xi_a} \frac{\hat{K}_{\xi_a}}{(\xi_a p)} \sin(\lambda_{\xi w}) \sin(\xi_a p \theta_{b1}) \quad (3.117)$$

3.5.2. Two flux barriers per pole

Analogously, the electromagnetic torque is computed for REL motor with two flux-barriers per pole, as computed for one barrier per pole case. The torque component of the first pole is computed as

$$\begin{aligned} \tau_m^{(1)} = & \frac{-\mu_o D^2 L_{stk}}{4} \left[\frac{U_{r2}^{(1)}}{A_1} \underbrace{\int_{\frac{\pi}{2p} - \theta_{b2}}^{\frac{\pi}{2p} - \theta_{b1}} K_s(\theta_r) d\theta_r}_{S'_1} + \frac{U_{r2}^{(1)}}{B_1} \underbrace{\int_{\frac{\pi}{2p} + \theta_{b1}}^{\frac{\pi}{2p} + \theta_{b2}} K_s(\theta_r) d\theta_r}_{S'_2} \right. \\ & \left. + \frac{U_{r1}^{(1)}}{\bar{g}_{(\frac{\pi}{2p} - \theta_{b1}) \rightarrow (\frac{\pi}{2p} + \theta_{b1})}} \underbrace{\int_{\frac{\pi}{2p} - \theta_{b1}}^{\frac{\pi}{2p} + \theta_{b1}} K_s(\theta_r) d\theta_r}_{S'_3} \right] \end{aligned} \quad (3.118)$$

The integrations S'_1 , S'_2 , and S'_3 are solved as

$$S'_1 = \int_{\frac{\pi}{2p} - \theta_{b2}}^{\frac{\pi}{2p} - \theta_{b1}} K_s(\theta_r) d\theta_r = \sum_{\xi_a} \frac{\hat{K}_{\xi_a}}{(\xi_a p)} [\cos(\lambda_{\xi 1} - \xi_a p \theta_{b2}) - \cos(\lambda_{\xi 1} - \xi_a p \theta_{b1})] \quad (3.119)$$

$$S'_2 = \int_{\frac{\pi}{2p} + \theta_{b1}}^{\frac{\pi}{2p} + \theta_{b2}} K_s(\theta_r) d\theta_r = \sum_{\xi_a} \frac{\hat{K}_{\xi_a}}{(\xi_a p)} [\cos(\lambda_{\xi_1} + \xi_a p \theta_{b1}) - \cos(\lambda_{\xi_1} + \xi_a p \theta_{b2})] \quad (3.120)$$

$$S'_3 = \int_{\frac{\pi}{2p} - \theta_{b1}}^{\frac{\pi}{2p} + \theta_{b1}} K_s(\theta_r) d\theta_r = \sum_{\xi_a} 2 \frac{\hat{K}_{\xi_a}}{(\xi_a p)} [\sin(\lambda_{\xi_1}) \cdot \sin(\xi_a p \theta_{b1})] \quad (3.121)$$

The electric loading is reported in eq. (2.20) and the rotor magnetic potentials of both inner and outer barrier are reported in eqs. (3.52) and (3.53). The average air-gap lengths A_1 and B_1 are computed in eqs. (3.41) and (3.42), in static eccentricity case, and in eqs. (3.43) and (3.44), in dynamic eccentricity case. Substituting all previous parameters and the three integrations solutions in eq. (3.118), it results

$$\begin{aligned} \tau_m^{(1)} = & \frac{-\mu_o D^2 L_{stk} U_{r2}^{(1)}}{4} \left[\frac{1}{A_1} \sum_{\xi_a} \frac{\hat{K}_{\xi_a}}{(\xi_a p)} [\cos(\lambda_{\xi_1} - \xi_a p \theta_{b2}) - \cos(\lambda_{\xi_1} - \xi_a p \theta_{b1})] + \right. \\ & \left. \frac{1}{B_1} \sum_{\xi_a} \frac{\hat{K}_{\xi_a}}{(\xi_a p)} [\cos(\lambda_{\xi_1} + \xi_a p \theta_{b1}) - \cos(\lambda_{\xi_1} + \xi_a p \theta_{b2})] \right] \\ & - \frac{\mu_o D^2 L_{stk} U_{r1}^{(1)}}{2\bar{g}_{(\frac{\pi}{2p} - \theta_{b1}) \rightarrow (\frac{\pi}{2p} + \theta_{b1})}} \sum_{\xi_a} \frac{\hat{K}_{\xi_a}}{(\xi_a p)} [\sin(\lambda_{\xi_1}) \sin(\xi_a p \theta_{b1})] \end{aligned} \quad (3.122)$$

The same approach is implemented on the computations of the torque components of the second and third pole. Then, the general formula of the electromagnetic torque component of the w -th pole is reported as

$$\begin{aligned} \tau_m^{(w)} = & \frac{-\mu_o D^2 L_{stk} U_{r2}^{(w)}}{4} \left[\frac{1}{A_w} \sum_{\xi_a} \frac{\hat{K}_{\xi_a}}{(\xi_a p)} [\cos(\lambda_{\xi_w} - \xi_a p \theta_{b2}) - \cos(\lambda_{\xi_w} - \xi_a p \theta_{b1})] + \right. \\ & \left. \frac{1}{B_w} \sum_{\xi_a} \frac{\hat{K}_{\xi_a}}{(\xi_a p)} [\cos(\lambda_{\xi_w} + \xi_a p \theta_{b1}) - \cos(\lambda_{\xi_w} + \xi_a p \theta_{b2})] \right] \\ & - \frac{\mu_o D^2 L_{stk} U_{r1}^{(w)}}{2\bar{g}_{(\frac{X(w)\pi}{2p} - \theta_{b1}) \rightarrow (\frac{X(w)\pi}{2p} + \theta_{b1})}} \sum_{\xi_a} \frac{\hat{K}_{\xi_a}}{(\xi_a p)} [\sin(\lambda_{\xi_w}) \sin(\xi_a p \theta_{b1})] \end{aligned} \quad (3.123)$$

Finally the total torque of the REL motor with $2p$ poles is estimated as

$$\begin{aligned} \tau_m = & \sum_{w=1}^{w=2p} \left(\frac{-\mu_o D^2 L_{stk} U_{r2}^{(w)}}{4} \left[\frac{1}{A_w} \sum_{\xi_a} \frac{\hat{K}_{\xi_a}}{(\xi_a p)} [\cos(\lambda_{\xi_w} - \xi_a p \theta_{b2}) - \cos(\lambda_{\xi_w} - \xi_a p \theta_{b1})] + \right. \right. \\ & \left. \frac{1}{B_w} \sum_{\xi_a} \frac{\hat{K}_{\xi_a}}{(\xi_a p)} [\cos(\lambda_{\xi_w} + \xi_a p \theta_{b1}) - \cos(\lambda_{\xi_w} + \xi_a p \theta_{b2})] \right] \\ & \left. - \frac{\mu_o D^2 L_{stk} U_{r1}^{(w)}}{2\bar{g}_{(\frac{X(w)\pi}{2p} - \theta_{b1}) \rightarrow (\frac{X(w)\pi}{2p} + \theta_{b1})}} \sum_{\xi_a} \frac{\hat{K}_{\xi_a}}{(\xi_a p)} [\sin(\lambda_{\xi_w}) \sin(\xi_a p \theta_{b1})] \right) \end{aligned} \quad (3.124)$$

3.5.3. Three flux barriers per pole

Once again, the electromagnetic torque is computed for REL motor with three flux barriers per pole. Both eccentricity cases are considered. The first pole torque component is computed as

$$\begin{aligned}
\tau_m^{(1)} = & \frac{-\mu_o D^2 L_{stk}}{4} \left[\frac{U_{r2}^{(1)}}{A_1} \underbrace{\int_{\frac{\pi}{2p}-\theta_{b2}}^{\frac{\pi}{2p}-\theta_{b1}} K_s(\theta_r) d\theta_r}_{S'_1} + \frac{U_{r2}^{(1)}}{B_1} \underbrace{\int_{\frac{\pi}{2p}+\theta_{b1}}^{\frac{\pi}{2p}+\theta_{b2}} K_s(\theta_r) d\theta_r}_{S'_2} \right. \\
& + \frac{U_{r1}^{(1)}}{\bar{g}_{(\frac{\pi}{2p}-\theta_{b1}) \rightarrow (\frac{\pi}{2p}+\theta_{b1})}} \underbrace{\int_{\frac{\pi}{2p}-\theta_{b1}}^{\frac{\pi}{2p}+\theta_{b1}} K_s(\theta_r) d\theta_r}_{S'_3} + \frac{U_{r3}^{(1)}}{x_1} \underbrace{\int_{\frac{\pi}{2p}-\theta_{b3}}^{\frac{\pi}{2p}-\theta_{b2}} K_s(\theta_r) d\theta_r}_{S'_4} \\
& \left. + \frac{U_{r3}^{(1)}}{y_1} \underbrace{\int_{\frac{\pi}{2p}+\theta_{b2}}^{\frac{\pi}{2p}+\theta_{b3}} K_s(\theta_r) d\theta_r}_{S'_5} \right] \quad (3.125)
\end{aligned}$$

where the averages of the air-gap lengths A_1 , B_1 , x_1 , and y_1 are computed, in case of static eccentricity as reported in eqs. (3.41), (3.42), (3.71) and (3.72). Besides, in dynamic eccentricity cases, they are computed as in eqs. (3.43), (3.44), (3.73) and (3.74). The scalar magnetic potentials of the three rotor islands $U_{r1}^{(1)}$, $U_{r2}^{(1)}$, and $U_{r3}^{(1)}$ are given by eqs. (3.86) to (3.88).

The solutions of the integrations S'_1 , S'_2 , and S'_3 are presented in eqs. (3.119) to (3.121). However, the integrations S'_4 , S'_5 are solved as

$$S'_4 = \int_{\frac{\pi}{2p}-\theta_{b3}}^{\frac{\pi}{2p}-\theta_{b2}} K_s(\theta_r) d\theta_r = \sum_{\xi_a} \frac{\hat{K}_{\xi_a}}{(\xi_a p)} [\cos(\lambda_{\xi 1} - \xi_a p \theta_{b3}) - \cos(\lambda_{\xi 1} - \xi_a p \theta_{b2})] \quad (3.126)$$

$$S'_5 = \int_{\frac{\pi}{2p}+\theta_{b2}}^{\frac{\pi}{2p}+\theta_{b3}} K_s(\theta_r) d\theta_r = \sum_{\xi_a} \frac{\hat{K}_{\xi_a}}{(\xi_a p)} [\cos(\lambda_{\xi 1} + \xi_a p \theta_{b2}) - \cos(\lambda_{\xi 1} + \xi_a p \theta_{b3})] \quad (3.127)$$

Consequently, the electromagnetic torque resulted from the first pole can be expressed as

$$\begin{aligned}
\tau_m^{(1)} = & \frac{-\mu_o D^2 L_{stk}}{4} \left[\frac{U_{r3}^{(1)}}{x_1} \sum_{\xi_a} \frac{\hat{K}_{\xi_a}}{(\xi_a p)} [\cos(\lambda_{\xi 1} - \xi_a p \theta_{b3}) - \cos(\lambda_{\xi 1} - \xi_a p \theta_{b2})] \right. \\
& + \frac{U_{r3}^{(1)}}{y_1} \sum_{\xi_a} \frac{\hat{K}_{\xi_a}}{(\xi_a p)} [\cos(\lambda_{\xi 1} + \xi_a p \theta_{b2}) - \cos(\lambda_{\xi 1} + \xi_a p \theta_{b3})] \\
& + \frac{U_{r2}^{(1)}}{A_1} \sum_{\xi_a} \frac{\hat{K}_{\xi_a}}{(\xi_a p)} [\cos(\lambda_{\xi 1} - \xi_a p \theta_{b2}) - \cos(\lambda_{\xi 1} - \xi_a p \theta_{b1})] \quad (3.128) \\
& \left. + \frac{U_{r2}^{(1)}}{B_1} \sum_{\xi_a} \frac{\hat{K}_{\xi_a}}{(\xi_a p)} [\cos(\lambda_{\xi 1} + \xi_a p \theta_{b1}) - \cos(\lambda_{\xi 1} + \xi_a p \theta_{b2})] \right] \\
& + \frac{-\mu_o D^2 L_{stk} U_{r1}^{(1)}}{2\bar{g}_{(\frac{\pi}{2p}-\theta_{b1}) \rightarrow (\frac{\pi}{2p}+\theta_{b1})}} \sum_{\xi_a} \frac{\hat{K}_{\xi_a}}{(\xi_a p)} [\sin(\lambda_{\xi 1}) \sin(\xi_a p \theta_{b1})]
\end{aligned}$$

Similarly, the electromagnetic torque components of the second and the third poles are computed. Then, the general formula of the electromagnetic torque per pole is achieved as

$$\begin{aligned}
\tau_m^{(w)} = & \frac{-\mu_o D^2 L_{stk}}{4} \left[\frac{U_{r3}^{(w)}}{x_w} \sum_{\xi_a} \frac{\hat{K}_{\xi_a}}{(\xi_a p)} [\cos(\lambda_{\xi w} - \xi_a p \theta_{b3}) - \cos(\lambda_{\xi w} - \xi_a p \theta_{b2})] \right. \\
& + \frac{U_{r3}^{(w)}}{y_w} \sum_{\xi_a} \frac{\hat{K}_{\xi_a}}{(\xi_a p)} [\cos(\lambda_{\xi w} + \xi_a p \theta_{b2}) - \cos(\lambda_{\xi w} + \xi_a p \theta_{b3})] \\
& + \frac{U_{r2}^{(w)}}{A_w} \sum_{\xi_a} \frac{\hat{K}_{\xi_a}}{(\xi_a p)} [\cos(\lambda_{\xi w} - \xi_a p \theta_{b2}) - \cos(\lambda_{\xi w} - \xi_a p \theta_{b1})] \\
& + \left. \frac{U_{r2}^{(w)}}{B_w} \sum_{\xi_a} \frac{\hat{K}_{\xi_a}}{(\xi_a p)} [\cos(\lambda_{\xi w} + \xi_a p \theta_{b1}) - \cos(\lambda_{\xi w} + \xi_a p \theta_{b2})] \right] \\
& + \frac{-\mu_o D^2 L_{stk} U_{r1}^{(w)}}{2\bar{g}_{(\frac{\pi}{2p} - \theta_{b1}) \rightarrow (\frac{\pi}{2p} + \theta_{b1})}} \sum_{\xi_a} \frac{\hat{K}_{\xi_a}}{(\xi_a p)} [\sin(\lambda_{\xi w}) \sin(\xi_a p \theta_{b1})]
\end{aligned} \tag{3.129}$$

By summing the electromagnetic torque components result from all poles, the total electromagnetic torque of the REL motor with three flux barriers per pole, in both cases of eccentricity, is achieved as

$$\begin{aligned}
\tau_m = & \sum_{w=1}^{w=2p} \left(\frac{-\mu_o D^2 L_{stk}}{4} \left[\frac{U_{r3}^{(w)}}{x_w} \sum_{\xi_a} \frac{\hat{K}_{\xi_a}}{(\xi_a p)} [\cos(\lambda_{\xi w} - \xi_a p \theta_{b3}) - \cos(\lambda_{\xi w} - \xi_a p \theta_{b2})] \right. \right. \\
& + \frac{U_{r3}^{(w)}}{y_w} \sum_{\xi_a} \frac{\hat{K}_{\xi_a}}{(\xi_a p)} [\cos(\lambda_{\xi w} + \xi_a p \theta_{b2}) - \cos(\lambda_{\xi w} + \xi_a p \theta_{b3})] \\
& + \frac{U_{r2}^{(w)}}{A_w} \sum_{\xi_a} \frac{\hat{K}_{\xi_a}}{(\xi_a p)} [\cos(\lambda_{\xi w} - \xi_a p \theta_{b2}) - \cos(\lambda_{\xi w} - \xi_a p \theta_{b1})] \\
& + \left. \frac{U_{r2}^{(w)}}{B_w} \sum_{\xi_a} \frac{\hat{K}_{\xi_a}}{(\xi_a p)} [\cos(\lambda_{\xi w} + \xi_a p \theta_{b1}) - \cos(\lambda_{\xi w} + \xi_a p \theta_{b2})] \right] \\
& + \left. \frac{-\mu_o D^2 L_{stk} U_{r1}^{(w)}}{2\bar{g}_{(\frac{\pi}{2p} - \theta_{b1}) \rightarrow (\frac{\pi}{2p} + \theta_{b1})}} \sum_{\xi_a} \frac{\hat{K}_{\xi_a}}{(\xi_a p)} [\sin(\lambda_{\xi w}) \sin(\xi_a p \theta_{b1})] \right)
\end{aligned} \tag{3.130}$$

3.6. Radial magnetic pressure and force

Since the air-gap flux density distribution is computed, the radial magnetic pressure distribution on the rotor surface can be computed from the following equation.

$$p_m(\theta_r) = \frac{B_g^2(\theta_r)}{2\mu_o} \quad (3.131)$$

The radial magnetic force acting on the rotor can be obtained by integrating the magnetic pressure distribution along the rotor surface. It is given by

$$F_r = \int_0^{2\pi} p_m(\theta_r) \frac{D}{2} L_{stk} e^{j\theta_r} d\theta_r \quad (3.132)$$

The magnetic radial force F_r can be split into F_x in x -axis direction, and F_y in y -axis direction. Both x and y axes are highlighted in Fig. 3.4 and Fig. 3.5. The radial forces in both axes direction are given by

$$F_x = \int_0^{2\pi} \frac{B_g^2(\theta_r) D L_{stk}}{4\mu_o} \cos(\theta_r) d\theta_r \quad (3.133)$$

$$F_y = \int_0^{2\pi} \frac{B_g^2(\theta_r) D L_{stk}}{4\mu_o} \sin(\theta_r) d\theta_r \quad (3.134)$$

3.7. Rotor iron losses

Once the air-gap flux density distribution is computed, the rotor iron losses can be easily estimated. The computation approach used for concentric REL motor can be implemented to compute the rotor iron losses of the eccentric REL motor. Due to the non-uniform air-gap flux density distribution over the motor poles, the iron losses of the rotor poles are different. Therefore, it is necessary to compute the iron losses for each pole separately.

Performance analysis of concentric and eccentric REL machine

In this chapter, a REL motor with defined geometry is analyzed by both analytical models of concentric and eccentric REL motor. Then, the results achieved by means of the analytical models are confirmed by the finite element (FE) analysis. REL motor with one, two, and three flux barriers per pole are considered in this study. Besides, the impact of both static and dynamic eccentricity cases on the main performance parameters, such as air-gap flux density, electromagnetic torque, radial magnetic force, is highlighted. In addition, the rotor iron losses are estimated in healthy and eccentricity cases. Different electric loading and eccentricity values are considered.

4.1. Geometrical data of the stator and rotor

As reported in Chapter 1, the reluctance torque depends on the rotor saliency ratio. For REL machines, typically two to four flux-barriers per pole is adjusted to achieve a good saliency ratio. However, PMAREL machine with one flux-barrier per pole can be designed. Thus, in this chapter, REL motors with one, two, and three flux-barriers per pole are investigated. The main geometrical data of the REL motor used in this analysis are reported in Table. 4.1. In addition, the geometrical data of the rotor with one, two, and three flux-barriers per pole are shown in Table. 4.2, Table. 4.3, and Table. 4.4, respectively.

Table 4.1: The main geometrical data of the REL motor

Stack length	L_{stk}	40 mm
Outer stator Diameter	D_e	200 mm
Inner stator Diameter	D	125 mm
Air-gap length	g	0.35 mm
Number of pole pairs	p	4
Number of stator slots	Q_s	36
Rated torque	T_N	12.5 Nm
Rated peak current	I_N	5.29 A
Rated frequency	f_N	166.67 Hz

Table 4.2: Rotor geometrical data of REL motor with one flux-barrier per pole.

Flux barrier ends angle	$2\theta_{b_1}$	52.42°
Thickness to length ratio of the barrier	$\frac{t_{b_1}}{l_{b_1}}$	0.0937

Table 4.3: Rotor geometrical data of REL motor with two flux-barriers per pole.

First flux barrier ends angle	$2\theta_{b_1}$	28°
Second flux barrier ends angle	$2\theta_{b_2}$	52.42°
Thickness to length ratio of the first barrier	$\frac{t_{b_1}}{l_{b_1}}$	0.1278
Thickness to length ratio of the second barrier	$\frac{t_{b_2}}{l_{b_2}}$	0.0937

Table 4.4: Rotor geometrical data of REL motor with three flux-barriers per pole.

First flux barrier ends angle	$2\theta_{b_1}$	28°
Second flux barrier ends angle	$2\theta_{b_2}$	52.42°
Third flux barrier ends angle	$2\theta_{b_3}$	76.48°
Thickness to length ratio of the first barrier	$\frac{t_{b_1}}{l_{b_1}}$	0.1278
Thickness to length ratio of the second barrier	$\frac{t_{b_2}}{l_{b_2}}$	0.0937
Thickness to length ratio of the third barrier	$\frac{t_{b_3}}{l_{b_3}}$	0.1156

4.2. FE model

In order to validate the analytical models, suitable FE models are built. Each FE analysis is carried out using Finite Element Method Magnetics package. The model is shown in Fig. 4.1, and it is based on the following assumptions.

- The stator model is simplified to a smooth bore (i.e., slot-less) machine. The stator MMF associated with each slot concentrated at points along the periphery. These points correspond to the center of each slot,
- The current of each point is set equal to the current of the corresponding slot, and it varies according to the rotor position θ_m .
- The relative iron permeability has been set equal to 5000 (i.e., very high value), which

leads to neglect the magnetic voltage drop along the iron paths,

- (d) The thickness of the mechanical iron ribs of each rotor flux-barrier is set equal to zero to allow the rotor islands to acquire a different potential each, otherwise the q -axis magnetic flux flows through the iron ribs due to the very low magnetic reluctance or the assumed linear iron.

The analytical and FE analysis are applied to rotors with one, two, and three flux-barriers per pole, in healthy (no eccentricity) case and in both cases of rotor eccentricity (static and dynamic). As an example, Fig. 4.2 (a) and (b) shows the flux density map of an REL motor with one flux-barrier per pole with and without eccentricity. It is noted that the flux density is symmetric for all poles in a healthy case. For both eccentricity cases, the flux density increases on the right-hand side, where the air-gap length is reduced and the flux density reduces on the left-hand side, where the air-gap length increased.

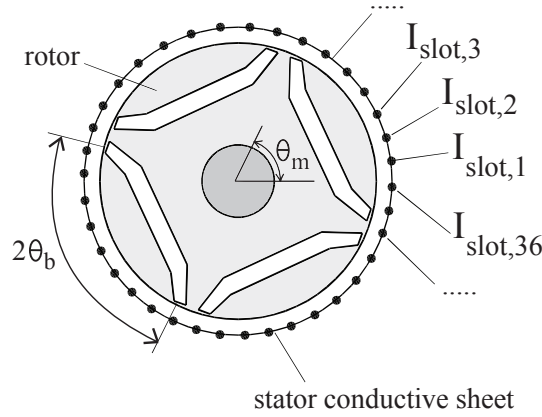


Figure 4.1: Cross section of REL motor with current sheet in the stator.

Based on the actual winding distribution in the stator slots, the electric loading is achieved, as shown in Fig. 4.3. This distribution is computed from eq. (2.15), where the rotor position is set equal to zero (at $\theta_m = 0^\circ$), the peak conductor current is set equal to 1 A ($\hat{I} = 1 A$), and the current angle (α_i^e) is equal to 45 electric degrees. As a consequent, a stepped stator scalar magnetic potential at the air-gap is raised, as shown in Fig. 4.4. This scalar magnetic potential allows the magnetic flux to flow through the air-gap and the rotor. Off course, both distributions of the electric loading and the scalar magnetic potential of the stator vary with the rotor position.

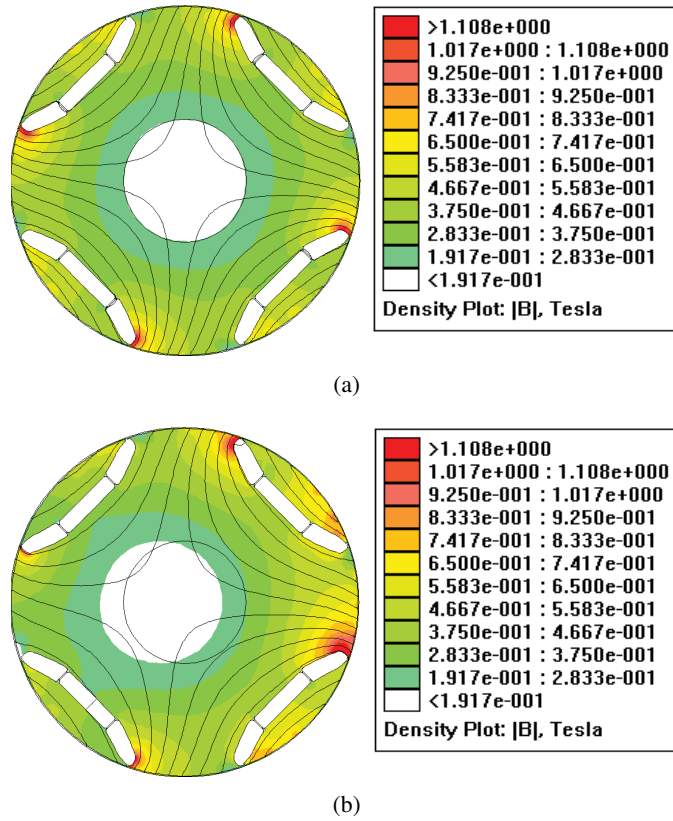


Figure 4.2: Flux density map of a REL motor with one flux-barrier per pole, in healthy and both eccentricity cases at rotor position $\theta_m = 0^\circ$. (a) Healthy case (no eccentricity). (b) Static or dynamic eccentricity case (the lower air-gap thickness is on the right hand side of the figure and eccentricity distance $e = 0.1 \text{ mm}$).

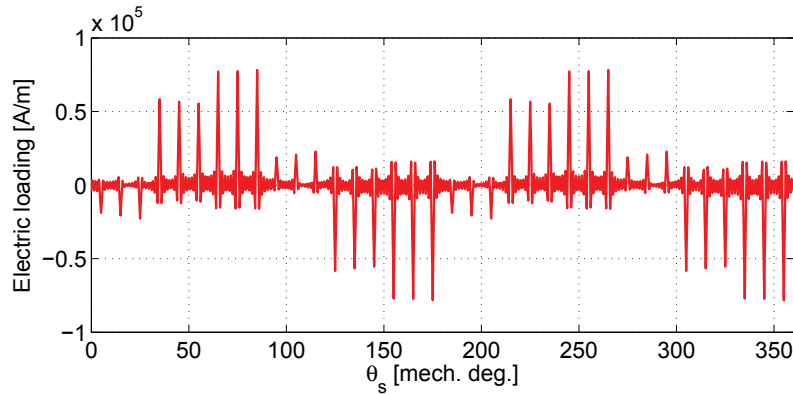


Figure 4.3: Electric loading of the stator current sheet at rotor position $\theta_m = 0^\circ$ and $\hat{I} = 1 \text{ A}$.

4.3. FE validation of the concentric REL motor analytical model

4.3.1. Air-gap flux density

The air-gap flux density distribution is estimated by the analytical model of the concentric REL motor. Then, it is confirmed by the FE model. Fig. 4.5, Fig. 4.6, and Fig. 4.7 show the air-gap

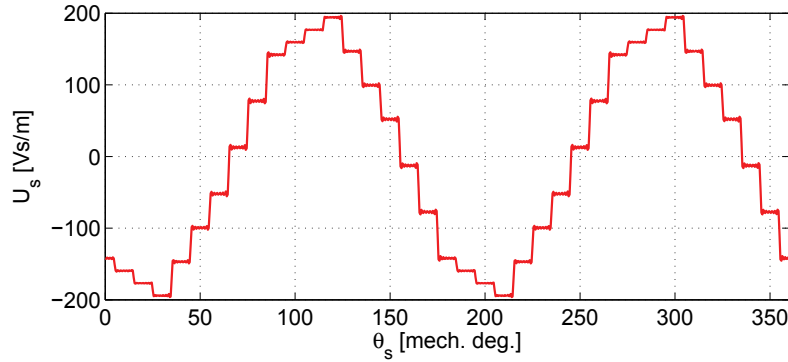


Figure 4.4: Scalar magnetic potential of the stator at rotor position $\theta_m = 0^\circ$ and $\hat{I} = 1 A$.

flux density distribution results from the analytical and FE models of REL motor with one, two, and three flux barriers per pole. The air-gap flux density distribution is estimated at different rotor positions, as an example, at $\theta_m = 0^\circ$ and $\theta_m = 60^\circ$. The symmetry of the air-gap flux density distribution for all poles is noticed. Besides, it is noted that there is a good agreement between the analytical and FE models results.

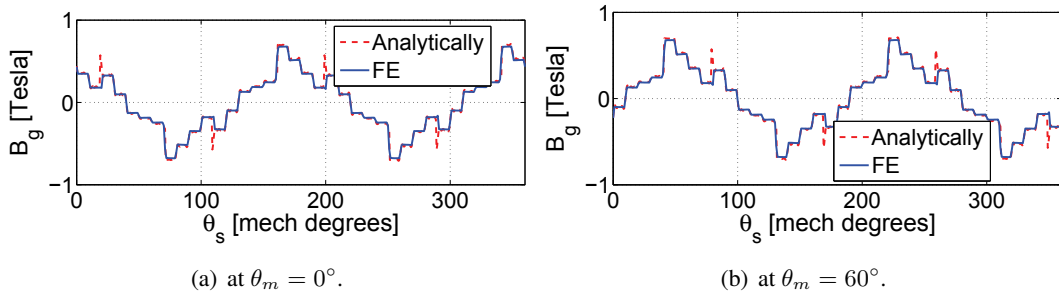


Figure 4.5: Air-gap flux density distribution achieved from the analytical and finite element model at healthy condition (no eccentricity), rotor with one flux-barrier per pole at $\alpha_i^e = 45^\circ$ and $\hat{I} = 1 A$.

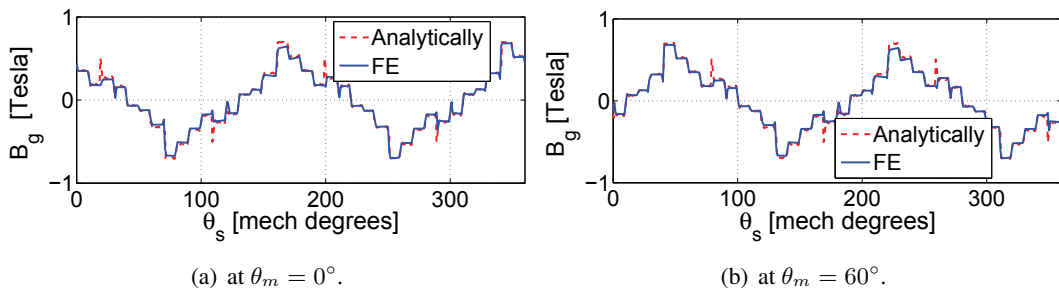


Figure 4.6: Air-gap flux density distribution achieved from the analytical and finite element model at healthy condition (no eccentricity), rotor with two flux-barriers per pole at $\alpha_i^e = 45^\circ$ and $\hat{I} = 1 A$.

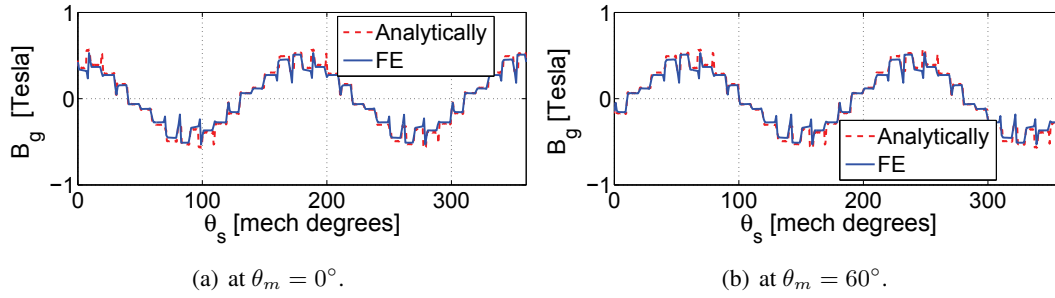


Figure 4.7: Air-gap flux density distribution achieved from the analytical and finite element model at healthy condition (no eccentricity), rotor with three flux-barriers per pole at $\alpha_i^e = 45^\circ$ and $\hat{I} = 1 A$.

4.3.2. Electromagnetic torque

The electromagnetic torque behavior versus rotor position is shown in Fig. 4.8 (a), (b), and (c) for one, two, and three flux-barriers, respectively. The repetition of 30 mechanical degrees (the same electromagnetic configuration appears every 60 electrical degrees) is due to the use of a three-phase system. A satisfactory agreement is noticed also in this case. However, the average torque from the analytical model is higher than that resulting from the FE model. The difference between the two models is due to the finite iron permeability in the FE analysis that slightly reduces the flux in the rotor path. Nevertheless, there is a good agreement between the torque ripple results from both analytical and FE models.

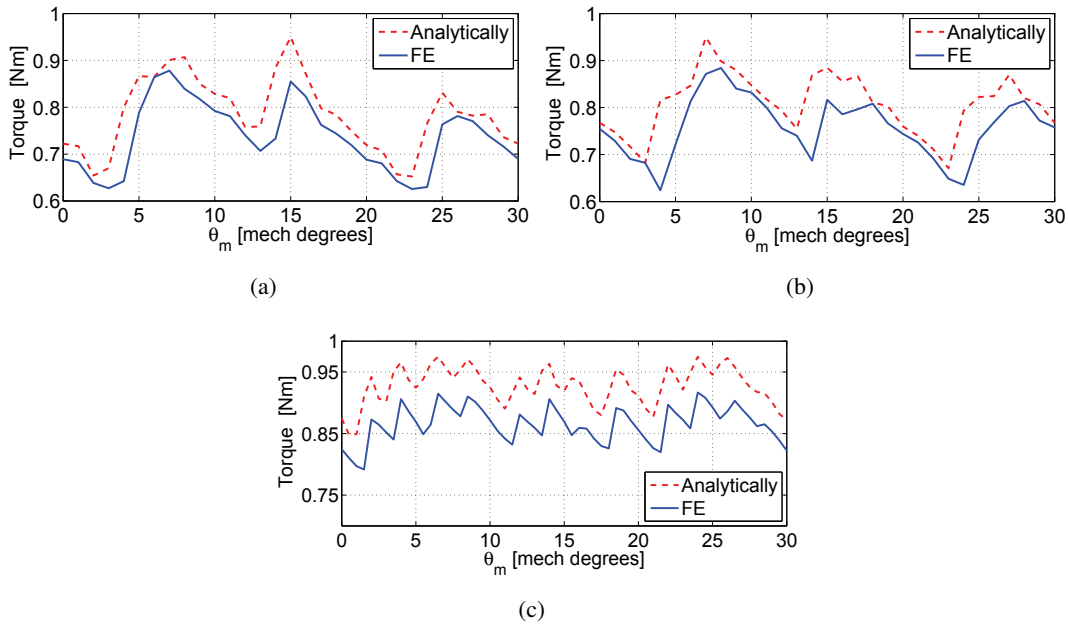


Figure 4.8: Torque results from the analytical and FE model at healthy condition (no eccentricity), rotor with one, two, and three flux-barriers per pole at $\alpha_i^e = 45^\circ$ and $\hat{I} = 1 A$. (a) One flux-barrier per pole. (b) Two flux-barriers per pole. (c) Three flux-barriers per pole.

4.3.3. Magnetic radial force

The magnetic radial force in x - axis direction (F_x) and in y - axis direction (F_y) are calculated using both the analytical model and FE simulation. For REL motor with one, two, and three flux-barriers per pole, Fig. 4.9, Fig. 4.10, and Fig. 4.11 show the magnetic forces F_x , and F_y versus the rotor position for one rotor turn, respectively. These force components are estimated at $\alpha_i^e = 45^\circ$ and $\hat{I} = 1 A$. It is noted that, with no eccentricity, the total radial force results to be negligible. The two main reasons of the difference between the results of the two models have been discussed before.

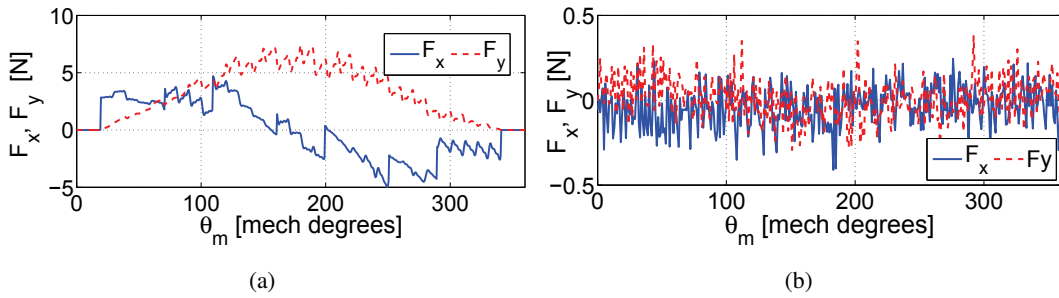


Figure 4.9: F_x and F_y at all rotor position in healthy condition (no eccentricity), rotor with one flux-barrier per pole. (a) Analytical model results. (b) FE model results.

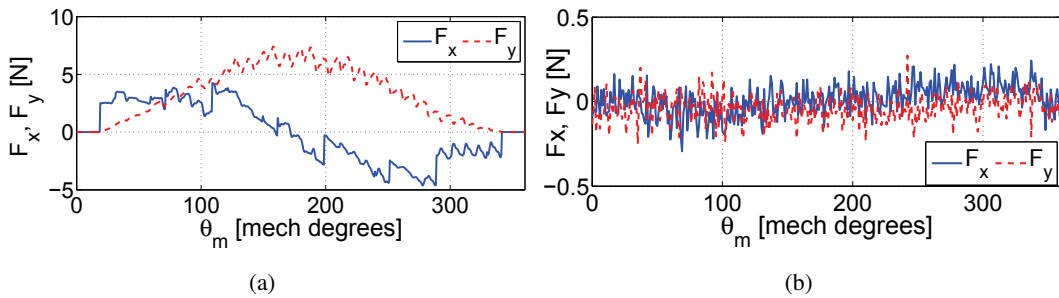


Figure 4.10: F_x and F_y at all rotor position in healthy condition (no eccentricity), rotor with two flux-barriers per pole. (a) Analytical model results. (b) FE model results.

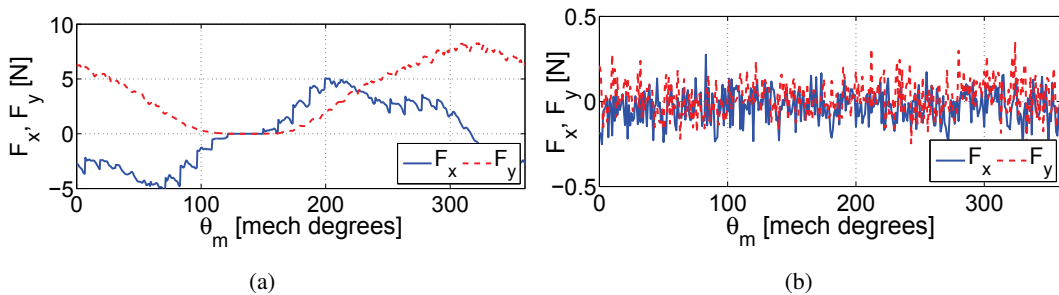


Figure 4.11: F_x and F_y at all rotor position in healthy condition (no eccentricity), rotor with three flux-barriers per pole. (a) Analytical model results. (b) FE model results.

4.3.4. Rotor iron losses

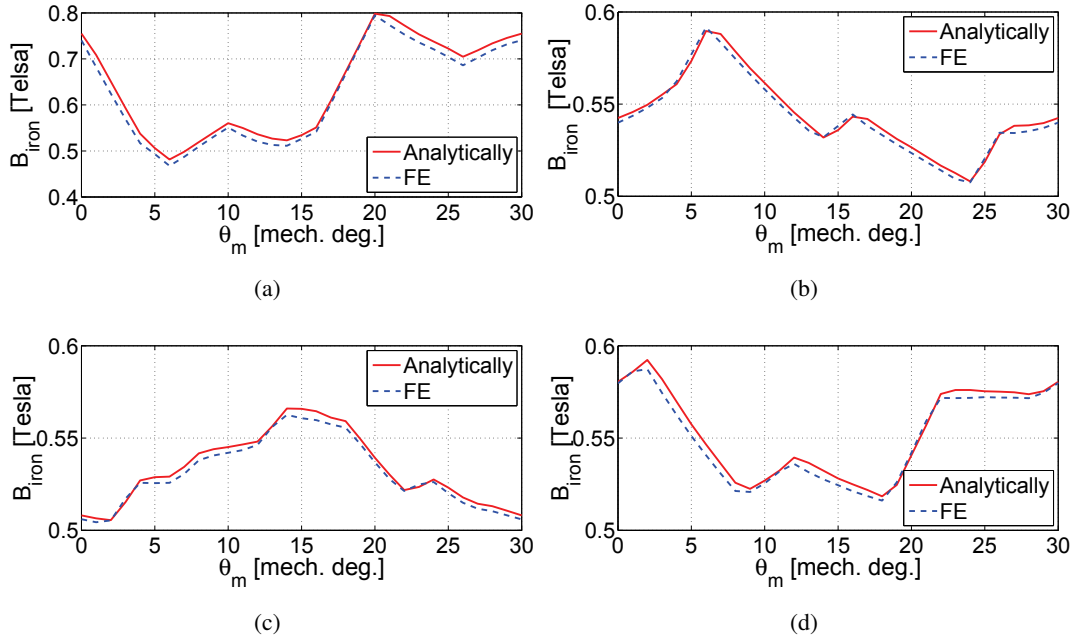


Figure 4.12: Flux densities variations in the different iron parts of the first rotor pole results from the analytical and FE models at $J = 1.06 \text{ A/mm}^2$ and $\alpha_i^e = 45^\circ$. (a) First island. (b) Second island. (c) Third island. (d) Channel.

The rotor eddy current losses are estimated in the different rotor iron parts (islands and channels). REL motor with one flux-barrier per pole has one island and one channel per pole, as shown in Fig.2.5 (a). Whereas, the REL motor with two flux-barriers per pole, has two islands and one channel per pole, as shown in Fig. 2.6 (a). Nevertheless, the REL motor with three-barriers per pole has three islands and one channel per pole, as reported in Fig. 2.7 (a). As mentioned in Chapter 2, the iron losses in the overall rotor are the summation of the iron losses in the rotor islands and channels. Thus, by increasing the number of barriers, the computations are extended for more rotor islands. This means that the rotor iron losses estimation of REL motor with three flux-barriers per pole is more general than REL motor with one and two flux barriers.

In addition, from Fig. 4.8, it is noted that the saliency ratio is increased by increasing the number of the flux-barriers. As a consequent, the average torque and torque ripple of REL motor with three barriers per pole are better than that with one and two flux-barriers per pole. Due to the previous reasons, this section deals with the analytical estimation of the rotor iron losses of REL motor with three flux-barriers per pole. The results achieved by means of the analytical model are confirmed by the FE analysis. The computations are carried out at two different current densities values ($J = 1.06 \text{ A/mm}^2$ and $J = 3 \text{ A/mm}^2$).

At each rotor position, from eqs. (2.89) to (2.93), the flux density in the rotor islands and channels can be predicted. Thanks to the symmetry of the air-gap flux density in the concentric REL motor, this leads to compute the iron losses in one pole. Then, the result is multiplied by the number of poles ($2p$). Fig. 4.12 shows the flux density variation in the three islands and the channel of the first pole. At first, the current density is set equal to $J = 1.06 \text{ A/mm}^2$. It is

noted that there is a satisfactory agreement between the analytical and FE models results.

According to eq. (2.86), these variations can be decomposed in their Fourier series. Then, their time-variation is computed, as in eq. (2.87). Hence, the eddy current losses are computed in each island and the channel, as reported in eq. (2.88), where a silicon iron lamination with specific iron losses equal to $3.6 [W/kg]$ at $1 T$ and $50 Hz$ is considered. If in these conditions the e.c. losses account for 30 %, we obtain $k_{ec} = 0.432 \cdot 10^{-3} W / (kg T^2 Hz^2)$. The flux density is repeated each 30 mechanical degree due to the three phase system. Therefore this variation is repeated 6 times for one mechanical rotor turn. In addition, the supply frequency of the motor is given by $f = pn/60$. Hence, the frequency of the flux density variation is equal to $6 \cdot f$, i.e., equal to $1200 Hz$, at motor speed equal to $6000 rpm$.

Table 4.5: The eddy current loss of a rotor pole, which results from the analytical and FE models at $J = 1.06 A/mm^2$ and $\alpha_i^e = 45^\circ$.

rotor part	Analytic [W/kg]	FE [W/kg]	volume [m ³]	mass [Kg]	Analytic [W]	FE [W]
first island	33.382	35.908	$1.342 \cdot 10^{-6}$	0.011	0.351	0.377
second island	1.606	1.713	$8.715 \cdot 10^{-6}$	0.068	0.109	0.117
third island	0.980	0.888	$2.282 \cdot 10^{-5}$	0.178	0.175	0.158
channel	1.866	1.759	$2.609 \cdot 10^{-5}$	0.204	0.380	0.358
total	37.834	40.268	$5.897 \cdot 10^{-5}$	0.461	1.1	1

The volume of the three islands and the channel are computed using the FE software, as reported in Table. 4.5. By considering the density of the rotor iron equal to $7800 Kg/m^3$, the mass of each rotor iron part is computed, as reported in Table. 4.5. The specific eddy current losses ($[W/kg]$) and the eddy current losses ($[W]$) of one rotor pole are reported in Table. 4.5. The total losses of the overall rotor results from the analytical and FE models are equal to $4.4 [W]$ and $4 [W]$, respectively. It is noted that there are a satisfactory agreement between the analytical and FE models. The small difference comes from the finite relative permeability of the iron in the FE model and the approximation of the shape of the rotor channel, as mentioned before in Fig. 2.8 (a).

Fig. 4.13 shows the specific iron losses result from both models. It is noted that the slot harmonic Q_s/p and its multiples have a high contribution in the iron losses. In addition, the specific iron losses in the first island are higher than the other islands and the channel.

Table 4.6: The eddy current loss of a rotor pole, which results from the analytical and FE models at $J = 3 A/mm^2$ and $\alpha_i^e = 45^\circ$.

rotor part	Analytic [W/kg]	FE [W/kg]	volume [m ³]	mass [Kg]	Analytic [W]	FE [W]
first island	296.244	279.219	$1.342 \cdot 10^{-6}$	0.011	2.962	3.071
second island	12.951	13.455	$8.715 \cdot 10^{-6}$	0.068	0.881	0.915
third island	7.906	7.079	$2.282 \cdot 10^{-5}$	0.178	1.407	1.260
channel	15.047	14.075	$2.609 \cdot 10^{-5}$	0.204	3.070	2.871
total	305.15	313.83	$5.897 \cdot 10^{-5}$	0.461	8.317	8.117

Similarly, the eddy current losses computations are repeated when the current density is

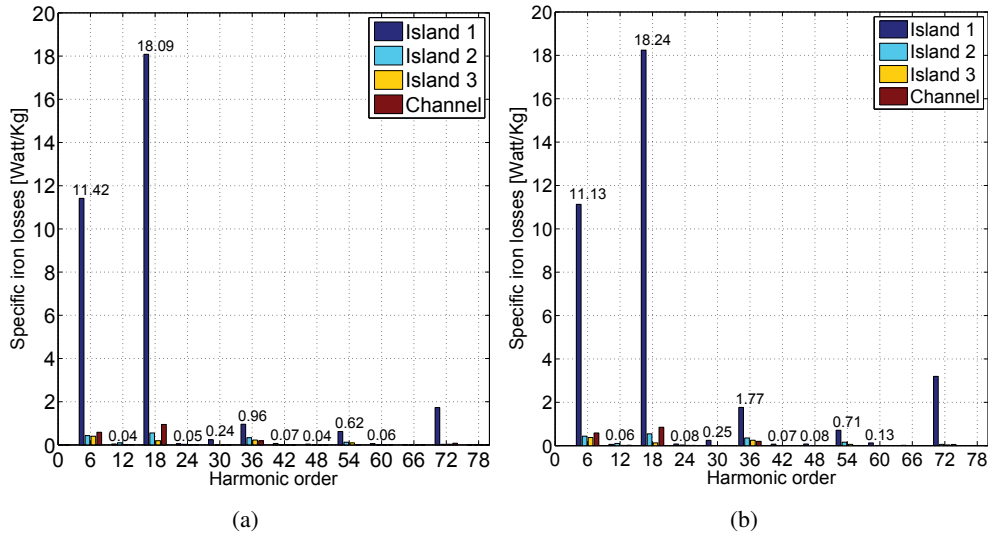


Figure 4.13: Specific eddy current losses in the different iron parts of a rotor pole at $J = 1.06 A/mm^2$ and $\alpha_i^e = 45^\circ$. (a) Analytical spectrum of the specific losses. (b) FE spectrum of the specific losses.

set equal to $J = 3A/mm^2$. The flux densities variations in the different iron parts of the first pole of the rotor are shown in Fig. 4.14. Then, the losses of the first island, second island, third island, and channel of the first pole are reported in Table. 4.6. Furthermore, the specific iron losses of the different iron parts of the first rotor pole are reported in Fig. 4.15. Once again, it is noted that there is a good agreement between the analytical and FE models results. The total iron losses of overall rotor result from the analytical and FE model are equal to 33.268 [W] and 32.468 [W], respectively.

4.4. FE validation of the eccentric REL motor analytical model

In this section, the impact of both static and dynamic eccentricity cases on the air-gap flux density distribution, the electromagnetic torque, the magnetic radial force acting on the rotor, and the rotor eddy current losses is studied. For simplicity, θ_e shown in Fig. 3.2 is set equal to zero, i.e., the rotor is shifted by distance e to the x -axis direction. In this section, the computations of both models are carried out according to an eccentricity equal to $e = 0.1 mm$, peak conductor current $\hat{I} = 1 A$, and electric current angle $\alpha_i^e = 45$ electric degrees. However, since the model is linear the comparison is the same also at full load ($\hat{I} = 5.29 A$).

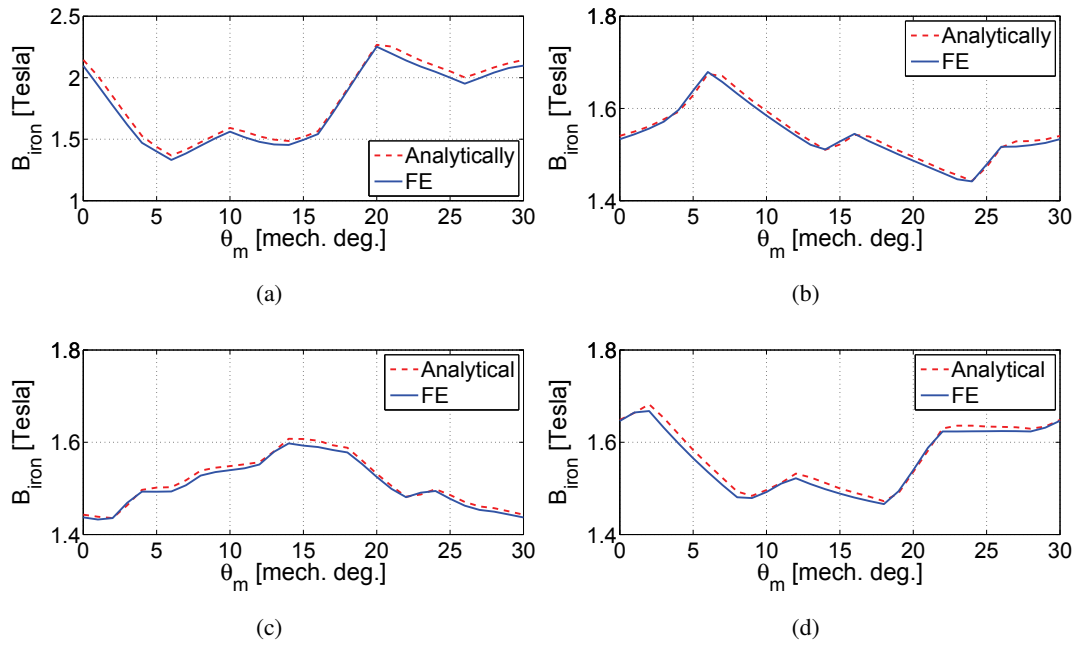


Figure 4.14: Flux densities variations in the different iron parts of the first rotor pole results from the analytical and FE models at $J = 3 A/mm^2$ and $\alpha_i^e = 45^\circ$. (a) First island. (b) Second island. (c) Third island. (d) Channel.

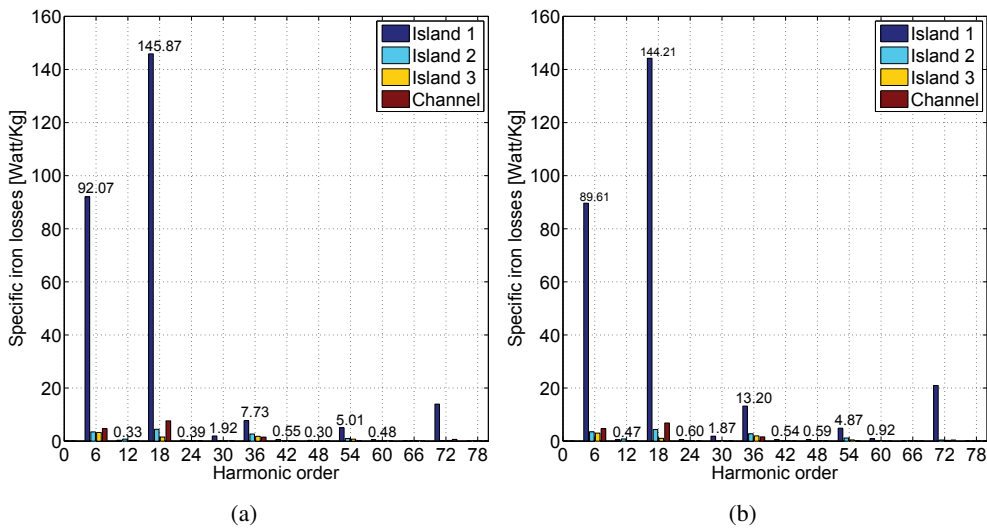


Figure 4.15: Specific eddy current losses in the different iron parts of a rotor pole at $J = 3 A/mm^2$ and $\alpha_i^e = 45^\circ$. (a) Analytical spectrum of the specific losses. (b) FE spectrum of the specific losses.

4.4.1. Static eccentricity case

Air-gap flux density

Fig. 4.16, Fig. 4.17, and Fig. 4.18 shows the air-gap flux density distribution results from the analytical and FE models of REL motor with one, two, and three flux barriers per pole, in case

of static eccentricity. Once again, the air-gap flux density distribution is estimated at different rotor positions, as an example, at $\theta_m = 0^\circ$ and $\theta_m = 60^\circ$. As expected, such a distribution is not the same over the different poles, due to the rotor eccentricity. The air-gap flux density is increased where the air-gap length is minimum and is decreased where the air-gap length is maximum.

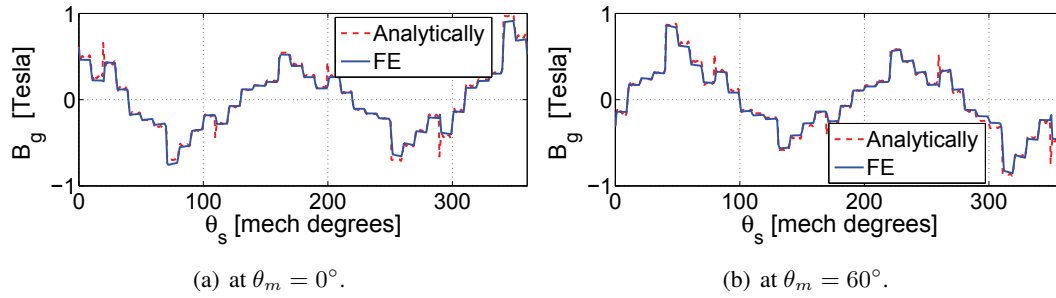


Figure 4.16: Air-gap flux density distribution achieved from the analytical and finite element model at static eccentricity, rotor with one flux-barrier per pole: (a) at $\theta_m = 0^\circ$, (b) at $\theta_m = 60^\circ$.

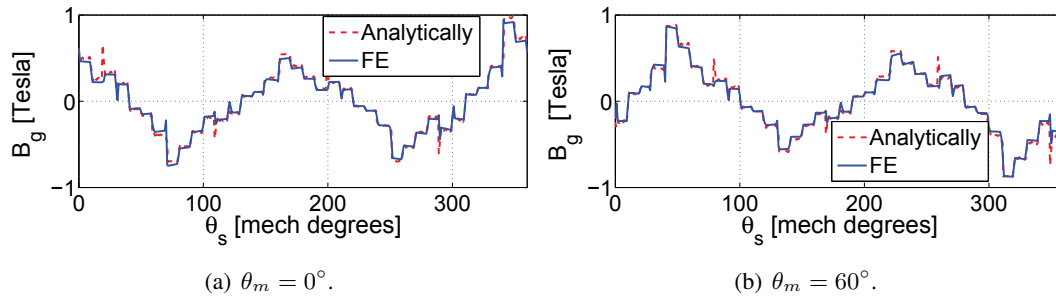


Figure 4.17: Air-gap flux density distribution achieved from the analytical and finite element model at static eccentricity, rotor with two flux-barriers per pole: (a) at $\theta_m = 0^\circ$, (b) at $\theta_m = 60^\circ$.

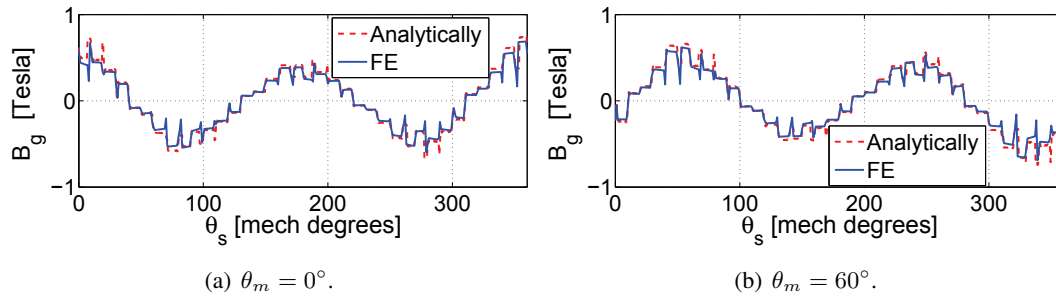


Figure 4.18: Air-gap flux density distribution achieved from the analytical and finite element model at static eccentricity, rotor with three flux-barriers per pole: (a) at $\theta_m = 0^\circ$, (b) at $\theta_m = 60^\circ$.

Electromagnetic Torque

Similarly, in case of static rotor eccentricity, the electromagnetic torque is computed. Fig. 4.19 shows the electromagnetic torque results from the analytical and FE models of REL motor with one, two, and three flux barriers per pole. Again, it is noted that there is a satisfactory agreement between the analytical and FE models. In addition, in presence of the static eccentricity, the torque remains almost the same as in a healthy condition and the torque ripple increases slightly. Therefore, the rotor eccentricity causes a negligible impact on the total torque.

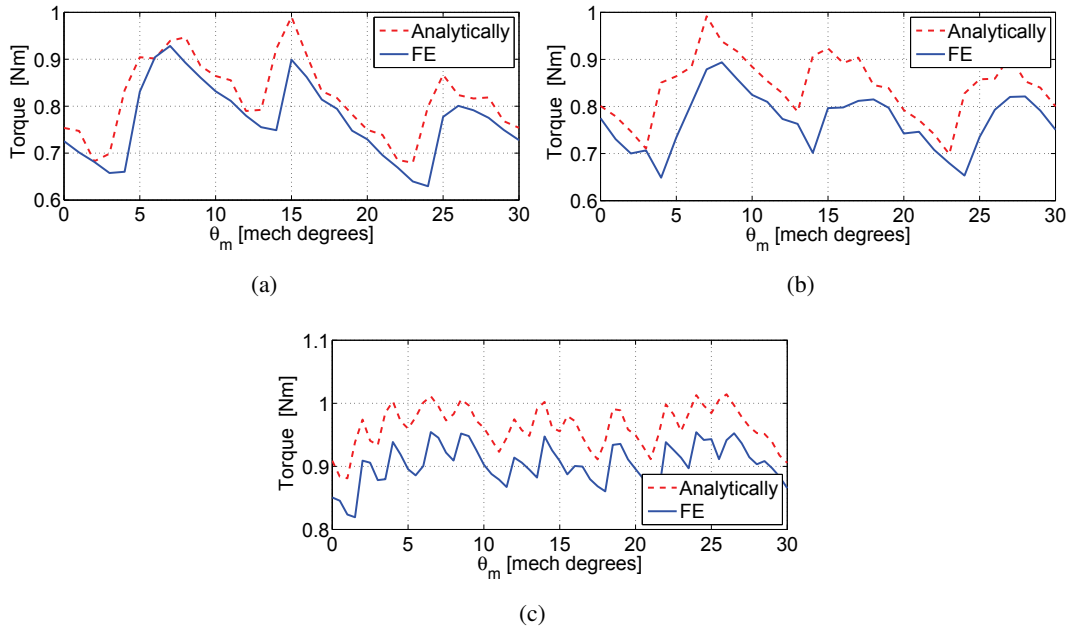


Figure 4.19: Torque results from the analytical and FE model at static eccentricity, rotor with one, two, and three flux-barriers per pole. (a) One flux-barrier per pole. (b) Two flux-barriers per pole. (c) Three flux-barriers per pole.

Magnetic Radial force

In static eccentricity case, the magnetic force components F_x and F_y are estimated by both analytical and FE models. Fig. 4.20, Fig. 4.21, and Fig. 4.22 shows the force components F_x and F_y acting on the rotor with one, two, and three flux barriers, respectively. Furthermore, the force components F_x and F_y result from both analytical and FE models can be presented in (xy) plan, as shown in Fig. 4.23.

Both models highlight a force in the direction of the smaller air-gap length in the range between 220 and 250 N for motor with one, and two flux-barriers and in the range between 150 and 200 N for motor with three flux-barriers. The difference between the two models is due to two main issues: (a) the approximation of air-gap lengths variations in front of the rotor islands and channels by their average values, (b) the finite permeability of iron in FE analysis that slightly reduces the flux in the rotor path, and hence, the force is reduced.

From Fig. 4.23, the analytical model overestimates the FE model. This overestimation changes with number of flux-barriers per pole. The force acting on the motor with two flux-

barriers per pole is slightly higher than that acting on motor with one flux-barrier per pole, but with three flux-barriers per pole, it tends to decrease.

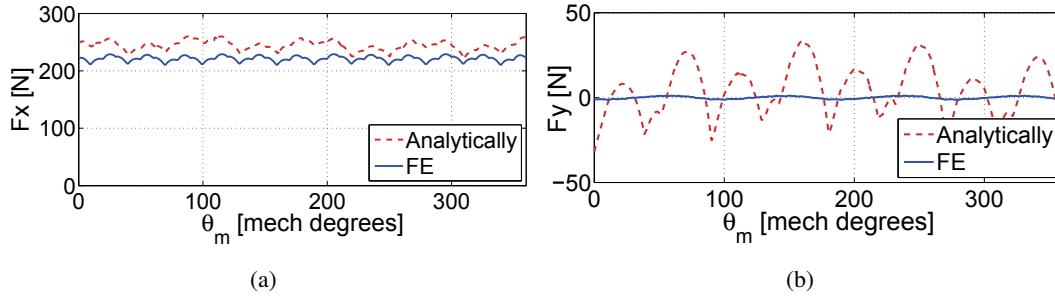


Figure 4.20: F_x and F_y at all rotor position in case of static eccentricity, rotor with one flux-barrier per pole. (a) F_x versus rotor position. (b) F_y versus rotor position.

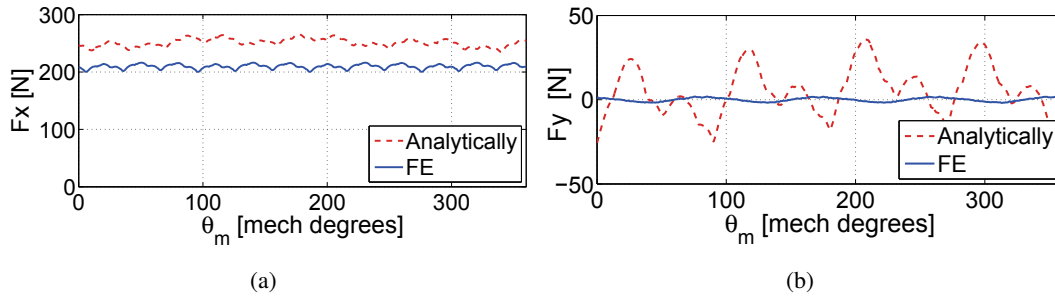


Figure 4.21: F_x and F_y at all rotor position in case of static eccentricity, rotor with two flux-barriers per pole. (a) F_x versus rotor position. (b) F_y versus rotor position.

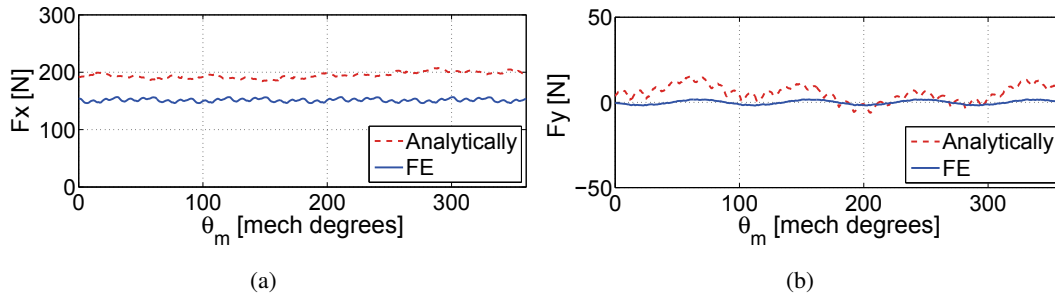


Figure 4.22: F_x and F_y at all rotor position in case of static eccentricity, rotor with three flux-barriers per pole. (a) F_x versus rotor position. (b) F_y versus rotor position.

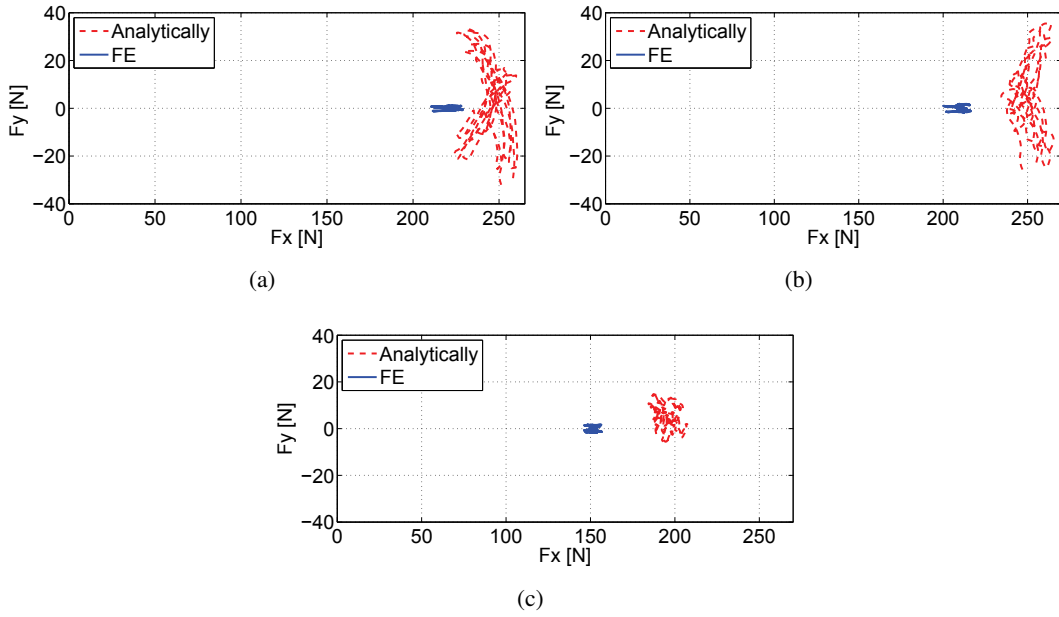


Figure 4.23: F_y versus F_x at all rotor position in case of one, two, and three flux-barriers per pole. (a) One flux barrier. (b) Two flux-barriers. (c) Three flux-barriers.

Rotor iron losses

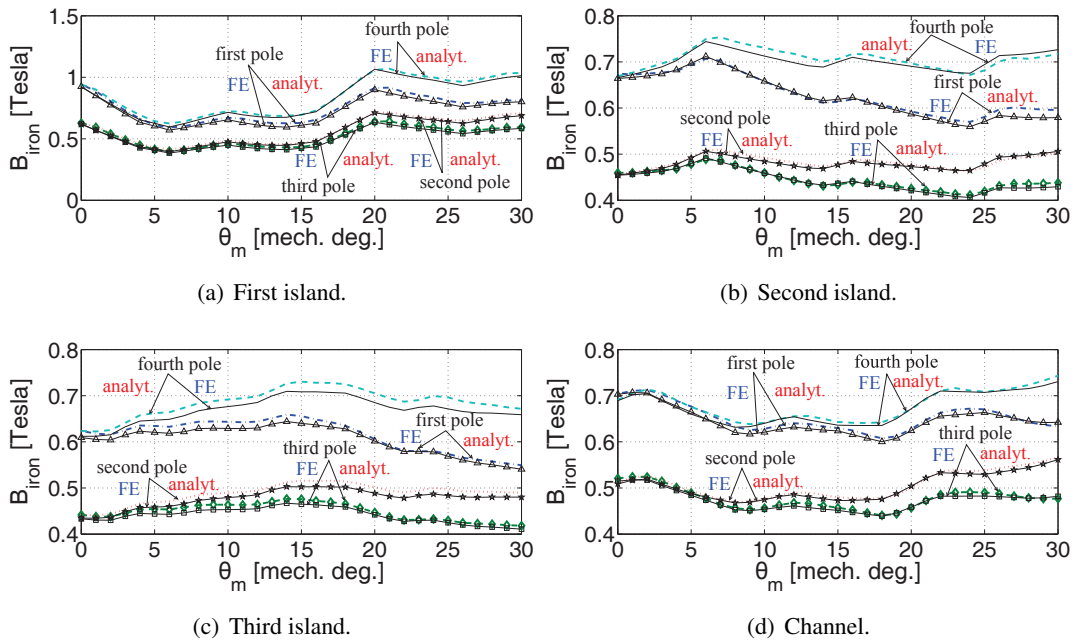


Figure 4.24: Flux density variation in the different iron parts of all rotor poles results from the analytical and FE models at $J = 1.06 \text{ A/mm}^2$.

As noted in Fig. 4.16, Fig. 4.17, and Fig. 4.18, the symmetry of the air-gap flux density

distribution per motor poles is lost due to the non-uniform air-gap length distribution. Hence, the flux density variation in the rotor islands and channels is computed for each pole, separately. Once again, a REL motor with three flux barriers per pole is considered in this section. Fig. 4.24 shows the flux density variation in the first island, second island, third island, and channel of each rotor pole. It is noted that there is a good agreement between the FE and analytical model results. The flux density variation in the islands and channels of the first pole and the fourth pole are higher than those of the second pole and the third pole. Because the first and the fourth pole are close the minimum air-gap length. On the contrary, the second and the third poles are close to the maximum air-gap length.

Table 4.7: The eddy current loss of the first pole of the rotor, which results from the analytical and FE models at $J = 1.06 \text{ A/mm}^2$.

rotor part	Analytic [W/kg]	FE [W/kg]	volume [m ³]	mass [Kg]	Analytic [W]	FE [W]
first island	67.315	72.663	$1.342 \cdot 10^{-6}$	0.011	0.741	0.799
second island	10.011	11.100	$8.715 \cdot 10^{-6}$	0.068	0.681	0.775
third island	7.890	6.464	$2.282 \cdot 10^{-5}$	0.178	1.404	1.151
channel	8.300	7.155	$2.609 \cdot 10^{-5}$	0.204	1.693	1.460
total	93.516	97.681	$5.897 \cdot 10^{-5}$	0.461	4.520	4.188

Table 4.8: The eddy current loss of the second pole of the rotor, which results from the analytical and FE models at $J = 1.06 \text{ A/mm}^2$.

rotor part	Analytic [W/kg]	FE [W/kg]	volume [m ³]	mass [Kg]	Analytic [W]	FE [W]
first island	22.983	27.306	$1.342 \cdot 10^{-6}$	0.011	0.253	0.300
second island	1.754	2.019	$8.715 \cdot 10^{-6}$	0.068	0.119	0.137
third island	1.301	1.126	$2.282 \cdot 10^{-5}$	0.178	0.232	0.200
channel	4.012	2.863	$2.609 \cdot 10^{-5}$	0.204	0.818	0.584
total	30.050	33.314	$5.897 \cdot 10^{-5}$	0.461	1.422	1.221

Table 4.9: The eddy current loss of the third pole of the rotor, which results from the analytical and FE models at $J = 1.06 \text{ A/mm}^2$.

rotor part	Analytic [W/kg]	FE [W/kg]	volume [m ³]	mass [Kg]	Analytic [W]	FE [W]
first island	31.202	31.578	$1.342 \cdot 10^{-6}$	0.011	0.343	0.347
second island	3.600	4.289	$8.715 \cdot 10^{-6}$	0.068	0.245	0.292
third island	3.724	3.327	$2.282 \cdot 10^{-5}$	0.178	0.663	0.592
channel	4.597	4.251	$2.609 \cdot 10^{-5}$	0.204	0.938	0.867
total	43.120	43.445	$5.897 \cdot 10^{-5}$	0.461	2.189	2.098

Similar to the concentric rotor (healthy case), the eddy current losses in the rotor islands and channels are estimated. However, in eccentricity case, the computations are applied for each pole, separately. Table. 4.7, Table. 4.8, Table. 4.9, and Table. 4.10 report the specific eddy

Table 4.10: The eddy current loss of the fourth pole of the rotor, which results from the analytical and FE models at $J = 1.06 A/mm^2$.

rotor part	Analytic [W/kg]	FE [W/kg]	volume [m ³]	mass [Kg]	Analytic [W]	FE [W]
first island	63.860	66.502	$1.342 \cdot 10^{-6}$	0.011	0.703	0.732
second island	5.127	7.004	$8.715 \cdot 10^{-6}$	0.068	0.349	0.476
third island	4.984	4.461	$2.282 \cdot 10^{-5}$	0.178	0.887	0.794
channel	5.193	4.441	$2.609 \cdot 10^{-5}$	0.204	1.059	0.906
total	79.164	82.408	$5.897 \cdot 10^{-5}$	0.461	2.998	2.908

current losses and the total eddy current losses in the islands and channels of the rotor first, second, third, fourth pole, respectively. Referring to the eddy current losses [W] per each pole, the analytical model is slightly higher than the FE model. From these tables, the total rotor eddy current losses results from the analytical and FE models are equal to 11.129 [W] and 10.415 [W], respectively. By comparing the static eccentricity and healthy cases, it is noted that the rotor eddy current losses in static eccentricity case is equal to $\simeq 250\%$ of that in healthy case.

Fig. 4.25 shows the analytic spectrum of the specific eddy current losses of the islands and channels of the first, second, third, and fourth pole, respectively. In addition, Fig. 4.26 shows the FE spectrum of the specific losses of the islands and channels of the different rotor poles. It is noted that the slot harmonic $Q_s=p$ and its multiples have high contribution in the iron losses. Besides, there is a good agreement between both models.

The rotor eddy current losses computations are repeated, when the current density is equal to $J = 3 A/mm^2$. The flux densities variations in the different iron parts of all rotor poles are shown in Fig. 4.27. Then, the eddy current losses of the different islands and channels of each pole are reported in Table. 4.11, Table. 4.12, Table. 4.13, and Table. 4.14. Once again, the total iron losses of overall rotor result from the analytical and FE model are equal to 89.746 [W] and 83.996 [W], respectively. By comparing the losses achieved in both healthy and static eccentricity cases, again, the rotor eddy current losses in static eccentricity case is equal to $\simeq 250\%$ of that in healthy case.

Table 4.11: The eddy current loss of the first pole of the rotor, which results from the analytical and FE models at $J = 3 A/mm^2$.

rotor part	Analytic [W/kg]	FE [W/kg]	volume [m ³]	mass [Kg]	Analytic [W]	FE [W]
first island	542.936	586.109	$1.342 \cdot 10^{-6}$	0.011	5.972	6.447
second island	80.743	91.951	$8.715 \cdot 10^{-6}$	0.068	5.491	6.253
third island	63.637	52.140	$2.282 \cdot 10^{-5}$	0.178	11.327	9.281
channel	66.947	57.710	$2.609 \cdot 10^{-5}$	0.204	13.657	11.773
total	754.262	787.910	$5.897 \cdot 10^{-5}$	0.461	36.447	33.754

Once again, the analytic and FE spectrum of the specific eddy current losses of the islands and channels of each pole are highlighted in Fig. 4.28 and Fig. 4.29, respectively. The same comments highlighted before are also noticed in these two figures.

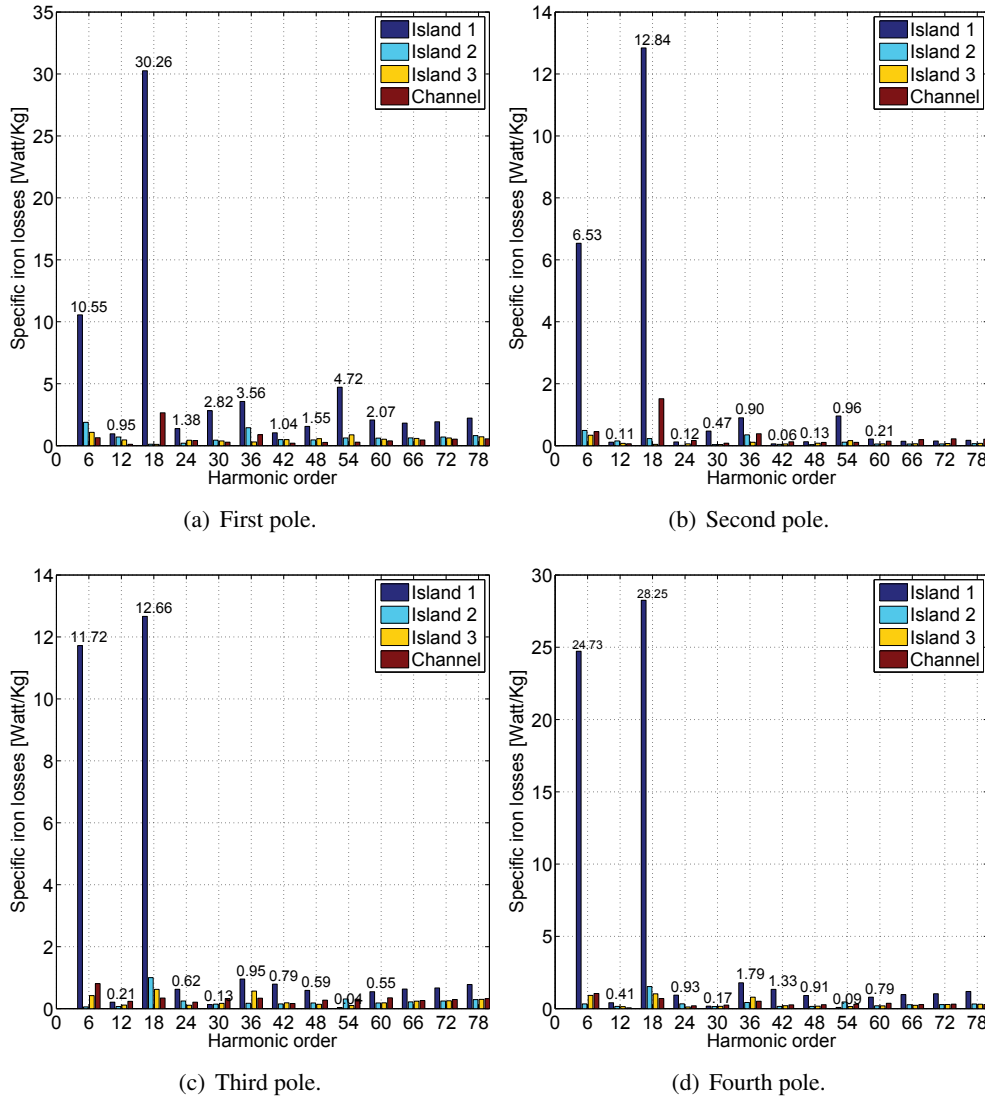


Figure 4.25: Analytic spectrum of the specific eddy current losses in the rotor islands and channels at $J = 1.06 \text{ A/mm}^2$.

Table 4.12: The eddy current loss of the second pole of the rotor, which results from the analytical and FE models at $J = 3 \text{ A/mm}^2$.

rotor part	Analytic [W/kg]	FE [W/kg]	volume [m ³]	mass [Kg]	Analytic [W]	FE [W]
first island	185.371	220.253	$1.342 \cdot 10^{-6}$	0.011	2.039	2.423
second island	14.150	16.287	$8.715 \cdot 10^{-6}$	0.068	0.962	1.108
third island	10.490	9.080	$2.282 \cdot 10^{-5}$	0.178	1.867	1.616
channel	32.359	23.094	$2.609 \cdot 10^{-5}$	0.204	6.601	4.711
total	242.370	268.713	$5.897 \cdot 10^{-5}$	0.461	11.469	9.858

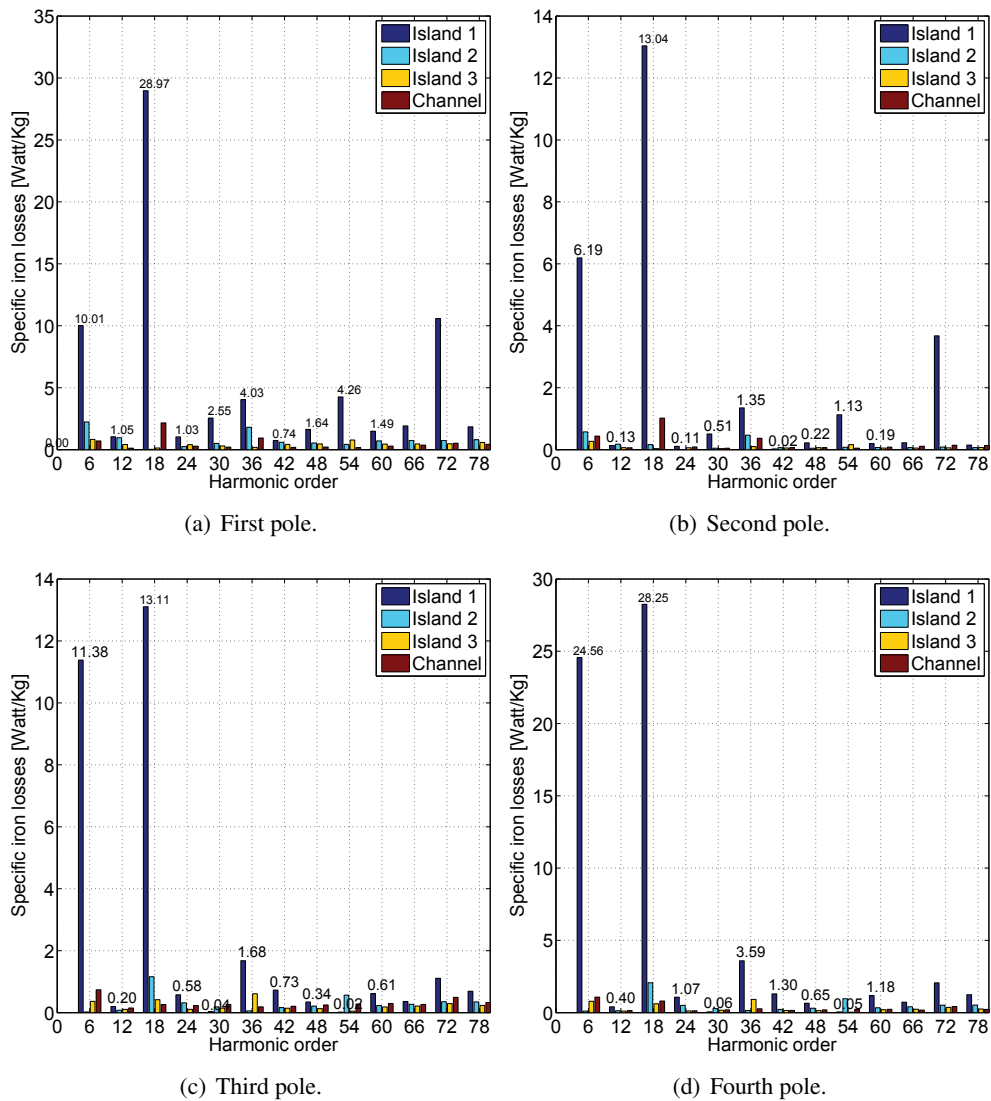


Figure 4.26: FE spectrum of the specific eddy current losses in the rotor islands and channels at $J = 1.06 \text{ A/mm}^2$.

Table 4.13: The eddy current loss of the third pole of the rotor, which results from the analytical and FE models at $J = 3 \text{ A/mm}^2$.

rotor part	Analytic [W/kg]	FE [W/kg]	volume [m ³]	mass [Kg]	Analytic [W]	FE [W]
first island	251.665	254.710	$1.342 \cdot 10^{-6}$	0.011	2.768	2.802
second island	29.009	34.599	$8.715 \cdot 10^{-6}$	0.068	1.973	2.353
third island	30.035	26.840	$2.282 \cdot 10^{-5}$	0.178	5.346	4.778
channel	37.079	34.290	$2.609 \cdot 10^{-5}$	0.204	7.564	6.995
total	347.787	350.438	$5.897 \cdot 10^{-5}$	0.461	17.651	16.928

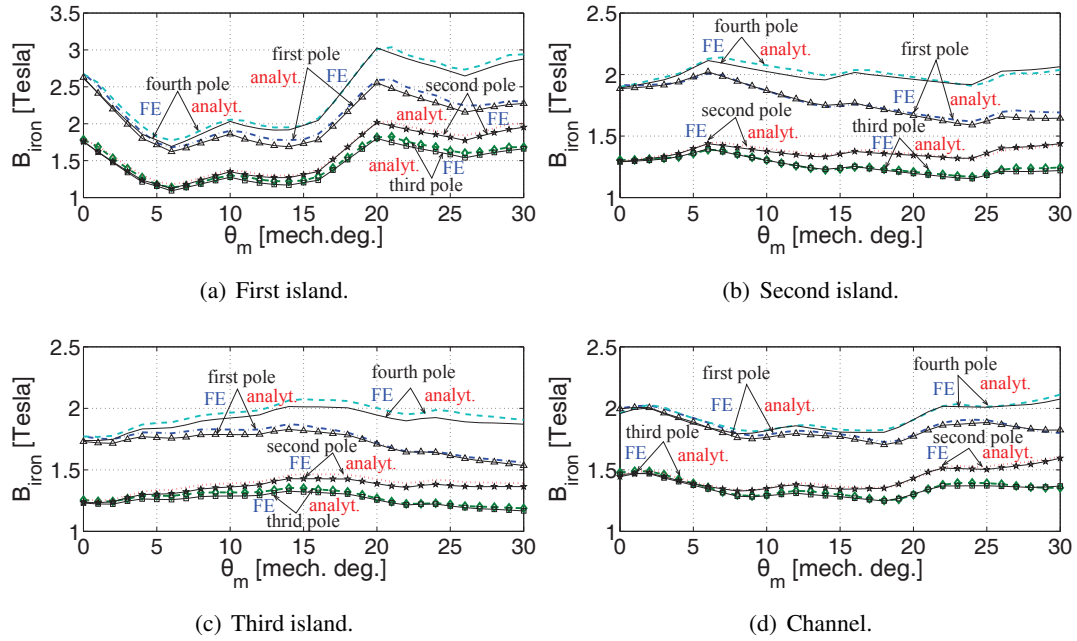


Figure 4.27: Flux density variation in the different iron parts of all rotor poles results from the analytical and FE models at $J = 3 \text{ A/mm}^2$.

Table 4.14: The eddy current loss of the fourth pole of the rotor, which results from the analytical and FE models at $J = 3 \text{ A/mm}^2$.

rotor part	Analytic [W/kg]	FE [W/kg]	volume [m ³]	mass [Kg]	Analytic [W]	FE [W]
first island	515.069	536.417	$1.342 \cdot 10^{-6}$	0.011	5.666	5.901
second island	41.352	56.498	$8.715 \cdot 10^{-6}$	0.068	2.812	3.842
third island	40.201	35.983	$2.282 \cdot 10^{-5}$	0.178	7.156	6.405
channel	41.886	35.824	$2.609 \cdot 10^{-5}$	0.204	8.545	7.308
total	638.508	664.721	$5.897 \cdot 10^{-5}$	0.461	24.179	23.456

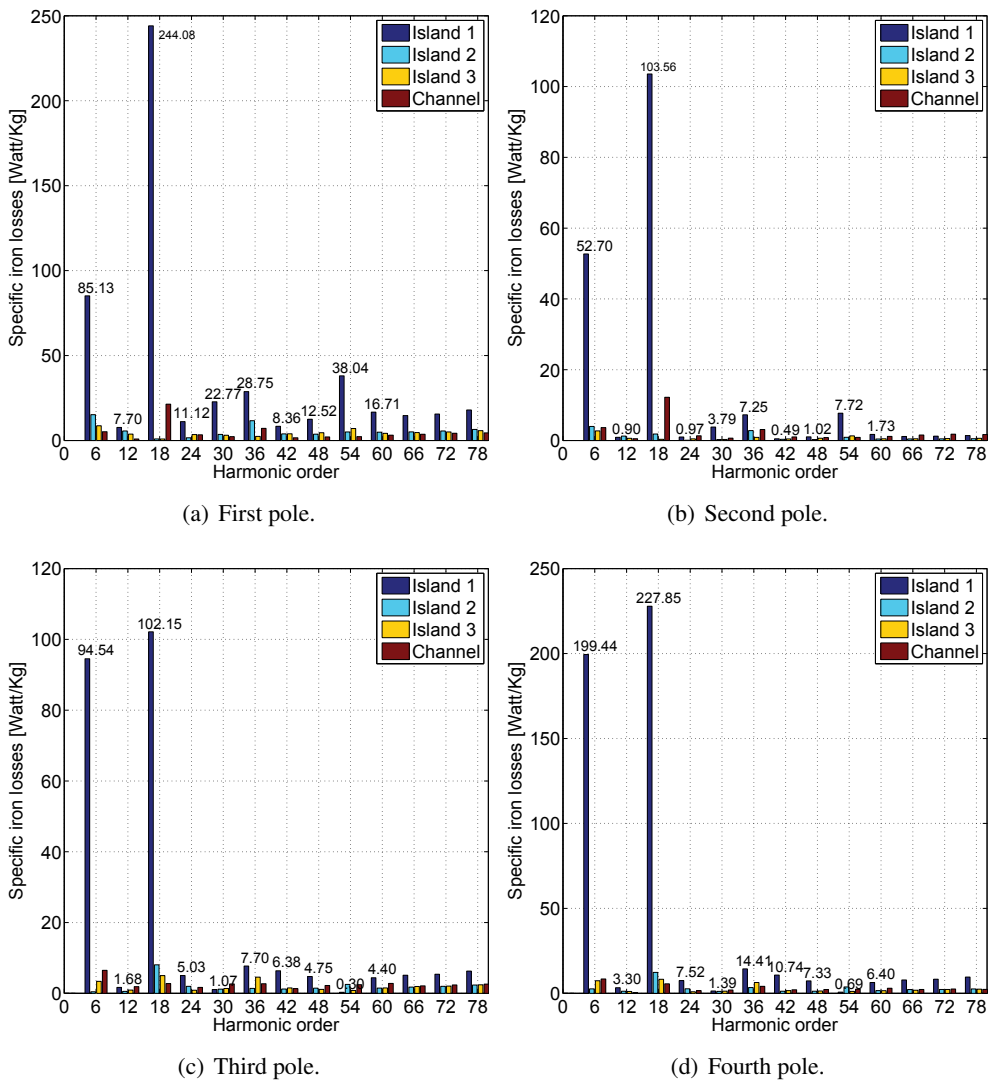


Figure 4.28: Analytic spectrum of the specific eddy current losses in the rotor islands and channels at $J = 3 \text{ A/mm}^2$.

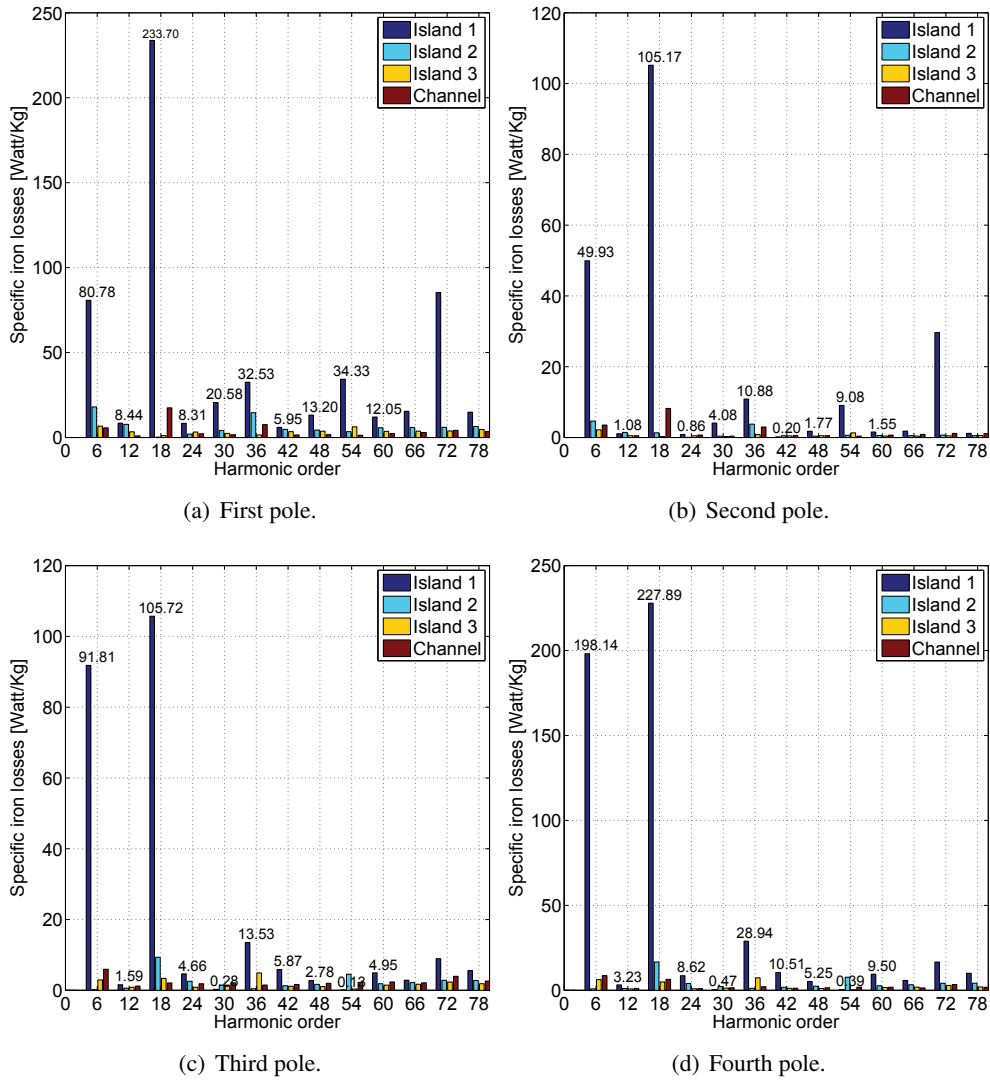


Figure 4.29: FE spectrum of the specific eddy current losses in the rotor islands and channels at $J = 3 \text{ A/mm}^2$.

4.4.2. Dynamic eccentricity case

Air-gap flux density

Similarly, the air-gap flux density distribution in case of dynamic eccentricity is estimated imposing the same eccentricity (i.e., equal to 0.1 mm). Fig. 4.30, Fig. 4.31, and Fig. 4.32 shows the air-gap flux density distributions of REL motor with one, two, and three flux-barriers per pole, at rotor positions $\theta_m = 0^\circ$ and $\theta_m = 60^\circ$. Since the position of the minimum air-gap length rotates with the rotor rotation, the peak of the air-gap flux density is also rotates. On the contrary, in static eccentricity case, the position of the minimum air-gap length is fixed on the right hand side. Thus, the peak of the air-gap flux density is fixed with the rotor rotation. As a consequent, the air-gap flux density distributions in both cases of eccentricity are the same at $\theta_m = 0^\circ$ and different at $\theta_m = 60^\circ$. This can be noted by comparing, as an example, Fig. 4.16 and Fig. 4.30.

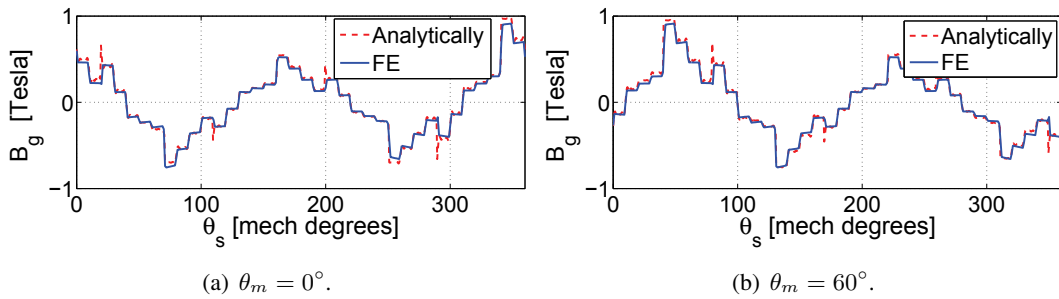


Figure 4.30: Air-gap flux density distribution achieved from the analytical and finite element model at dynamic eccentricity, rotor with one flux-barrier per pole: (a) at $\theta_m = 0^\circ$, (b) at $\theta_m = 60^\circ$.

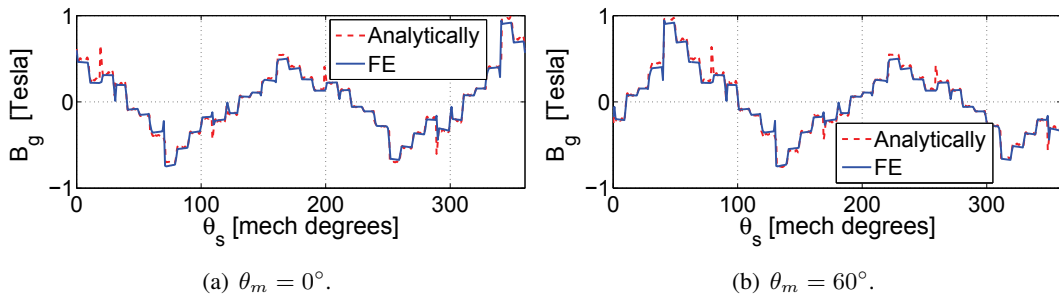


Figure 4.31: Air-gap flux density distribution achieved from the analytical and finite element model at dynamic eccentricity, rotor with two flux-barriers per pole: (a) at $\theta_m = 0^\circ$, (b) at $\theta_m = 60^\circ$.

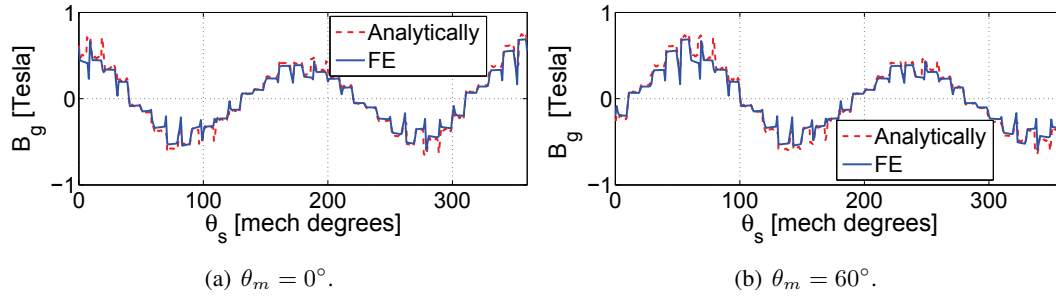


Figure 4.32: Air-gap flux density distribution achieved from the analytical and finite element model at dynamic eccentricity, rotor with three flux-barriers per pole: (a) at $\theta_m = 0^\circ$, (b) at $\theta_m = 60^\circ$.

Electromagnetic Torque

The electromagnetic torque is estimated, in case of dynamic rotor eccentricity, for motor with one, two, and three flux-barriers per pole. Fig. 4.33 shows the results of both analytical and FE models. The average torque and the torque ripple are similar to those of static eccentricity case. Consequently, the dynamic eccentricity has a negligible effect on the torque ripple.

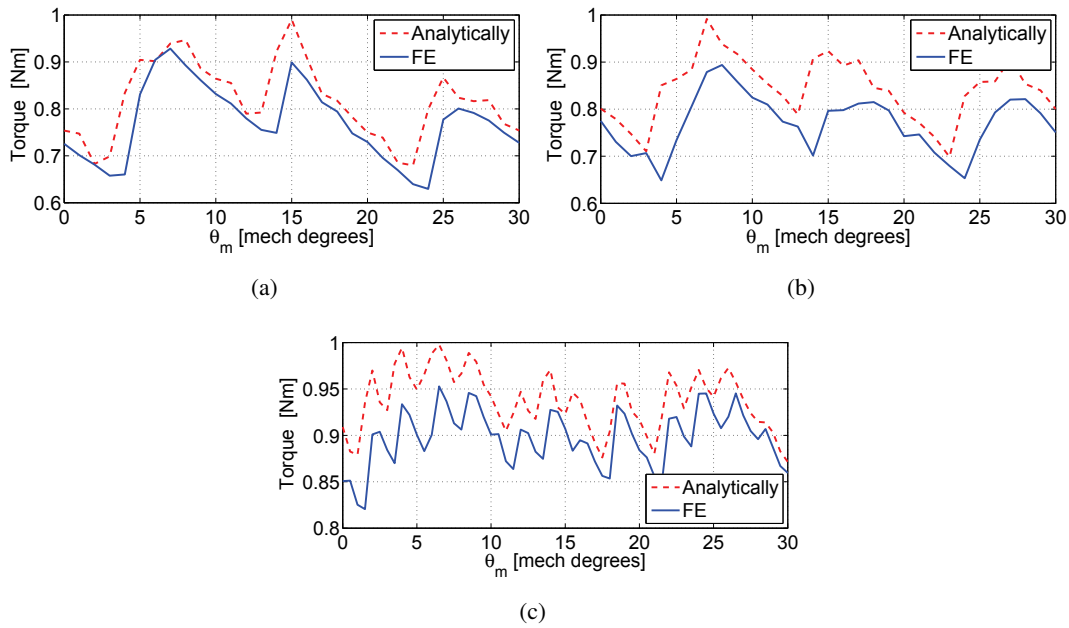


Figure 4.33: Torque results from the analytical and FE model at dynamic eccentricity, rotor with one, two, and three flux-barriers per pole. (a) One flux-barrier per pole. (b) Two flux-barriers per pole. (c) Three flux-barriers per pole.

Magnetic Radial force

In dynamic eccentricity case, the analytical and FE models estimate the force components F_x and F_y for REL motor with one, two, and three flux-barriers per pole, as shown in Fig. 4.34, Fig. 4.35, and Fig. 4.36, respectively. Both F_x and F_y components are presented in (xy) plane, as shown in Fig. 4.37. Since, the radial force in the direction of the minimum air-gap length, which rotates with the rotor rotation, this force rotates with the rotor rotation too.

Both models predict a maximum radial force in the range between 220 and 250 N for REL motor with one or two flux-barriers per pole. In addition, they predict a maximum force in the range between 150 and 200 N for REL motor with three flux-barriers per pole. Once again, the analytical computation tends to overestimate the radial force. The force amplitude is slightly lower with three flux-barriers per pole. As mentioned before, the difference between the two models is due to the approximation of the average air-gap length and the finite permeability of iron in FE analysis that slightly reduces the flux in the rotor path.

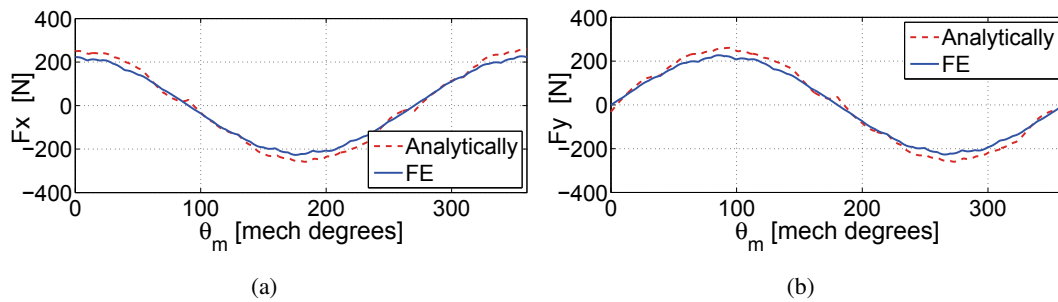


Figure 4.34: F_x and F_y at all rotor position in case of dynamic eccentricity, rotor with one flux-barrier per pole. (a) F_x versus rotor position. (b) F_y versus rotor position.

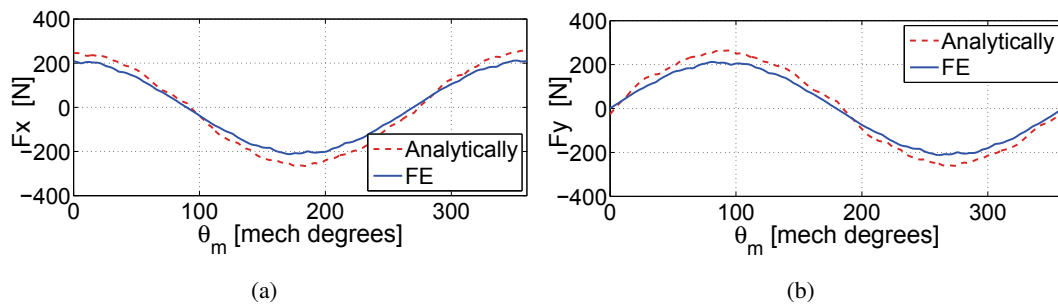


Figure 4.35: F_x and F_y at all rotor position in case of dynamic eccentricity, rotor with two flux-barriers per pole. (a) F_x versus rotor position. (b) F_y versus rotor position.

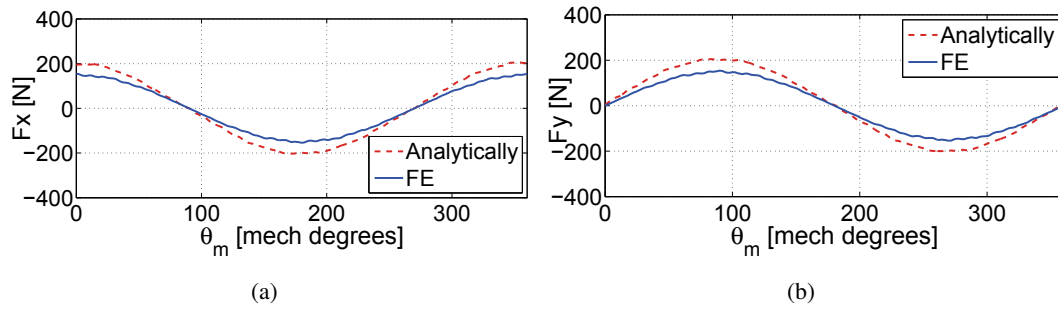


Figure 4.36: F_x and F_y at all rotor position in case of dynamic eccentricity, rotor with three flux-barriers per pole. (a) F_x versus rotor position. (b) F_y versus rotor position.

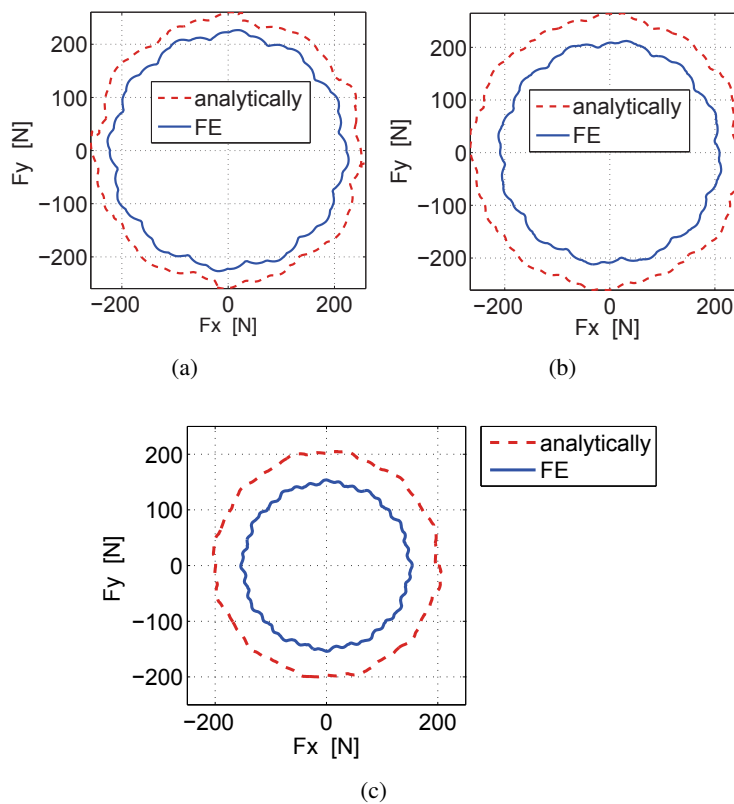


Figure 4.37: F_y versus F_x at all rotor position in case of one, two, and three flux-barriers per pole. (a) One flux barrier. (b) Two flux-barriers. (c) Three flux-barriers.

Rotor iron losses

Similar to static eccentricity case, the flux densities variations in the rotor islands and channels are estimated by both analytical and FE models of REL motor with three-barriers per pole. Again, referring to the i -th island of each pole, the flux density variation in this island is not the same for all poles, due to the non-uniform distribution of the air-gap length over the poles. Thus, the flux density variation in the i -th island is computed for each pole, separately. Fig. 4.38 shows the flux density distribution in the different islands and channels of each rotor pole at

current density equal to $J = 1.06 A/mm^2$.

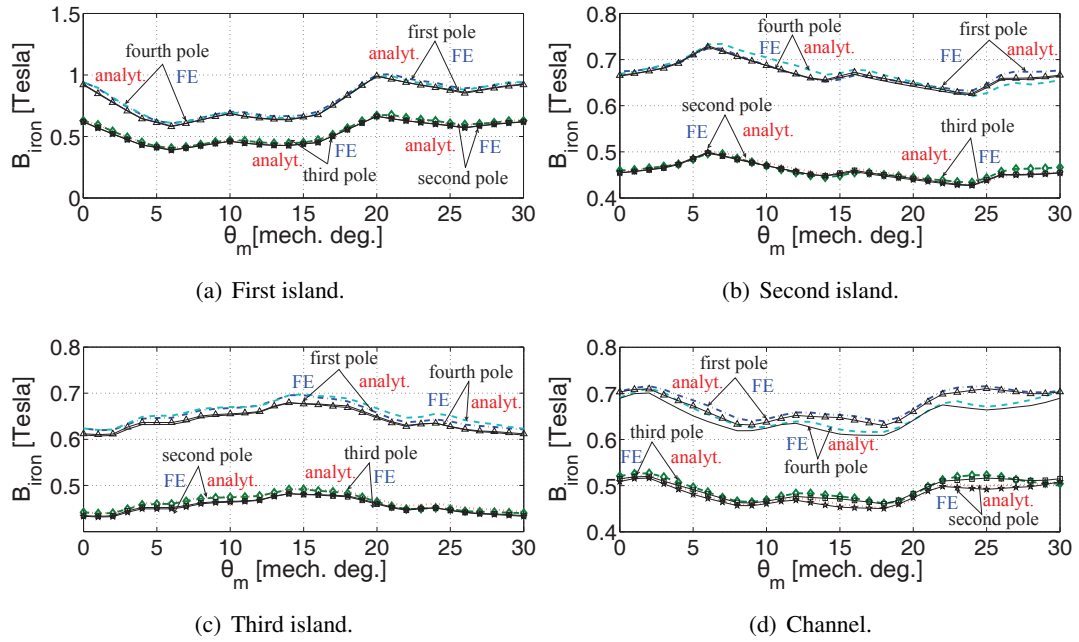


Figure 4.38: Flux densities variations in the different iron parts of all rotor poles results from the analytical and FE models at $J = 1.06 A/mm^2$.

Table 4.15: The eddy current loss of the first pole of the rotor, which results from the analytical and FE models at $J = 1.06 A/mm^2$.

rotor part	Analytic [W/kg]	FE [W/kg]	volume [m ³]	mass [Kg]	Analytic [W]	FE [W]
first island	49.733	55.058	$1.342 \cdot 10^{-6}$	0.011	0.547	0.606
second island	2.387	2.629	$8.715 \cdot 10^{-6}$	0.068	0.162	0.179
third island	1.443	1.299	$2.282 \cdot 10^{-5}$	0.178	0.257	0.231
channel	2.418	2.572	$2.609 \cdot 10^{-5}$	0.204	0.493	0.525
total	55.982	61.557	$5.897 \cdot 10^{-5}$	0.461	1.459	1.541

Table 4.16: The eddy current loss of the second pole of the rotor, which results from the analytical and FE models at $J = 1.06 A/mm^2$.

rotor part	Analytic [W/kg]	FE [W/kg]	volume [m ³]	mass [Kg]	Analytic [W]	FE [W]
first island	22.107	25.525	$1.342 \cdot 10^{-6}$	0.011	0.243	0.281
second island	1.193	1.257	$8.715 \cdot 10^{-6}$	0.068	0.081	0.086
third island	0.713	0.657	$2.282 \cdot 10^{-5}$	0.178	0.127	0.117
channel	2.037	1.346	$2.609 \cdot 10^{-5}$	0.204	0.416	0.275
total	26.050	28.785	$5.897 \cdot 10^{-5}$	0.461	0.867	0.759

Table 4.17: The eddy current loss of the third pole of the rotor, which results from the analytical and FE models at $J = 1.06 \text{ A/mm}^2$.

rotor part	Analytic [W/kg]	FE [W/kg]	volume [m ³]	mass [Kg]	Analytic [W]	FE [W]
first island	22.147	26.056	$1.342 \cdot 10^{-6}$	0.011	0.244	0.287
second island	1.168	1.237	$8.715 \cdot 10^{-6}$	0.068	0.079	0.084
third island	0.730	0.661	$2.282 \cdot 10^{-5}$	0.178	0.130	0.118
channel	1.713	1.462	$2.609 \cdot 10^{-5}$	0.204	0.350	0.298
total	25.757	29.417	$5.897 \cdot 10^{-5}$	0.461	0.803	0.787

Table 4.18: The eddy current loss of the fourth pole of the rotor, which results from the analytical and FE models at $J = 1.06 \text{ A/mm}^2$.

rotor part	Analytic [W/kg]	FE [W/kg]	volume [m ³]	mass [Kg]	Analytic [W]	FE [W]
first island	49.889	55.966	$1.342 \cdot 10^{-6}$	0.011	0.549	0.616
second island	2.838	2.531	$8.715 \cdot 10^{-6}$	0.068	0.193	0.172
third island	1.540	1.296	$2.282 \cdot 10^{-5}$	0.178	0.274	0.231
channel	2.851	2.881	$2.609 \cdot 10^{-5}$	0.204	0.582	0.588
total	57.119	62.674	$5.897 \cdot 10^{-5}$	0.461	1.598	1.607

It is noted that there is a good agreement between the FE and analytical model results. The flux density variation in the islands and channels of the first pole and the fourth pole are higher than those of the second pole and the third pole. Because the first and the fourth pole are close the minimum air-gap length. On the contrary, the second and the third poles are close to the maximum air-gap length. Due to the rotation of the minimum air-gap length, the flux densities variations in the islands and channels of the first and fourth pole are high for all rotor position.

Table. 4.15, Table. 4.16, Table. 4.17, and Table. 4.18 report the specific eddy current losses and the total eddy current losses in the islands and channels of the rotor first, second, third, fourth pole, respectively. From these tables, the total rotor eddy current losses results from the analytical and FE models are equal to 4.727 [W] and 4.694 [W], respectively. Referring to the eddy current losses per each pole, the analytical model is slightly higher than the FE model. By comparing the dynamic eccentricity and healthy cases, it is noted that the rotor eddy current losses in static eccentricity case is equal to $\simeq 112\%$ of that in healthy case.

Fig. 4.39 and Fig. 4.40 shows the analytic and FE spectrum of the specific eddy current losses of the islands and channels of the first, second, third, and fourth pole, respectively. It is noted that the slot harmonic $Q_s = p$ and its multiples have high contribution in the iron losses.

At $J = 3 \text{ A/mm}^2$, the flux density variation in the different iron parts of all poles is shown in Fig. 4.41. Then, the eddy current losses of the different islands and channels of each pole are reported in Table. 4.19, Table. 4.20, Table. 4.21, and Table. 4.22. The total iron losses of overall rotor result from the analytical and FE model are equal to 38.120 [W] and 37.632 [W], respectively. By comparing the dynamic eccentricity and healthy cases, again, the rotor eddy current losses in dynamic eccentricity case are equal to $\simeq 115\%$ of those in healthy case. Comparing the rotor eddy current losses of both static and dynamic eccentricity cases, at

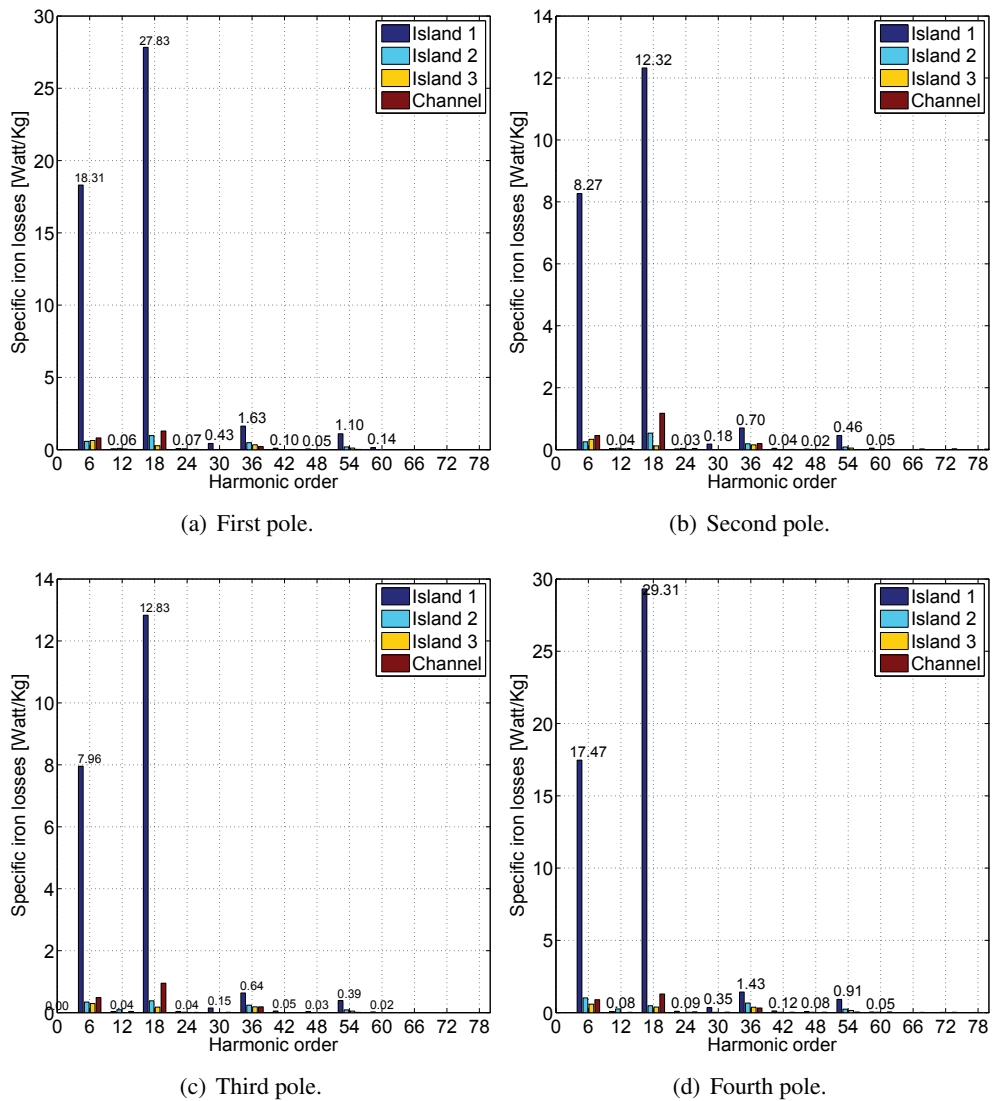


Figure 4.39: Analytic spectrum of the specific eddy current losses in the rotor islands and channels at $J = 1.06 \text{ A/mm}^2$.

different current density levels, the impact of the static eccentricity on the eddy current losses can be approximately considered as twice of the corresponding of the dynamic eccentricity.

Then, the analytic and FE spectrum of the specific iron losses of the islands and channels of each pole are highlighted in Fig. 4.42 and Fig. 4.43, respectively. The same comments highlighted before are also noticed in these two figures.

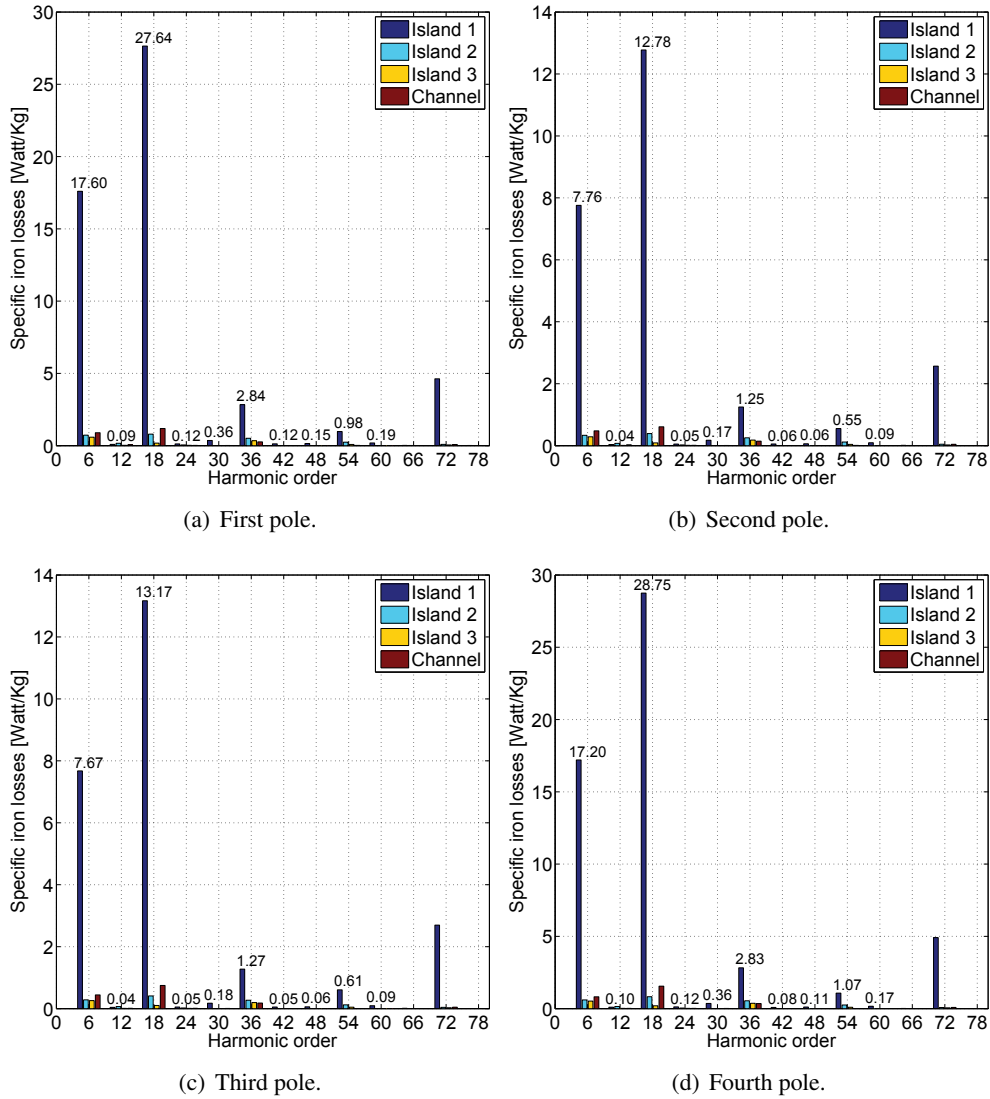


Figure 4.40: FE spectrum of the specific eddy current losses in the rotor islands and channels at $J = 1.06 \text{ A/mm}^2$.

Table 4.19: The eddy current loss of the first pole of the rotor, which results from the analytical and FE models at $J = 3 \text{ A/mm}^2$.

rotor part	Analytic [W/kg]	FE [W/kg]	volume [m ³]	mass [Kg]	Analytic [W]	FE [W]
first island	401.127	444.105	$1.342 \cdot 10^{-6}$	0.011	4.412	4.885
second island	19.256	21.204	$8.715 \cdot 10^{-6}$	0.068	1.309	1.442
third island	11.641	10.482	$2.282 \cdot 10^{-5}$	0.178	2.072	1.866
channel	19.504	20.743	$2.609 \cdot 10^{-5}$	0.204	3.979	4.232
total	451.528	496.532	$5.897 \cdot 10^{-5}$	0.461	11.772	12.425

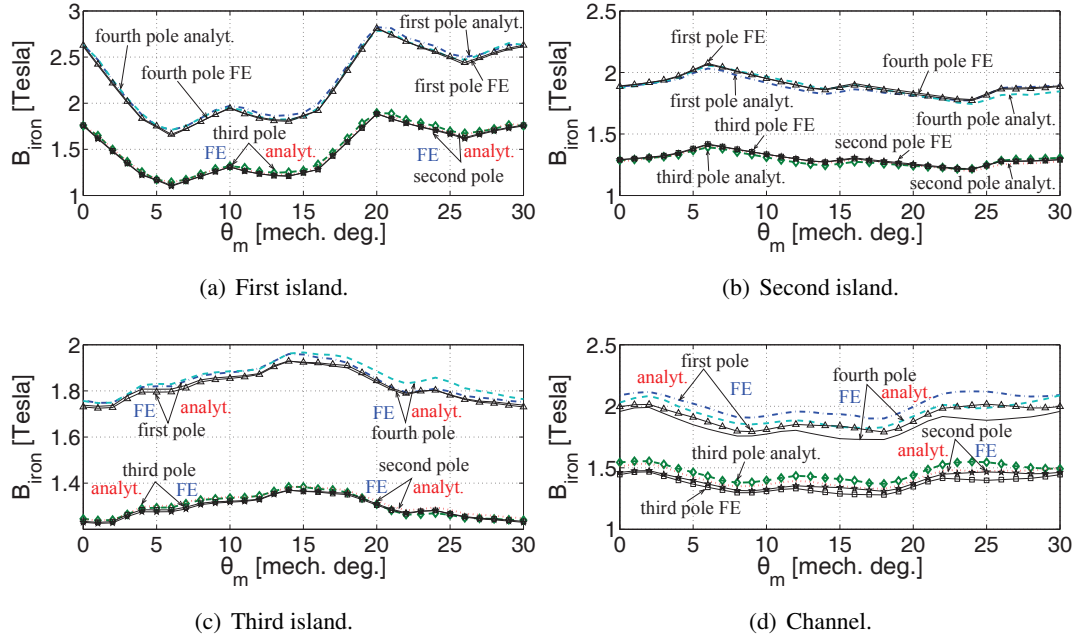


Figure 4.41: Flux densities variations in the different iron parts of all rotor poles results from the analytical and FE models at $J = 3 \text{ A/mm}^2$.

Table 4.20: The eddy current loss of the second pole of the rotor, which results from the analytical and FE models at $J = 3 \text{ A/mm}^2$.

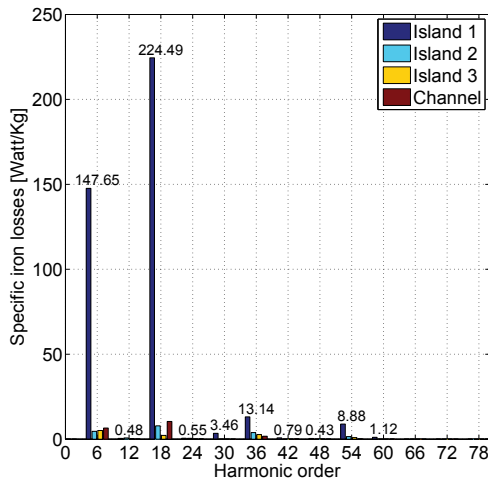
rotor part	Analytic [W/kg]	FE [W/kg]	volume [m ³]	mass [Kg]	Analytic [W]	FE [W]
first island	178.303	205.888	$1.342 \cdot 10^{-6}$	0.011	1.961	2.059
second island	9.621	10.137	$8.715 \cdot 10^{-6}$	0.068	0.654	0.689
third island	5.752	5.300	$2.282 \cdot 10^{-5}$	0.178	1.024	0.943
channel	16.433	10.860	$2.609 \cdot 10^{-5}$	0.204	3.352	2.215
total	210.108	232.184	$5.897 \cdot 10^{-5}$	0.461	6.991	5.906

Table 4.21: The eddy current loss of the third pole of the rotor, which results from the analytical and FE models at $J = 3 \text{ A/mm}^2$.

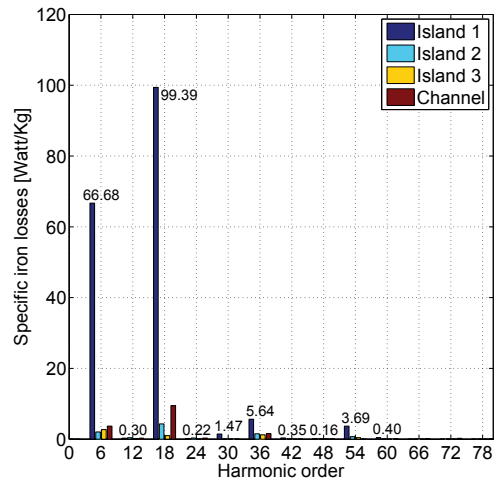
rotor part	Analytic [W/kg]	FE [W/kg]	volume [m ³]	mass [Kg]	Analytic [W]	FE [W]
first island	178.629	210.172	$1.342 \cdot 10^{-6}$	0.011	1.965	2.312
second island	9.417	9.979	$8.715 \cdot 10^{-6}$	0.068	0.640	0.679
third island	5.884	5.333	$2.282 \cdot 10^{-5}$	0.178	1.047	0.949
channel	13.814	11.796	$2.609 \cdot 10^{-5}$	0.204	2.818	2.406
total	207.444	237.280	$5.897 \cdot 10^{-5}$	0.461	6.470	6.346

Table 4.22: The eddy current loss of the fourth pole of the rotor, which results from the analytical and FE models at $J = 3 \text{ A/mm}^2$.

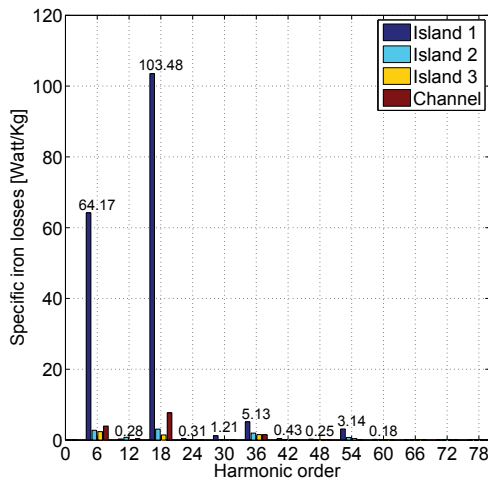
rotor part	Analytic [W/kg]	FE [W/kg]	volume [m^3]	mass [Kg]	Analytic [W]	FE [W]
first island	402.384	451.430	$1.342 \cdot 10^{-6}$	0.011	4.426	4.966
second island	22.891	20.417	$8.715 \cdot 10^{-6}$	0.068	1.557	1.388
third island	12.425	10.456	$2.282 \cdot 10^{-5}$	0.178	2.212	1.861
channel	22.999	23.237	$2.609 \cdot 10^{-5}$	0.204	4.692	4.740
total	460.697	505.540	$5.897 \cdot 10^{-5}$	0.461	12.887	12.955



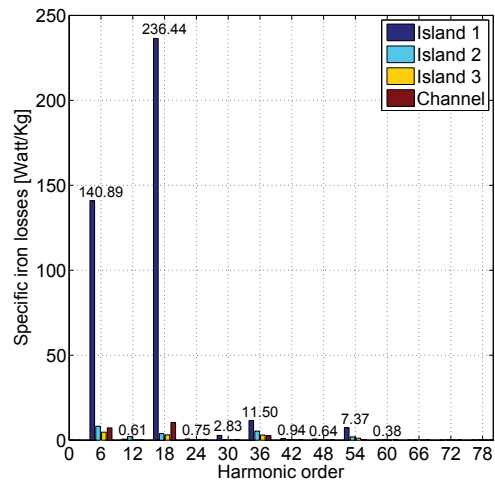
(a) First pole.



(b) Second pole.



(c) Third pole.



(d) Fourth pole.

Figure 4.42: Analytic spectrum of the specific eddy current losses in the rotor islands and channels at $J = 3 \text{ A/mm}^2$.

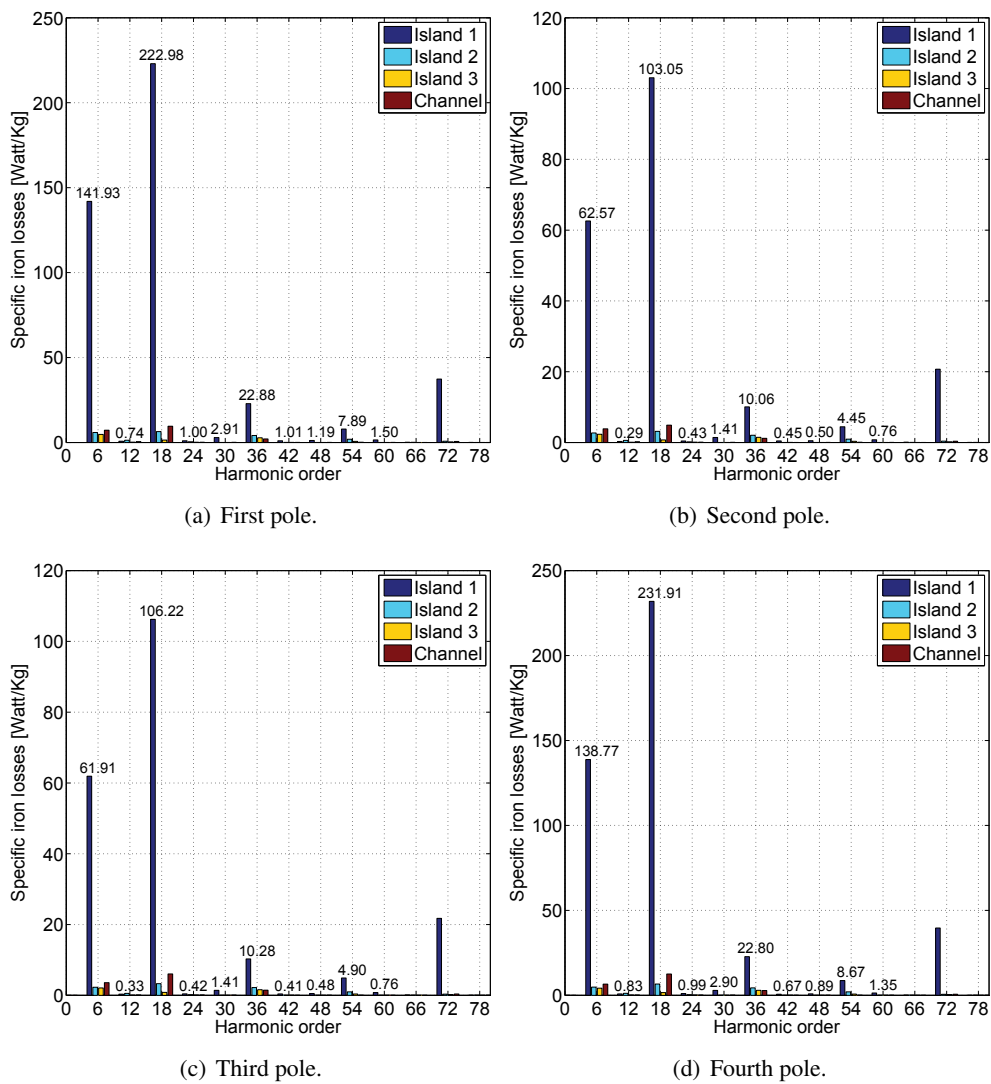
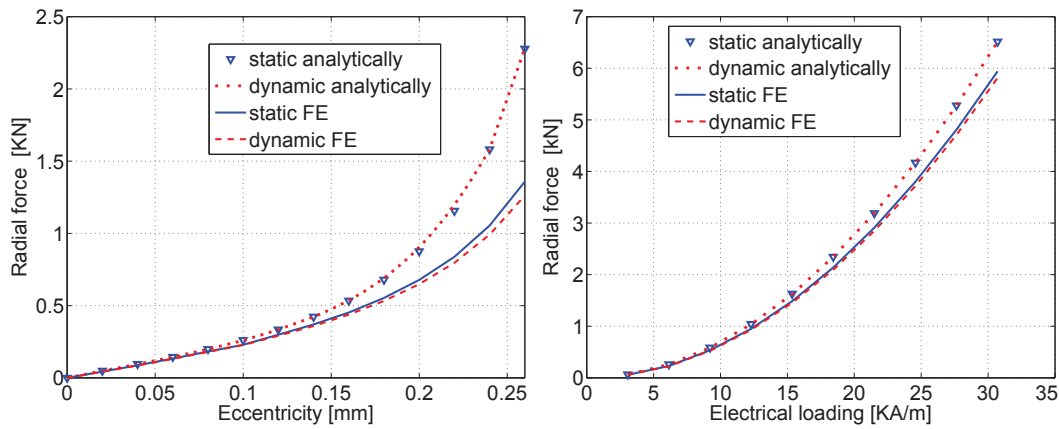


Figure 4.43: FE spectrum of the specific eddy current losses in the rotor islands and channels at $J = 3 \text{ A/mm}^2$.

4.4.3. The effect of eccentricity distance and electrical loading on the radial force

Fig. 4.44 (a) shows the radial force (the peak value is reported) versus the eccentricity. All computations are carried out for REL motor with one flux-barrier per pole, as an example. The radial force increases rapidly with the eccentricity. Static and dynamic eccentricity cause similar maximum radial force. The analytical model matches the FE analysis fairly well, up to an eccentricity equal to half the air-gap length, while it overestimates the force for higher eccentricity.

Fig. 4.44 (b) shows the radial force versus the electrical loading. The force increases with the power of two with respect to the electrical loading. Again, there is a satisfactory agreement between the two models when, eccentricity is lower than 50% of the air-gap length.



(a) Radial force versus the eccentricity distance in both cases of eccentricity results from the analytical and FE cases of eccentricity ($e = 0.1 \text{ mm}$) results from the models. Electrical loading is 6200 A/m or $\hat{I} = 1 \text{ A}$. (b) Radial force versus the electrical loading in both analytical and FE models.

Figure 4.44: The variation of the radial force with (a) the eccentricity distance and (b) the electrical loading, in both cases of eccentricity.

Different rotor geometries and stator windings

In this chapter, the analytical model proposed in Chapter 3 is used to compare the performance of the REL motors with different rotor geometries such as symmetric rotor (rotor with symmetric flux barriers) and asymmetric rotor (rotor with asymmetric flux barriers) in both eccentricity cases. As an example, a four pole machine with one, two, and three flux-barriers per pole is used. In addition, the analytical model is also applied to REL motors with fractional-slot coil windings to study the impact of these windings arrangements on the radial forces acting on the rotor in both healthy (no eccentricity) and eccentricity cases. Both single- and double-layer windings are compared with integral-slot distributed windings. As an example, a six-slot four-pole machine with concentrated windings and 36-slot four pole machine with distributed windings are compared. A finite-element analysis confirms the results achieved by means of the analytical model.

5.1. Introduction

In a synchronous reluctance (REL) motor, the anisotropic rotor strongly interacts with the magneto-motive force (MMF) harmonics, which are due to the discrete distribution of the winding within the slots. The main effect investigated up now is the torque ripple. Several works about the torque ripple reduction are based on a proper design of the rotor geometry. A practical design criterion has been proposed in [30] for symmetrical rotor poles geometry. An alternative approach is represented by the introduction of asymmetries in the rotor flux-barriers. They allow one or more torque ripple harmonics to be minimized or even cancelled [25, 27]. Such techniques have been also adopted in [26, 49]. All these works highlight that both REL and interior permanent magnet (IPM) machines exhibit a strong non-linear behaviour so that their design is rather complex.

In addition, an interest is growing up on synchronous machines with high efficiency and high power density. To this aim, fractional-slot non overlapped coil windings (FSCW) are used. Several researches have been carried out about FSCW configurations to achieve merits such as reduction of the end winding length which leads to reduce the stator copper loss and to increase the efficiency [50], increasing the self-inductance of each phase which leads to reduce the short

circuit current [51], allowing the phases to be mutually separated so as to avoid the propagation of the fault. FSCW allows the fault tolerance [52–54] and flux weakening capability [55,56] to be increased.

On the other hand, there are some drawbacks in adopting FSCW such as an increase of magneto-motive force (MMF) harmonic content. This causes iron saturation, a decrease of the average torque, unbalanced radial forces, and torque ripples. Sub harmonics increase the rotor losses due to currents induced in the rotor metallic parts. Unbalanced radial forces cause stress on the bearing and magnetic noise [57–59]. Several works are available in literature dealing with proper selection of number of slots and number of poles [41].

Among all those studies, the impact of the rotor eccentricity in these machines has been only marginally considered or not dealt with at all. This chapter aims to fill this gap, focusing on the impact of both static and dynamic eccentricity of synchronous REL machines. Hereafter, a REL motor is considered, however the same analysis may be easily extended to an IPM machine. A symmetric rotor with a single flux-barrier per pole is adopted, even if, the same analysis is valid for two and three flux-barriers per pole.

The purpose of this chapter is to apply the analytical model presented in Chapter 3 to study the eccentricity effect in a REL machine taking into account rotor structures with symmetric and asymmetric flux-barriers geometry and with single- and double-layer FSCW. The main focus is on the radial force on the rotor that represents the main effect of eccentricity. Finite element is used again to confirm the results of the analytical model as shown in Chapter 4. All results in this chapter are carried out considering the eccentricity equal to $e = 0.1 \text{ mm}$, eccentricity initial angle $\theta_e = 0$, peak conductor current $\hat{I} = 1 \text{ A}$, and electric current angle $\alpha_i^e = 45$ electric degrees. Again, since the model is linear the comparison is the same also at full load ($\hat{I} = 5.29 \text{ A}$).

5.2. Rotor structure with symmetric and asymmetric flux-barriers

Rotor geometry with symmetric flux-barriers is shown in Fig. 5.1 (a). All flux-barriers have the same dimensions (t_{b1}, l_{b1}) and end tip angle θ_{b1} . A typical problem of this rotor structure is a high torque ripple superimposed to the average torque [60]. The fundamental stator magneto motive force (MMF) harmonic is synchronous with the rotor and it produces the average torque. High anisotropy is required in synchronous REL motor to get high torque. The other MMF harmonics move asynchronously with the rotor causing torque ripple. They interact with the rotor anisotropic structure. Rotor geometries with asymmetric flux-barriers, also called "machaon" rotor structures, are adopted to reduce one or more torque harmonics. Fig. 5.1 (b) shows the machaon rotor structure. In the 4-pole rotor the flux barriers of the first and third pole have dimensions (t_{b1}, l_{b1}) and end tip angle θ_{b1} while the flux barriers of the second and fourth pole have dimensions (t_{b2}, l_{b2}) and end tip angle θ_{b2} , different from the previous ones.

In this section, the same analytical model of the REL motor with symmetric flux-barriers per pole is implemented. However, the diversity of the flux barriers dimensions, shown in Fig. 5.1 (b), is taken into consideration during the computations. Table. 5.1, Table. 5.2, and Table. 5.3 shows the geometry of the flux-barriers of the different rotor poles of REL motor with one, two, and three flux-barriers per pole, respectively.

The analytical and simplified FE models for REL motor are applied in both static and dynamic eccentricity cases. The results are reported hereafter. All results in this section are

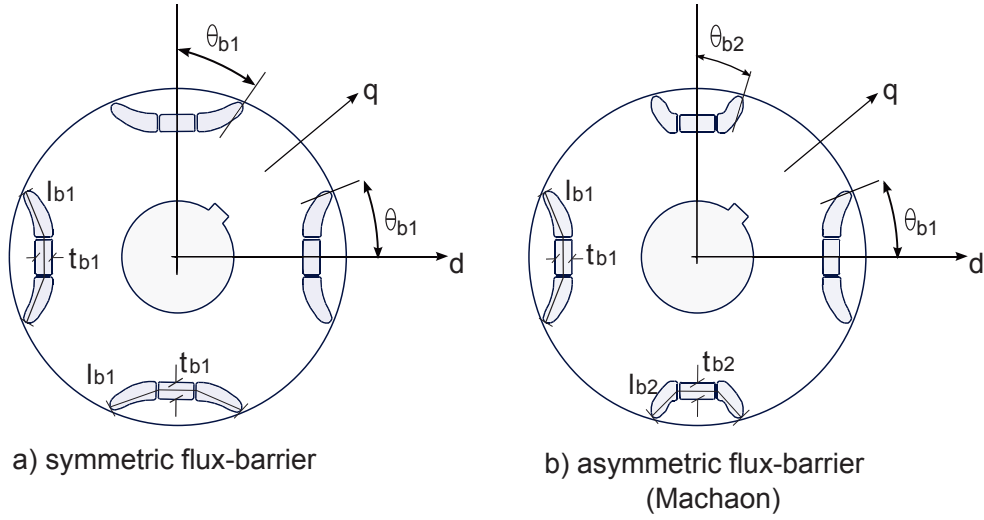


Figure 5.1: Rotor geometry with symmetric and asymmetric flux-barriers.

Table 5.1: Geometrical data of asymmetric rotor with one flux-barrier per pole.

first and third pole	$2\theta_{b_1} = 28^\circ$ $\frac{t_{b_1}}{l_{b_1}} = 0.13$	second and fourth pole	$2\theta_{b_1} = 31^\circ$ $\frac{t_{b_1}}{l_{b_1}} = 0.12$
----------------------	--	------------------------	--

Table 5.2: Geometrical data of asymmetric rotor with two flux-barriers per pole.

first and third pole	$2\theta_{b_1} = 28^\circ$	second and fourth pole	$2\theta_{b_1} = 31^\circ$
	$2\theta_{b_2} = 52^\circ$		$2\theta_{b_2} = 56^\circ$
	$\frac{t_{b_1}}{l_{b_1}} = 0.13$ $\frac{t_{b_2}}{l_{b_2}} = 0.096$		$\frac{t_{b_1}}{l_{b_1}} = 0.12$ $\frac{t_{b_2}}{l_{b_2}} = 0.083$

Table 5.3: Geometrical data of asymmetric rotor with three flux-barriers per pole.

first and third pole	$2\theta_{b_1} = 28^\circ$	second and fourth pole	$2\theta_{b_1} = 31^\circ$
	$2\theta_{b_2} = 52^\circ$		$2\theta_{b_2} = 56^\circ$
	$2\theta_{b_3} = 77.2^\circ$		$2\theta_{b_3} = 80.3^\circ$
	$\frac{t_{b_1}}{l_{b_1}} = 0.13$		$\frac{t_{b_1}}{l_{b_1}} = 0.12$
	$\frac{t_{b_2}}{l_{b_2}} = 0.096$		$\frac{t_{b_2}}{l_{b_2}} = 0.083$
	$\frac{t_{b_3}}{l_{b_3}} = 0.063$		$\frac{t_{b_3}}{l_{b_3}} = 0.61$

carried out considering a slot-less stator with distributed non-chorded winding, equivalent to a 36-slot stator.

5.2.1. Comparison in case of static rotor eccentricity

The analytical and FE model computes the electromagnetic torque of the REL motor with asymmetric rotor, in static eccentricity case. Fig. 5.2 shows the torque for motor with one, two, and three flux-barriers per pole. It is noted that there is a satisfactory agreement between both models results. The analytical model estimates the same torque ripple as the FE model. The difference in the average torque is due to the reasons mentioned before in chapter 4. To clarify the effect of asymmetric flux-barriers in the rotor on reducing the torque ripple, Fig. 5.3 shows the comparison between the torque of the REL motor with symmetric and asymmetric rotor structures. As expected, it is noted that the torque ripple of a motor with asymmetric rotor structure is smaller than that with symmetric rotor structure.

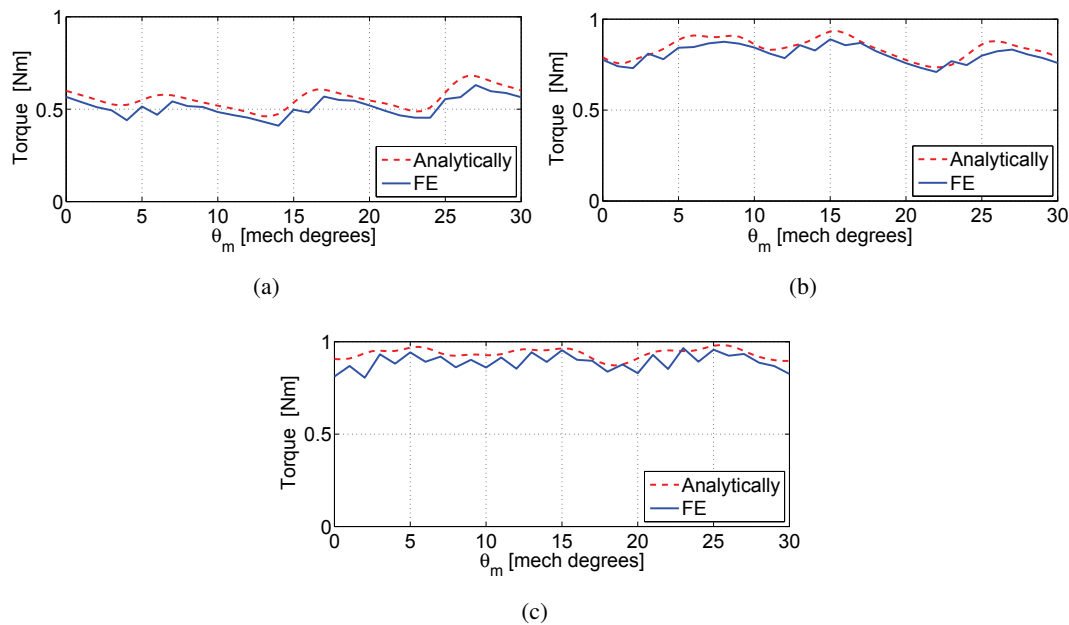


Figure 5.2: Torque behaviour results from both analytical and FE models at static eccentricity, $e = 0.1$ mm, for REL motor with asymmetric rotor geometry with one, two, and three flux-barriers per pole. (a) One flux-barrier per pole. (b) Two flux-barriers per pole. (c) Three flux-barriers per pole.

In case of static eccentricity, the radial force components F_x and F_y are shown in Fig. 5.4 (a), Fig. 5.4 (b), and Fig. 5.4 (c) for rotor with one, two, and three asymmetric flux-barriers per pole, respectively. With symmetric flux-barriers per pole, the force components are shown in Fig. 4.23 (a), Fig. 4.23 (b), and Fig. 4.23 (c), respectively. Referring to rotor with one and two flux-barriers per pole, the force is in the direction of the smaller air-gap length in the range between 220 and 250 N, in case of symmetric rotor, and it is in the range between 220 and 300 N, with asymmetric rotor. Besides, referring to rotor with three barriers per pole, the force is in the range between 150 and 200 N, in case of symmetric rotor, and it is in the range between 160 and 220 N, with asymmetric rotor. Both analytical and FE models gives similar force. It is noted that the radial force on the rotor in case of asymmetric rotor and symmetric rotor structure is comparable. It is $\simeq 25\%$ higher in case of asymmetric rotor with one flux-barrier, but it reduces to $\simeq 7\%$ and $\simeq 8\%$ higher with two and three flux-barriers rotor, respectively. Therefore, the two structures will exhibit similar noise and vibration.

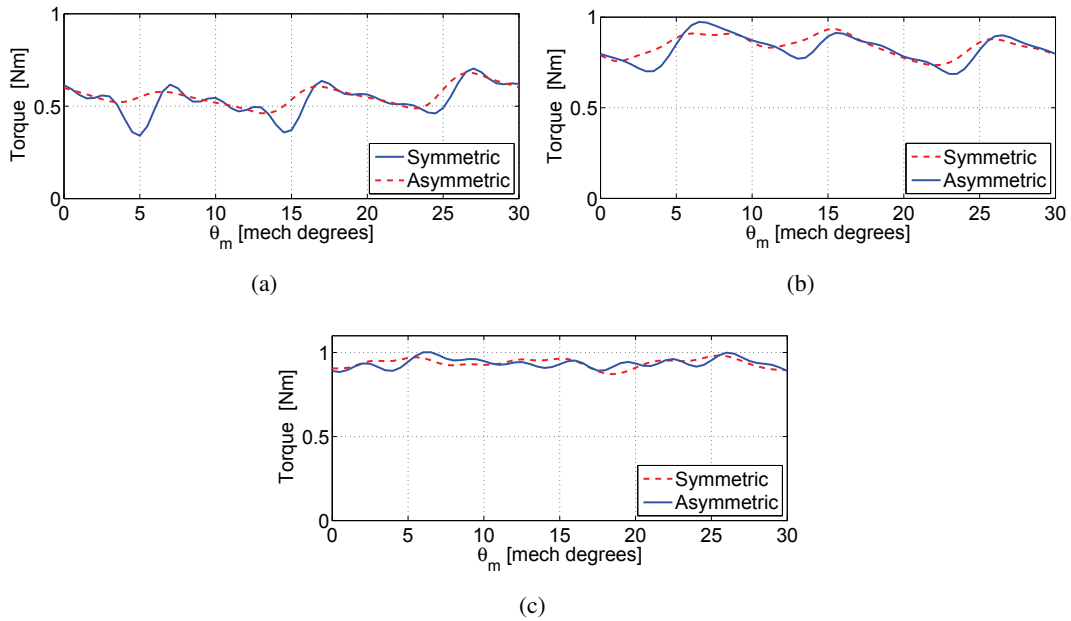


Figure 5.3: Torque behavior at static eccentricity, $e = 0.1$ mm, for REL motor with asymmetric and symmetric rotor geometries with: (a) one flux-barrier, (b) two flux-barriers, and (c) three flux-barriers per pole.

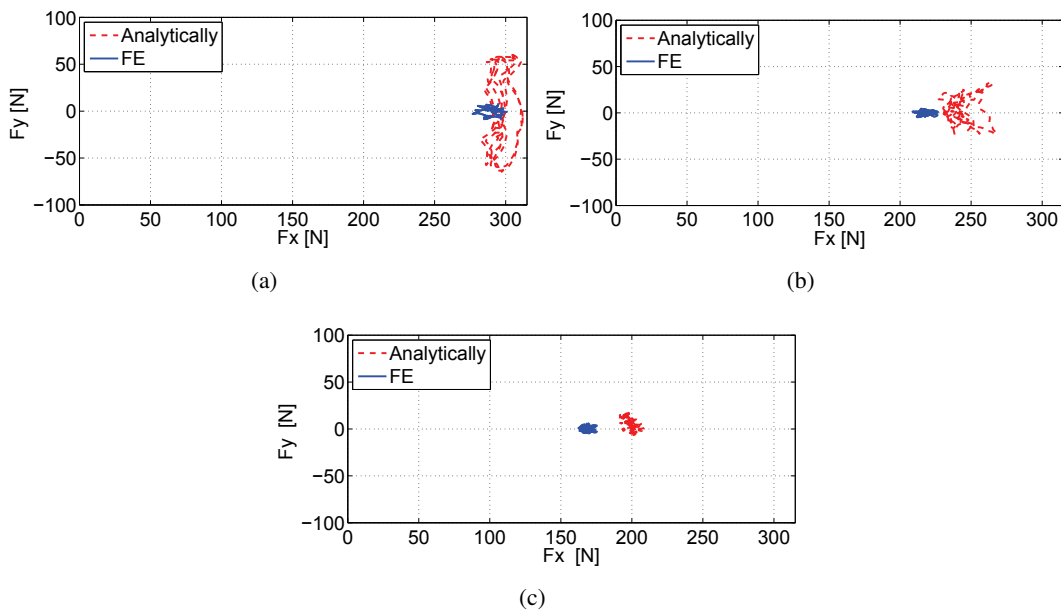


Figure 5.4: F_y versus F_x at all positions of asymmetric rotor in static eccentricity case. (a) One flux-barrier, (b) Two flux-barriers, and (c) Three flux-barriers per pole.

5.2.2. Comparison in case of dynamic rotor eccentricity

Similarly, in dynamic eccentricity case, the electromagnetic torque is estimated by both analytical and FE models of REL motor with asymmetric rotor. Fig. 5.5 shows the torque for a

motor with one, two, and three flux-barriers per pole. Fig. 5.6 confirms that the electromagnetic torque is similar in both static and dynamic eccentricity cases. Once again, there is a good agreement between the FE and the analytical models results.

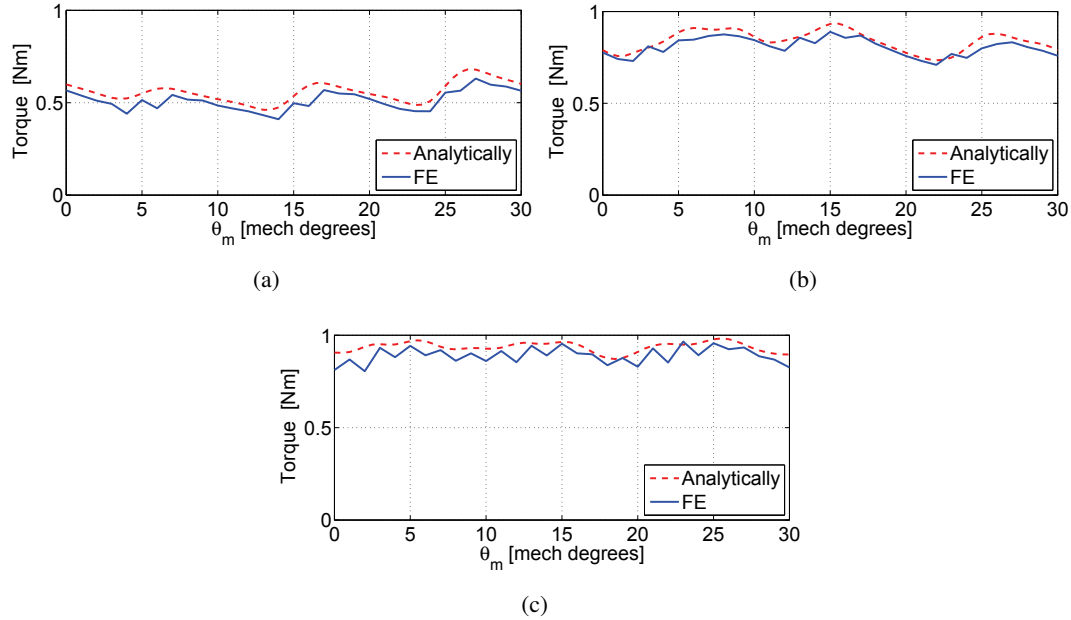


Figure 5.5: Torque behavior at static eccentricity for REL motor with asymmetric rotor geometry with: (a) one flux-barrier, (b) two flux-barriers, and (c) three flux-barriers per pole.

In case of dynamic eccentricity, Fig. 5.7 and Fig. 4.37 show the force components F_x and F_y for asymmetric and symmetric rotor structure with one, two, and three flux-barriers per pole, respectively. The radial force is in direction of the smaller air-gap length which rotates with the rotor. In asymmetric rotor case, the force computed by means of both models results in the range between 200 and 320 N in all cases. Once again, the radial force on asymmetric rotor in comparison with the case of symmetric rotor is slightly higher (20%) with one flux-barrier rotor, and comparable with two and three flux-barriers rotor.

The analytical model tends to slightly overestimate the radial force, with respect to the FE model. As said in chapter 4, the difference is due (i) to the approximation of the average air-gap length in front of each rotor iron path and (ii) to the finite permeability of iron in FE analysis that slightly reduces the flux in the rotor path in comparison to the analytical model. In addition, the results show that increasing the number of flux-barriers (and then bounding the flux paths) the radial forces tend to decrease.

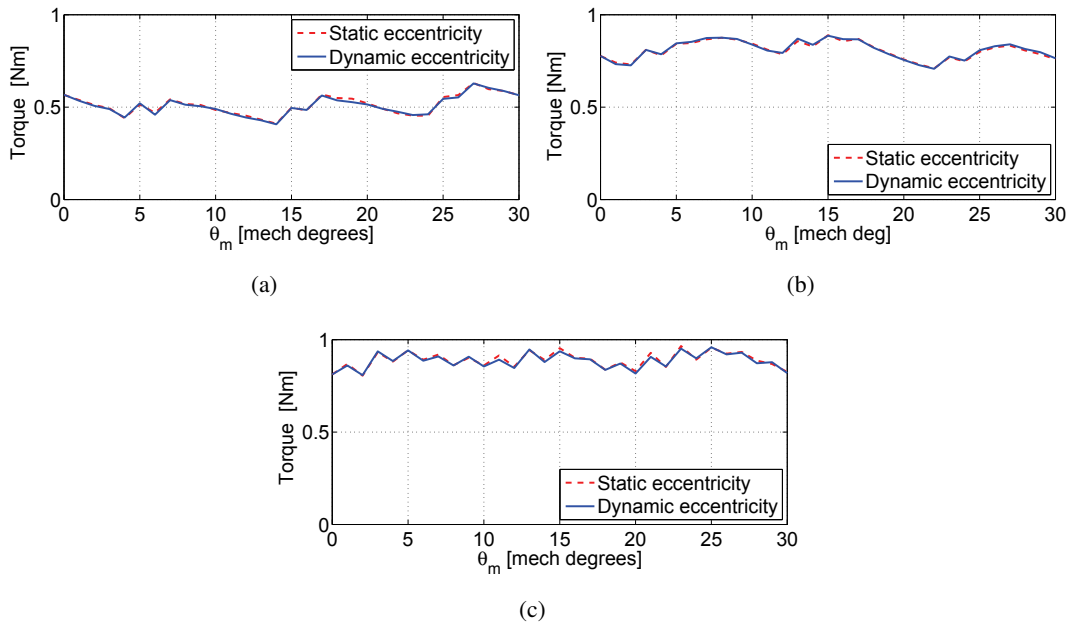


Figure 5.6: Torque behavior results at both static and dynamic eccentricity cases for REL motor with asymmetric rotor geometry with: (a) one flux-barrier, (b) two flux-barriers, and (c) three flux-barriers per pole.

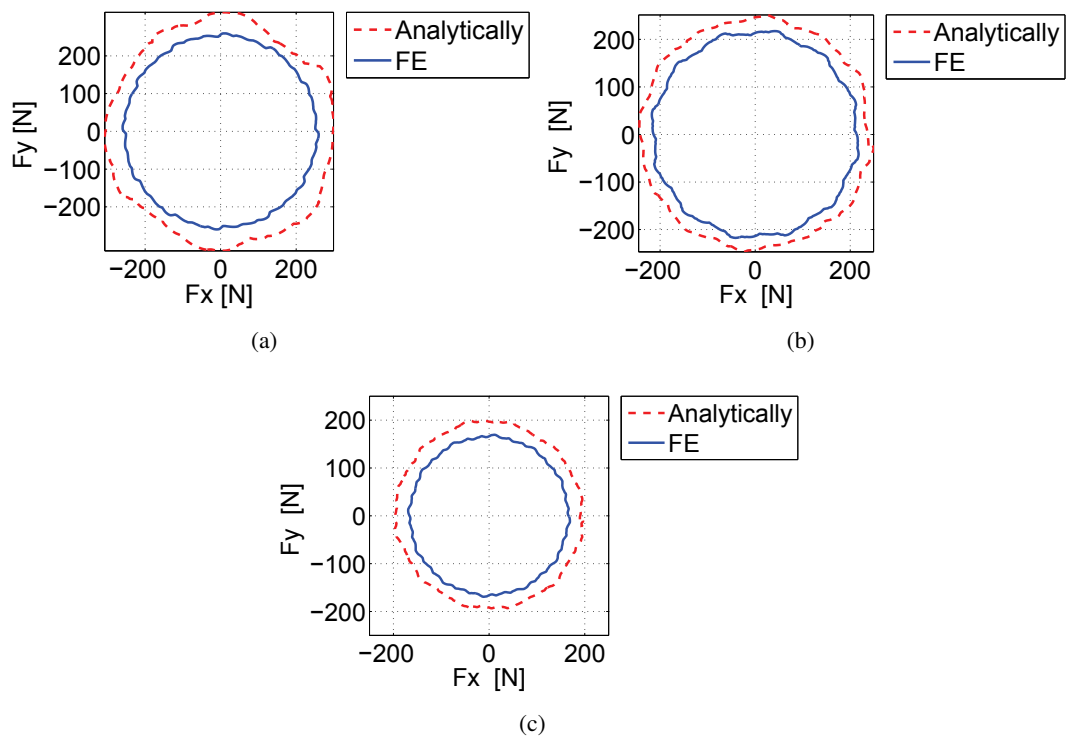


Figure 5.7: F_y versus F_x at all positions of asymmetric rotor in dynamic eccentricity case. (a) One flux-barrier, (b) Two flux-barriers, and (c) Three flux-barriers per pole.

5.3. Fractional-Slot Stator windings

Fig. 5.8 shows the structure of a 6-slot 4-pole REL machine with single- and double-layer non-overlapped coil windings (FSCW), considering a symmetric rotor with one flux-barrier per pole. For the sake of comparison, a REL machine with integral-slot distributed windings is also considered: a 36-slot 4-pole machine with the same size and the same symmetric rotor geometry of the FSCW REL machine.

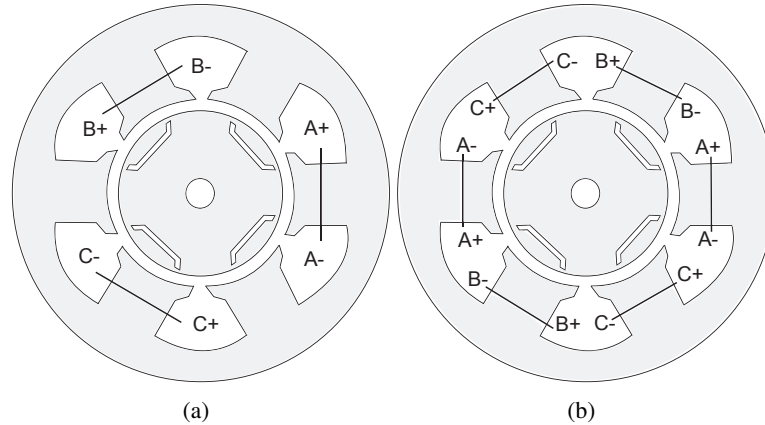


Figure 5.8: Six-slot four-pole REL machine with (a) single-layer and (b) double-layers FSCW.

Fig. 5.9 shows the map of the magnetic flux density with a double-layer FSCW, in healthy case and both eccentricity cases. These maps can be compared with that of REL motor with distributed windings shown in Fig. 4.2. In case of distributed windings, there are small symmetric saturation for four poles. In case of double layer FSCW (see Fig. 5.9 (a)), this saturation increase in two poles only due to increase of space harmonics. The flux density distribution is shifted from the axis of symmetry in both cases of eccentricity. Therefore, the flux density on the right hand side is increased and the flux density on left hand side is decreased, as shown in Fig. 5.9 (b).

5.3.1. Winding comparison in case of no eccentricity

Fig. 5.10 shows the stator scalar magnetic potential (MMF_s) referring to stator with distributed integral-slot winding (with three slots per pole per phase), double-, and single-layers FSCW, respectively. The rotor position is fixed to $\theta_m = 0^\circ$. When distributed winding is used, the MMF_s approximates a sinusoidal waveform. On the contrary, a large harmonic content is noticed when FSCW is adopted. Because, the distributed windings produces only odd harmonic in the MMF_s , however, the double-layer FSCW produces odd and even harmonics in the MMF_s . Whereas, the MMF_s in case of single-layer FSCW has odd, even, and sub-harmonic. In addition, it is noted that the peak values of the MMF_s are quite different: single layer FSCW yields a peak two times the peak of the other two windings.

Fig. 5.11 shows the rotor magnetic potential (MMF_r) for REL motor with the different stator windings. There is a periodical waveform in the first two cases: the MMF_r is the same every pole pair pitch. On the contrary, there is rotor magnetic unbalance with single layer

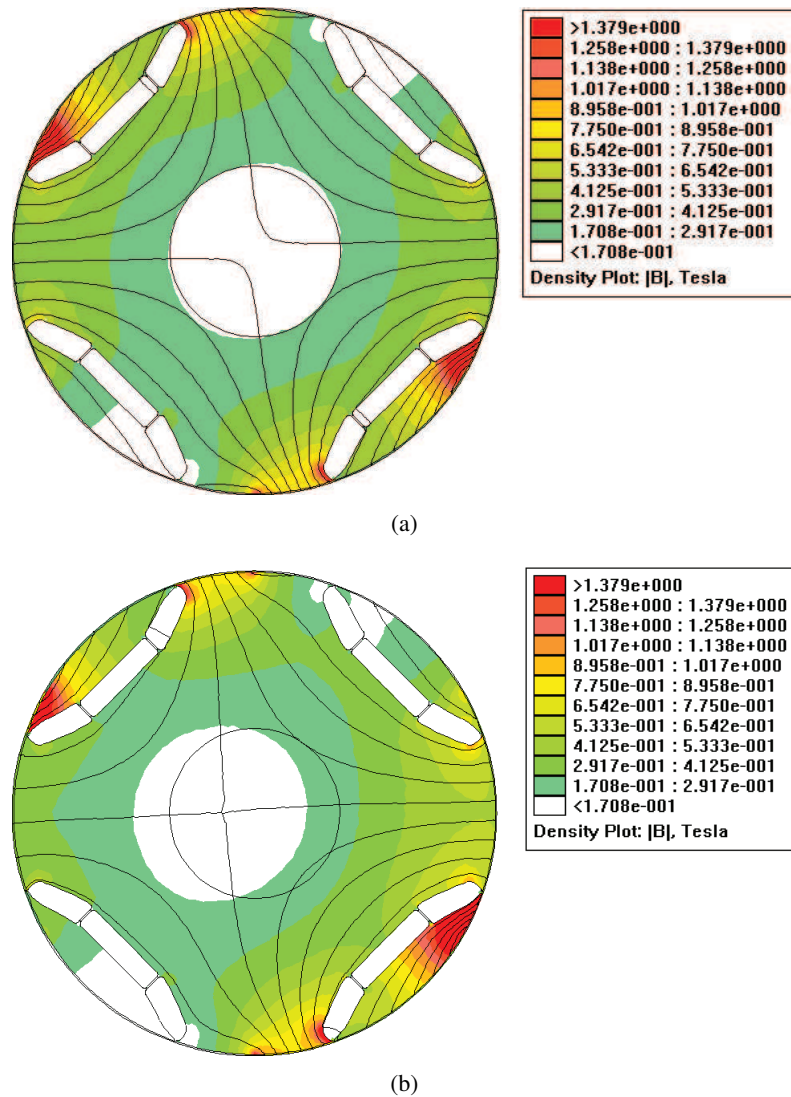


Figure 5.9: Magnetic flux density mapping of REL motor with double layer FSCW in the stator and single flux-barrier per rotor pole. (a) Healthy case (no eccentricity). (b) Static or dynamic eccentricity case (at rotor position $\theta_m = 0^\circ$).

FSCW, also in case of no eccentricity. This is due to the sub-harmonic of order $\nu = 1$. This rotor magnetic unbalance causes unbalanced pull forces, as will be shown in the following.

From the stator and rotor scalar magnetic potentials, the air-gap flux density distribution can be computed at any rotor position. As an example, in this section, the air-gap flux density distribution is computed at $\theta_m = 0^\circ$ and $\theta_m = 60^\circ$. Fig. 5.12 and Fig. 5.13 shows these distributions of REL motor with double- and single-layers FSCW, respectively. It is noted a satisfactory agreement between the analytical and FE model. Comparing these distributions with those result from the distributed windings shown in Fig. 4.5, as expected, the harmonic contents in Fig. 5.12 and Fig. 5.13 are higher.

In case of stator with distributed integral-slot windings and double layer FSCW with no eccentricity, the radial force results to be almost zero, as shown in Fig. 4.9 and Fig. 5.14. On

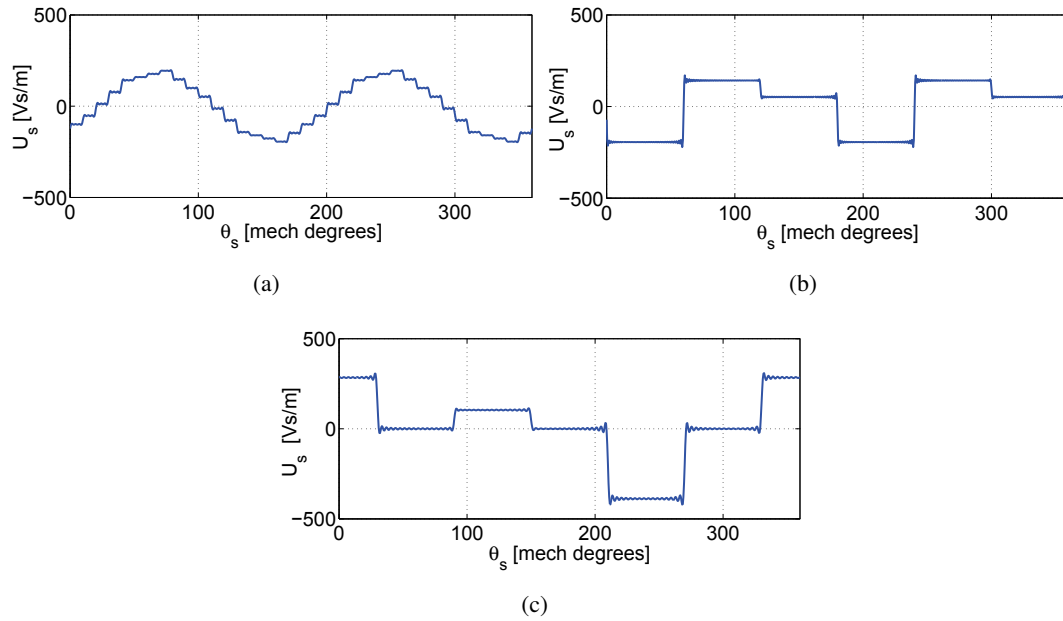


Figure 5.10: Scalar magnetic potential of the stator at rotor position $\theta_m = 0^\circ$: (a) distributed integral-slot winding, (b) double-layers FSCW, (c) single-layer FSCW.

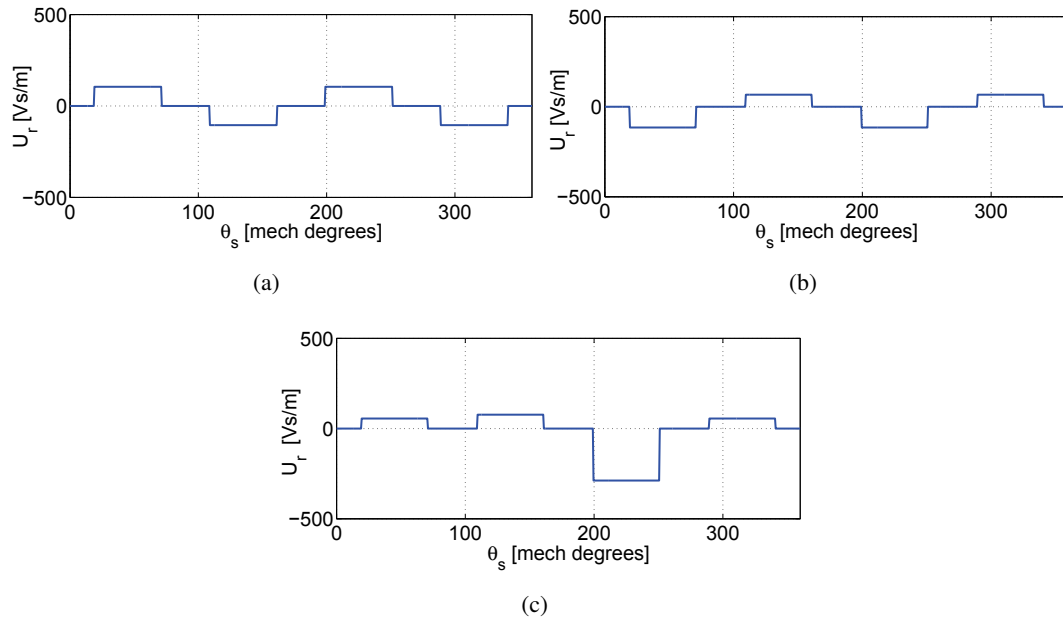


Figure 5.11: Scalar magnetic potential of the concentric rotor at rotor position $\theta_m = 0^\circ$: (a) distributed integral-slot winding, (b) double-layers FSCW, (c) single-layer FSCW.

the contrary, with single layer FSCW, Fig. 5.15 and Fig. 5.16 show the radial force components on the rotor. According to the currents, the radial force on the rotor is about 975 N from the FE results and 1075 N from the analytical results. A satisfactory agreement between FE and analytical model is shown.

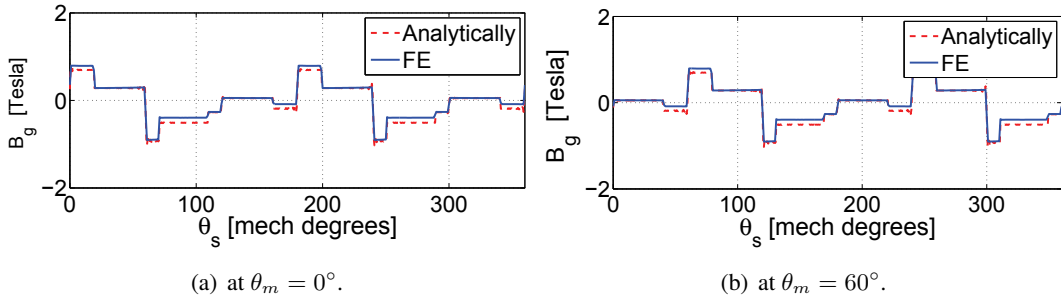


Figure 5.12: Air-gap flux density distribution results from the analytical and finite element model at healthy condition (no eccentricity), double-layer FSCW is adopted.

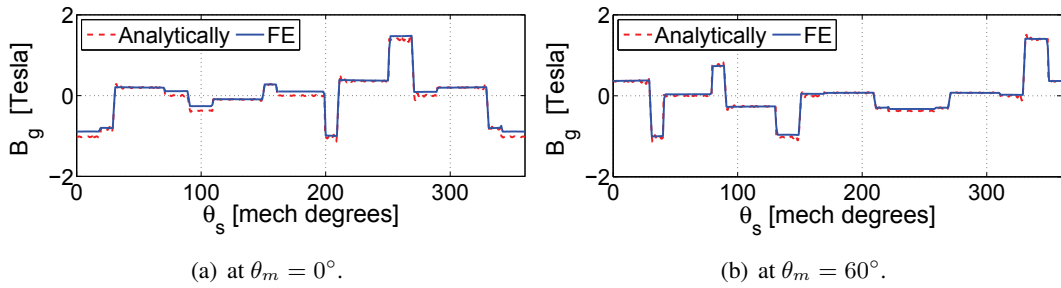


Figure 5.13: Air-gap flux density distribution results from the analytical and finite element model at healthy condition (no eccentricity), single-layer FSCW is adopted.

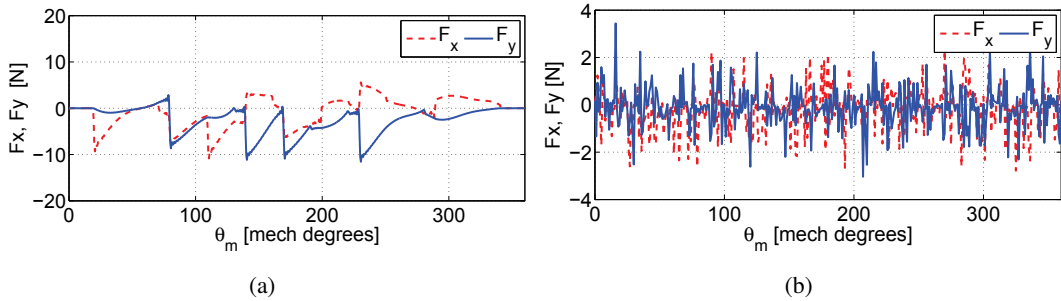


Figure 5.14: F_x and F_y at all rotor position in healthy condition (no eccentricity), double-layer FSCW is adopted. (a) Analytical model results. (b) FE model results.

5.3.2. Winding comparison in case of static rotor eccentricity

The air-gap flux density distribution of REL motor with double- and single-layer FSCW is estimated by the analytical and FE models in static eccentricity case. They are shown in Fig. 5.17 and Fig. 5.18 at rotor positions $\theta_m = 0^\circ$ and $\theta_m = 60^\circ$. It is possible to compare these distributions with those of REL motor with distributed integral-slot winding as shown in Fig. 4.16.

Fig. 4.23 (a), Fig. 5.19 (a), and Fig. 5.19 (b) show the radial force on the REL rotor with distributed integral-slot windings, double layer FSCW, and single layer FSCW, respectively. The radial force is in the direction of the smaller air-gap length (i.e x -direction) in the range

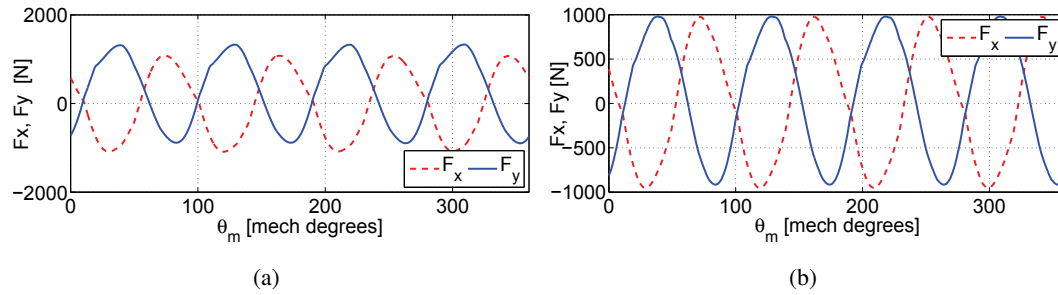


Figure 5.15: F_x and F_y at all rotor position in healthy condition (no eccentricity), single-layer FSCW is adopted. (a) Analytical model results. (b) FE model results.

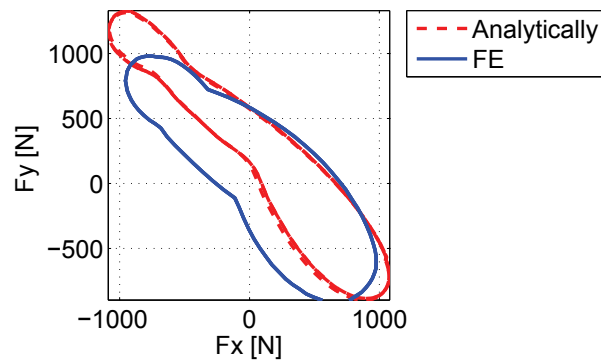


Figure 5.16: F_y versus F_x at all rotor positions in case of single-layer FSCW (no eccentricity).

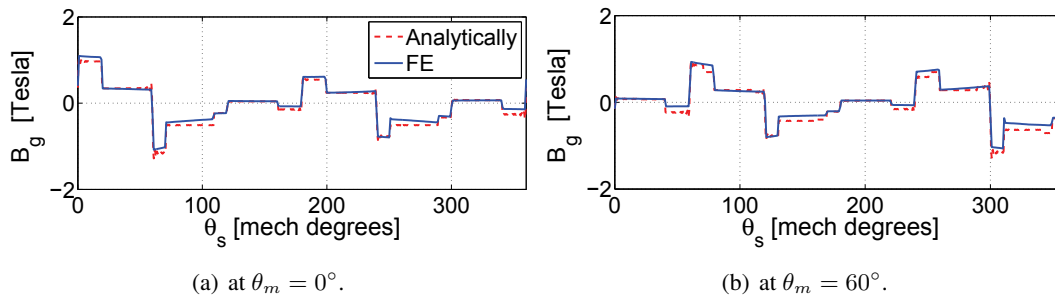


Figure 5.17: Air-gap flux density distribution results from the analytical and finite element model at static eccentricity, double-layer FSCW is adopted.

between 220 and 250 N with distributed windings and in the range between 500 and 510 N with double layer FSCW (more than two times). The force with the double layer FSCW is higher than that with the distributed windings because of the higher harmonic content (higher amplitude of all harmonics and presence of even order harmonics). With the single layer FSCW, both F_x and F_y are very high but F_x is greater than F_y because the direction of the smaller air-gap length is in x -direction. From Fig. 5.19 (b), it is noted that the analytical and FE models predict a force in the range between 1850 and 2300 N, respectively. It is about 5 times higher than the distributed windings case. From Fig. 5.19 (b) and Fig. 5.16, it is noted that the radial force F_y assumes almost the same value in healthy and static eccentricity cases, but the radial force F_x

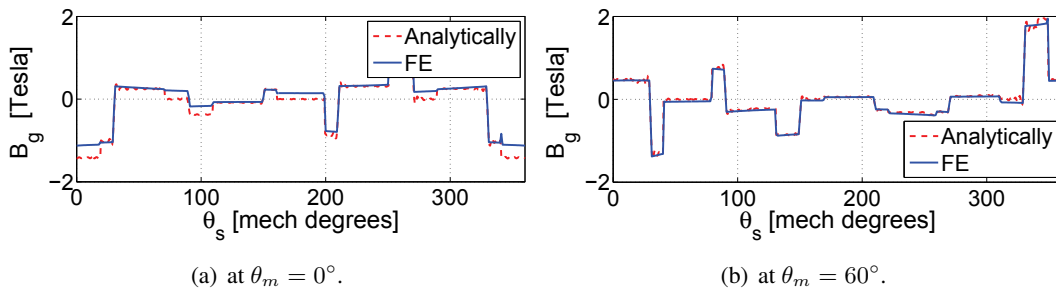


Figure 5.18: Air-gap flux density distribution results from the analytical and finite element model at static eccentricity, single-layer FSCW is adopted.

in case of static eccentricity is two times the value in case of no eccentricity (healthy case).

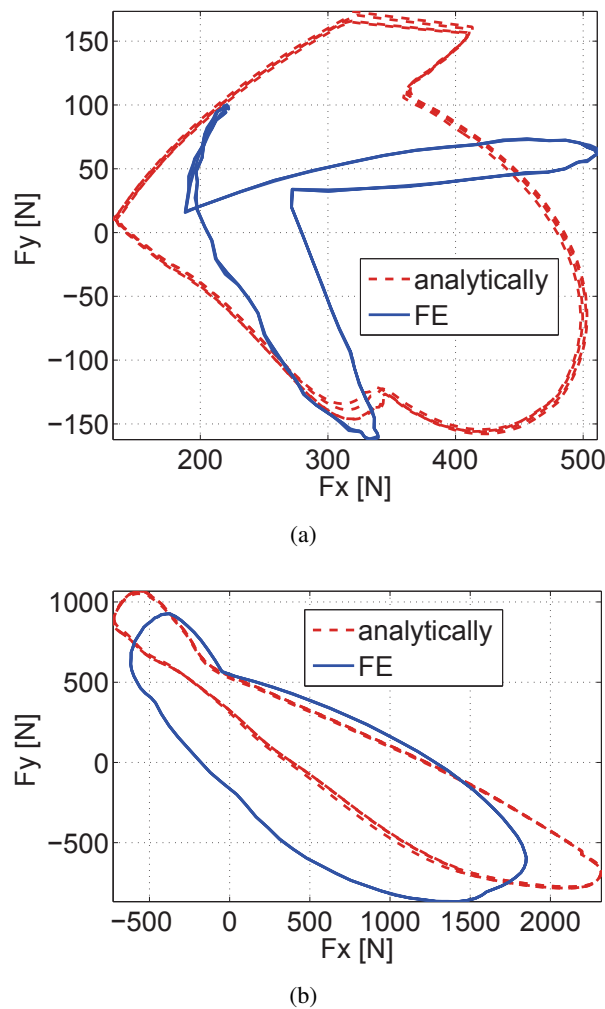


Figure 5.19: F_y versus F_x at all rotor positions in case of REL motor with double- and single-layers FSCW (at static eccentricity). (a) Double-layer FSCW. (b) Single-layer FSCW.

5.3.3. Windings comparison in case of dynamic rotor eccentricity

Analogously, the air-gap flux density distribution is computed by both analytical and FE models in dynamic eccentricity case. Fig. 5.20 and Fig. 5.21 show those distributions for REL motor with double- and single-layers FSCW, respectively. Once again, they are compared at rotor positions $\theta_m = 0^\circ$ and $\theta_m = 60^\circ$ with the air-gap flux density distribution of REL motor with distributed windings shown in Fig. 4.30. The distortion in the waveform of FSCW case due to the added harmonic is noted. Again, a good agreement between both models is noticed.

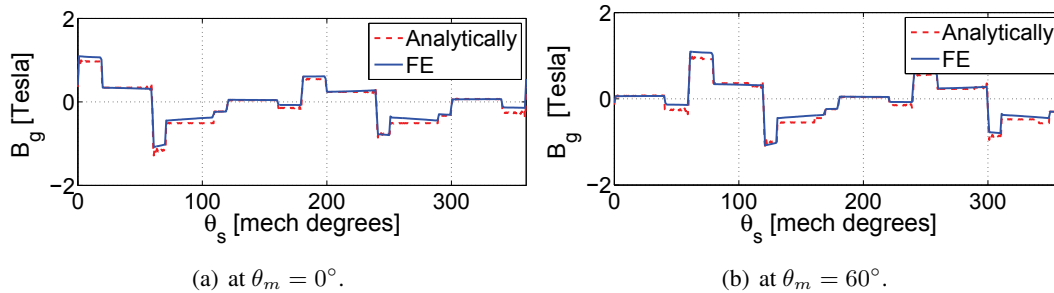


Figure 5.20: Air-gap flux density distribution results from the analytical and finite element model at dynamic eccentricity, double-layer FSCW is adopted.

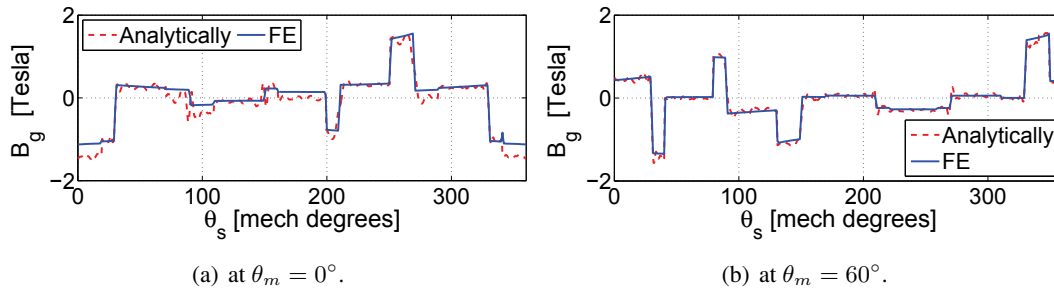
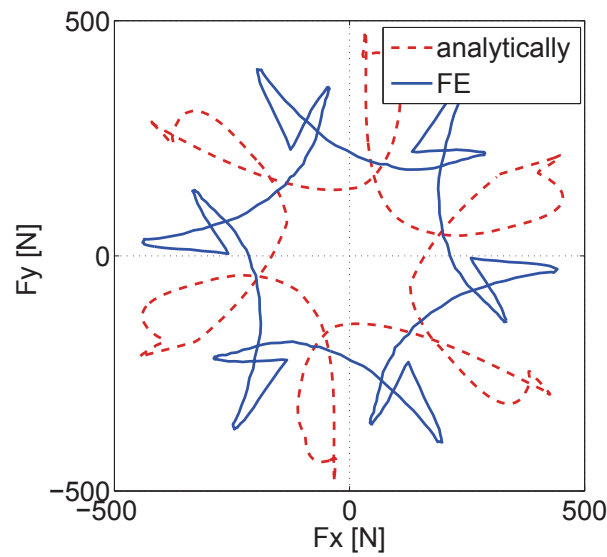


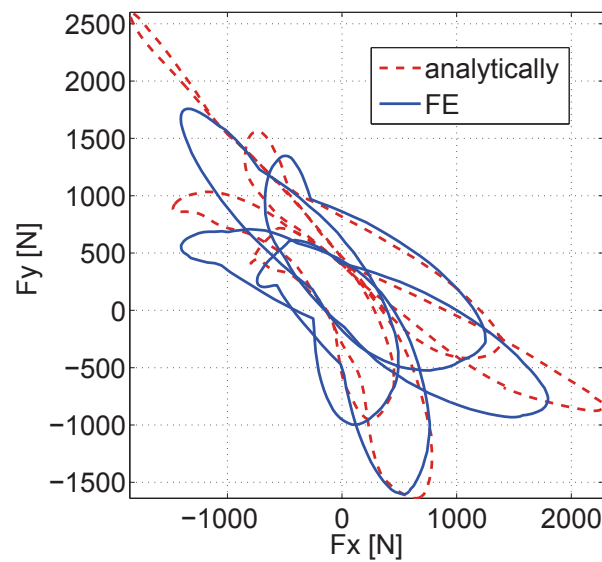
Figure 5.21: Air-gap flux density distribution results from the analytical and finite element model at dynamic eccentricity, single-layer FSCW is adopted.

Radial force components F_x and F_y are also calculated in case of dynamic rotor eccentricity. Fig. 4.37 (a), Fig. 5.22 (a), and Fig. 5.22 (b) show the radial force components F_y versus F_x according to the different windings. It is in the range between 220 and 250 N with integral-slot distributed windings, between 440 and 450 N with double-layer FSCW, and in the range between 1800 and 2600 N in case of single-layer FSCW.

The results of the previous three cases are summarized in Table 5.4 for the purpose of a rapid comparison. All computations are carried out with the same electrical loading for the main harmonic (i.e., of order $\nu = p$). From Table 5.4, the radial force in case of distributed windings is lower than that in case of FSCW in both cases of eccentricity. The radial forces with single layer FSCW stator are much higher than with the other two windings. Thus, the single layer FSCW is not recommended with REL motor.



(a)



(b)

Figure 5.22: F_y versus F_x at all rotor positions in case of REL motor with double- and single-layers FSCW (at dynamic eccentricity). (a) Double-layer FSCW. (b) Single-layer FSCW.

To complete the analysis, Table 5.5 reports a comparison referring to rotors with different number of flux barriers per pole. The results refer to REL motor with double layers FSCW. It is noted that, adding additional rotor barriers monotonically reduces the force values.

Table 5.4: Peak value of the radial force on the symmetric rotor according to different cases of stator windings.

Eccentricity case	No eccentricity	Static eccentricity	Dynamic eccentricity
The FE model results [N]			
distributed windings	0	230	227
double-layers FSCW	0	510	440
single-layer FSCW	976	1850	1800
The Analytical model results [N]			
distributed windings	0	260	250
double-layers FSCW	0	500	450
single-layer FSCW	1075	2300	2600

Table 5.5: Peak radial force on rotor with one, two, and three flux-barriers per pole resulting from both analytical and FE models. Double layer FSCW stator is considered.

Eccentricity case	No eccentricity	Static eccentricity	Dynamic eccentricity
The FE model results [N]			
one flux-barrier	0	510	440
two flux-barriers	0	452	408
three flux-barriers	0	335	282
The Analytical model results [N]			
one flux-barrier	0	500	450
two flux-barriers	0	483	506
three flux-barriers	0	480	430

5.3.4. Iron saturation impact including the complete stator FE model

A REL motor with a complete stator including slots, teeth, and back iron has been analysed by means of FE model. A first set of simulations has been carried out considering the iron with actual B-H curve instead of linear iron, at first without iron bridges in the rotor. Fig. 5.23 shows the results with linear iron and actual B-H curve iron in case of static eccentricity. Fig. 5.24 also shows the results of both FE models in case of dynamic eccentricity. It is noticed that the radial force has the same behaviour for both FE models. However, when the actual B-H curve is considered, the radial force is lower due to a reduction of the flux density caused by the iron saturation.

A second set of simulations has been carried out, including the rotor iron bridges (actual B-H curve is again considered). Fig. 5.25 shows the radial forces, when iron bridges are included in case of static eccentricity for double layers and single layer FSCW, respectively. In case of dynamic eccentricity, Fig. 5.26 shows the same results. This means that the impact of the iron bridges on the radial force is quite negligible.

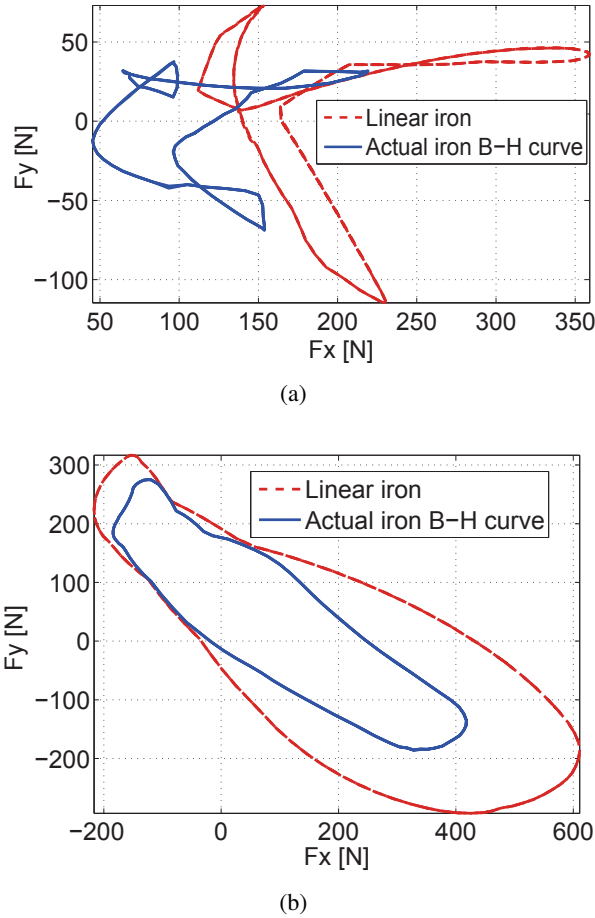
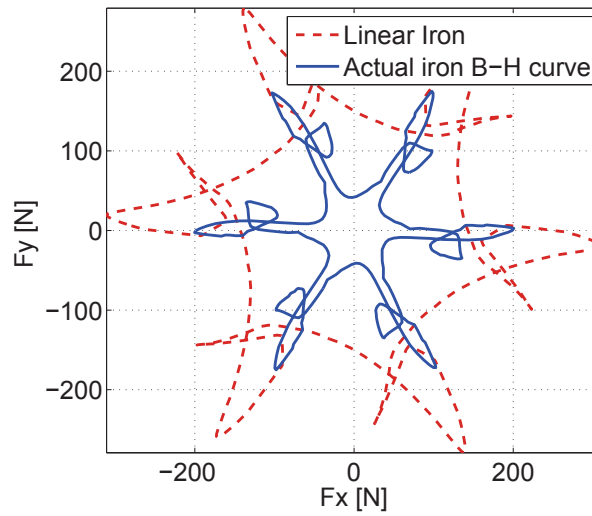


Figure 5.23: F_y versus F_x in both cases of linear iron and actual iron B-H curve used in REL motor with double and single layers FSCW stator and symmetric rotor in case of static eccentricity.

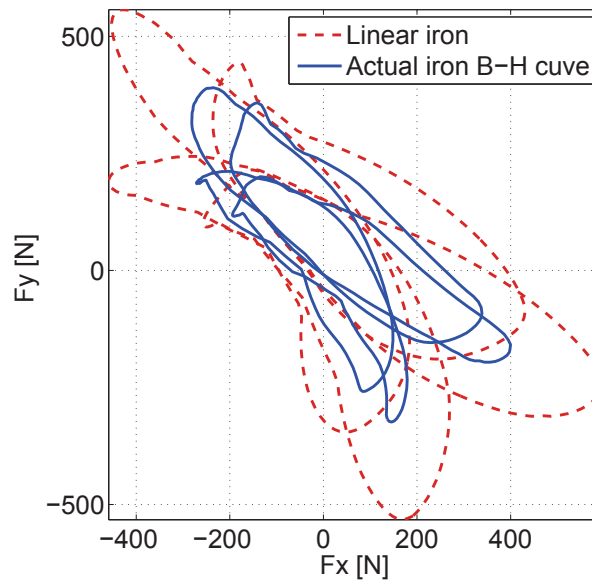
5.4. Conclusions

The analytical model proposed in chapter 3 is used for computing the impact of the rotor eccentricity for a wide set of configurations of REL motors (but the analysis is valid in general for any machines with anisotropic rotors). At first, a REL motor with asymmetric rotor flux-barriers has been analysed. It is noticed that, the force in case of asymmetric rotor is not much larger than the force in case of symmetric rotor. Therefore, the "Machaon" rotor geometry, which is useful for reducing the torque ripples, exhibits approximately the same radial force of symmetric rotor geometry in case of rotor eccentricity.

In addition, the analytical model is applied on REL motor with concentrated coil windings including single and double-layer configuration. The analytical model results to be proper also for such configurations. The drawbacks of single layer FSCW configuration is highlighted. A REL motor with a complete stator has been analysed, again comparing single layer and double layer windings. The iron saturation is effective on reducing the radial force value, while the iron bridges have a negligible impact on the radial force. The comparison with FE results shows a proper agreement. For the sake of REL motor design purpose, it is required to overestimate the radial force as factor of safety and the analytical approach tends to overestimate the radial



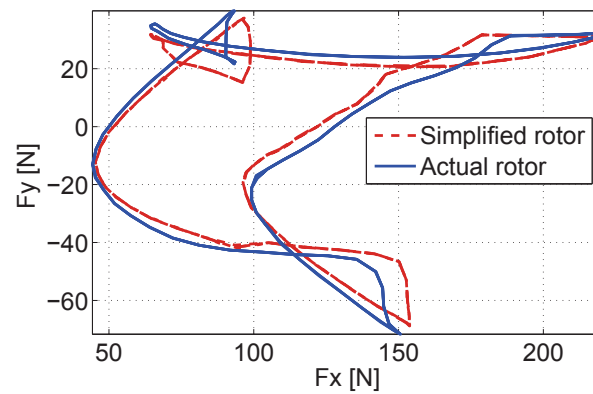
(a)



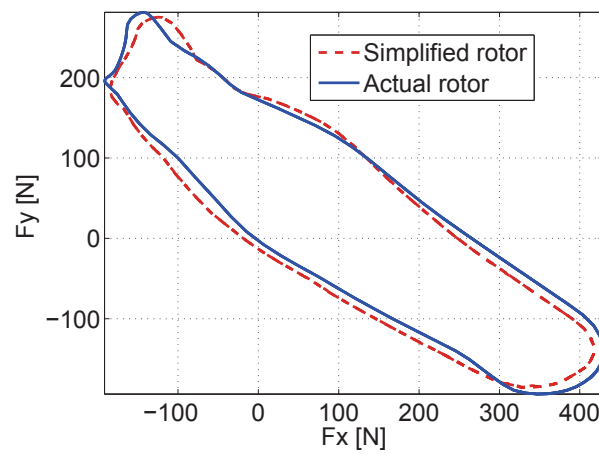
(b)

Figure 5.24: F_y versus F_x in both cases of linear iron and actual iron B-H curve used in REL motor with double and single layers FSCW stator and symmetric rotor in case of dynamic eccentricity.

forces. So the analytical model is useful for REL motor design. However, let us remember that, the analytical model simulation time is about a few seconds, where the finite element simulation requires some hours. So the analytical model allows to save time and its results are suitable for the motor design purpose. The analytical model does not include the stator slotting, so that the same slot-less model is used with FE analysis, to compare the results.

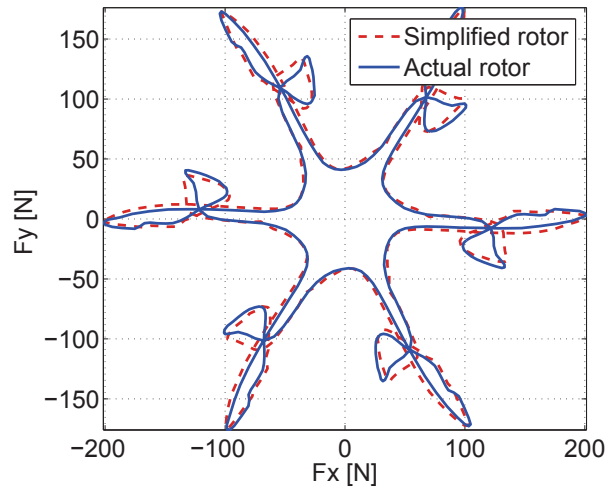


(a) double layers FSCW

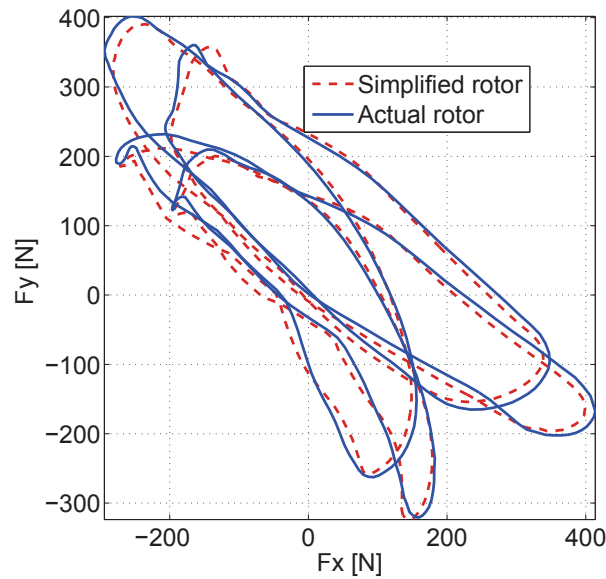


(b) single layer FSCW

Figure 5.25: F_y versus F_x in both cases of ideal rotor and actual rotor (including iron bridges) used in REL motor with double and single layers FSCW stator and symmetric rotor in case of static eccentricity.



(a) double layers FSCW



(b) single layer FSCW

Figure 5.26: F_y versus F_x in both cases of ideal rotor and actual rotor (including iron bridges) used in REL motor with double and single layers FSCW stator and symmetric rotor in case of dynamic eccentricity.

Comparison between eccentric REL and PMAREL motors

This chapter deals with the finite element analysis of REL and PMAREL machines with different eccentricity scenarios. Static and dynamic eccentricity cases and a combination of them are studied. Symmetric and asymmetric rotor structures are considered for both REL and PMAREL machines. In addition, two symmetric rotors with different flux-barriers dimensions are studied. This work focuses on the computation of the unbalanced radial force acting on the rotor when eccentricity occurs. Furthermore, the radial forces acting on the rotor parts bordered by the flux-barriers, i.e., rotor islands, are computed. The REL motor is compared with PMAREL motor with both Ferrite and NdFeB PMs. As an example, a 36-slots 4-pole machines with the same geometrical dimensions are compared.

6.1. Introduction

During the manufacturing process, the machines are probably prone to some manufacturing imprecision, such as mass unbalance, shaft bow, and bearing tolerance. Indeed, it is significant to point out the effect of the eccentricity on those machines. In this perspective, the eccentricity yields magnetic and dynamic problems with additional vibrations and noises.

There are several works in literature dealing with the effect of eccentricity on surface mounted permanent magnet (SPM) and induction machines [37, 42–45, 48, 61–67]. On the contrary, eccentricity impact on the performance of REL and PMAREL machines is only marginally considered [37, 45, 63], while there are several comparisons between the performance of REL, PMAREL, and SPM motors, with concentric rotor [36, 56]. A comparison between PMAREL and SPM motor, with eccentricity, is shown in [43, 68, 69]. However, this comparison did not consider all possible eccentricity cases. Moreover, [43, 68, 69] did not consider the comparison with REL motor.

In addition, the effect of the eccentricity on the radial forces acting on the rotor islands, in case of REL and PMAREL motors, and acting on the poles, in case of SPM motor, is not considered. This radial forces is important for designing the rotor iron ribs for REL or PMAREL motor and designing PMs thickness for SPM motor. For correct design of rotor bearings, the radial forces on the overall rotor is also computed.

To fill this gap this work deals with the comparison between the impact of the eccentricity on the REL and PMAREL machines. Their performance are compared in order to highlight the worst case. Furthermore, the eccentricity effect is studied for different REL and PMAREL rotor geometry.

Static rotor eccentricity, dynamic rotor eccentricity, and their combination are considered [45, 70, 71]. Fig. 6.1 shows the different kinds of the rotor eccentricity. In all cases, the rotor center is shifted from the stator center. Once again, in case of static eccentricity, the rotor rotates around its own center, as sketched in Fig. 6.1 (a). Besides, in case of dynamic eccentricity, the rotor rotates around the stator center, as in Fig. 6.1 (b). Hence, in the combined eccentricity case, the rotor rotates out of both stator and rotor centers, around another different point. In this study, the rotation axis of the rotor in case of combined eccentricity is chosen, as an example, in the middle of the stator and rotor centers, as shown in Fig. 6.1 (c).

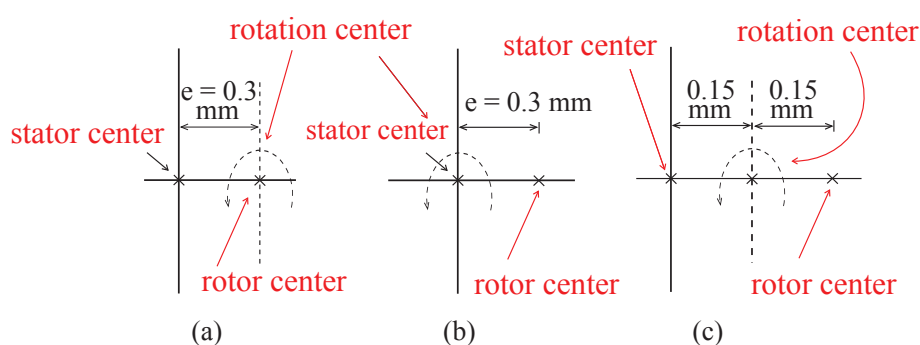


Figure 6.1: Different cases of the rotor eccentricity. (a) static eccentricity, (b) dynamic eccentricity, and (c) combined eccentricity.

For the purpose of comparing REL and PMAREL motors, two different rotor geometries are considered. They are: (a) symmetric rotor and (b) asymmetric (Machao) rotor. In case of symmetric rotor geometry, the flux-barriers have the same dimensions for all poles. On the contrary, the flux-barriers exhibit different dimensions for adjacent poles in case of asymmetric rotor geometry. Again, this asymmetry is adopted to minimize one or more torque ripple harmonics. The impact of the rotor geometry on the motor performance and the impact of the flux barrier dimensions is studied too.

Both REL and PMAREL motors are characterized by three flux barriers per pole. Two of this rotor geometries are with symmetric flux-barriers. They are called symmetric rotor A and symmetric rotor B. The flux-barrier angles of rotor B are higher than that of rotor A, as reported in Table 6.1. The third rotor geometry is an asymmetric rotor with flux barrier dimensions of the first and third poles as in symmetric rotor A. The flux-barriers of the second and the fourth poles are as in symmetric rotor B.

The radial force on the whole rotor and on each flux-barrier of the REL and PMAREL machines are calculated. The computations of the forces on the rotor islands are carried out at the rotor position when the radial force is maximum. Fig. 6.2 shows the REL or PMAREL motor considered in this study. In addition, the main geometrical data of both REL and PMAREL motors are reported in Table 4.1. The finite element (FE) analysis are used to analyse the two machines and to compare them, in case of eccentricity.

In this chapter, the comparison between the two motors in healthy case (no eccentricity) and eccentricity cases is carried out at the same eccentricity, electric loading, and electric current

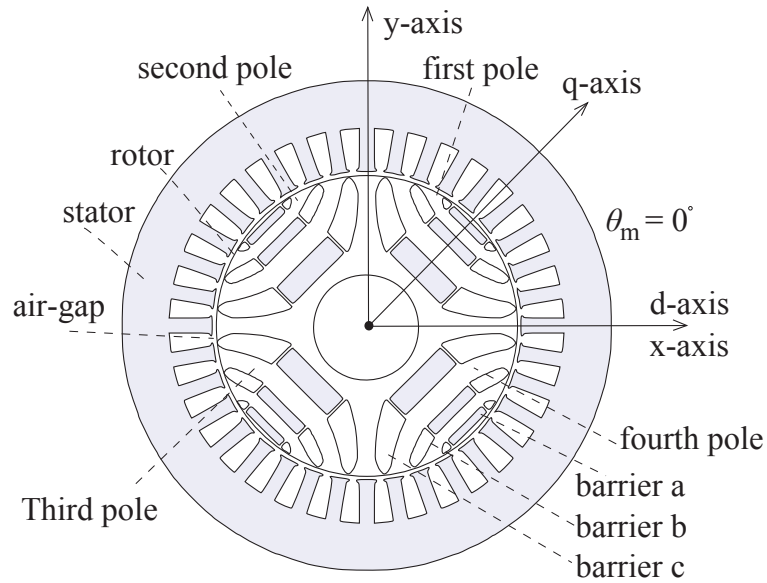


Figure 6.2: Cross section of REL or PMAREL (if the magnets are added inside the flux-barriers) machine under analysis.

angle. The eccentricity is set equal to $e = 0.3\text{mm}$. The peak value of the fundamental of the electric loading is set equal to 32490 A/mm , where the stator conductor current density is equal to 6 A/mm^2 . The electric current angle is 60° for both motors which results maximum torque per ampere (MTPA).

Table 6.1: Flux-barriers ends angles for both symmetric rotor A and symmetric rotor B.

First flux barrier ends angle (symmetric A)	$2\theta_{b_1}$	28°
Second flux barrier ends angle (symmetric A)	$2\theta_{b_2}$	53°
Third flux barrier ends angle (symmetric A)	$2\theta_{b_3}$	77°
First flux barrier ends angle (symmetric B)	$2\theta_{b_1}$	32°
Second flux barrier ends angle (symmetric B)	$2\theta_{b_2}$	57°
Third flux barrier ends angle (symmetric B)	$2\theta_{b_3}$	81°

6.2. Comparison in healthy case (no eccentricity)

At first, the FE analysis of the REL and PMAREL motors with concentric rotor is carried out. The three different rotor geometries (symmetric A and B, and asymmetric rotor) are considered. The value of the radial force is a few Newtons for all rotor geometries and it can be approximated to be zero.

By introducing an arc in the middle of the air-gap in front of each rotor island bordered by each flux-barrier, as shown in Fig. 6.3, the radial force acting on the corresponding rotor island is computed by integrating the Maxwell stress tensor. Table 6.2 and Table 6.3 show the radial forces on the rotor islands of all poles of both REL and Ferrite PMAREL motors. The computations are carried out for both motors with different rotor geometries. This computations are

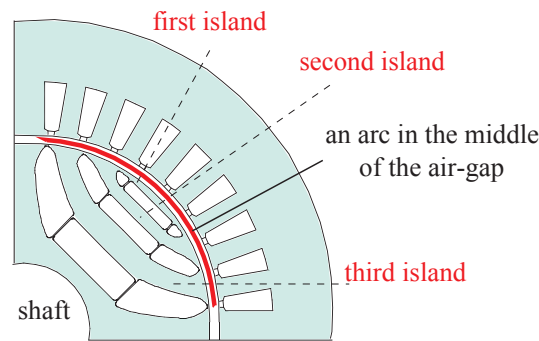


Figure 6.3: Cross section describes the method of computation of the radial force acting on the third rotor island which bordered by the flux-barrier c , as an example.

carried out at $\theta_m = 0^\circ$, where the radial force on the overall rotor is maximum. From Table 6.2 and Table 6.3, as expected, the forces are the same for all poles. In both motors, the first rotor islands (the outer islands) are subjected to forces of the order of tens of Newtons, while the inner islands (the second and third island) are subjected to forces of the order of hundreds of Newtons.

In addition, in the symmetric rotors A and B, the radial forces are distributed evenly over the poles, offsetting to each other. Thus, the total force acting on the overall rotor is very low (a few Newtons). In the case of asymmetric rotor, the forces are not the same over the poles, due to the diversity of flux barriers. The forces on the rotor islands of the second and fourth pole are the same acting on the rotor islands of symmetric rotor B. The forces on the rotor islands of the first and third pole are the same acting on the rotor islands of the symmetric rotor A. Anyway, the resultant force on the overall rotor is always very low, since the forces are two by two equal and in opposite direction.

Referring to PMAREL motor with Ferrite PMs, there are no significant changes in the forces acting on the rotor islands boarded by the flux barriers. On the contrary, by comparing the REL motor with PMAREL motor with NdFeB PMs, it is noted that the radial force on the first rotor island of symmetric rotors A, B, and asymmetric rotor is increased by 190 %, 120 %, and 250 %, respectively. However, high energy PMs slightly increases the radial force acting on the second and third rotor islands, as noticed in Table 6.2 and Table 6.4.

Hence, the magnetic force acting on the rotor islands are increases due to the high energy PMs. However, they have no effect on the overall rotor force. Because the PMs increase the flux density in front of all poles so that the radial forces caused by the added PMs are in opposite directions and cancelled each other. Thus, the radial force on the overall rotor is very low (a few Newtons).

Table 6.2: Radial forces acting on the rotor islands of different rotor geometries of REL motor at $\theta_m = 0^\circ$ in healthy case (with no eccentricity).

		$F_r[N]$		
pole order	rotor island	symmetric A	symmetric B	asymmetric
pole 1 or 3	first island	38.6	53.8	36.4
	second island	203	222	194
	third island	485	473	466
pole 2 or 4	first island	38.6	54.4	54.2
	second island	203	225	226
	third island	486	478	479

Table 6.3: Radial forces acting on the rotor islands of different rotor geometries of PMAREL (with Ferrite PMs) motor at $\theta_m = 0^\circ$ in healthy case (with no eccentricity).

		$F_r[N]$		
pole order	rotor island	symmetric A	symmetric B	asymmetric
pole 1 or 3	first island	41.0	52.6	38.4
	second island	201	218	192
	third island	488	476	470
pole 2 or 4	first island	41.1	53.3	53.4
	second island	201	222	222
	third island	488	480	481

Table 6.4: Radial forces acting on the rotor islands of different rotor geometries of PMAREL (with NdFeB PMs) motor at $\theta_m = 0^\circ$ in healthy case (with no eccentricity).

		$F_r[N]$		
pole order	rotor island	symmetric A	symmetric B	asymmetric
pole 1 or 3	first island	115	119	131
	second island	228	228	278
	third island	514	471	526
pole 2 or 4	first island	115	121	108
	second island	228	233	268
	third island	515	477	507

6.3. Comparison in static eccentricity case

Static eccentricity is studied when the rotor is shifted to the right hand side of $e = 0.3 \text{ mm}$. Firstly, the radial forces acting on the different rotors of the REL and PMAREL machines are computed according to the same eccentricity, electric loading, and electric current angle.

Fig. 6.4 (a), (b), and (c) show the radial force acting on the different rotor geometries of the REL and PMAREL motor, respectively. It is noted that, the radial force acting on the symmetric rotor B is slightly lower than that acting on symmetric rotor A highlighting the effect of the flux-barrier dimensions on the radial force. It is also worth noticing the small difference between the symmetric rotor B and asymmetric rotor. There are high force in x-axis direction where there are minimum air-gap length. The radial force component in y-axis direction is increased only of a few Newtons in case of asymmetric rotor.

By comparing Fig. 6.4 (a), (b), and (c), it is noted that the added PMs has no significant effect on the radial force on overall rotor. In addition, the PM type has little effect on this radial force. This is due to the symmetric effect of the added PMs on all rotor poles. The PMs increase the flux density not only in front of the two poles closest to the minimum air-gap length, but also in front of the other two poles.

The forces acting on the rotor islands are maximum when they are close to the minimum air-gap length and vice versa. Since, the variation of the air-gap length is constant with the rotor rotation, the forces are variable during its rotation. Therefore, the computation of the forces is carried out at the rotor position which gives the maximum radial force on the rotor. They are reported in Table 6.5, Table 6.6, and Table 6.7 for both REL and PMAREL motor.

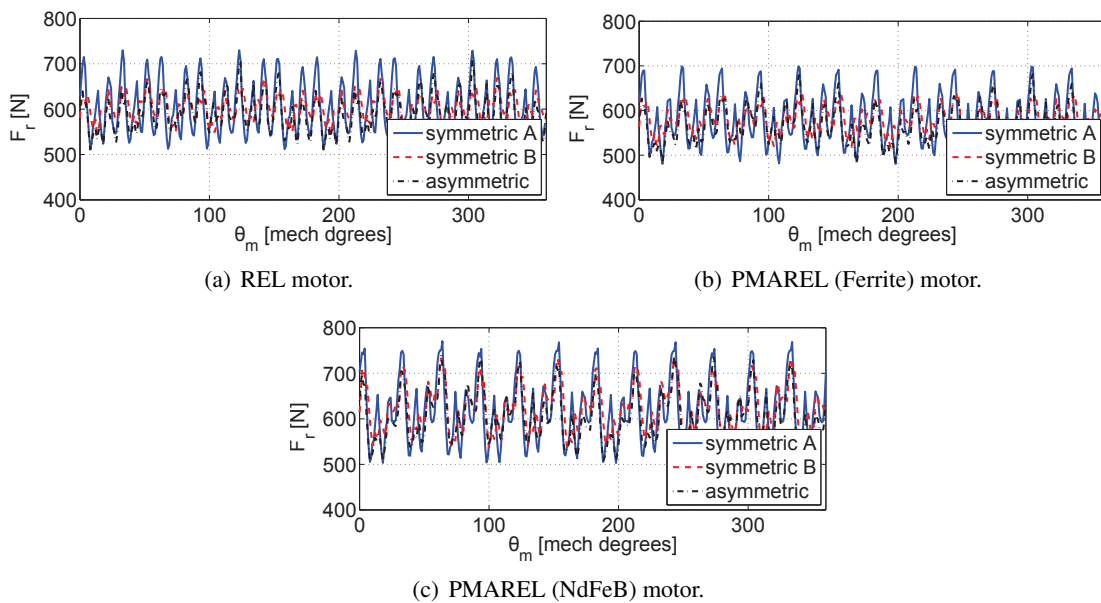


Figure 6.4: Radial forces versus the rotor position in case of REL, PMAREL (with Ferrite PMs), and PMAREL (with NdFeB PMs) motor with different rotor geometries, with static eccentricity ($e = 0.3 \text{ mm}$).

From Table 6.5, Table 6.6, and Table 6.7, the forces acting on the different poles are not

Table 6.5: Radial forces acting on the rotor islands of different rotor geometries of REL motor, with static eccentricity.

		$F_r [N]$ (worst case)		
	θ_m	33°	52°	123°
pole order	rotor island	symmetric A	symmetric B	asymmetric
pole 4	first island	41.3	111	47.0
	second island	398	387	260
	third island	813	773	547
pole 1	first island	28.4	57.1	18.7
	second island	247	196	135
	third island	568	465	297
pole 2	first island	19.6	43.3	39.9
	second island	140	133	212
	third island	307	312	452
pole 3	first island	26.0	62.7	37.4
	second island	204	224	370
	third island	468	522	777

symmetric. This leads to unbalanced radial force on the overall rotor, as shown in Fig. 6.5 (a), (b), and (c). In case of REL motor, by considering the third rotor island of the worst pole which is closer to stator, it is noted that the radial forces on the third island of symmetric rotor B are similar to that on asymmetric rotor island. It is lower than that of symmetric rotor A.

Once again, there are no significant difference between the forces when Ferrite PMs are inset in the flux-barriers. From, Table 6.7 and Table 6.5, referring to the third island of the worst pole of symmetric rotor A, the forces are increased by 14% when NdFeB PMs are inset in the flux-barriers and no significant difference (slightly increases) in case of symmetric rotor B and asymmetric rotor.

By comparing Tables 6.5 and 6.2, it is noted that the radial forces on the third island of the worst pole of symmetric rotor A, symmetric rotor B, and asymmetric rotor is increased by 68%, 63%, and 17% of those of healthy case, respectively, due to the static eccentricity.

Table 6.6: Radial forces acting on the rotor islands of different rotor geometries of PMAREL (with Ferrite PMs) motor, with static eccentricity.

		$F_r[N]$ (worst case)		
	θ_m	33°	35°	124°
pole order	rotor island	symmetric A	symmetric B	asymmetric
pole 4	first island	46.0	57.4	34.4
	second island	384	361	259
	third island	803	736	552
pole 1	first island	27.0	25.4	9.74
	second island	244	247	124
	third island	574	549	308
pole 2	first island	10.4	13.2	21.2
	second island	132	147	202
	third island	322	330	443
pole 3	first island	16.1	18.8	42.0
	second island	193	195	358
	third island	467	444	770

6.4. Comparison in dynamic eccentricity case

The rotor is shifted horizontally to the right. Therefore, the position of the minimum air-gap length is between the first and fourth poles. The position of the minimum air-gap length rotates together with the rotor. Then, the radial force rotates with the rotor. In the $(F_x F_y)$ plane, it exhibits a circle shape for a complete rotation of the rotor.

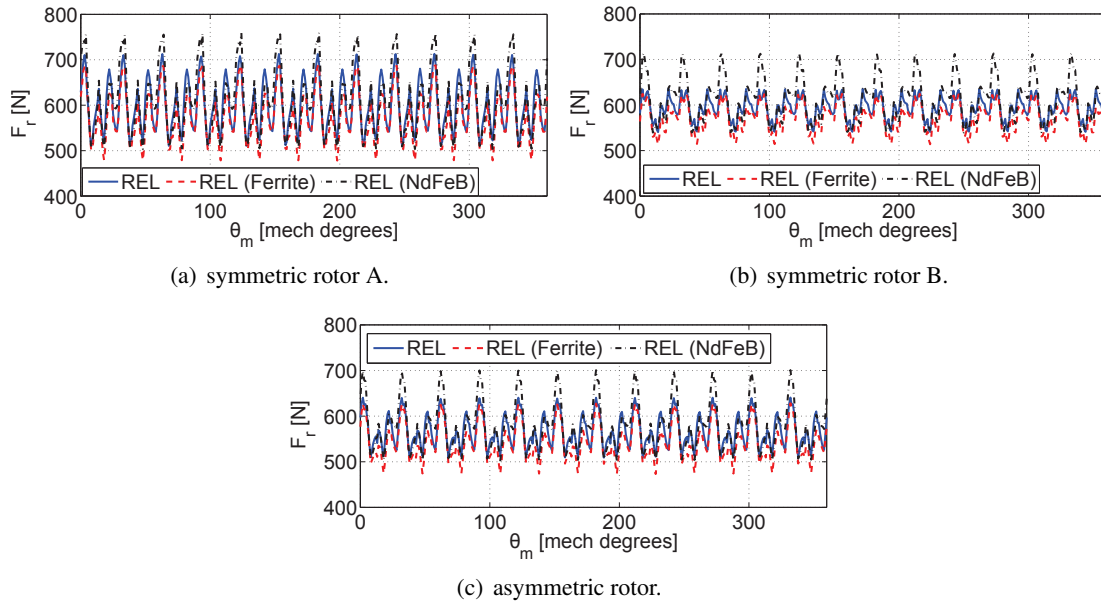
Fig. 6.5 shows the radial force on overall the rotor of REL machine and PMAREL machine, with dynamic rotor eccentricity ($e= 0.3mm$). Different rotor geometries are also considered for both machines at the same eccentricity, electric loading, and current angle.

From Fig. 6.5, once again, the radial force acting on the symmetric rotor B and the asymmetric rotor are close and slightly lower than that acting on the symmetric rotor A. In addition, the introduction of the Ferrite PMs within the flux-barriers yields a slight reduction of the radial force acting on overall the rotor. In case of introduction of NdFeB PMs, the radial force on overall the rotor is comparable with that in case of REL motor also.

Table 6.8, Table 6.9, and Table 6.10 shows the radial forces acting on the rotor islands of different rotors of the REL, PMAREL (with Ferrite PMs), and PMAREL (with NdFeB PMs) motor, respectively. This computations are carried out at the rotor position which results the maximum value of the radial force on the overall rotor of the three motors. It is noted that the rotor islands of poles 1 and 4 are more stressed than the rotor islands of poles 2 and 3, because poles 1 and 4 are always near to the minimum air-gap length. In addition, the radial forces acting on the outer rotor islands (first island) are of order of tens of Newtons and the radial

Table 6.7: Radial forces acting on the rotor islands of different rotor geometries of PMAREL (with NdFeB PMs) motor, with static eccentricity.

		$F_r [N]$ (worst case)		
	θ_m	64°	243°	243°
pole order	rotor island	symmetric A	symmetric B	asymmetric
pole 4	first island	207	80.0	79.9
	second island	496	188	187
	third island	922	363	359
pole 1	first island	120	121	143
	second island	248	304	322
	third island	477	575	603
pole 2	first island	101	190	188
	second island	202	528	483
	third island	383	747	801
pole 3	first island	145	98.4	121
	second island	328	235	245
	third island	613	451	463

Figure 6.5: Radial forces in case of REL, PMAREL (with Ferrite PMs), and PMAREL (with NdFeB PMs) motor with different rotor geometries, with dynamic eccentricity ($e = 0.3 \text{ mm}$).

forces on the second and third rotor islands are of order of hundreds of Newtons as occurs in static eccentricity case.

Table 6.8: Radial forces acting on the rotor islands of different rotor geometries of REL motor, with dynamic eccentricity.

		$F_r [N]$ (worst case)		
	θ_m	273°	22°	332°
pole order	rotor island	symmetric A	symmetric B	asymmetric
pole 4	first island	33.9	90.0	41.3
	second island	333	314	299
	third island	718	669	665
pole 1	first island	19.3	46.9	38.1
	second island	159	151	173
	third island	359	357	368
pole 2	first island	21.5	49.7	24.8
	second island	161	156	158
	third island	360	360	359
pole 3	first island	37.4	84.3	61.0
	second island	341	311	341
	third island	719	679	698

Also in this case, there are no significant effect of adding the Ferrite PMs in the flux-barriers. However, the forces on the third island of the worst pole is increased by 15%, 6%, and 16% for symmetric rotor A, symmetric rotor B and asymmetric, respectively, due to adopting NdFeB PMs in the flux-barriers.

Furthermore, Table 6.8 is compared with Table 6.2. It is noted that the radial forces on the rotor islands are increased by 48%, 40%, and 43% for symmetric rotor A, symmetric rotor B and asymmetric rotor due to dynamic eccentricity, respectively.

6.5. Comparison in combined eccentricity case

The combined eccentricity occurs when the machine is subjected simultaneously to the static and dynamic eccentricity. The distance between the rotor and stator axes is constant in static and dynamic eccentricity cases. On the contrary, in combined eccentricity case, the relative position of the rotor axis is varied by varying the position of the rotor. This study assumes that the stator is shifted horizontally to the left hand side by 0.15 mm and the rotor axis is shifted horizontally to the right hand side by 0.15 mm at $\theta_m = 0^\circ$. Therefore, the maximum distance between the stator and rotor axis is $e_0 = 0.3 \text{ mm}$ at $\theta_m = 0^\circ$. By increasing θ_m with the rotor rotation, this distance is reduced till to reach zero value at $\theta_m = 180^\circ$ (i.e., when the stator and rotor axis are coincident). Then, by increasing θ_m , the eccentricity distance increases again, until it returns to the maximum distance at $\theta_m = 360^\circ$.

Table 6.9: Radial forces acting on the rotor islands of different rotor geometries of PMAREL (with Ferrite PMs) motor, with dynamic eccentricity.

		$F_r [N]$ (worst case)		
	θ_m	184°	216°	332°
pole order	rotor island	symmetric A	symmetric B	asymmetric
pole 4	first island	36.2	52.2	41.7
	second island	322	315	306
	third island	731	686	676
pole 1	first island	11.4	17.1	25.3
	second island	145	161	162
	third island	361	371	375
pole 2	first island	11.4	15.8	15.1
	second island	145	155	148
	third island	363	358	370
pole 3	first island	39.0	42.4	60.2
	second island	319	278	333
	third island	691	612	695

The eccentricity distance is a function of the rotor position θ_m . It is given by:

$$e(\theta_m) = e_0 \cos\left(\frac{\theta_m}{2}\right) \quad (6.1)$$

when θ_m varies between 0° and 180° , and

$$e(\theta_m) = e_0 \cos\left(\frac{360 - \theta_m}{2}\right) \quad (6.2)$$

when θ_m varies between 180° and 360° . Then, the maximum and minimum air-gap length are given by:

$$\begin{aligned} g_{min} &= g_0 - e(\theta_m) \\ g_{max} &= g_0 + e(\theta_m) \end{aligned} \quad (6.3)$$

The radial force acting on the three different rotors of the REL, PMAREL (with Ferrite PMs), and PMAREL (with NdFeB PMs) machines are shown in Fig. 6.6. The radial forces assumes its maximum value at the minimum air-gap length at $\theta_m = 0^\circ$ and then it reduced to zero value at $\theta_m = 180^\circ$ and then it increased again to the maximum value at $\theta_m = 360^\circ$. The comparison between the three rotor geometries is the same as in static and dynamic rotor eccentricity cases.

The radial forces acting on the rotor islands of the three rotor geometries of REL, PMAREL (with Ferrite PMs), and PMAREL (with NdFeB PMs) motor are shown in Table 6.11, Table 6.12, and Table 6.13, respectively. Since, the rotor is horizontally shifted to the right hand

Table 6.10: Radial forces acting on the rotor islands of different rotor geometries of PMAREL (with NdFeB PMs) motor, with dynamic eccentricity.

		$F_r [N]$ (worst case)		
	θ_m	184°	3°	332°
pole order	rotor island	symmetric A	symmetric B	asymmetric
pole 4	first island	180	165	182
	second island	418	461	433
	third island	825	712	772
pole 1	first island	109	87.7	90.1
	second island	218	202	202
	third island	408	385	381
pole 2	first island	102	83.3	109
	second island	218	204	218
	third island	422	402	423
pole 3	first island	180	160	165
	second island	415	393	394
	third island	742	701	714

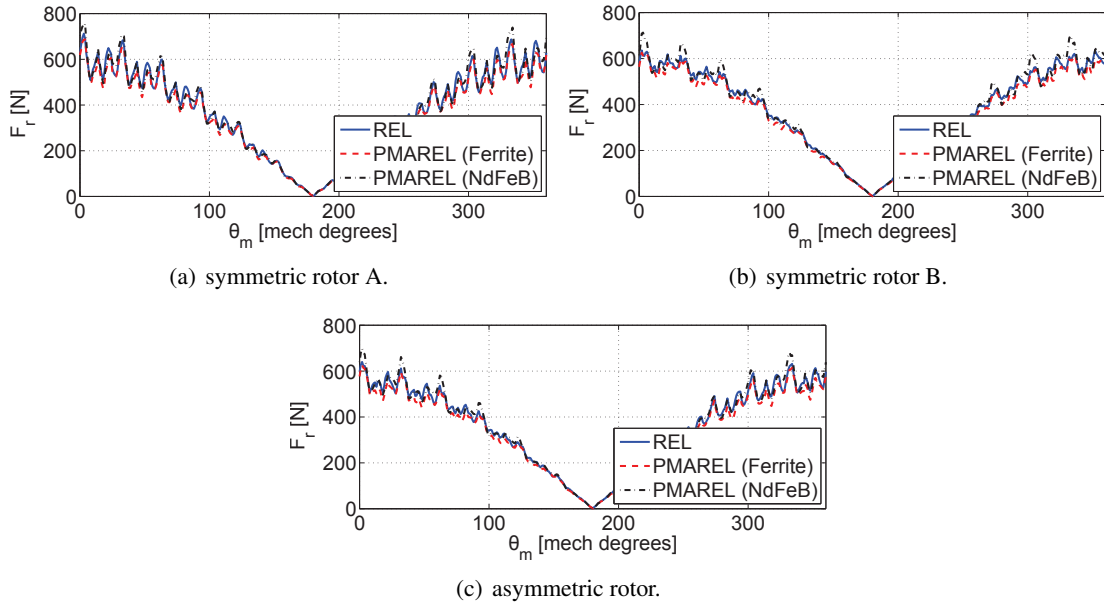


Figure 6.6: Radial forces in case of REL, PMAREL (with Ferrite PMs), and PMAREL (with NdFeB PMs) motor with different rotor geometries, with combined eccentricity ($e_0 = 0.3 \text{ mm}$).

side, the most stressed rotor islands are of pole 1 and 4 as shown in Table 6.11. In case of asymmetric rotor, the barriers of poles 2 and 4, are higher than the barriers of the poles 1 and 3.

Therefore forces on rotor islands of poles 2 and 4 are slightly higher. Specifying better, the rotor islands of pole 4 are subjected to forces slightly higher than that on the rotor islands of pole 1. Besides, rotor islands of pole 2 are subjected to forces slightly higher than those acting on the rotor islands of pole 3.

As noted before, there are no significant change when adding the Ferrite PMs within the flux-barriers, as in case of static and dynamic rotor eccentricity. However, in case of adding the NdFeB PMs within the flux-barriers of symmetric rotor A, the radial forces are increased by 245%, 25%, and 15% for the first, second, and third rotor island, respectively. Analogously, for symmetric rotor B, the forces are increased by 430%, 38%, and 7% for the first, second, and third rotor island, respectively. Besides, in case of asymmetric rotor, the forces are increased by 440%, 30%, and 8% for the first, second, and third rotor island, respectively.

Table 6.11: Radial forces acting on the rotor islands of different rotor geometries of REL motor, with combined eccentricity.

		$F_r[N]$ (worst case)		
	θ_m	3°	352°	2°
pole order	rotor island	symmetric A	symmetric B	asymmetric
pole 4	first island	33.7	93.5	34.7
	second island	329	326	297
	third island	708	684	660
pole 1	first island	20.1	47.9	38.4
	second island	157	155	173
	third island	354	368	366
pole 2	first island	22.3	47.8	23.8
	second island	163	151	158
	third island	365	353	362
pole 3	first island	37.1	80.9	59.1
	second island	341	299	340
	third island	721	657	695

From Tables 6.11 and 6.12, the effect of the mixed eccentricity on the radial forces acting on the rotor islands can be studied. Referring to the third island of the worst pole, this force is increased by 48%, 46%, and 45% for symmetric rotor A, symmetric rotor B and asymmetric rotor, respectively.

Table 6.12: Radial forces acting on the rotor islands of different rotor geometries of PMAREL (with Ferrite PMs) motor, with combined eccentricity.

		$F_r [N]$ (worst case)		
	θ_m	4°	2°	2°
pole order	rotor island	symmetric A	symmetric B	asymmetric
pole 4	first island	35.2	60.8	42.4
	second island	317	332	304
	third island	719	689	671
pole 1	first island	11.5	25.7	25.7
	second island	144	162	162
	third island	359	375	373
pole 2	first island	11.5	23.1	14.6
	second island	148	166	149
	third island	371	390	372
pole 3	first island	38.9	58.2	58.3
	second island	320	332	332
	third island	693	701	692

6.6. Conclusions

The computation of the radial magnetic force acting on the overall rotor of REL and PMAREL motors, in different eccentricity cases, is necessary for the robust design of the rotor bearings against the vibration and noise. In this study, not only asymmetric rotor structure is considered, but also, two symmetric rotors (A and B) with different flux barriers dimensions are considered. For eccentric REL motor, it is noted that the radial force acting on the symmetric rotor B and the asymmetric rotor are close and slightly lower than that acting on the symmetric rotor A. The introduction of the Ferrite or NdFeB PMs within the flux-barriers yields a slight (negligible) reduction of the radial force acting on overall the rotor. In other words, both REL and PMAREL motor have the same radial magnetic force on the overall rotor in the different eccentricity cases.

For designing the rotor iron ribs in both motors, the radial magnetic forces acting on the rotor islands are computed. The computations are carried out at the rotor position which results the maximum value of the radial force on the overall rotor. In case of eccentric (static, dynamic, and combined) REL motor, referring to the third rotor island of the worst pole which close to the minimum air-gap length, the radial force on the island of symmetric rotor B is similar to that of asymmetric rotor. However, it is lower than that of symmetric rotor A.

In static eccentricity case, the radial force acting on the third island of the symmetric rotor A, symmetric rotor B, and asymmetric rotor is increased by 68%, 63%, and 17% of those of healthy case, respectively. However, this radial force is increased by 43% to 48% for all rotor geometries, due to the dynamic and combined eccentricity.

Table 6.13: Radial forces acting on the rotor islands of different rotor geometries of PMAREL (with NdFeB PMs) motor, with combined eccentricity.

		$F_r [N]$ (worst case)		
	θ_m	4°	2°	2°
pole order	rotor island	symmetric A	symmetric B	asymmetric
pole 4	first island	117	179	181
	second island	410	454	426
	third island	813	759	766
pole 1	first island	108	90.5	90
	second island	216	201	201
	third island	405	381	379
pole 2	first island	106	86.4	109
	second island	220	206	219
	third island	426	411	426
pole 3	first island	181	166	166
	second island	418	408	407
	third island	750	722	696

Off course, due to adding the PMs within the flux-barriers, the air-gap flux density in front to each rotor island is increased, which leads to increase the magnetic force on the rotor islands. Since, the Ferrite PM has much lower residual flux density than the NdFeB PM, there are no significant changes in the forces acting on the rotor islands of PMAREL (with Ferrite PMs) motor than those of the REL motor. However, by comparing the REL motor with PMAREL motor with NdFeB PMs, it is noted that the radial forces acting on the rotor islands is increased, specially, the forces acting on the outer islands.

Finally, the robust design of the rotor bearings against the vibration and noise for the three motors can be applied. Besides, the thickness of the rotor iron ribs of REL and PMAREL motor can be designed.

Analytical comparison of REL and SPM machines with eccentricity

This work describes an analytical model of concentric SPM motor. Then, the air-gap length variation in eccentricity case is introduced in the analytical model. Hence, the air-gap flux density distribution, the magnetic radial force acting on the rotor can be estimated. The results of the analytical model are confirmed by the FE analysis. Then, an analytical comparison between the eccentric REL and SPM motors is carried out. The two machines are with the same geometrical dimensions. In addition, an accuracy comparison between the analytical models of both motors is presented. Furthermore, a rapid prediction of the maximum and minimum values of the air-gap flux density of both motors is carried out. Finally, FE comparison between a complete stator eccentric SPM, PMAREL, and REL motors is carried out at different electric current angles, different number of poles, and different stator windings arrangements.

7.1. Introduction

Nowadays, the advancement in the field of power electronics and high energy permanent magnet materials has been broadened the field of application of permanent magnet (PM) machines greatly. It has been adopted for many applications such as electric/hybrid vehicles, aerospace, generation with renewable energy sources etc. The permanent magnet machines are preferred over the traditional machines such as brush commutated direct current (DC) machines, induction machines, synchronous machines because of its merits. These merits are listed as:

- (a) air-gap flux density is relatively high,
- (b) high torque and output power density,
- (c) flux weakening operation capability,
- (d) high fault tolerant,
- (e) overload capability,
- (f) lower copper losses which results in higher efficiency.

The permanent magnet synchronous machine (PMSM) has permanent magnets in the rotor and the stator consists of the three phase, sine distributed windings, or fractional slot windings, depending on the application of the motor. The PMSM are built with a number of rotor configurations. Among them, surface mounted and interior magnet rotors are the most commonly used configurations. The magnet poles are buried inside the rotor in case of interior PM (IPM) rotor configuration as shown in Fig.7.1 (b). Whereas the magnet poles are mounted on the rotor surface in case of surface mounted PM (SPM) rotor configuration as shown in Fig.7.1 (a).

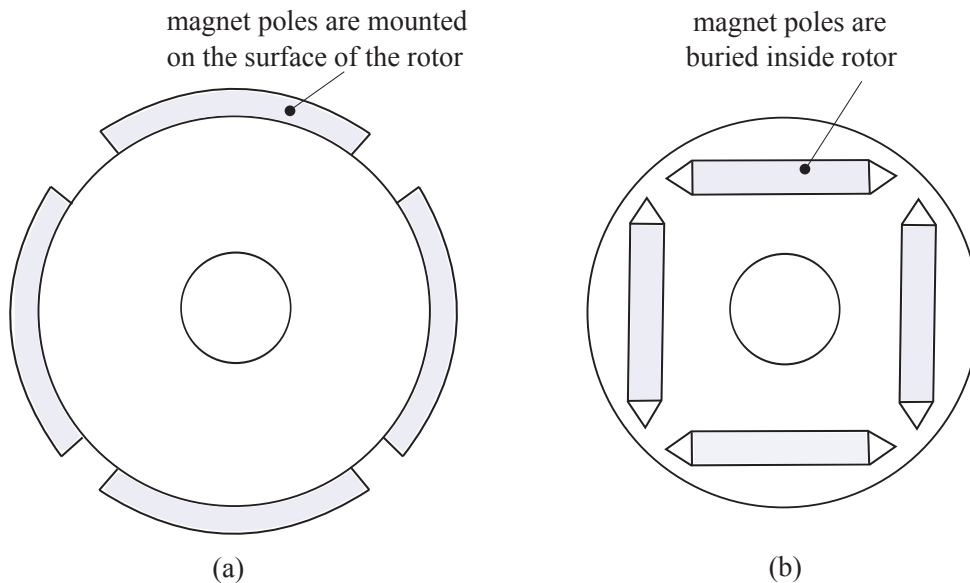


Figure 7.1: Cross section of (a) SPM rotor and (b) IPM rotor.

The IPM motor has very small air-gap length. Hence, the air-gap flux density can be weakened effectively by negative armature reaction. The IPM motor has additional reluctance torque because of the rotor saliency. Therefore, it has large constant power range during flux weakening. Additionally, the effect of the centrifugal force on the rotor magnet at high speed is minimal. Since, the relative permeability of the rare-earth magnets is close to the air permeability, the effective air-gap length is high in SPM motor. Moreover, the SPM motor is magnetically non salient machine, hence, there is no reluctance torque contribution. In case of SPM, the centrifugal force has more effect on the magnet poles comparing with that in case of IPM motor. As a result, the IPM structure is preferred over the SPM structure in many applications, especially, when the machines need to operate above the base speed with constant power.

Most of SPM machines are based on rare-earth magnetic materials, namely, NdFeB grades. This is due to their high remanence and coercivity values. Recently, the increase of Nd magnet price has forced the manufacturers of these kind of machines to search for alternative solutions, especially in those applications where the quantity of PM material is significant, as in mass production (e.g., home appliances, automotive, washing machines, etc.). These solutions could be the REL and PMAREL (or can be called IPM) with multiple barriers. Therefore, it important to compare the SPM machine with these machines not only in healthy case, but also in faulty cases. This study focuses on the eccentricity faults result during the manufacturing process.

Firstly, an analytical models are used to compare between the REL and SPM motors. The

analytical model of the REL motor already has been presented in chapter 3. However, this model is extended in this chapter to include the non-uniform displacement of the rotor axis from the stator axis. The analytical model of the concentric and eccentric SPM motor is discussed in this chapter. Since, the results of these analytical models are confirmed by the FE analysis, they can be used for a fast comparison between the two machines in different eccentricity cases. Finally, the eccentric SPM, PMAREL, and REL motors with a complete stator including slots, teeth, and back iron, has been compared together by means of FE models. These models consider the iron with actual B-H curve instead of linear iron. To the aim of a general comparison, both motors are compared at different current angles, number of poles, and stator windings.

7.2. Analytical model of concentric SPM motor

This section describes the 2D analytical model of SPM motor [44, 61, 62, 72, 73]. The main target of this model is to predict the air-gap flux density distribution. Then, the magnetic pressure and radial force on the rotor are derived. Fig. 7.2 shows a 4-pole SPM machine with slot-less stator and concentric rotor. Since the stator and rotor magnetic voltage drop is neglected (i.e., relative permeability of the iron is assumed to be infinity), there are only two regions to be considered, as shown in Fig. 7.2: Region *I* is the air-gap region, Region *II* is the magnets region.

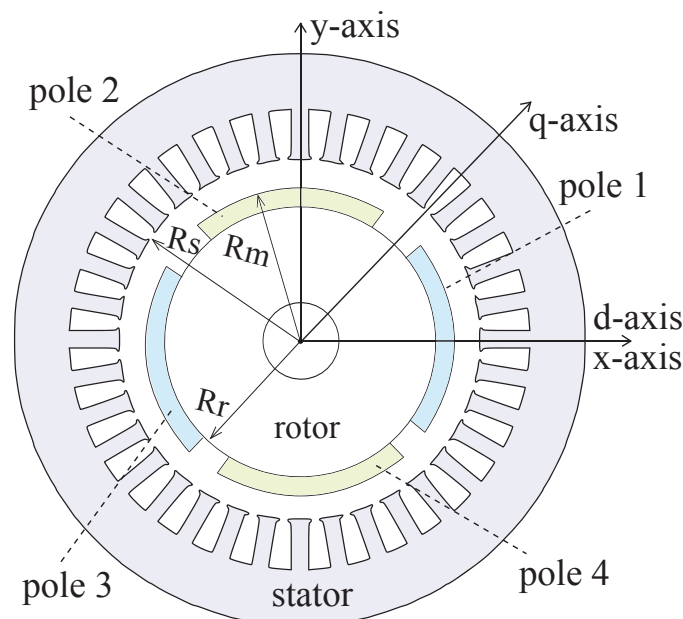


Figure 7.2: Cross section of concentric internal rotor SPM machine.

7.2.1. Relation between the field intensity and flux density for different regions

According to the material properties of Region *I*, the relation between the magnetic field intensity (H) (A/m) and the flux density (B) (Tesla) is given by:

$$B_I = \mu_o H_I \quad (7.1)$$

where μ_o is a permeability of the free space with a value of $4\pi \times 10^{-7}$ (H/m).

For Region *II*, PM can be characterizing by a hysteresis loop which relates H to B . A typical B-H curve for a rare-earth magnet is presented in Fig. 7.3 (a). The second quadrant of the B-H curve, referred to as the demagnetizing curve. From Fig. 7.3 (b), it can be found that rare-earth magnet exhibits nearly linear demagnetization property. The slope of this demagnetization curve is defined as the recoil permeability μ_{rec} (H/m), or $\mu_o \mu_r$, where dimensionless quantity μ_r is called relative recoil permeability of magnet having typical value between 1.05 and 1.2. Therefore, the demagnetization curve can be presented by:

$$B_{II} = \mu_o \mu_r H_{II} + \mu_o M \quad (7.2)$$

where $M = \frac{B_{rem}}{\mu_o}$ (A/m) is the residual magnetization vector and B_{rem} is remanence of PM.

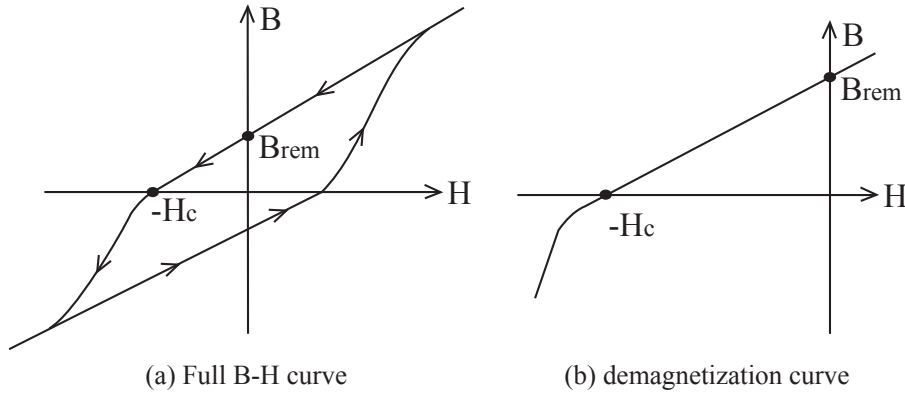


Figure 7.3: B-H relation of rare-earth magnet.

7.2.2. Analytical solution of magnetic field in region *I* and *II*

The magnetic field in region *I* and *II* satisfies the basic equations of magneto-statics

$$\begin{aligned} \vec{\nabla} \cdot \vec{B}_{I,II} &= 0 \\ \vec{\nabla} \times \vec{H}_{I,II} &= 0 \end{aligned} \quad (7.3)$$

The magnetic flux density can be expressed in terms of the magnetic vector potential $A_{I,II}$ as

$$\vec{B}_{I,II} = \vec{\nabla} \times \vec{A}_{I,II} \quad (7.4)$$

From eqs. (7.3) and (7.4), the magnetic vector potential distribution in air-gap (\vec{A}_I) is given by the solution of Laplace's equation as follows:

$$\vec{\nabla}^2 \vec{A}_I = 0 \quad (7.5)$$

Substituting eq. (7.3) in eq. (7.2), it results

$$\vec{\nabla} \vec{B}_{II} = -\mu_o \vec{\nabla} \times \vec{M} \quad (7.6)$$

Then, by substituting eq. (7.4) in eq. (7.6), the magnetic vector distribution in the PM (\vec{A}_{II}) is achieved by the solution of Poisson's equation, as follows:

$$\vec{\nabla}^2 \vec{A}_{II} = -\mu_o \vec{\nabla} \times \vec{M} \quad (7.7)$$

The magnetization is assumed to be uniform throughout the cross-section of the magnets and \vec{M} is given by:

$$\vec{M} = M_r \vec{r} + M_\theta \vec{\theta} \quad (7.8)$$

where M_r and M_θ are computed as

$$M_r = \sum_{\nu^e=1,3,5,\dots}^{\infty} M_{\nu^e} \cos(\nu^e p \theta_r) \quad (7.9)$$

$$M_\theta = 0 \quad (7.10)$$

The Fourier decomposition of the magnetization vector in the radius direction is expressed as

$$M_{\nu^e} = \frac{2B_{rem}}{\mu_o} \alpha_p \frac{\sin(\frac{\nu^e \pi \alpha_p}{2})}{\frac{\nu^e \pi \alpha_p}{2}} \quad (7.11)$$

where ν^e is the space harmonic, α_p is the pole-arc to pole-pitch ratio, and angle θ_r is the angular coordinate expressed in the rotor reference frame according to the center of the magnetic pole, as shown in Fig. 7.2. It is given by

$$\theta_r = \theta_s - w_r t - \theta_e = \theta_s - \varphi_r \quad (7.12)$$

where θ_s is the angular coordinate in the stator reference frame, w_r is the rotor angular velocity, and θ_e is the rotor position at time $t = 0$, as shown in Fig. 7.2.

Then, both Laplace's and Poisson's equations eqs. (7.5) and (7.7) can be rewritten in polar coordinates, respectively, as follows:

$$\frac{\partial^2 \vec{A}_I}{\partial r^2} + \frac{1}{r} \frac{\partial \vec{A}_I}{\partial r} + \frac{1}{r^2} \frac{\partial^2 \vec{A}_I}{\partial \theta^2} = 0 \quad (7.13)$$

$$\frac{\partial^2 \vec{A}_{II}}{\partial r^2} + \frac{1}{r} \frac{\partial \vec{A}_{II}}{\partial r} + \frac{1}{r^2} \frac{\partial^2 \vec{A}_{II}}{\partial \theta^2} = -\mu_o \vec{\nabla} \times \vec{M} \quad (7.14)$$

The general solution of eq. (7.13) gives the magnetic vector potential distribution in air-gap (\vec{A}_I) as

$$\vec{A}_I(r, \theta_r) = \sum_{\nu^e=1}^{\infty} (a_{I\nu^e} r^{\nu^e p} + b_{I\nu^e} r^{-\nu^e p}) \sin(\nu^e p \theta_r) + \sum_{\nu^e=1}^{\infty} (c_{I\nu^e} r^{\nu^e p} + d_{I\nu^e} r^{-\nu^e p}) \cos(\nu^e p \theta_r) \quad (7.15)$$

The magnetic vector potential distribution in PM region (\vec{A}_{II}) is obtained from the general solution of eq. (7.14), as

$$\begin{aligned} \vec{A}_{II}(r, \theta_r) = & \sum_{\nu^e=1}^{\infty} (a_{II\nu^e} r^{\nu^e p} + b_{II\nu^e} r^{-\nu^e p}) \sin(\nu^e p \theta_r) + \\ & + \sum_{\nu^e=1}^{\infty} (c_{II\nu^e} r^{\nu^e p} + d_{II\nu^e} r^{-\nu^e p}) \cos(\nu^e p \theta_r) + A_p \end{aligned} \quad (7.16)$$

where A_p is particular solution at $\nu^e p \neq 1$ and is given by:

$$A_p = \sum_{\nu^e=1}^{\infty} M_{\nu^e} \mu_0 \frac{\nu^e p}{(\nu^e p)^2 - 1} r \sin(\nu^e p \theta_r) \quad (7.17)$$

The coefficients $a_{I\nu^e}$, $b_{I\nu^e}$, $c_{I\nu^e}$ and $d_{I\nu^e}$ and $a_{II\nu^e}$, $b_{II\nu^e}$, $c_{II\nu^e}$ and $d_{II\nu^e}$ are determined by applying the appropriate boundary conditions. The boundary conditions are listed as:

(a) the boundary condition at the surface of the rotor iron is

$$H_{\theta II} = 0|_{r=R_r} \quad (7.18)$$

(b) the boundary condition at the surface of the permanent magnets is

$$H_{\theta I}|_{r=R_m} = H_{\theta II}|_{r=R_m} \quad \text{and} \quad B_{r I}|_{r=R_m} = B_{r II}|_{r=R_m} \quad (7.19)$$

where B_r is the radial component of the flux density and R_r and R_m , as shown in Fig.7.2, are the rotor the and magnet radius, respectively.

(c) the boundary condition at the stator surface is

$$H_{\theta I}|_{r=R_s^+} - H_{\theta I}|_{r=R_s^-} = K_s \quad (7.20)$$

where $H_{\theta I}$ is the circumferential component of the magnetic field, R_s is the stator bore radius as shown in Fig.7.2, and K_s is the stator winding equivalent current sheet, which presented in eq. (2.20).

By applying the previous boundary conditions, the coefficients $a_{I\nu^e}$, $b_{I\nu^e}$, $c_{I\nu^e}$ and $d_{I\nu^e}$ and $a_{II\nu^e}$, $b_{II\nu^e}$, $c_{II\nu^e}$ and $d_{II\nu^e}$ can be computed. Because of the main purpose of this study is to compute the air-gap flux density, the computation of the parameters $a_{I\nu^e} \times r^{\nu^e p}$, $b_{I\nu^e} \times r^{-\nu^e p}$, $c_{I\nu^e} \times r^{\nu^e p}$ and $d_{I\nu^e} \times r^{-\nu^e p}$ is shown in eq. (7.21).

$$\begin{aligned} a_{I\nu^e} \times r^{\nu^e p} &= - \left(\frac{r}{R_m} \right)^{\nu^e p} \times \{aa + bb\} \\ b_{I\nu^e} \times r^{-\nu^e p} &= - \left(\frac{R_m}{r} \right)^{\nu^e p} \times \{cc + hh\} \\ c_{I\nu^e} \times r^{\nu^e p} &= - \left(\frac{r}{R_m} \right)^{\nu^e p} \times \{ee + ff\} \\ d_{I\nu^e} \times r^{-\nu^e p} &= - \left(\frac{R_m}{r} \right)^{\nu^e p} \times \{xx + yy\} \end{aligned} \quad (7.21)$$

where

$$aa = \frac{R_m \gamma_{\nu^e 1} \mu_r - \delta_{\nu^e 1} + \left(\frac{R_m}{R_r}\right)^{2\nu^e p} [\delta_{\nu^e 1} + R_m \gamma_{\nu^e 1} \mu_r] + \left(\frac{R_s}{R_r}\right)^{\nu^e p} \left(\frac{R_m}{R_r}\right)^{\nu^e p} \alpha_{\nu^e 1} R_s [\mu_r + 1]}{\left[\left(\frac{R_m}{R_r}\right)^{2\nu^e p} - \left(\frac{R_s}{R_m}\right)^{2\nu^e p}\right] (\mu_r - 1) - \left[\left(\frac{R_s}{R_r}\right)^{2\nu^e p} - 1\right] (\mu_r + 1)} \quad (7.22)$$

$$bb = \frac{\left(\frac{R_s}{R_m}\right)^{\nu^e p} R_s \alpha_{\nu^e 1} [\mu_r - 1] + 2R_r \beta_{\nu^e 1} \left(\frac{R_m}{R_r}\right)^{\nu^e p}}{\left[\left(\frac{R_m}{R_r}\right)^{2\nu^e p} - \left(\frac{R_s}{R_m}\right)^{2\nu^e p}\right] (\mu_r - 1) - \left[\left(\frac{R_s}{R_r}\right)^{2\nu^e p} - 1\right] (\mu_r + 1)} \quad (7.23)$$

$$cc = \frac{\left(\frac{R_s}{R_m}\right)^{2\nu^e p} (R_m \gamma_{\nu^e 1} \mu_r - \delta_{\nu^e 1}) + 2 \left(\frac{R_s}{R_r}\right)^{\nu^e p} \left(\frac{R_s}{R_m}\right)^{\nu^e p} R_r \beta_{\nu^e 1} + \left(\frac{R_s}{R_r}\right)^{2\nu^e p} (R_m \gamma_{\nu^e 1} \mu_r + \delta_{\nu^e 1})}{\left[\left(\frac{R_m}{R_r}\right)^{2\nu^e p} - \left(\frac{R_s}{R_m}\right)^{2\nu^e p}\right] (\mu_r - 1) - \left[\left(\frac{R_s}{R_r}\right)^{2\nu^e p} - 1\right] (\mu_r + 1)} \quad (7.24)$$

$$hh = \frac{\left(\frac{R_s}{R_m}\right)^{\nu^e p} R_s \alpha_{\nu^e 1} [\mu_r + 1] + \left(\frac{R_s}{R_m}\right)^{\nu^e p} \left(\frac{R_m}{R_r}\right)^{2\nu^e p} R_s \alpha_{\nu^e 1} [\mu_r - 1]}{\left[\left(\frac{R_m}{R_r}\right)^{2\nu^e p} - \left(\frac{R_s}{R_m}\right)^{2\nu^e p}\right] (\mu_r - 1) - \left[\left(\frac{R_s}{R_r}\right)^{2\nu^e p} - 1\right] (\mu_r + 1)} \quad (7.25)$$

$$ee = \frac{R_m \gamma_{\nu^e 2} \mu_r - \delta_{\nu^e 2} + \left(\frac{R_m}{R_r}\right)^{2\nu^e p} [\delta_{\nu^e 2} + R_m \gamma_{\nu^e 2} \mu_r] + \left(\frac{R_s}{R_r}\right)^{\nu^e p} \left(\frac{R_m}{R_r}\right)^{\nu^e p} \alpha_{\nu^e 2} R_s [\mu_r + 1]}{\left[\left(\frac{R_m}{R_r}\right)^{2\nu^e p} - \left(\frac{R_s}{R_m}\right)^{2\nu^e p}\right] (\mu_r - 1) - \left[\left(\frac{R_s}{R_r}\right)^{2\nu^e p} - 1\right] (\mu_r + 1)} \quad (7.26)$$

$$ff = \frac{\left(\frac{R_s}{R_m}\right)^{\nu^e p} R_s \alpha_{\nu^e 2} [\mu_r - 1] + 2R_r \beta_{\nu^e 2} \left(\frac{R_m}{R_r}\right)^{\nu^e p}}{\left[\left(\frac{R_m}{R_r}\right)^{2\nu^e p} - \left(\frac{R_s}{R_m}\right)^{2\nu^e p}\right] (\mu_r - 1) - \left[\left(\frac{R_s}{R_r}\right)^{2\nu^e p} - 1\right] (\mu_r + 1)} \quad (7.27)$$

$$xx = \frac{\left(\frac{R_s}{R_m}\right)^{2\nu^e p} (R_m \gamma_{\nu^e 2} \mu_r - \delta_{\nu^e 2}) + 2 \left(\frac{R_s}{R_r}\right)^{\nu^e p} \left(\frac{R_s}{R_m}\right)^{\nu^e p} R_r \beta_{\nu^e 2} + \left(\frac{R_s}{R_r}\right)^{2\nu^e p} (R_m \gamma_{\nu^e 2} \mu_r + \delta_{\nu^e 2})}{\left[\left(\frac{R_m}{R_r}\right)^{2\nu^e p} - \left(\frac{R_s}{R_m}\right)^{2\nu^e p}\right] (\mu_r - 1) - \left[\left(\frac{R_s}{R_r}\right)^{2\nu^e p} - 1\right] (\mu_r + 1)} \quad (7.28)$$

$$yy = \frac{\left(\frac{R_s}{R_m}\right)^{\nu^e p} R_s \alpha_{\nu^e 2} [\mu_r + 1] + \left(\frac{R_s}{R_m}\right)^{\nu^e p} \left(\frac{R_m}{R_r}\right)^{2\nu^e p} R_s \alpha_{\nu^e 2} [\mu_r - 1]}{\left[\left(\frac{R_m}{R_r}\right)^{2\nu^e p} - \left(\frac{R_s}{R_m}\right)^{2\nu^e p}\right] (\mu_r - 1) - \left[\left(\frac{R_s}{R_r}\right)^{2\nu^e p} - 1\right] (\mu_r + 1)} \quad (7.29)$$

where the parameters $\alpha_{\nu^e 1}$, $\beta_{\nu^e 1}$, $\gamma_{\nu^e 1}$, and $\delta_{\nu^e 1}$ and $\alpha_{\nu^e 2}$, $\beta_{\nu^e 2}$, $\gamma_{\nu^e 2}$, and $\delta_{\nu^e 2}$ are given by:

$$\alpha_{\nu^e 1} = \begin{cases} \frac{\mu_0 \hat{K}_{sv^e}}{\nu^e p} \sin(p\theta_m), & \nu^e = (6k + 1), k = 0, 1, 2, 3, \dots \\ \frac{\mu_0 \hat{K}_{sv^e}}{\nu^e p} \sin(p\theta_m), & \nu^e = (3k - m), k = -1, -2, -3, \dots \\ 0 & \text{elsewhere} \end{cases} \quad (7.30)$$

$$\beta_{\nu^e 1} = \frac{\mu_o M_{\nu^e}}{1 - (\nu^e p)^2} \cos(\nu^e p \varphi_r) \quad (7.31)$$

$$\gamma_{\nu^e 1} = \frac{\mu_o M_{\nu^e}}{\mu_r (1 - (\nu^e p)^2)} \cos(\nu^e p \varphi_r) \quad (7.32)$$

$$\delta_{\nu^e 1} = \frac{\mu_o M_{\nu^e} \nu^e p}{(\nu^e p)^2 - 1} R_m \cos(\nu^e p \varphi_r) \quad (7.33)$$

$$\alpha_{\nu^e 2} = \begin{cases} \frac{\mu_o \hat{K}_{s\nu^e}}{\nu^e p} \cos(p\theta_m), & \nu^e = (6k + 1), k = 0, 1, 2, 3, \dots \\ \frac{-\mu_o \hat{K}_{s\nu^e}}{\nu^e p} \cos(p\theta_m), & \nu^e = (6k + 1), k = -1, -2, -3, \dots \\ 0 & \text{elsewhere} \end{cases} \quad (7.34)$$

$$\beta_{\nu^e 2} = \frac{\mu_o M_{\nu^e}}{1 - (\nu^e p)^2} \sin(\nu^e p \varphi_r) \quad (7.35)$$

$$\gamma_{\nu^e 2} = \frac{-\mu_o M_{\nu^e}}{\mu_r (1 - (\nu^e p)^2)} \sin(\nu^e p \varphi_r) \quad (7.36)$$

$$\delta_{\nu^e 2} = \frac{-\mu_o M_{\nu^e} \nu^e p}{(\nu^e p)^2 - 1} R_m \sin(\nu^e p \varphi_r) \quad (7.37)$$

Then, the parameters of eq. (7.21) are implemented in eq. (7.15) to determine the air-gap magnetic vector potential distribution. Finally the air-gap flux density can be computed as follows:

$$B_{rI} = \frac{1}{r} \frac{\partial A_I}{\partial \theta} \quad \text{and} \quad B_{\theta I} = -\frac{\partial A_I}{\partial r} \quad (7.38)$$

However, this study focuses on the computation of the radial component of the air-gap flux density to compute the radial magnetic pressure and the radial force on the rotor. Form eqs. (7.21) and (7.38), it is computed as

$$B_{rI}(r, \theta_r) = \left(\frac{\nu^e p}{r} \right) \left[\sum_{\nu^e=1}^{\infty} (a_{I\nu^e} r^{\nu^e p} + b_{I\nu^e} r^{-\nu^e p}) \cos(\nu^e p \theta_r) - \sum_{\nu^e=1}^{\infty} (c_{I\nu^e} r^{\nu^e p} + d_{I\nu^e} r^{-\nu^e p}) \sin(\nu^e p \theta_r) \right] \quad (7.39)$$

By substituting r by $R_s - g/2$, the air-gap flux density can be computed. Therefore, the flux density can be computed on the surface of the magnet and on the inner stator surface by implementing $r = R_m$ and $r = R_s$, respectively. In addition, the flux density can be computed inside the magnet B_{rII} by applying the same previous procedure for region II.

7.3. Analytical model of eccentric SPM motor

Both static and dynamic eccentricity, in case of uniform displacement of the rotor axis from the stator axis, are considered in the analytical model of the REL motor, as shown in chapter 3. However, in this section, the different scenarios of the non-uniform displacement of the rotor axis from the stator axis are described. Fig. 7.4 (a) shows the uniform displacement of the rotor axis from the stator axis, Fig. 7.4 (b) shows non-uniform similar and opposite displacement of the rotor axis from the stator axis, Fig. 7.4 (c) shows the non uniform displacement of the rotor axis from the stator axis at one end only. In addition, the rotor may exhibit a rotation around its center (i.e., static eccentricity) or a rotation around the stator center (i.e., dynamic eccentricity).

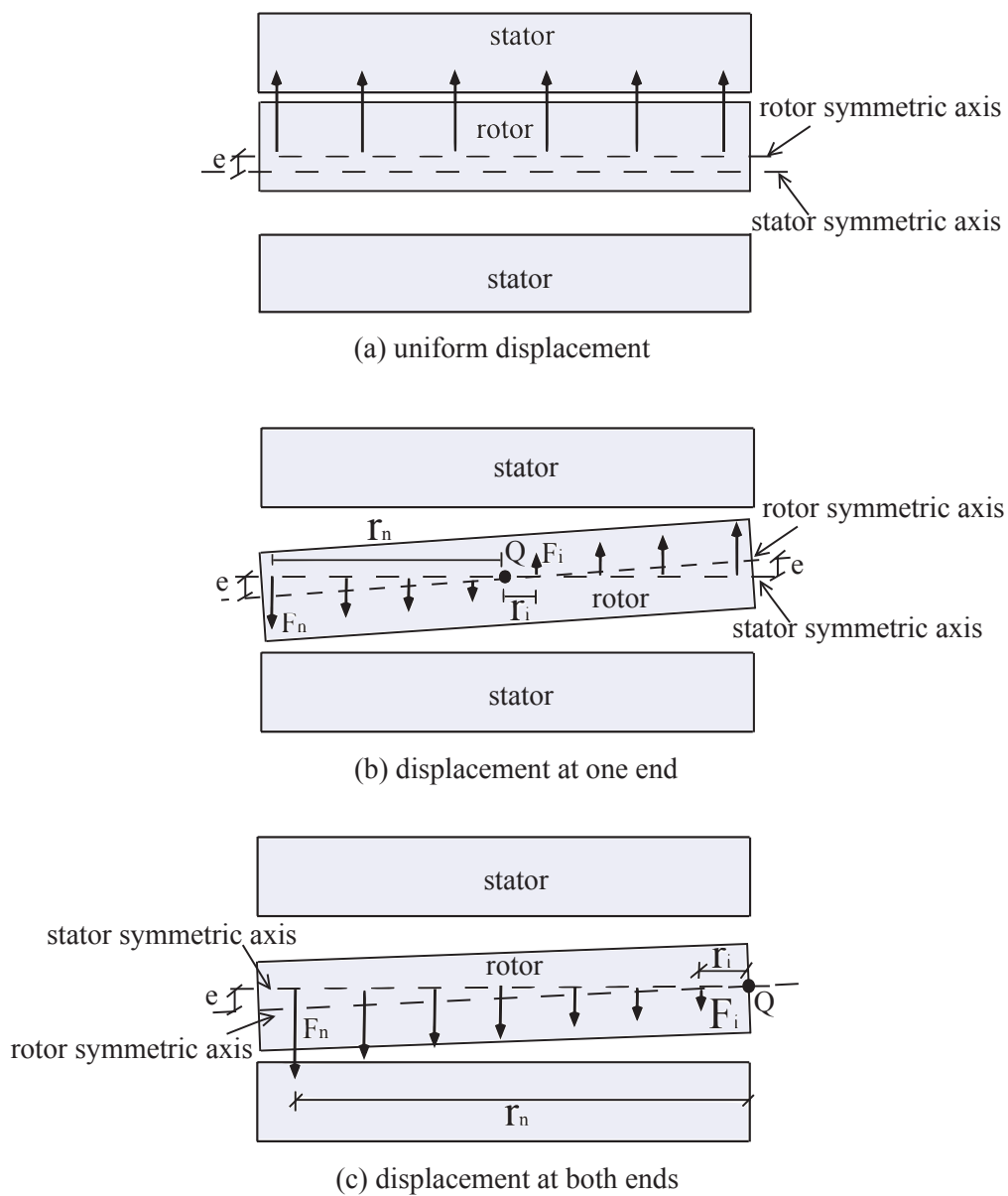


Figure 7.4: Three different axial eccentricity cases.

The three different displacements of the rotor axis from the stator axis are considered in the analytical model of SPM motor. At the beginning, the analytical model of the SPM is introduced for the uniform displacement or the rotor symmetric axis from the stator symmetric axis. This analytical model is used to compute the air-gap flux density distribution, radial force on the rotor in case of eccentricity. Then, for the other two eccentricity cases, the rotor is divided to finite number of slides and the analytical model is applied to each slide. Hence, the total radial force on the rotor is the summation of the radial force on each rotor slide. Analogously, the analytical model of the REL motor is extended to the two different non uniform rotor axis displacements for the stator axis.

Fig. 7.5 shows cross section of an eccentric rotor SPM machine, where the point of symmetry of the rotor O_r is shifted from the point of symmetry of the stator O_s , by distance e and angle θ_e . To the aim of considering the air-gap length variation, as shown in Fig. 7.5, the constant value of the internal stator radius (i.e, R_s) is replaced by variable radius computed according to the rotor symmetric point O_r (i.e, R_{sr}), as presented in [44].

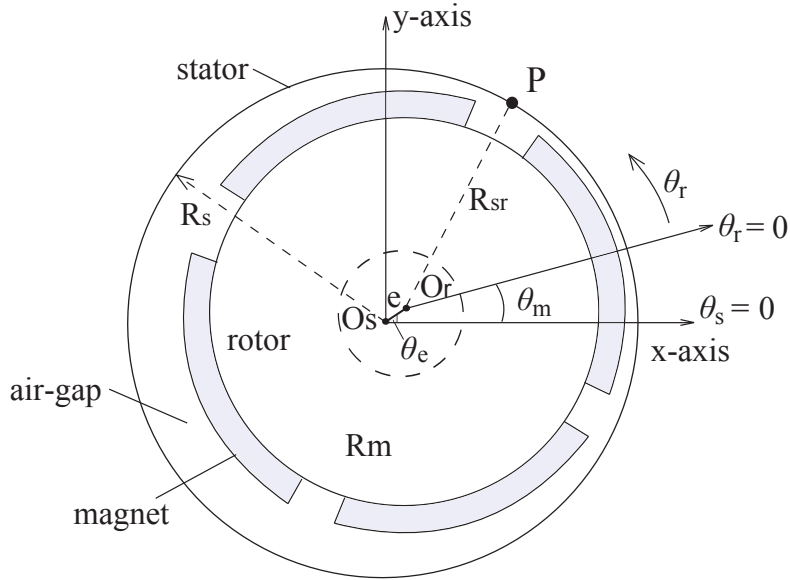


Figure 7.5: Cross section of eccentric internal rotor SPM machine.

As shown in Fig. 7.5 and Fig. 7.6, point P is located on the inner surface of the stator. In Fig. 7.6, this point is defined by R_s and θ_s in stator polar reference frame and by R_{sr} and θ_{sr} in rotor polar reference frame, where R_{sr} is not constant in case of eccentricity. To calculate the R_{sr} and θ_{sr} of the point P , when the rotor axis is displaced from the stator axis by angle θ_e , a transformation from the stator to the rotor reference frame is performed, as shown in Fig. 7.6. The Cartesian coordinates of point P in stator reference frame are

$$P_{xs} = R_s \cos(\theta_s) \quad \text{and} \quad P_{ys} = R_s \sin(\theta_s) \quad (7.40)$$

The transformation of the Cartesian coordinates of point P from the stator to the rotor reference frame are as follows:

$$\begin{bmatrix} P'_{xr} \\ P'_{yr} \end{bmatrix} = \begin{bmatrix} \cos(\theta_e) & \sin(\theta_e) \\ -\sin(\theta_e) & \cos(\theta_e) \end{bmatrix} \times \begin{bmatrix} P_{xs} \\ P_{ys} \end{bmatrix} \quad (7.41)$$

and then

$$P_{xr} = P'_{xr} - e \quad \text{and} \quad P_{yr} = P'_{yr} \quad (7.42)$$

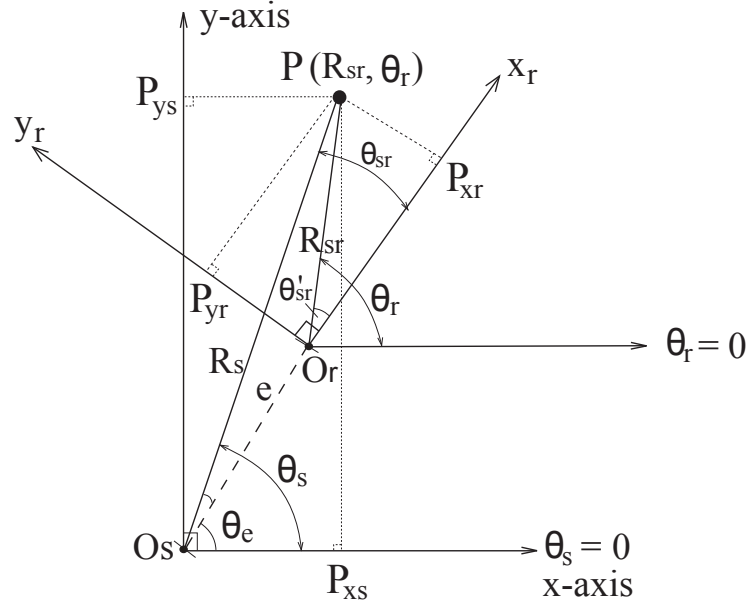


Figure 7.6: Transformation from stator to rotor reference frame.

Then, R_{sr} and θ_{sr} are given by:

$$R_{sr} = \sqrt{P_{xr}^2 + P_{yr}^2} \quad \text{and} \quad \theta_{sr} = \tan^{-1}(P_{yr}/P_{xr}) \quad (7.43)$$

The stator current sheet and the rotor magnetization should be modified with respect to the new rotor polar reference frame. Therefore, they should be referred to the angle θ_{sr} which results in correct boundary conditions implementation.

From Fig. 7.6, the relation between θ_s and θ_{sr} is expressed as

$$\theta_s = \theta'_{sr} + \theta_e \approx \theta_{sr} + \theta_e \quad (7.44)$$

Then, the current sheet is modified by introducing an additional shift angle θ_e . Therefore, the total shift is given by $p\theta_m - \nu^e p_s \theta_e$. In addition, the magnetization phase shift angle is also modified as

$$\theta_r = \theta_s - \varphi_r = \theta_{sr} + \theta_e - \varphi_r = \theta_{sr} - \varphi'_r \quad \text{where} \quad \varphi'_r = \varphi_r - \theta_e \quad (7.45)$$

Replacing each R_s by R_{sr} in eqs. (7.22) to (7.29) and φ_r by φ'_r in eqs. (7.31) to (7.33) and (7.35) to (7.37), the air-gap flux density can be computed in the eccentricity case. Then, the electromagnetic pressure on the rotor is computed as in eq. (3.131). Hence, the total radial force on the rotor and its components in x and y axes directions can be computed, as in eqs. (3.132) to (3.134), respectively.

In case of non-uniform displacement of the rotor axis from the stator axis, as shown in Fig. 7.4 (b) and Fig. 7.4 (c), the symmetric axis of the rotor is divided into a finite number of

slides n_s . Then, the previous analytical models of eccentric SPM and REL motor are applied considering each slide stack length equal to L_{stk}/n_s . The total force in x -axis and y -axis directions are given by:

$$F_x = \sum_{n=1}^{n_s} F_{xn} \quad \text{and} \quad F_y = \sum_{n=1}^{n_s} F_{yn} \quad (7.46)$$

where F_{xn} and F_{yn} are the force components acting on the n -th slide. In addition, the torque with respect to the Q -axis perpendicular to the stator symmetric axis, as shown in Fig. 7.4 (b) and Fig. 7.4 (c), is given by:

$$T_Q = \sum_{n=1}^{n_s} F_n \times r_n \quad (7.47)$$

where r_n is the distance from Q -axis and the center of n -th slide. The location of Q -axis depends on the type of eccentricity as shown in Fig. 7.4 (b) and Fig. 7.4 (c).

7.4. Results of the analytical model of concentric SPM motor

Fig. 7.7 (a) and Fig. 7.7 (b) shows the air-gap flux density at no eccentricity case at $\theta_m = 0$ and $\theta_m = 20$, respectively. It is noted that, there are satisfactory agreement between the analytical model and FE model results. In addition, it is noted that, the air-gap flux density is similar for the all poles at different rotor position.

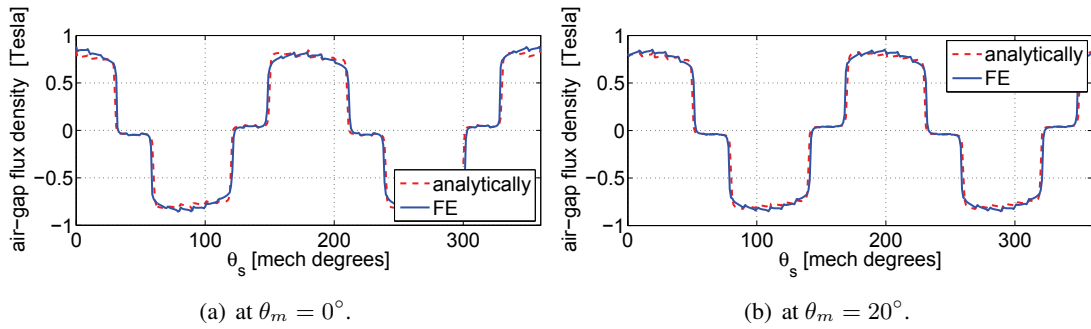


Figure 7.7: Air-gap flux density of a SPM motor at loading condition with concentric rotor at different positions ($\theta_m = 0^\circ$ and 60°).

The radial force components in x axis direction and y axis direction are also computed for healthy SPM motor. Fig. 7.8 shows the analytical and FE results. It is noted that, the radial force assumes zero value for both models.

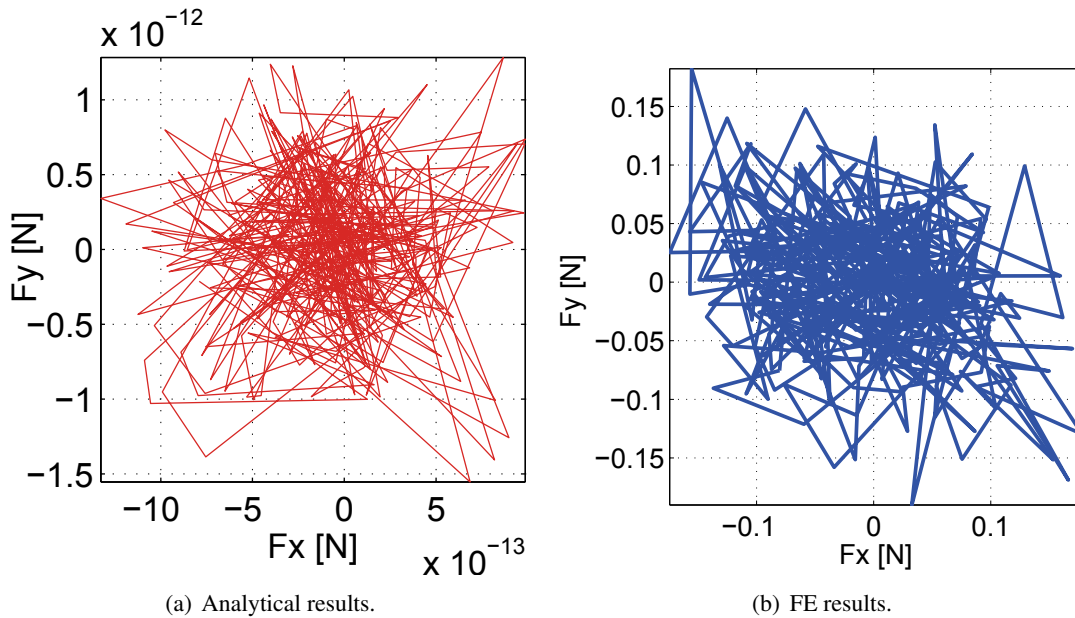


Figure 7.8: F_y versus F_x at all rotor positions in case of no eccentricity.

7.5. Analytical comparison between SPM and REL motors

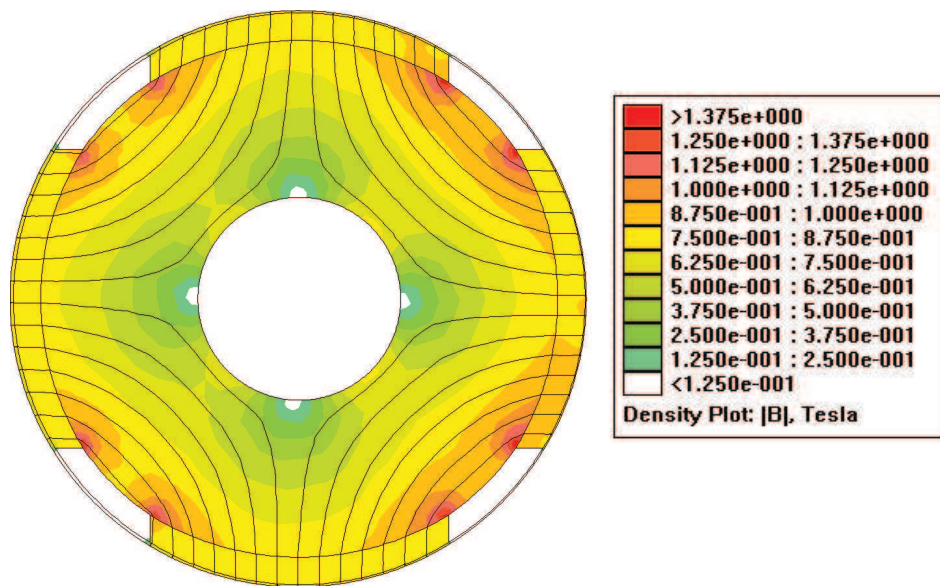
To the aim of comparison between the REL and SPM machines, both machines have the same geometrical dimensions. The main geometrical data of REL motor are reported in Table. 4.1 and Table. 4.2. For SPM machine, the main data used in the analytical and FE simulation are listed in Table 7.1. A mechanical air-gap length of 0.35 mm is considered. In the SPM machine, a bandage thickness 0.15 mm is added so that the total magnetic air-gap becomes equal to 0.5 mm .

Table 7.1: Geometrical data of the SPM machine.

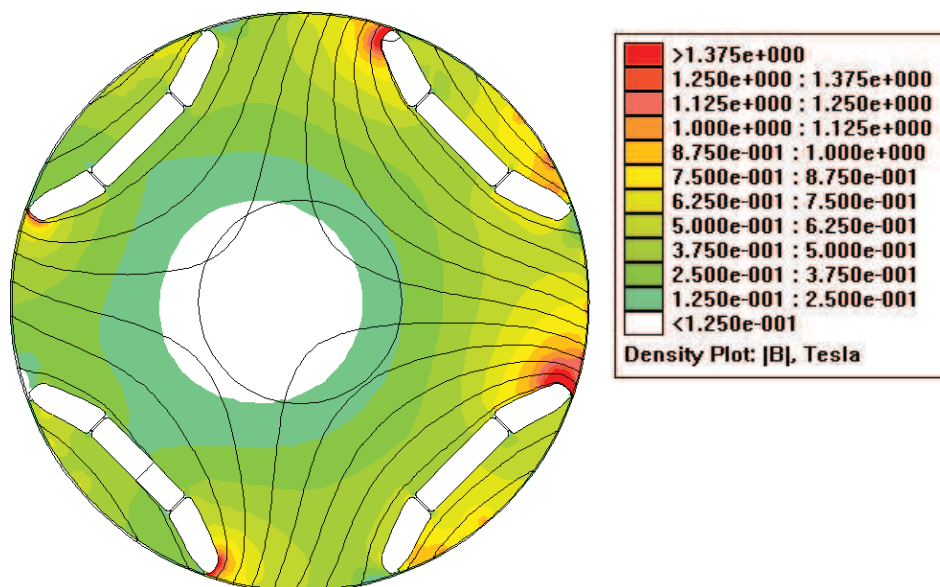
Outer stator radius	R_{se}	100 mm
Inner stator radius	R_s	62.5 mm
Magnet radius	R_m	62 mm
Rotor radius	R_r	57 mm
Stack length	L_{stk}	40 mm
Number of stator pole pairs	p_s	4
Number of rotor magnets pole pairs	p	4
Number of stator slots	Q_s	36
Pole-arc to pole pitch ratio	α_p	0.67
Permanent magnet thickness	h_m	5 mm
Remanent flux density	B_{rem}	0.905 T
Relative permeability	μ_r	1.08

The 2D FE model is used to validate the results achieved by the analytical model. Each FE analysis is carried out using FEMM package. Fig. 7.9 shows both the flux lines and the flux density map of the SPM machine and REL machine with eccentricity $e = 0.2 \text{ mm}$ and electrical loading equal to 6200 A/m at $\theta_e = 0^\circ$ when the rotor is at the position $\theta_m = 0^\circ$. A displacement $e = 0.2 \text{ mm}$ is quite high, however it allows the eccentricity effect to be better highlighted. For both machines, the flux density increases on the right hand side where the air-gap length is reduced and decreases on the left hand side where the air-gap length is increased, respectively.

It is worth noting that in the SPM machine the flux lines remain quite symmetrical and the flux density quite similar among the poles. The main reason is the presence of the surface PMs which tend to keep a constant flux density even with the air-gap variation. On the contrary, in the REL machine the flux lines are quite distorted and the flux density increases greatly near the lower air-gap length. This is mainly due to the low distance between the stator and the rotor iron.



(a) eccentricity case.



(b) eccentricity case.

Figure 7.9: Flux density map (a) SPM machine and (b) REL machine with eccentricity on the right hand side by $e = 0.2 \text{ mm}$ at $\theta_e = 0^\circ$, rotor position $\theta_m = 0^\circ$. Electrical loading is 6200 A/m.

7.5.1. Case of uniform displacement of the rotor axis

Fig. 7.10 shows the air-gap flux density of SPM and REL machines with and without rotor eccentricity. The flux density behaviours in case of eccentricity correspond to the maps in Fig. 7.9. With uniform air-gap, the flux density is the same in all four poles, while it is not in case of eccentricity. It increases where the air-gap length is reduced and decreases where the air gap length is increased. Fig. 7.10 shows that in the REL machine where a higher variation of flux density occurs.

Fig. 7.11 shows the air-gap flux density computed from the analytical and FE models of SPM and REL machine with eccentricity equal to 0.2 mm . It is noted that there is a satisfactory agreement between the analytical models and the FE analysis. A discrepancy is found near the lower air-gap length. It is more evident analysing the REL machine, which is characterized by a lower difference between stator and rotor radius, i.e., $(R_s - R_r)$. The analytical model tends to overestimate the flux density. A lower difference is found when the rotor is characterized by a number of flux barriers per pole higher than two, as shown in chapter 4 and [37, 63].

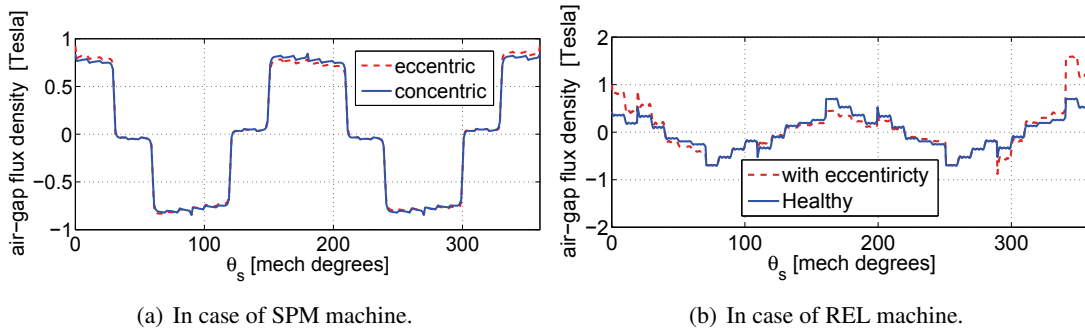


Figure 7.10: Air-gap flux density for SPM and REL machine with and without rotor eccentricity, at loading condition, at $\theta_m = 0^\circ$ ($e = 0.2 \text{ mm}$). Electrical loading is 6200 A/m .

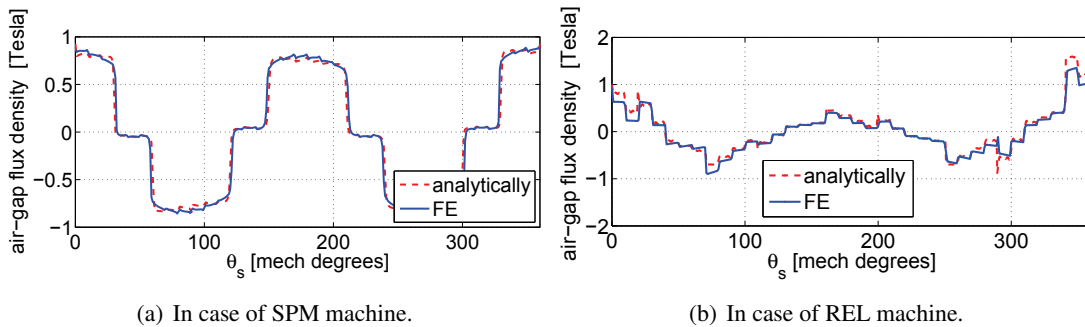


Figure 7.11: Air-gap flux density results from the analytical and FE models of SPM and REL machines, at loading condition, at $\theta_m = 0^\circ$ ($e = 0.2 \text{ mm}$). Electrical loading is 6200 A/m .

Fig. 7.12 shows the radial force on the rotor of both machines, in case of no load and load conditions (electric loading = 6200 A/m), versus different eccentricity distances. In case of SPM machine with eccentricity, the radial force on the rotor at both no load and load conditions are quite similar. There is also a good agreement between the results of the analytical model and the FE analysis.

As far as the REL machine is concerned, at no load condition, the radial force on the rotor with eccentricity assumes zero value, since the stator current is zero so that the stator magnetic potential is zero too. Therefore, the magnetic pressure and the radial force on the rotor are zero, as shown in Fig. 7.12 (b). On the contrary, the radial force increases rapidly with the eccentricity when the machine operates under load. It is worth noticing that the radial force increases more than proportionally with respect to the rotor eccentricity. Due to the small air-gap, the radial forces are higher than the radial forces in the SPM machine, as noticed

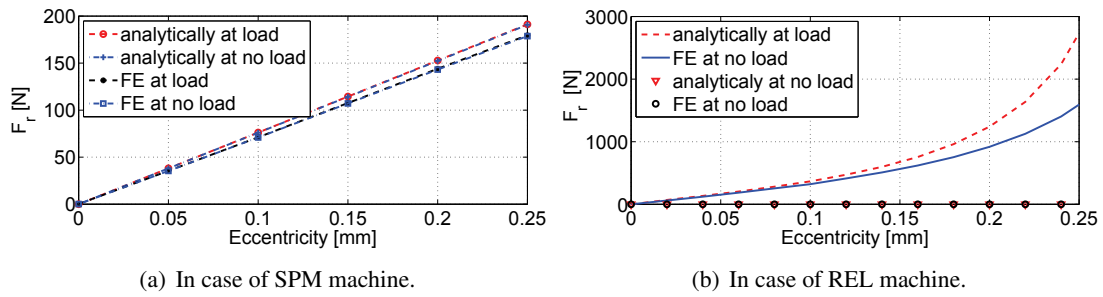


Figure 7.12: F_r versus eccentricity distance in case of SPM and REL machine at no load and load conditions, with uniform displacement between the rotor and the stator symmetric axes. Electrical loading is 6200 A/m.

by comparing Fig. 7.12 (a) and Fig. 7.12 (b). It is again observed an overestimation of the analytical computation with respect the FE analysis. Such an overestimation increases with the eccentricity e .

7.5.2. Case of displacement of rotor axis at one end

This section deals with the second case of eccentricity where the rotor axis has a displacement from the stator axis at one end, as shown in Fig. 7.4 (c). The total radial force on the rotor of both machines at different eccentricity values is shown in Fig. 7.13. The effect of eccentricity on the REL machine is again higher than the effect on the SPM machine with the same geometrical dimensions. There are also a satisfactory agreement between the results of the analytical and the FE model in both figures.

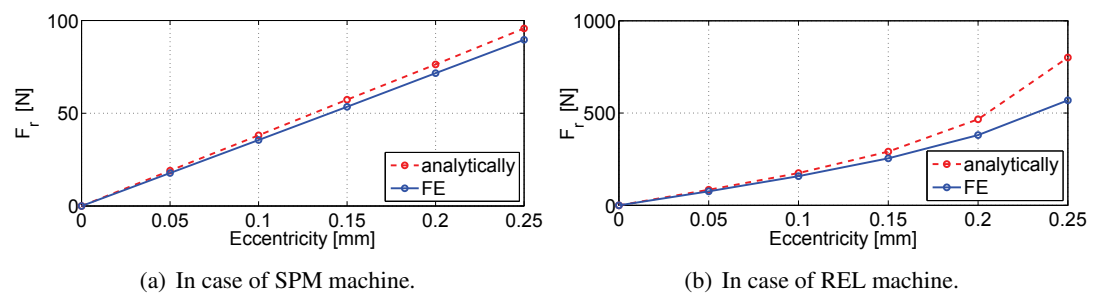


Figure 7.13: F_r versus eccentricity distance in case of SPM and REL machine with displacement between the rotor and the stator axis at one end. Electrical loading is 6200 A/m.

Fig. 7.14 shows the unbalanced axial torque on the rotor of both SPM and REL machine. In REL machine the torque is higher than in SPM machine. There are again a satisfactory agreement between both analytical and FE model results.

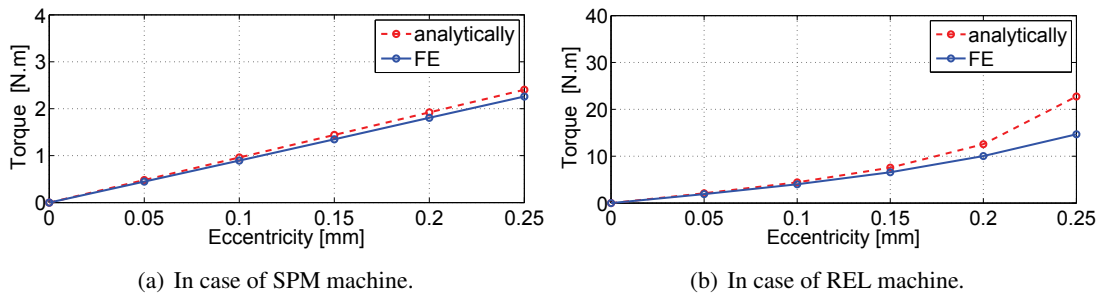


Figure 7.14: Torque due to unbalanced magnetic force in case of rotor displacement at one end, for both SPM and REL machines. Electrical loading is 6200 A/m.

7.5.3. Case of similar and opposite displacement of rotor axis

In case of similar and opposite displacement of rotor axis from the stator axis, the total radial force on the rotor is equal to zero for both machines. However, there are torques due to the unbalance magnetic force around the axis of stator, as shown in Fig. 7.4 (b). Fig. 7.15 (a) and Fig. 7.15 (b) show that the unbalanced torque in case of REL machine is again higher than that of SPM machine. In addition, there are also agreement between the results of both analytical and FE models. From Fig. 7.15 and Fig. 7.14, it is noted that the unbalanced torque around the Q -axis with a displacement of rotor axis at one end (second eccentricity case) is higher than that with a similar and opposite displacement of rotor axis at both ends (third eccentricity case).

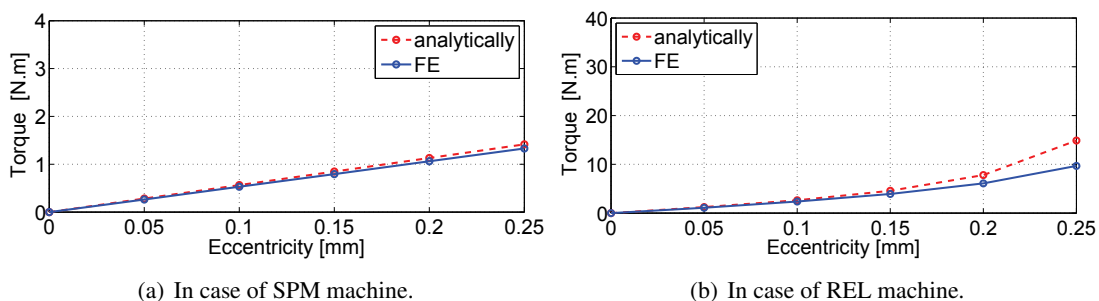


Figure 7.15: Torque due to unbalanced magnetic force, in case of similar and opposite rotor displacement at both ends, for both SPM and REL machines. Electrical loading is 6200 A/m.

7.6. Accuracy comparison of the two models

The aim of this section is to compare the robustness of the two analytical models. To do that, an ideal cylindrical rotor is considered, as shown in Fig. 7.16. Such a system is studied as a limit case of both the analytical models presented above, considering

- an SPM machine without PMs, and
- an REL machine without flux barriers.

In both machines, $R_s = 62.15 \text{ mm}$.

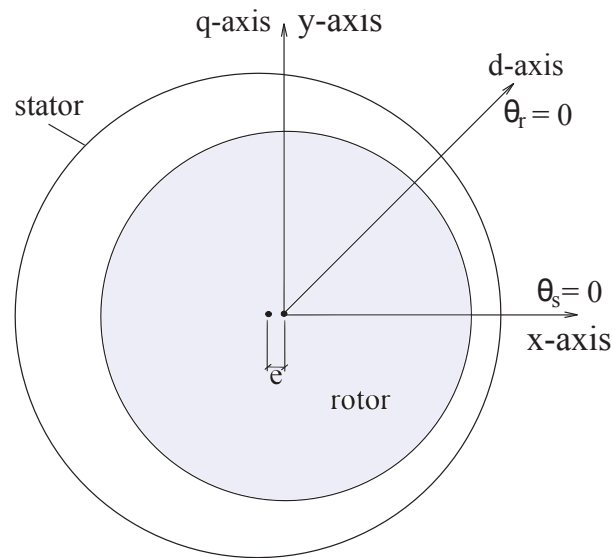


Figure 7.16: Cross section of an ideal eccentric rotor.

The results of both models at the same air-gap length are reported in Table 7.2. A satisfactory agreement between both analytical models is observed. In addition, the analytical results are similar to those achieved from FE analysis. The discrepancy between the analytical models and the FE analysis increases with the eccentricity (from half of the air-gap length to higher values).

Table 7.2: Unbalanced forces from both analytical models and comparison with FE results.

eccentricity (<i>mm</i>)	Analytical		FE model
	SPM model	REL model	
0.05	204	205	191
0.1	457	460	414
0.15	842	847	712
0.2	1575	1582	1185

Such a comparison shows that both analytical models yield an acceptable results. For very high eccentricity (about half the air-gap length) they both tend to overestimate the unbalanced forces, since they suffer from their approximations. Anyways, an eccentricity equal or higher than half the air-gap length means that there is a heavy fault in the machine rather than a problem in the machine assembling.

7.7. A rapid prediction of the air-gap flux density

The aim of this last Section is to show how to get a rapid estimation of the air-gap flux density and the unbalanced forces in the two machine topologies presented above.

As far as the SPM machine is concerned, the PM imposes the flux in the machine. A rapid prediction of the no-load air-gap flux density is achieved by means of

$$\hat{B}_g \approx \frac{B_{rem}}{1 + \frac{\mu_{rec} g_0}{t_m}} \quad (7.48)$$

Therefore, the variation of the air-gap flux density is computed by substituting $(g_0 + e)$ and $(g_0 - e)$ for g_0 . By introducing the data of Table 7.1 it is possible to verify that a variation about 8% is found according to an eccentricity displacement of $e = 0.2 \text{ mm}$. In addition, the PM limits the stator current reaction, too. Let us refer to a sinusoidally distributed stator electric loading, that is, to its fundamental harmonic only, whose amplitude is \hat{K}_s . The flux density due to such an electric loading results in

$$\hat{B}_g \approx \frac{\mu_0}{g_0 + t_m/\mu_{rec}} \cdot \frac{\hat{K}_s R_s}{p} \quad (7.49)$$

which is limited not only by the air-gap but also by the PM thickness. Also in this case, the substitution of $(g_0 + e)$ and $(g_0 - e)$ for g_0 yields a very limited flux density variation. The maximum flux density variations computed with this simplified model agree with those shown in Fig. 7.10.

As far as the REL machine is concerned, the distance between stator and rotor iron is quite low, so that any change of the air-gap length causes a high flux density variation. With the same assumption of a sinusoidally distributed stator electric loading, the flux density is estimated as

$$\hat{B}_g \approx \frac{\mu_0}{g_0} \cdot \frac{\hat{K}_s R_s}{p} \quad (7.50)$$

According to this relationship, it is evident that the substitution of $(g_0 + e)$ and $(g_0 - e)$ for g_0 yields a quite high variation of the air-gap flux density.

7.8. FE comparison of complete stator SPM, REL, and PMAREL motors

This section deals with the comparison between eccentric SPM, REL, and PMAREL machines by means of FE models. The three machines are with a complete stator including slots, teeth, and back iron, as shown in Fig. 7.2 and Fig. 6.2 for SPM and REL or PMAREL machines, respectively. The iron with actual B-H curve is considered instead of linear iron. To the aim of a general comparison, both motors are compared at different current angles, number of poles, and stator windings.

The results of both REL and PMAREL have been shown in Chapter 6. However, the results of the SPM motor are presented in this section. Then, they are compared by those of REL and PMAREL machines. The overall radial force on the SPM rotor for all rotor position is also computed. Additionally, the maximum radial forces on the PMs are computed. Then, the performance of this motor is compared with that of the other two motors. For the purpose of fair comparison between the three motors, the used SPM motor has the same main geometrical dimensions of the other two motors, as reported in Table 7.1.

7.8.1. Comparison in healthy case (no eccentricity)

In case of SPM motor with concentric rotor, the radial force of each pole is computed. The results are shown in Table 7.3. It is noted that the force of the third pole compensates that acting on the first pole. Similarly, the force of the second pole almost cancels the force acting on the fourth pole. Therefore, the overall force on the rotor is equal to a few Newtons (can be approximated to zero). By comparing this motor with the other two motors in healthy case, it is noted that, the three motors exhibit the same radial force on the overall rotor.

Table 7.3: Radial forces acting on the poles of the SPM motor at $\theta_m = 0^\circ$ in healthy case (with no eccentricity).

F_r acting on the PMs [N]			
pole 1	pole 2	pole 3	pole4
588.9	588.4	588.7	588.9

7.8.2. Comparison in static eccentricity case

To compare the three motors, the same conditions of the static eccentricity, load angle and electric loading are considered. For the purpose of achieving lower torque ripple in PMAREL or REL motor [27], the asymmetric rotor geometry is preferred. Besides, from Fig. 6.5 (a), (b), and (c), it is noted that there is no significant difference between the radial forces acting on the overall rotor of REL and PMAREL motor in different eccentricity cases. Therefore, SPM motor is compared with PMAREL motor with asymmetric rotor geometry. Table 7.4 shows the worst radial forces on the rotor of PMAREL and SPM motor. It is noted that, the radial force on PMAREL rotor is 450 % and 510% of that acting on SPM rotor, in case of considering Ferrite and NdFeB PMs, respectively.

Table 7.4: Worst radial forces acting on the rotor PMAREL and SPM motor, with static eccentricity.

	SPM (NdFeB PMs)	PMAREL (Ferrite PMs)	PMAREL (NdFeB PMs)
rotor position	$\theta_m = 121^\circ$	$\theta_m = 304^\circ$	$\theta_m = 243^\circ$
F_r [N]	146	685	740

According to the rotor position which results the maximum radial force on the rotor ($\theta_m = 121^\circ$), the radial force acting each pole is computed as reported in Table 7.5. From Table 7.5, the fourth and the third poles are the most stressed because they are close to the minimum air-gap length. The worst radial force is on the fourth pole. By comparing Table 7.3 and Table 7.5, the radial force acting on worst pole is increased by 12% due to the static eccentricity.

Table 7.5: Radial forces acting on the poles of the SPM motor, with static eccentricity, at $\theta_m = 121^\circ$.

F_r acting on the PMs [N]			
pole 1	pole 2	pole 3	pole 4
559.8	547.2	622.3	661.5

Due to the variation of the air-gap flux density with the load angle, the comparison is carried out at different values of load angles, as shown in Fig. 7.17. It is noted that, the unbalanced forces in case of PMAREL and REL motor are higher than that in case of SPM motor for the possible range of load angle.

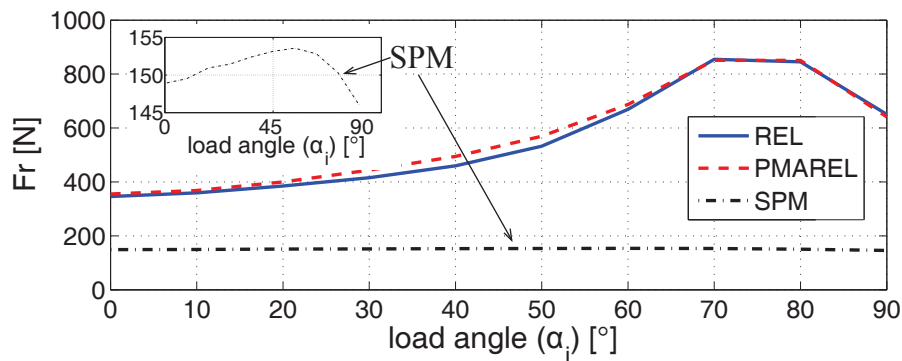


Figure 7.17: Radial forces versus load angle for REL, PMAREL, and SPM motors at rotor positions of worst cases.

The previous comparison is carried out when the distributed windings are considered in the stator. Therefore, this comparison is repeated when fractional slot concentrated windings (FSCW) is adopted in order to identify which is the worst winding configuration in case of eccentricity. Due to the high unbalanced radial force for single layer FSCW at healthy case, as shown in [63] and Chapter 4, the comparison is carried out only for double layer FSCW. As

an example 6-slot four-pole motors are adopted for this comparison. The radial force acting on the rotor of SPM and PMAREL motor is 116 N and 335 N, respectively. Therefore, with double layers FSCW, PMAREL motor is the worst motor in case of static eccentricity.

To ensure the generality of this comparison, the analysis is repeated for two different 36-slot six-pole motors. The radial force on SPM and PMAREL motor is 180 N and 1220 N, respectively. Once again, PMAREL motor is the worst in case of static eccentricity.

7.8.3. Comparison in dynamic eccentricity case

The same dynamic eccentricity described before, as shown in Fig. 6.1 (b), are applied on the SPM motor. The radial force on the rotor of PMAREL motor is about 430% and 480% of that on the rotor of the SPM motor, in case of using Ferrite and NdFeB PMs, respectively. The maximum force acting on the rotor of SPM motor is at $\theta_m = 240^\circ$. Table 7.6 shows the radial force acting on each pole. The most stressed PM is that of the first pole. From, Table 7.3 and Table 7.6, the force acting on that pole is increased by 10% due to the dynamic eccentricity.

Table 7.6: Radial forces acting on the poles of the SPM motor, with dynamic eccentricity, at $\theta_m = 240^\circ$.

F_r acting on the PMs [N]			
pole 1	pole 2	pole 3	pole4
648.2	584.7	536.1	593.2

Once again, this comparison is carried out at the following conditions: a) different load angles, b) different number of poles, and c) double layer FSCW in the stator. As expected, PMAREL motor is the worst for all load angles range, as in static eccentricity case.

In case of using FSCW, the radial force on SPM and PMAREL motor is 113 N and 282 N, respectively. Considering six pole motors, the radial force on SPM and PMAREL motor is 179 N and 1288 N, respectively. Therefore, PMAREL is the worst motor also in case of dynamic eccentricity.

Furthermore, Fig. 7.18 shows the electro-magnetic torque of both motors in both healthy and eccentricity. It is noted that, there are negligible effect of eccentricity on the torque. The impact of eccentricity on the flux linkage in d and q axes is shown in Fig. 7.19 for both motors. It is noted that, there are slight reduction in d -axis in case of PMAREL motor. There are negligible effect on flux linkage in case of SPM motor.

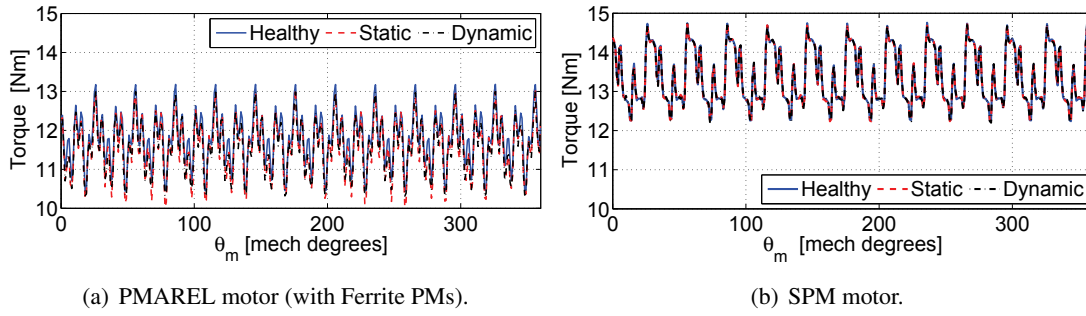


Figure 7.18: Torque versus rotor position at healthy condition (no eccentricity) and eccentricity in case of (a) PMAREL motor (with Ferrite), (b) SPM motor.

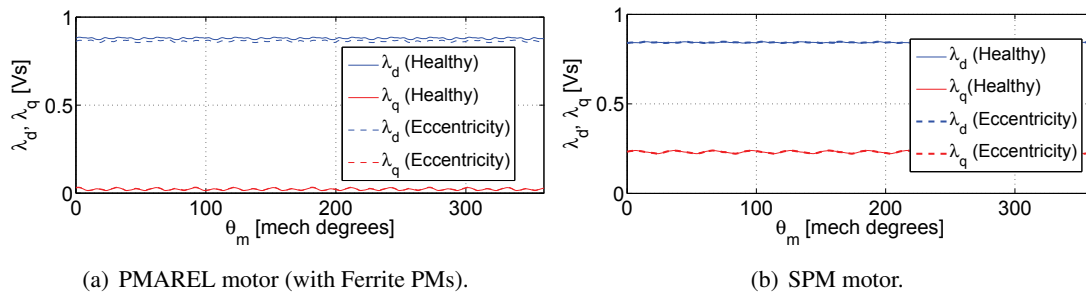


Figure 7.19: Flux linkage versus rotor position at healthy condition (no eccentricity) and eccentricity in case of (a) PMAREL motor (with Ferrite), (b) SPM motor.

7.8.4. Comparison in combined eccentricity case

The previous two eccentricity scenarios are combined together. Then, it is applied to the SPM motor with the same axis of rotation used for both another motors, as shown in Fig. 6.1 (c). The radial force on the rotor of PMAREL motor is about 430% and 480% of that on the rotor of the SPM motor, in case of using Ferrite and NdFeB PMs, respectively. The radial forces acting on each pole is computed, as reported in Table 7.7. The most stressed pole is the first pole, as occurs in the dynamic eccentricity. Once again, the same comparison is repeated in case of adopting FSCW, wide range of load angles, and different number of pole. As expected, the PMAREL motor is the worst in case of combined eccentricity too.

Table 7.7: Radial forces acting on the poles of the SPM motor, with combined eccentricity, at $\theta_m = 0^\circ$.

F_r acting on the PMs [N]			
pole 1	pole 2	pole 3	pole4
647.9	584.8	536.1	593.0

7.9. Conclusions

Two analytical models are described for analysing SPM and REL machines with rotor eccentricity. The analytical models allow to compute the air-gap flux density, the magnetic pressure and the unbalanced radial force on the rotor.

The analytical models are used to compute the impact of the rotor eccentricity and to highlight which machine is more affected by such a phenomenon. A SPM and a REL machine with the same main geometrical dimensions are analysed, comparing them with different rotor eccentricities.

It is noted that, the eccentricity impact on the REL machine is much higher than that on the SPM machine. The FE analysis is carried out in order to validate the results achieved by means of both analytical models. There is a satisfactory agreement between FE and analytical results. Even if the analytical models tend to overestimate the unbalanced radial force when the eccentricity is higher than half an air-gap, they allow simulation time to be saved: both analytical models require few seconds, while the FE analysis needs some hours.

The REL and PMAREL machines are compared with the SPM machine. The complete stator and actual B-H curve of the iron are considered in the FE models of the three machines. Due to the slight difference between the REL and PMAREL (with Ferrite PMs) machines, in case of eccentricity, as concluded in Chapter 6, the comparison between PMAREL and SPM machines is enough. It is noted that, the radial force acting on PMAREL with Ferrite PMs machines is about 450%, 430%, and 430% with respect to SPM machine, in case of static, dynamic, and combined eccentricity cases, respectively. In case of NdFeB PMs, the radial force acting on PMAREL machines is about 510%, 480%, and 480% with respect to SPM machine, in case of static, dynamic, and combined eccentricity cases, respectively. Therefore, the impact of the eccentricity on SPM machines is lower than that on REL or PMAREL machines, even if there are high radial forces acting on the rotor poles.

The comparison between PMAREL or REL motor with SPM motor is carried out at different load angles, when FSCW is adopting, and when different number of poles is considered. It is noted that PMAREL or REL motor exhibits the highest forces for all previous conditions, in different eccentricity scenarios.

Part II

Non-Linear Analytical Computation

Analytical model of REL motor considering iron saturation and slotting effect

In this chapter, the analytical models of both concentric and eccentric REL motor, which presented in chapters 2 and 3, are improved by considering the stator slotting effect and the magnetic saturation in the stator and rotor iron paths. The slotting effect can be included by introducing an air-gap permeance function, which leads to improve the air-gap flux density distribution waveform. The saturation effect is considered by increasing the air-gap length by a specific quantity: the saturation factor K_{sat} . This factor presents the magnetic voltage drop in the stator and rotor iron parts. The parameters of both magnetic models are changed iteratively according to the saturation level in the various parts of the machine, when the convergence is achieved, the iterations stop. As an example, 36-slot 4-pole machine is analysed, considering three flux barriers per pole. Finite element analyses confirm the results achieved by means of the analytical models.

8.1. The effect of stator slotting

This section summarizes the history of the research carried out to consider the stator slotting effect in the analytical models of the electric machines. Then, the relative permeance function presented in [74] is used with the analytical models of the concentric and eccentric REL motor. Both models predicts the radial component of the air-gap flux density distribution. The tangential component has small value for this machine. Hence, the radial component of the relative complex permeance function presented in [74] will be multiplied by the air-gap flux density distributions result from the analytical models.

The presence of slotting influences the magnetic behavior in the air-gap region. As a consequence the flux density field within the air-gap is strongly modified by both slot opening geometry and air-gap length. As it is well known, the first studies of slotting effect were performed by Carter [75] in exploiting conformal transformation techniques. A further approach can be found in [62] following the guidelines analyzed deeply in [76]: a conformal transformation reduces the complex slotted geometry into slot-less geometry. The relative permeance

function ($\lambda_r(r, \theta_s)$) is calculated by analyzing a model of one slot of the PM machine. This permeance function is multiplied by the radial component of air-gap flux density ($B_g(r, \theta_s)$), to get the modified flux density. The relative permeance expression can be expressed in the form of a Fourier series, as

$$\lambda_r(r, \theta_s) = \Lambda_0(r) + \sum_{h=1}^{\infty} \Lambda_h(r) \cos(hQ_s\theta_s). \quad (8.1)$$

where Λ_h as well as Λ_0 are proper coefficients reported in [62], and Q_s is the number of stator slots. In [77], a similar formulation is presented.

All the previous techniques rely on the unique presence of radial magnetic field in the air-gap. However recently another method has been proposed [74] assuming a conformal mapping transformation based upon cylindrical coordinates: the magnetic field thus consists of its two real different radial and tangential components. From the Schwarz-Christoffel conformal mapping, the development of the formulation of a complex permeance function can be estimated in order to rescale the flux density slot-less waveform according to: $B(r, \theta_s) = B_{slotless}(r, \theta_s) \lambda(r, \theta_s)$.

A peculiarity of the last method is represented by the fact that the permeability exhibits a complex algebraic form:

$$\lambda(r, \theta_s) = \lambda_a(r, \theta_s) + j \lambda_b(r, \theta_s). \quad (8.2)$$

The flux density field waveform at the air-gap results in:

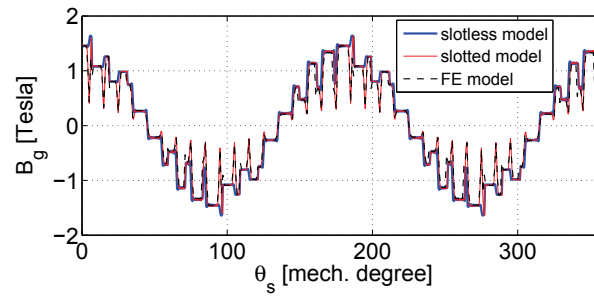
$$B_{sr} = B_r \lambda_a + B_\theta \lambda_b; \quad B_{s\theta} = B_\theta \lambda_a - B_r \lambda_b. \quad (8.3)$$

where all quantities are function of θ_s and r . The expressions for λ_a and λ_b are by far more complicated in terms of mathematical formulation and are reported in [74]. Once again, since, the analytical model of the REL motor estimates only the radial component of the air-gap flux density, the radial component of the relative permeability function, which described in [74], is only used. Hence, the modified air-flux density distribution can be achieved as

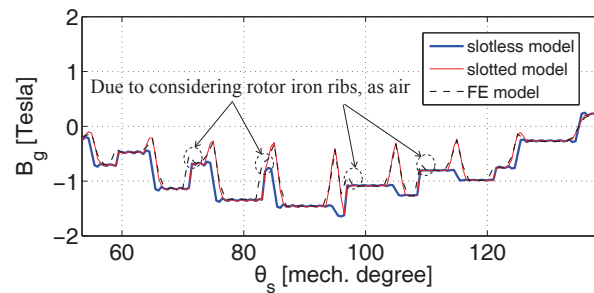
$$B_g(\theta_s) = B_{g_{slotless}}(\theta_s) \lambda_a(r, \theta_s) \quad (8.4)$$

Fig. 8.1 and Fig. 8.2 highlight the difference between the slot-less model and the slotted one, in healthy (no eccentricity) and eccentricity case, respectively. In fact, the flux density obtained by means of the procedure described by Zarko in [74], the slotted effect adjustment foresees very good agreement with FE results. Particularly, due to consistent permeance variation in front of the teeth, the flux density dips are fairly taken into account and represented correctly. Once again, the rotor iron ribs are neglected in both analytical and FE models. These ribs behave as slot opening causing some dips in the air-gap flux density waveform. A practical approach, which describes how to consider the iron ribs in the analytical model, will be presented at Appendix A.

Since the slotted air-gap flux density distribution (B_g) is obtained, the magnetic pressure and magnetic forces in x -axis and y -axis directions can be computed. The effect of slotting on the radial magnetic force can be noted, as in Fig. 8.3. There is a negligible difference between the analytical and FE slotted model. As expected, including the stator slots effect, the magnetic force is reduced comparing with slot-less model. Both dynamic and static eccentricity cases are shown in Fig. 8.3.

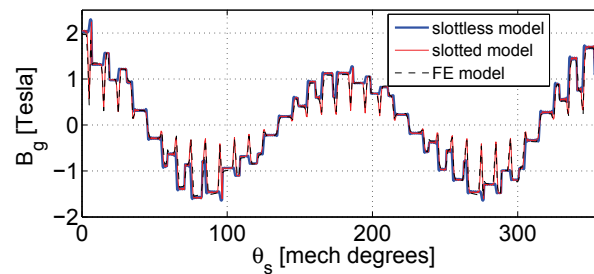


(a) Complete air-gap flux density distribution waveform

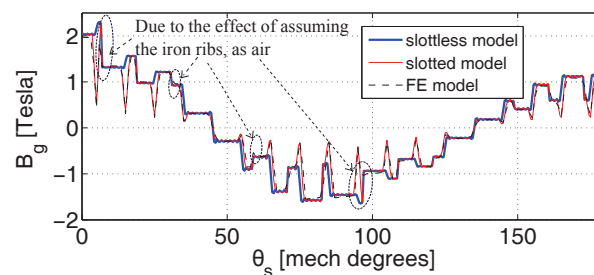


(b) Part of the air-gap flux density distribution waveform

Figure 8.1: Air-gap flux density distribution results from the analytical and FE models of concentric REL motor, without and with considering the stator slotting effect.



(a) Complete air-gap flux density distribution waveform



(b) First two poles air-gap flux density distribution waveform.

Figure 8.2: Air-gap flux density distribution results from the analytical and FE models of eccentric REL motor, without and with considering the stator slotting effect.

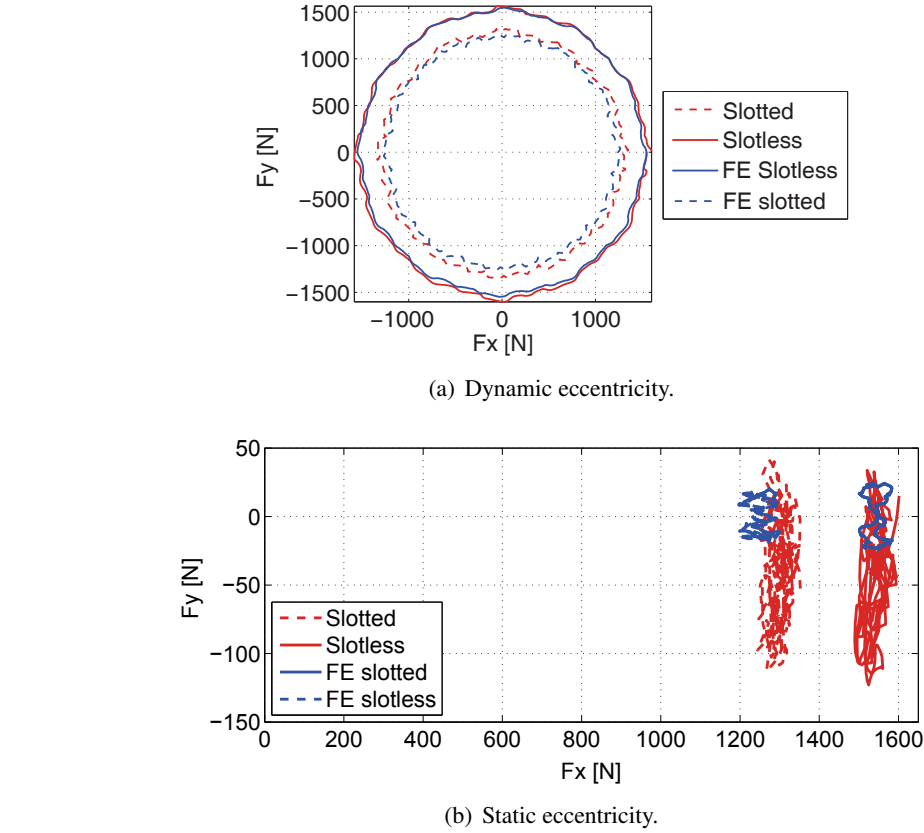


Figure 8.3: F_y versus F_x acting on the rotor of the REL machine with both eccentricity cases.

8.2. Saturation effect modeling

8.2.1. Basic idea of the saturation factor computation

The simple magnetic circuit shown in Fig. 8.4 is used to clarify the main idea of presenting the magnetic voltage drop in the real iron by means of saturation factor. The magnetic voltage drop occurs in the real iron path can be substituted by an equivalent voltage drop in the air-gap. This can be implemented by using higher equivalent air-gap length (g_e), as reported in eq. (8.5). As in eq. (8.6), this equivalent air-gap length is achieved by multiplying the air-gap length by a specific quantity, which is called saturation factor (K_{sat}). Since, the equivalent air-gap length is achieved, the accurate air-gap magnetic flux can be computed, and hence, the machine performance can be predicted, accurately.

$$MMF = H_g g + H_{fe} L_{fe} = H_g g_e \tag{8.5}$$

$$g_e = g \cdot K_{sat} \tag{8.6}$$

H_g and H_{fe} are the magnetic field intensity in the air-gap and the iron, respectively. L_{fe} is the length of the iron path shown in Fig. 8.4. From eqs. (8.5) and (8.6), the saturation factor can be expressed as

$$K_{sat} = \frac{H_g g + H_{fe} L_{fe}}{H_g g} \tag{8.7}$$

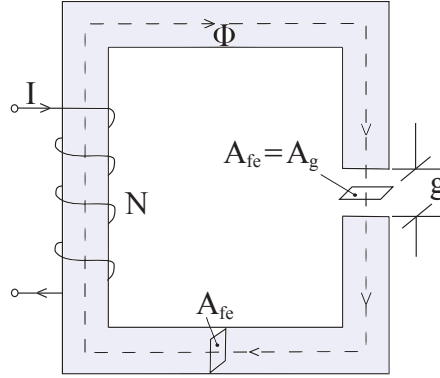


Figure 8.4: Simple Magnetic circuit

At the beginning, the magnetic voltage drop is neglected. Then, the air-gap magnetic flux is computed as $\phi = NI/R_g$. Since, the cross section of the iron part is constant and the fringing is neglected, as shown in Fig. 8.4, the magnetic flux density in the air-gap B_g and the iron B_{fe} are equal. Hence, the magnetic field intensity in the air-gap is given by ($H_g = B_g/\mu_0$). From B_{fe} and the B-H characteristic of the iron, the magnetic field intensity in the iron H_{fe} can be achieved. Finally, the saturation factor can be computed from eq. (8.7). However, this saturation factor is not accurate enough, because it is based on the neglecting of the voltage drop occurs in the iron. Therefore, an iterative approach is proposed to search for the proper saturation factor while the analytical results converge to the FE results. This iterative approach is shown in Fig. 8.5. To the aim of validating this iterative technique, two simple examples are analytically investigated and confirmed by the FE results.

The first example

As shown in Fig. 8.6, the model consists of the windings, which produces the magnetic flux, the air-gap, and ferromagnetic material with actual B-H curve. The boundary conditions are adopted to force the magnetic flux to flow through the air-gap in perpendicular direction, as in motor case. Then, it flows through the ferromagnetic material. The geometrical dimensions of the model are reported in Table 8.1. In addition, A_g is the area perpendicular to the air-gap flux considering the fringing effect. It is given by $w_{fe}L_{stk}/k_{fr}$, where k_{fr} is a factor to consider the fringing effect and is given by $\frac{w_{fe}}{w_{fe}+2*g}$. The magnetization curve of the used ferromagnetic material is shown in Fig. 8.7.

Table 8.1: The geometrical dimensions of the FE model of the first example.

g	the air-gap length = 0.0004 m,
L_{fe}	the iron path length = 0.0396 m,
w_{fe}	the iron block width = 0.04 m,
NI or MMF	the magneto motive force = 1500 AT,
L_{stk}	the iron block stack length = 0.04 m,

The analytical computations and the iterative approach shown in Fig. 8.5 have been carried out. Fig. 8.8 (b) shows the conversion of the iron flux density resulted from the analytical model

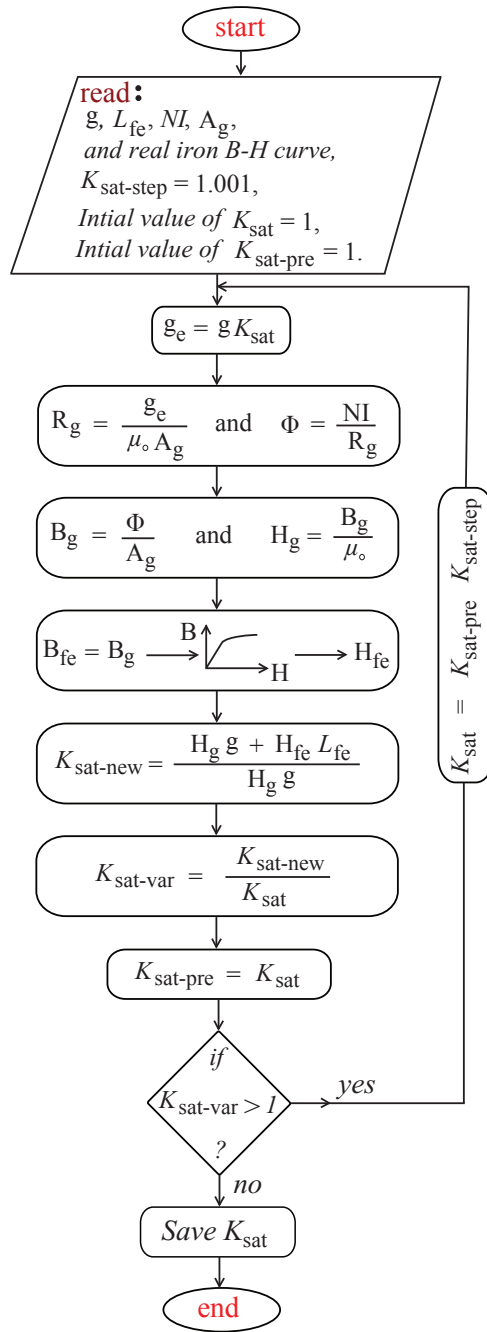


Figure 8.5: Iterative approach for computing the proper saturation factor.

to that resulted from the FE model, with increasing the number of iterations. The saturation factor is increased, until the variation of the saturation factor $K_{sat-var}$ is equal to one. From Fig. 8.8 (a), the final saturation factor is achieved equal to 2.4683.

Finally, B_g , H_g , B_{fe} , and H_{fe} are computed. To check the results, the total voltage drop $H_g g + H_{fe} L_{fe}$ is computed and compared with MMF, as reported in Table 8.2. It is noted that there are very good agreement between the total voltage drop and the MMF.

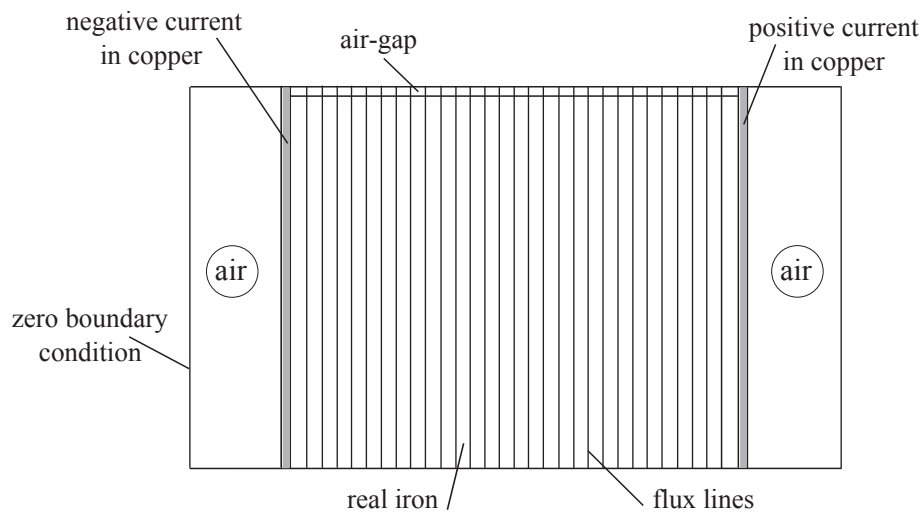


Figure 8.6: Cross section of the first example FE model.

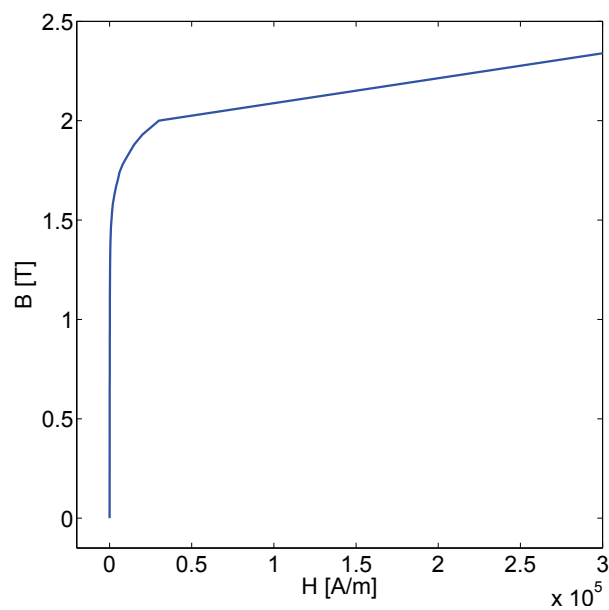


Figure 8.7: Magnetization curve of the ferromagnetic material used.

Table 8.2: Comparison between the results of the FE and the analytical model.

	FE model	Analytical model
B_g (Tesla)	1.89	1.91
H_g (A/m)	1503000	1519000
B_{fe} (Tesla)	1.96	1.95
H_{fe} (A/m)	24100	22500
NI (AT) (as check)	1500	1497.6

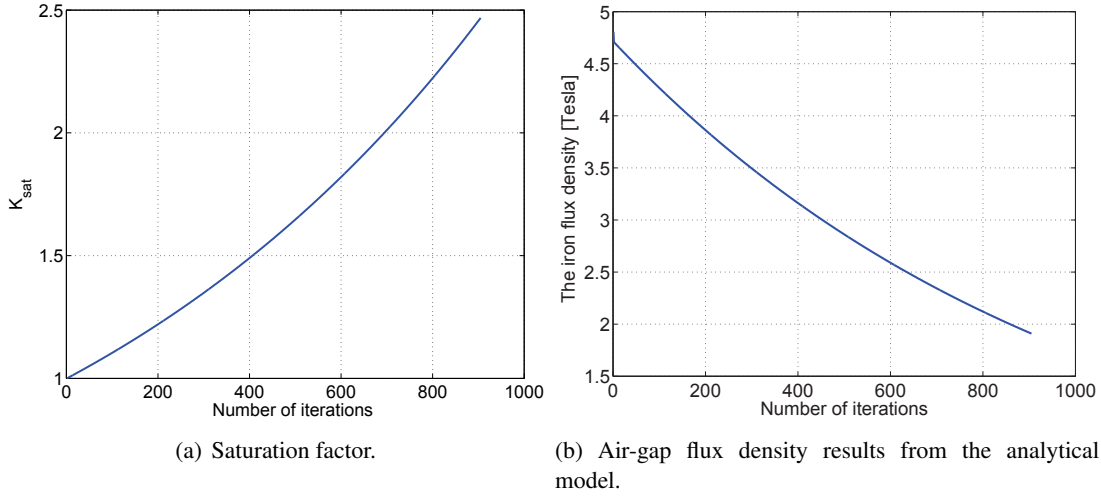


Figure 8.8: The saturation factor and the air-gap flux density versus the number of iterations.

8.2.2. The second example

To the aim of checking the reliability of the iterative approach, another model is built with different geometry, as shown in Fig. 8.9. To increase the accuracy of the results, the iron block is divided into N_{step} numbers of small blocks have equal iron path length, as shown in Fig. 8.9 ($N_{step} = 8$ is taken, as an example). Besides, the saturation factor step $K_{sat,step}$ is set equal to 1.0001.

The iron path length of each block ($L_{fe_{bi}}$) can be calculated by dividing the total iron path length L_{fe} into the number of blocks N_{step} . The width of the i -th iron block (w_{bi}) can be computed as in eq. (8.8). The dimensions of the second model are similar to those of the first model, however, the width w_g (is the width of the upper part of the iron block) is equal to 0.04 m and w_e (is the width of the lower part of the iron block) is equal to 0.02 m. Once again, the same iron B-H characteristic shown in Fig. 8.7 is used.

At first, the magnetic voltage drop in the iron is neglected, then, the magnetic flux is computed. After that, the flux density in each block ($B_{fe_{bi}}$) is computed. From the B-H curve of the ferromagnetic material and the $B_{fe_{bi}}$, the magnetic field intensity of each block ($H_{fe_{bi}}$) is achieved. Then, the saturation factor is computed as in eq. (8.9). Finally, iteration approach shown in Fig. 8.5 is applied on the second model.

$$w_{bi} = w_g - \frac{(w_g - w_e)}{N_{step}}i + \frac{(w_g - w_e)}{2N_{step}} \quad (8.8)$$

$$K_{sat-new} = \frac{H_g g + \sum_{i=1}^{i=N_{step}} H_{fe_{bi}} L_{fe_{bi}}}{H_g g} \quad (8.9)$$

The final saturation factor is resulted equal to 4.0323. Besides, the results of the analytical model and the FE model are compared together, as shown in Table 8.3. From the comparison, it is noted that there are a good agreement between the two model results. The final check of total MMF is carried out, as reported in Table 8.3. From the results of the two previous examples,

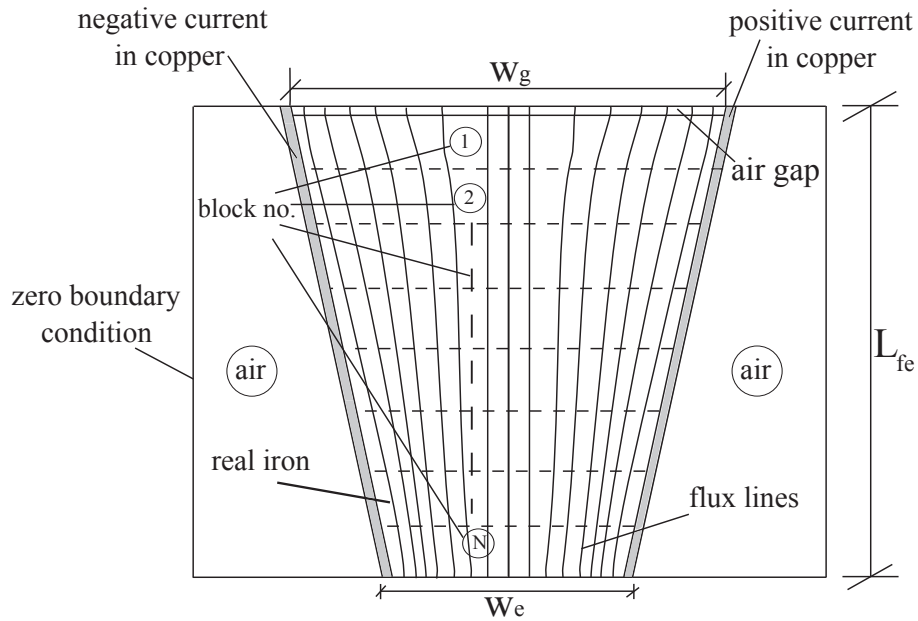


Figure 8.9: Cross section of the second example FE model.

Table 8.3: Comparison between the results of the FE and the analytical model of the second example.

	FE model results	The Analytical model results
B_g (Tesla)	1.19	1.17
H_g (A/m)	948700	930000
B_{fe1} (Tesla)	1.262	1.2064
B_{fe1} (Tesla)	1.364	1.29
B_{fe1} (Tesla)	1.469	1.385
B_{fe1} (Tesla)	1.585	1.496
B_{fe1} (Tesla)	1.714	1.63
B_{fe1} (Tesla)	1.858	1.781
B_{fe1} (Tesla)	2.016	1.97
B_{fe1} (Tesla)	2.185	2.1998
H_{fe} (A/m)	303.6	268.8
H_{fe} (A/m)	561.1	347.48
H_{fe} (A/m)	1160	550.294
H_{fe} (A/m)	2887	1132.5
H_{fe} (A/m)	6505	2919.5
H_{fe} (A/m)	16450	8055.2
H_{fe} (A/m)	61880	25469
H_{fe} (A/m)	155300	189030
NI (AT) (as check)	1500	1499.5

it is concluded that the iterative approach is a practical approach and it can be implemented on the REL motor analytical model.

8.2.3. Saturation factors of concentric REL motor

Some analytical works have already taken into account the magnetic saturation of the motor iron parts, as in [78–82]. For the induction motor, in [78], the air-gap is modelled in the sinusoidal form to consider the magnetic voltage drop in the iron parts. For the surface PM motors, the magnetic saturation in the teeth are considered in [80]. The magnetic saturation in the teeth tips, as well as, the stator and rotor back iron is considered in [81, 82]. The saturation effect is considered by increasing the air-gap length by a specific quantity: the saturation factor K_{sat} . This factor considers the magnetic voltage drop in the stator and rotor iron parts. The parameters of the magnetic model are changed iteratively according to the saturation level in the various parts of the machine, when the convergence is achieved, the iterations stop: This technique has not been introduced in [81]. Thus, the complete matching between the analytical and FEA results has not been achieved yet. This section aims to fill this gap.

In the REL machine, due to the high non-linearity in the rotor geometry, it is not easy to consider the saturation effect of the rotor and stator iron in one unique saturation factor, as in [81, 82]. Thus, independent saturation factors for both stator and rotor are computed. Firstly, the saturation effect of the stator iron is considered. Secondly, the saturation effect of the rotor iron is considered.

8.2.4. Stator saturation factors

From the linear analytical model presented in section II and III, the radial air-gap flux density distribution $B_g(\theta_s)$ is computed. From Fig. 8.10, the magnetic flux flows through each tooth is given by

$$\phi_{t_i} = \int_{\gamma_s + (i-1)\alpha_{slot}}^{\gamma_s + i\alpha_{slot}} B_g(\theta_s) \frac{D}{2} L_{stk} d\theta_s \tag{8.10}$$

where α_{slot} and γ_s are the slot angle and the angle between the first slot center and the d-axis, respectively.

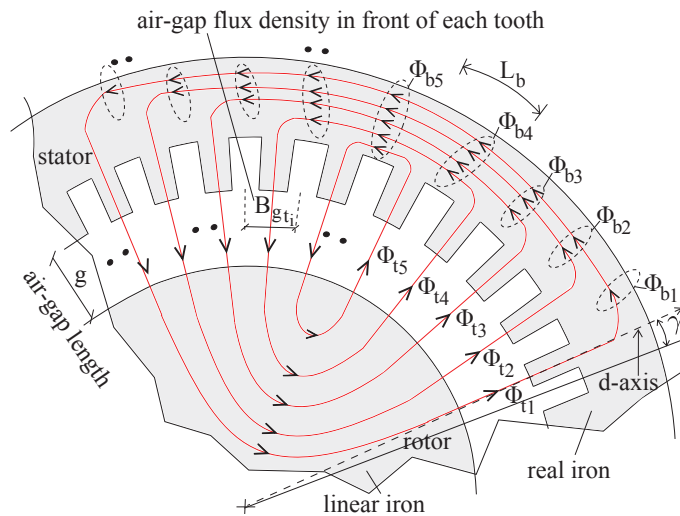


Figure 8.10: Cross section of the stator of REL machine considering rotor with linear iron.

Then, the flux density in each tooth, $B_{t_i} = \phi_{t_i}/(w_t h_t)$, can be computed, and from the B-H iron characteristic, the field intensity for each tooth, H_{t_i} , is achieved. Consequently, the magnetic voltage drop on each tooth $U_{t_i} = H_{t_i} h_t$ is computed, where w_t and h_t are the width and the height of the stator tooth, respectively.

The fluxes which flow through the different parts of the stator back iron, as shown in Fig. 8.10, have to be computed in order to derive the magnetic voltage drop in these parts. The main issue for computing these fluxes resides on the position dependency of the peak of $B_g(\theta_s)$, which in turns depends on the operating current angle. Therefore, the flux computations are generalized, as follows. Starting from any tooth (let us start with the first tooth), let's consider $\phi_{b_1} = \phi_{t_1}$. Then, the other fluxes are computed as $\phi_{b_i} = \phi_{t_i} + \phi_{b_{i-1}}$. To calibrate the starting point assumption, the average of the computed back iron fluxes is subtracted from the flux of each back iron part.

Similarly, the flux density in each back iron part is computed as $B_{b_i} = \phi_{b_i}/(L_{stk} h_b)$, where h_b is the back iron height. Once again, the flux intensity in each back iron part H_{b_i} is obtained from the B-H iron curve. Then, the magnetic voltage drop in each back iron part is computed as $U_{b_i} = H_{b_i} l_b$, where l_b is the flux path length of each back iron part, as shown in Fig. 8.10, given by $\pi(D_{se} - h_b)/Q_s$, where D_{se} is the external stator diameter.

The saturation factors ($K_{sat-new}$) in front of the stator teeth are computed, as explained in Fig. 8.11, where $U_{path_{b_i}}$ and H_{gt_i} are the magnetic voltage drop in each stator back iron complete path, as shown in Fig. 8.10, and the field intensity in front to each stator tooth, respectively.

Finally, the computations of these saturation factors are carried out within an iterative scheme to get the accurate saturation factor to modify the air-gap length in front to each stator tooth. This iterative approach is deeply explained in Fig. 8.12.

The air-gap flux density distribution for the first half pole considering the stator saturation effect is compared with FE results, as shown in Fig. 8.13. It is noted that there is a good agreement between both models. To test the generality of the modified analytical model, the air-gap flux density distributions which result from both analytical and FE models, are compared together at different rotor positions, current angles, and electric loading. From Fig. 8.13 and Fig. 8.14, it is noted that there is a good agreement at different rotor positions. From Fig. 8.13 and Fig. 8.15, the model is valid for different electric current angles. In addition, the modified analytical model is valid for different electric current angle (i.e., different saturation levels), as noted from Fig. 8.13 and Fig. 8.16.

8.2.5. Rotor saturation factors

Analogously, the saturation factor of the rotor islands and rotor channels, shown in Fig. 8.17, can be computed as presented for the stator part. The main idea is to compute the magnetic voltage drop which occurs in each rotor island and rotor channel. In the example, REL machine, with three flux-barriers per pole, has three rotor islands and one channel per pole, as shown in Fig. 8.17. From the air-gap flux density distribution resulting from the previous section, the fluxes entering and going out from the first rotor island can be computed as

$$\phi_{in_1} = \int_{\frac{\pi}{2p} - \theta_{b1}}^{\frac{\pi}{2p}} B_g(\theta_s) \frac{D}{2} L_{stk} d\theta_s \quad \text{and} \quad \phi_{out_1} = \int_{\frac{\pi}{2p}}^{\frac{\pi}{2p} + \theta_{b1}} B_g(\theta_s) \frac{D}{2} L_{stk} d\theta_s \quad (8.11)$$

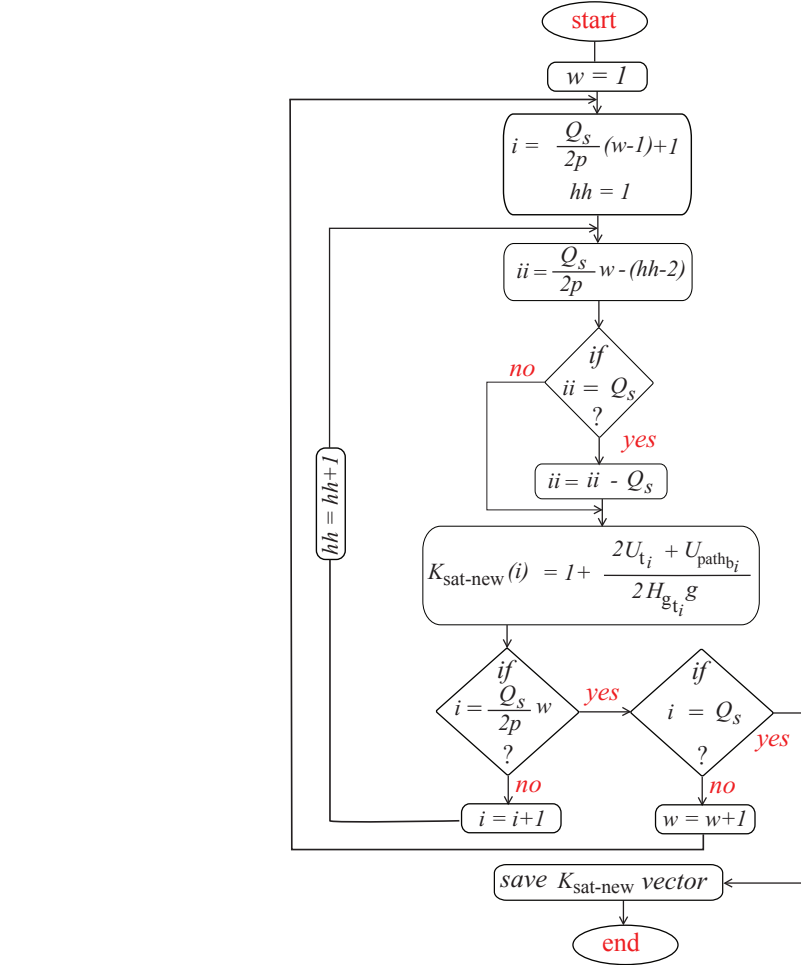


Figure 8.11: Computation of the saturation factors of the different stator parts, in case of no eccentricity.

From ϕ_{in1} and ϕ_{out1} , the magnetic flux flowing through the first barrier (ϕ_{b1}) is given by $\phi_{in1} - \phi_{out1}$. Hence, the flux flowing through the first island $\phi_{island1}$ is given by $\phi_{in1} - \phi_{b1}$. However, the flux flows through the second island is given by $\phi_{in2} - \phi_{b2} + \phi_{b1}$ as explained in Fig. 8.17, where ϕ_{in2} and ϕ_{out2} are given by

$$\phi_{in2} = \int_{\frac{\pi}{2p} - \theta_{b2}}^{\frac{\pi}{2p} - \theta_{b1}} B_g(\theta_s) \frac{D}{2} L_{stk} d\theta_s \quad \text{and} \quad \phi_{out2} = \int_{\frac{\pi}{2p} + \theta_{b1}}^{\frac{\pi}{2p} + \theta_{b2}} B_g(\theta_s) \frac{D}{2} L_{stk} d\theta_s \quad (8.12)$$

The same procedure is repeated for the third island. Then, the flux-density in these islands can be computed as $B_{island_i} = \phi_{island_i} / (w_{r_i} L_{stk})$, where w_{r_i} is the width of the i -th iron path [83]. Hence, the field intensity H_{island_i} is obtained from the B-H iron curve. Finally, the saturation factor for the i -th rotor island is given by

$$K_{sat_{island_i}} = 1 + \frac{\mu_o H_{island_i} L_{island}}{2 B_{g_{island_i}} g} \quad (8.13)$$

where $B_{g_{island_i}}$ is the average air-gap flux density in front of the i -th rotor island. The rotor channel is approximated, as shown in Fig. 8.17. Similarly, the saturation factor of this channel

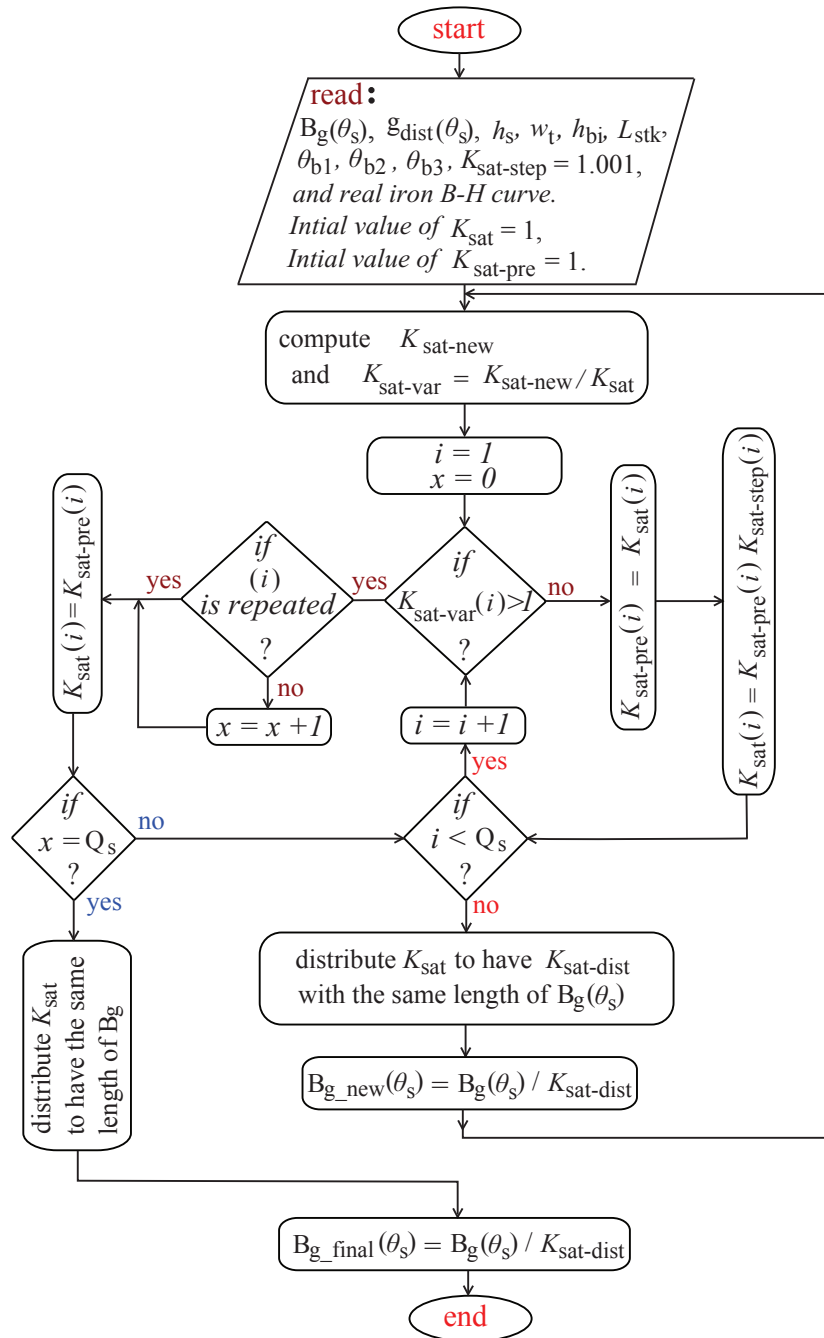


Figure 8.12: Iterative approach for computing the proper saturation factors of the different stator iron parts.

is computed, as carried out for the first island. Thanks to the symmetry, in healthy case, the computed saturation factors for the first pole are the same for the other poles. Again, as for the stator, an iterative technique shown in Fig. 8.12 is combined to this computation to get the most accurate values of these saturation factors. The final air-gap flux density distribution for the first half pole considering the stator and rotor saturation effects is shown in Fig. 8.18.

Once again, the results of the improved analytical model are confirmed by the FE analysis

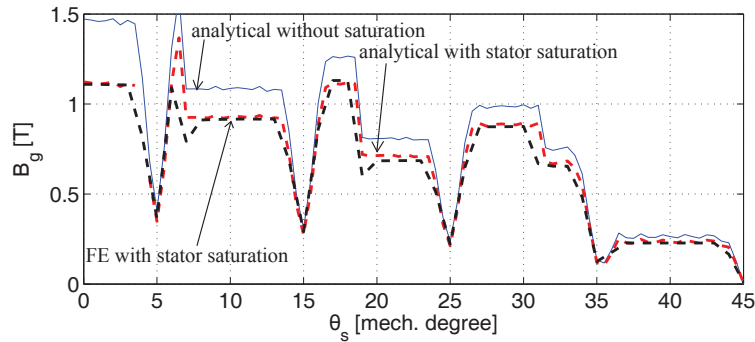


Figure 8.13: Air-gap flux density distribution results from the analytical and FE models considering the stator saturation effect at rotor position $\theta_m = 0^\circ$, with electric current angle $\alpha_i^e = 45^\circ$ and electric loading $\hat{K}_s = 6200A/m$.

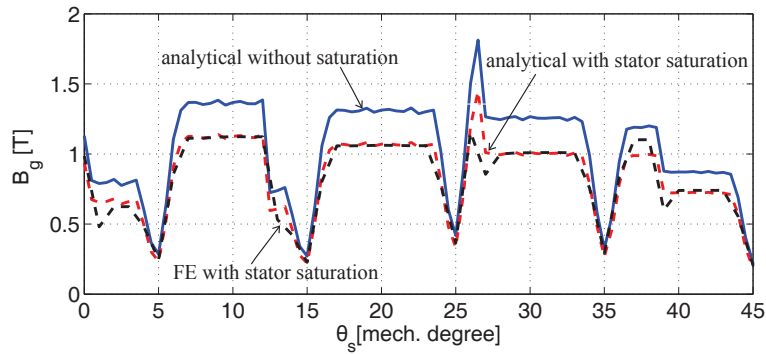


Figure 8.14: Air-gap flux density distribution results from the analytical and FE models considering the stator saturation effect at rotor position $\theta_m = 20^\circ$, with electric current angle $\alpha_i^e = 45^\circ$ and electric loading $\hat{K}_s = 6200A/m$.

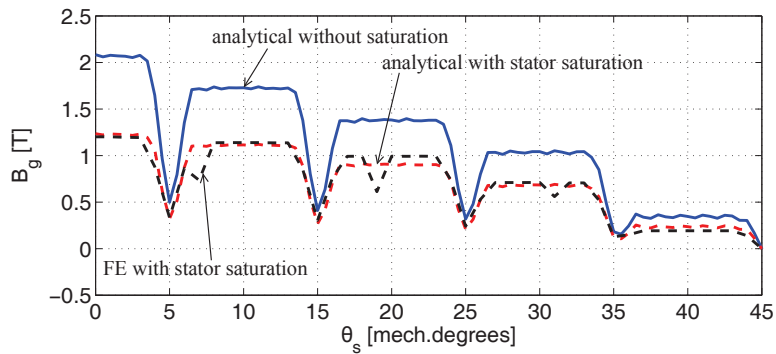


Figure 8.15: Air-gap flux density distribution results from the analytical and FE models considering the stator saturation effect at rotor position $\theta_m = 0^\circ$, with electric current angle $\alpha_i^e = 0^\circ$ and electric loading $\hat{K}_s = 6200A/m$.

at different rotor position, current angle, and electric loading or saturation level, as shown in Fig. 8.19, Fig. 8.20, and Fig. 8.21, respectively. It is noted that the modified analytical model is valid for a general operating condition.

Since, the air-gap flux density is computed, the electro-magnetic torque can be estimated.

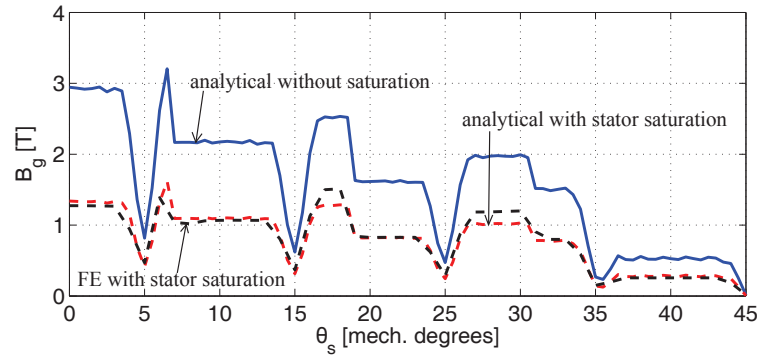


Figure 8.16: Air-gap flux density distribution results from the analytical and FE models considering the stator saturation effect at rotor position $\theta_m = 0^\circ$, with electric current angle $\alpha_i^e = 45^\circ$ and electric loading $\hat{K}_s = 17650 A/m$.

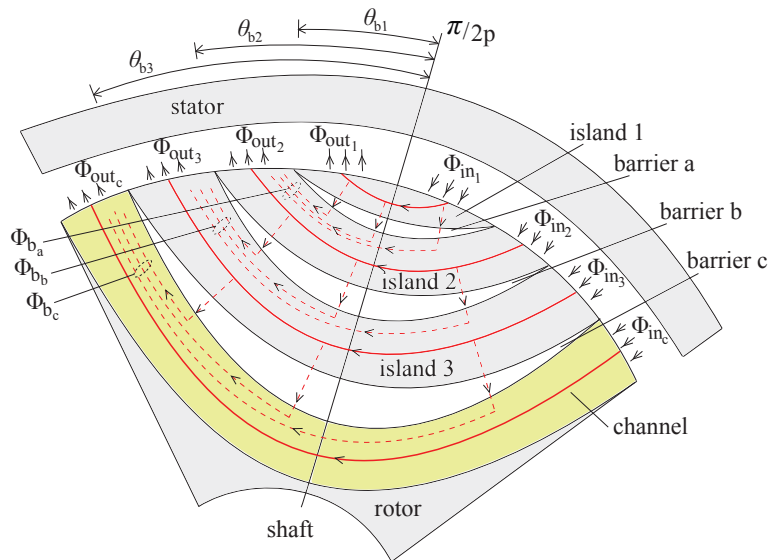


Figure 8.17: Cross section of the rotor of REL machine considering stator with linear iron.

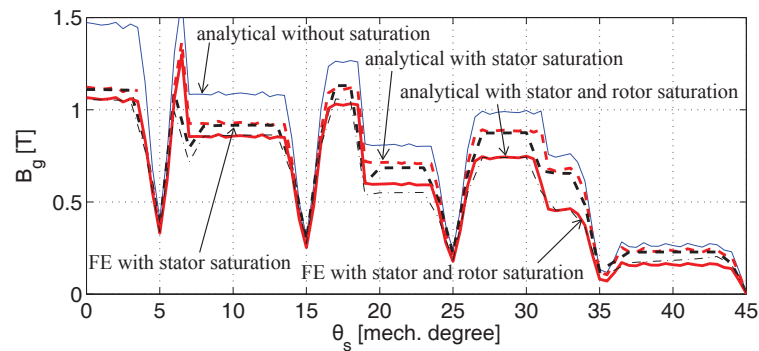


Figure 8.18: Air-gap flux density distribution results from the analytical and FE models considering the stator and rotor saturation effect at rotor position $\theta_m = 0^\circ$, with electric current angle $\alpha_i^e = 45^\circ$ and electric loading $\hat{K}_s = 6200 A/m$.

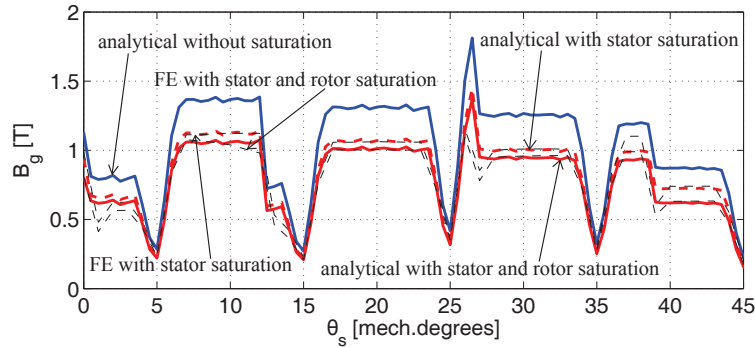


Figure 8.19: Air-gap flux density distribution results from the analytical and FE models considering the stator and rotor saturation effect at rotor position $\theta_m = 20^\circ$, with electric current angle $\alpha_i^e = 45^\circ$ and electric loading $\hat{K}_s = 6200 A/m$.

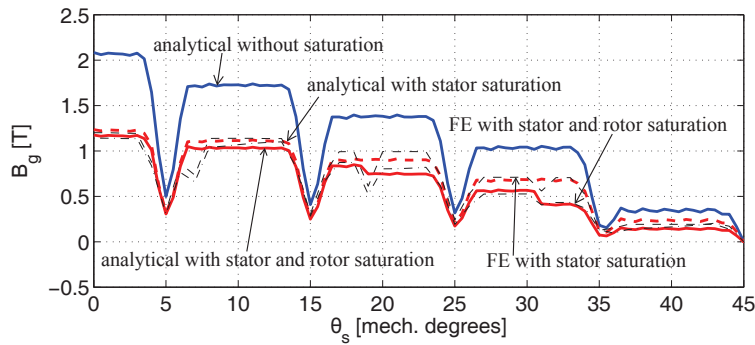


Figure 8.20: Air-gap flux density distribution results from the analytical and FE models considering the stator and rotor saturation effect at rotor position $\theta_m = 0^\circ$, with electric current angle $\alpha_i^e = 0^\circ$ and electric loading $\hat{K}_s = 6200 A/m$.

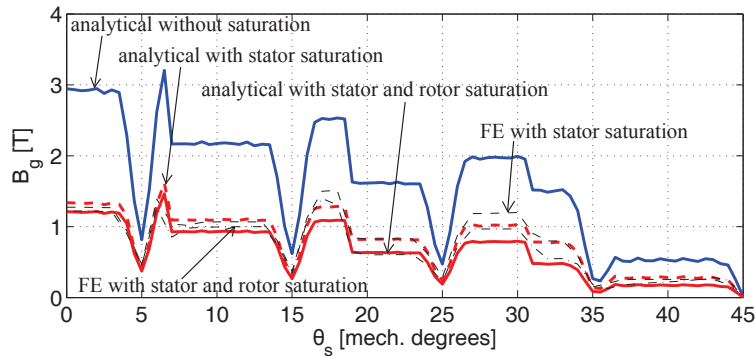


Figure 8.21: Air-gap flux density distribution results from the analytical and FE models considering the stator and rotor saturation effect at rotor position $\theta_m = 0^\circ$, with electric current angle $\alpha_i^e = 45^\circ$ and electric loading $\hat{K}_s = 17650 A/m$.

Fig. 8.22 (a) and Fig. 8.23 (a), shows the electro-magnetic torque waveforms result from the analytical model at different electric loading values (at $\hat{K}_s = 6200 A/m$ and $\hat{K}_s = 17650 A/m$, respectively). In addition, the electro-magnetic torque waveforms result from the FE analysis, at the same electric loading conditions, are shown in Fig. 8.22 (b) and Fig. 8.23 (b).

It is noted that the behaviour is different, even though the averages are close. In particular, while the analytical waveform resembles the linear one, shown in Chapter 4, the FE waveform is smooth out, showing a higher torque ripple though, mostly due to the slot harmonics (i.e., 18th harmonic and its multiples). This can be noted by comparing the torque spectrum of both models. The analytical torque spectrum is shown in Fig. 8.22 (c) and Fig. 8.23 (c) at $\hat{K}_s = 6200A/m$ and $\hat{K}_s = 17650A/m$, respectively. Besides, the FE torque spectrums are shown in Fig. 8.22 (d) and Fig. 8.23 (d), respectively.

The average torque and the torque ripple resulted from both models at different electric loading are reported in Table 8.4 and Table 8.5. It is noted that the improved analytical model accurately predicts the average torque at different electric loading values. However, it underestimate the torque ripple. Several FE simulations are carried out to identify the reason of the peaks of Fig. 8.22 (b) and Fig. 8.23 (b). It is noted that, they are caused by the interaction between the local saturation occurs close to the barrier ends and the stator teeth. By sharpening the barrier ends, a lower torque ripple and a smaller 18th harmonic effect in the FE results is achieved. Besides, the FE torque trend resembled more that of the linear case. The improved analytical model does not consider the local saturation occurs close to the barrier ends.

Table 8.4: Comparison between the electro-magnetic torque results from the FE and the analytical model at electric loading equal to 6200A/m.

	FE model	Analytical model
Average torque (Nm)	0.72	0.71
Torque ripples %	38	19

Table 8.5: Comparison between the electro-magnetic torque results from the FE and the analytical model at electric loading equal to 17650A/m.

	FE model	Analytical model
Average torque (Nm)	4.72	4.68
Torque ripples %	43.53	32.35

Table 8.6 reports the specific eddy current losses and the total eddy current losses in the islands and channels of a rotor pole. The electric loading is set equal to 6200A/m (at $J = 1.06A/mm^2$). The total rotor eddy current losses results from the analytical and FE models are equal to 12.176 [W] and 10.5 [W], respectively. Similarly, the iron losses computation are repeated at higher electric loading 17650A/m (at $J = 3A/mm^2$). Then, the results are reported in Table 8.7. The total rotor eddy current losses results from the analytical and FE models are equal to 94.72 [W] and 43.9 [W], respectively.

It is noted that the results are quite different with respect to the linear case. In addition, the analytical model overestimates the FE model. Fig. 8.24 and Fig. 8.25 show the analytic and FE spectrum of the specific eddy current losses of the islands and channels at $\hat{K}_s = 6200A/m$ and $\hat{K}_s = 17650A/m$, respectively. From the harmonic spectrum of both models shown in Fig. 8.24, it is noted that all harmonics are close a part from the 18th one. On the contrary, Fig. 8.25 shows that there is not a general behavior for the rotor losses at higher current: some are underestimated and some other are overestimated. Thus, the analytical model does not predict the rotor eddy current losses accurately.

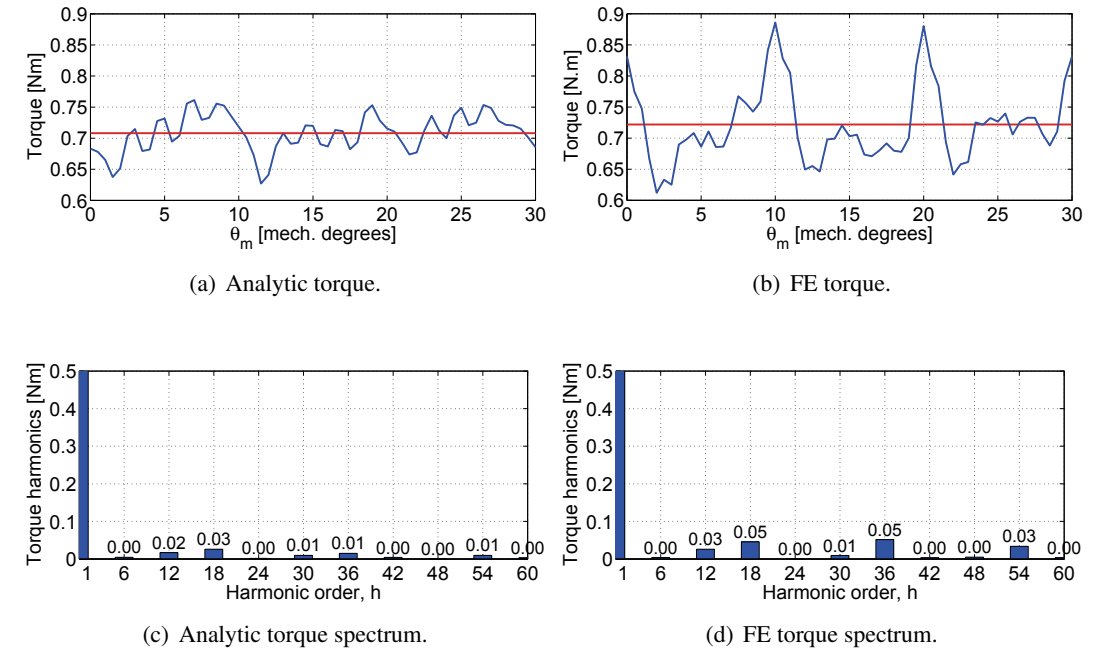


Figure 8.22: Comparison between the analytical and FE torque with electric current angle $\alpha_i^e = 45^\circ$ and electric loading $\hat{K}_s = 6200A/m$.

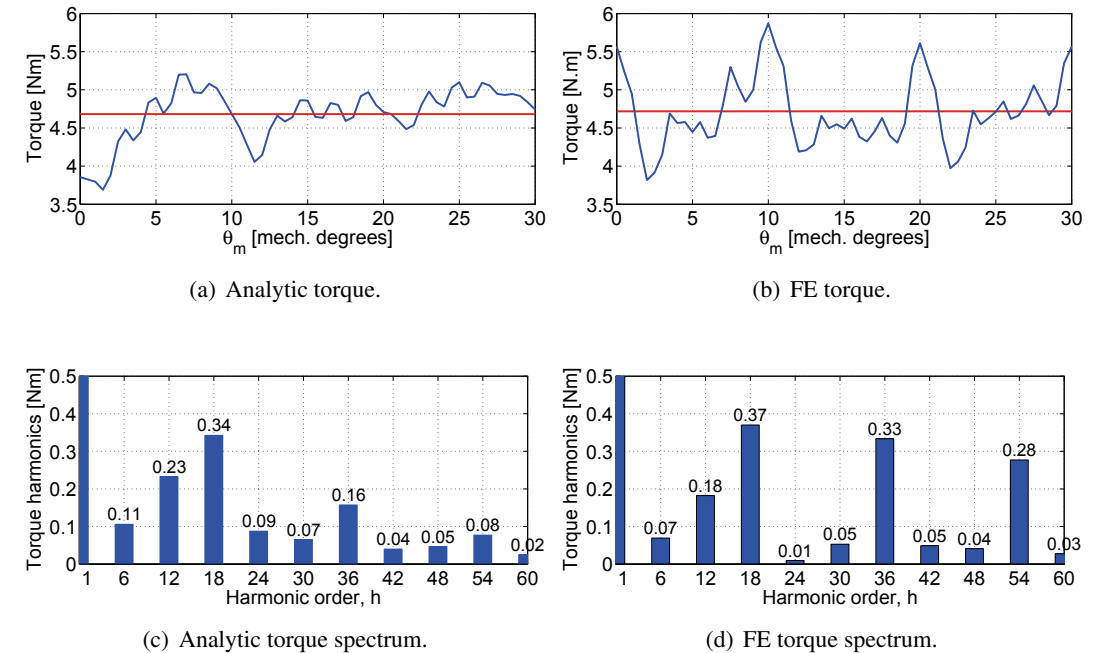


Figure 8.23: Comparison between the analytical and FE torque with electric current angle $\alpha_i^e = 45^\circ$ and electric loading $\hat{K}_s = 17650A/m$.

8.2.6. Saturation factors of eccentric REL motor

One of advantages of the analytical model is the short simulation time consuming. However, this analytical model is based on some assumption, as mentioned before in Chapter 3. One of

Table 8.6: The eddy current loss of a rotor pole, which results from the analytical and FE model at $J = 1.06A/mm^2$ and $\alpha_i^e = 45^\circ$.

rotor part	Analytic [W/kg]	FE [W/kg]	volume [m ³]	mass [Kg]	Analytic [W]	FE [W]
first island	25.171	24.619	$1.342 \cdot 10^{-6}$	0.011	0.277	0.271
second island	7.452	6.504	$8.715 \cdot 10^{-6}$	0.068	0.507	0.442
third island	3.874	3.487	$2.282 \cdot 10^{-5}$	0.178	0.690	0.621
channel	7.696	6.329	$2.609 \cdot 10^{-5}$	0.204	1.570	1.291
total	44.193	40.939	$5.897 \cdot 10^{-5}$	0.461	3.044	2.625

Table 8.7: The eddy current loss of a rotor pole, which results from the analytical and FE model at $J = 3A/mm^2$ and $\alpha_i^e = 45^\circ$.

rotor part	Analytic [W/kg]	FE [W/kg]	volume [m ³]	mass [Kg]	Analytic [W]	FE [W]
first island	85.316	128.345	$1.342 \cdot 10^{-6}$	0.011	0.938	1.412
second island	58.985	30.402	$8.715 \cdot 10^{-6}$	0.068	4.011	2.067
third island	27.370	14.942	$2.282 \cdot 10^{-5}$	0.178	4.872	2.660
channel	67.939	23.352	$2.609 \cdot 10^{-5}$	0.204	13.860	4.764
total	239.61	197.04	$5.897 \cdot 10^{-5}$	0.461	23.68	10.9

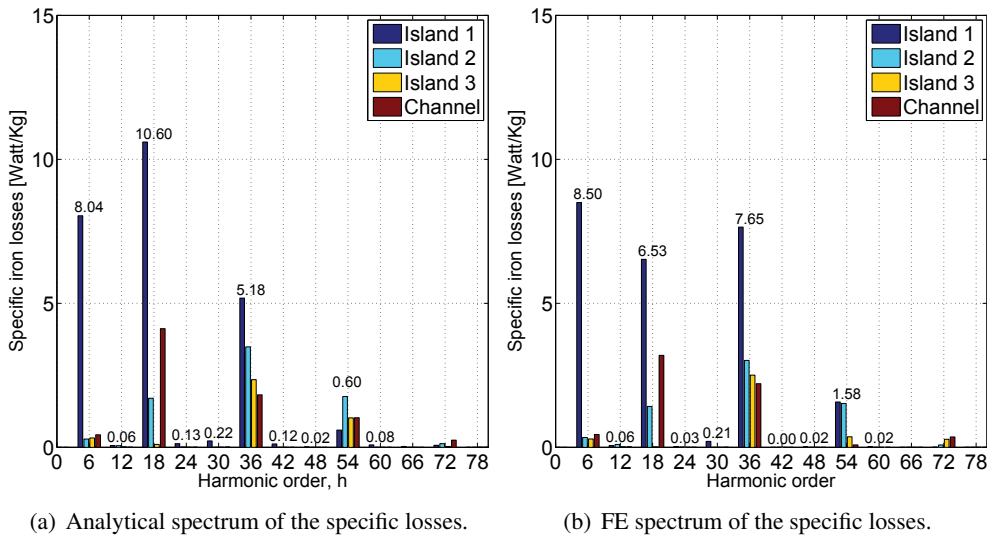


Figure 8.24: Specific eddy current losses in the different iron parts of a rotor pole at $J = 1 A/mm^2$ and $\alpha_i^e = 45^\circ$.

these is that the magnetic saturation has been neglected. This assumption yields an overestimation of the air-gap flux density, as shown in Fig. 8.26. As a consequent, such an overestimation causes an even higher overestimation of the magnetic pressure and of the magnetic force on the rotor, especially for higher electrical loading. This overestimation is noticed in Figs. 8.26, 8.27. Therefore, this linear analytical model is not precise to accurately predict the radial magnetic force. A wrong computation of the UMF causes a design of unnecessarily high iron rib widths.

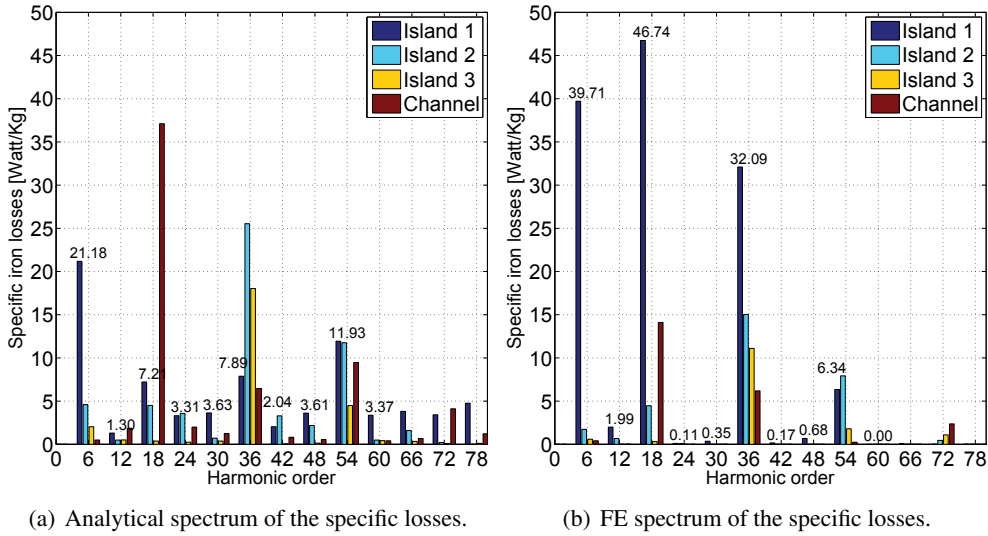


Figure 8.25: Specific eddy current losses in the different iron parts of a rotor pole at $J = 3 A/mm^2$ and $\alpha_i^e = 45^\circ$.

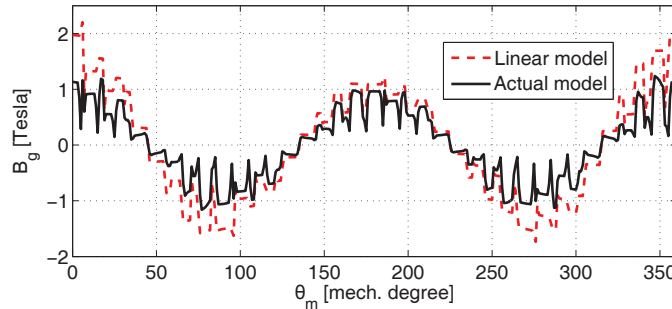
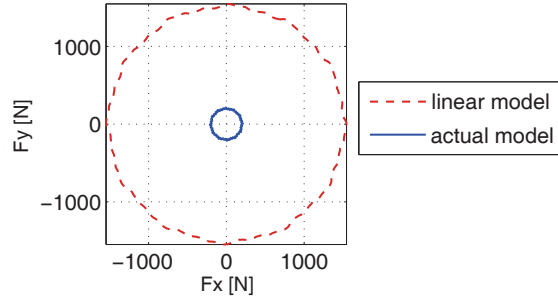


Figure 8.26: Air-gap flux density distribution in case of eccentricity, considering both linear and actual B-H iron characteristic.

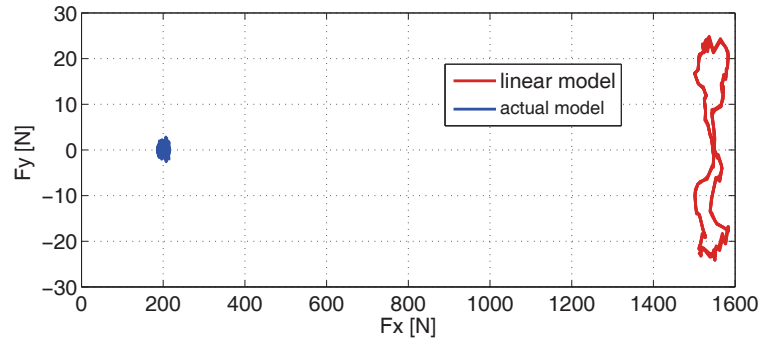
Consequently, it is mandatory to adopt an approach to include the non-linear behavior of the motor iron. An approach is proposed in the previous Section to consider the saturation effect by increasing the air-gap length by a specific quantity: the saturation factor K_{sat} .

Once again, to compute the proper K_{sat} , the magnetic fluxes in different iron parts have to be computed accurately. An iterative approach has been adopted to determine the magnetic saturation in the motor iron. The saturation effect of the stator iron is considered by determining Q_s saturation factors so as to calibrate the air-gap flux density in front of each stator tooth. Then, the saturation effect of the rotor iron is considered by means of $2p(N_b + 1)$ saturation factors to compensate $B_g(\theta_s)$ in front of each rotor island and rotor channel, where N_b is the number of flux-barriers per pole.

To the aim of comparing the results of the improved analytical model with those of the linear one, which shown in Chapter 4, the same eccentricity, electric loading, and current angle are used (i.e., $e = 0.1mm$, $\hat{K}_s = 6200A/mm$, and $\alpha_i^e = 45^\circ$). Since, the eccentricity has



(a) Dynamic eccentricity.



(b) Static eccentricity.

Figure 8.27: F_y versus F_x acting on the rotor of the REL with both eccentricity cases, which result from both linear and actual motor FE models.

high effect on the radial forces acting on the rotor, this section focuses on the computation of the radial forces.

8.2.7. Stator saturation factors

Fig. 8.28 shows the magnetic flux paths in the various stator iron parts. The magnetic flux flowing through the i -th stator tooth (ϕ_{t_i}) is computed by integrating the air-gap flux density $B_g(\theta_s)$ over this tooth, as reported in eq. (8.10). Then, the flux density in each tooth is computed, as $B_{t_i} = \phi_{t_i}/(w_t h_t)$. From the B-H iron characteristic, the field intensity in each tooth, i.e., H_{t_i} is obtained so that the magnetic voltage drop in each i -th tooth is calculated as $U_{t_i} = H_{t_i} h_t$.

As shown in Fig. 8.28, the flux flowing through the stator back iron between the first and second tooth, i.e. ϕ_{b_1} , is the same flux of the first tooth, ϕ_{t_1} . Then, the fluxes flowing through the stator back iron between the other teeth are computed, as $\phi_{b_i} = \phi_{t_i} + \phi_{b_{i-1}}$. The flux density in these iron parts can be obtained, as $B_{b_i} = \phi_{b_i}/(L_{stk} h_b)$. Hence, the field intensity in these iron parts is achieved from the B-H iron characteristic. Then, the magnetic voltage drop in each iron part is given by $U_{b_i} = H_{b_i} l_b$. From Fig. 8.28, by summing the corresponding U_{b_i} for each actual elementary stator back iron path, the magnetic voltage drop in the complete flux path $U_{path_{b_i}}$ can be achieved.

It is noted that, the previous computations of magnetic voltage drop in the stator teeth is general for any rotor position and for any eccentricity. On the contrary, the computation of ϕ_{b_1} should be synchronized with the first tooth of each pole. Thus, similar to the healthy case

computations, the average value of the computed flux in the back iron parts should be subtracted from each ϕ_{b_i} so as to obtain the actual values of U_{b_i} .

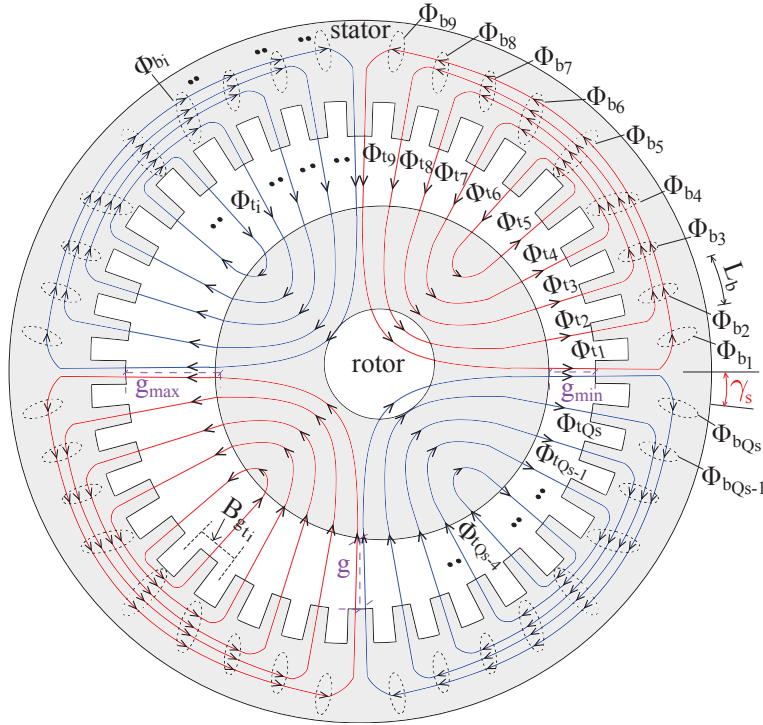


Figure 8.28: Cross section of an eccentric REL motor shows the magnetic saturation in the stator.

For the healthy case (no eccentricity), from U_{t_i} and $U_{path_{b_i}}$, the saturation factors of each flux path are easily computed, because the two teeth of each flux path have the same flux density. However, in case of eccentricity, the saturation factors of the air-gap in front to each stator tooth are different. Therefore, even the voltage drop occurring in the two teeth of each flux path (i.e., distant a pole pitch) is different. The computation of the saturation factors in the stator are deeply discussed in Fig. 8.29.

where, H_{g_t} and g_t are the magnetic field intensity in the air-gap and the average air-gap length in front to the i -th tooth, respectively. An iterative computation is carried out to achieve the proper saturation factor of each stator flux path. This loop is explained in the flow chart of Fig. 8.12.

The air-gap flux density distribution is improved by considering the Q_s saturation factors in front of the stator teeth, i.e., $B_{g_{stator}}(\theta_s)$. The radial magnetic pressure and radial forces are accurately estimated. Fig. 8.30 shows F_y versus F_x , in both cases of eccentricity. FE model with actual stator and linear rotor is compared with the analytical model showing a good agreement between the two models results.

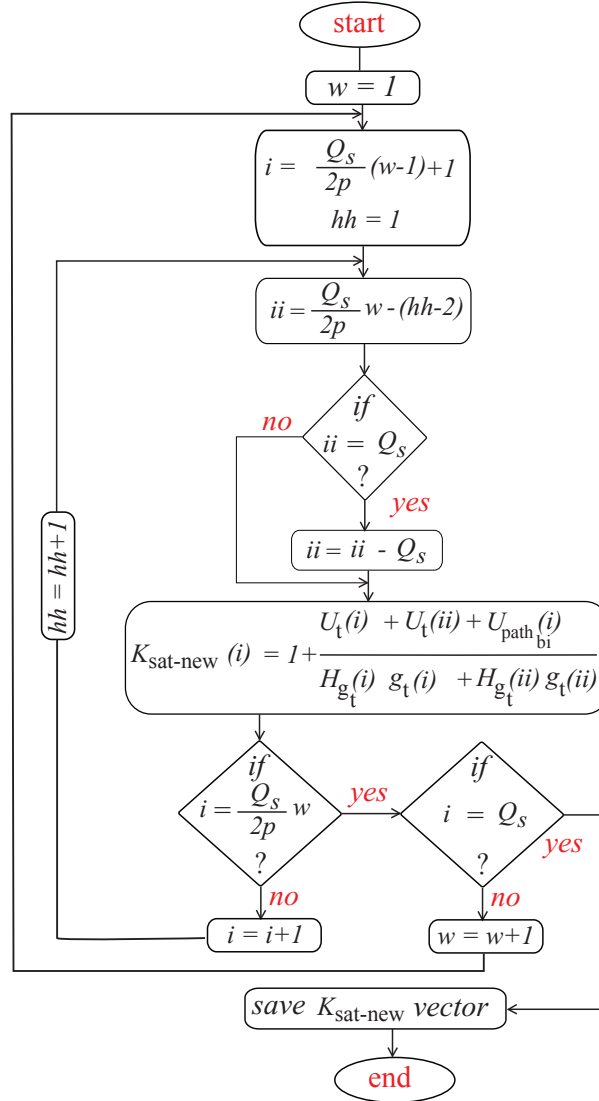
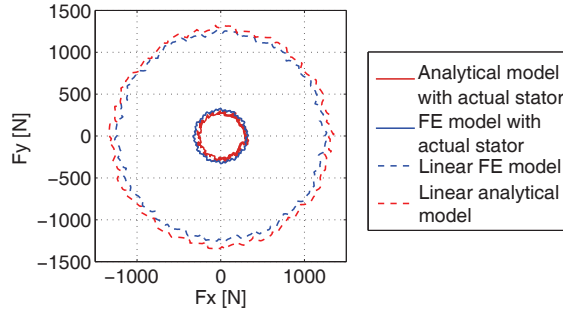


Figure 8.29: Computation of the saturation factors of the different stator parts, in case of eccentricity.

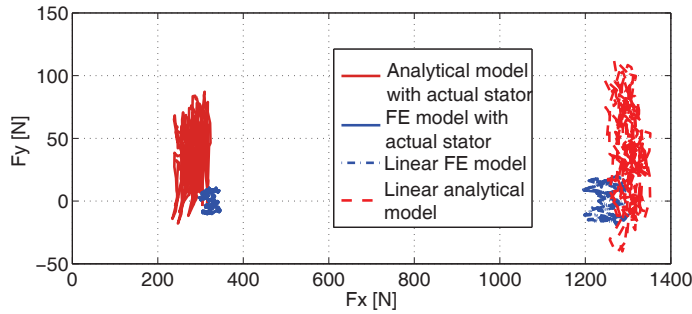
8.2.8. Rotor saturation factors

For the REL motor with three flux-barrier considered, as an example in this chapter, there are three islands and one channel in the rotor, as shown in Fig. 8.31. Since, the magnetic flux concentration in the rotor channel is not high, the rotor channel is approximated, as shown in Fig. 8.31. To compute the magnetic voltage drop in the rotor islands and channels, the flux density is computed starting from the improved air-gap flux density, which consider the stator saturation effect, i.e., $B_{g_{stator}}(\theta_s)$. Once again, due to the eccentricity and the asymmetric distribution of the air-gap flux density over the various poles, the computations should be applied to all islands of all rotor poles. For, the first island of each pole, these fluxes are given by

$$\phi_{in_1}^w = \int_{\frac{X(w)\pi}{2p} - \theta_{b1}}^{\frac{X(w)\pi}{2p}} B_{g_{stator}}(\theta_s) \frac{D}{2} L_{stk} d\theta_s \quad (8.14)$$



(a) Dynamic eccentricity.



(b) Static eccentricity.

Figure 8.30: F_y versus F_x acting on the rotor of the REL with both eccentricity cases, result from both analytical and FE models consider the linear and non linear stator iron.

and

$$\phi_{out_1}^w = \int_{\frac{X(w)\pi}{2p}}^{\frac{X(w)\pi}{2p} + \theta_{b1}} B_{g_{stator}}(\theta_s) \frac{D}{2} L_{stk} d\theta_s \quad (8.15)$$

Then, the magnetic flux flows through the first barrier for different poles, i.e., $\phi_{b_1}^w$ is given by $\phi_{in_1}^w - \phi_{out_1}^w$. The fluxes flowing in the first island of the different poles are given by $\phi_{in_1}^w - \phi_{b_1}^w$. Once gain, the fluxes flowing in the second island of the different poles are $\phi_{in_2}^w - \phi_{b_2}^w + \phi_{b_1}^w$ as highlighted in Fig. 8.31, where $\phi_{in_2}^w$ and $\phi_{out_2}^w$ are given by

$$\phi_{in_2}^w = \int_{\frac{X(w)\pi}{2p} - \theta_{b2}}^{\frac{X(w)\pi}{2p} - \theta_{b1}} B_{g_{stator}}(\theta_s) \frac{D}{2} L_{stk} d\theta_s \quad (8.16)$$

$$\phi_{out_2}^w = \int_{\frac{X(w)\pi}{2p} + \theta_{b1}}^{\frac{X(w)\pi}{2p} + \theta_{b2}} B_{g_{stator}}(\theta_s) \frac{D}{2} L_{stk} d\theta_s \quad (8.17)$$

Similarly, the fluxes following in the third island and in the channel of the different poles are computed.

Again, the flux density in the rotor islands and channels are given by $B_{island_i}^w = \phi_{island_i}^w / (w_{r_i} L_{stk})$, where w_{r_i} is the width of the i -th iron path [83]. From the B-H iron curve, the magnetic field intensity $H_{island_i}^w$ is obtained. Hence, the magnetic voltage drop in all the rotor islands and rotor channels are computed as $H_{island_i}^w L_{island}$. Finally, the saturation factors of the different

rotor parts is given by

$$K_{sat_{island_i}}^w = 1 + \frac{\mu_o H_{island_i}^w L_{island}}{B_{g_{in_{island_i}}}^w g_{in_{island_i}}^w + B_{g_{out_{island_i}}}^w g_{out_{island_i}}^w} \quad (8.18)$$

where $B_{g_{in_{island_i}}}^w$ and $g_{in_{island_i}}^w$ are the average air-gap flux density entering in the i -th rotor island of the w -th pole and the average air-gap length in front of the input part of the i -th rotor island of the w -th pole, respectively. Similarly, $B_{g_{out_{island_i}}}^w$ and $g_{out_{island_i}}^w$ are the average air-gap flux density going out from the i -th rotor island of the w -th pole and the average air-gap length in front of the output part of the i -th rotor island of the w -th pole, respectively.

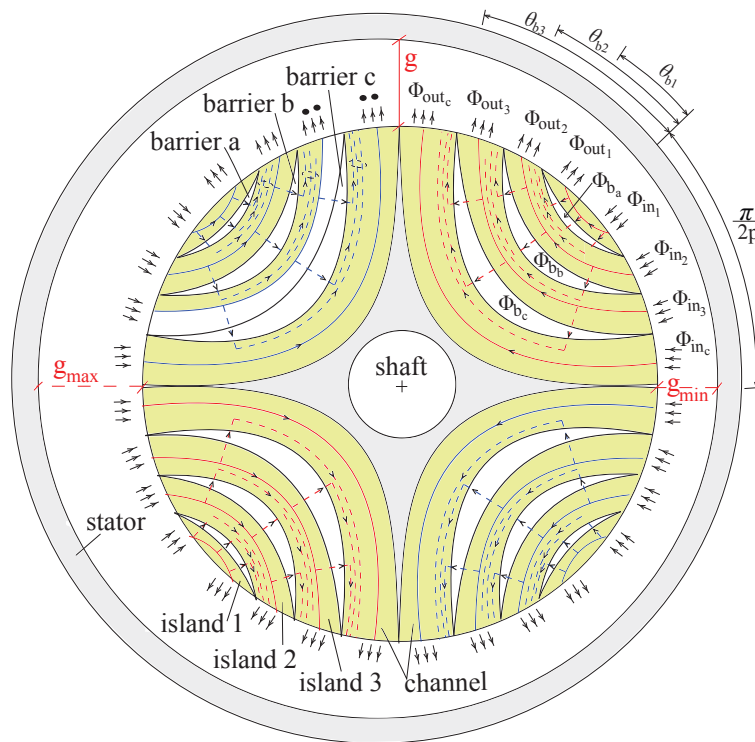
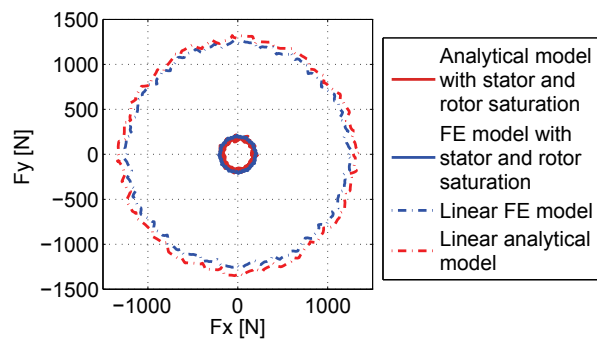
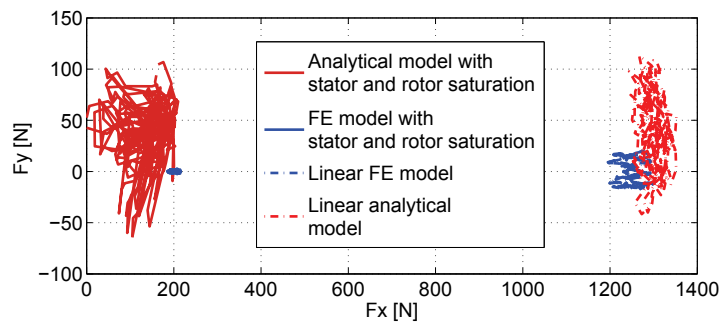


Figure 8.31: Cross section of an eccentric REL motor shows the magnetic saturation in the rotor.



(a) Dynamic eccentricity.



(b) Static eccentricity.

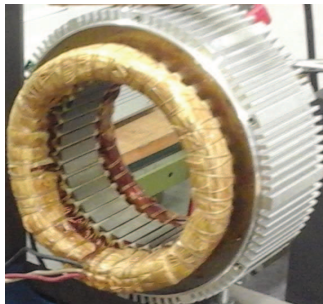
Figure 8.32: F_y versus F_x acting on the rotor of the REL with both eccentricity cases, result from both analytical and FE models consider the linear and non linear motor iron.

8.3. Experimental validation

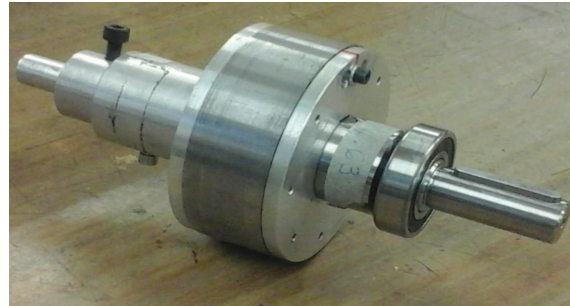
In this section, a test bench has been designed in order to validate the prediction of the unbalanced magnetic force acting on the rotor of the REL motor, in eccentricity case. The measured magnetic force is compared with those of both analytical and FE models.

8.3.1. The machine

A three-phase four-pole REL machine is used. Fig. 8.33 (a) and Fig. 8.33 (b) show the stator and rotor of the used motor, respectively. Distributed windings are adopted in the 36-slot of the stator. This windings are connected in delta configuration. The rotor of this machine is symmetric rotor and has three flux barriers per pole. The machine has the same geometrical dimensions of that used in Chapter 4 and Chapter 8. The main geometrical dimensions of the machine are reported in Table. 4.1. Besides, the rotor geometrical data are reported in Table. 4.4.



(a)



(b)

Figure 8.33: Three-phase REL motor prototype: photo of (a) stator and (b) rotor.

8.3.2. Bench layout

Fig. 8.34 shows the test bench, which used to validate the results of both analytical and FE model of eccentric REL motor. This bench consists of the following:

- (a) mechanical frame to fix the stator of the motor,
- (b) the REL motor under test,
- (c) DC isolated power supply with its imbedded ammeter,
- (d) variable resistance, which used to control the motor current value,
- (e) identical pair of weights, which presents the measured magnetic force.

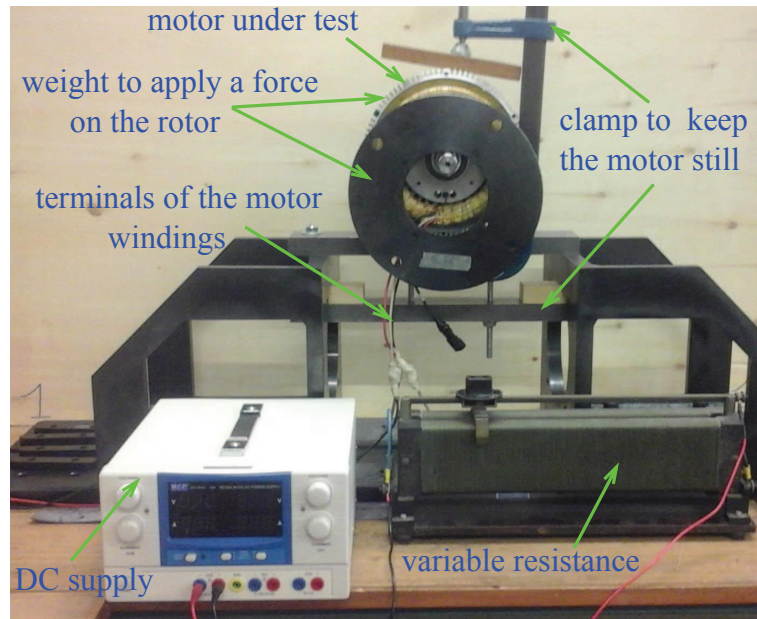


Figure 8.34: Structure of the test bench.

8.3.3. Implementation procedure

This section presents a simple technique to validate the results of both FE and analytical models of the eccentric REL motor by the experimental results. Firstly, the covers, the bearings, are removed from the motor. Then, the stator is fed by DC current, as shown in Fig. 8.34 and Fig. 8.35. As a consequent, the magnetic flux is generated. Since, the rotor is kept concentric with the stator, the rotor rotates to align the d-axis with the stator flux, hence, the direction of the flux and the d-axis of the rotor can be defined.

Secondly, the supply is disconnected and the stator can be rotated in order to enforce the peak of the stator magnetic flux to be against the earth gravity (i.e., to be at the upper part of the stator), as shown in Fig. 8.36. Besides, the rotor *d*-axis is aligned with the new stator flux direction, as shown in Fig. 8.36. After that, a piece of electrical insulation paper, with known thickness ($t_{insulation}$) is placed between the stator and the upper part of the rotor. To the aim of computing the maximum value of the force, the eccentricity have been carried out at the upper direction too (i.e., at the d-axis direction or the flux direction). Eccentricity can be computed as $g - t_{insulation}$.

Thirdly, the supply is connected to the stator. Consequently, there is a magnetic force acting on the rotor in the upper direction. The stator current should be high enough to produce magnetic force able to raise the rotor weight, because the mechanical element which initiate the eccentricity should be removed. At this moment, there are only two forces acting on the rotor: the magnetic force due to the eccentricity F_r and the gravity force due to the rotor weight $F_{rw} = m_{rotor}g$.

Fourthly, the supply current is reduced slowly till the rotor start to fall. At this instant, the current is reported. This current produces the magnetic force, which is equal to the rotor weight at the given eccentricity value. Therefore, the current and the magnetic force are known and reported.

Finally, the rotor weight can be increased by adding identical known weights at both ends of the rotor. Then, the test procedure can be repeated. In addition, the experiment can be repeated at different eccentricity values by using insulation papers with different thicknesses.

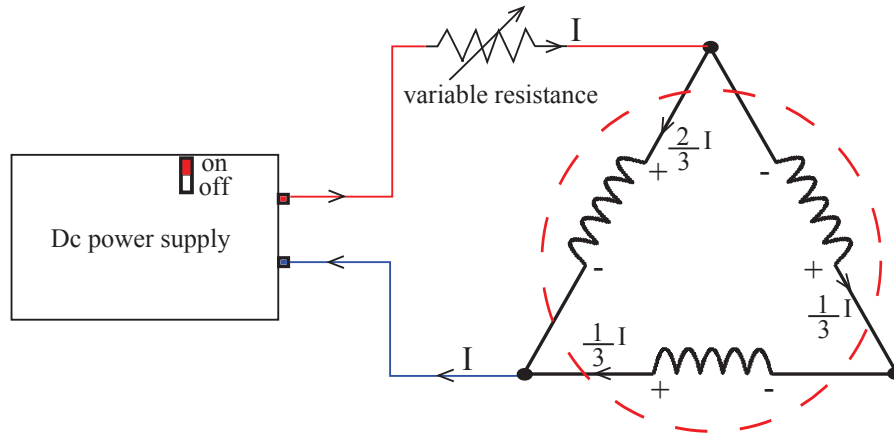


Figure 8.35: Schematic diagram shows the connection of the stator windings with the DC supply.

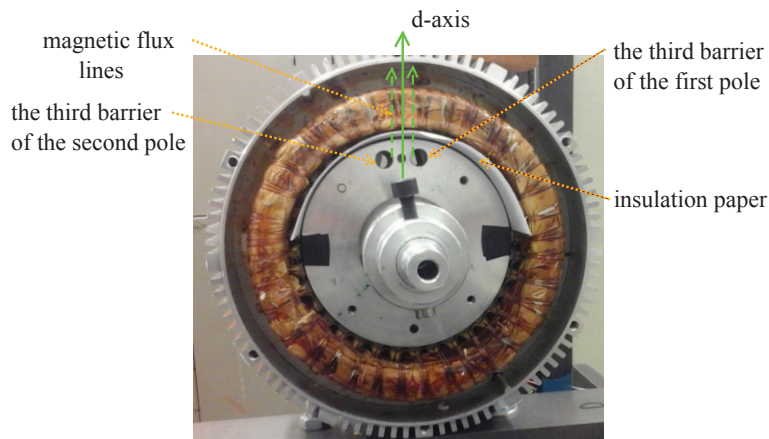


Figure 8.36: Cross section of the REL motor under test shows the alignment of the d-axis of the rotor with the stator magnetic flux.

8.3.4. Results Comparison and discussion

The simulation of both analytical and FE models should be carried out at the same current values obtained from the experimental test. Then, the magnetic force results from these models can be compared with those of the experimental test. However, to the aim of fair comparison, the two models should be modified in order to consider the three phase currents, as shown in Fig. 8.35. In Fig. 8.35, only two terminals of the stator are connected to the DC supply, hence, the currents of the three phases are given by:

$$i_a = \frac{2}{3} \hat{I} \quad \text{and} \quad i_b = i_c = -\frac{1}{3} \hat{I} \quad (8.19)$$

By substituting eq. (8.19) in eq. (2.14) and considering the current angle $\alpha_i^e = 0^\circ$ and rotor position $\theta_m = 0^\circ$, the electric loading is achieved as

$$K_s(\theta_s) = \sum_{\nu^e=1}^{+\infty} \frac{2}{3} \hat{K}_{s\nu^e} \sin(\nu^e p \theta_s) \quad (8.20)$$

It is noted that the peak value of the electric loading is multiplied by $2/3$ due to the stator winding connection shown in Fig. 8.35.

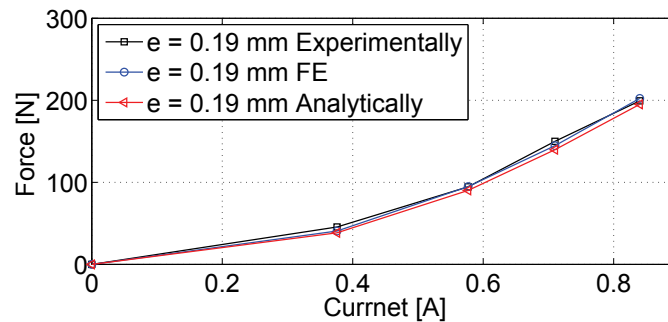


Figure 8.37: The variation of the magnetic force with the current, which results from the analytical model, FE analysis, and experimental test. Eccentricity is set equal to 0.19 mm.

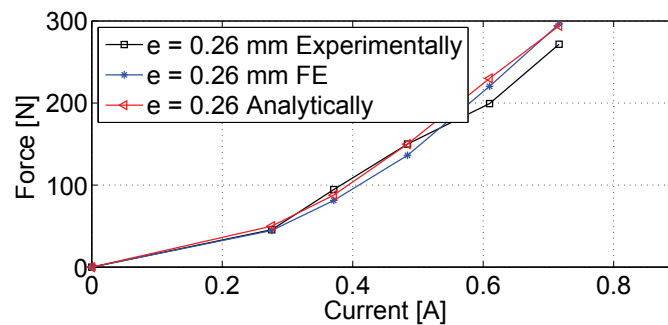


Figure 8.38: The variation of the magnetic force with the current, which results from the analytical model, FE analysis, and experimental test. Eccentricity is set equal to 0.26 mm.

Fig. 8.37 and Fig. 8.38 show the comparison between the results of both analytical and FE models and the experimental test at different eccentricity values. As an example, eccentricity equal to 0.19 mm and 0.26 mm are considered. It is noted that there are a good agreement between both models and the experimental test. Since, the analytical model accurately predicts the magnetic force, in case of static eccentricity, the same behaviour is expected in case of dynamic eccentricity. Because, as it is known, the static eccentricity is a screen shoot of the dynamic eccentricity at one rotor position.

8.4. Conclusions

Firstly, the slotting and the magnetic saturation effect are included in an analytical model to compute the magnetic features of a concentric synchronous REL motor. The results achieved by means of the analytical model are confirmed by the FE model. The analytical model predicts the performance of the machine in few seconds, so that it results to be very useful for designing this kind of machines, which exhibits significant non-linear features.

The torque computation and a comparison between the results achieved by means of the linear and non-linear model are presented. It is noted that the average torque is accurately estimated by the non-linear analytical model.

Secondly, the stator slots effect is considered to improve the analytical model of an eccentric REL motor. As a consequent, the influence of the stator slots on the air-gap flux density and radial magnetic force on the rotor is studied. FE model confirms the results achieved by the slotted linear analytical model, in both cases of eccentricity.

Thirdly, the non-linear behavior of the stator iron is included. The air-gap length is improved in front to Q_s parts by means of Q_s independent saturation factors. These saturation factors are computed based on the linear model. Then, an iterative approach is applied to these computations to achieve a number of Q_s independent saturation factors. Then, the effect of considering the magnetic voltage drop in the stator teeth and back iron on the radial force is evident: the UMF is reduced to one fourth. The results of the modified analytical model of this step are compared with the FE model. There is a good agreement between both models for both eccentricity cases.

Finally, the magnetic voltage drops in the different islands and channels of the rotor are computed. Then, the saturation factors are computed and merged with the air-gap length in front of these islands and channels. Once again, due to computing these saturation factors based on the linear analytical model, the iterative approach is applied to define the suitable rotor saturation factors. For both eccentricity cases, the effect of the magnetic saturation occurs in the different rotor iron parts on the magnetic force is presented. Both FE analysis and experimental tests confirm the results achieved by means of the improved analytical model proposed in this paper. It is noted that, the magnetic force results from the improved model is accurate enough to get an indication of the additional stress on the iron ribs due to the eccentricity. Thus, it is useful for designing the rotor iron ribs.

Part III

Analytical Design of the REL and PMAREL Motors

Practical approach to design the PM in PMAREL motors robust toward the demagnetization

In the permanent magnet assisted reluctance motors, low-energy permanent magnet (PM), such as Ferrite PM, is used to get a cheap rotor. As far as the design choices are concerned, the PM width has to be selected so as to achieve the desired air-gap flux density at no load condition and the PM thickness has to be selected to avoid the demagnetization of the PM under full load conditions. This chapter presents a practical analytical approach to compute PM width and thickness according to a given air-gap flux density and stress on the PM itself. Two approaches, based on a complete model and a simplified model, are considered and compared. As an example, a 36-slot 4-pole machine is designed. Finite element analysis confirms the results achieved by means of both analytical analyses.

9.1. Introduction

The selection of the PM dimensions is a key step during the design procedure of PMAREL motor, often requiring a cut-and-try process. The PM width is selected to achieve the desired air-gap flux density at no load (\hat{B}_g), as in [84–86]. Then, the PM thickness is modified so as to limit the flux-density variation and to avoid an irreversible demagnetization of the PM itself [84–86].

This chapter deals with a practical analytical approach based on the magnetic network analysis of PMAREL motor, as in [87, 88]. The no load flux density of the PM (B_{mo}) which implicitly depends on the desired \hat{B}_g is computed for a given PM width. Then, the current reaction and the stress on the PM are computed for a given PM thickness. The operating point of the PM under load, B_{mL} , is achieved, as shown in Fig. 9.1. This operating point is compared with the knee point flux-density (B_{knee}) in order to check the PM demagnetization.

Two analytical approaches are presented. The first one is based on the complete model of the magnetic network of the PMAREL motor. Then, to the purpose of obtaining practical relationships between the magnetic fields and the main PM dimensions, a simplified magnetic

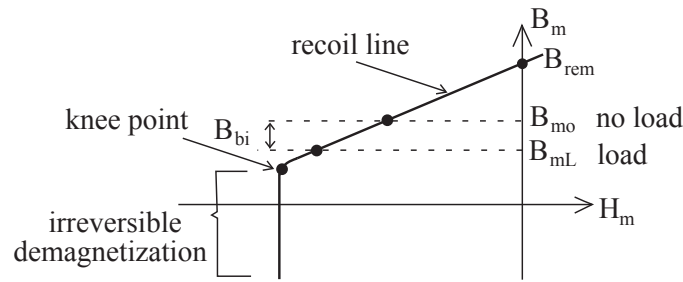


Figure 9.1: Demagnetization curve of the PM material.

network model is proposed. Such relationships facilitate the designer to select the proper PM width and thickness.

At first, both analyses are presented neglecting the effect of the rotor iron ribs. Later on, the effect of these ribs is considered. Finite element analysis is used to confirm the results of both analytical approaches.

As an example, a 36-slot 4-pole machine, with three flux-barriers per rotor pole, is considered. Its detailed geometrical data are reported in Table 9.1. Some experimental results are reported in [89, 90].

Table 9.1: Geometrical data of the PMAREL machine used in the example.

external stator diameter	D_{se}	200	mm
internal stator diameter	D	125	mm
stack length	L_{stk}	40	mm
number of stator slots	Q_s	36	
number of pole pairs	p	2	
air-gap length	g	0.35	mm
half angle of the first barrier ends	θ_{b_1}	12.9	deg
half angle of the second barrier ends	θ_{b_2}	25.7	deg
half angle of the third barrier ends	θ_{b_3}	38.6	deg
PM thickness of the first barrier	t_{m_1}	3	mm
PM thickness of the second barrier	t_{m_2}	6	mm
PM thickness of the third barrier	t_{m_3}	10	mm
width of the first PM	w_{m_1}	14	mm
width of the second PM	w_{m_2}	26	mm
width of the third PM	w_{m_3}	30	mm
Ferrite remanence flux density	B_{rem}	0.314	T
total width of first barrier iron ribs	t_{r_1}	0.8	mm
total width of second barrier iron ribs	t_{r_2}	1.6	mm
total width of third barrier iron ribs	t_{r_3}	1.6	mm

9.2. The no load flux density of the PM

This section discusses the complete and simplified models of the PMAREL motor at no load condition. Both models are based on the magnetic network analysis. Once the width of each i -th PM (w_{m_i}) is fixed, the no load flux density $B_{m_{o_i}}$ in each i -th PM can be computed. Firstly, the dimensions of the holes addressing the PMs are assumed with the same dimensions of the PMs. Then, holes slightly higher than the PMs will be taken into account.

9.2.1. Complete model to predict the no-load flux density

A lumped-parameter representation of the PM is shown in Fig. 9.2: a flux source ϕ_{rem} in parallel with a PM reluctance R_m , given by

$$\phi_{rem} = B_{rem} w_m L_{stk} \quad (9.1)$$

$$R_m = \frac{t_m}{\mu_{rec} \mu_o w_m L_{stk}} \quad (9.2)$$

The actual flux of the PM ϕ_m is the flux resulting from this parallel. As shown in Fig. 9.2, R_m is parallel connected with R_{bl} and R_{br} which are the reluctances of the left and the right parts of the barrier where the PM is inset. R_{bm} is the equivalent parallel reluctance of these two parts, given by

$$R_{bm} = \frac{t_b}{\mu_o (l_b - w_m) L_{stk}} \quad (9.3)$$

where w_m , t_b , and l_b are the PM width, the thickness, and the length of the flux barrier, respectively.

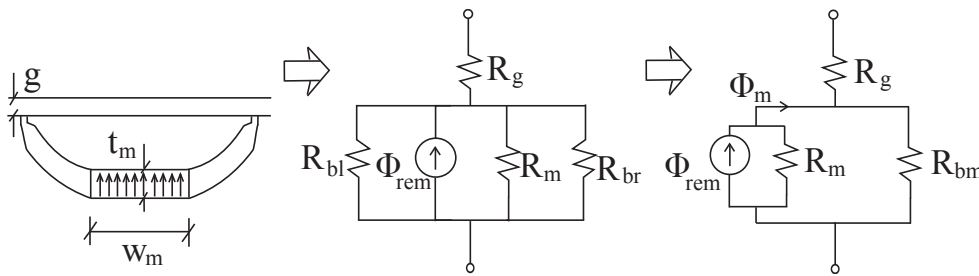


Figure 9.2: Sketch of one flux-barrier of the PMAREL motor and its equivalent lumped-parameter magnetic circuit.

In this perspective, the complete magnetic network of one pole of PMAREL motor with three flux-barriers can be derived, as shown in Fig. 9.3. For the purpose of simplifying the magnetic circuit analysis, the magnetic circuit is redrawn, as shown in Fig. 9.4, using the equivalent magnetic potential generators U_{rem_i} computed as

$$U_{rem_i} = \phi_{rem_i} R_{b_i} \quad (9.4)$$

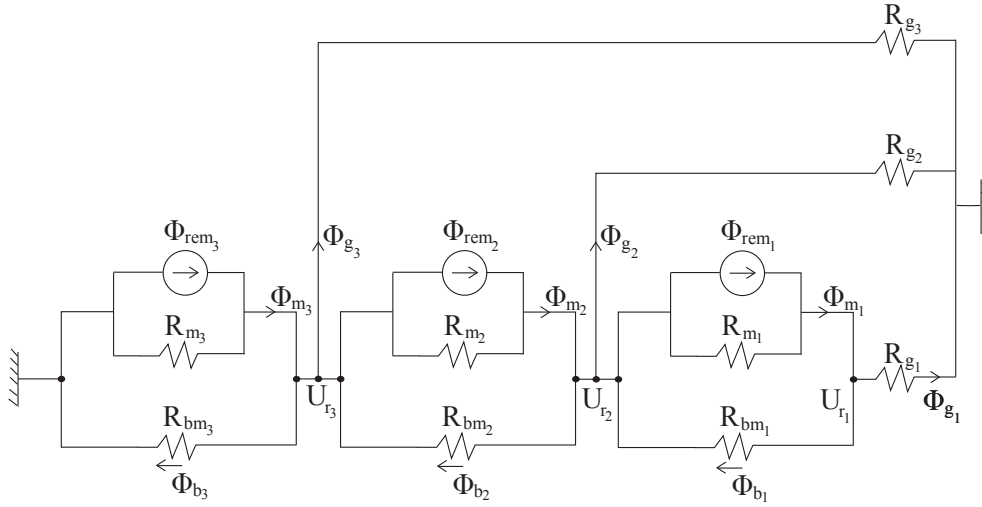


Figure 9.3: Magnetic network of one pole of PMAREL motor at no load.

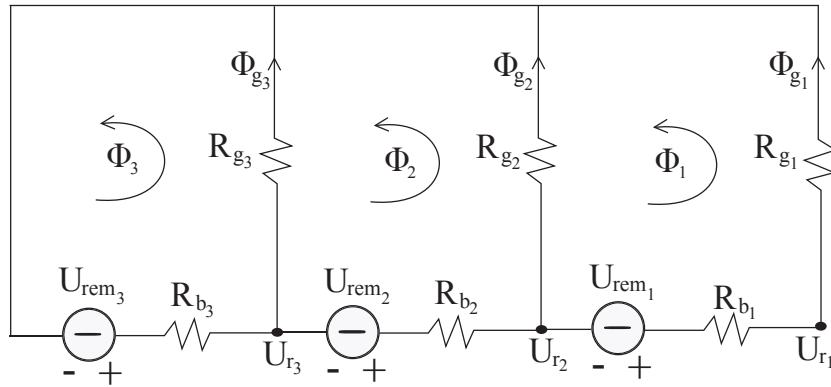


Figure 9.4: Redrawing of the magnetic network of one pole of PMAREL motor at no load.

Applying the Kirchhoff's voltage law, the fluxes flowing in each i -th loop, i.e., ϕ_i (with $i = 1, 2, 3$), are computed from

$$\begin{bmatrix} U_{rem_1} \\ U_{rem_2} \\ U_{rem_3} \end{bmatrix} = \begin{bmatrix} R_{g_1} + R_{g_2} + R_{b_1} & -R_{g_2} & 0 \\ -R_{g_2} & R_{g_2} + R_{g_3} + R_{b_2} & -R_{g_3} \\ 0 & -R_{g_3} & R_{g_3} + R_{b_3} \end{bmatrix} \cdot \begin{bmatrix} \phi_1 \\ \phi_2 \\ \phi_3 \end{bmatrix} \quad (9.5)$$

where R_{b_i} and R_{g_i} are the magnetic reluctances corresponding to the i -th flux barrier and to the portions of air-gap in front of the i -th flux-barrier, respectively. By simplifying $\mu_{rec} \simeq 1$, they are given by

$$R_{b_i} = \frac{t_{b_i}}{\mu_o l_{b_i} L_{stk}} \quad (9.6)$$

$$R_{g_i} = \frac{g}{\mu_o (\theta_{b_i} - \theta_{b_{i-1}}) (D - g) L_{stk}} \quad (9.7)$$

Consequently, the flux flowing in the air-gap in front of each i -th flux-barrier is

$$\phi_{g_i} = \phi_i - \phi_{i-1} \quad (9.8)$$

and the scalar magnetic potential of the i -th rotor island is

$$U_{r_i} = \phi_{g_i} R_{g_i} \quad (9.9)$$

From Fig. 9.3, the flux flowing through the left and right parts of the i -th flux-barrier (with respect to the PM) is given by

$$\phi_{b_i} = \frac{U_{r_i} - U_{r_{i+1}}}{R_{b_{m_i}}} \quad (9.10)$$

Applying the Kirchhoff's current law at the nodes shown in Fig. 9.3, the flux of the i -th PM is computed as

$$\phi_{m_i} = \phi_{g_i} + \phi_{b_i} + \phi_{m_{i-1}} - \phi_{b_{i-1}} \quad (9.11)$$

Then, the no load flux density of the i -th PM results in

$$B_{m_{oi}} = \frac{\phi_{m_i}}{w_{m_i} L_{stk}} \quad (9.12)$$

Since the thickness t_b of the flux-barrier is not constant along its length l_b , the flux density flowing through the barrier is not uniformly distributed. The actual barrier is conveniently replaced by an equivalent barrier with the same reluctance but an uniform thickness of the barrier t_{be} which is assumed to be the same thickness of the middle part of the barrier addressing the PM (i.e., t_m). Consequently, the length of the equivalent barrier l_{be} is adjusted so as to keep the ratio t_{be}/l_{be} equal to the ratio t_b/l_b , that is, the same reluctance of the actual barrier. Then, the flux density flowing through the equivalent barrier is uniform.

9.2.2. Correction for lower size PM

If the dimensions of the hole where the PM is inset are higher than those of the PM itself, as shown in Fig. 9.5, the previous computation is slightly modified [91, 92]. In order to keep the same previous analytical procedure, the PM characteristics (i.e., ϕ_{rem} and R_m) are modified to equivalent values ($\phi_{rem_{eq}}$ and R''_m) according to the equivalent network shown in Fig. 9.6.

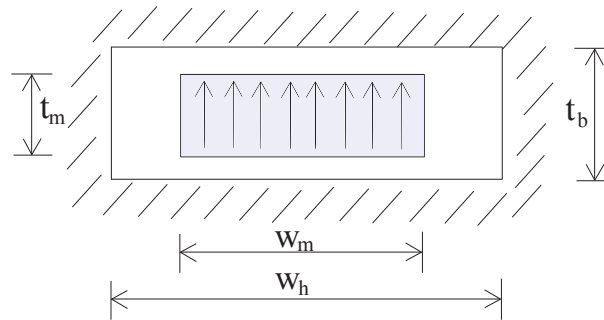


Figure 9.5: Cross section of the PM inset in the middle part of the flux-barrier (PM size lower than the hole size).

R'_t is the reluctance of the lateral space on the two sides of the PM and R''_t is the reluctance of the space above and below the PM. They are given by

$$R'_t = \frac{t_b}{\mu_o(w_h - w_m)L_{stk}} \quad (9.13)$$

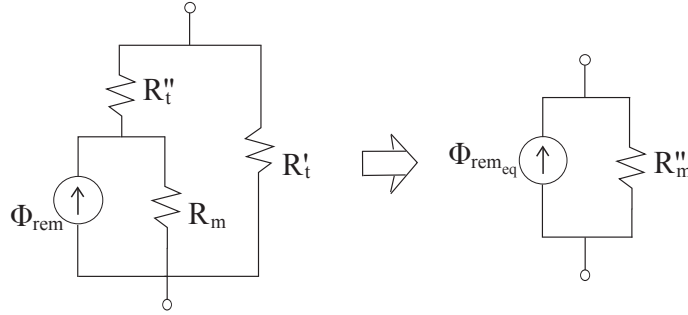


Figure 9.6: Magnetic network of the middle part of the flux-barrier containing the PM with lower dimension.

$$R_t'' = \frac{t_h - t_m}{\mu_o w_m L_{stk}} \quad (9.14)$$

The reluctance R_t'' influences both ϕ_{rem} and R_m . ϕ_{rem} decreases and its equivalent value is estimated by

$$\begin{aligned} \phi_{rem,eq} &= \phi_{rem} \frac{R_m}{R_m + R_t''} \\ &= \phi_{rem} \frac{t_m / \mu_{rec}}{t_m / \mu_{rec} + (t_b - t_m)} \simeq \phi_{rem} \frac{t_m}{t_b \mu_{rec}} \end{aligned} \quad (9.15)$$

where R_m' is computed as

$$R_m' = \frac{t_m - \mu_{rec}(t_b - t_m)}{\mu_o \mu_{rec} w_m L_{stk}} \quad (9.16)$$

Substituting $\mu_{rec} \simeq 1$, it is given by

$$R_m' \simeq \frac{t_b}{\mu_o \mu_{rec} w_m L_{stk}} \quad (9.17)$$

The reluctance R_t' can be combined into the PM reluctance R_m' , which is referred to as the equivalent R_m'' , calculated as

$$R_m'' = \frac{t_m}{\mu_o \mu_{rec} \left[w_m + (w_h - w_m) \frac{t_m}{t_b \mu_{rec}} \right] L_{stk}} \quad (9.18)$$

It corresponds to consider an equivalent PM width given by

$$w_{m,eq} = w_m \left[1 + \frac{(w_h - w_m)}{w_m} \frac{t_m}{t_b \mu_{rec}} \right] \quad (9.19)$$

9.2.3. Simplified model to compute the no-load flux density

The analytical approach described above allows a precise estimation of the air-gap and PM flux density. However, for a design approach, a practical simplification is proposed to obtain a direct relation between the i -th PM width w_{m_i} and the no load flux density $B_{m_{o_i}}$ of the i -th PM. This allows a rapid determination of the PM widths. Fig. 9.7 shows the approximated paths of the air-gap flux ϕ_{g_i} , according to the following assumptions:

- (a) the air-gap flux in front of the first flux barrier, ϕ_{g_1} , flows through the first PM and the same portion of PM of the second and third flux-barrier. These portions of width are equal to the first PM width, i.e., w_{m_1} .
- (b) the air-gap flux flowing between the first and second barrier ends, ϕ_{g_2} , flows in a portion of the second and third PM whose width is $(w_{m_2} - w_{m_1})$.
- (c) the air-gap flux between the second and third flux-barriers ends, ϕ_{g_3} , flows through the portion of the third PM whose width is $(w_{m_3} - w_{m_2})$.

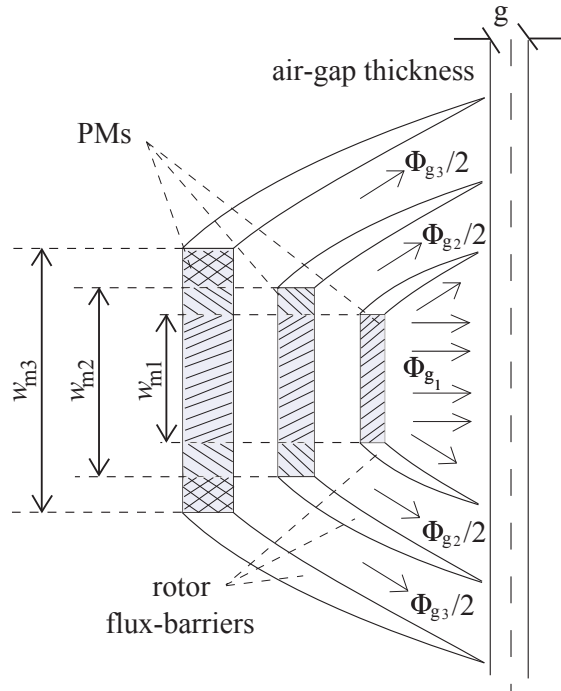


Figure 9.7: Sketch of a rotor pole with approximated paths of the no load air-gap flux due to the different PMs.

Fig. 9.8, Fig. 9.9, and Fig. 9.10 show the equivalent magnetic networks according to the first, the second, and the third assumption, respectively. Then, three independent networks are achieved from which the relationships between the i -th PM width and the i -th air-gap flux ϕ_{g_i} are

$$\phi_{g_i} = \frac{U_{m_i}}{R_{g_i} + R_{m_i}} \quad (9.20)$$

where U_{m_i} is

$$U_{m_i} = B_{rem}(w_{m_i} - w_{m_{i-1}})L_{stk}R_{m_i} \quad (9.21)$$

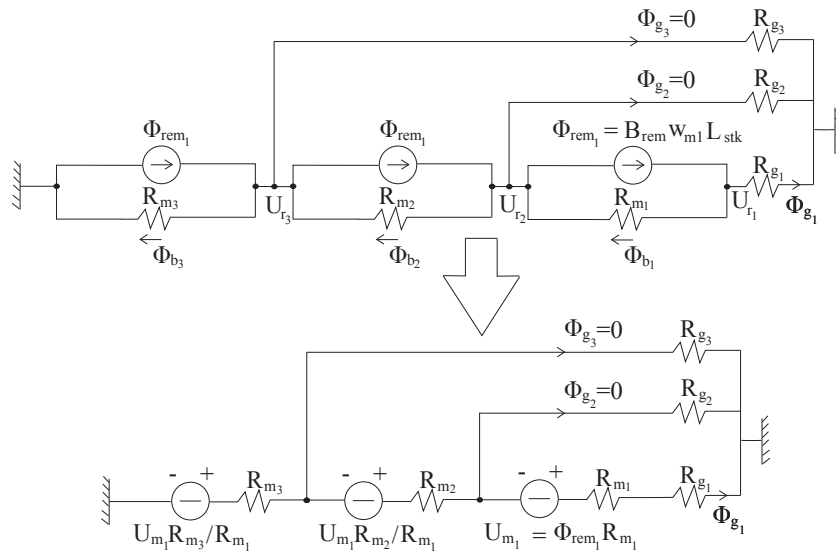


Figure 9.8: Magnetic network according to the first assumption, all PM widths are equal to w_{m1} .

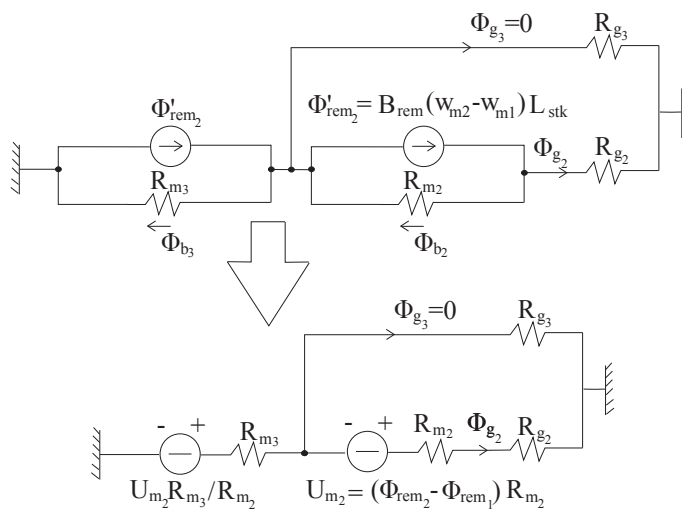


Figure 9.9: Magnetic network according to the second assumption, the second and the third PM widths are equal to $(w_{m2} - w_{m1})$.

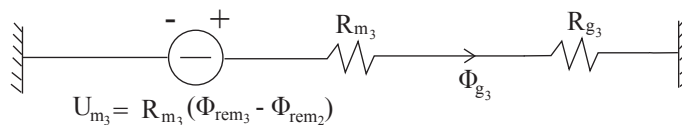


Figure 9.10: Magnetic network according to the third assumption, the third PM width is equal to $(w_{m3} - w_{m2})$.

The simplified method may yield a different flux density in the PMs, and also in the different parts of the same PM. However, with standard rotor geometries, that is, with several flux barriers per pole which properly guide the flux lines, the PM operating points are close each other, as noted in the flux density map shown later in Fig. 9.11.

9.2.4. PM width selection

The last two equations, together with eq. (9.2) and eq. (9.7), are useful to determine the PM widths according to the desired flux density distribution in the air-gap. Hence, starting from ϕ_{g_i} , the eqs. (9.9) to (9.12) are applied to compute the no-load flux density of the i -th PM, i.e., B_{mo_i} .

However, let us note that the choice of the air-gap flux density \hat{B}_g is not independent from the adopted PM material: \hat{B}_g has to be chosen according to the PM residual flux density, e.g., using Ferrite PM (see Table 9.1), it can be assumed to be lower than 0.1 T.

9.2.5. Example and FE validation

The results of the previous analytical analysis are compared with those of FE analysis referring to the 4-pole PMAREL motor with three flux-barriers per pole, whose geometrical data are reported in Table 9.1. Fig. 9.11 shows the flux density map at no load condition. ϕ_{rem_i} and R_{m_i} are computed from eq. (9.1) and eq. (9.2), respectively. Then, the relation between the thickness and the length of the i -th flux barrier (t_{b_i}/l_{b_i}) is computed, e.g. as reported in the Appendix B. The thickness of the i -th flux barrier is assumed to be equal to the thickness of the i -th PM, i.e., t_{m_i} . Then, l_{b_i} can be computed, and hence R_{bm_i} and R_{b_i} can be computed as in eqs. (9.3) and (9.6).

After that, both complete and simplified analytical models are applied. The results of these two models are compared with FE analysis, as shown in Table 9.2 and Fig. 9.12. The flux density in the PM is almost constant in the whole PM volume, and the average value is reported. It is noted that, there is a good agreement between the FE and the complete analytical model results. The simplified analytical model results are reasonably close to the previous ones, confirming that the practical approximations carried out in the simplified model are consistent.

Table 9.2: The analytical and FE model results for PMAREL motor at no load, neglecting the rotor iron ribs.

	FE model	Analytical model	
		complete	simplified
$B_{mo_1} (T)$	0.309	0.311	0.299
$B_{mo_2} (T)$	0.309	0.310	0.302
$B_{mo_3} (T)$	0.312	0.313	0.300
$B_{g_1} (T)$	0.152	0.153	0.140
$B_{g_2} (T)$	0.126	0.128	0.128
$B_{g_3} (T)$	0.049	0.049	0.033

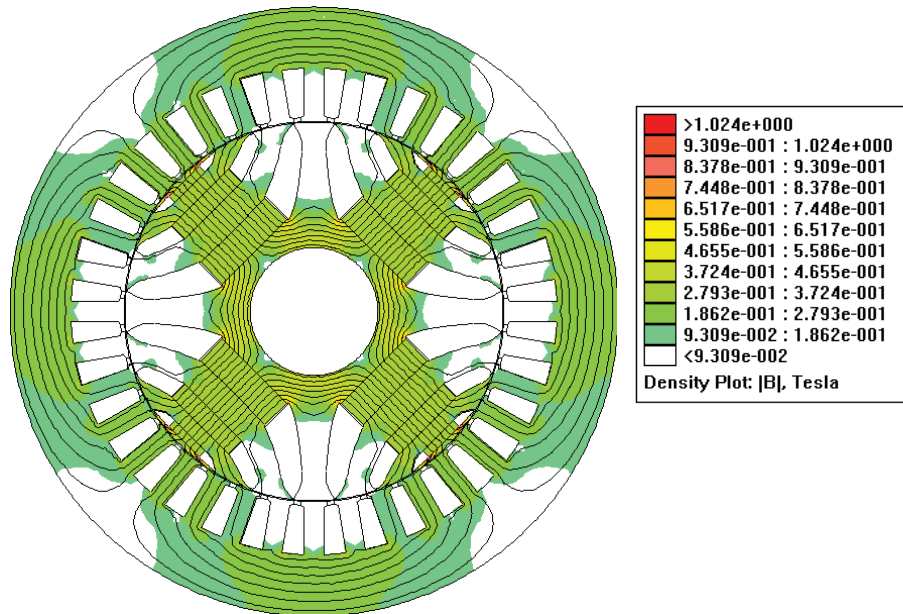


Figure 9.11: Flux density map of PMAREL motor at no-load operating condition.

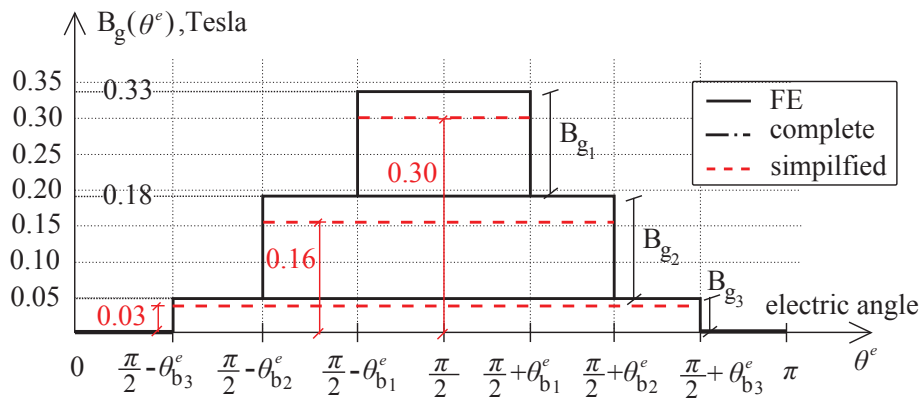


Figure 9.12: Air-gap flux density results from the PMs according to the approximated paths of the flux at no load condition.

9.3. Computation of the current reaction

To compute the flux due to the stator current, the PMs are removed. The motor is analyzed as a REL motor. The worst condition is considered, that is, when the stator current is producing a magneto-motive force (MMF) completely along the q -axis, as shown in Fig. 9.13. Of course, the resulting flux is the flux against the PM magnetization direction (negative q -axis) so that the stator current is referred to as a demagnetizing current. A sinusoidal waveform of the stator MMF (distributed winding machine) is assumed and the iron ribs effect is neglected.

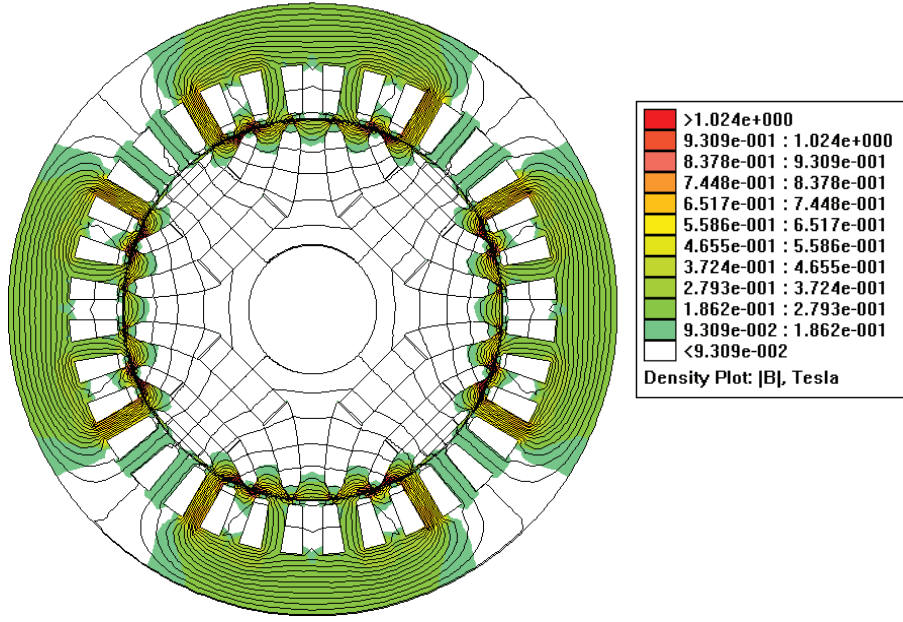


Figure 9.13: Flux density map of REL motor fed by q -axis current only (i.e., a demagnetizing current).

9.3.1. Complete model to predict the PM stress

Fig. 9.15 shows the complete magnetic network of the REL motor fed by the demagnetizing current referring to a single pole shown in Fig. 9.14. From the analysis of the magnetic network, the (demagnetizing) flux in the i -th rotor flux-barrier, i.e., ϕ_{b_i} , can be computed from:

$$\begin{bmatrix} U_{s_1} - U_{s_2} \\ U_{s_2} - U_{s_3} \\ U_{s_3} \end{bmatrix} = \begin{bmatrix} R_{g_1} + R_{g_2} + R_{b_1} & -R_{g_2} & 0 \\ -R_{g_2} & R_{g_2} + R_{g_3} + R_{b_2} & -R_{g_3} \\ 0 & -R_{g_3} & R_{g_3} + R_{b_3} \end{bmatrix} \times \begin{bmatrix} \phi_{b_1} \\ \phi_{b_2} \\ \phi_{b_3} \end{bmatrix} \quad (9.22)$$

where U_{s_i} is the average value of the stator magnetic potential in front of the i -th flux-barrier, as shown in Fig. 9.16, given by

$$U_{s_i} = \frac{\sin(p\theta_{b_i}) - \sin(p\theta_{b_{i-1}})}{p(\theta_{b_i} - \theta_{b_{i-1}})} \cdot \hat{U}_s \quad (9.23)$$

and \hat{U}_s is the peak value of the stator scalar magnetic potential, i.e., $\hat{U}_s = \hat{K}_s D / (2p)$, and \hat{K}_s is the electrical loading. R_{b_i} and R_{g_i} are the magnetic reluctances corresponding to the i -th flux barrier and to the portions of air-gap in front of the i -th flux-barrier, respectively. They are given by eqs. (9.6) and (9.7).

The flux density in the region where the PM is inset (which corresponds to the PM flux density variation from no-load to full load) is the same flux-density in the middle part of the flux-barrier. Such a flux density on the i -th PM results in

$$B_{b_i} = \frac{\phi_{b_i}}{l_{b_i} L_{stk}} \quad (9.24)$$

and it is shown in Fig. 9.1 in the PM B-H curve.

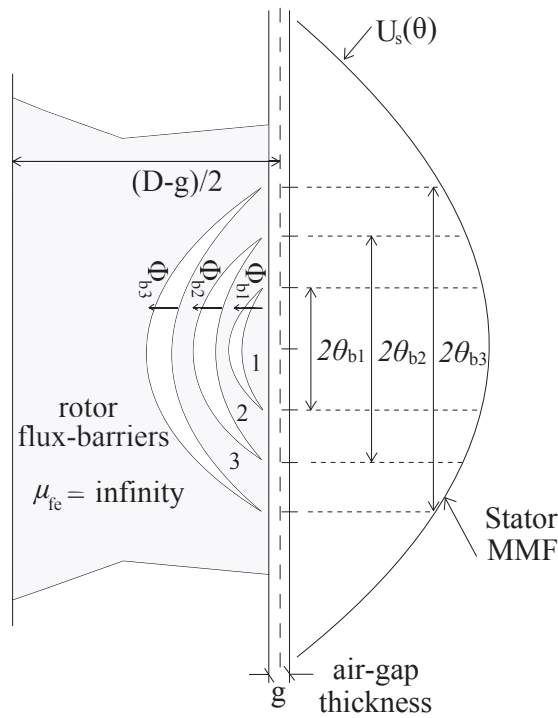


Figure 9.14: Sketch of a rotor pole with three flux-barriers.

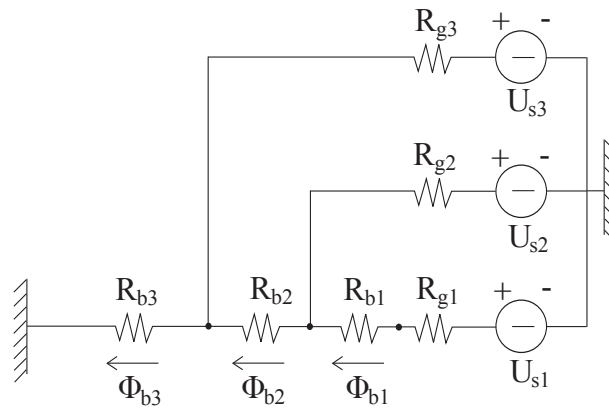


Figure 9.15: Magnetic network, referring to a single pole of the REL motor with three flux-barriers.

9.3.2. Simplified model to predict the PM stress

It is known that in REL and PMAREL motors, in order to maximize the average torque, the air-gap thickness is kept as low as possible and the flux-barrier thickness are designed quite high so as to limit the q -axis flux, i.e., to increase the rotor saliency. It follows that the reluctances R_{g_i} are negligible with respect to the R_{b_i} . Therefore, the complete magnetic network shown in Fig. 9.15 can be simplified by neglecting the R_{g_i} , as shown in Fig. 9.17. The flux flowing through the i -th flux barrier is

$$\phi_{b_i} = \frac{U_{s_i} - U_{s_{i+1}}}{R_{b_i}}, \quad i \neq N_b \quad (9.25)$$

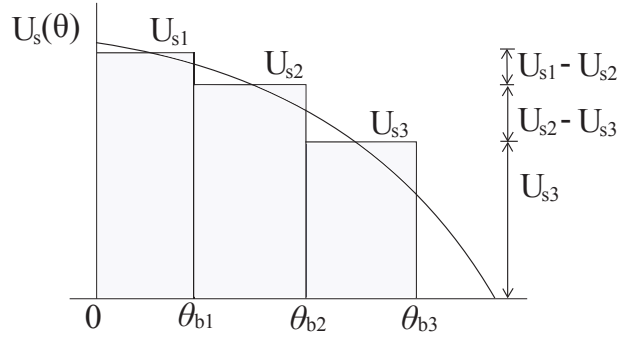


Figure 9.16: Computation of average stator scalar magnetic potential in front of each flux-barrier.

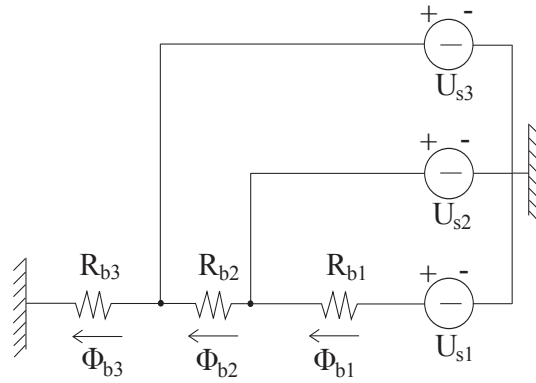


Figure 9.17: Simplified magnetic network, referring to one pole with three flux-barriers.

By substituting eq. (9.25) in eq. (9.24), the stress on the i -th PM due to the demagnetizing current can be directly computed as

$$B_{b_i} = \frac{\mu_o}{t_{m_i}} (U_{s_i} - U_{s_{i+1}}) \quad (9.26)$$

B_{b_i} is proportional to the stator scalar magnetic potential which implicitly depends on the electrical loading and the angles of the flux-barrier ends. The former depends on the rated current of the motor, while the latter depends on the flux-barrier geometry.

9.3.3. PM thickness selection

To avoid an irreversible PM demagnetization, the PM thickness has to be high enough and increased if necessary. Let us note that B_{b_i} in eq. (9.26) is inversely proportional to the i -th PM thickness t_{m_i} . Then, the thickness of the PM can be rapidly determined during the design procedure by rearranging eq. (9.26), according to a given \hat{K}_s . Since R_{g_i} is neglected, the flux density stress is slightly overestimated (increasing the safety).

9.3.4. Flux barriers end angles

The choice of the position of the flux barrier ends affects marginally the average torque in a multi-flux-barrier machine, but it plays an important role in the torque ripple production. There are many techniques to select these angles such as the adoption of two different flux barrier geometries in the same lamination [27], so as to compensate the impact of the stator magneto-motive force (MMF) harmonics [29, 93]. Several optimizations were carried out to reduce the torque ripple and several solutions have been found [94–96]. In [30, 84–86, 97], a method to select the angles of the barrier ends is illustrated, based on having an equal space between the flux barrier ends, as shown in Fig. 9.18. The electrical angle between two adjacent flux barrier ends is given by

$$\Delta\theta_b^e = \frac{2\pi p}{n_r} \quad (9.27)$$

and the number of rotor equivalent slots per pole pair, n_r , is selected according to the number of stator slots per pole pair, n_s . Superscript e is used to indicate the electrical angles.

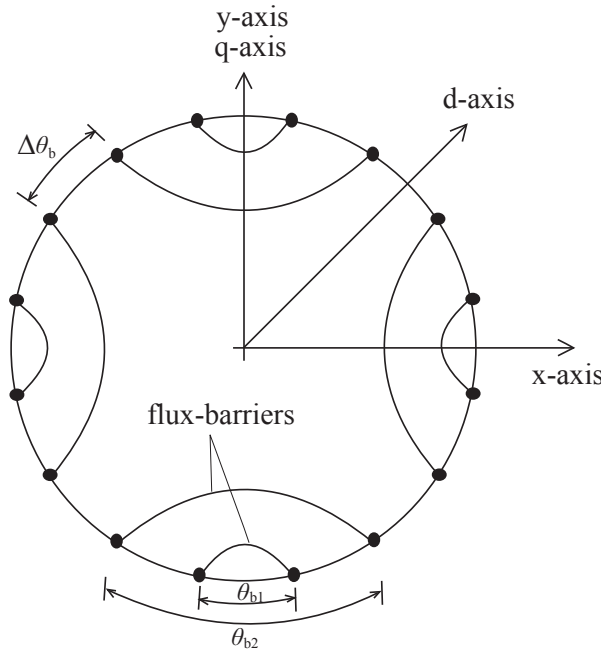


Figure 9.18: Rotor with equal space between the flux-barriers ends.

In eq. (9.26), B_{b_i} does not depend on the technique used to define the angles of the flux-barriers ends. However, if the flux barrier ends are equally spaced, its expression can be further reduced. The angle of the i -th flux barrier end can be expressed as $\theta_{b_i}^e = k_i \Delta\theta_b^e$, where k_i depends on the rotor geometry [30, 97]. Some examples are reported in Table 9.3.

Substituting eq. (9.23) in eq. (9.26), the general expression of flux density in the i -th flux barrier is given by

$$B_{b_i} = \frac{\mu_0 \hat{U}_s}{t_{be_i}} \left[\frac{\sin(p\theta_{b_i}) - \sin(p\theta_{b_{i-1}})}{p(\theta_{b_i} - \theta_{b_{i-1}})} - \frac{\sin(p\theta_{b_{i+1}}) - \sin(p\theta_{b_i})}{p(\theta_{b_{i+1}} - \theta_{b_i})} \right] \quad (9.28)$$

This expression can be simplified as

$$\begin{aligned}
 B_{b_i} &= \frac{\mu_o \hat{U}_s}{t_{e_{b_i}}} \left[\frac{\sin(\theta_{b_i}^e) - \sin(\theta_{b_{i-1}}^e)}{(\theta_{b_i}^e - \theta_{b_{i-1}}^e)} - \frac{\sin(\theta_{b_{i+1}}^e) - \sin(\theta_{b_i}^e)}{(\theta_{b_{i+1}}^e - \theta_{b_i}^e)} \right] \\
 &= \frac{\mu_o \hat{U}_s}{t_{e_{b_i}}} \left[\frac{-(\theta_{b_i}^e - \theta_{b_{i-1}}^e) \sin(\theta_{b_{i+1}}^e) + (\theta_{b_{i+1}}^e - \theta_{b_{i-1}}^e) \sin(\theta_{b_i}^e) - (\theta_{b_{i+1}}^e - \theta_{b_i}^e) \sin(\theta_{b_{i-1}}^e)}{(\theta_{b_{i+1}}^e - \theta_{b_i}^e)(\theta_{b_i}^e - \theta_{b_{i-1}}^e)} \right]
 \end{aligned} \tag{9.29}$$

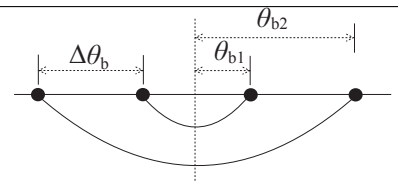
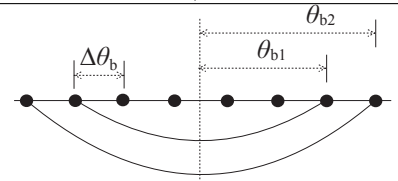
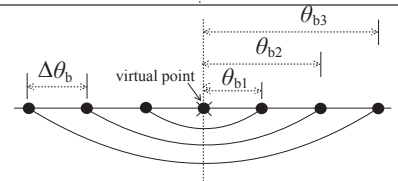
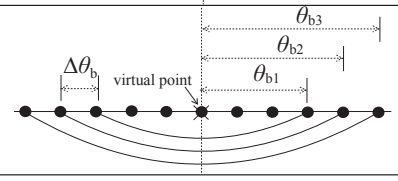
Then, by substituting $\theta_{b_i}^e = k_i \Delta \theta_b^e$ in eq. (9.28), it results

$$B_{b_i} = \frac{\mu_o \hat{U}_s}{t_{e_{b_i}}} \left[\frac{-\Delta \theta_b^e \sin((k_i + 1)\Delta \theta_b^e) + 2\Delta \theta_b^e \sin(k_i \Delta \theta_b^e) - \Delta \theta_b^e \sin((k_i - 1)\Delta \theta_b^e)}{(\Delta \theta_b^e)^2} \right] \tag{9.30}$$

Finally, eq. (9.29) can be simplified as

$$B_{b_i} = \frac{\mu_o \hat{U}_s}{t_{m_i}} \left[\frac{2 \sin(k \Delta \theta_b^e) [1 - \cos(\Delta \theta_b^e)]}{\Delta \theta_b^e} \right] \tag{9.31}$$

Table 9.3: Examples for different rotor geometry with equal space between the equivalent rotor slots per pole pair.

Number of Stator slots	Number of poles	n_s	n_r	N_b	Drawing of one pole	rotor type
24	4	12	8	2		complete $k_i = 0.5, 1.5$
24	4	12	16	2		incomplete $k_i = 2.5, 3.5$
36	4	18	14	3		complete with virtual point $k_i = 1, 2, 3$
36	4	18	22	3		incomplete with virtual point $k_i = 3, 4, 5$

9.3.5. Example and FE validation

The ratio t_{b_i}/l_{b_i} is computed as described in Appendix B according to the motor data in Table 9.1. As stated above, the thickness of the i -th equivalent flux-barrier t_{b_i} is equal to the thickness of the i -th PM t_{m_i} . From t_{b_i} and t_{b_i}/l_{b_i} , the length of the i -th equivalent flux-barrier l_{b_i} is equal to 41, 78, and 140 mm for the first, second, and third flux-barrier, respectively. Then, from eq. (9.6), the reluctances of the i -th equivalent barrier are equal to 1.44×10^6 , 1.54×10^6 , and $1.42 \times 10^6 H^{-1}$, respectively.

In this example, the electric loading \hat{K}_s is adjusted at the rated value that is 30.9 kA/m. Then, the peak value of the scalar stator magnetic potential \hat{U}_s is computed as $\hat{K}_s D_i / (2p)$, resulting in 964 A.

The results achieved from the complete, the simplified and the FE models are compared in Table 9.4. There is a satisfactory agreement between FE and analytical results. In particular, the simplified analytical model yields a satisfactory agreement with both complete analytical model and FE model. This confirms that the simplified analytical model is well suited to predict the maximum stress on the PMs of PMAREL motor due to the loading current. It is confirmed that the air-gap length has a negligible effect on the results. As a consequence, any rotor eccentricity in these machines [37, 63] has a negligible impact on the PMs stress, that is, on the PM demagnetization.

Table 9.4: The analytical and FE model results for REL motor with demagnetization current.

	FE model	Analytical model	
		complete	simplified
$B_{b_1} (T)$	0.076	0.074	0.077
$B_{b_2} (T)$	0.071	0.069	0.070
$B_{b_3} (T)$	0.046	0.050	0.052

Moreover, the superposition of the effect is applied on magnetic networks of the PMAREL motor since the iron flux density is quite low in these operating conditions. The operating points under load for the i -th PM B_{mL_i} can be achieved. The results of both analytical and FE analysis are summarized in Table 9.5, showing a good agreement. Furthermore, the operating points derived from the simplified analytical analysis are slightly lower than the complete analytical and FE analysis. Hence, this introduces an implicitly safety factor from the point of view of the PM demagnetization.

The PM operating points are identified in Fig. 9.19. From Table 9.5 and Fig. 9.19, it is noted that the greatest reduction in flux density due to the electric loading (the worst operating point) is for the PM inset in the first flux-barrier (the smaller barrier).

The proposed procedure has a direct application in selecting the PM width, according to the imposed electric loading and the given maximum stress on the PM. As an example, Fig. 9.20 highlights the relationship between the PM thickness and the electrical loading, for given PM flux density variations, which correspond to the flux density in the flux barriers due to the stator current, i.e., B_b . The results reported in Fig. 9.20 refer to the smaller flux-barrier, where the PM stress and the risk of demagnetization are higher.

Table 9.5: The PMs operating points resulting from the analytical and FE analysis of PMAREL motor, neglecting rotor iron ribs.

	FE model	Analytical model	
		complete	simplified
B_{mL_1} (T)	0.233	0.237	0.222
B_{mL_2} (T)	0.238	0.241	0.232
B_{mL_3} (T)	0.266	0.263	0.250

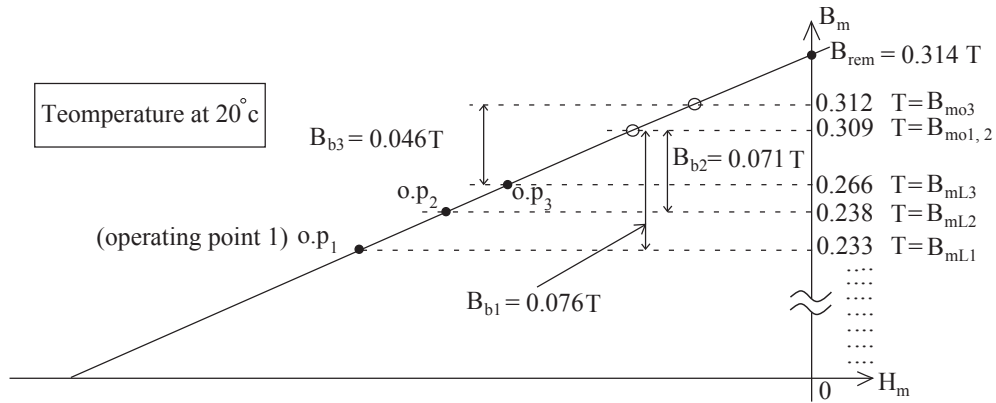


Figure 9.19: Demagnetization curve of the PM material (Ferrite) with the operating points of PMAREL motor fed by nominal electric loading with neglecting the rotor iron ribs.

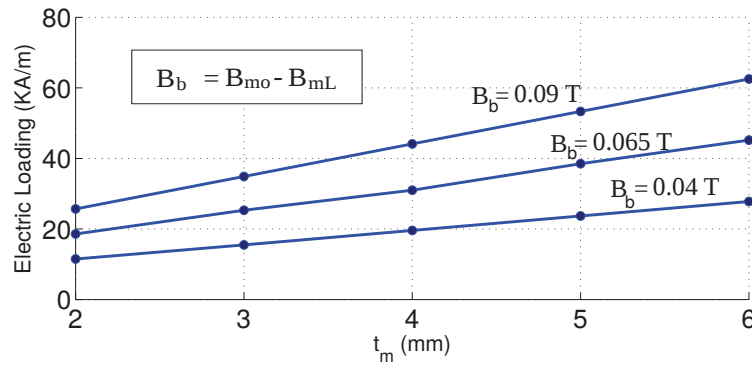


Figure 9.20: Relationship between electric loading and PM thickness for different PM flux density variations under load.

9.4. Rotor iron ribs effect

This section illustrates the effect of the rotor iron ribs. The analysis of PMAREL motor is achieved by means of the magnetic networks shown in Fig. 9.3 and Fig. 9.15, considering the effect of the iron ribs at no load condition. The system is linearized: the leakage flux in the ribs is considered as a flux source ($\phi_{sat_i} = B_{sat_i} t_{r_i} L_{stk}$) in the opposite direction of the PM flux, where B_{sat_i} is the saturated flux density in the iron ribs. In this perspective, the effective flux

of the i -th PM $\phi_{rem_{eff_i}}$ is given by

$$\begin{aligned}\phi_{rem_{eff_i}} &= \phi_{rem_i} - \phi_{sat_i} \\ &= B_{rem} w_{m_i} L_{stk} - B_{sat_i} t_{r_i} L_{stk} \\ &= B_{rem} \left(w_{m_i} - \frac{B_{sat_i} t_{r_i}}{B_{rem}} \right) L_{stk}\end{aligned}\quad (9.32)$$

This equation highlights that a portion of PM is necessary for saturating the iron ribs, whose width results to be equal to $t_{r_i} B_{sat_i} / B_{rem}$. Therefore, the PM can be ideally split into two parts: one to saturate the ribs, the other to produce air-gap flux. The effective width of the i -th PM producing the air-gap flux, $w_{m_{eff_i}}$, is defined by the term within the parenthesis in eq. (9.32), that is

$$w_{m_{eff_i}} = w_{m_i} - \frac{B_{sat_i} t_{r_i}}{B_{rem}} \quad (9.33)$$

The iron ribs effect is considered in both complete and simplified magnetic networks, as described hereafter.

9.4.1. Complete model

The magnetic networks shown in Fig. 9.3 and Fig. 9.4 are modified as shown in Fig. 9.21 and Fig. 9.22 in order to consider the iron ribs effect. If the effective PM widths $w_{m_{eff_i}}$ are considered instead of the whole PM widths w_{m_i} , the flux in each loop, as shown in Fig. 9.22, is computed as in eq. (9.5). According to the effective PM lengths, the vector U_{rem_i} in eq. (9.5) is replaced by the vector U_i given by

$$U_i = \phi_{rem_{eff_i}} R_{b_i} \quad (9.34)$$

Then, from eqs. (9.8) to (9.10), the flux flowing in the air-gap in front of the i -th flux-barrier ϕ_{g_i} , the scalar magnetic potential of the i -th rotor island U_{r_i} , and the flux flowing through the left and right parts of the i -th flux-barriers ϕ_{b_i} , can be computed, respectively. Hence, the flux of the i -th PM is computed as follows:

$$\phi_{m_i} = \phi_{g_i} + \phi_{b_i} + \phi_{m_{i-1}} - \phi_{b_{i-1}} + \phi_{sat_i} - \phi_{sat_{i-1}} \quad (9.35)$$

Consequently, the no load flux densities of the i -th PM is computed as in eq. (9.12).

9.4.2. Simplified model

Analogously, the same approximations, shown in Fig. 9.8, Fig. 9.9, and Fig. 9.10 can be applied in case of considering the iron ribs. Then, the value of each i -th ϕ_{g_i} is given by

$$\phi_{g_i} = \frac{U_{m_{eff_i}}}{R_{g_i} + R_{m_i}} \quad (9.36)$$

where the scalar magnetic potential $U_{m_{eff_i}}$ is

$$U_{m_{eff_i}} = B_{rem} (w_{m_{eff_i}} - w_{m_{eff_{i-1}}}) L_{stk} R_{m_i} \quad (9.37)$$

Starting from ϕ_{g_i} , from eqs. (9.9) to (9.12), $B_{m_{o_i}}$ can be computed, considering the iron ribs effect.

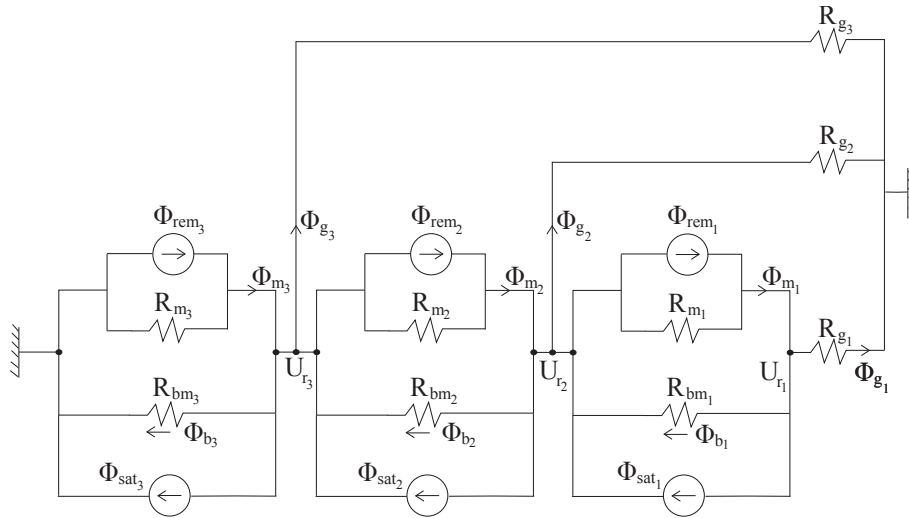


Figure 9.21: Magnetic network of one pole of PMAREL motor at no load, considering the rotor iron ribs.

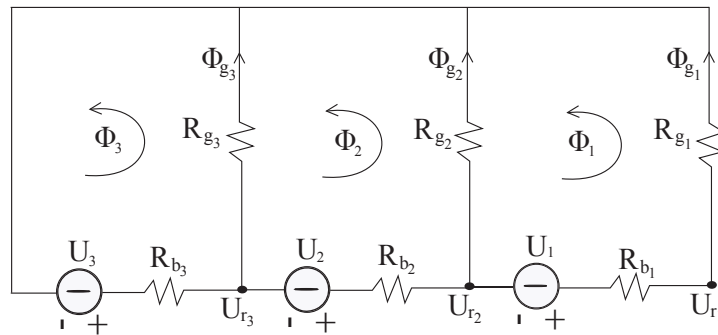


Figure 9.22: Redrawing of the magnetic network of one pole of PMAREL motor at no load, considering the rotor iron ribs.

9.4.3. Example and FE Validation

The saturation flux of the i -th flux barrier ϕ_{sat_i} can be computed by using the values of t_{r_i} and B_{rem} as in Table 9.1. Then, both analytical analyses described above are carried out. The results of both analytical and FE models are shown in Table 9.6. There is a satisfactory agreement between the analytical and the FE analysis. Once again, the simplified analytical model results to be suitable for the analysis.

By comparing Table 9.2 and Table 9.6, it is noted that, the rotor iron ribs cause a slightly increase of the no load PM flux density of the first and second flux-barrier. Additionally, the effect of the iron ribs on the magnets inset in the third flux-barrier is very low (i.e., so low that can be neglected).

The PM operating points under load of the PMs inset in the three flux-barriers are computed and reported in Table 9.7. They are also shown in Fig. 9.23. It is noted that, the operating points of the PM inset in the first and second flux-barriers are improved due to the iron ribs effect while the operating point of the third magnet approximately remains the same as in case of neglecting the iron ribs.

Table 9.6: The analytical and FE model results for PMAREL motor at no load, considering the rotor iron ribs.

	FE model	Analytical model	
		complete	simplified
$B_{mo_1} (T)$	0.310	0.313	0.308
$B_{mo_2} (T)$	0.311	0.312	0.308
$B_{mo_3} (T)$	0.312	0.313	0.309

Table 9.7: The PM operating points resulting from analytical and FE analysis for PMAREL motor, considering the rotor iron ribs.

	FE model	Analytical model	
		complete	simplified
$B_{mL_1} (T)$	0.234	0.239	0.231
$B_{mL_2} (T)$	0.240	0.243	0.240
$B_{mL_3} (T)$	0.266	0.263	0.257

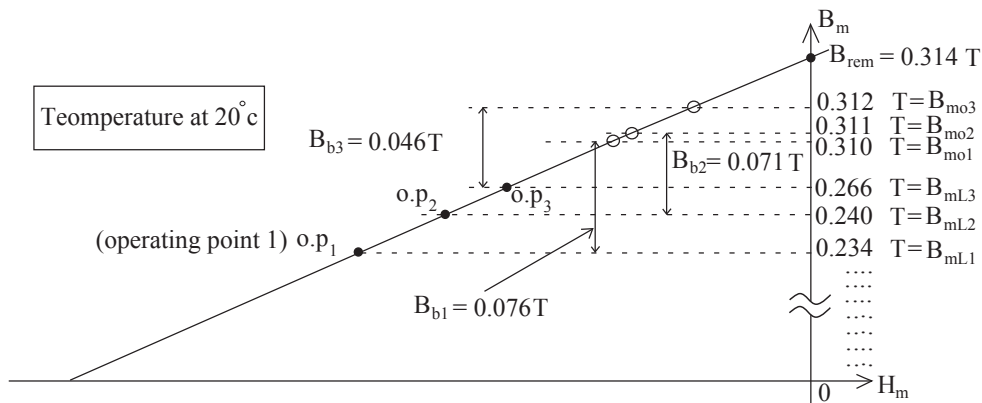


Figure 9.23: Demagnetization curve of the PM material (Ferrite) with the operating points of PMAREL motor fed by nominal electric loading, considering the rotor iron ribs.

9.4.4. Electric loading effect on the operating points of the PMs

To the aim of studying the effect of the electric loading on the operating points of the PMs, the electric loading is changed, as an example \hat{K}_s is adjusted at different value equal to 25 (kA/m). Table 9.8 shows the exact and simplified analytical models and FE model results. By comparing Table 9.4 and Table 9.8, it is noted that the stress on the PMs is decreased due to electric loading decreasing and vice versa. Once again, there is a good agreement between the analytical and FE models. In addition, the operating points of the PMs are increased in both cases of considering and neglecting the rotor iron bridges.

In this perspective, the maximum demagnetizing current I_{demag} which enforces the operating point of the first barrier magnet (the worst PM, as shown in Fig. 9.23 and Fig. 9.19) to be equal to 0 T (i.e., at Knee point) can be computed as

$$I_{demg} = I_n \frac{B_{mo_1} - B_{knee}}{B_{mo_1} - B_{ml_1}} \quad (9.38)$$

Table 9.8: The analytical and FE model results for REL motor with low demagnetizing current

	Exact analytical model	Simplified analytical model	FE model
$B_{b_1} (T)$	0.060	0.063	0.061
$B_{b_2} (T)$	0.056	0.057	0.060
$B_{b_3} (T)$	0.041	0.042	0.040

The operating point of the first barrier magnet equals to 0.233 and 0.234 T , as shown in Fig.9.19 and Fig.9.23, at the rated current, which is set equal to 5.012 A . Therefore, the maximum demagnetizing current I_{demag} is achieved equal to 20.18 and 20.44 A in case of considering and neglecting the rotor iron bridges, respectively. It is noted that, the maximum demagnetizing current is about four times of the rated times at operating temperature equal to 20°.

Finally, the analysis can be easily extended to different temperature, as well as, to various PM types. The iron ribs effect can be also considered in both analytical analysis, showing a slight variation in the PM flux density.

9.5. Conclusions

This chapter dealt with two analytical models for the magnetic analysis of PMAREL motors, focusing on the no load flux density and the PM demagnetization under load. In particular, a simplified approach is proposed, based on effective assumptions, allowing the main PM dimensions to be directly estimated. The key relationships between magnetic fields and the PM geometry are rewritten, highlighting the direct link between the PM thickness and the stress on the PM (demagnetization limit), and between the PM width and the desired air-gap flux density. These relationships yield to rapidly estimate the PM dimensions during the design procedure, without requiring iterations.

There is a satisfactory agreement between the results of both analytical and FE analysis. The PM operating points under load of the simplified model are slightly lower than those achieved from the complete analytical model and the FE model. This can be considered as an implicit safety margin to avoid the PM demagnetization.

The analysis can be easily extended to different temperature, as well as, to various PM types. The iron ribs effect can be also considered in both analytical analyses, showing a slight variation in the PM flux density.

Chapter 10

Fast Synthesis of REL and PMAREL Motors

This chapter describes a procedure for a practical synthesis of a Synchronous Reluctance Motor, as well as, a Permanent Magnet Assisted Synchronous Reluctance Motor. The procedure is completely analytical, yielding a rapid prediction of the motor geometry, taking into account both magnetic and mechanical considerations. From the application requirements, the external volume of the motor is computed. The further practical needs, such as maximum outer space, maximum available length, existing stator lamination, and so on are considered. Then, the design of the rotor geometry is carried out. Referring to the permanent assisted synchronous reluctance motor, the PM size is determined considering the demagnetization limit according to the maximum current loading.

10.1. Introduction

The synchronous reluctance machine is becoming of great interest in the latest years, due to two key factors: (i) the increase of rare earth Permanent Magnet (PM) cost, and (ii) the increasing request of high-efficiency machines. Therefore, the REL motor and the Ferrite PM assisted REL (Ferrite PMAREL) motor are becoming competitors of both surface-mounted PM machines and induction machines in many applications [29]. It is also becoming particularly interesting when the motor control is based on the sensorless rotor position detection [98–100].

A sketch of a four-pole synchronous REL rotor with three flux barriers per pole is shown in Fig. 10.1. The synchronous PMAREL motor is achieved when PMs are inset within the flux barriers [101, 102]. The PMs are introduced into the flux barriers to the aim of saturating the iron ribs, increasing the power factor (PF), which is quite low in the REL machines.

Even if, there is a great interest in this kind of machines, there is a poor knowledge about their design, that is, about which are the effective size for a given torque and, in particular, how to select the rotor geometry. In order to fill this gap, the aim of this chapter is to give useful suggestions for reaching a preliminary motor geometry, needed for a fast comparison with other motor types or as the starting point for a successive optimization.

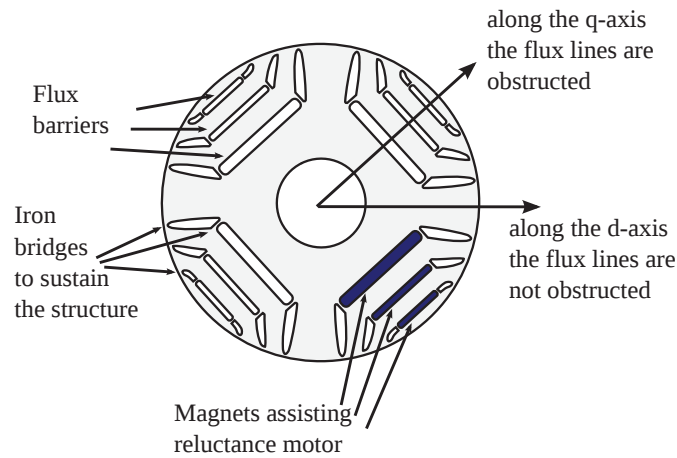


Figure 10.1: Cross section of synchronous reluctance rotor.

At first, the stator size is estimated adopting a torque density factor derived from the past experience. The proper stator has to be characterized by a number of slots per pole per phase greater than two and a distributed winding, so as to reduce the stator magneto-motive force (MMF) harmonics, avoiding a high torque ripple. In the following, the stator is selected with three slots per pole per phase and a distributed winding.

Then, the focus is posed on the rotor geometry and, especially, on the geometry of the rotor flux barriers. In fact, there is a high influence of such a geometry on the machine capability, as far as, both average torque and ripple is concerned [30].

The attention is mainly focused on the rotor geometry, that is, on the flux barriers geometry. There is a high influence of such a geometry on the machine capability, as far as both average torque and ripple are concerned [30]. To achieve a high rotor saliency, the number of flux barriers per pole ranges between two and four. Hereafter, a rotor with three flux-barriers per pole will be referred to. Their thickness is computed from magnetic considerations, as will be shown in section 10.4. Magnetic ribs are determined according to the centrifugal forces on the rotor islands bordered by the flux barriers themselves (section 10.5). PMs are inset in each flux barrier to assist the REL motor. The width of the PMs is linked to the magnetic flux in the air-gap (section 10.6). The thickness of each PM is selected according to prevent the irreversible demagnetization due to the maximum current reaction (section 10.7).

10.2. Determination of the main REL motor dimensions

The determination of the main dimensions of the REL motor (outer stator diameter D_e and the stack length L_{stk}) is based on the past experience about this kind of machines. Being the rated torque T_n of the machine related to the active volume, the adopted procedure is based on the ratio between the torque and the outer volume of the machine itself. To this aim the factor k_{TV} is defined, which corresponds to this ratio.

The air gap volume is typically related to the rated motor torque, since the tangential (shear) stress due to the interaction between the electric and magnetic fields occurs at the air gap surface. However, the volume considered here refers to the outer diameter. For the application point of view, the outer volume has a more direct link with the machine size.

Since the ratio between outer and inner stator diameters, D_e and D , respectively, changes with the machine dimensions (small size machines exhibit a D_e -to- D ratio larger than large size machines), it results that the factor k_{TV} also depends on the rated torque. Anyway, for typical application requirements, e.g., rated torque in the range between 5 to 50 Nm, a proper value (expressed in Nm over liter) is

$$k_{TV} \approx 10 \frac{Nm}{l} \quad (10.1)$$

Table 10.1: Determination of the factor k_{TV} in different cases of the literature.

D_e (mm)	L_{stk} (mm)	T_n (Nm)	k_{TV} (Nm/l)	Reference
72	60	2.4	9.82	[38]
112	40	4.5	11.42	[103]
150	105	18	9.7	[92]
135	60	7	8.2	[95]
200	70	20	9.1	[95]
340	250	260	11.45	[95]
125	27	2	6	[95]
203.2	133.4	57.3	13.2	[17]
203.2	133.4	35	8.1	[17]

Table 10.1 shows the computation of the factor k_{TV} for different motors used in the literature. It is noted that the value of k_{TV} is within range between 8 and 12 Nm/l. This range depends on the cooling effectiveness.

Once the outer volume is fixed, D_e and L_{stk} are segregated on the basis of further practical needs, such as maximum outer space, maximum available length, existing stator lamination, and so on.

10.3. Selection of the ends of the flux barriers

The selection of the ends of the flux barriers in a REL machine is a design step requiring a particular care. Even if such a choice affects only marginally the average torque in a multi-flux-barrier machine, it plays a very important role in the torque ripple production.

This ripple is caused by the interaction between the spatial harmonics of magneto-motive force (MMF) due to the stator currents and the rotor geometry. The main harmonic of the stator MMF is synchronous with the rotor and produces the average electromagnetic torque. The other harmonics are not synchronous and cause variations of the flux across the flux barriers, i.e., oscillations of the rotor magnetic potential. The main effect is a high torque ripple.

There are some techniques proposed in literature to reduce the torque ripple in synchronous REL machines [23, 24, 26, 28]. The rotor skewing can be considered to reduce the ripple, even if this technique is not enough to smooth completely the torque [24, 28, 30]. Another strategy consists in introducing a slight shift of the flux barriers [25, 104] or adopting two different flux barrier geometries in the same lamination [27, 49], so as to compensate the impact of the

stator magneto-motive force (MMF) harmonics [29, 93]. The resulting motor is referred to as "Machaon" motor. Several optimizations were carried out to the purpose of smoothing the torque and several solutions have been founded [49, 94, 95].

In this chapter, the proposed technique in [30] is referred, even if this technique does not always give the solution with the lowest torque ripple [1, 27], it provides a good starting point in the rotor geometry definition. Among the others, the main advantage is that the position of the rotor flux-barriers can be determined analytically. It results to be a good starting point for the design. Then, a successive optimization can be used to refine the geometry.

As stated in [30], the rotor periphery is divided into equally spaced separation points n_r . These points n_r are called equivalent rotor slots per pole pair. They must be properly related to the stator number of slots per pole pair $n_s = Q_s/p$ in order to minimize the torque ripple. As a consequence, the following relationship is suggested in [30], relating n_s , with n_r , that is

$$n_r = n_s \pm 4 \quad (10.2)$$

Therefore, the flux-barrier ends (actual and fictitious) are assumed to be equally spaced along the rotor periphery, during our design procedure.

In addition, there are two types of rotor geometry are introduced in [30]. The former is a complete rotor structure, while no flux barrier is omitted. The latter is an incomplete rotor structure, while there are some flux barriers close to the q-axis are omitted, in case of high n_r values. Of course, there are spurious harmonics, in case of incomplete rotor structure. However, this still represents the best solution with respect to the given n_s .

In order to compare between both rotor structures, as an example, a 4-pole REL motor with 36 slots in the stator (i.e., $n_s = 18$) and three flux barrier per the rotor pole ($N_b = 3$), is considered. From eq. (10.2), there are two choices of n_r . According to the rotor structure needed, n_r can be selected. If $n_r = 14$ is selected, a complete rotor structure is designed, as shown in Fig. 10.2. However, if $n_r = 22$ is selected, an incomplete rotor structure is designed, as shown in Fig. 10.3. Besides, in this example, there are virtual point is appeared because $n_r/2$ is odd. At first, this virtual point is placed at the q-axis, as recommended by [30]. However, the effect of putting this virtual point in the d-axis will be investigated later.

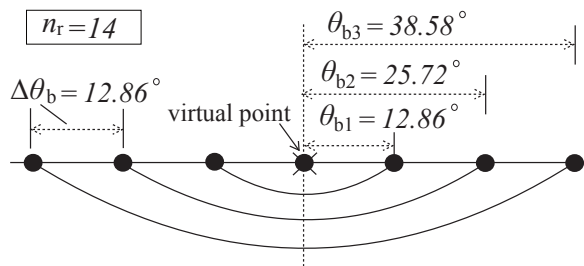


Figure 10.2: Schematic diagram of one pole of complete rotor structure of a 4-pole REL machine with $n_s = 18$ slots per pole pair.

Both REL motors with different rotor structure are designed and simulated by means of FE software at the nominal current (i.e., $I_n = 5.29A$ and $\alpha_i^e = 63^\circ$). Knowing that, the design of the flux barriers geometries will be discussed later in this chapter. Fig. 10.4 and Fig. 10.5 show the flux density map of both motors. The average torque and torque ripple are computed for

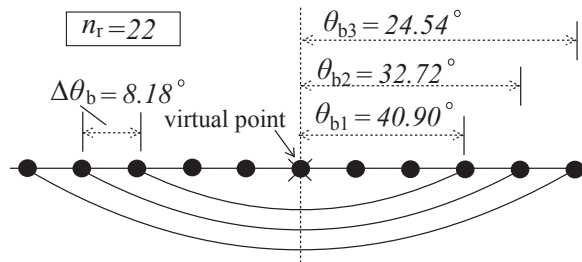


Figure 10.3: Schematic diagram of one pole of incomplete rotor structure of a 4-pole REL machine with $n_s = 18$ slots per pole pair.

REL motor with both types of rotor structure, as shown in Fig. 10.6. They are equal 11.9 Nm and 23%, in case of complete rotor, and are equal 11 Nm and 36.3%, in case of incomplete rotor. Of course, it is clear that the spurious harmonics, due to incomplete rotor, increase the torque ripple and slightly reduce the average torque. Therefore, for this motor, the best choice is the complete rotor. However, sometimes, the value of n_r is high depending on the stator. In this case, it is recommended, to choose n_r which offers lower omitted flux barriers (i.e., the nearest solution to the complete design).

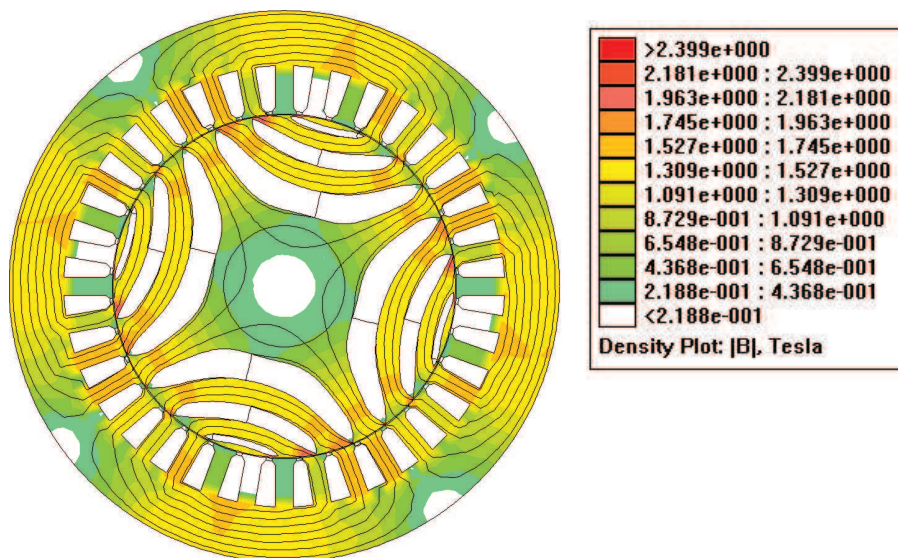


Figure 10.4: Flux density map of a 4-pole REL motor with a complete rotor structure at the rated loading condition and $\theta_m = 30^\circ$

Once again, [30] suggested that, in case of $n_r/2$ is odd, the virtual point should be in front of the q-axis. However, the effect of considering this virtual point in front of d-axis, as shown in Fig. 10.7. It is noted that, the flux barriers angles are changed. In order to compare between the two cases of considering the virtual points in front to the q-axis and d-axis, the same motor used in the previous example is redesigned again. Fig. 10.8 shows the map of the flux density of the new redesigned motor, in case of considering the virtual point in front to the d-axis. From Fig. 10.5 and Fig. 10.8, it is noted that, the space between the poles is double the distance between the points within the pole itself. By comparing the torque and torque ripple

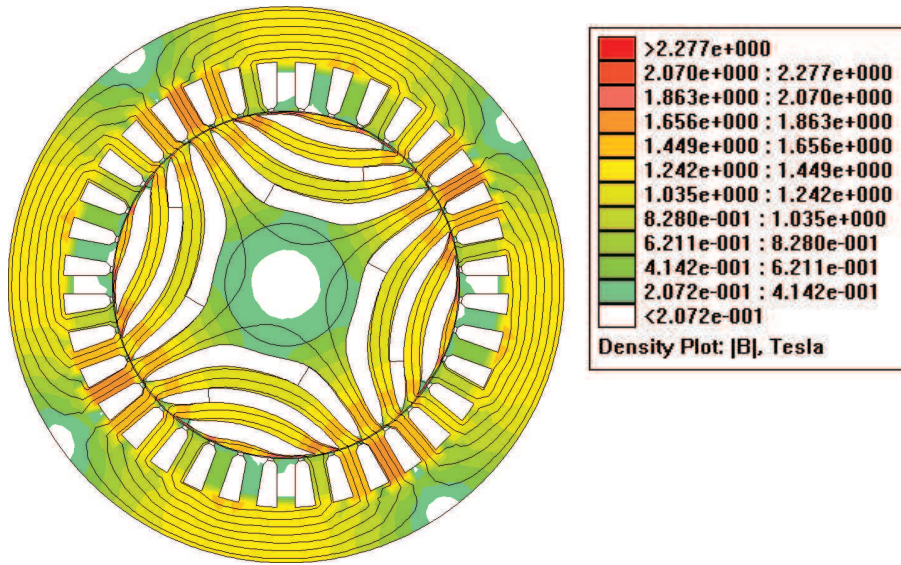


Figure 10.5: Flux density map of a 4-pole REL motor with an incomplete rotor structure at the rated loading condition and $\theta_m = 30^\circ$

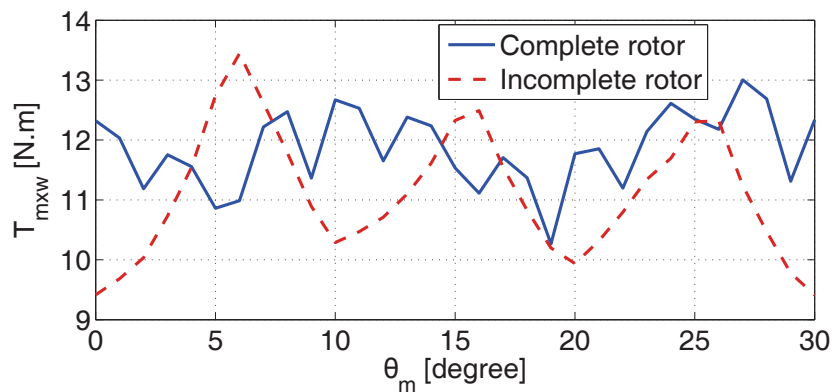


Figure 10.6: Electromagnetic torque versus the rotor position for REL motor with both complete and incomplete rotor structure.

result from the FE simulations, the torque and the ripples at this case are equal to 10.5 Nm and 41% , respectively. From Fig. 10.9, due to considering virtual point in front to d-axis, the average torque is reduced and the torque ripple is doubled with respect to the case of complete rotor and virtual point in front to the q-axis, as expected. Now, the recommendations given by [30] for selecting the end barriers angles are now clear and understandable. Therefore, this recommendations should be follows in order to select good initial design of the rotor with low torque ripple as possible.

As a consequence, according to the selected stator, as stated before in section 10.2 and the rotor design, the values of n_s and N_b are known. Then, there are two values of n_r (i.e., n_{r1} and n_{r2}) referring to eq. (10.2). In order to achieve the lowest torque possible ripple, n_r must be selected to obtain a complete rotor structure or the closest structure to the complete one, in case of high value of n_r . This step can be carried out automatically and analytically by using the algorithms shown in Fig. 10.10. The steps of this algorithm are explained as follows:

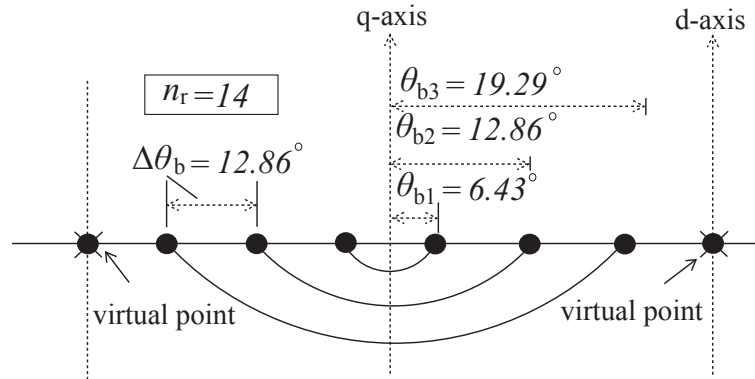


Figure 10.7: Schematic diagram of one pole of complete rotor structure of a 4-pole REL machine with $n_s = 18$ slots per pole pair, in case of virtual point in front to d-axis.

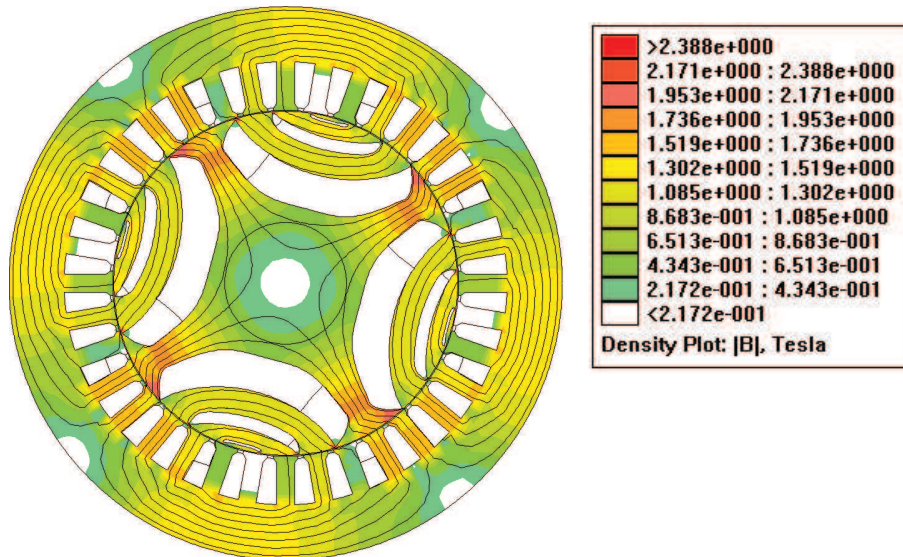


Figure 10.8: Flux density map of a 4-pole REL motor with a complete rotor structure at the rated loading condition and the virtual point in front to the d-axis and $\theta_m = 30^\circ$

Firstly, the value of n_{r_1} (n_{r_1}) is checked, if it is enough to construct the requiring flux barriers or not (i.e., $\geq 4N_b$ or not). Then, if it is enough, it is checked if is exactly equal to the points required for the flux barrier or not (i.e., $= 4N_b$ or not). If it is equal to $4N_b$, the rotor is a complete rotor and the value of n_{r_1} is the best solution. But, if it is greater than $4N_b$, the rotor is incomplete rotor and the second value of n_{r_1} (n_{r_2}) should be checked. Secondly, in the similar way, n_{r_2} is checked. If it results a complete rotor, it must be selected. If it gives incomplete rotor also, the two solutions of incomplete rotor should be compared together. The solution which results lower omitted flux barriers (i.e., the closest solution to the complete motor), must be selected. Finally, depending on the value of the selected n_r , the end barriers angles can be computed. In case of n_{r_1} and n_{r_2} not enough for the flux barriers points, the design requirements should be modified. The first possible modification is in the stator number of slots Q_s to modify the values of n_s , and hence, to change the value of n_r . The second possible modification is to reduce the number of flux barriers per pole in the rotor N_b , and hence, the number of the requiring points is reduced.

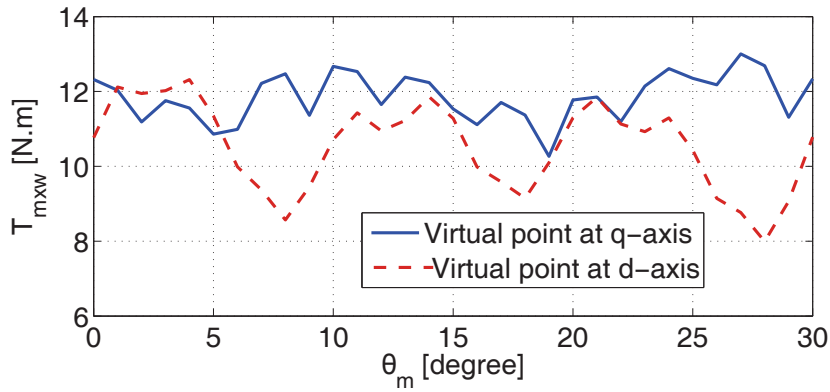


Figure 10.9: Impact of choosing the virtual point at *d*-axis or *q*-axis on the electromagnetic torque of the REL motor.

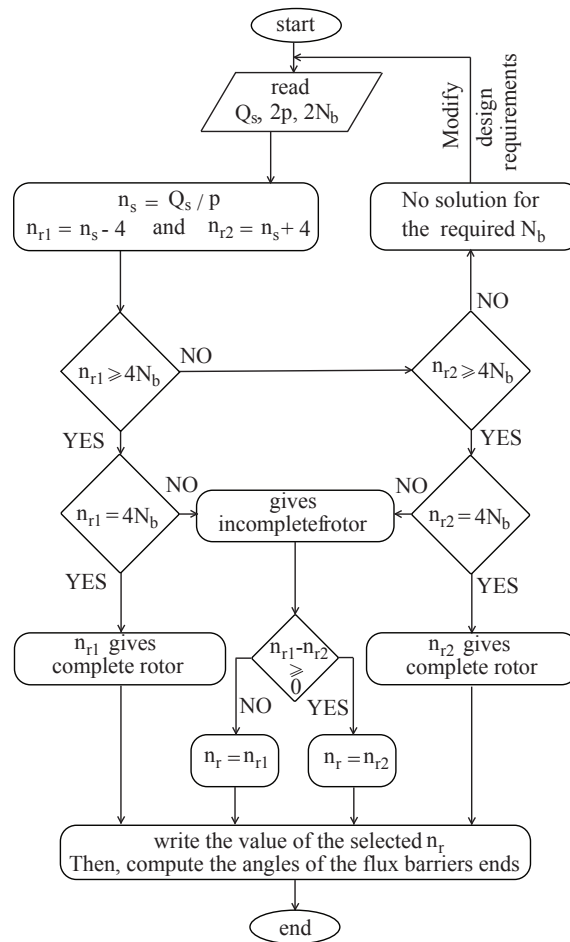


Figure 10.10: A Flow chart describes the automatic algorithm used for obtaining the best value of n_r according to the design requirements.

10.4. Selection of the geometry of the flux barriers

For the purpose of taking into account the thickness of the flux-barrier, which affects the level of saturation of the machine, a coefficient k_{air} [105, 106] has been defined as

$$k_{air} = \frac{\sum_i t_{bi}}{(D_r - D_{sh})/2} = \frac{t_{bt}}{(D_r - D_{sh})/2} \tag{10.3}$$

where, the terms t_{b_i} is the thickness of the i -th flux-barriers, D_r is the external rotor diameter and D_{sh} is the shaft diameter.

Coefficient k_{air} has to be chosen according to the stator geometry (e.g. tooth width and back-iron height). In this way, it is possible to define a coefficient $k_{air,s}$ related to the stator geometry as $k_{air,s} = (p_s - w_t)/p_s$ in which p_s is the stator slot pitch defined as: $p_s = \pi D_i/Q_s$ and w_t is the stator tooth width. It is evident that the k_{air} of the rotor should be close to the $k_{air,s}$ of the stator, so as the machine results to be equally saturated. For the purpose of limiting the iron losses, $k_{air,s}$ should be slightly lower than k_{air} .

A high rotor saturation factor k_{air} causes a decrease of torque and power since the rotor path limits the flux along the d -axis direction [105]. The stator iron path is characterized by a lower flux density (since it is limited by the rotor) so that the stator iron losses decrease. Both power factor and efficiency don't present considerable variations with k_{air} . As a final consideration, a k_{air} a little higher than that of the stator seems to be the proper choice, considering both torque and losses.

Once the total rotor iron width $(1 - k_{air})(D_r - D_{sh})/2$ has been decided, the width of each rotor iron path w_{r_p} is computed referring to the flux density distribution of the d -axis flux, as shown in Fig. 10.11. Then, w_{r_p} results to be proportional to the average flux density in that path. $w_{r_{p_i}}$ of i -th path (with $i = 1, 2, 3,$ and 4) is given by

$$w_{r_{p_i}} = \frac{(1 - k_{air}) \left[\frac{D_r - D_{sh}}{2} \right] \frac{1}{(\theta_{b_i}^e - \theta_{b_{i-1}}^e)} \int_{\theta_{b_{i-1}}^e}^{\theta_{b_i}^e} \sin \theta^e d\theta^e}{\sum_{\kappa=1}^{\kappa=N_b} \frac{1}{(\theta_{b_\kappa}^e - \theta_{b_{\kappa-1}}^e)} \int_{\theta_{b_{\kappa-1}}^e}^{\theta_{b_\kappa}^e} \sin \theta^e d\theta^e + \frac{1}{2(\frac{\pi}{2} - \theta_{b_{N_b}}^e)} \int_{\theta_{b_{N_b}}^e}^{\frac{\pi}{2}} \sin \theta^e d\theta^e} \quad (10.4)$$

where $2\theta_{b_i}^e$ is the electrical angle of the i -th flux-barrier ends ($i = 1, 2,$ and 3 in the example), as shown in Fig. 10.11.

In [16], the optimum distribution of the air isolation t_{b_t} is suggested. The stator magnetic potential in the q -axis direction is shown in Fig. 9.16. The average stator scalar magnetic potential (U_{s_i}), in front to the i -th flux barrier, is computed, as reported in eq. (9.23). Referring to Fig. 9.17, the magnetic voltage drop on the i -th flux-barrier (ΔU_{s_i}) is given by

$$\Delta U_{s_i} = U_{s_i} - U_{s_{i+1}} \quad (10.5)$$

The ratio between the thicknesses of the i -th and $i + 1$ -th barrier is reported in [16] as

$$\frac{t_{b_i}}{t_{b_{i+1}}} = \frac{\Delta U_{s_i}}{\Delta U_{s_{i+1}}} \sqrt{\frac{l_{b_i}}{l_{b_{i+1}}}} \simeq \frac{\Delta U_{s_i}}{\Delta U_{s_{i+1}}} \sqrt{\frac{\theta_{b_i}}{\theta_{b_{i+1}}}} \quad (10.6)$$

Thus,

$$\frac{t_{b_2}}{t_{b_1}} = \frac{\Delta U_{s_2}}{\Delta U_{s_1}} \sqrt{\frac{\theta_{b_2}}{\theta_{b_1}}} = c_{12} \quad (10.7)$$

$$\frac{t_{b_3}}{t_{b_1}} = \frac{\Delta U_{s_3}}{\Delta U_{s_1}} \sqrt{\frac{\theta_{b_3}}{\theta_{b_1}}} = c_{13} \quad (10.8)$$

Referring to the REL motor with three flux-barriers per pole, the thickness of each barrier is computed as

$$t_{b_1} = \frac{k_{air} (D_r - D_{sh})}{1 + c_{12} + c_{13}} \quad (10.9)$$

$$t_{b2} = \frac{k_{air} \frac{(D_r - D_{sh})}{2} c_{12}}{1 + c_{12} + c_{13}} \quad (10.10)$$

$$t_{b3} = \frac{k_{air} \frac{(D_r - D_{sh})}{2} c_{13}}{1 + c_{12} + c_{13}} \quad (10.11)$$

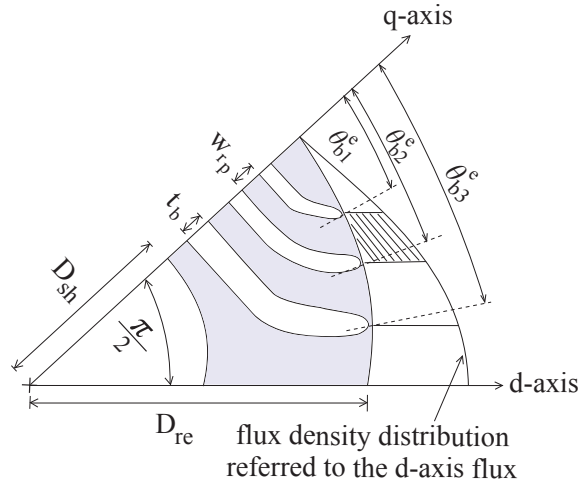


Figure 10.11: Iron path width referring to the d-axis flux density distribution.

From the results of [107], it is founded that, the fluid barriers (circular and angled shape) shapes is the better than the traditional rectangular or I2U shaped barriers (i.e., one I-shaped plus two U-shaped barriers). Because, the REL motor with fluid barriers less saturated than that with the traditional barriers, with the same electric loading. Therefore, the REL motor with fluid barriers has higher torque than the counterpart motor. In addition, it still keep low torque ripple. Both configuration of fluid barriers and I2U shaped barriers are shown in Fig. 10.12.

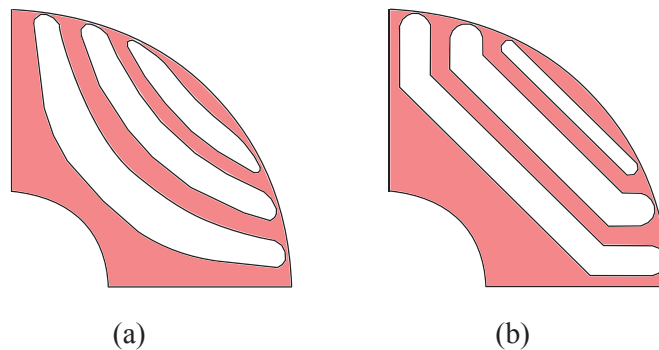


Figure 10.12: Rotor pole with (a) fluid barriers, (b) I2U shaped barriers.

From [107, 108], the steps of drawing the fluid flux barriers are clarified. The profiles of the barriers are based on the potential lines of the magnetic field in the rotor, as shown in

Fig. 10.13. This lines are described in polar coordinates by

$$c(r, \theta) = \sin(p\theta) \frac{\left(\frac{2r}{D_{sh}}\right)^{2p} - 1}{\left(\frac{2r}{D_{sh}}\right)^p} \quad (10.12)$$

and

$$r(\theta, c) = \frac{D_{sh}}{2} \left[\frac{c + \sqrt{c^2 + 4 \sin^2(p\theta)}}{2 \sin(p\theta)} \right]^{1/p} \quad 0 \leq \theta \leq \frac{\pi}{p} \quad (10.13)$$

where, r and θ are the radius and angle of a point on the potential line.

Each barrier is defined by three potential lines, as shown in Fig. 10.13 [107]. The central potential line is defined by substituting the barrier end angle and the outer rotor radius $D_r/2$ in eq. (10.12). The radius of the mid-point of this line ($r_{m,bi}$) is computed at angle $\pi/2p$ from eq. (10.13). Then, depending on the barrier thickness, the upper and lower points surrounding the mid-point of the barrier ($r_{m1,bi}$ and $r_{m2,bi}$) are computed, as reported in eqs. (10.14) and (10.15), respectively. After that, by substituting these points in eq. (10.12), the potential lines of the barrier borders can be obtained. Hereafter, the flux barrier can be drawn, as shown in Fig. 10.13. All previous steps are summarized in the flowchart given in Fig. 10.14.

$$r_{m1,bi} = r_{m,bi} - \frac{t_{bi}}{2} (1 - \Delta m_i) \quad \theta = \frac{\pi}{2p} \quad (10.14)$$

$$r_{m2,bi} = r_{m,bi} + \frac{t_{bi}}{2} (1 + \Delta m_i) \quad \theta = \frac{\pi}{2p} \quad (10.15)$$

where, Δm_i is the per-unit offset factor. It varies in the range $[-1, 1]$. However, it commonly used as zero value in order to split the barrier 50 – 50 around the virtual midline of the barrier.

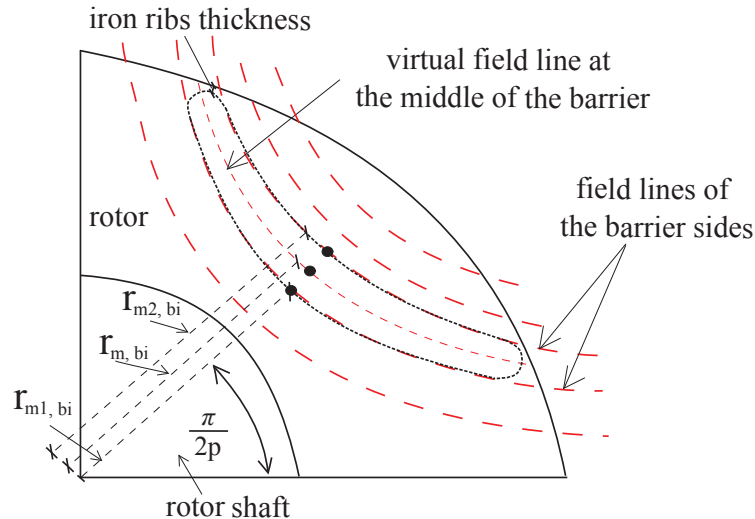


Figure 10.13: Drawing of the flux-barrier according to the potential lines of the rotor field.

Surely, the total thickness of the barriers shouldn't exceed the available length through the q-axis $(D_r - D_{sh})/2$. Also, the summation of the angles of the barrier ends shouldn't exceed the

angular span $\pi/(2p)$. If one of these conditions are not satisfied during the design, there is an overlapping between the barriers which is considered an unfeasible design. However, in our design, k_{air} is always less than one. Therefore, the total air thickness is always less than $(D_r - D_{sh})/2$. In addition, the angles of the barrier ends are computed based on equally spaced points on the rotor periphery, as shown in Fig. 10.10. Therefore, there is no possibility to obtain a summation of angles greater than $\pi/(2p)$. Therefore, our design is robust toward overlapping between the barriers and always results in a feasible design. Additionally, [107] approved that the optimization results for the barrier ends angles are very close to that proposed in [30]. This means that our design is not very far from the optimum design and is considered a good starting point for optimization.

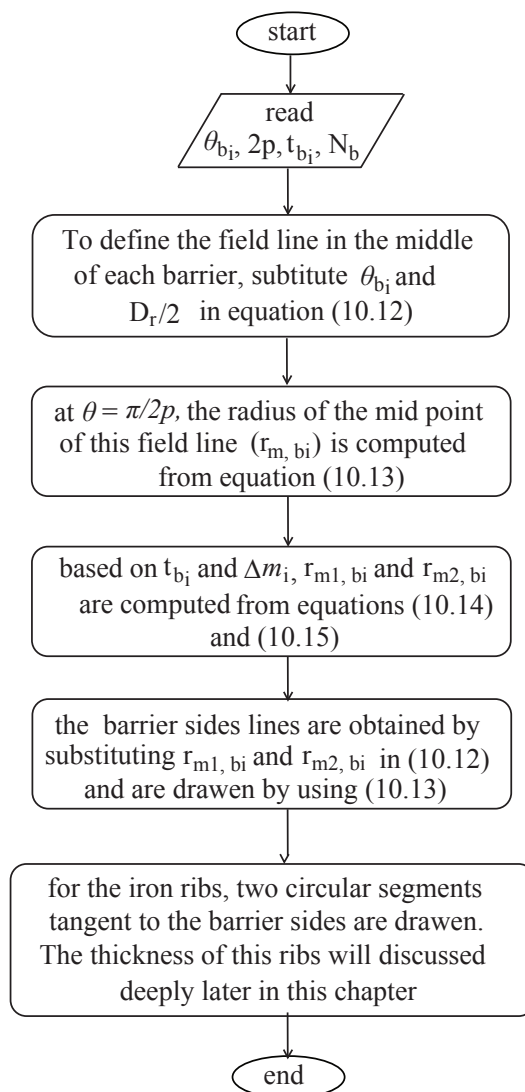


Figure 10.14: A Flow chart describes the steps of drawing the fluid flux barriers.

10.5. Computation of the iron rib thickness

The typical flux barrier geometries are represented in Fig. 10.15(a) and (c): a rectangular and a circular flux barrier. In Fig. 10.15(b) and (d), there are the corresponding geometrical approximations. The rotor magnetic island between the flux-barrier and the air-gap is highlighted in gray color. According to Fig. 10.15 (b), the cross-area section of the rotor island is

$$S_{isl} = \frac{R_r^2}{2} [2\theta_b - \sin(2\theta_b)] \quad (10.16)$$

and the cross-area section of the rotor island of Fig. 10.15 (d) is two times the previous one.

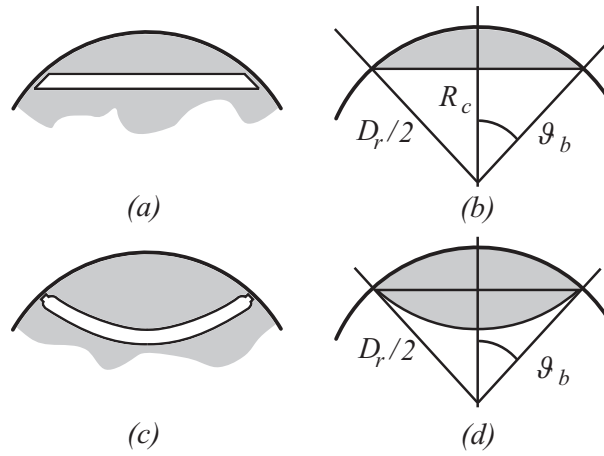


Figure 10.15: Approximation of the region between the flux barrier and the air-gap. (a) Rectangular flux barrier geometry. (b) Geometrical approximation of the rectangular flux barrier. (c) Circular flux barrier geometry. (d) Geometrical approximation of the circular flux barrier.

The force acting on these rotor islands is the sum of the magnetic force and the centrifugal force. The magnetic force is computed from the magnetic pressure $B^2/(2\mu_0)$ on the rotor surface $\theta_b D_r L_{stk}$, according to the air-gap flux density B . A reasonable value for such a flux density is between 1 and 1.2 T. This value tends to overestimate the magnetic force, increasing the mechanical safety margin.

The centrifugal force is computed as $m\omega_m^2 R_c$ where $m = \gamma S_{isl} L_{stk}$ is the mass of the iron island, ω_m is the rotor speed, and R_c is the radius of the center of gravity of the rotor island. It can be assumed to be about $R_c = (D_r \cos \theta_b)/2$. This is correct in case of the island of Fig. 10.15 (d), while it is slightly underestimated in case of the island of Fig. 10.15 (b). In commonly used lamination, the mass density γ is about 7800 kg/m^3 .

Referring to the circular flux barrier, the total force that the rotor ribs have to sustain is given by

$$F_r = \theta_b D_r L_{stk} \left\{ \frac{B^2}{2\mu_0} + \frac{\gamma_{fe} D_r^2 \omega_m^2 \cos \theta_b}{4} \left[1 - \frac{\sin(2\theta_b)}{2\theta_b} \right] \right\} \quad (10.17)$$

The tensile strength of non-oriented steel is in the range between 400 and 500 N/mm². A safety factor between 2 and 3 is kept [109, 110], so as to limit the strength of the rib σ_r to 150 and 200 N/mm².

Finally, the total thickness of the inner iron ribs corresponding to the flux barrier under study [109, 110] is given by

$$\sum t_r = \frac{F_r}{\sigma_r L_{stk}} \quad (10.18)$$

The different arrangements of the inner iron ribs are shown in Fig. 10.16. However, in order to assist the REL motor with PM, the first arrangement, as shown in Fig. 10.16 (a) is adopted. In addition, the outer two iron ribs thickness t_{ro} are set with respect to the minimum practical thickness which is based on the lamination thickness (i.e., in a lamination whose thickness is 0.35 mm , the minimum rib thickness is about 0.4 mm).

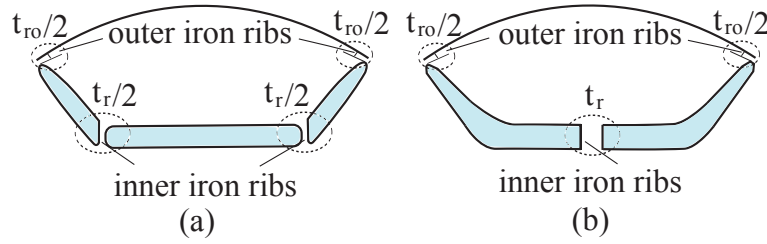


Figure 10.16: Different arrangements of the inner iron ribs in the REL machine.

Hereafter, the total thickness of the iron ribs t_{rt} (i.e., the summation of the inner and the outer ribs) is given by

$$t_{rt} = t_r + t_{ro} \quad (10.19)$$

10.6. Selection of the PM width

The purpose of this section is to choose the width of the PM to be inset in each flux-barrier. As stated before in the previous chapter, the PM width determine the magnetic flux of the PM (ϕ_m). Part of this flux flows through the iron ribs (ϕ_{sat}) up to saturate them, and the other part flows through the air gap (ϕ_g) linking the stator winding. This is referred to as the no-load flux linkage due to the PM. Starting from the remanence flux of the PM, that is, $\phi_{rem} = B_{rem} w_m L_{stk}$, it is possible to define an effective remanence flux $\phi_{rem_{eff}}$ as in eq. (9.32) and can be rewritten as

$$\phi_{rem_{eff}} = B_{rem} w_{m_{eff}} L_{stk} \quad (10.20)$$

where, $w_{m_{eff}}$ is the effective PM width useful for the air-gap flux density. Fig. 10.17 shows $w_{m_{eff}}$, as well as, the PM width Δw_m lost to saturate the iron ribs whose thickness is t_{rt} . Then, $w_{m_{eff}}$ is given by eq. (9.33) and Δw_m is given by

$$\Delta w_m = \frac{B_{sat}}{B_{rem}} t_{rt} \quad (10.21)$$

where, B_{sat} is the saturated flux density in the iron ribs. Using Ferrite magnet, whose $B_{rem} \simeq 0.35 \text{ T}$, $\Delta w_m \simeq 6 \cdot t_r$.

The flux saturating the iron ribs remains almost the same, while the air-gap flux increases with the PM width. The PM widths are limited by the length of the flux-barriers themselves. In particular, the PM width in the first flux-barrier, the shorter one, is referred to as w_{m_1} .

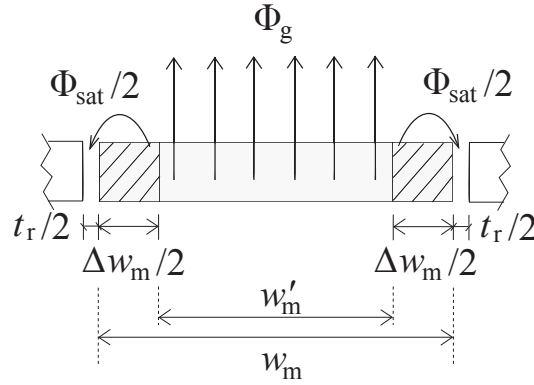


Figure 10.17: PM width and flux lines: ϕ_g is the useful flux through the air-gap and ϕ_{sat} is the flux lost in the ribs.

The computation of the PM widths is based on the air-gap flux density distribution at no load, as shown in Fig. 10.18. It is staircase distribution and it is approximated as a sine wave distribution. The average air-gap flux density ($B_{g_{avg}}$) in front to the i -th flux-barrier is given by

$$\begin{aligned} B_{g_{avg}} &= \frac{1}{\theta_{b_i} - \theta_{b_{i-1}}} \int_{\theta_{b_{i-1}}}^{\theta_{b_i}} \hat{B}_g \cos(p\theta) d\theta \\ &= \hat{B}_g \frac{\sin(\theta_{b_i}^e) - \sin(\theta_{b_{i-1}}^e)}{\theta_{b_i}^e - \theta_{b_{i-1}}^e} \end{aligned} \quad (10.22)$$

where \hat{B}_g is the peak value of the air-gap flux density at no load. Using Ferrite PM, the flux in the air-gap is quite low. Therefore, \hat{B}_g is assumed to be ≤ 0.1 T. Then, the average flux

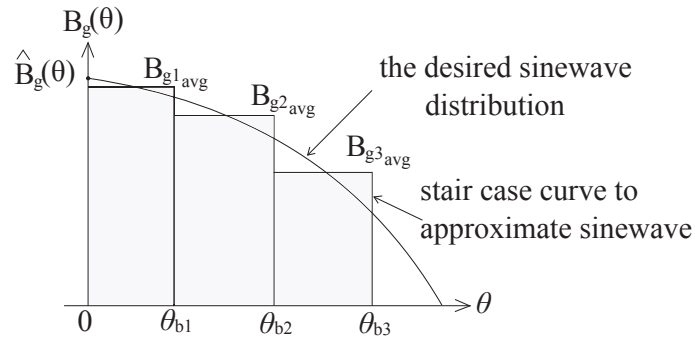


Figure 10.18: Air-gap flux density distribution at no load for half pole.

flowing through the air-gap in front to the rotor island bordered by the i -th flux-barrier can be computed as

$$\phi_{g_i} = B_{g_{avg}} (l_{b_i} - l_{b_{i-1}}) L_{stk} \quad (10.23)$$

where, l_{b_i} is the length of the i -th flux-barrier, which is assumed to be the same of the rotor arc in front of it, i.e., $\theta_{b_i} D_i$.

Starting from ϕ_{g_i} , the PM widths can be computed by two methods. Both methods are based on the complete and the simplified magnetic network of the motor at no load, which

proposed in the previous chapter. Firstly, the computation of the PM widths based on the complete model is presented. Secondly, the same computation are repeated based on the simplified model.

10.6.1. complete model analysis

To compute the effective PM width which responsible for producing the air-gap flux, the effective remanence flux $\phi_{rem_{eff_i}}$ should be computed. This computation is reported in eq. (9.32) and eq. (9.33). To the aim of computing $\phi_{rem_{eff_i}}$, the magnetic network shown in Fig.9.21 is modified, as shown in Fig.10.19.

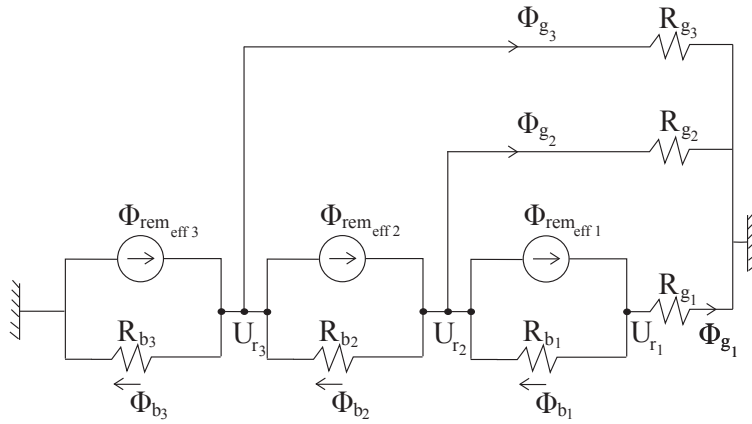


Figure 10.19: Complete magnetic network of PMAREL motor at no load considering the rotor iron ribs.

Applying Kirchhoff's current law at the different nodes of the magnetic network shown in Fig.10.19, $\phi_{rem_{eff_i}}$ is computed as

$$\phi_{rem_{eff_i}} = \sum_{i=1}^i \phi_{g_i} + \phi_{b_i} \quad (10.24)$$

Besides, ϕ_{b_i} is given by

$$\phi_{b_i} = \frac{U_{r_i} - U_{r_{i+1}}}{R_{b_i}} \quad (10.25)$$

By substituting eqs. (9.9) and (10.25) in eq. (10.24), $\phi_{rem_{eff_i}}$ is expressed as

$$\phi_{rem_{eff_i}} = \sum_{i=1}^i \phi_{g_i} + \frac{\phi_{g_i} R_{g_i} - \phi_{g_{i+1}} R_{g_{i+1}}}{R_{b_i}} \quad (10.26)$$

Then, by substituting eqs. (10.23) and (10.26) in eq. (9.32), the direct relation, which computes the active width of each PM, can be deduced as

$$w_{m_{eff_i}} = \frac{1}{B_{rem}} \left[(l_{b_i} - l_{b_{i-1}}) \sum_{i=1}^i B_{g_{i_{avg}}} + \frac{g l_{b_i} (B_{g_{i_{avg}}} - B_{g_{(i+1)_{avg}}})}{t_{b_i}} \right] \quad (10.27)$$

Therefore, from the desired air-gap flux-density in front to each barrier, the barrier geometry, and the PM type (i.e., B_{rem}), and the air-gap length, the effective width of each PM can be computed. Finally, the total width of the PM is given by

$$w_{m_i} = \Delta w_{m_i} + w_{m_{eff_i}} \quad (10.28)$$

10.6.2. Simplified model analysis

The computation procedure of the effective PM widths is based on the practical simplified magnetic network of the PMAREL motor at no load which proposed in the previous chapter. However, the rotor iron ribs are considered. Once again, from Fig.9.7, the same assumptions according to a rotor with three flux-barriers per pole, are used as follows

- the air-gap flux density in front to the first flux-barrier is referred to as ϕ_{g_1} . This flux flows through a portion of the PMs in the three flux-barriers, whose width is $w_{m_{eff_1}}$ that is the same effective width of the first PM.
- the remain effective width of the second PM is $(w_{m_{eff_2}} - w_{m_{eff_1}})$. ϕ_{g_2} flows in the portions of PM of the second and third flux-barriers, whose effective width is $(w_{m_{eff_2}} - w_{m_{eff_1}})$.
- similarly, the remain effective width of the third flux-barrier is $(w_{m_{eff_3}} - w_{m_{eff_2}})$. ϕ_{g_3} flows through this remaining width.

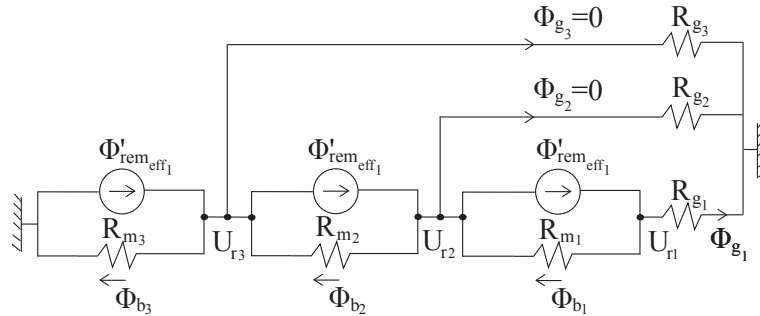


Figure 10.20: Magnetic network according to the first assumption. All the PM widths are equal to $w_{m_{eff_1}}$, then $\phi'_{rem_eff_1} = B_{rem} w_{m_{eff_1}} L_{stk}$.

Then, from the previous assumptions and by considering the rotor iron ribs, Fig.10.20, Fig.10.21 can be deduced. Consequently, the general equation of air-gap flux corresponding to the portions of air-gap in front to the i -th flux-barrier is

$$\phi_{g_i} = \frac{\phi'_{rem_eff_i} R_{m_i}}{R_{g_i} + R_{m_i}} \quad (10.29)$$

Once again, the magnetic reluctance corresponding to the portions of air-gap in front to the i -th flux-barrier, as in eq. (9.7) and R_{m_i} is the magnetic reluctance of the i -th PM, as in eq. (9.2),

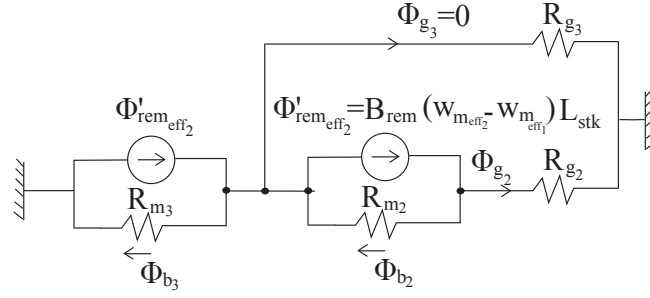


Figure 10.21: Magnetic network according to the second assumption. All the PM widths are equal to $w_{m_{eff_2}} - w_{m_{eff_1}}$, then $\phi'_{rem_{eff_2}} = B_{rem}(w_{m_{eff_2}} - w_{m_{eff_1}})L_{stk}$.

where the PM thickness is assumed the same thickness of the flux barrier (i.e., $t_{m_i} = t_{b_i}$). They can be rewritten as

$$R_{g_i} = \frac{g}{\mu_0(l_{b_i} - l_{b_{i-1}})L_{stk}} \quad \text{and} \quad R_{m_i} = \frac{t_{b_i}}{\mu_0 w_{m_{eff_i}} L_{stk}} \quad (10.30)$$

From Fig.10.20, Fig.10.21 and eq. (9.32), the value of the effective remanence flux is given by

$$\phi'_{rem_{eff_i}} = B_{rem}(w_{m_{eff_i}} - w_{m_{eff_{i-1}}})L_{stk} \quad (10.31)$$

Then, by substituting eqs. (10.30) and (10.31) in eq. (10.29), an expression for the ϕ_{g_i} can be obtained, as

$$\phi_{g_i} = B_{rem}(w_{m_{eff_i}} - w_{m_{eff_{i-1}}}) \left[\frac{t_{b_i}(l_{b_i} - l_{b_{i-1}})}{w_{m_{eff_i}}g + t_{b_i}(l_{b_i} - l_{b_{i-1}})} \right] L_{stk} \quad (10.32)$$

Then, by equalling this expression with eq. (10.23), the final expression of computing the effective width of the i-th PM is given by

$$w_{m_{eff_i}} = \left[\frac{B_{rem}t_{b_i}}{B_{rem}t_{b_i} - B_{avg_i}g} \right] \left[w_{m_{eff_{i-1}}} + (l_{b_i} - l_{b_{i-1}}) \frac{B_{avg_i}}{B_{rem}} \right] \quad (10.33)$$

Finally, the total width of the i-th PM is computed as in eq. (10.28) in the previous subsection.

10.7. Computation of the PM thickness

In this section, the stress on the PM is computed in order to check if the PM thickness is enough to avoid the PM demagnetization or not (i.e., the flux density of PM operating point is higher than the flux density at knee point B_{knee}). This check is carried out in order to enable the design procedure to be more robust towards the demagnetization problem.

As stated before, the stress on the PM is caused by the flux due to the stator current. The worst condition is when the stator current produces flux completely against the PM flux, as shown in Fig. 9.13. This is referred to as the demagnetization current. The flux due to the current is computed applying the superposition of the effect: The PMs are removed and the computation is carried out on a REL motor. The actual PM flux-density is achieved by subtracting the demagnetization current flux density from the no-load flux density.

The analytical approach which proposed in the previous chapter, is used to perform this check on the PMs thicknesses. This model is based on the complete and simplified magnetic network analysis. Both analysis will be investigated in this chapter in order to evaluate the effect of the simplification on the design of the motor.

10.7.1. complete model analysis

From the complete network of one rotor pole with three flux-barriers of a REL motor, as in Fig.9.15, the flux flowing through each flux barrier ϕ_{b_i} can be computed, as in eq. (9.22). Hence, the uniform flux density in each barrier (i.e., the stress on each PM) can be computed as in eq. (9.24). Then, the PM thickness can be chosen so as to avoid the irreversible demagnetization.

10.7.2. Simplified model analysis

As stated in the previous chapter, the magnetic network shown in Fig.9.15 is properly simplified, as shown in Fig.9.17, in order to enable the designer to compute the stress by using practical equations. Since R_{g_i} have been neglected, the flux density stress is overestimated, that means a high safety margin.

The flux flowing in the i -th flux barrier is computed as in eq. (9.25). Then, the flux density is computed, as in eq. (9.24). In addition, if the flux barriers are equally spaced according to [30], the flux density is computed, as in eq. (9.31).

From eqs. (9.24) and (9.31), it is noted that, the stress on the PMs depends on the electrical loading and flux-barrier thickness. Therefore, at the nominal electric loading, the selected thickness of the PM can be checked by eqs. (9.24) and (9.31). Then, the thickness of the PM can be minimized as possible without exceeds the demagnetization margins. Hence, the suitable volume of the PM can be achieved.

10.8. Example

The design procedure described above is applied hereafter to determine the main dimensions of a PMAREL motor. The required nominal torque T_N and speed n_N are 12.5 Nm and 5000 rpm, respectively.

As stated above, a torque density $k_{TV} \simeq 10 \text{ Nm/l}$ is assumed to determine the outer stator volume. Then, $D_e^2 L_{stk}$ is computed and it is equal to 0.00159 m^3 .

From the application needs, the external diameter of the motor D_e is selected to be 200 mm. Consequently, the stack length of the motor results in 40 mm. The inner diameter D_i of the stator is estimated to be equal to $D_i \simeq 0.6 D_e$ resulting in 120 mm. Rather than a custom stator geometry, a commercial lamination is selected according to D_e and D_i . The selected commercial lamination is a MEC 132 for a 4-pole machine. Its geometrical data are given in Table 10.2.

The design of the rotor is a crucial point. It is split into six steps. The first step is to determine the end points of the flux-barriers. A number of three flux barriers per pole is chosen. As a preliminary choice, rotor geometry with equal spaced equivalent slots per pole pair is

Table 10.2: The geometrical data of the commercial lamination MEC 132 for a 4-pole machine.

External stator diameter	D_e	200	mm
Inner stator diameter	D	125	mm
Number of slots	Q_s	36	
Tooth width	w_t	6	mm
Slot height	h_s	17.5	mm
Slot opening height	h_{so}	0.5	mm
Slot opening width	w_{so}	2.5	mm

selected, as suggested in [30]. The number of stator slots per pole pair is $n_s = 18$, then n_r is computed as in eq. (10.2) and it is equal to 14. Then, the rotor of this example can be expressed as shown in Fig. 10.22. Referring to [30], it can be defined as a "complete" rotor with one "virtual" point. Hence, $k_i = 1, 2, 3$. Then, the angular distance between each two points is $\Delta\theta_b^e = 25.71^\circ$, and hence, $\theta_{b_1}^e$, $\theta_{b_2}^e$, and $\theta_{b_3}^e$ are equal to 25.71° , 51.42° , and 77.13° , respectively.

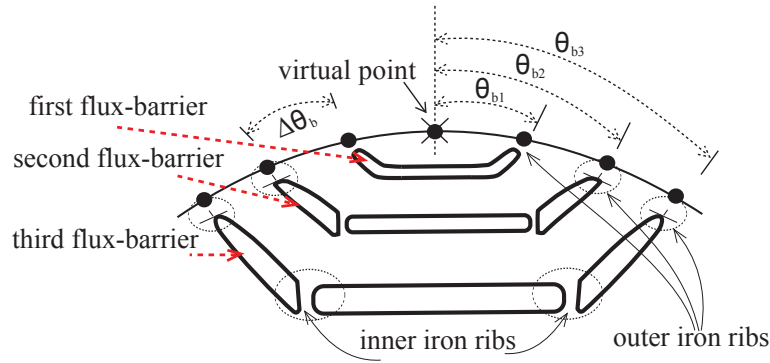


Figure 10.22: Sketch of a rotor pole with three flux barriers per pole, equally spaced flux barrier ends and different types of the iron ribs.

The second step deals with the computation of the flux barrier thickness, according to the coefficient k_{air} which is fixed to 0.45. The total air thickness is computed and then it is split into the three barriers. According to the position of the barrier ends, rotor iron paths are computed from eq. (10.4), then the barrier thicknesses t_{b_1} , t_{b_2} , and t_{b_3} are chosen to be 3 mm, 6 mm, and 10 mm, respectively, according to eqs. (10.9) to (10.11).

The third step is the computation of the flux-barriers length. Starting from the barrier ends and the outer rotor diameter, the lengths are $l_{b_1} = 28$ mm, $l_{b_2} = 56$ mm, and $l_{b_3} = 84$ mm, respectively.

The fourth step is the computation of the iron rib thickness. Fig. 10.22 shows the positions of the rotor iron ribs. It is worth noticing that the minimum thickness of the rib should be about equal to the thickness of the lamination, e.g., 0.4 mm for a lamination thickness of 0.35 mm. The outer iron ribs (at the end of each flux-barrier) are set equal to the minimum practical thickness since these ribs have a limited mechanical capacity. The thickness computed using eq. (10.17) and eq. (10.18) yields 0.1 mm, 0.33 mm, and 0.72 mm for the first, second, and third barrier ribs, respectively. Then, the inner iron ribs of the first flux-barrier (the shortest one) can be omitted considering that the two ribs at the barrier ends are enough ($t_{r_1} = 0.8$ mm).

The total iron rib thicknesses for the second and third barriers are split into four ribs whose thickness is fixed to 0.4 mm, i.e., two ribs for the outer iron ribs and two ribs for the inner iron ribs, as shown in Fig.10.22, according to the minimum practical constraint. Thus the total thickness of the iron ribs results in $t_{r_2} = 1.6$ mm, and $t_{r_3} = 1.6$ mm, respectively.

The fifth step is the computation of the PMs widths. From eqs. (10.27) and (10.28), the PMs widths which results from the complete model are $w_{m_1} = 13$ mm, $w_{m_2} = 25$ mm, and $w_{m_3} = 28$ mm, respectively. In addition, the PMs widths which results from the simplified model are $w_{m_1} = 13$ mm, $w_{m_2} = 25$ mm, and $w_{m_3} = 29$ mm, respectively. It is noted that the simplified model results are feasible.

The sixth step is the computation of the maximum magnetic stress on each PM. This stress depends on the electrical loading \hat{K}_s of the motor which is linked to the conductor current density J_s . The recommended range of the conductor current density is between 6 and 9 A/mm² according to a air-cooled machine (for a continuous duty higher for an intermittent duty). The current density J_s is selected equal to 6 A/mm², the electrical loading \hat{K}_s resulting in 33500 A/m. The stress on the first, second, and third PM, which results from the complete model, are 0.102 T, 0.094 T, and 0.069 T, respectively. Besides, the stress on the first, second, and third PM, which results from the simplified model, are 0.107 T, 0.096 T, and 0.072 T, respectively. It is noted that the simplified model overestimates the stress on the PM.

Then, the PMs operating points result from the complete and simplified analysis are shown in Table 10.3.

Table 10.3: The PMs operating points result form both complete and simplified analyses.

	Complete analysis	Simplified analysis
B_{m_1}	0.212	0.200
B_{m_2}	0.218	0.213
B_{m_3}	0.242	0.238

Referring to both analysis results, it is possible to verify that all operating points of the PMs are above the knee point B_{knee} . Therefore, the thickness of the PMs is enough for this electrical loading. In addition, it is noted that there is a good agreements between both complete and simplified analysis results. Moreover, the operating points of the PMs which result from the simplified analysis are slightly lower than those results from the complete analysis. Once again, it considered more robust towards the demagnetization.

From eq. (9.38), it was also verified that the maximum electrical loading which cause an irreversible PM demagnetization, which results from the complete and simplified analysis, is equal to 310% and 290% of the nominal electrical loading, respectively. The maximum electrical loading results from the simplified analysis lower than that results from the complete analysis. This also is referred to as a safety factor towards the demagnetization.

Since the simplified analysis results are feasible and have a higher safety factor, they are used to design the width and thickness of the PMs. Once defined the rotor geometry, it has been verified by means of a finite element analysis, [111]. A flux density map is shown in Fig.10.23. The resulting average torque is 12.47 Nm and the torque ripple is around 26%. Consequently, this result highlights that the proposed design procedure rapidly yields a satisfactory initial

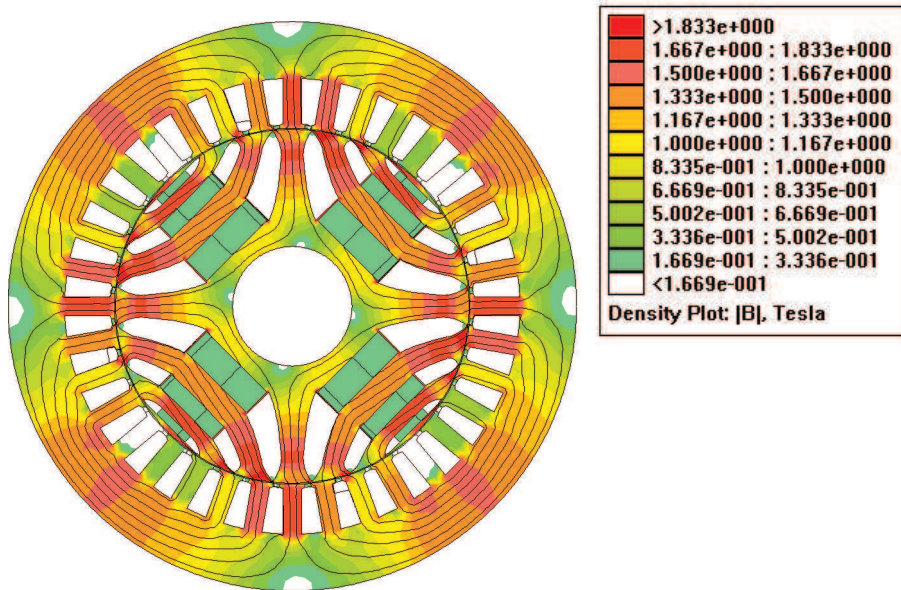


Figure 10.23: Flux density map of PMAREL motor with electrical loading $\hat{K}_s = 42500 \text{ A/m}$ at rotor position $\theta_m = 0^\circ$

motor sizing. Then, the rotor has been optimized adopting finite element method to reduce the torque ripple.

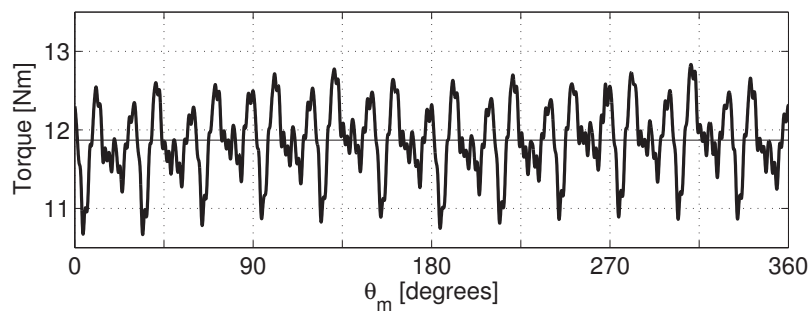
The optimization mainly focused on the position of the flux barrier ends. After that, two motors prototypes, a synchronous REL motor and a PMAREL motor were manufactured. Fig. 10.24 shows the measured torque of two motor prototypes at rated current.

10.9. Conclusion

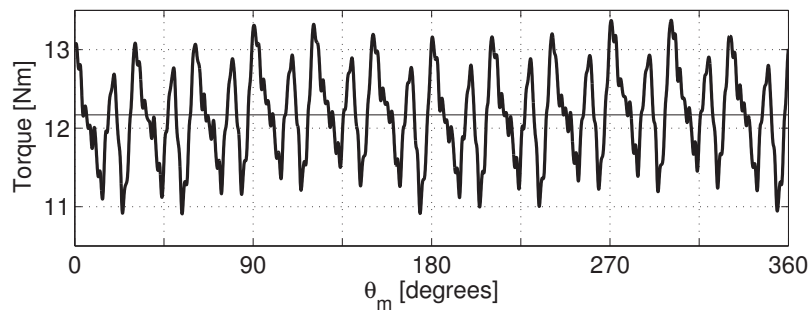
A rapid procedure to estimate the main dimensions of a synchronous reluctance motor, with or without the assistance of a permanent magnet, is fully described in this chapter.

A practical torque density factor is given so as the motor size is rapidly determined. According to the practical approach followed by the industry, the geometry of the stator lamination is selected from the geometries available of the induction motors.

On the contrary, the rotor required a deeper computation. Its geometry is achieved step-by-step, starting from the selection of the flux-barrier ends, lengths and thicknesses. The iron ribs and PM sizes are determined according to centrifugal and magnetic forces, no-load flux density distribution and stator current reaction, respectively. Finally, a practical example, concludes the computations carried out in this chapter.



(a) measurements on the REL motor.



(b) measurements on the PMAREL motor.

Figure 10.24: Experimental torque in (a) a REL motor prototype and (b) a PMAREL motor prototype.

Part IV

Graphical User Interface Application

Chapter 11

User interface application for concentric and eccentric REL motor

In this chapter, the analytical models presented in chapters 2 and 3 are rewritten in C++ code. Then, using Qt software [112], a graphical user interface application is developed. This application is able to analyze a REL motor with one, two, and three flux-barriers. In addition, healthy case and different eccentricity cases are involved in this application. Furthermore, both symmetric and asymmetric rotor geometries are considered. The inputs of this application are the motor geometrical data, the value and the type of the eccentricity, the loading conditions of the motor, and the rotor geometry type. The outputs of the application are the stator and rotor scalar magnetic potential, the air-gap flux density distribution, the electromagnetic torque, the radial magnetic pressure acting on the rotor, and the radial magnetic force acting on the rotor.

11.1. The main body of the application

Fig. 11.1 shows a simple flow chart which explains how the user interface application works. At first, the user should import the input data of the application through the different widgets of the main interface window, where the widgets are the primary elements for creating user interfaces in Qt. Besides, they can receive user inputs, display data and status information, and provide a container for other widgets that should be grouped together.

These widgets should be linked to the main c++ code parameters. The main c++ code consists of three classes responsible for presenting the analytical models of REL motors with one, two, and three flux barriers per pole, respectively. These classes are `REL_analytical_one`, `REL_analytical_two`, and `REL_analytical_three`. Based on the number of the barriers imported by the user, the suitable class is implemented. The results of each class are the stator magnetic potential (U_s), the rotor magnetic potential (U_r), the air-gap flux density distribution (B_g), the electromagnetic torque (τ_m), the magnetic pressure acting on the rotor (p_m), and the magnetic forces in x and y -axes direction (F_x and F_y).

Again, the output results are linked to the main user window widgets. The results are graphically presented. A Qt widget for plotting and data visualization is used to plot the main C++ code results. This widget is called `QCustomPlot` [113]. In the following sections, the main parts of the graphical user application shown in Fig. 11.1, are deeply discussed.

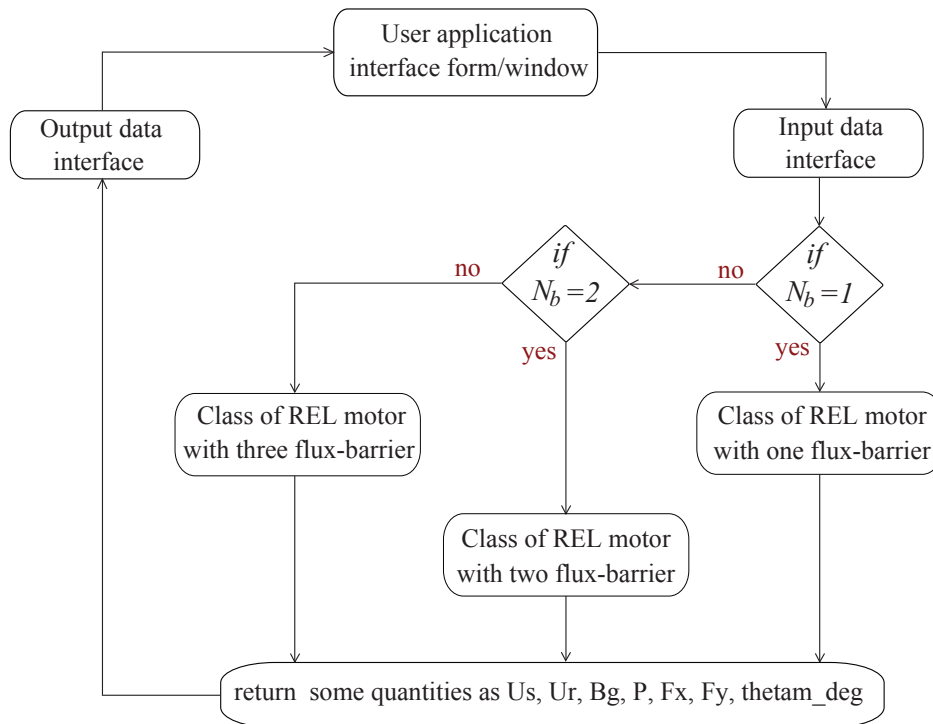


Figure 11.1: Flow chart shows the main components of the proposed graphical user interface application.

11.2. User application interface form

The main form is designed using the Qt environment, as shown in Fig. 11.2, Fig. 11.3, Fig. 11.4, Fig. 11.5, and Fig. 11.6. The main form contains the tool bar and five tab windows. The name of the first tab is "General data". From Fig. 11.2, the aim of this tab window is to import the geometrical data of the stator, eccentricity value and type, the rotor position, the electric loading, and the electric current angle. The second tab name is "Rotor data". From Fig. 11.3, the rotor geometrical data and the rotor geometry type can be inserted in this tab window. The other three tab windows are designed to show the results of the C++ code of the analytical model. The stator and rotor magnetic potentials and the air-gap flux density distribution are shown in the third tab window, as shown in Fig. 11.4. The name of this tab is the "Magnetic Field Computations". From Fig. 11.5, the fourth tab window shows the electromagnetic torque and the magnetic pressure on the rotor and its name is "Torque and Radial Pressure Computation". The fifth tab window name is the "Radial Magnetic Force Computation". It shows the radial magnetic force components in both x and y axes directions, as shown in Fig. 11.6.

The first tab window has some input widgets as the spin box and the radio button. From Fig. 11.2, the spin boxes enable the user to import the number of pole pairs, the number of stator slots, the stator diameter, the stack length, the air-gap length, the eccentricity values, the initial and final rotor position, the electric loading, the electric current angle, and the winding chording angle. Besides, the radio button allow the user to select the eccentricity type, as shown in Fig. 11.2.

In the second tab window, a radio button allows the user to select the rotor geometry type,

as shown in Fig. 11.3. In addition, the spin boxes are used to define the number of the flux-barriers per pole, the thickness of the flux-barriers, and the flux-barriers end angles. To start the

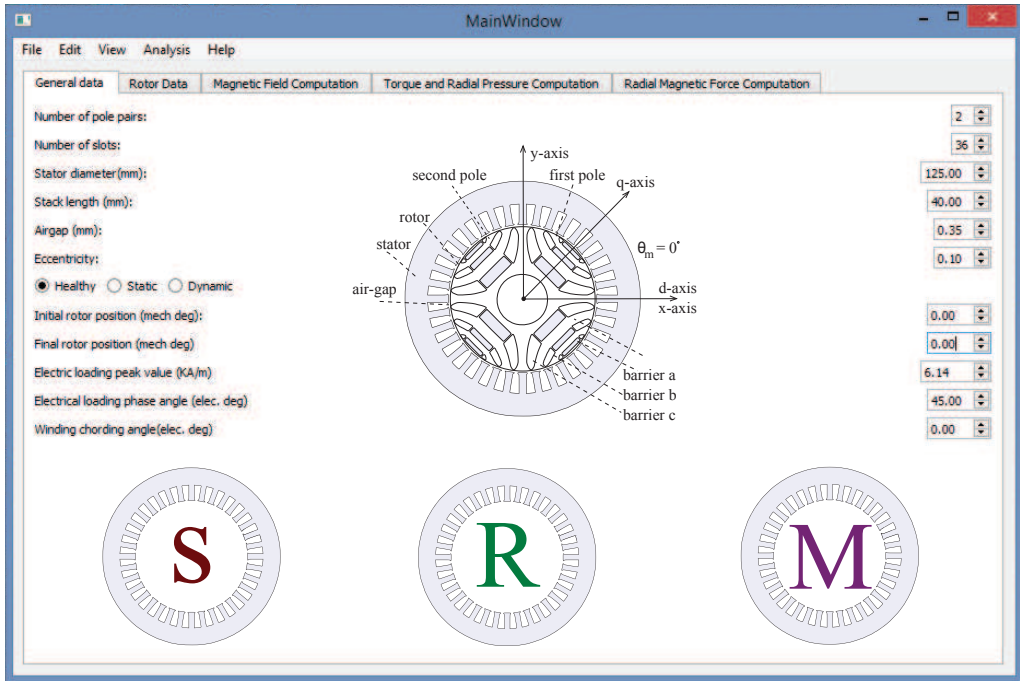


Figure 11.2: Interface window allows the user to import the main data of the motor.

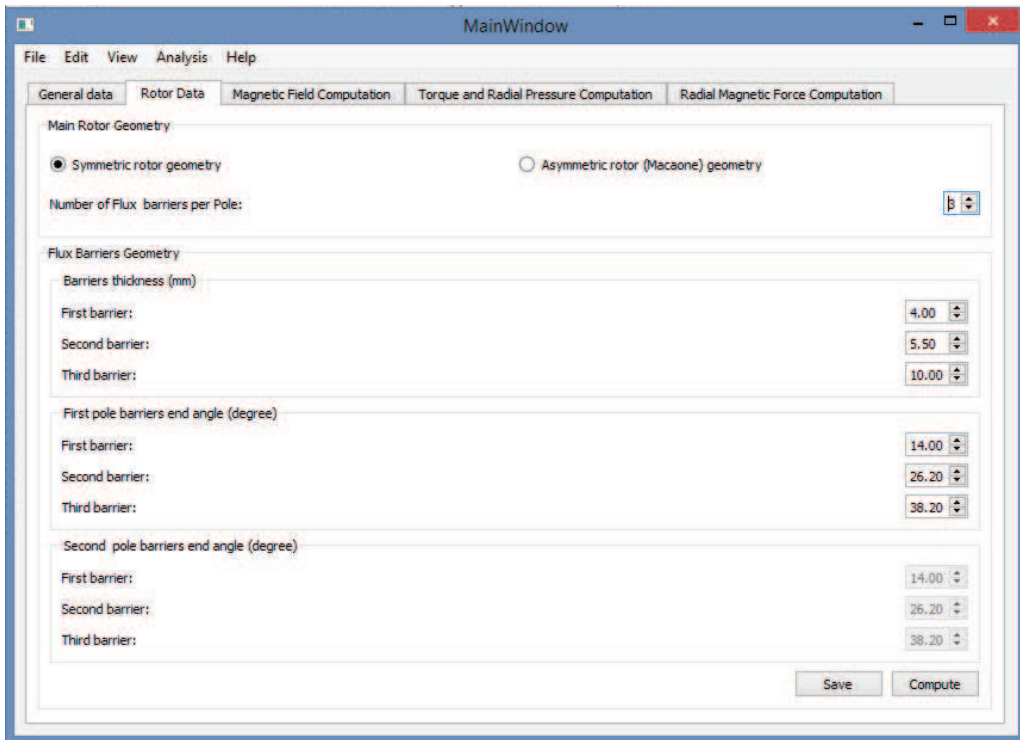


Figure 11.3: Interface window allows the user to import the main data of the rotor.

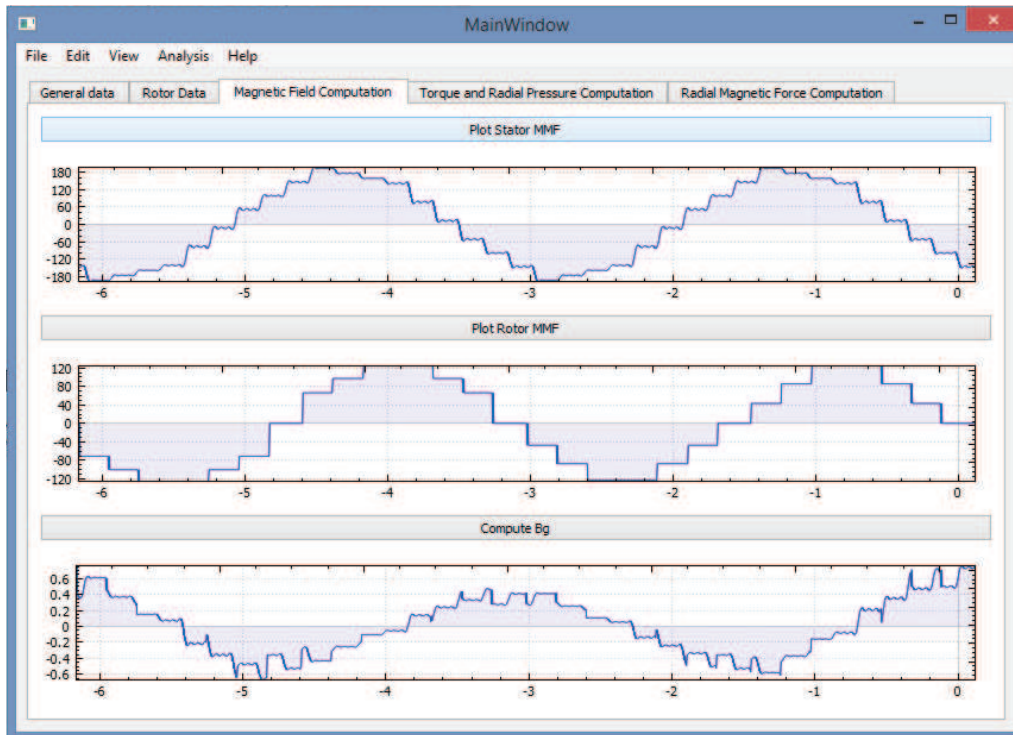


Figure 11.4: Interface window allows the user to export the results such as U_s , U_r , and B_g .

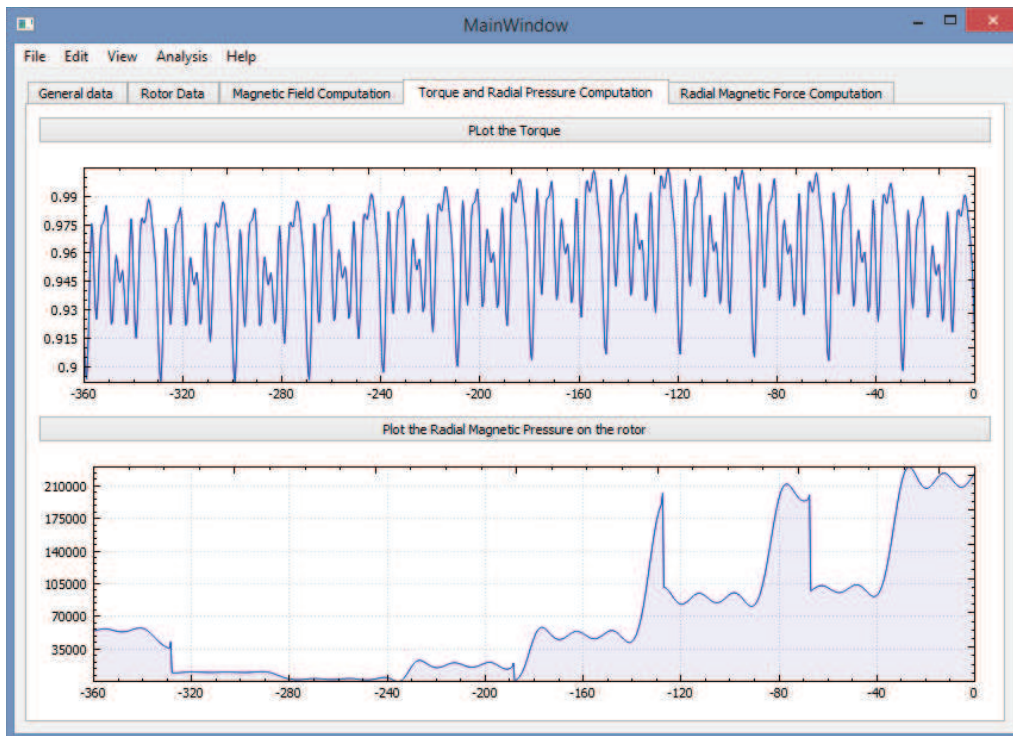


Figure 11.5: Interface window allows the user to export the results such as τ_m and p_m .

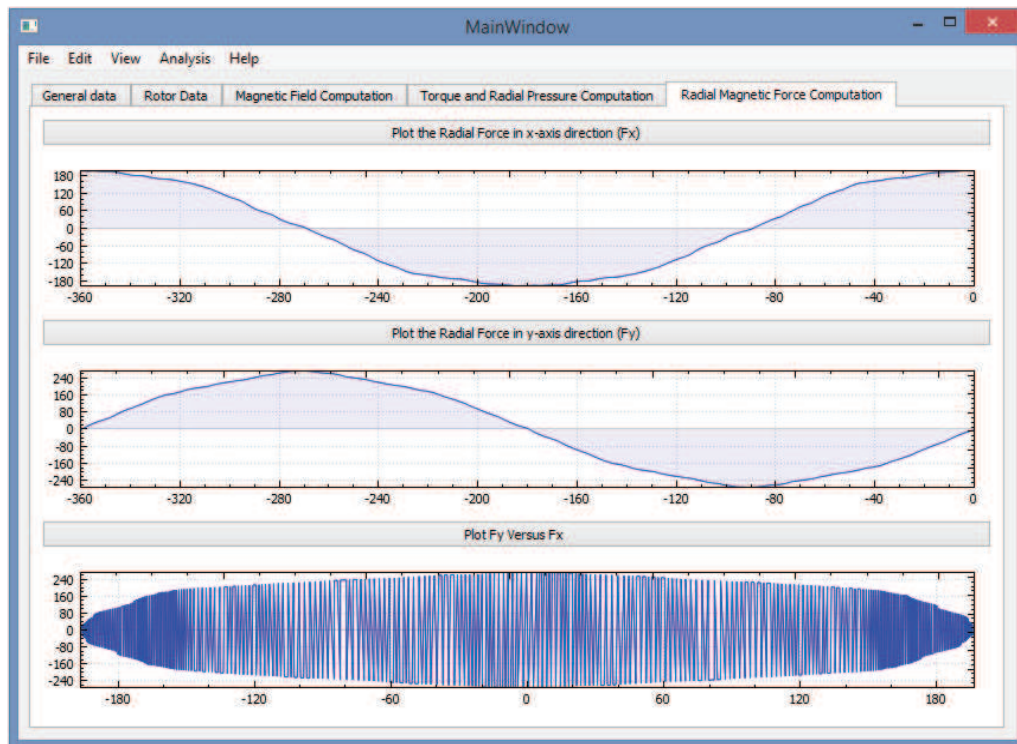


Figure 11.6: Interface window allows the user to export the results such as F_x and F_y .

analysis, a push button is used. The label of this push button is "Compute". Besides, another push button is used to save the inserted data of the motor. Its label is "Save".

In the other three tab windows shown in Fig. 11.4, Fig. 11.5, and Fig. 11.6, the push buttons allow the user to plot the results that he need. In addition, a display widgets are used to view the results.

11.3. Input and output data interface

The user interface (UI) of this application is designed completely using Qt Designer [112]. The result is a UI file describing the form, the widgets used, any signal-slot connections between them, and other standard user interface properties. When the project is built, user interface compiler (UIC) will create a header file that lets us construct the form.

The user interface form is created by a class `REL_Widget`. To access the form and its contents, we need to include the `ui_rel_widget.h` header file created by UIC during the build process:

```
#include "ui_rel_widget.h"
```

The `REL_Widget` class is defined by sub-classing `QWidget` because the form itself is based on `QWidget`:

```
class REL_Widget : public QWidget
{
    Q_OBJECT
```

```

public:
    explicit REL_Widget (QWidget *parent = 0);
    ~REL_Widget ();

private slots:

    void compute ();    // TO START THE ANALYSIS
    void save ();      // TO SAVE THE MOTOR SIMULATION DATA

private:
    Ui::REL_Widget *ui;
    REL_analytical_one    One_Barrier_model;
    REL_analytical_two    Two_Barrier_model;
    REL_analytical_three  Three_Barrier_model;
};

```

Apart from the constructor, the class contains private slots that are responsible for some actions. As an example, two slots are shown. They are responsible for starting the analysis and saving the simulation data. The private ui member variable refers to the form, and is used to access the contents of the user interface.

To implement the REL_Widget class, firstly, the constructor simply calls the base class's constructor and sets up the form's user interface, as

```

REL_Widget::REL_Widget (QWidget *parent) :
    QWidget (parent),
    ui (new Ui::REL_Widget)
{
    ui->setupUi (this);

    connect (ui->pbCompute, SIGNAL (clicked (bool)), this, SLOT (compute ()));
    connect (ui->pbSave, SIGNAL (clicked (bool)), this, SLOT (save ()));
}

```

The user interface is set up with the setupUI () function. We pass 'this' as the argument to this function to use the REL_Widget widget itself as the container for the user interface. In addition, the connection of the slots and the signals is reported. As an example, the signals of the two push buttons shown in Fig. 11.3 are connected to the two slots shown before (compute and save slots). The same procedure is implemented for the other input widgets and their corresponding slots.

The input widgets are linked to the main analytical model parameters. As an example, the user insert the number of pole pairs using the spin box as shown in Fig. 11.2. This spin box can be linked to the parameters p of the analytical model, as

```

int p = ui->sb_p->value ();

```

Analogously, the other inputs widgets are linked to its corresponding parameters in the analytical model. As mentioned before, there are three classes for the three analytical models of the REL motor with one, two, and three flux-barrier per pole. Based on the number of barrier imported by the user, the suited class is selected. This can be applied as

```

if (ui->sb_Nb->value() == 1) {
    One_Barrier_model.set_data(p, Qs, D, L, g, e, eccentricity,
        thetam_initial, thetam_final, thetabdeg11, thetabdeg12, tb1, Ks,
        alphaie_deg, betare);
    One_Barrier_model.compute_potential();
    One_Barrier_model.print_result();
}

if (ui->sb_Nb->value() == 2) {
    Two_Barrier_model.set_data(p, Qs, D, L, g, e, eccentricity,
        thetam_initial, thetam_final, thetabdeg11, thetabdeg12, tb1,
        thetabdeg21, thetabdeg22, tb2, Ks, alphaie_deg, betare);
    Two_Barrier_model.compute_potential();
    Two_Barrier_model.print_result();
}

if (ui->sb_Nb->value() == 3) {
    Three_Barrier_model.set_data(p, Qs, D, L, g, e, eccentricity,
        thetam_initial, thetam_final, thetabdeg11, thetabdeg12, tb1,
        thetabdeg21, thetabdeg22, tb2, thetabdeg31, thetabdeg32, tb3, Ks,
        alphaie_deg, betare);
    Three_Barrier_model.compute_potential();
    Three_Barrier_model.print_result();
}

```

For the output widgets interface, the main C++ code results are plotted in the user interface form or window. This can be done using the QCustomPlot widget [113]. Several examples explain how to use this widget are available in [113].

11.4. Model of REL motor with one barrier

The class REL_analytical_one is used when the number of the flux-barriers is set equal to three. The push button "compute" is linked to the function compute_potential. This function is responsible for computing the stator and rotor magnetic potential, the electromagnetic torque, the magnetic pressure and the magnetic force acting on the rotor.

```
One_Barrier_model.compute_potential();
```

This function, firstly, split the air-gap into different regions. The number of these regions is computed as

```
regions_num = 4*p*nb;
```

Then, the different angles of the air-gap regions are computed as

```

for (int m = 0 ; m < (2*p) ; m++) // TO DEFINE THE CENTER ANGLE OF EACH
    POLE
    w.push_back(2*m+1);
for (int m = 0 ; m <= (2*p) ; m++) {
    if (m%2 == 0)
        thetab1= thetab11;
    else
        thetab1= thetab12;
}

```

```

if (m == (2*p)){
    thetab1= thetab11;
    beta_rad.push_back((w[0]*pi/(2*p)-thetab1)+2*pi);}
else{
    beta_rad.push_back(w[m]*pi/(2*p)-thetab1);
    beta_rad.push_back(w[m]*pi/(2*p)+thetab1);}
}

```

In addition, the winding factor of the stator distributed winding and the electric loading are computed as

```

alphase = p * 2*pi / Qs;
q = Qs / 3 / (2*p);

//==> INSERTION OF NU ELEMENTS AND ITS CHECK
nu.push_back(1); nu.push_back(-5); nu.push_back(7); nu.push_back
(-11);
nu.push_back(13); nu.push_back(-17);nu.push_back(19);nu.push_back
(-23);
nu.push_back(25); nu.push_back(-29);nu.push_back(31);nu.push_back
(-35);
nu.push_back(37); nu.push_back(-41);nu.push_back(43);nu.push_back
(-47);
nu.push_back(49); nu.push_back(-53);nu.push_back(55);nu.push_back
(-59);
nu.push_back(61);

for(int i=0; i < nu.size(); i++) {
    kwdnu.push_back(sin(nu[i] * q * alphase/2) / (q * sin (nu[i] *
    alphase/2)));
    kwpmu.push_back(cos(nu[i] * betare / 2));
    kwnu.push_back(kwdnu[i] * kwpmu[i]);
    Knu.push_back(Ks * kwnu[i]);
}

```

The stator scalar magnetic potential reported in eq. (2.18) is rewritten using C++ language as

```

for ( int xx = 0 ; xx< 360/step ; xx++) {
    double Us = 0.00;

    for ( int nn =0 ; nn < nu.size(); nn++) {
        Us = Us - (D/(2*p))* Knu[nn]/(nu[nn]) * cos(nu[nn]*p*
        thetas_rad[xx]-p*thetam_rad[jj] - alphaie_deg*pi/180);
    }
    us.push_back(Us);
}

```

From eq. (3.12), the scalar magnetic potential of the rotor islands is achieved. Then, the magnetic potentials of the different rotor regions are presented in a vector. This vector rotates with the rotor rotation. The programming script of the rotor magnetic potential is written as

```

int h=0;
for (int m = 0 ; m < regions_num; m=m+2) {
    if (h == 0)
        t1b1 = t1b11;
}

```



```

else
    tblb1 = tblb12;
Ur_vector.push_back((compute_a(beta_rad[m],beta_rad[m+1],tblb1)*
    compute_usi(beta_rad[m],beta_rad[m+1])));
Ur_vector.push_back(0);
h=h+1;
}
//==> ALLOCATION OF THE COMPUTED ROTOR POTENTIAL FOR THE DIFFERENT
      ROTOR ISLANDS
h=0;
for (int m =0 ; m <regions_num; m++) {
    for (double ss = (beta_rad[m]*180/pi)/step + step ; ss < (beta_rad
        [m+1]*180/pi)/step; ss++) {
        Ur.push_back(Ur_vector[m]);
        h=h+1;
    }
}
reverse(Ur.begin(), Ur.end());
double shift;
shift = -1*(thetam_deg[jj])/step ;
rotate(Ur.rbegin(), Ur.rbegin() + shift , Ur.rend());

```

where the integration of the stator magnetic potential between two general angles is computed by the following function

```

double REL_analytical_one::compute_usi(double beta1, double beta2) {
    double Usi = 0;
    double lm;
    for ( int nn =0 ; nn < nu.size(); nn++) {
        lm = (nu[nn]-1)*p*thetam_actual - alphaie_deg*pi/180 + nu[nn]
            ]*p*(beta1+beta2)/2;
        Usi = Usi- D * (Knu[nn]/(pow((nu[nn]*p),2)))* cos(lm)*sin(nu
            [nn]*p*(beta2-beta1)/2);
    }
    return Usi;
}

```

and the constant a is computed as

```

double REL_analytical_one::compute_a(double beta1, double beta2,
    double tblb1) {
    double aNum;
    double aDen;
    double a_c;
    aNum = (D*tblb1) / (2*compute_airgap(beta1,beta2));
    aDen = 1 + aNum *(beta2-beta1);
    a_c = aNum/aDen ;
return a_c;
}

```

and the average air-gap length between two general angles is obtained from the following function

```

double REL_analytical_one::compute_airgap(double beta1, double beta2
) {

    switch( eccentricity ) {
    case Healthy:
        return g;
        break;
    case Static:
        thetam_g = 0;
        break;
    case Dynamic:
        thetam_g = thetam_actual;
        break;
    }

    return g * ( 1 - 2*delta/(beta2-beta1)*cos((beta1+beta2)/2+
        thetam_g)*sin((beta2-beta1)/2) );
}

```

From the stator and rotor scalar magnetic potential, as reported in eq. (3.5), the air-gap flux density can be computed as

```

h=0;
for (int m =0 ; m < regions_num; m++) {
    for (double ss = (beta_rad[regions_num-(m+1)]*180/pi)/step + step
; ss < (beta_rad[regions_num-m]*180/pi)/step; ss++) {
        Bg.push_back(mu0*(-us[h]+Ur[h])/compute_airgap(beta_rad[
            regions_num-(m+1)],beta_rad[regions_num-m]));
        h=h+1;
    }
}

```

Since the air-gap flux density is computed, the electromagnetic torque can be estimated as reported in eq. (2.68). The C++ script estimates the torque is reported as follows

```

double ttq = 0;
for (int m =0 ; m < regions_num; m=m+1) {
    ttq = ttq - ((mu0*pow(D,2)*L)/(2*compute_airgap(beta_rad[m],
        beta_rad[m+1]))) *
        Ur_vector[m]*compute_Ksi(beta_rad[m],beta_rad[m+1]);
}
ttq.push_back(ttq);
}

```

where the integration of the electric loading between two general angles is carried out using the following function.

```

double REL_analytical_one::compute_Ksi(double beta1, double beta2) {
    double Ksi = 0;
    double lm;
    for ( int nn =0 ; nn < nu.size(); nn++) {
        lm = (nu[nn]-1)*p*thetam_actual - alphaie_deg*pi/180 + nu[nn]
            *p*(beta1+beta2)/2;
        Ksi = Ksi + Knu[nn]*sin(nu[nn]*pi/2)/(nu[nn]*p) * sin(lm)*sin
            (nu[nn]*p*(beta2-beta1)/2);
    }
}

```



```

    }

    return Ksi;
}

```

Based on the air-gap flux density, the electromagnetic pressure is estimated as

```

for ( int ss = 0 ; ss <360/step; ss++)
    pressure.push_back (pow(Bg[ss], 2) / (2*mu0) );

```

Finally, the radial magnetic force components in x and y axes directions are computed as in the following script.

```

force_x = 0.00;
force_y = 0.00;
Np      = thetas_rad.size()-1;
dthetar = 2*pi/Np;

for ( int nn =0 ; nn <= Np; nn++) {
    force_x = force_x + pressure[nn]*L*D/2*dthetar * cos(-1*
        thetas_rad[nn]);
    force_y = force_y + pressure[nn]*L*D/2*dthetar * sin(-1*
        thetas_rad[nn]);
}
Force = sqrt( pow(force_x,2) + pow(force_y,2) );
F_x.push_back(force_x);
F_y.push_back(force_y);
F_radial.push_back(Force);
}

```

11.5. Model of REL motor with two barrier

Analogously, when the number of flux-barriers is set equal to two, the class REL_analytical_two is run. If the push button "compute" is clicked, the analysis is carried out using the following function

```

Two_Barrier_model.compute_potential();

```

The computation of the number of the air-gap regions is similar to that carried out at the previous section. Besides, the computation of the angles of this regions is little bit changed, due to the presence of the second flux barrier.

The stator scalar magnetic potential is computed as shown in the previous section. However, the rotor magnetic potential is estimated as

```

int h=0;
for (int m =0 ; m <=regions_num ; m=m+2*nb) {
    if (h%2 == 0){
        tblb1 = tblb11;
        tblb2 = tblb21;}
    else{
        tblb1 = tblb12;
        tblb2 = tblb22;}
}

```

```

Ur2= compute_c(beta_rad[m+1], beta_rad[m+2], beta_rad[m], beta_rad[
m+3], tblb1, tblb2)
    * compute_usi(beta_rad[m+1], beta_rad[m+2])+ compute_d(
        beta_rad[m+1], beta_rad[m+2],
        beta_rad[m], beta_rad[m+3], tblb1, tblb2)* compute_usi(
        beta_rad[m], beta_rad[m+1])
    + compute_f(beta_rad[m+1], beta_rad[m+2], beta_rad[m],
        beta_rad[m+3], tblb1, tblb2)
    * compute_usi(beta_rad[m+2], beta_rad[m+3]);
Ur1= compute_a(beta_rad[m+1],beta_rad[m+2],tblb1) * compute_usi(
    beta_rad[m+1],beta_rad[m+2])
    + compute_b(beta_rad[m+1],beta_rad[m+2],tblb1) *Ur2 ;

Ur_vector.push_back(Ur2);
Ur_vector.push_back(Ur1);
Ur_vector.push_back(Ur2);
Ur_vector.push_back(0);
h=h+1;
}

```

As shown before, the constant a is estimated by calling its corresponding function. Similarly, the constants b , c , d , and f are estimated by calling the function of each constant.

Once again, from U_s and U_r , the air-gap flux density is computed. Then, the electromagnetic torque, the radial magnetic pressure, the radial magnetic force components are estimated, using the same functions introduced in the first class REL_analytical_one.

11.6. Model of REL motor with three barrier

The class REL_analytical_three is used when the number of the flux-barriers is set equal to three. To start the analysis, the following function is called.

```
Three_Barrier_model.compute_potential();
```

Analogously, the number of the air-gap regions, the angles of the air-gap regions, the winding factor, and the stator scalar magnetic potential are computed. Due to the change occurs in the number of the flux-barriers, the rotor magnetic potential is estimated as

```

int h=0;
for (int m =0 ; m <regions_num ; m=m+2*nb) {
if (h%2 == 0){
    tblb1= tblb11;
    tblb2= tblb21;
    tblb3= tblb31;}
else{
    tblb1= tblb12;
    tblb2= tblb22;
    tblb3= tblb32;}

Ur3 = compute_m(beta_rad[m+2], beta_rad[m+3], beta_rad[m+1],
    beta_rad[m+4], beta_rad[m], beta_rad[m+5],tblb1, tblb2,tblb3)
    * compute_usi(beta_rad[m+2], beta_rad[m+3])

```

```

+ compute_n(beta_rad[m+2], beta_rad[m+3], beta_rad[m+1],
  beta_rad[m+4], beta_rad[m], beta_rad[m+5], tblb1, tblb2, tblb3
)
* compute_usi(beta_rad[m+1], beta_rad[m+2])
+ compute_q(beta_rad[m+2], beta_rad[m+3], beta_rad[m+1],
  beta_rad[m+4], beta_rad[m], beta_rad[m+5], tblb1, tblb2, tblb3
)
* compute_usi(beta_rad[m+3], beta_rad[m+4])
+ compute_j(beta_rad[m+2], beta_rad[m+3], beta_rad[m+1],
  beta_rad[m+4], beta_rad[m], beta_rad[m+5], tblb1, tblb2, tblb3
)
* compute_usi(beta_rad[m], beta_rad[m+1])
+ compute_h(beta_rad[m+2], beta_rad[m+3], beta_rad[m+1],
  beta_rad[m+4], beta_rad[m], beta_rad[m+5], tblb1, tblb2, tblb3
)
* compute_usi(beta_rad[m+4], beta_rad[m+5]);

Ur2= compute_c(beta_rad[m+2], beta_rad[m+3], beta_rad[m+1],
  beta_rad[m+4], tblb1, tblb2)
  * compute_usi(beta_rad[m+2], beta_rad[m+3]) + compute_d(
    beta_rad[m+2], beta_rad[m+3],
    beta_rad[m+1], beta_rad[m+4], tblb1, tblb2) * compute_usi(
      beta_rad[m+1], beta_rad[m+2])
  + compute_f(beta_rad[m+2], beta_rad[m+3], beta_rad[m+1],
    beta_rad[m+4], tblb1, tblb2)
  * compute_usi(beta_rad[m+3], beta_rad[m+4])
  + compute_z(beta_rad[m+2], beta_rad[m+3], beta_rad[m+1],
    beta_rad[m+4], tblb1, tblb2) * Ur3 ;

Ur1= compute_a(beta_rad[m+2], beta_rad[m+3], tblb1) * compute_usi(
  beta_rad[m+2], beta_rad[m+3])
  + compute_b(beta_rad[m+2], beta_rad[m+3], tblb1) * Ur2 ;

Ur_vector.push_back(Ur3);
Ur_vector.push_back(Ur2);
Ur_vector.push_back(Ur1);
Ur_vector.push_back(Ur2);
Ur_vector.push_back(Ur3);
Ur_vector.push_back(0);

h=h+1;
}

```

The functions of computing the constants z , m , n , q , j , and h are written similar to that of the constant a , shown before.

11.7. The results of the application

The graphical user interface application is checked at the healthy case, different eccentricity cases, different number of poles, different rotor geometry, different eccentricity values, different electric loading, and different electric current angles. It is noted that there is a good agreement between the application results and the FE results. As an example, the geometrical data reported in Table. 4.1 and Table. 4.4 are imported to the application. Then, the compute push button is clicked. Hence, the analytical model of the REL motor with three flux-barriers per pole, which presented in class `REL_analytical_three` is applied. Since, the push buttons of plotting the stator scalar magnetic potential, the rotor scalar magnetic potential, and the air-gap flux density are pressed, the results are viewed, as shown in Fig. 11.4. Similarly, the electromagnetic torque, the radial magnetic pressure distribution on the rotor are plotted, as shown in Fig. 11.5, if their corresponding plotting push buttons are pressed. Finally, the radial magnetic force components in x and y directions are plotted versus the rotor position. Besides, F_y versus F_x is shown. These figures are shown in Fig. 11.6.

Conclusions and future work

The first part of this thesis dealt with an analytical model of REL motor. The model combines a differential computation together with a lumped parameter network to consider the rotor anisotropy. REL motor with one, two, and three flux-barriers per pole is considered.

Next, an analytical model of eccentric REL motor is proposed. Both static and dynamic eccentricity cases are considered. It is noticed that, the main effect of static and dynamic eccentricity is a large force in direction of the smaller air-gap.

The analytical model is extended to compute the impact of the eccentricity for a wide set of configurations of REL motor. It is noticed that, the asymmetric rotor geometry exhibits approximately the same radial force of symmetric rotor geometry in case of eccentricity. In addition, the analytical model is applied on REL motor with concentrated coil windings including single- and double-layer configuration. The model results to be proper also for such configurations. The drawbacks of single-layer FSCW configuration are highlighted.

Both REL and PMAREL motors are compared at different eccentricity scenarios. Different rotor geometries are considered. The impact of the dimensions of the flux-barriers on the radial forces is highlighted. It is noted that, there is no significant difference between the two motors in different eccentricity cases.

An analytical model is described for analyzing SPM machines with and without rotor eccentricity. The models of both REL and SPM motors are used to compute the impact of the eccentricity and to highlight which machine is more affected by such a phenomenon. It is noted that, the eccentricity impact on the REL machine is much higher than that on the SPM machine, at different eccentricity cases.

At the second part of the thesis, the slotting and the magnetic saturation effect are included in the analytical models of concentric and eccentric REL. It is noted that the average torque is accurately estimated by the model of the concentric REL motor. In addition, the radial magnetic force, which results from of the eccentric motor model, is precisely computed. The results are confirmed by FE analysis and experimental measurements.

At the third part of the thesis, two analytical approaches for designing the permanent magnet of the PMAREL motor are proposed. The width and the thickness are selected so as to achieve the desired no-load air-gap flux density and resist the demagnetization under the desired loading conditions, respectively. Then, the iron ribs effect is also considered in both analytical analyses.

A rapid procedure to estimate the main dimensions of a synchronous reluctance motor, with or without the assistance of a PM, is fully described.

At the fourth part of the thesis, a graphical user interface application has been developed for the linear analytical models of concentric and eccentric REL motor.

Ultimately, some further improvements could be applied to the presented models (future work):

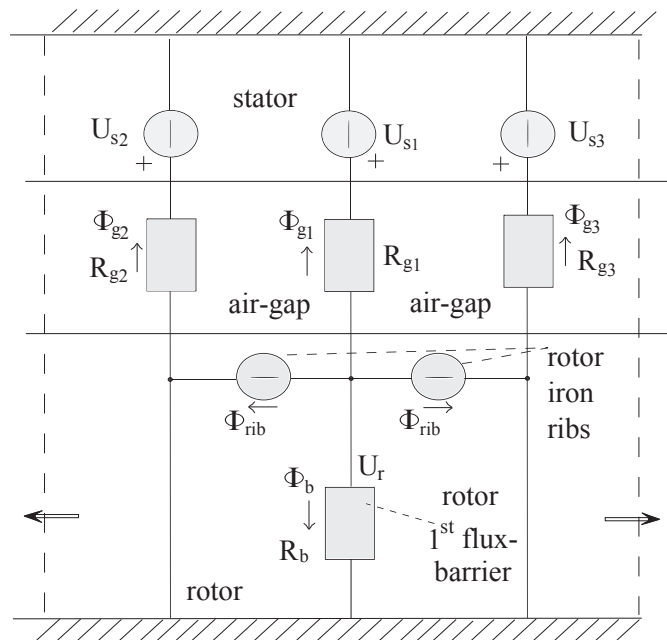
- considering the local saturation occurs in the rotor channels and islands,
- including the rotor iron ribs in the magnetic network of the REL motor,
- implementing other approaches of computing the electromagnetic torque,
- applying optimization approaches to the improved analytical model so as to get the proper rotor geometry. This helps to reduce the torque ripples and eddy-current losses,
- evaluating the influent of the infinite permeability assumption on the magnetic radial forces calculation (linear analytical model) with respect to the approximation of air-gap lengths,
- carrying out structural analysis to study the mechanical stress acting on the rotor iron ribs in both healthy and eccentricity cases,
- verifying the analytical model of the eccentric REL motor by 3D FE model, specially, in case of non-uniform displacement of the rotor axis from the stator axis.

Appendix A

As an example, REL motor with one flux-barrier per pole is considered. As it is known, the rotor iron ribs are commonly saturated. It is assumed that the ribs are saturated at constant flux density B_{sat} according to the B-H characteristic of the rotor iron laminations. The saturated magnetic ribs are presented in the magnetic circuit by means of flux sources. These flux sources are given by

$$\phi_{rib} = B_{sat} t_r L_{stk}$$

where t_r is the thickness of the iron rib.



The aforementioned figure shows the magnetic network of REL motor with one flux-barrier per pole considering the saturation occurs in the rotor iron ribs. The magnetic flux flowing through the first flux-barrier is computed as

$$\phi_b = [-\phi_{g1} - 2\phi_{rib}]$$

Then, the magnetic potential of the first flux-barrier is given by

$$\begin{aligned} U_r &= \phi_b \cdot R_b \\ &= -aD \sum_{\nu^e} \frac{\hat{K}_{\nu^e}}{(\nu^e p)^2} \cos(\lambda_{\nu^e}) \cdot \sin(\nu^e p \theta_b) - a k_{rib} \end{aligned}$$

where θ_b is the barrier angle, and the constants a and k_{rib} are as follows

$$\begin{aligned} a &= \frac{\frac{Dt_b}{2gl_b}}{1 + \frac{Dt_b}{2gl_b} 2\theta_b} \\ k_{rib} &= \frac{4B_{sat} t_r g}{\mu_o D} \end{aligned}$$

By neglecting the magnetic voltage drop in iron paths, the air-gap flux density is estimated as

$$B_g(\theta_r) = \mu_o \frac{-U_s(\theta_r) + U_r}{g}$$

The total electromechanical torque is given by:

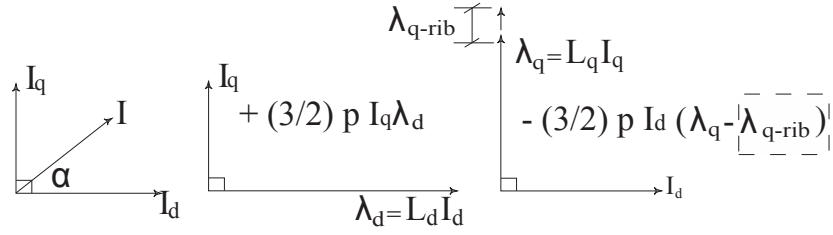
$$\begin{aligned} \tau_m &= k_\tau D \sum_{\nu^e} \frac{\hat{K}_{\nu^e}}{(\nu^e p)^2} \cos(\lambda_{\nu^e}) \sin(\nu^e p \theta_b) \\ &\cdot \sum_{\xi} \frac{\hat{K}_{\xi}}{(\xi p)} \sin(\lambda_{\xi}) \sin(\xi p \theta_b) \\ &+ k_\tau k_{rib} \sum_{\xi} \frac{\hat{K}_{\xi}}{(\xi p)} \sin(\lambda_{\xi}) \sin(\xi p \theta_b) \end{aligned}$$

where λ_{ν^e} , λ_{ξ} , k_τ and are defined as following:

$$\begin{aligned} \lambda_{\nu^e} &= \frac{\nu^e \pi}{2} + (\nu^e - 1)\omega_{me} t - \alpha_i^e \\ \lambda_{\xi} &= \frac{\xi \pi}{2} + (\xi - 1)\omega_{me} t - \alpha_i^e \quad (1) \\ k_\tau &= \frac{a \mu_o D^2 L_{stk}}{g} \end{aligned}$$

The vector representation for the flux-linkage components in d-axis and q-axis directions in case of considering the rotor iron ribs is shown in the following. It is noted that the iron ribs produce flux-linkage in q-axis direction as shown in the vector diagram. This flux linkage λ_{q-rib} interacts with the d-axis current I_d and produces negative torque component. Therefore, the iron ribs cause reduction in the torque by constant value equal to $\frac{-3}{2} p \lambda_{q-bridge} I_d$ as in following:

$$\tau_m = \frac{3}{2} p (\lambda_d I_q - \lambda_q I_d - \lambda_{q-rib} I_d)$$



For the aim of analytical computation of the torque reduction caused by the consideration of the rotor iron bridges, the q-axis flux-linkage produced by the iron ribs should be calculated. This flux-linkage is the difference between the q-axis flux-linkage in both cases of considering and neglecting the iron ribs. To calculate this difference, the current is imposed only in q-axis by letting the current angle $\alpha = 90^\circ$. For the purpose of computation simplification, the fundamental component is used for calculating the iron bridge torque reduction. Therefore, the fourier analysis are applied to the q-axis flux-density in both cases of considering and neglecting the rotor iron ribs. The fundamental flux per pole in q-axis in both cases can be calculated from the fundamental component of the flux-density as

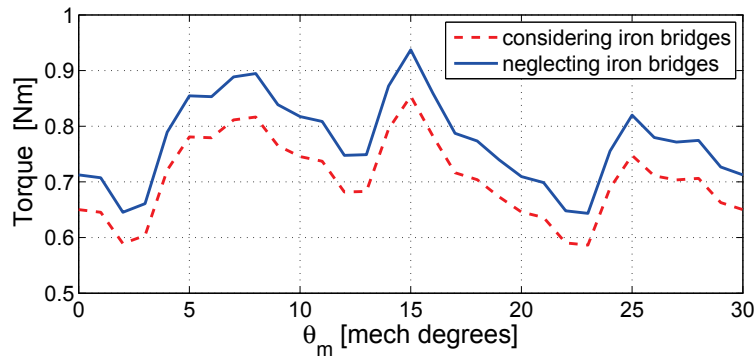
$$\phi_{pole} = \frac{2}{\pi} \hat{B} \tau_p L_{stk} = \hat{B}_g \frac{DL_{stk}}{p}$$

where \hat{B} is the peak value of the fundamental component of the air-gap flux-density and τ_p is the pole pitch. The q-axis flux-linkage is calculated in both cases as

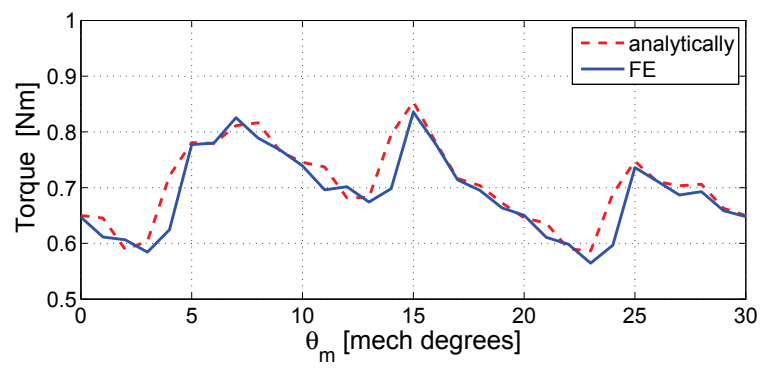
$$\lambda_q = \frac{k_w N_s}{2} \hat{B} \frac{DL_{stk}}{p}$$

where N_s is the number of series conductor per phase and k_w is the winding factor.

Finally, the difference between the λ_q in both cases of considering and neglecting the iron ribs can be estimated. Hence, the reduction in the electromagnetic torque due to considering the iron ribs, as shown in the following figure, can be estimated.



This approach is applied in the analytical model and FE model. Then, a satisfactory agreement between both models is achieved as shown in the following figure

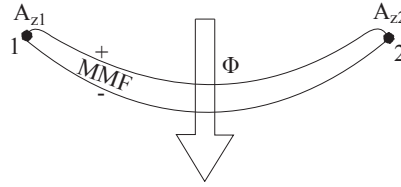


Appendix B

This Appendix describes how the ratio between the thickness and the length of the i -th flux-barrier (t_{b_i}/l_{b_i}) can be computed. Due to the non uniform thickness of the flux barriers, it is not easy to compute this ratio analytically. Thus, a simple FE model for computing the accurate ratio between thickness and the length of the each i -th flux barrier (t_{b_i}/l_{b_i}) is presented in the following figure. Hence, the flux flows through each i -th flux barrier is computed as

$$\phi_{b_i} = [A_{z_1} - A_{z_2}] \cdot L_{stk}$$

where A_{z_1} and A_{z_2} are the magnetic potential vector which are imposed at the points 1 and 2, respectively.



Then, the average magnetic potential drop on each flux-barrier is given by

$$MMF_{avg_i} = \int H_{ti} dl$$

So that R_{b_i} and the ratio t_{b_i}/l_{b_i} are given by:

$$R_{b_i} = \frac{MMF_{avg_i}}{\phi_{b_i}}$$

and

$$\frac{t_{b_i}}{l_{b_i}} = \mu_0 L_{stk} \frac{MMF_{avg_i}}{\phi_{b_i}}$$

This previous approach is applied to the motor described in the example. The values of A_{z_1} and A_{z_2} are imposed to be equal to 0.01 and -0.01 Wb/m , respectively. Then, the flux flowing through the flux -barriers is computed. It is given by 0.8 mWb . Then, the average magnetic voltage drop on each flux-barrier is computed by using the FE software according the aforementioned equation. It is given by 115, 123, and 114 A for the first, second, and third flux-barrier, respectively. After that, the ratio t_{b_i}/l_{b_i} can be estimated. Their values are equal to 0.073, 0.077, and 0.072 for the first, second, and third flux-barrier, respectively.

Bibliography

- [1] R. R. Moghaddam, "Synchronous reluctance machine (synrm) in variable speed drives (vsd) applications," Ph.D. dissertation, Stockholm, Sweden, 2011.
- [2] J. Kostko, "Polyphase reaction synchronous motors," *Journal of the American Institute of Electrical Engineers*, vol. 42, no. 11, pp. 1162–1168, Nov 1923.
- [3] R. R. Moghaddam, "Synchronous reluctance machine (synrm) design," Master's thesis, Royal Institute of Technology, 2007.
- [4] T. A. Lipo, "Synchronous reluctance machines-a viable alternative for ac drives?" in *Electric Machines and Power Systems*, pp. 659–671, Nov. 1991.
- [5] T. Fukao, A. Chiba, and M. Matsui, "Test results on a super-high-speed amorphous-iron reluctance motor," *IEEE Transactions on Industry Applications*, vol. 25, no. 1, pp. 119–125, Jan 1989.
- [6] D. A. Staton, T. J. E. Miller, and S. E. Wood, "Maximising the saliency ratio of the synchronous reluctance motor," *IEE Proceedings B - Electric Power Applications*, vol. 140, no. 4, pp. 249–259, July 1993.
- [7] O. A. Hassan, S.A. and A. Mohamadein, "Performance of different types of reluctance motors: experimental comparative study," *Elect. Mach. Elerrromech.*, vol. 5, pp. 225–236, 1980.
- [8] I. Boldea, *Reluctance synchronous machines and drives*. Oxford: Clarendon Press (1), 1996.
- [9] A. Vagati, "The synchronous reluctance solution: a new alternative in ac drives," in *20th International Conference on Industrial Electronics, Control and Instrumentation, 1994. IECON '94*, vol. 1, Sep 1994, pp. 1–13 vol.1.
- [10] A. A. A.J. Cruickshank, R.W. Menzies, "Theory and performance of reluctance motors with axially laminated anisotropic rotors," *Proceedings of the Institution of Electrical Engineers*, vol. 118, no. 7, pp. 887–894, July 1971.
- [11] I. Boldea, Z. X. Fu, and S. A. Nasar, "Performance evaluation of axially-laminated anisotropic (ala) rotor reluctance synchronous motors," *IEEE Transactions on Industry Applications*, vol. 30, no. 4, pp. 977–985, Jul 1994.

- [12] P. LAWRENSEN and S. GUPTA, "Developments in the performance and theory of segmental-rotor reluctance motors," *Proceedings of the Institution of Electrical Engineers*, vol. 114, no. 5, pp. 645–653, May 1967.
- [13] V. HONSINGER, "The inductances L_d and L_q of reluctance machines," *IEEE Trans.*, vol. PAS-90, (1), pp. 298–304, 1971.
- [14] —, "Steady-state performance of reluctance machines," *IEEE Trans.*, vol. PAS-90, (1), pp. 305–317, 1971.
- [15] A. Fratta, A. Vagati, and F. Villata, "On the evolution of ac machines for spindle drive applications," in *Conference Record of the IEEE Industry Applications Society Annual Meeting*, Oct 1989, pp. 699–704 vol.1.
- [16] A. Vagati, G. Franceschini, I. Marongiu, and G. P. Troglia, "Design criteria of high performance synchronous reluctance motors," in *Conference Record of the Industry Applications Society Annual Meeting*, Oct 1992, pp. 66–73 vol.1.
- [17] M. J. Kamper, F. S. V. der Merwe, and S. Williamson, "Direct finite element design optimisation of the cageless reluctance synchronous machine," *IEEE Transactions on Energy Conversion*, vol. 11, no. 3, pp. 547–555, Sep 1996.
- [18] B. J. Chalmers and L. Musaba, "Design and field-weakening performance of a synchronous reluctance motor with axially laminated rotor," *IEEE Transactions on Industry Applications*, vol. 34, no. 5, pp. 1035–1041, Sep 1998.
- [19] J. Pyrhönen, "Lecture notes in electric drives."
- [20] M. Barcaro, "Design and analysis of interior permanent magnet synchronous machines for electric vehicles," Ph.D. dissertation, Padova University, 2011.
- [21] D. Mingardi, M. Morandini, S. Bolognani, and N. Bianchi, "On the properties of the differential cross-saturation inductance in synchronous machines," in *IEEE Energy Conversion Congress and Exposition (ECCE)*, Sept 2015, pp. 2964–2971.
- [22] E. Armando, P. Guglielmi, G. Pellegrino, M. Pastorelli, and A. Vagati, "Accurate modeling and performance analysis of ipm-pmsm motors," *IEEE Transactions on Industry Applications*, vol. 45, no. 1, pp. 123–130, Jan 2009.
- [23] A. Fratta, G. P. Troglia, A. Vagati, and F. Villata, "Evaluation of torque ripple in high performance synchronous reluctance machines," in *Conference Record of IEEE Industry Applications Society Annual Meeting*, Oct 1993, pp. 163–170 vol.1.
- [24] T. M. Jahns and W. L. Soong, "Pulsating torque minimization techniques for permanent magnet ac motor drives—a review," *IEEE Transactions on Industrial Electronics*, vol. 43, no. 2, pp. 321–330, Apr 1996.
- [25] M. Sanada, K. Hiramoto, S. Morimoto, and Y. Takeda, "Torque ripple improvement for synchronous reluctance motor using an asymmetric flux barrier arrangement," *IEEE Transactions on Industry Applications*, vol. 40, no. 4, pp. 1076–1082, July 2004.

- [26] J. M. Park, S. I. Kim, J. P. Hong, and J. H. Lee, "Rotor design on torque ripple reduction for a synchronous reluctance motor with concentrated winding using response surface methodology," *IEEE Transactions on Magnetics*, vol. 42, no. 10, pp. 3479–3481, Oct 2006.
- [27] N. Bianchi, S. Bolognani, D. Bon, and M. D. Prè, "Rotor flux-barrier design for torque ripple reduction in synchronous reluctance and pm-assisted synchronous reluctance motors," *IEEE Transactions on Industry Applications*, vol. 45, no. 3, pp. 921–928, May 2009.
- [28] S. H. Han, T. M. Jahns, W. L. Soong, M. K. Güven, and M. S. Illindala, "Torque ripple reduction in interior permanent magnet synchronous machines using stators with odd number of slots per pole pair," *IEEE Transactions on Energy Conversion*, vol. 25, no. 1, pp. 118–127, March 2010.
- [29] M. Barcaro and N. Bianchi, "Torque ripple reduction in fractional-slot interior pm machines optimizing the flux-barrier geometries," in *XXth International Conference on Electrical Machines (ICEM)*, Sept 2012, pp. 1496–1502.
- [30] A. Vagati, M. Pastorelli, G. Francheschini, and S. Petrache, "Design of low-torque-ripple synchronous reluctance motors," *IEEE Transactions on Industry Applications*, vol. 34, no. 4, pp. 758–765, Jul 1998.
- [31] M. Morandin, "Electric drives with permanent magnet synchronous machines connected to internal combustion engines," Ph.D. dissertation, UNIVERSITÀ DEGLI STUDI DI PADOVA, 2013.
- [32] N. Bianchi, M. D. Prè, L. Alberti, and E. Fornasiero, *Theory and Design of Fractional-Slot PM Machines*, S. by the IEEE-IAS Electrical Machines Committee, Ed. Padova: CLEUP (ISBN 978-88-6129-122-5), 2007., 2007.
- [33] N. Bianchi and M. Barcaro, "Iron losses reduction in synchronous motors with anisotropic rotor," in *34th Annual Conference of IEEE Industrial Electronics, IECON*, Nov 2008, pp. 1258–1263.
- [34] M. Barcaro, N. Bianchi, and F. Magnussen, "Rotor flux-barrier geometry design to reduce iron losses in synchronous ipm motors under fw operations," in *IEEE International Electric Machines and Drives Conference. IEMDC '09.*, May 2009, pp. 928–935.
- [35] N. Bianchi, "Analysis of the IPM motor – Part II, Finite Element approach", in *Design, Analysis, and Control of Interior PM Synchronous Machines*, T. Jahns, Ed. IEEE IAS Tutorial Course notes, IAS Annual Meeting, Seattle, October 3, 2004, CLEUP press, in pp. 3.34–3.66, ISBN 88–7178–898–2.
- [36] G. Pellegrino, A. Vagati, P. Guglielmi, and B. Boazzo, "Performance comparison between surface-mounted and interior pm motor drives for electric vehicle application," *IEEE Transactions on Industrial Electronics*, vol. 59, no. 2, pp. 803–811, Feb 2012.
- [37] H. Mahmoud and N. Bianchi, "Eccentricity in synchronous reluctance motors –part I: Analytical and finite-element models," *IEEE Transactions on Energy Conversion*, vol. 30, no. 2, pp. 745–753, June 2015.

- [38] S.-H. Han, T. Jahns, and W. Soong, "Torque ripple reduction in interior permanent magnet synchronous machines using the principle of mutual harmonics exclusion," in *Record of the 42nd IEEE in Industry Applications Annual Meeting*, Sept 2007, pp. 558–565.
- [39] W.-H. Kim, K.-S. Kim, S.-J. Kim, D.-W. Kang, S.-C. Go, Y.-D. Chun, and J. Lee, "Optimal pm design of pma-synrm for wide constant-power operation and torque ripple reduction," *IEEE Transactions on Magnetics*, vol. 45, no. 10, pp. 4660–4663, Oct 2009.
- [40] U.-J. Seo, Y.-D. Chun, J.-H. Choi, P.-W. Han, D.-H. Koo, and J. Lee, "A technique of torque ripple reduction in interior permanent magnet synchronous motor," *IEEE Transactions on Magnetics*, vol. 47, no. 10, pp. 3240–3243, Oct 2011.
- [41] C. Spargo, B. Mecrow, and J. Widmer, "Higher pole number synchronous reluctance machines with fractional slot concentrated windings," in *7th IET International Conference on Power Electronics, Machines and Drives (PEMD 2014)*, April 2014, pp. 1–6.
- [42] D.-J. Kim, H.-J. Kim, J.-P. Hong, and C.-J. Park, "Estimation of acoustic noise and vibration in an induction machine considering rotor eccentricity," *IEEE Transactions on Magnetics*, vol. 50, no. 2, pp. 857–860, Feb 2014.
- [43] K.-T. Kim, K.-S. Kim, S.-M. Hwang, T.-J. Kim, and Y.-H. Jung, "Comparison of magnetic forces for IPM and SPM motor with rotor eccentricity," *IEEE Transactions on Magnetics*, vol. 37, no. 5, pp. 3448–3451, Sep 2001.
- [44] M. Michon, R. Holehouse, K. Atallah, and J. Wang, "Unbalanced magnetic pull in permanent magnet machines," in *7th IET International Conference on Power Electronics, Machines and Drives (PEMD 2014)*, April 2014, pp. 1–6.
- [45] A. Smith and D. Dorrell, "Calculation and measurement of unbalanced magnetic pull in cage induction motors with eccentric rotors. i. analytical model," *IEE Proceedings - Electric Power Applications*, vol. 143, no. 3, pp. 193–201, May 1996.
- [46] S. Swann, "Effect of rotor eccentricity on the magnetic field in the air-gap of a non-salient-pole machine," *Proceedings of the Institution of Electrical Engineers*, vol. 110, no. 5, pp. 903–915, May 1963.
- [47] D. Dorrell, W. Thomson, and S. Roach, "Combined effects of static and dynamic eccentricity on airgap flux waves and the application of current monitoring to detect dynamic eccentricity in 3-phase induction motors," in *Seventh International Conference on (Conf. Publ. No. 412) in Electrical Machines and Drives*, Sep 1995, pp. 151–155.
- [48] G. Joksimovic, M. Durovic, J. Penman, and N. Arthur, "Dynamic simulation of dynamic eccentricity in induction machines-winding function approach," *IEEE Transactions on Energy Conversion*, vol. 15, no. 2, pp. 143–148, June 2000.
- [49] D. Ionel, "Interior permanent magnet motor including rotor with unequal poles," *U.S. Patent, 8,102,091, Jan. 24, 2102*.
- [50] N. Bianchi, S. Bolognani, and P. Frare, "Design criteria of high efficiency SPM synchronous motors," in *IEEE International Conference in Electric Machines and Drives.*, vol. 2, June 2003, pp. 1042–1048 vol.2.

- [51] B. Mecrow, A. Jack, D. Atkinson, S. Green, G. Atkinson, A. King, and B. Green, "Design and testing of a four-phase fault-tolerant permanent-magnet machine for an engine fuel pump," *IEEE Transactions on Energy Conversion*, vol. 19, no. 4, pp. 671–678, Dec 2004.
- [52] B. Mecrow, A. Jack, J. Haylock, and J. Coles, "Fault-tolerant permanent magnet machine drives," *IEE Proceedings on Electric Power Applications*, vol. 143, no. 6, pp. 437–442, Nov 1996.
- [53] A. Jack, B. Mecrow, and J. Haylock, "A comparative study of permanent magnet and switched reluctance motors for high-performance fault-tolerant applications," *IEEE Transactions on Industry Applications*, vol. 32, no. 4, pp. 889–895, Jul 1996.
- [54] N. Bianchi, S. Bolognani, M. Pre, and G. Grezzani, "Design considerations for fractional-slot winding configurations of synchronous machines," *IEEE Transactions on Industry Applications*, vol. 42, no. 4, pp. 997–1006, July 2006.
- [55] J. Cros, J. Figuerola, and P. Viarouge, "BLDC motors with surface mounted PM rotor for wide constant power operation," in *Conference Record of the 38th IAS Annual Meeting in Industry Applications*, vol. 3, Oct 2003, pp. 1933–1940 vol.3.
- [56] A. EL-Refaie and T. Jahns, "Comparison of synchronous pm machine types for wide constant-power speed range operation," in *Conference Record of the Fourtieth Annual Meeting in Industry Applications*, vol. 2, Oct 2005, pp. 1015–1022 Vol. 2.
- [57] J. Wang, Z. P. Xia, and D. Howe, "Analysis of three-phase surface-mounted magnet modular permanent magnet machines," in *Second International Conference on Power Electronics, Machines and Drives (PEMD)*, vol. 3, March 2004, pp. 27–32.
- [58] F. Magnussen and H. Lendenmann, "Parasitic effects in PM machines with concentrated windings," in *Conference Record of the Fourtieth Annual Meeting in industry Applications*, vol. 2, Oct 2005, pp. 1044–1049 Vol. 2.
- [59] D. Ishak, Z. Zhu, and D. Howe, "Unbalanced magnetic forces in permanent magnet brushless machines with diametrically asymmetric phase windings," in *Conference Record of the Fourtieth Annual Meeting in Industry Applications*, vol. 2, Oct 2005, pp. 1037–1043 Vol. 2.
- [60] N. Bianchi, S. Bolognani, D. Bon, and M. D. Prè, "Torque harmonic compensation in a synchronous reluctance motor," *IEEE Transactions on Energy Conversion*, vol. 23, no. 2, pp. 466–473, June 2008.
- [61] Z. Zhu, D. Howe, E. Bolte, and B. Ackermann, "Instantaneous magnetic field distribution in brushless permanent magnet dc motors. i. open-circuit field," *IEEE Transactions on Magnetics*, vol. 29, no. 1, pp. 124–135, Jan 1993.
- [62] Z. Zhu and D. Howe, "Instantaneous magnetic field distribution in brushless permanent magnet dc motors. iii. effect of stator slotting," *IEEE Transactions on Magnetics*, vol. 29, no. 1, pp. 143–151, Jan 1993.
- [63] H. Mahmoud and N. Bianchi, "Eccentricity in synchronous reluctance motors-part II: Different rotor geometry and stator windings," *IEEE Transactions on Energy Conversion*, vol. 30, no. 2, pp. 754–760, June 2015.

- [64] U. Kim and D. Lieu, "Magnetic field calculation in permanent magnet motors with rotor eccentricity: without slotting effect," *IEEE Transactions on Magnetics*, vol. 34, no. 4, pp. 2243–2252, Jul 1998.
- [65] —, "Magnetic field calculation in permanent magnet motors with rotor eccentricity: with slotting effect considered," *IEEE Transactions on Magnetics*, vol. 34, no. 4, pp. 2253–2266, Jul 1998.
- [66] D. Dorrell, M. Popescu, C. Cossar, and D. Ionel, "Unbalanced magnetic pull in fractional-slot brushless pm motors," in *Industry Applications Society Annual Meeting, 2008. IAS '08. IEEE*, Oct 2008, pp. 1–8.
- [67] M. Michon, R. Holehouse, K. Atallah, and G. Johnstone, "Effect of rotor eccentricity in large synchronous machines," *IEEE Transactions on Magnetics*, vol. 50, no. 11, pp. 1–4, Nov 2014.
- [68] C. Hwang, C. Chang, S. Cheng, C. Chan, C. Pan, and T. Chang, "Comparison of performances between IPM and SPM motors with rotor eccentricity," *Journal of Magnetism and Magnetic Materials*, vol. 282, no. 0, pp. 360 – 363, 2004, international Symposium on Advanced Magnetic Technologies.
- [69] T.-J. Kim, S.-M. Hwang, K.-T. Kim, W.-B. Jung, and C.-U. Kim, "Comparison of dynamic responses for ipm and spm motors by considering mechanical and magnetic coupling," *IEEE Transactions on Magnetics*, vol. 37, no. 4, pp. 2818–2820, Jul 2001.
- [70] J.-K. Park, I.-M. Seo, and J. Hur, "Fault type detection using frequency pattern of stator current in ipm-type bldc motor under stator inter-turn, dynamic eccentricity, and coupled faults," in *IEEE Energy Conversion Congress and Exposition (ECCE)*, Sept 2013, pp. 2516–2521.
- [71] F. Li, Q. Lv, Y. Fang, N. Liang, and X. Bao, "Analysis of electromagnetic stiffness in submersible motors with inclined rotor eccentricity," in *17th International Conference on Electrical Machines and Systems (ICEMS)*, Oct 2014, pp. 2940–2944.
- [72] T. Lubin, S. Mezani, and A. Rezzoug, "Two-dimensional analytical calculation of magnetic field and electromagnetic torque for surface-inset permanent-magnet motors," *IEEE Transactions on Magnetics*, vol. 48, no. 6, pp. 2080–2091, June 2012.
- [73] H. Xiaohong and X. Penghu, "Calculation of air gap flux density for the surface motor," in *4th International Conference on Electric Utility Deregulation and Restructuring and Power Technologies (DRPT)*, July 2011, pp. 1769–1773.
- [74] D. Zarko, D. Ban, and T. Lipo, "Analytical calculation of magnetic field distribution in the slotted air gap of a surface permanent-magnet motor using complex relative air-gap permeance," *IEEE Transactions on Magnetics*, vol. 42, no. 7, pp. 1828–1837, July 2006.
- [75] F. Carter, "Note on air-gap and interpolar induction," *Journal of the Institution of Electrical Engineers*, vol. 29, no. 146, pp. 925–933, July 1900.
- [76] B. Heller and V. Hamata, *Harmonic Field Effects in Induction Machines*. New York: Elsevier, 1977.

- [77] J. Gieras, "Analytical approach to cogging torque calculation of pm brushless motors," *IEEE Transactions on Industry Applications*, vol. 40, no. 5, pp. 1310–1316, Sept 2004.
- [78] J. Moreira and T. Lipo, "Modeling of saturated ac machines including air gap flux harmonic components," *IEEE Transactions on Industry Applications*, vol. 28, no. 2, pp. 343–349, Mar 1992.
- [79] D. F. M. Hafner and K. Hameyer, "Accounting for saturation in conformal mapping modeling of a permanent magnet synchronous machine," *COMPEL, Int. J. Comput. Math. Elect. Electron. Eng.*, vol. 30, no. 3, pp. 916–928, 2011.
- [80] M. Ojaghi and S. Nasiri, "Modeling eccentric squirrel-cage induction motors with slotting effect and saturable teeth reluctances," *IEEE Transactions on Energy Conversion*, vol. 29, no. 3, pp. 619–627, Sept 2014.
- [81] K. Abbaszadeh and F. Rezaee Alam, "On-load field component separation in surface mounted permanent magnet motors using an improved conformal mapping method," *IEEE Transactions on Magnetics*, vol. PP, no. 99, pp. 1–1, 2015.
- [82] F. Rezaee Alam and K. Abbaszadeh, "Magnetic field analysis in eccentric surface-mounted permanent-magnet motors using an improved conformal mapping method," *Energy Conversion, IEEE Transactions on*, vol. in press, no. 99, 2015.
- [83] N. Bianchi, H. Mahmoud, and S. Bolognani, "Fast synthesis of permanent magnet assisted synchronous reluctance motors," *IET Electric Power Applications*, April 2016. [Online]. Available: <http://digital-library.theiet.org/content/journals/10.1049/iet-epa.2015.0240>
- [84] A. Vagati, B. Boazzo, P. Guglielmi, and G. Pellegrino, "Ferrite assisted synchronous reluctance machines: A general approach," in *XXth International Conference on Electrical Machines (ICEM)*, Sept 2012, pp. 1315–1321.
- [85] —, "Design of ferrite-assisted synchronous reluctance machines robust toward demagnetization," *IEEE Transactions on Industry Applications*, vol. 50, no. 3, pp. 1768–1779, May 2014.
- [86] B. Boazzo, A. Vagati, G. Pellegrino, E. Armando, and P. Guglielmi, "Multipolar ferrite-assisted synchronous reluctance machines: A general design approach," *IEEE Transactions on Industrial Electronics*, vol. 62, no. 2, pp. 832–845, Feb 2015.
- [87] R. Qu and T. A. Lipo, "Analysis and modeling of airgap amp; zigzag leakage fluxes in a surface-mounted-pm machine," in *37th IAS Annual Meeting. Conference Record of the Industry Applications Conference*, vol. 4, Oct 2002, pp. 2507–2513 vol.4.
- [88] Y. Kano, T. Kosaka, and N. Matsui, "Simple nonlinear magnetic analysis for permanent-magnet motors," *IEEE Transactions on Industry Applications*, vol. 41, no. 5, pp. 1205–1214, Sept 2005.
- [89] N. Bianchi, E. Fornasiero, M. Ferrari, and M. Castiello, "Experimental comparison of pm assisted synchronous reluctance motors," in *IEEE Energy Conversion Congress and Exposition (ECCE)*, Sept 2014, pp. 4499–4506.

- [90] N. Bianchi, E. Fornasiero, E. Carraro, S. Bolognani, and M. Castiello, "Electric vehicle traction based on a pm assisted synchronous reluctance motor," in *IEEE International Electric Vehicle Conference (IEVC)*, Dec 2014, pp. 1–6.
- [91] P. Guglielmi, B. Boazzo, E. Armando, G. Pellegrino, and A. Vagati, "Magnet minimization in ipm-pmasr motor design for wide speed range application," in *IEEE Energy Conversion Congress and Exposition*, Sept 2011, pp. 4201–4207.
- [92] —, "Permanent-magnet minimization in pm-assisted synchronous reluctance motors for wide speed range," *IEEE Transactions on Industry Applications*, vol. 49, no. 1, pp. 31–41, Jan 2013.
- [93] L. Alberti, M. Barcaro, and N. Bianchi, "Design of a low-torque-ripple fractional-slot interior permanent-magnet motor," *IEEE Transactions on Industry Applications*, vol. 50, no. 3, pp. 1801–1808, May 2014.
- [94] G. Pellegrino and F. Cupertino, "FEA-based multi-objective optimization of IPM motor design including rotor losses," in *IEEE Energy Conversion Congress and Exposition*, Sept 2010, pp. 3659–3666.
- [95] N. Bianchi, M. Degano, and E. Fornasiero, "Sensitivity analysis of torque ripple reduction of synchronous reluctance and interior PM motors," *IEEE Transactions on Industry Applications*, vol. 51, no. 1, pp. 187–195, Jan 2015.
- [96] G. Y. Sizov, P. Zhang, D. M. Ionel, N. A. O. Demerdash, I. P. Brown, A. O. Smith, and M. G. Solveson, "Modeling and analysis of effects of skew on torque ripple and stator tooth forces in permanent magnet ac machines," in *IEEE Energy Conversion Congress and Exposition (ECCE)*, Sept 2012, pp. 3055–3061.
- [97] A. Vagati, M. Pastorelli, G. Franceschini, and C. Petrace, "Design of low-torque-ripple synchronous reluctance motors," in *Conference Record of the IEEE Industry Applications Conference, Thirty-Second IAS Annual Meeting, IAS '97.*, vol. 1, Oct 1997, pp. 286–293 vol.1.
- [98] P. Guglielmi, M. Pastorelli, and A. Vagati, "Cross-saturation effects in ipm motors and related impact on sensorless control," *IEEE Transactions on Industry Applications*, vol. 42, no. 6, pp. 1516–1522, Nov 2006.
- [99] N. Bianchi, S. Bolognani, J. H. Jang, and S. K. Sul, "Comparison of pm motor structures and sensorless control techniques for zero-speed rotor position detection," *IEEE Transactions on Power Electronics*, vol. 22, no. 6, pp. 2466–2475, Nov 2007.
- [100] L. Wang and R. D. Lorenz, "Rotor position estimation for permanent magnet synchronous motor using saliency-tracking self-sensing method," in *Conference Record of the IEEE Industry Applications Conference*, vol. 1, 2000, pp. 445–450 vol.1.
- [101] A. V. A. Fratta and F. Villata., "Permanent magnet assisted synchronous reluctance drive for constant-power application: Drive power limit," *Proc. of Intelligent Motion European Conference, PCIM*, pp. 196–203, 1992.
- [102] W. H. Kim, K. S. Kim, S. J. Kim, D. W. Kang, S. C. Go, Y. D. Chun, and J. Lee, "Optimal pm design of pma-synrm for wide constant-power operation and torque ripple reduction," *IEEE Transactions on Magnetics*, vol. 45, no. 10, pp. 4660–4663, Oct 2009.

- [103] K. Imamura, M. Sanada, S. Morimoto, and Y. Inoue, "Improvement of demagnetization by rotor structure of ipmsm with dy-free rare-earth magnet," in *15th International Conference on Electrical Machines and Systems (ICEMS)*, Oct 2012, pp. 1–6.
- [104] N. Bianchi and S. Bolognani, "Reducing torque ripple in PM synchronous motors by pole shifting," *Proceeding of International Conference on Electrical Machines (ICEM)*, pp. 1222–1226, 2000.
- [105] M. Ferrari, N. Bianchi, and E. Fornasiero, "Rotor saturation impact in synchronous reluctance and pm assisted reluctance motors," in *IEEE Energy Conversion Congress and Exposition (ECCE)*, Sept 2013, pp. 1235–1242.
- [106] —, "Analysis of rotor saturation in synchronous reluctance and pm-assisted reluctance motors," *IEEE Transactions on Industry Applications*, vol. 51, no. 1, pp. 169–177, Jan 2015.
- [107] M. Gamba, G. Pellegrino, and F. Cupertino, "Optimal number of rotor parameters for the automatic design of synchronous reluctance machines," in *International Conference on Electrical Machines (ICEM)*, Sept 2014, pp. 1334–1340.
- [108] C. T. K.J. Binns, P.J. Lawrenson, *The analytical and numerical solution of electric and magnetic fields*. John Wiley and Sons copyright, 1992.
- [109] M. Barcaro, G. Meneghetti, and N. Bianchi, "Structural analysis of the interior pm rotor considering both static and fatigue loading," in *IEEE Energy Conversion Congress and Exposition (ECCE)*, Sept 2012, pp. 4338–4345.
- [110] —, "Structural analysis of the interior pm rotor considering both static and fatigue loading," *IEEE Transactions on Industry Applications*, vol. 50, no. 1, pp. 253–260, Jan 2014.
- [111] *Finite Element Method Magnetics*, Ver. 4.2 user's manual ed., February 5, 2009, [Online] available: <http://www.femm.info/Archives/doc/manual.pdf>.
- [112] <https://www.qt.io/>.
- [113] <http://qcustomplot.com/>.

List of Symbols

The symbols are divided into Roman symbols and Greek symbols. The dimensionless coefficients defined in chapter 2 and 3 are not reported, since they may cause misunderstanding with other symbols. However, it should be noted that these coefficients are not further adopted in the others chapters.

Roman symbols

A_g	air-gap cross section area
A_{fe}	iron cross section area
\vec{A}_I	magnetic vector potential in region I
\vec{A}_{II}	magnetic vector potential in region II
B	the viscous friction coefficient
B_g	air-gap flux density
B_{b_i}	flux density in the i -th part of the stator yoke
B_{rI}	the radial flux density in region I
B_{t_i}	flux density in the i -th stator tooth
B_{ml_i}	load flux density of the i -th PM
B_{moi}	no load flux density of the i -th PM
B_{rem}	the remanence of the PM
B_{island_i}	flux density in the i -th rotor island
B_I	flux density in region I
B_{II}	flux density in region II
$B_{\theta I}$	tangential flux density in region I
D	the inner diameter of the stator
D_e	the external diameter of the stator
D_r	the outer rotor diameter
D_{sh}	the shaft diameter
e	the eccentricity distance between the stator and rotor axes
f	the machine frequency

F_r	radial magnetic force acting on the rotor
F_x	magnetic force acting on the rotor in x -axis direction
F_y	magnetic force acting on the rotor in y -axis direction
g	air-gap length
g_e	equivalent air-gap length
$\bar{g}_{\gamma_1 \rightarrow \gamma_2}$	average air-gap length over a region boarded by the angles γ_1 and γ_2
H_b	length of the stator yoke
H_g	field intensity in the air-gap
H_{b_i}	field intensity in the i -th part of the stator yoke
H_{t_i}	field intensity in the i -th tooth of the stator
H_{fe}	field intensity in the iron
H_I	field intensity in region I
H_{II}	field intensity in region II
i_a	current flowing through phase a winding
i_b	current flowing through phase b winding
i_c	current flowing through phase c winding
i_d	d -axis current component
I_d	peak value of the d -axis current component
I_N	the peak value of the nominal current
i_q	q -axis current component
I_q	peak value of the q -axis current component
\hat{i}_s	stator current space vector
I_{demg}	demagnetizing current of the PM
I_{slot}	peak current in the stator slot
$I_{nominal}$	peak value phase rated current
J	moment of inertia of the rotor
K_s	linear current density or the electric loading of the stator
$\hat{K}_{s\nu^e}$	peak value of the ν^e -th harmonic of the electric loading
$\hat{K}_w^{\nu^e}$	winding factor of the ν^e -th harmonic
\hat{K}_{air}	ratio between the air length to the total length in the rotor
\hat{K}_{sat}	saturation factor referring to the magnetic voltage drop in the iron parts of the machine
$\hat{K}_{sat_{island_i}}$	saturation factor representing the voltage drop occurs in i -th rotor island
L_d	the d -axis component of the machine inductance
L_m	phase magnetizing inductance
L_q	the q -axis component of the machine inductance
$l_{b_{1,2,3}}$	first, second, and third flux-barrier length, respectively
L_{fe}	iron path length
L_{md}	the d -axis component of the magnetizing inductance
L_{mq}	the q -axis component of the magnetizing inductance
$L_{s\sigma}$	leakage inductance per phase
\vec{M}	residual magnetization vector of the PM
M_r	radial magnetization of the PM
M_θ	tangential magnetization of the PM

N	number of turns in the coil
N_b	number of the flux-barriers per rotor pole
n_r	number of equivalent rotor slots per pole pair
n_s	number of equivalent stator slots per pole pair
N_s	number of series conductors per phase
\hat{n}	amplitude of the impulse fuction
$n_d(\theta_s)$	conductor density distribution function
$n_{da}(\theta_s)$	conductor density distribution function of phase a
$n_{db}(\theta_s)$	conductor density distribution function of phase b
$n_{dc}(\theta_s)$	conductor density distribution function of phase c
p	number of pole pairs
p_m	radial magnetic pressure on the rotor
p_{ec}	eddy current losses
p_{fe}	total iron losses
p_{hy}	hysteresis losses
$p_{ec_{island}_i}$	specific eddy current losses in the i -th rotor island
q	number of slots per pole per phase
Q_s	number of the stator slots
R_m	magnetic reluctance of the PM
R_r	outer radius of the rotor
R_s	inner radius of the stator
R_t'	magnetic reluctance of the lateral space of the two sides of the PM
R_t''	magnetic reluctance of the space above and below the PM
$R_{b_{1,2,3}}$	magnetic reluctance of the first, second , and third flux-barrier, respectively
R_{g_i}	reluctance referring to the portions of the air-gap in front to the i -th flux-barrier
R_{bm}	equivalent of the parallel reluctance of the lateral parts of the flux-barrier
R_{se}	external radius of the stator
T	electromagnetic torque
T_N	nominal torque
T_Q	axial torque on the rotor in case of non uniform axial eccentricity
$t_{b_{1,2,3}}$	thickness of the first, second , and third flux-barrier, respectively
$t_{r_{1,2,3}}$	iron rib thickness of the first, second , and third flux-barrier, respectively
t_{m_i}	thickness of the i -th PM
U_d	the d -axis component of the peak value of the nominal phase voltage
U_N	peak value of the nominal phase voltage
U_r	rotor scalar magnetic potential
U_q	the q -axis component of the peak value of the nominal phase voltage
U_s	rotor scalar magnetic potential
U_{b_i}	magnetic voltage drop in the stator yoke
U_{r_i}	scalar magnetic potential of the i -th rotor island
U_{s_i}	average value of the stator magnetic potential in front to the i -th flux-barrier
U_{t_i}	magnetic voltage drop in the i -th stator tooth
U_{rem}	equivalent magnetic potential potential generator of the PM

v_d	the d -axis component of the stator voltage vector
v_q	the q -axis component of the stator voltage vector
v_s	stator terminal voltage vector in stationary reference frame
W'_m	magnetic coenergy
w_m	permanent magnet width
w_t	stator tooth width
w_{meq}	equivalent PM width
w_{meff_i}	effective width of the i -th PM
w_{rpi}	thickness of the i -th rotor island

Greek symbols

α_p	ratio between the pole arc and the pole pitch
α_i^e	electrical angle of the current vector referring to the d -axis
α_{slot}	slot angle
γ_s	angle between the first slot center and the d -axis
$\Delta = e/g$	relative eccentricity
δ	angle between the magnetic field and d -axis
δ_m	angle between the air-gap flux linkage and d -axis
$\delta(\cdot)$	Dirac delta impulse
ξ	saliency ratio
θ	angle between the d -axis and the a -axis
θ_m	refers to the rotor position
θ_r	coordinate angles of the $d - q$ reference frame
θ_s	coordinate angles of the stator reference frame
$2\theta_{b1,2,3}$	end angle of the first, second, and third flux-barrier, respectively
λ_m	air-gap flux-linkage
λ_r	relative permeance function
λ_s	stator flux linkage
λ_{md}	the d -axis component of the air-gap flux-linkage
λ_{mq}	the q -axis component of the air-gap flux-linkage
λ_{sd}	the d -axis component of the stator flux-linkage
λ_{sq}	the q -axis component of the stator flux-linkage
$\lambda_{s\sigma}$	leakage flux of the stator
$\lambda_{s\sigma d}$	the d -axis component of the leakage flux
$\lambda_{s\sigma q}$	the q -axis component of the leakage flux
μ_o	vacuum magnetic permeance
μ_r	relative magnetic permeance
ν	mechanical space harmonic order

ν^e	electrical space harmonic order
τ_m	analytical electromagnetic torque
ϕ	angle between the stator voltage and current space vectors
$\phi_{b_{1,2,3}}$	flux flowing through the first, second, and third flux-barrier, respectively
ϕ_{g_i}	flux flowing through the air-gap in front to the i -th flux-barrier
ϕ_{m_i}	flux of the i -th PM
ϕ_{t_i}	flux flowing through the i -th stator tooth
ϕ_{in_i}	flux enters the i -th rotor island
ϕ_{out_i}	flux leaves the i -th rotor island
$\phi_{f.b_i}$	flux crossing the i -th flux-barrier
ω_B	base angular speed of the motor
$\omega_{B'}$	maximum angular speed of the Field weakening operating condition (region II)
ω_m	mechanical angular speed of the motor
ω_{me}	electrical angular speed of the motor